

REPORT

SEISMIC CONFIRMATORY
PROGRAM
**Virgil C. Summer
Nuclear Station
Unit 1**

OL NO. NPF-12



SOUTH CAROLINA ELECTRIC & GAS COMPANY

8302100224 830201
PDR ABOCK 05000395
P PDR

FEBRUARY -1983

SEISMIC CONFIRMATORY PROGRAM

Virgil C. Summer Nuclear Station

Unit 1

OL No. NPF-12

SOUTH CAROLINA ELECTRIC & GAS COMPANY

February 1983

TABLE OF CONTENTS

<u>ITEM</u>		<u>PAGE</u>
I.	INTRODUCTION	1
II.	APPLICABILITY OF EXPLOSION TESTS TO EARTHQUAKES	3
III.	ACCELEROGRAPH PAD EFFECTS.	6
IV.	FOUNDATION EFFECTS	8
V.	CONCLUSIONS.	12

FIGURES

APPENDIX A: SOIL-STRUCTURE INTERACTION AND ITS INFLUENCE
ON EARTHQUAKE MOTIONS RECORDED AT THE
JENKINSVILLE, S.C. ACCELEROGRAPH STATION
(Ertec Western, Inc.)

APPENDIX B: EXPERIMENTAL INVESTIGATION OF RELATIVE RESPONSE
OF ACCELEROGRAPH PAD, FREE FIELD AND STRUCTURAL
FOUNDATIONS AT THE VIRGIL C. SUMNER NUCLEAR
STATION (URS/John A. Blume & Associates, Engineers)

SEISMIC CONFIRMATORY PROGRAM

I. INTRODUCTION

In its Partial Initial Decision (PID) dated 20 July 1982 (Docket No. 50-395 OL) in the matter of South Carolina Electric and Gas Co. et al. (Virgil C. Summer Nuclear Station, Unit 1), the Atomic Safety and Licensing Board (ASLB) required two licensing conditions to be met by the Applicants. The first is a requirement to continue seismic monitoring. The second condition involves a confirmatory program on plant equipment and components, to ensure seismic safety during shallow reservoir-induced earthquakes.

Additionally, as a result of Advisory Committee on Reactor Safeguards (ACRS) meetings held in early 1981, there is also a commitment of the Licensees (contained in a letter from T.C. Nichols to H.R. Denton, dated 4/15/81) to continue seismic margin analysis for equipment and components necessary for continued heat removal. At the time of the ACRS commitment, the response spectrum of concern was the $M_L^{4.5}$ response spectrum proposed by the Licensees for the Monticello Reservoir-induced seismicity (RIS). This spectrum applies to normal depth RIS.

The procedures and conclusions described herein constitute results obtained during the experimental stage of the Licensees' program to satisfy the ASLB licensing condition. This program is described in the document entitled "Seismic Confirmatory Program for Equipment and Components, Virgil C. Summer Nuclear Station," dated September 24, 1982.

The first set of results (Section III) are quantitative estimates of the amplification effects of the concrete pad at the Monticello Dam abutment on the accelerograph records of earthquake motion at that site. These estimates were made using two independent methods, both of which confirm the opinions of expert witnesses expressed during ASLB hearings in 1982.

The second set of results documents the reduction in motion at the lower foundation levels of plant structures caused by the composite influence of embedment, wave scattering, foundation size and rigidity, rock-foundation interaction, and other effects on the incident waves. These effects were evaluated by conducting explosion tests and recording the resulting motions in the nuclear plant structures and on the soil surface in the free field. Section II discusses the applicability of this type of active field experiment to demonstrate the reductions to be expected during actual earthquakes. The results, in terms of response spectra at the basement level of structures, are presented in Section IV for the Auxiliary Building, Service Water Pumphouse, and Diesel Generator Sump.

Finally, conclusions resulting from this program are discussed in Section V. These are, generally, that the ACRS commitment to analyze equipment for the effects of a M_L 4.5 earthquake at normal depth is more stringent than the envelope spectrum referenced by the ASLB licensing condition after reduction as demonstrated by this program. Two appendices to this report describe details of the field work, data analysis, and interpretation conducted by Ertec Western, Inc. (Appendix A) and URS/John A. Blume & Associates, Engineers (Appendix B), upon which these conclusions are based.

II. APPLICABILITY OF EXPLOSION TESTS TO EARTHQUAKES

Five series of explosion tests were conducted to establish the nature of vibratory motion at the floor level of various structures comprising the Virgil C. Summer Nuclear Station (VCSNS), compared to ground motion at nearby free-field locations. Two of the test series (Tests 4 and 5) were designed also to compare signal levels on the USGS accelerograph pad with those at nearby free-field locations on the dam abutment. Test 5 explosions were located at or very near the hypocenter of the 16 October 1979 earthquake so that source-to-receiver propagation effects would be similar. Test 2 and Test 5 explosions were also recorded on the foundation of the Fairfield Pumped Storage Facility (hydroplant). Tests 3 and 4 provided data from different azimuths but at almost the same distance (approximately 4000 ft) to the receivers in the VCSNS structures and various free-field locations. Test 1, conducted in 1981, provided foundation and free-field data from another azimuth and from a greater distance (approximately 14,000 ft).

There are several reasons why these explosion test results are applicable to shallow RIS events in the vicinity of the VCSNS. First, the RIS events are all very shallow so that the paths of propagation from source to receiver are approximately the same as for explosions detonated in the granite bedrock; all of the explosions were detonated well into the granite bedrock except for a few of the Test 5 shots.

Second, all wave types show similar foundation to free-field reductions, implying that earthquake motions would be similarly reduced. All available recordings of earthquakes and explosions in the Monticello Reservoir area are characterized by two large amplitude segments. Based on travel-time observations and other signal characteristics, the first segment is comprised of energy that has traveled from source to receiver primarily as P waves and the second is comprised of energy that has propagated as S+higher-mode surface waves. Therefore, while the energy partitioning between P waves and S+higher-mode waves generated by the source is expected to be different for earthquakes compared with explosions (earthquakes generating proportionally more shear

energy than explosions), the observed reduction factors from foundation to free field should be the same for both earthquakes and explosions. The same is true for the accelerograph pad to free-field amplification factors. Because of the strong effects of the heterogeneous structure on detailed features of the signals, it was not possible to isolate specific wavelets and compare them individually among receivers; indeed, the detailed wave shapes exhibit a very high temporal and spatial variability, manifested by chaotic particle motions and poor phase coherence between nearby receivers, whereas the overall signal levels behave systematically from receiver to receiver as discussed above.

Third, the consistency of spectral reductions observed both for P waves and S+higher-mode waves for different foundation receiver-to-source azimuths (200°; 240°; 30°) and distances (3700 ft; 4300 ft; 14,000 ft) indicates that neither direction of arrival nor angle of incidence is important. That is, the spectral reductions are approximately the same regardless of the direction of arrival or angle of incidence of the input signals. Therefore, the explosion test results are appropriate for shallow RIS events located anywhere in the vicinity of the VCSNS.

Fourth, the question of possible large differences in fundamental mode excitation by earthquakes and explosions at different depths where there is a shallow saprolite layer is not relevant because fundamental mode waves in the frequency band 10 to 40 Hz have been observed in only one instance, specifically where the saprolite layer was continuous from source to receiver. In that case, the group velocity was approximately 0.2 km/sec compared with a minimum observed group velocity of about 2 km/sec for the S+higher-mode window that consistently contains most of the signal energy. There are extreme variations in the thickness of the saprolite layer in the vicinity of the VCSNS, effectively eliminating it as a waveguide. For example, the saprolite layer is totally absent in the hydroplant - tailrace portion of the propagation path to the accelerograph pad from the Test 5 shots and the 1979 earthquake source. Fundamental mode waves generated in the immediate vicinity of a

receiver by the incident P wave or S+higher-mode wave fields would be generated by both source types, and corresponding foundation to free-field reductions would apply to both.

Finally, the smaller motions observed in the hydroplant foundation, compared with the accelerograph pad and nearby free-field locations for Test 5 explosions, are consistent with the observation that the 16 October 1979 RIS event that caused a 0.36g peak acceleration on the USGS pad did not cause any damage to structures or equipment in the hydroplant.

Therefore, these explosion tests provide an appropriate quantitative basis to establish adjusted response spectra for VCSNS structures.

III. ACCELEROGRAPH PAD EFFECTS

The dynamic interaction between the concrete pad at Monticello Dam abutment and the saprolite on which it rests was suspected to contribute to the high peak ground accelerations recorded on the pad by the USGS SMA-1 accelerograph during small reservoir-induced earthquakes. To investigate and quantify any potential effect, several methods are available. The two most direct and timely methods are forced vibration tests (with mathematical modeling of dynamic response) and explosion tests (with instrument recording of ground motion on the pad and adjacent to it in the free field). Both of these methods were used, and both indicated that the pad-soil system increases the recorded ground motions compared with motions in the free field (without any pad-soil interaction). The fact that both of these independent methods indicate a pad amplification demonstrates that this effect is real.

The forced-vibration tests are described in detail in Appendix A. Briefly, the natural frequencies, modal dampings, and mode shapes of the soil-pad system were derived by recording responses of the pad to continuous forced vibrations at controlled frequencies. These modal parameters were then used to construct a mathematical model of the dynamic system. The motions recorded on the pad during the 1978 and 1979 earthquakes were input to the structural model to determine the equivalent motion in the free field (i.e., without any soil-pad effects). The average ratio (over all horizontal components of these records) of free-field/pad motion, in terms of 5 percent damped spectral velocity, is shown in Figure 1. It varies as a function of frequency, but indicates substantial reductions in motion (from 5 to 30 percent) at frequencies above 20 Hz.

Details of the explosion tests are described in Appendix B. The pad and several surrounding free-field sites were instrumented, and motions during a series of explosions were recorded. Response spectra of these motions were computed to compare free-field and pad motion. Figure 2 gives a summary of the ratio of free-field to pad response spectral amplitudes. While differing in detail from the forced vibration test results, the explosion test

results indicate substantially the same overall effect, i.e., motions in the free field are smaller than those on the pad by approximately 20 to 30 percent for frequencies above 20 Hz.

Based on these two independent tests, it is appropriate to reduce earthquake motions recorded on the dam abutment pad to represent free-field motions. The reductions indicated by each test are used in conjunction with the nuclear plant structure test results to indicate overall reductions in the recorded ground motions, as discussed in Section IV.

These pad amplification effects apparently are not unique to the Monticello Reservoir site. At the Fall 1982 American Geophysical Union, a paper was presented* that indicated the peak acceleration recorded near Enola, Arkansas by an SMA instrument on a concrete pad was significantly larger than observed on a nearby free-field recording of the same near-field earthquake. It is our understanding that the USGS is carrying out further analysis of these data, but that this amplification appears to be a real effect (Fletcher, 1982; personal communication).

* Haar, L.C., J.B. Fletcher, and E. Semberra; A Preliminary Analysis of Digital Seismograms from the Arkansas Earthquake Swarm of 1982; EOS, Vol. 63, No. 45, p. 1024, November, 1982

IV. FOUNDATION EFFECTS

To determine the composite influence of foundation size and rigidity, wave scattering, embedment, foundation-rock interaction, and other effects, blast motions were recorded simultaneously in nuclear plant structures and free-field sites.

These field experiments were designed to establish experimentally the difference between foundation and free-field motions, including the possible range in effects due to differences in source location, travel path, and free-field site conditions. The details of these experiments are given in Appendix B.

As a general result, foundation motions were found to be significantly less than those in the free field at the same source-receiver distance. This applies for all tests (including the 1981 experiments) and for all structures.

It is important to note that foundation reductions should be applied after the effect of the accelerograph pad-soil system has been taken into account. The reductions for various types of foundations have been computed by comparison to free-field motions. These reductions apply in addition to reductions of motions recorded on the accelerograph pad discussed in the previous section.

A further point is that the motions recorded during these experiments are used to compute reduced earthquake motions for structures and to assess effects of these motions on equipment. Response spectra for these reduced earthquake motions represent spectra at the basement levels of structures; they must be compared with floor spectra at the appropriate elevation to make preliminary determinations of the adequacy of equipment qualification. At the basement elevation of structures, the floor spectrum is in general higher than the ground input motion spectrum because foundation springs were used in the original structural analysis to model the interaction of the structure and the rock on which it is founded.

Results for Auxiliary Building

Motions in the Auxiliary Building are representative of motions in the Reactor and Control Building, which are also founded on rock. The Auxiliary Building motions are also representative of motions to be expected in the Intermediate Building, which is founded on caissons but which is tied on its west side to the Control Building at the foundation level, and is laterally stiffened on its east side by a structural shear wall anchored to rock.

Figures 3 and 4 show reduced envelope response spectra for the two horizontal components of the 1979 earthquake accelerograph record obtained at the dam abutment. In Figure 3, the forced-vibration transfer function has been used to quantify the accelerograph pad-soil effect, and the reduction for plant structures has been applied, so the spectra shown represent an Auxiliary Building basement motion equivalent to that recorded on the USGS accelerograph pad in 1979. Figure 4 is similar except that the explosion test data were used to correct for the accelerograph pad effect. These two figures show the range of results obtained for different components of motion and different analysis techniques. Also shown on the figures are the original envelope spectrum, the SSE spectrum for rock structures anchored at 0.15 g, the reservoir-induced seismicity (RIS) spectrum anchored at 0.22 g, and the Auxiliary Building floor spectrum for the basement level.

Except for a small frequency range, the reduced 1979 spectra fall below the RIS spectrum so that the latter provides a more stringent input. Therefore, it is concluded that the analyses to be performed under the Advisory Committee on Reactor Safeguards (ACRS) commitment to review equipment will govern the acceptability (or unacceptability) of current qualification data.

Conclusions about the acceptability of equipment qualification can be made by comparison of equipment qualification spectra to floor spectra and evaluation of available margins.

Results for Service Water Pumphouse

Reduced 1979 spectra are shown in Figures 5 and 6 for the Service Water Pumphouse. Again, these spectra show the range of results from different methods of determining the accelerograph pad-soil effect, and for the two components of the 1979 earthquake record. In this case, these adjusted spectra are compared to the RIS spectrum (which is anchored to 0.22g). The adjusted 1979 spectra fall below the RIS spectrum so that equipment in this structure can be considered under the qualification program for the ACRS commitment.

Results for Diesel Generator Building

Explosion test data were recorded on the sump floor of the Diesel Generator Building. The sump is a structural appendage (approximately 12 ft by 65 ft in plan dimensions) situated below the main building. The structure itself is founded on caissons which extend through saprolite to bedrock. Because of the instrument location (in the long, narrow sump), the motions recorded may overestimate the motions expected on the main floor of the Diesel Generator Building. These motions apply to the Diesel Generator Building and to the Fuel Handling Building, which is also founded on caissons.

Figures 7 and 8 show the reduced 1979 spectra, compared to the SSE spectrum, the RIS spectrum, and the envelope spectrum. In this case there is a small frequency range in which the reduced spectra exceed the RIS spectrum, but this exceedance is not large, so that few pieces of equipment are likely to be affected. Therefore, the evaluation of equipment in this structure can most logically and efficiently be accomplished during the program for the ACRS commitment.

V. CONCLUSIONS

The experiments and analyses conducted for this program have indicated that the envelope spectrum obtained from accelerograms recorded on the USGS accelerometer pad at the Monticello dam abutment is inappropriate to represent ground motion in the nuclear plant structures. The effect of the pad-soil system has been to amplify motions over what would be obtained in the free field. Moreover, the nuclear plant structures reduce motions further because of the composite influence of embedment, foundation size and rigidity, wave scattering, rock-foundation interaction, and other effects which cannot individually be quantified. The total reduction has been well-documented and quantified by the work reported herein.

For structures founded on rock, the ACRS commitment to review equipment for a magnitude M_L 4.5 earthquake will cover the review necessary to satisfy the ASLB licensing condition (the ACRS criterion implies higher levels of ground motion at virtually all frequencies than the reduced envelope spectra and is therefore more conservative). This is also the case for structures founded on soil (the Service Water Pumphouse). For structures founded on caissons, the reduced spectra exceed the RIS spectra only in a small frequency range. For the small amount of equipment involved in the Diesel Generator Building and the Fuel Handling Building the determination of effects on equipment can logically be made during the review of equipment for the Advisory Committee on Reactor Safeguards (ACRS) commitment.

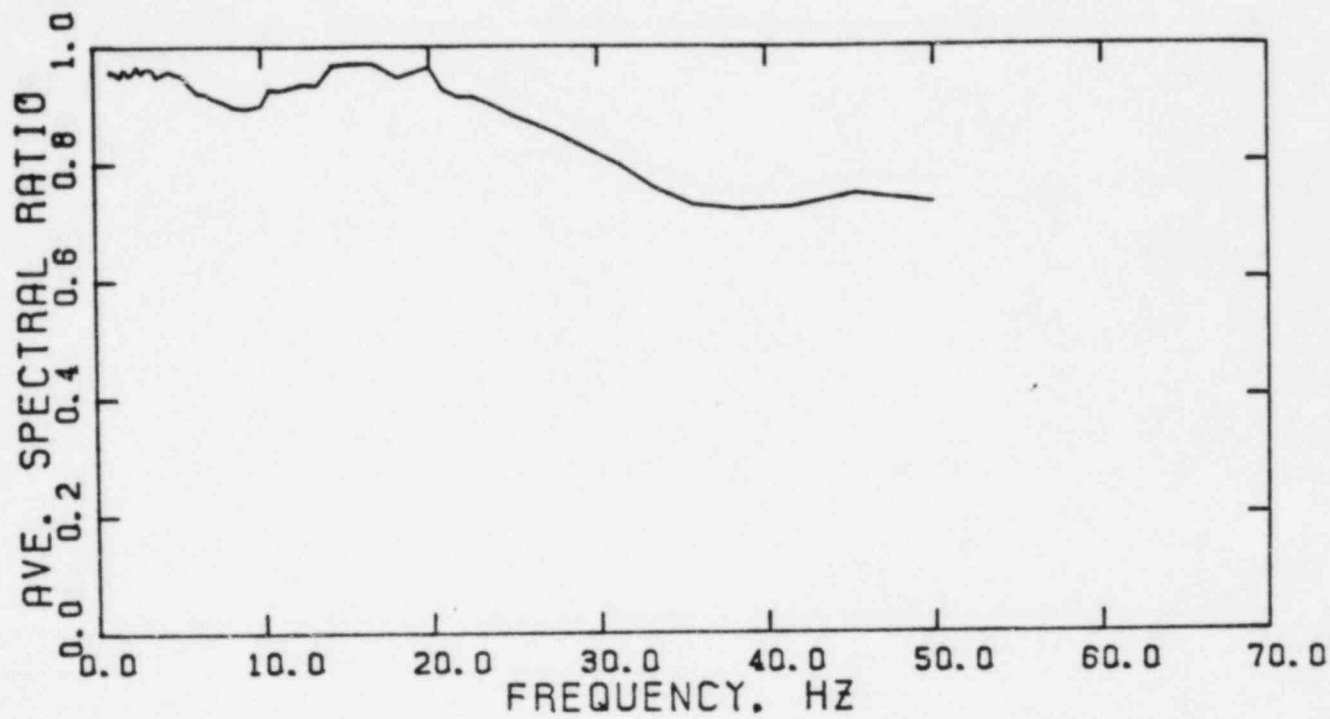
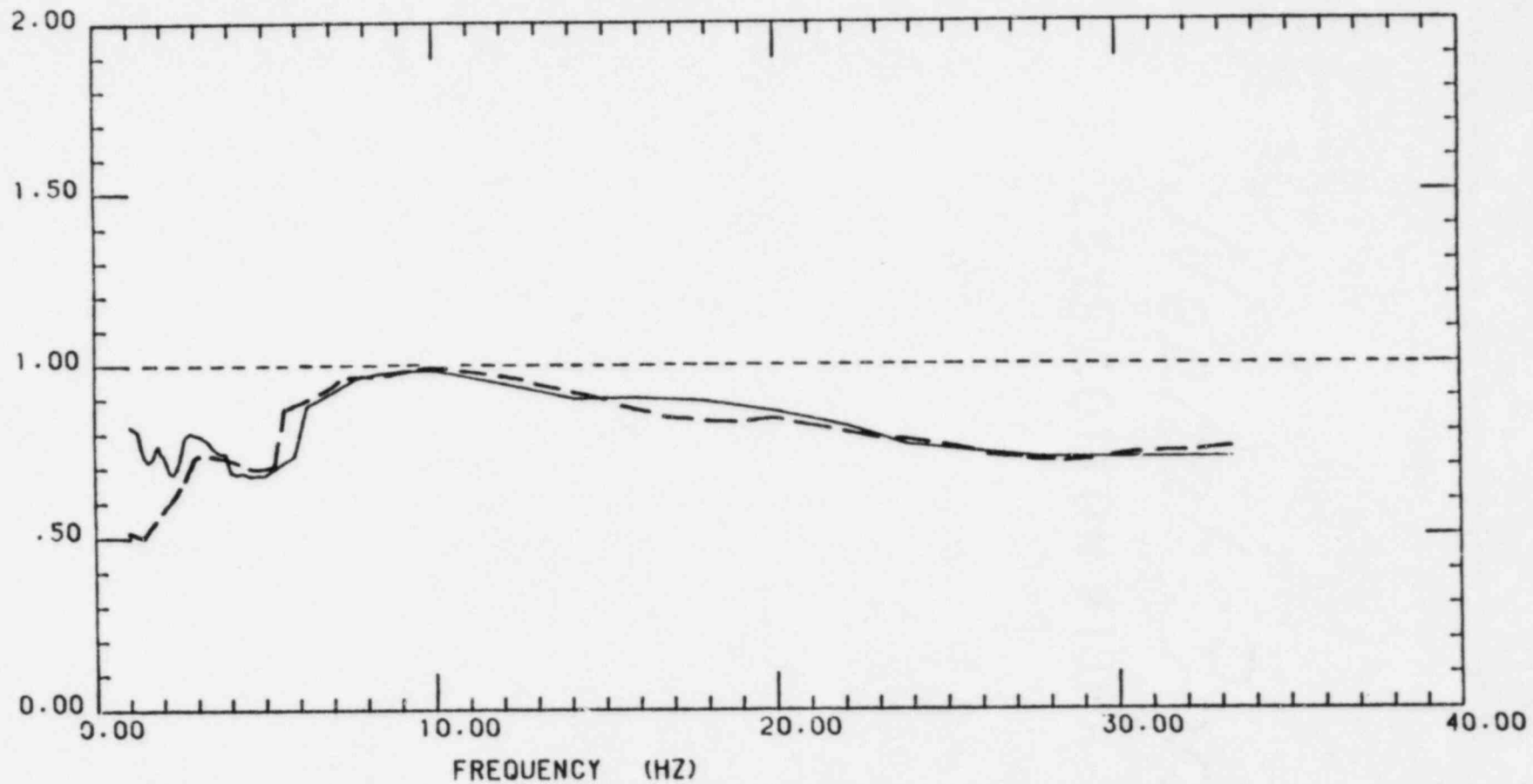


Figure 1: Ratio of free field to pad spectral velocity (5% damping) versus frequency, from forced vibration tests.



————— 180° Component of 1979 record
 - - - - - 90° Component of 1979 record

Figure 2: Ratio of free field to pad spectral velocity (5% damping) versus frequency, from explosion tests.

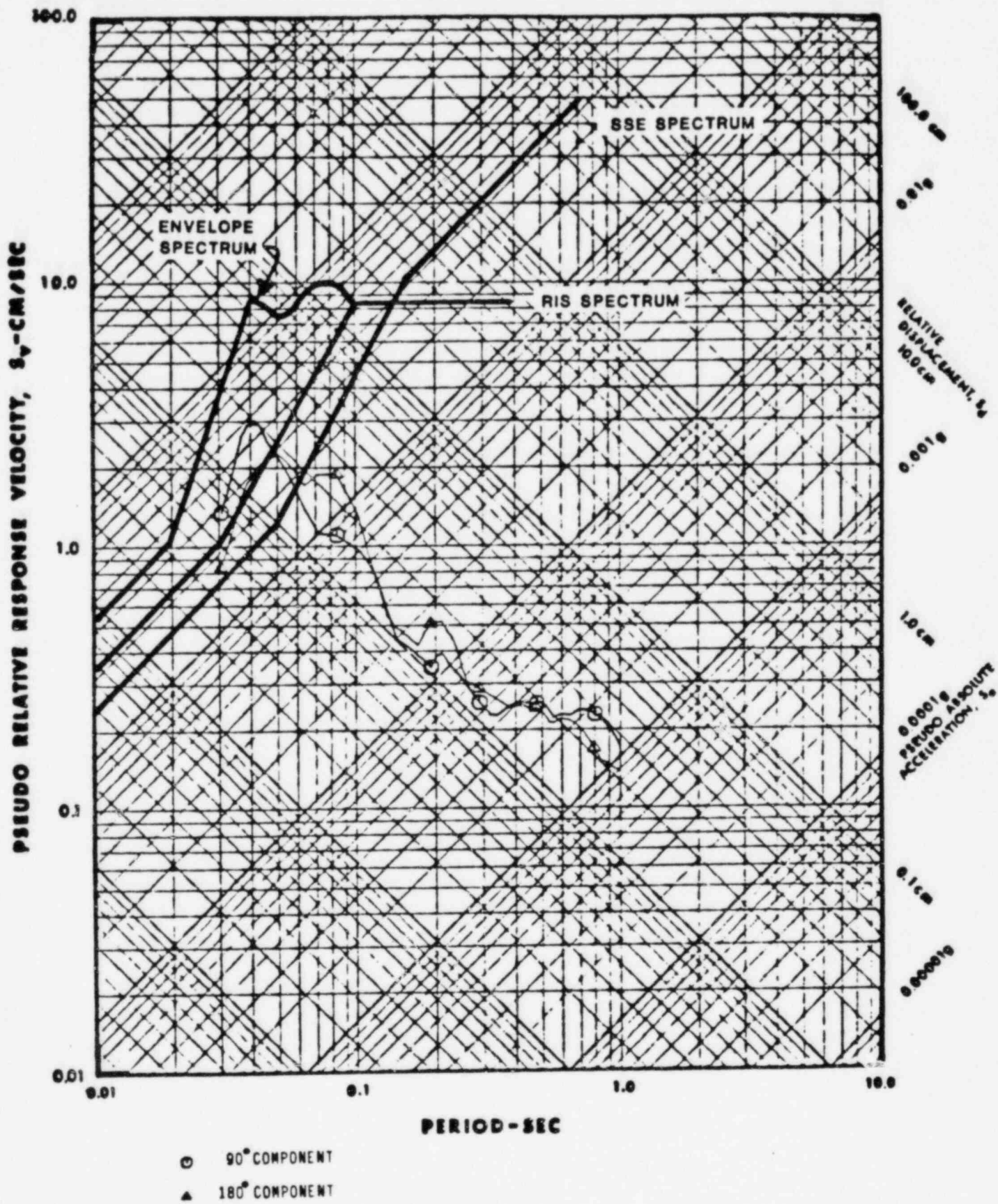


Figure 3: Reduced Auxiliary Building spectra (5% damping) for 1979 record (from forced vibration pad results and explosion foundation results) compared to envelope, RIS, and SSE spectra,

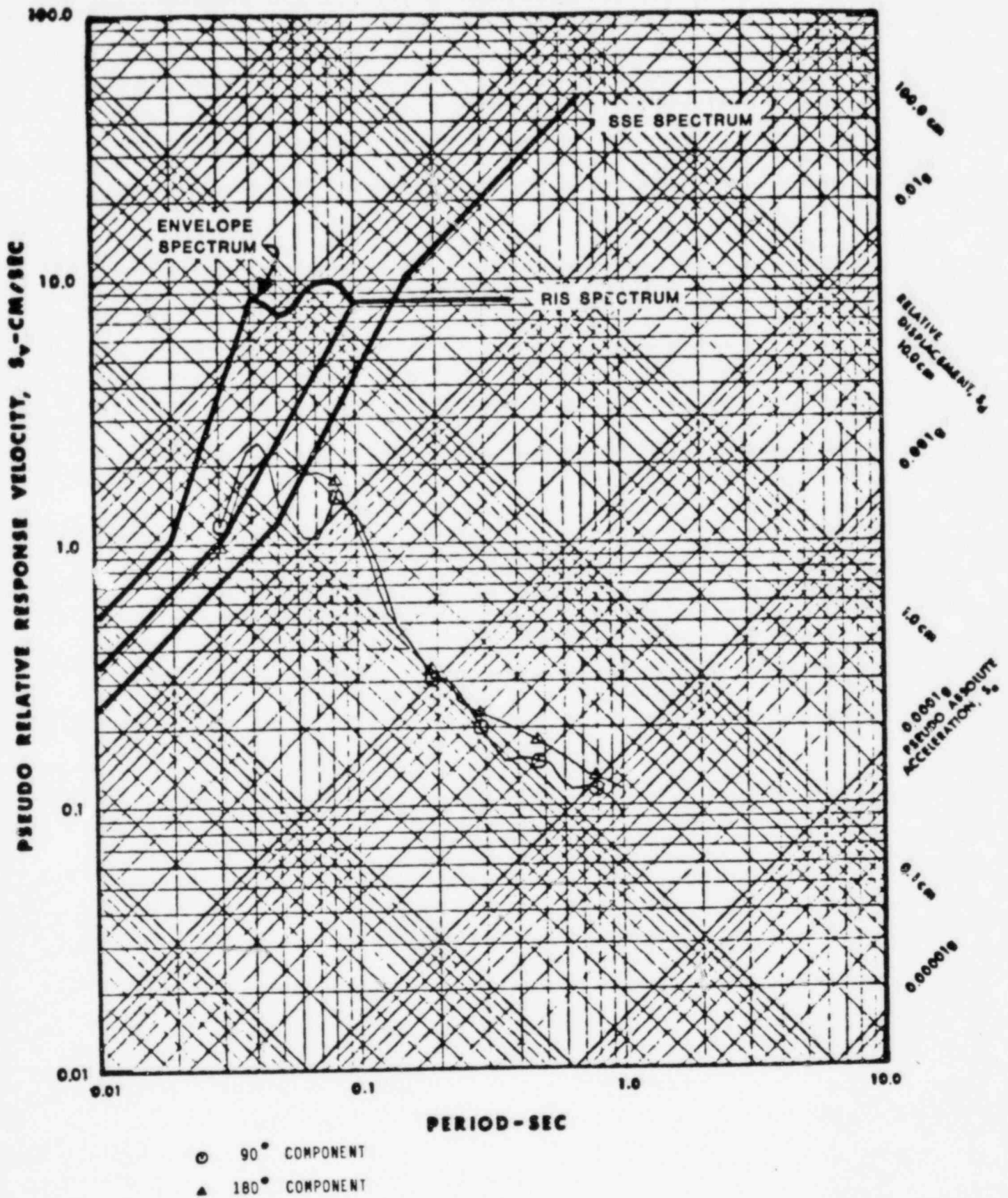


Figure 4: Reduced Auxiliary Building spectra, (5% damping) for 1979 record (from explosion pad and foundation results) compared to envelope, RIS, and SSE spectra.

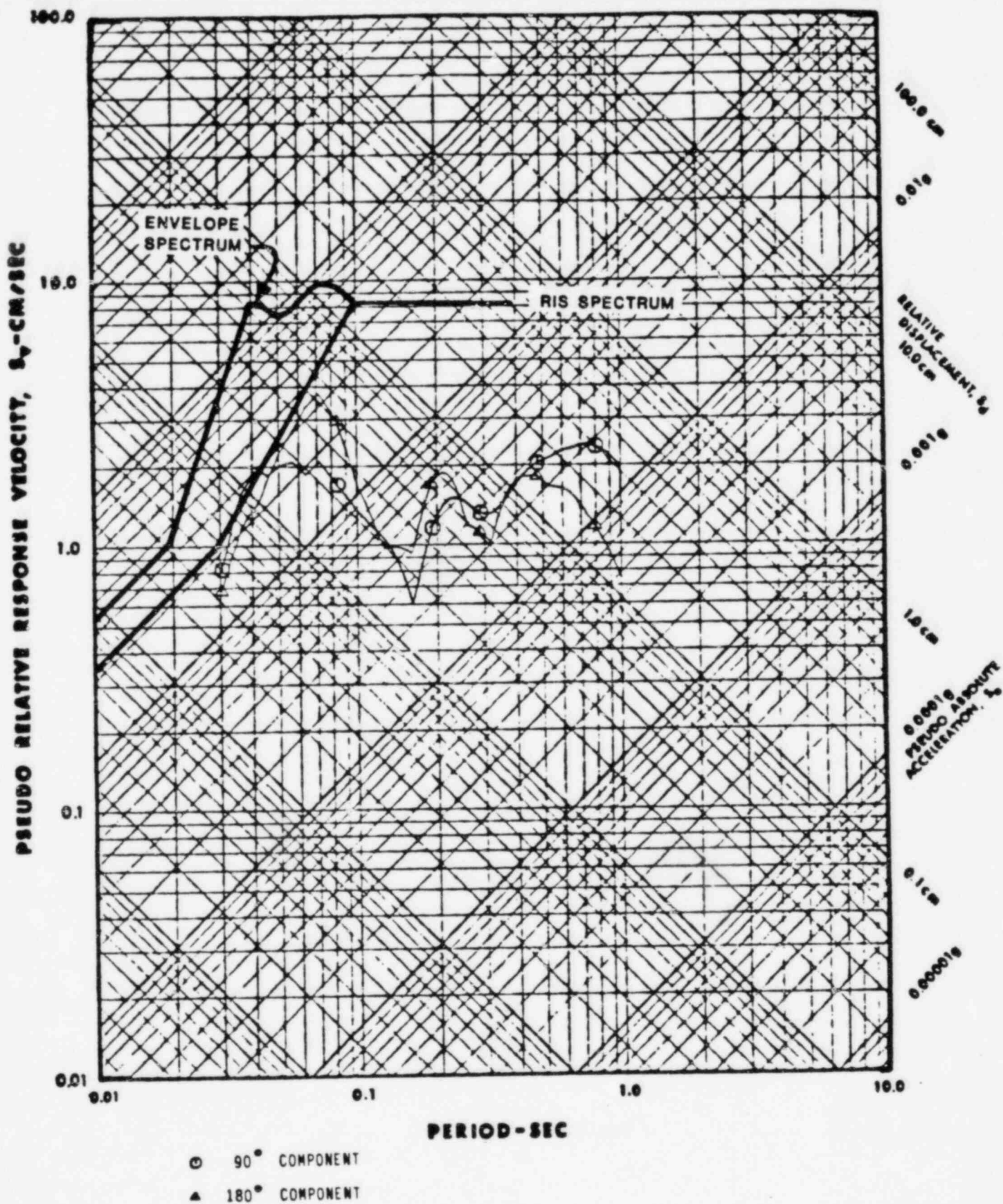


Figure 5: Reduced Service Water Pumphouse spectra (5% damping) for 1979 record (from forced vibration pad results and explosion foundation results) compared to envelope, and RIS spectra.

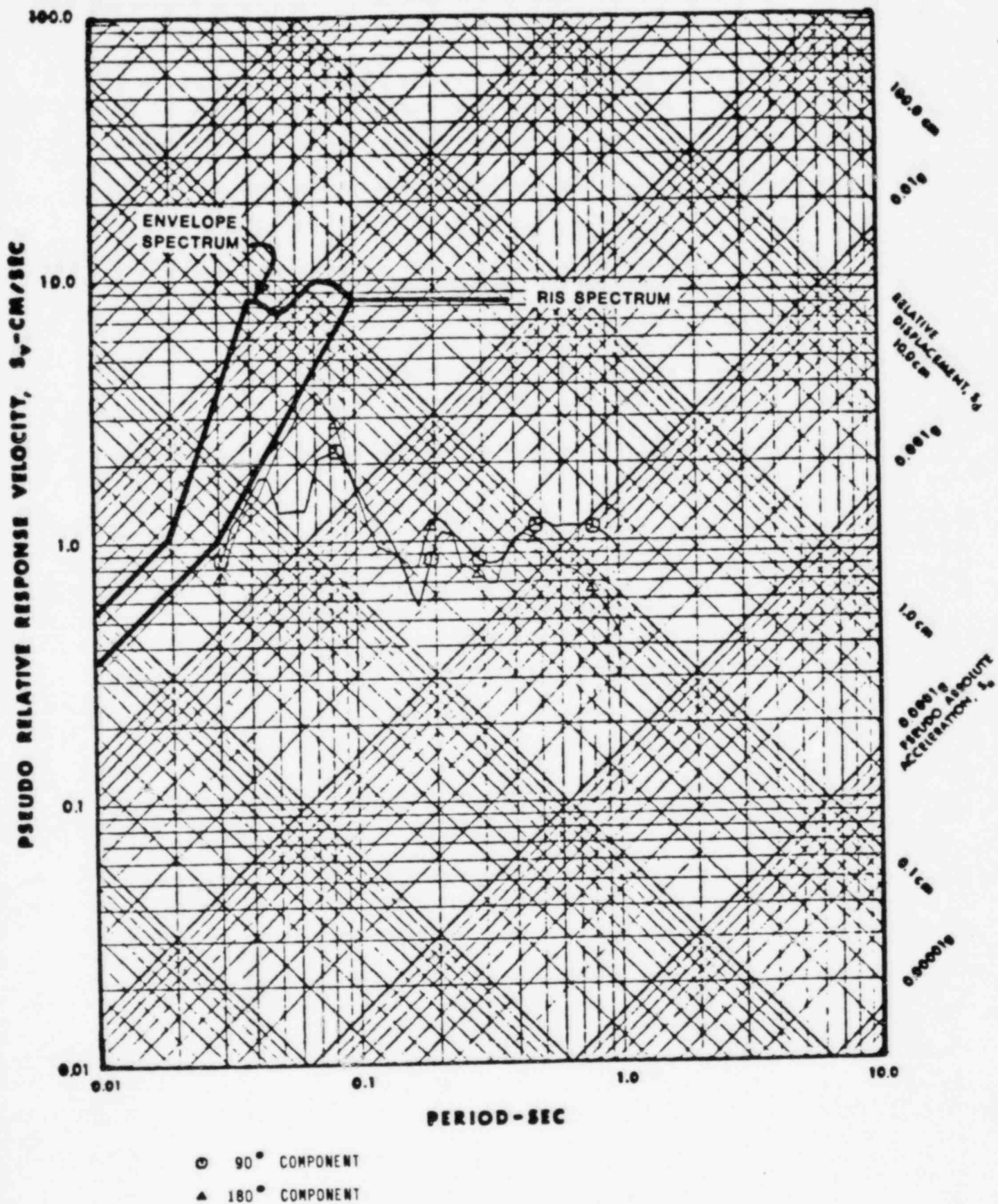


Figure 6: Reduced Service Water Pumphouse spectra (5% damping) for 1979 record (from explosion pad and foundation results) compared to envelope and RIS spectra.

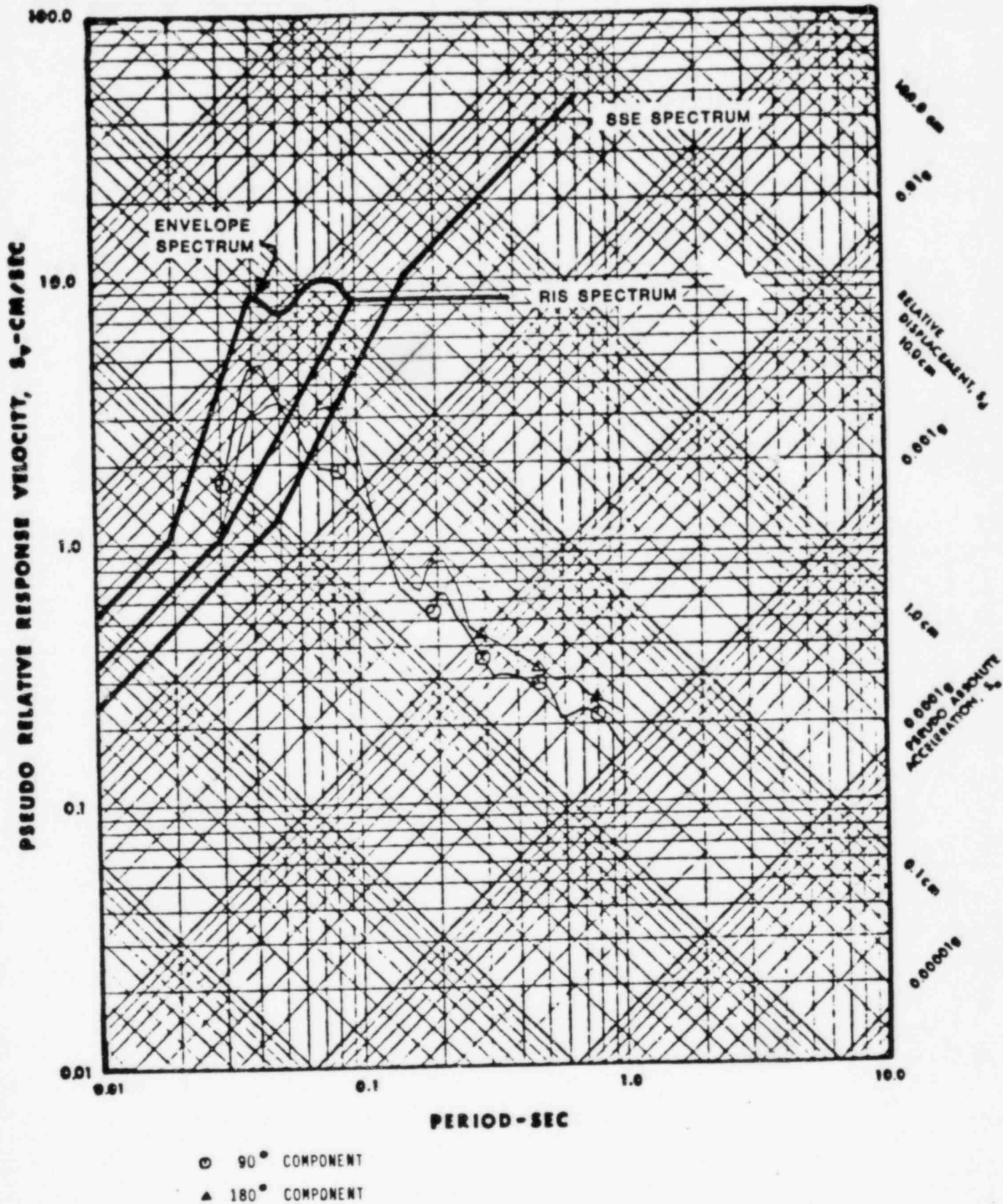


Figure 7: Reduced Diesel Generator Sump spectra (5% damping) for 1979 record (from forced vibration pad results and explosion foundation results) compared to envelope, RIS and SSE spectra.

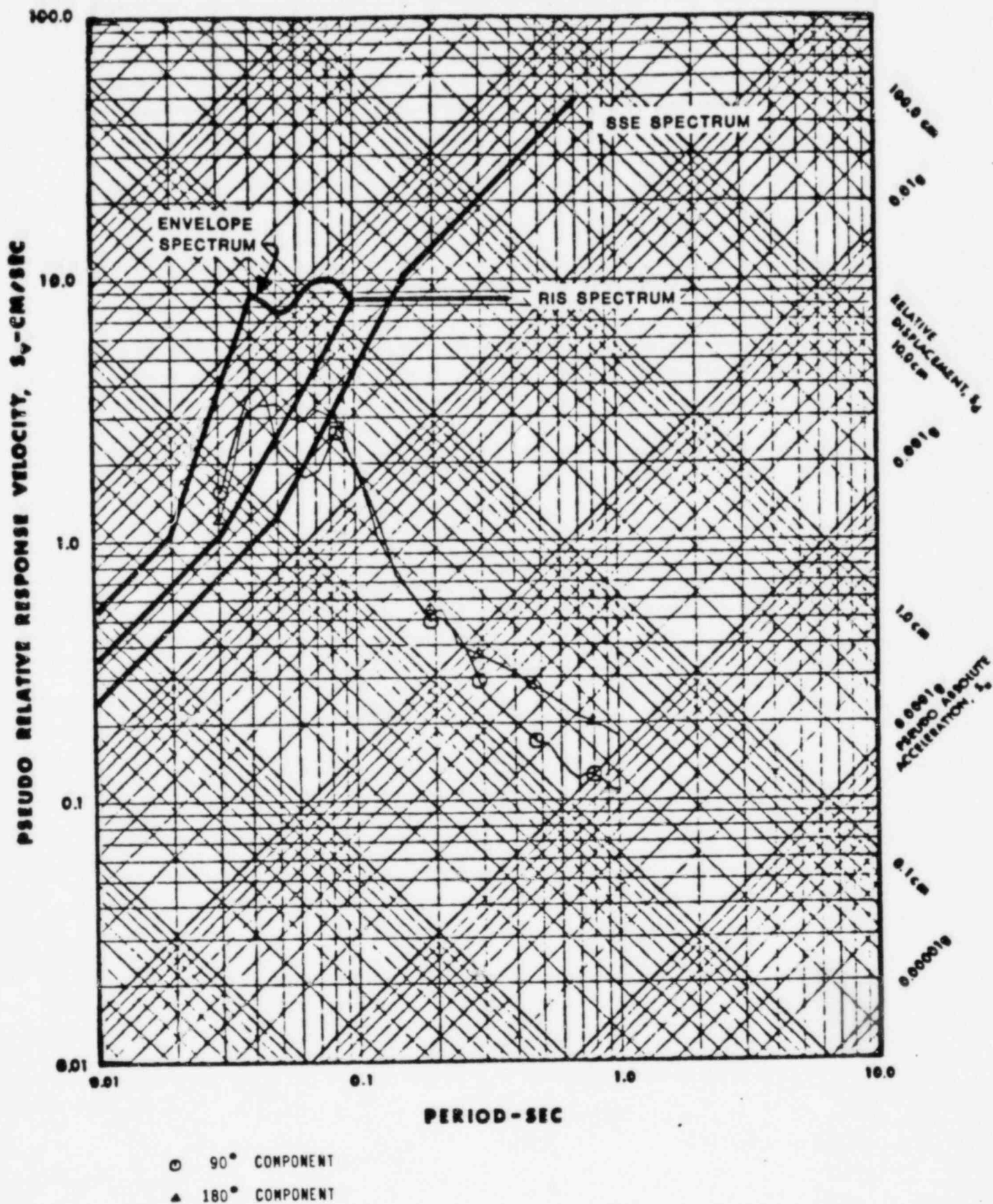


Figure 8: Reduced Diesel Generator Sump spectra (5% damping) for 1979 record (from explosion pad and foundation results) compared to envelope, RIS, and SSE spectra.

SOIL-STRUCTURE INTERACTION
AND ITS INFLUENCE ON
EARTHQUAKE MOTIONS RECORDED
AT THE JENKINSVILLE, S.C.
ACCELEROGRAPH STATION

Submitted to:

South Carolina Electric and Gas Company
P.O. Box 764
Columbia, S.C. 29218

Submitted by:

Ertec, Inc.
3777 Long Beach Boulevard
Long Beach, CA 90807

February, 1983

83-164

TABLE OF CONTENTS

	<u>Page</u>
1.0 SUMMARY	1
2.0 INTRODUCTION	3
3.0 SOIL-STRUCTURE INTERACTION MODELS	6
3.1 Equations of Motion for Earthquake Response	6
3.2 Solution of Equations of Motion	9
3.3 Derivation of Free-Field Motion	10
4.0 FORCED VIBRATION TESTS	12
4.1 Field Testing Program	12
4.2 Response Data from Vibration Tests	14
5.0 DATA ANALYSIS	15
5.1 Reduction of Data from Forced Vibration Tests	15
5.2 Determination of Stiffness Matrix	17
5.3 Determination of of Modal Parameters	22
6.0 CALCULATION OF FREE-FIELD MOTIONS	24
7.0 REFERENCES	26

1.0 SUMMARY

Forced vibration tests, using small eccentric mass shakers, were conducted at the Jenkinsville, S.C. accelerograph station to determine the effect soil-structure interaction had on the motions recorded at the station during 4 small reservoir-induced earthquakes. The tests and subsequent analysis clearly indicated that soil-structure interaction amplified the 5 percent damped response spectra of the recorded horizontal motions by an average of about 20 percent in the frequency range 20 to 50 Hz. No significant amplification was noted in the vertical direction.

The Jenkinsville accelerograph station consists of a 4 ft x 4 ft x 2 ft concrete pad partially embedded in the soil and a 5-ft-high wooden hut, which is attached to the pad. The Kinematics SMA-1 accelerograph, mounted on the pad, recorded the earthquakes' motions. In the frequency range from 5 to 60 Hz the vibration tests revealed that the soil-pad-hut system had 2 natural frequencies in each horizontal direction. No natural frequency was identified in the vertical direction. The natural frequencies and the associated modal dampings were:

Direction	1st Mode		2nd Mode	
	f_1 - Hz	ζ_1 - %	f_2 - Hz	ζ_2 - %
x (N50°E)	16.7	4.0	49.8	20
y (N40°W)	10.6	6.0	47.9	21

Both modes exhibited strongly coupled translational and rocking response. The first mode involved mostly the response of the hut while the second mode involved a greater response of the pad.

Based on the results of the vibration tests, linear lumped parameter soil-structure models of the soil-pad-hut system were constructed. The equations of motion for the models were solved for the unknown free-field motions in terms of the earthquake motions recorded by the SMA-1 and the dynamic properties of the soil-pad-hut system. The flow chart presented in Figure 1 shows the chronological steps of the investigation, beginning with the field experiment and ending with the computation of the free-field response spectra.

The computed free-field accelerograms had smaller amplitudes than the corresponding SMA-1 accelerograms. On the average the response spectra of the horizontal free-field accelerograms were: 5 percent less than the SMA-1 response spectra in the frequency range from 1 to 20 Hz; between 5 and 27 percent less in the frequency range from 20 to 36 Hz; and 27 percent less from 36 to 50 Hz. The differences between the vertical free-field and SMA-1 response spectra were negligible.

The differences between the horizontal free-field and SMA-1 response spectra demonstrate that a reduction in the envelope spectrum developed by the NRC for the Monticello accelerograms (NRC, 1982) is appropriate. The recommended reduced spectrum, shown in Figure 20, is based on the average reduction obtained from the results of the soil-pad-hut interaction analysis displayed in Figure 19.

2.0 INTRODUCTION

The Jenkinsville accelerograph station, located near Monticello dam at the Virgil C. Summer nuclear site, recorded motions from 3 small earthquakes on 27 August 1978 and another small shock on 16 October 1979. Although the earthquakes caused no damage, they produced large peak accelerations at the accelerograph station. These accelerations were recorded by a Kinematics SMA-1 accelerograph, which was bolted to a concrete pad (4 ft x 4 ft x 2 ft) that was partially embedded in the ground. A 5-ft-high wooden hut was attached to the slab to provide a shelter for the SMA-1.

There was some question whether these high peak accelerations were truly representative of free-field ground motions or whether they had been influenced by the interaction between the concrete pad and the ground. To obtain an indication of whether the motions were influenced by interaction, the firm of Stoll, Evans, Woods and Associates conducted plucking tests on the concrete pad in January, 1982. The purpose of the tests was to determine the natural frequencies and dampings of the soil-pad-hut system. Their results showed coupled rocking and translational motion in both N50E and N40W horizontal directions. Whereas, there was some uncertainty in distinguishing between rocking and translational modes, it was judged that the predominantly rocking modes had natural frequencies of 18 to 20 Hz and 12 Hz in the N50E and N40W directions, respectively. The predominantly translational mode had similar natural frequencies between 40 and 50 Hz in each direction.

These results suggested that soil-structure interaction may have significantly influenced the earthquake motions recorded by the SMA-1 accelerograph. This conclusion was based on the observation that the natural frequencies measured during the plucking tests were in the frequency range where significant energy is contained in the SMA-1 accelerograms. However, additional field tests were required to accurately quantify this interaction.

Forced vibration tests, which were considered the most reliable means of quantifying the dynamic properties of the station, were conducted by ANCO

Engineers and Ertec, Inc. in November, 1982. The data collected during these tests were used to construct dynamic soil-structure interaction models of the soil-pad-hut system. These models were then used to deconvolve the SMA-1 accelerograms through transfer functions to generate corresponding free-field, ground-motion accelerograms.

As outlined in the 10 September 1982 proposal from SCE&G to the NRC, the theoretical free-field earthquake motions were to be computed by 2 methods. The first and most direct approach involved: (1) the determination of the stiffness matrix of the equations of motion of the system from the forced vibration data, and (2) the deconvolution in the frequency domain of the accelerograms recorded by the SMA-1 instrument through the transfer functions for the soil-structure models. The inverse Fourier Transform gives the free-field motions in the time domain. The second approach involved the straightforward use of the modal quantities (natural frequencies, dampings, mode shapes, and participation factors) in the modal equations of motion of the system. The first approach, which was to be the prime analysis tool, had the advantage of preserving all the information at each frequency. The second approach offered simplicity and was to be used to check the first approach. However, during the analysis, it became apparent that the first approach was extremely sensitive to the phases, or the time lags, between the harmonic force applied by the shaker and the accelerations measured on the pad and hut. The computed stiffnesses in some cases had a negative imaginary part, which implied negative damping, and this in turn resulted in extremely small estimates of the free-field motions. This did not seem to be realistic, and so a decision was made to use the second approach, which did not depend on the phase measurements, as the prime analysis tool.

In the second approach the response spectra of the theoretical free-field accelerograms were computed and compared to the response spectra of the recorded SMA-1 motions. The response spectra computation was carried out to 50 Hz for 5 percent critical damping. The ratio of the recorded spectra to the free-field spectra indicated the influence of soil-pad-hut interaction on the recorded earthquake motions.

The remainder of this report is organized as follows. Section 3.0 presents the theoretical formulation of the soil-pad-hut interaction. Section 4.0 describes the forced vibration tests that were conducted on the pad. Section 5.0 presents the methods used to reduce the data from the vibration tests and the methods used to determine the dynamic properties of the soil-pad-hut system. Section 6.0 presents the theoretical free-field motions and compares them to the recorded SMA-1 motions to determine the significance of the interaction.

3.0 SOIL-STRUCTURE INTERACTION MODELS

Preliminary forced vibration tests conducted on the pad indicated that the fundamental mode of vibration in both horizontal directions was heavily influenced by the wooden hut attached to the concrete pad. Therefore, the hut was included in the soil-structure model for the response calculations. The soil-structure model for both the forced vibration experiments and earthquake response analyses is shown in Figure 2 for horizontal translation and rocking.

The model in Figure 2 has 3 degrees of freedom: horizontal translation (v_{ob}) and rocking (ϕ) of the concrete pad, and rotation (θ) of the wooden hut. A rotational spring was considered sufficient to model the connection between the hut and the pad. The base of the hut was separated from the concrete pad by a 5/8-inch-thick foam-rubber pad. During the vibration experiments the hut appeared to rock about the base as evidenced by the compression visible in the front and back ends of the foam rubber.

3.1 Equations of Motion for Earthquake Response

Under the assumption of small displacements and linear response, the equation of motion in the frequency domain for the model shown in Figure 1 is:

$$M \ddot{\bar{v}} + K \bar{v} = \bar{f} \quad (3-1)$$

where the 2 dots above the variable indicate double differentiation with respect to time and the bar over the quantity indicates the Fourier Transform. In Equation (3-1) M and K are the mass and stiffness matrices, respectively; \bar{v} is the transformed displacement vector; and \bar{f} is the transformed force vector. These quantities are:

$$\bar{v} = \{\bar{v}_{ob}, \bar{\phi}, \bar{\theta}\}^T \quad (3-2)$$

$$\underline{\ddot{x}} = -\{(m+m_h)\ddot{v}_{gh}, (mh_o+m_h(2h_o+h_h))\ddot{v}_{gh}, m_h h_h \ddot{v}_{gh}\}^T \quad (3-3)$$

$$M = \begin{bmatrix} m+m_h & mh_o+m_h(2h_o+h_h) & m_h h_h \\ mh_o+m_h(2h_o+h_h) & mh_o^2 + I + m_h(2h_o+h_h)^2 + I_h & m_h h_h(2h_o+h_h) + I_h \\ m_h h_h & m_h h_h(2h_o+h_h) + I_h & m_h h_h^2 + I_h \end{bmatrix} \quad (3-4)$$

$$K = \begin{bmatrix} K_{11} & K_{12} & 0 \\ K_{21} & K_{22} & 0 \\ 0 & 0 & K_{\theta} \end{bmatrix} \quad (3-5)$$

In the above equations: the symbols m and I are the mass and moment of inertia of the concrete pad; m_h and I_h are the mass and moment of inertia of the wooden hut; h_o is the height of the center of gravity (c.g.) of the concrete pad above the soil-pad interface; h_h is the height of the c.g. of the hut above the top of the concrete pad; K_{ij} ($i, j=1, 2$) are the foundation impedance functions; K_{θ} is the rotational stiffness between the hut and concrete pad; and \ddot{v}_{gh} is the horizontal free-field acceleration. The displacement, v_{ob} , is measured with respect to the free-field motion.

The mass matrix, M , is real and symmetric, while the stiffness matrix, K , is complex and symmetric. All elements of the stiffness matrix are frequency dependent and represent the unknowns in the soil-structure models that were to be determined from the forced-vibration experiments. The elements of the mass matrix were determined from measurements made on the pad and hut after the forced vibration experiments were completed. The mass and moment of inertia of both the concrete pad and hut were based on: (1) the dimensions of each structure, (2) the concrete density computed from a standard NX core of the concrete pad, and (3) the wood densities computed from small plywood and 2 by 4 sections cut from the hut.

In deriving Equation (3-1) the pad-foundation forces, P and Q in Figure 2, were expressed in terms of the pad-foundation displacements, v_{ob} and ϕ , through the impedance functions, K_{ij} (Bielak, 1971). In theory, $K_{ij} = K_{ji}$, because the model is linear. This equality was not assumed when deriving the stiffnesses from the data obtained during the forced vibration tests.

One assumption of the soil-structure model shown in Figure 2 is that the theoretical free-field motion, \ddot{v}_{gh} , is the pad-foundation-input motion. In theory the pad-foundation-input motion will generally be different from the free-field motion because of the scattering of the incident seismic waves off the pad-foundation interface (Luco, 1980). However, for the Monticello accelerograph pad this effect was considered to be negligible in the frequency range of interest from 1 to 60 Hz.

Another assumption of the soil-structure models, which was confirmed by the forced vibration experiments, was that torsional motion, arising from any accidental eccentricity between the c.g. of the pad and center of stiffness of the soil, was negligible. Furthermore, torsional input motions resulting from non-vertically incident shear waves are expected to be negligible for frequencies less than 60 Hz.

Alternatively, Equation (3-1) can be expressed in terms of normal coordinates under the assumption that classical normal modes exist for the soil-structure model. Thus, Equation (3-1) can be expressed as:

$$\ddot{\bar{\eta}}_i + 2\omega_i \zeta_i \dot{\bar{\eta}}_i + \omega_i^2 \bar{\eta}_i = -\Gamma_i \ddot{v}_{gh} \quad (3-6)$$

where η_i is the i^{th} normal coordinate; ω_i and ζ_i are the i^{th} natural frequency and damping, respectively; and Γ_i is the participation factor for the i^{th} mode. The vector of participation factors, $\underline{\Gamma}$, is given by:

$$\underline{\Gamma} = \psi^T \{ m+m_h, m h_o+m_h(2h_o+h_h), m_h h_h \}^T \quad (3-7)$$

where Ψ is the mode shape matrix, i.e., the i^{th} column of Ψ is the i^{th} mode shape. The matrix Ψ is normalized such that $\Psi^T M \Psi = I$, the identity matrix. The displacement vectors $\underline{\eta}$ and \underline{v} are related by:

$$\underline{v} = \Psi \underline{\eta} \quad (3-8)$$

3.2 Solution of Equations of Motion

The solution to the equations of motion was obtained by 2 methods: (1) direct approach involving equation (3-1), and (2) modal superposition. The stiffness matrix needed to be determined to apply the direct approach, and the natural frequencies, modal dampings and mode shapes were required for the modal superposition method. These inputs are determined in Section 5.0 from the forced vibration tests discussed in Section 4.0.

With the mass and stiffness matrices known, the solution to Equation (3-1) can be written as:

$$\underline{\ddot{v}} = - [M - K/\omega^2]^{-1} \underline{\bar{f}} \quad (3-9)$$

The relationship, $\underline{v} = - \underline{\ddot{v}} / \omega^2$, which is applicable assuming zero initial conditions, was used in the derivation.

In terms of the modal quantities, the solution can be easily obtained by solving Equation (3-7) and substituting the resulting expression into Equation (3-8). In terms of $\underline{\ddot{v}}$ the solution can be written as:

$$\underline{\ddot{v}} = \underline{\ddot{v}}_{gh} \Psi \underline{\bar{A}}^T \quad (3-10)$$

where the i^{th} element of the $\underline{\bar{A}}$ vector is the amplification factor for the i^{th} mode. It is given by:

$$\bar{A}_i = \Gamma_i / \left[1 - (\omega/\omega_i)^2 - j 2 (\omega/\omega_i) \zeta_i \right] \quad (3-11)$$

where $j = \sqrt{-1}$ for this equation only.

3.3 Derivation of Free-Field Motion

The objective of this investigation was to determine the free-field accelerations from the 4 earthquake accelerograms recorded by the SMA-1 accelerograph, which was mounted to the pad as shown in Figure 2. This was accomplished by expressing the recorded SMA-1 motions, v_{SMA} , in terms of the elements of the displacement vector \underline{v} . For example, the translational acceleration recorded by the SMA-1, v_{SMA}^h , is:

$$\ddot{v}_{SMA}^h = \ddot{v}_{gh} + \ddot{v}_{ob} + (h_o + h_3) \ddot{\phi} \quad (3-12)$$

where h_3 is the height of the transducer element in the SMA-1 above the c.g. of the concrete pad. For vertical motion, the analogous equation is:

$$\ddot{v}_{SMA}^v = \ddot{v}_{gv} - e_x \ddot{\phi}_y \quad (3-13)$$

where e_x is the distance in the x direction between the vertical transducer in the SMA-1 and the c.g. of the concrete pad (Figure 2), and $\ddot{\phi}_y$ is the pad rotation about the y axis.

By substituting the solutions to the equations of motion given by Equation (3-9) into Equation (3-12), one can obtain an expression for the transformed free-field motion \bar{v}_{gh}^h in terms of \bar{v}_{SMA}^h through the appropriate transfer function:

$$\bar{v}_{gh}^h = \bar{v}_{SMA}^h / \left[1 - (1/\det B) \left(\sum_{j=1}^3 B_{1j} f_j + (h_o+h_3) \sum_{j=1}^3 B_{2j} f_j \right) \right] \quad (3-14)$$

where $\det B$ is the determinant of the matrix $[M - K/\omega^2]$; B_{1j} are the elements of the adjoint of $[M - K/\omega^2]$; and f_j are the elements of $(-\bar{f} / \bar{v}_{gh}^h)$.

Similarly, by substituting Equation (3-10) into (3-12), an analogous equation can be derived in terms of the modal quantities:

$$\bar{V}_{gh} = \bar{V}_{SMA}^h / \left[1 + \sum_{j=1}^3 \psi_{1j} \bar{A}_j + (h_0 + h_3) \sum_{j=1}^3 \psi_{2j} \bar{A}_j \right] \quad (3-15)$$

where ψ_{ij} are the elements of the mode shape matrix, Ψ .

By following the same basic procedures, similar equations can be derived for the vertical free-field motion as well.

4.0 FORCED VIBRATION TESTS

Forced vibration tests of the concrete pad were conducted to determine the dynamic characteristics of the soil-pad-hut system. In these tests eccentric-mass shakers were used to provide harmonic excitation to the pad over a frequency range of 5 to 60 Hz. Triaxial accelerometer packages placed on each corner of the pad and near the roof of the hut measured the amplitudes and phases of the horizontal and vertical motions. These measurements were used to determine the stiffness and modal quantities that appear in the frequency-dependent transfer functions, which are, for example, the denominators of the right hand sides of Equations (3-14) and (3-15).

4.1 Field Testing Program

The field testing program was conducted by ANCO Engineers of Culver City, California, and was monitored by Ertec, Inc. of Long Beach, California. The vibration generation equipment consisted of 2 eccentric mass shakers, MK-11 and MK-12, capable of producing low- and high-force levels similar to those experienced by the pad during the recorded earthquakes. Endevco piezoelectric accelerometers (5241A), which have a flat frequency response between 2 and 500 Hz, were used to measure the pad and hut accelerations.

Signals from the accelerometers were passed through a STI differential amplifier and antialias filter, which removed frequencies greater than 100 Hz. The output was passed through an analog-to-digital converter and stored on a Data General Nova 3 Computer. A Hewlett-Packard HP3582A Spectrum Analyzer, and HP7015B x-y plotter, as well as a Houston Instruments plotter were used to monitor the tests.

To determine the frequency-dependent foundation impedances, K_{ij} ($i, j=1, 2$), for coupled translation and rocking response, 2 independent forced-vibration tests were performed for each horizontal direction; that is, in the x and y directions (see Section 5.2 for theory).

For one test in the x direction, for example, ANCO mounted the MK-11 eccentric mass shaker to the top of the pad over the center of gravity (c.g.) and excited the pad with a x-directional horizontal harmonic force at a fixed frequency. The resulting coupled translational and rocking accelerations were measured with triaxial accelerometer packages. The tests were repeated over a range of frequencies from 5 to 60 Hz. The frequencies were incremented such that the frequency of a given test was 1 percent larger than the frequency of the preceding test. The applied force in pounds equaled $1.051 ef^2$, where e = eccentricity and f = frequency in Hz. To keep the force levels from becoming too large, the eccentricity was lowered at 20 Hz and again at 35 Hz. The eccentricity values selected were: 1.0 (5 to 20 Hz); 0.40 (20 to 35 Hz); and 0.15 (35 to 60 Hz).

For the other independent test, the shaker was moved from over the c.g. to a point about halfway between the c.g. and the end of the pad. The shaker weights were oriented to produce a force in the vertical direction. This induced a moment to the pad, and the coupled rocking and translational motions were measured in the same manner as in the first test.

A third test was performed to determine the frequency-dependent stiffnesses for vertical response. Theoretically, the second test described above would also provide response data to determine the stiffnesses. However, because of the asymmetric stress distribution that resulted beneath the pad during this test, the shaker was placed over the c.g. for the vertical test.

Three confirmation tests, one for each direction, were conducted to verify the experimental results. One confirmation test consisted of repeating the test where the shaker provided a vertical eccentric force. However, in the verification test, the shaker was moved to the same location on the other side of the c.g. Through a comparison with the original vertical eccentric force test, this test also indicated the effect of the asymmetric stress distribution beneath the pad.

The entire test procedure described above (comprising a total of 8 tests) was repeated twice: first at low-force levels, using the MK-11 shaker, and then at high-force levels, using the MK-12 shaker. The high-force-level tests were conducted with the MK-12 shaker. The results of the 2 tests indicated whether or not non-linear response was significant.

In addition to the pad-response measurements, other quantities were also obtained: (1) the dimensions, density, mass, moment of inertia and location of the c.g. of the pad, (2) the location of the applied force within the MK-11 and MK-12 shakers, (3) the locations of the transducer elements within the SMA-1 instrument that recorded the earthquake ground motions, and (4) the locations on the pad of the accelerometers recording the motions generated during the vibration tests. All of these quantities were measured directly, obtained from specification sheets, or computed.

4.2 Response Data from Vibration Tests

The steady-state acceleration amplitudes and phases for the acceleration-time histories recorded by the Endevco accelerometers were determined by Fourier analysis at each frequency of excitation. The modulus was taken as the amplitude of the steady-state acceleration and the phase angle was computed from the real and imaginary parts. The phase angle (p) was defined with respect to the applied force; i.e., if the shaker force was $F = F_0 \sin \omega t$, then the response measured by a particular accelerometer was $a = a_0 \sin (\omega t + p)$. The shaker force and the measured accelerations were considered to be positive along the coordinate axes shown in Figure 3. To time the application of the harmonic force, a sensor was placed on the rotating shaft of the shaker. This sensor recorded the times at which the shaker force reached its maximum positive value during each revolution.

5.0 DATA ANALYSIS

5.1 Reduction of Data from Forced Vibration Tests

The steady-state amplitude and phase data obtained from the forced vibration tests were transformed into the 3 translational and 3 rotational accelerations of the center of gravity (c.g.) of the concrete pad and the rotation and vertical translation of the wooden hut. The equations that describe the rigid body motion of the concrete pad for small displacements (see Figure 1) are:

$$U_i = U_x + (z_i - z_c) \theta_y - (y_i - y_c) \theta_z \dots (i=1,4,7,10) \quad (5-1)$$

$$V_i = U_y - (z_i - z_c) \theta_x + (x_i - x_c) \theta_z \dots (i=2,5,8,11) \quad (5-2)$$

$$W_i = U_z + (y_i - y_c) \theta_x - (x_i - x_c) \theta_y \dots (i=3,6,9,12) \quad (5-3)$$

Equation (5-1) applies to accelerations U_i recorded on the i^{th} accelerometer oriented in the x direction. Similar definitions apply to Equations (5-2) and (5-3) in the y and z directions, respectively. In the above equations U_x , U_y , and U_z are the horizontal accelerations of the c.g. of the concrete pad in the x , y , and z directions, respectively. The rotational accelerations about principal axes through the pad's c.g. are represented by θ_x , θ_y , and θ_z . The coordinates (x_c, y_c, z_c) designate the location of the c.g. of the pad while (x_i, y_i, z_i) designate the location of the i^{th} accelerometer.

In general, 4 separate equations involving 3 unknown responses can be written for each one of the equations (5-1), (5-2) and (5-3). Each response quantity in these equations is of the form $a_o \sin(\omega t + p)$. Thus, the response quantities can be expressed, for convenience, as complex variables, and existing computer software can be used to solve the simultaneous equations for the unknown responses, U_x , U_y , U_z , θ_x , θ_y and θ_z .

For our transducer arrangement on the pad, the quantity $z_1 - z_c$ was constant for all i . Therefore, θ_y and θ_x could not be obtained from Equations (5-1) and (5-2). Furthermore, because some of the x_i , y_i and z_i pairs were nearly equal (e.g., x_1 and x_4), equations involving these pairs were nearly dependent, and therefore, ill-conditioned for solving simultaneously. Thus, 4 different sets of 2 simultaneous equations were written for each one of Equations (5-1) and (5-2). Because of noise, some of the W_1 recordings had to be eliminated, and only 1 or 2 sets of 3 simultaneous equations were written for Equation (5-3). The solutions for each set were averaged to reduce any random noise that may have been present.

Because the wooden hut was assumed to act as a rigid body attached to the concrete pad by flexible springs, the hut's motions at its c.g. were easily computed from the recorded roof motions and the calculated pad motions.

The calculations of translational accelerations (U_x , U_y , U_z) and rotational accelerations (θ_x , θ_y , θ_z) in Equations (5-1), (5-2), (5-3) showed that torsional accelerations (θ_z) were small. As expected, translations perpendicular to the direction of the applied shaker force were small compared to the translations in the direction of the force.

Typical plots of the U_x displacement amplitude and phase data versus frequency are shown in Figure 4 for the first low-force-level test. The displacement amplitudes have been normalized by the shaker force. The discontinuities at 20 Hz and 35 Hz reflect the change to lower eccentricities (and hence lower force levels) during the test. Theoretically, if the soil-structure system were completely linear and if the eccentricities were precisely set, then discontinuities would not appear. However, they are small and of no practical consequence.

The narrow peak at 16 Hz and the broad peak at 48 Hz in Figure 4 correspond to the first and second natural frequencies of the soil-pad-hut system. Similar plots for the corresponding high-force-level test are shown

in Figure 5. The amplitude and phase plots are considerably different from those in Figure 4. For example, the second natural frequency was reduced from about 50 Hz during the low-level tests (Figure 4) to approximately 25 Hz during the first high-level test (Figure 5). This indicates that the high-force-level tests induced a severe non-linear response by degrading the soil stiffness and/or creating a small gap at the interface between the side of the pad and the surrounding soil. The same conclusions were reached upon inspection of the results of all the high-force-level tests. These tests, because of their long duration at high-force levels and the attendant non-linear response, were not considered indicative of the behavior of the soil-pad-hut system during the reservoir-induced earthquakes, which essentially applied impulsive loads lasting less than 1 second. Consequently, only the low-force-level data were considered in the subsequent analysis.

5.2 Determination of Stiffness Matrix

The elements of the stiffness matrix in Equation (3-8) were determined from the equations of motion for the forced vibration experiments. The equations are similar to the matrix Equation (3-1); the only difference is the forcing term, \underline{f} , on the right-hand side.

Theory. To determine the elements of the complex stiffness matrix, K_{ij} ($i = 1, 2$) and K_{θ} , in 1 horizontal direction, 2 independent forced vibration tests were performed as discussed in Section 4.0. The first one consisted of a horizontal harmonic force applied above the c.g. of the pad (Figure 2). The second one consisted of vertical harmonic force applied at a point located away from the c.g. For each experiment 3 equations of motion involving the base translation, v_{ob} , and rotation, ϕ , of the pad and the rotation of the hut, θ , were written.

The equations of motion for the first experiment are:

$$M \ddot{\underline{v}}^1 + K \underline{v}^1 = \underline{f}^1 \quad (5-4)$$

where:

$$\underline{v}^1 = \{v_{ob}^1, \phi^1, \theta^1\}^T \quad (5-5)$$

$$\underline{f}^1 = \{F, F(h_o+h_l) + M_e, 0\}^T \quad (5-6)$$

$$M = \begin{bmatrix} m+m_h & mh_o+m_h(2h_o+h_h) & m_h h_h \\ mh_o+m_h(2h_o+h_h) & mh_o^2+I+m_h(2h_o+h_h)^2+I_h & m_h h_h(2h_o+h_h)+I_h \\ m_h h_h & m_h h_h(2h_o+h_h)+I_h & m_h h_h^2+I_h \end{bmatrix} \quad (5-7)$$

$$K = \begin{bmatrix} K_{11} & K_{12} & 0 \\ K_{21} & K_{22} & 0 \\ 0 & 0 & K_\theta \end{bmatrix} \quad (5-8)$$

Note that the M and K above are identical to M and K given by Equations (3-4) and (3-5), which were used in the equations of motion for the earthquake response.

The equations of motion for the second experiment are:

$$M\underline{\ddot{v}}^2 + K\underline{v}^2 = \underline{f}^2 \quad (5-9)$$

where:

$$\underline{v}^2 = \{v_{ob}^2, \phi^2, \theta^2\}^T \quad (5-10)$$

$$\underline{f}^2 = \{0, Fa, 0\}^T$$

In the above equations, \underline{v}^i and \underline{f}^i represent the displacement and force vectors respectively, measured during the i^{th} experiment; F is the applied harmonic shaker force; a is the horizontal distance from the applied vertical shaker force to the pad's c.g.; M_e is the moment applied by the shaker when the shaker force is in the horizontal direction; and h_1 is the vertical distance of the horizontal shaker force above the pad's c.g. The remaining symbols were defined in Section 3.0.

The matrix equations (5-4) and (5-9) can be written out as 6 equations involving the unknown stiffness. Because K_θ is not coupled to K_{ij} in the stiffness matrix, 2 of the equations involve the unknown K_θ only. The remaining 4 equations involve the unknown K_{ij} only. Thus, two independent estimates of K_θ were obtained, and under the assumption $K_{12} \neq K_{21}$, unique estimates of the K_{ij} were obtained. Details of the solution procedure are given below.

Because the applied shaker force is harmonic, then:

$$\underline{f}^i = \underline{\bar{f}}^i e^{i\omega t} \quad (5-11)$$

$$\underline{v}^i = \underline{\bar{v}}^i e^{i\omega t} \quad (5-12)$$

where $\underline{\bar{f}}^i$ and $\underline{\bar{v}}^i$ represent the complex amplitudes and are functions of the circular frequency, ω , in radians/sec. The $\underline{\bar{v}}^i$ were determined using the data reduction methods discussed in Subsection 5.1.

By substituting Equations (5-11) and (5-12) into Equations (5-4) and (5-9) and by making use of $-\omega^2 \underline{\bar{v}}^i = \underline{\bar{v}}^i$, the following equations are obtained for the unknown stiffnesses:

$$K_{\theta} = (\omega^2 / \bar{\theta}^1) \{M_3\}^T \bar{v}^1 \quad (5-13)$$

$$K_{\theta} = (\omega^2 / \bar{\theta}^2) \{M_3\}^T \bar{v}^2 \quad (5-14)$$

$$\bar{v}_{ob}^1 K_{11} + \bar{\phi}^1 K_{12} = -\omega^2 \bar{f}_1^1 + \omega^2 \{M_1\}^T \bar{v}^1 \quad (5-15)$$

$$\bar{v}_{ob}^2 K_{11} + \bar{\phi}^2 K_{12} = \omega^2 \{M_1\}^T \bar{v}^2 \quad (5-16)$$

$$\bar{v}_{ob}^1 K_{21} + \bar{\phi}^1 K_{22} = -\omega^2 \bar{f}_2^1 + \omega^2 \{M_2\}^T \bar{v}^1 \quad (5-17)$$

$$\bar{v}_{ob}^2 K_{21} + \bar{\phi}^2 K_{22} = -\omega^2 \bar{f}_2^2 + \omega^2 \{M_2\}^T \bar{v}^2 \quad (5-18)$$

In the above equations \bar{f}_j^1 is the j^{th} element of the vector \bar{f}^1 , and $\{M_j\}$ is the vector whose elements are given by the j^{th} column of the mass matrix.

Equations (5-15) and (5-16) were solved simultaneously for K_{11} and K_{12} , and Equations (5-17) and (5-18) were solved for K_{21} and K_{22} at each frequency, ω , in the range from 5 to 60 Hz.

The stiffnesses in the vertical direction were obtained from the third vibration test where the harmonic shaker force was applied in the vertical direction over the pad's c.g. However, because the vertical tests showed no natural frequencies in this direction, the stiffnesses were not used in the earthquake response calculations for the vertical direction, and they are not presented in this report.

Results. The real and imaginary parts of the complex stiffnesses, K_{ij} and K_{θ} , are shown in Figures 6 through 9 for the x direction. Some observations in these figures are of particular interest. For example,

the real part of the stiffness K_{11} in Figure 6 increases with frequency. This is not consistent with the theory for embedded rectangular foundations (Dominguez, 1978), which shows the stiffness, K_{11} , decreasing slightly with frequency. The real parts of K_{12} and K_{21} , (Figure 7) although roughly equal, are much larger than expected on the basis of theory (Dominguez, 1978). The imaginary parts are clearly not equal, and in fact, $\text{Im}(K_{12})$ is negative for nearly all frequencies. The stiffness K_{22} (Figure 8) exhibits erratic behavior, especially near the natural frequencies of 16.7 Hz and 49.8 Hz. The imaginary part of K_{22} is negative for nearly all frequencies, which implies negative damping. The stiffness associated with the hut, K_{θ} , seemed fairly well behaved in comparison with the impedances K_{1j} ($j=1,2$). However, the K_{θ} were not obtained from a simultaneous solution as were the K_{1j} . Rather, independent estimates of K_{θ} were obtained from both vibration tests; whereas, both tests were required to obtain single estimates of K_{1j} .

The relative stability of the K_{θ} suggested that the data from both tests and the resulting simultaneous equations were not well conditioned for solution by this procedure. To test this hypothesis, the off diagonal terms, K_{12} and K_{21} , were set equal to zero. Equations (5-15) and (5-16) were each solved for K_{11} , and Equations (5-17) and (5-18) were each solved for K_{22} . The results, presented in Figures 10 and 11, show a reduction in fluctuations with frequency. The differences between both independent estimates of K_{11} and K_{22} are considered small by experimental standards. Nonetheless, they were apparently large enough to cause the erratic behavior observed in Figures 6, 7 and 8.

Even though they are more stable, the stiffnesses K_{11} and K_{22} shown in Figures 10 and 11 still exhibit some anomalies. For example, the increases in the real part of K_{11} , with frequency up to the first and second natural frequencies, are not expected. The negative imaginary part of K_{11} around the natural frequency (16.7 Hz) is also not expected. The same comments apply to K_{22} , except the negative imaginary part is observed at all frequencies greater than 12 Hz. The reasons for these anomalies are not entirely clear. One explanation is the soil-pad-hut model is more sophisticated than the one

considered and that the stiffnesses are simply reflecting these differences. Another explanation lies with the phases between the applied shaker forces and measured accelerations. The calculations showed that the stiffnesses were sensitive to these phases. Thus, experimental error, noise, or some other phenomena could have affected the phase measurements, which could have contributed to the behavior in the K_{1j} noted above, especially with regard to the imaginary part.

Even with the anomalies in the K_{1j} it was still possible that the substitution of these stiffnesses into Equation (3-9) would lead to reasonable estimates of the earthquake response of the soil-pad-hut system. This is explored further in Section 6.0.

5.3 Determination of Modal Parameters

To obtain the free-field earthquake ground motions by modal superposition (e.g., Equation 3-15), the natural frequencies (ω_1), modal dampings (ζ_1), and mode shapes (ψ_1) must be determined. These parameters were obtained from the data generated during the low-level forced vibration tests.

The natural frequencies and dampings were determined by applying a procedure developed by Beck (1980). The procedure consists of fitting a theoretical amplification curve for a single-degree-of-freedom system to the observed response data. The method is applicable to modes which are well separated and have low damping, which is the case for the soil-pad-hut system. A computer program for the curve fitting was taken from Appendix A.2 of Lin (1982). The program was applied to pad displacement data normalized by the applied shaker force. The displacement data were computed by dividing the pad accelerations, determined in Subsection 5.1, by $-\omega^2$.

An example of the response data from the low-level vibration tests was shown in Figure 4. Two peaks are apparent in the plot: one near 16 Hz and the other near 47 Hz. The response data that defined each peak were used in the curve fitting procedure. This procedure was repeated for the y direction also. The resulting ω_1 and ζ_1 are presented in Table 1.

The mode shapes were obtained from the response data at each natural frequency. For example, at the i^{th} natural frequency the response data $\{ \ddot{v}_{ob}, \ddot{\phi}, \ddot{\theta} \}^T$, obtained from the data reduction procedures described in Subsection 5.1, would represent the i^{th} mode shape, ψ_i , to within a scale factor (Nielsen, 1964). The scale factors and hence the mode shapes were then determined by solving:

$$\Psi^T M \Psi = I \quad (5-19)$$

where Ψ is the mode shape matrix, M is the mass matrix, and I is the identity matrix. The mode shapes ψ_i (i.e. the columns of Ψ) are also presented in Table 1.

Discussion. The natural frequencies (ω_i) and modal dampings (ζ_i) determined from the forced vibration tests are similar to those obtained during the pluck tests conducted by Stoll, Evans, Woods and Associates on 9 January 1982. This indicates that the dynamic characteristics of the soil-pad-hut system did not change appreciably in the 10 months between the experiments, and therefore, they probably did not change between the time of the earthquakes and the experiments.

The forced vibration tests clearly showed (Table 1) that the first natural frequency in each direction was influenced by the hut. On the other hand, the second natural frequency in each horizontal direction was predominantly the response of the pad. The similarity of the second natural frequencies in the x and y directions is to be expected because the soil properties are not expected to vary significantly in the 2 directions. However, the differences in the first natural frequency in the x and y directions are expected because the stiffness of the hut is different in each direction.

6.0 CALCULATION OF FREE-FIELD MOTIONS

An indication of the amount of soil-structure interaction that affected the SMA-1 accelerograms recorded on the concrete pad was obtained from the transfer function, $\frac{\bar{v}_{SMA}}{\bar{v}_{gh}}$. These functions were computed from equations such as (3-14) and (3-15). Graphs of the transfer functions, both the modulus and phase, versus frequency are shown in Figure 12 for the x direction. These plots were derived from Equation (3-14), which used the stiffnesses shown in Figures 9, 10, and 11. The transfer functions computed from Equation (3-15), which involved the modal quantities, are shown in Figures 13 and 14 for the x and y directions. A general transfer function for the vertical (z) direction cannot be computed because it depends on both the horizontal and vertical SMA motions. Individual transfer functions for each vertical component of the SMA accelerogram can be calculated but they show little amplification and are not presented.

The transfer function obtained by the stiffness approach (Figure 12) indicated that the motions recorded by the SMA-1 were greater than the free-field motions by factors larger than 10 over a wide frequency range, which did not seem physically possible. The transfer functions were sensitive to the phases, and the large values for the modulus were mostly attributed to the negative imaginary parts of K_{11} and K_{22} , which implied negative damping in the system. At this point, it was concluded that the stiffness approach would not give realistic estimates of the transfer function or the free-field ground motions, and this approach was not pursued further.

The transfer functions obtained from the modal approach (Figures 13 and 14) are reasonable and consistent with physical intuition. One of the reasons for the regular behavior of these transfer functions is that they do not depend on the phases measured during the vibration tests. The damping in the system and the other modal parameters were obtained only from the modulus versus frequency plots, as discussed in Subsection 5.3. The phase information was not needed for this approach.

The free-field earthquake ground motions, corresponding to the 4 accelerograms recorded by the SMA-1, were computed by taking the inverse Fourier Transform of Equation (3-15) and the analogous equation for the vertical direction. A comparison between the SMA-1 and free-field accelerograms is shown in Figures 15 and 16 for the 090° and 180° directions, respectively. These directions corresponded to the transducer directions in the SMA-1. Thus, the x and y free-field motions, computed from the transfer functions, were transformed into the 090° and 180° directions.

Figures 15 and 16 show that the computed horizontal free-field accelerograms are somewhat less than the SMA-1 accelerograms, both in amplitude and frequency content. The differences for vertical motions were negligible and these results are not presented.

The 5 percent damped response spectra of the SMA-1 and free-field accelerograms are shown in Figures 17 and 18 for the 090° and 180° directions. The differences in the SMA-1 and free-field response spectra are also consistent with the transfer functions.

The average reduction in the horizontal free-field motions was obtained by averaging the ratio, $PSV_{f-f}(f)/PSV_{SMA}(f)$, where $PSV_{f-f}(f)$ and $PSV_{SMA}(f)$ are the 5 percent damped pseudovelocities at frequency f for the free-field and SMA-1 accelerograms, respectively. The ratios for the 8 horizontal components were averaged arithmetically at each frequency and the results are plotted in Figure 19. The average reduction in $PSV_{f-f}(f)$ for frequencies between 1 and 20 Hz is about 5 percent. The reduction is linear between 20 and 36 Hz; its value at 36 Hz is 27 percent. The average reduction for frequencies between 36 and 50 Hz is about 27 percent.

The average reduction factors indicated above were used to modify the envelope spectrum developed by the NRC for the Monticello accelerograms (NRC, 1982). The 5 percent damped response spectrum in Figure 2-1 of that reference was reduced by these reduction factors and the results are plotted in Figure 20. The reduced spectrum in Figure 20 is the corresponding free-field spectrum for the Monticello accelerograms.

7.0 REFERENCES

- Beck, J. L., 1980, Determining modes for structures from earthquake records: Earthquake Engineering Research Laboratory, Report EERL 80-01, California Institute of Technology, Pasadena, California.
- Bielak, J., 1971, Earthquake response of building foundation systems: Earthquake Engineering Research Laboratory, Report EERL 71-04, California Institute of Technology, Pasadena, California.
- Dominguez, J., 1978, Dynamic stiffness of rectangular foundations. Department of Civil Engineering, Report No. R78-20, Massachusetts Institute of Technology, Cambridge, Massachusetts.
- Luco, J. E., 1980, Linear soil-structure interaction: Report UCRL-15272, PSA #7249809 submitted to Lawrence Livermore Laboratory.
- Lin, A. N., 1982, Experimental observations of the effect of foundation embedment on structural response: Earthquake Engineering Research Laboratory, Report EERL 82-01, California Institute of Technology, Pasadena, California.
- Nielsen, N. N., 1964, Dynamic response of multistory buildings: Earthquake Engineering Research Laboratory, California Institute of Technology, Pasadena, California.
- Nuclear Regulatory Commission (NRC), 1982, Safety Evaluation Report related to the operation of Virgil C. Summer Nuclear Station, Unit No. 1, Docket No. 50-395, South Carolina Electric and Gas Company, NUREG-0717, Supplement No. 4, August.

TABLE 1
MODAL PARAMETERS FOR SOIL-PAD-HUT MODELS

Direction	1st mode			2nd mode		
	ω	ζ	Ψ	ω	ζ	Ψ
x	16.7 Hz	.04	1.45E-2	49.8 Hz	.20	5.67E-2
			5.77E-4			1.87E-3
			4.64E-3			-3.90E-3
y	10.6 Hz	.06	9.34E-3	47.9 Hz	.21	5.16E-2
			4.39E-4			1.63E-3
			5.04E-3			-5.88E-3

VIBRATION TESTS

APPLIED FORCE
 ● Harmonic Excitation of Pad
 at Low & High Force Levels
 MEASURED RESPONSES
 ● Acceleration Amplitudes
 ● Phases

DATA REDUCTION

TRANSFORM MEASURED RESPONSE DATA
 INTO TRANSLATIONS & ROTATIONS
 OF PAD & HUT c.g.'s

EXAMINE DATA FROM
 LOW-FORCE-LEVEL
 TESTS

EXAMINE DATA FROM
 HIGH-FORCE-LEVEL
 TESTS

SEVERE
 STIFFNESS
 DEGRADATION,
 DO NOT USE

SELECT DATA
 FOR ANALYSIS

DYNAMIC PROPERTIES DETERMINATION

STIFFNESS MATRIX FROM
 AMPLITUDE & PHASE DATA

NATURAL FREQUENCIES, DAMPINGS,
 & MODE SHAPES FROM AMPLITUDE DATA

SOIL-STRUCTURE INTERACTION ANALYSIS

COMPUTE SMA-1
 TO FREE-FIELD
 TRANSFER FUNCTION

UNREALISTIC
 RESULTS
 DO NOT USE

COMPUTE SMA-1
 TO FREE-FIELD
 TRANSFER FUNCTION

FREE-FIELD MOTION COMPUTATION

COMPUTE FREE-FIELD
 ACCELEROGRAMS &
 RESPONSE SPECTRA

FREE-FIELD
 SIGNIFICANTLY LESS
 THAN SMA-1

090° & 180° DIR. COMPARE FREE-FIELD TO SMA-1 MOTIONS UP DIR. DIFFERENCES SMALL. NEGLECT

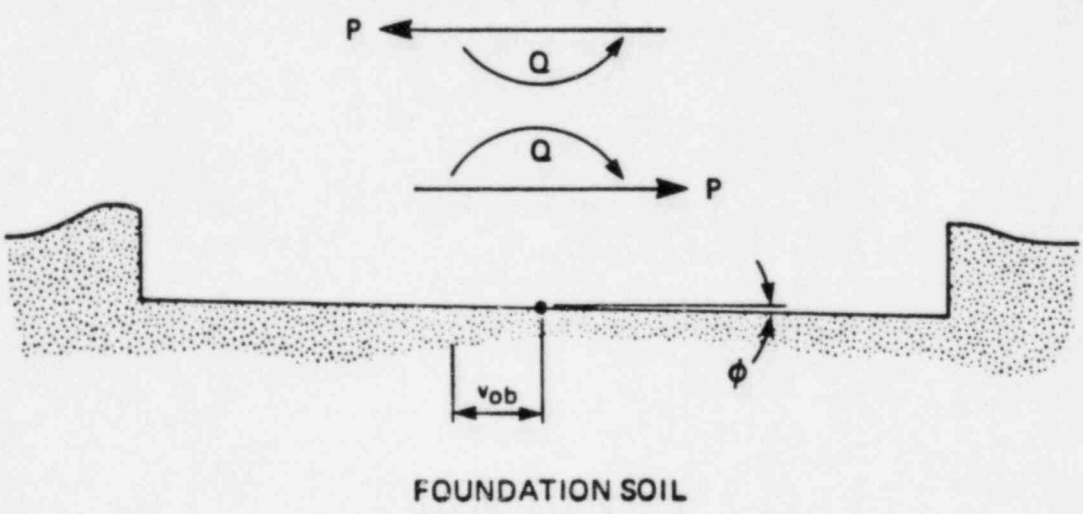
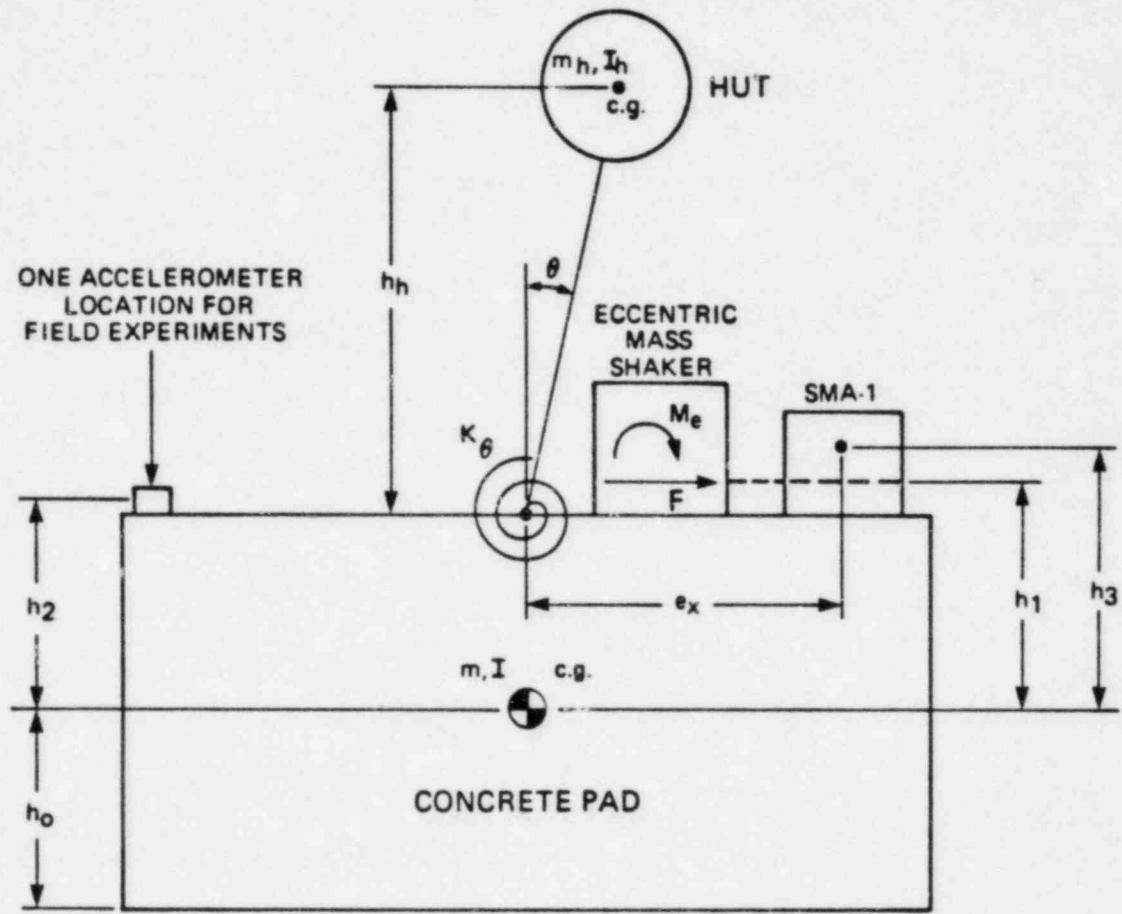
CONCLUSION

REDUCE NRC (1982)
 ENVELOP SPECTRUM

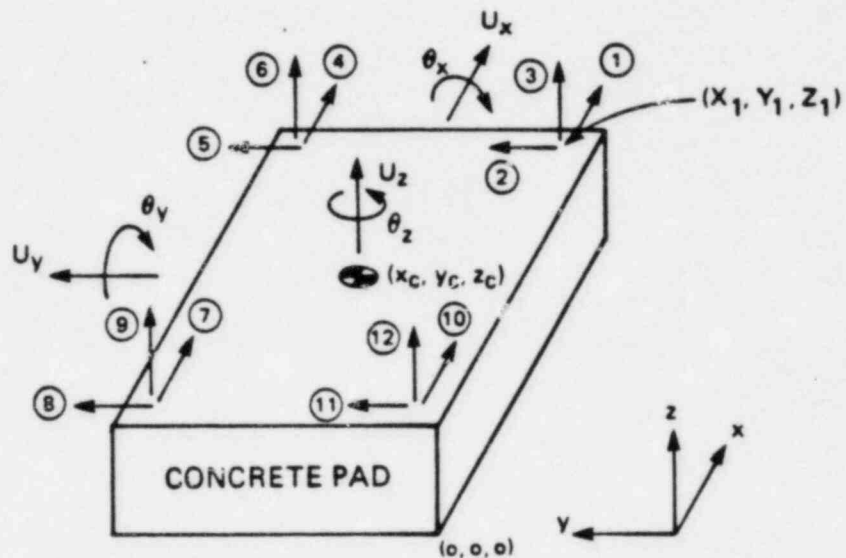


PROJECT NO.: 83-164
 SCE&G

SOIL-STRUCTURE INTERACTION
 INVESTIGATION AT JENKINSVILLE
 ACCELEROGRAPH STATION



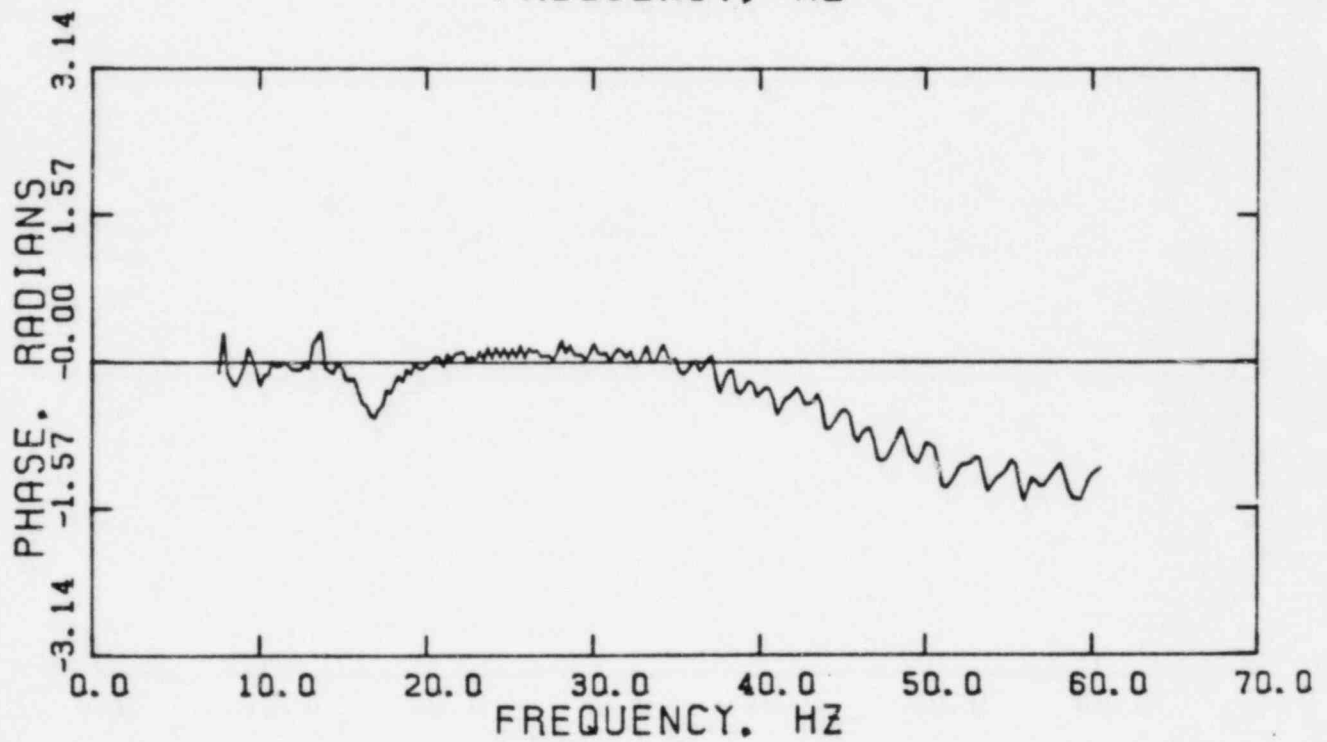
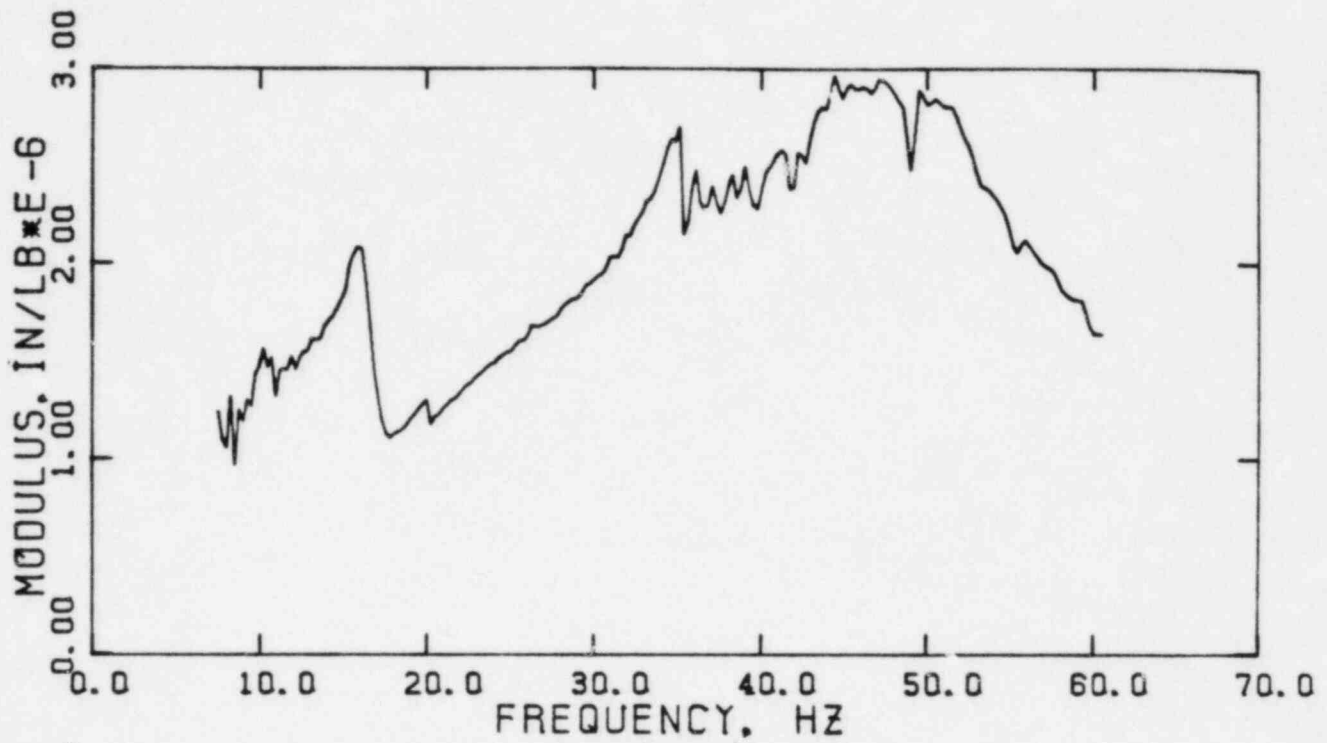
	PROJECT NO.:	83 164
	SCE&G	
SOIL-PAD-HUT INTERACTION MODEL FOR HORIZONTAL TRANSLATION AND ROCKING		
12-82	FIGURE 2	



- ↑ ① DIRECTION OF POSITIVE ACCELERATION FOR ACCELEROMETER *i*
- (*x_i*, *y_i*, *z_i*) COORDINATE OF ACCELEROMETER *i*
- (*x_c*, *y_c*, *z_c*) COORDINATE FOR CENTER OF GRAVITY (c.g.) OF THE PAD
- U_x*, *U_y*, *U_z* ARE THE TRANSLATIONAL MOTIONS OF THE PAD c.g.
- θ_x*, *θ_y*, *θ_z* ARE THE ROTATIONAL MOTIONS OF THE PAD

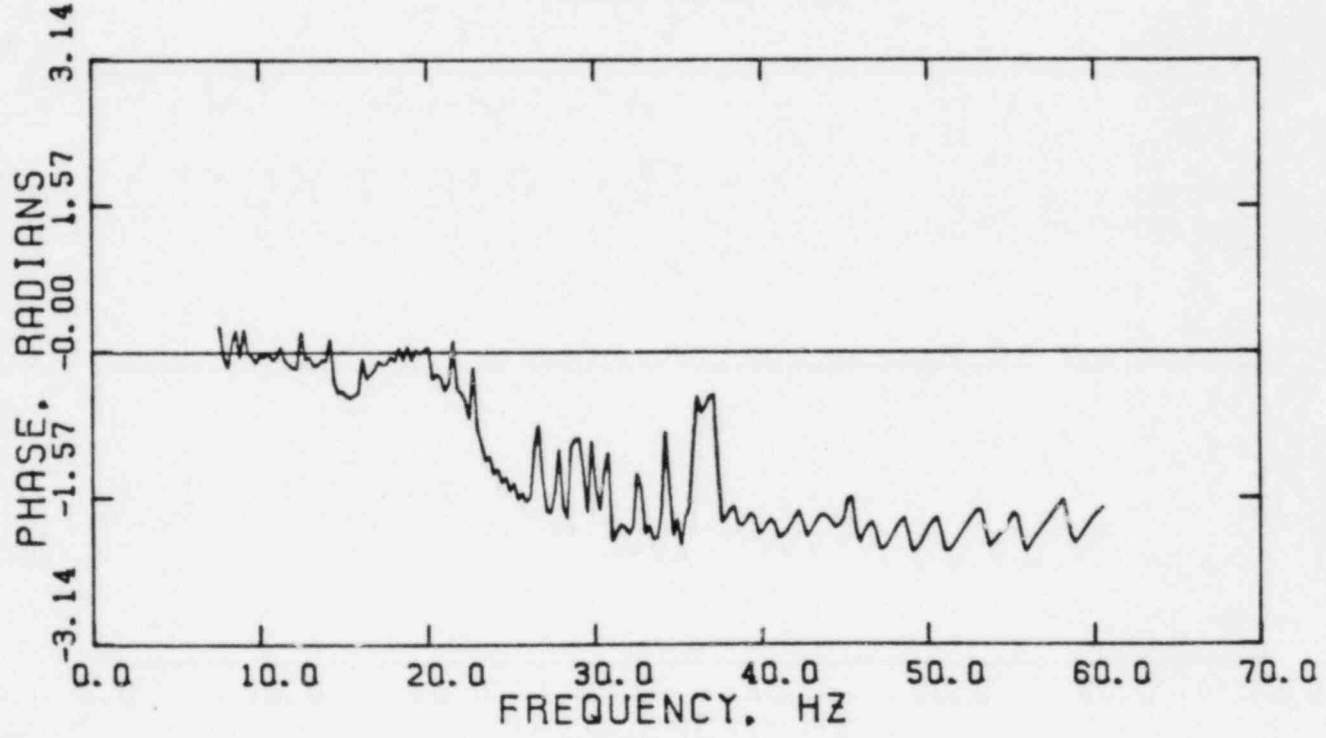
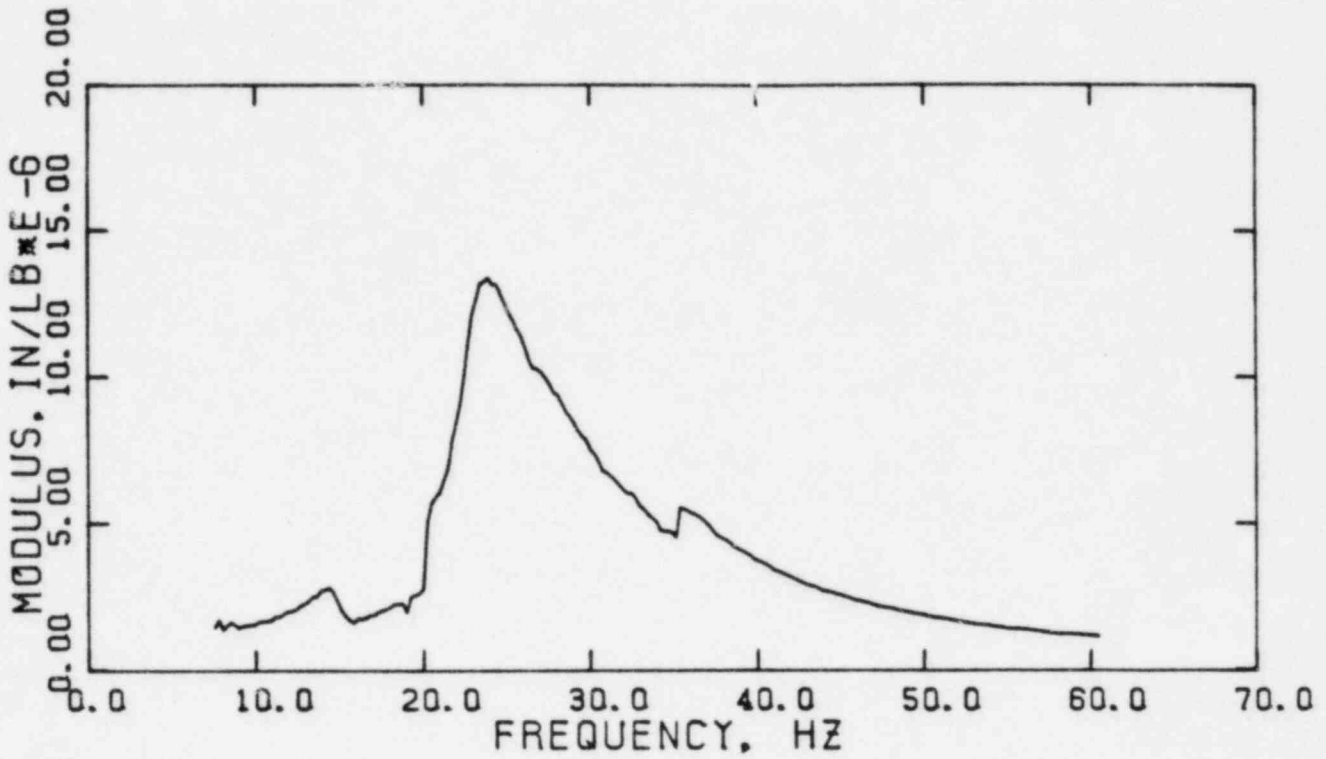
	PROJECT NO.:	B3 164
	SC&G	
ACCELEROMETER LOCATIONS, COORDINATE AXES, AND SYMBOL NOTATION FOR THE FORCED VIBRATION EXPERIMENTS		
12-82	FIGURE 3	

Approved by /
Checked by /
Drawn by /
Compiled by /



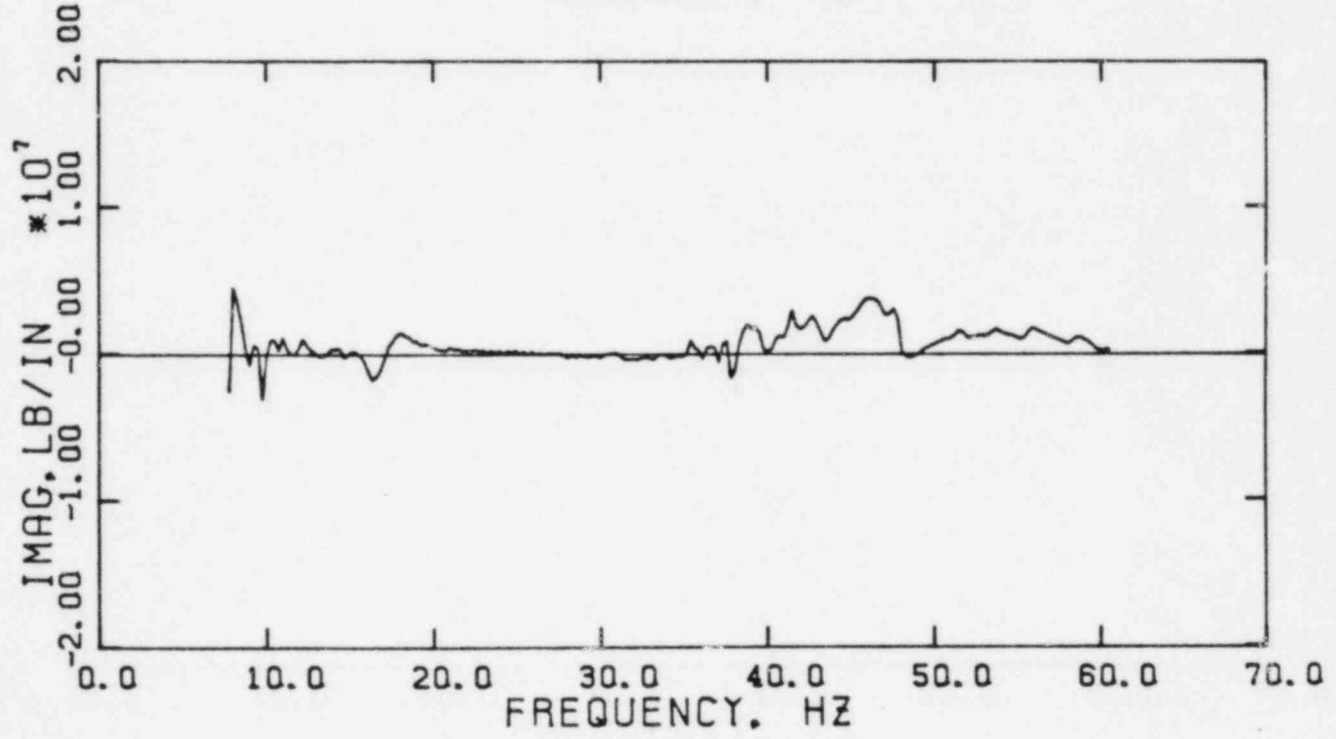
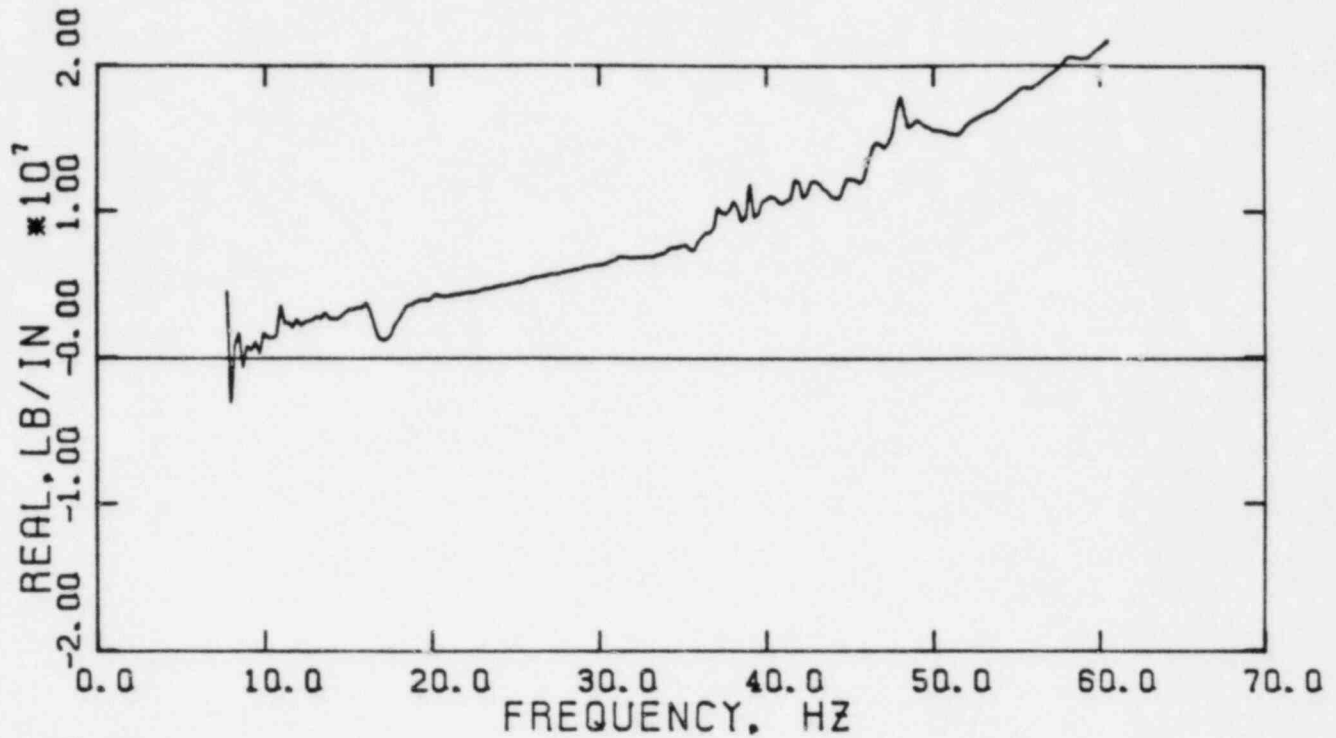
 The Earth Technology Corporation	PROJECT NO.: 83 164
	SCE&G
DISPLACEMENT AMPLITUDES, U_x , AND PHASES FROM FIRST LOW FORCE-LEVEL VIBRATION TEST	
1-83	FIGURE 4

Approved by _____
Checked by _____
Drawn by _____
Compiled by _____



 The Earth Technology Corporation	PROJECT NO.: 83-164
	SCE&G
DISPLACEMENT AMPLITUDES, U_x , AND PHASES FROM FIRST HIGH FORCE-LEVEL VIBRATION TEST	
1-83	FIGURE 5

Approved by _____
Checked by _____
Drawn by _____
Compiled by _____



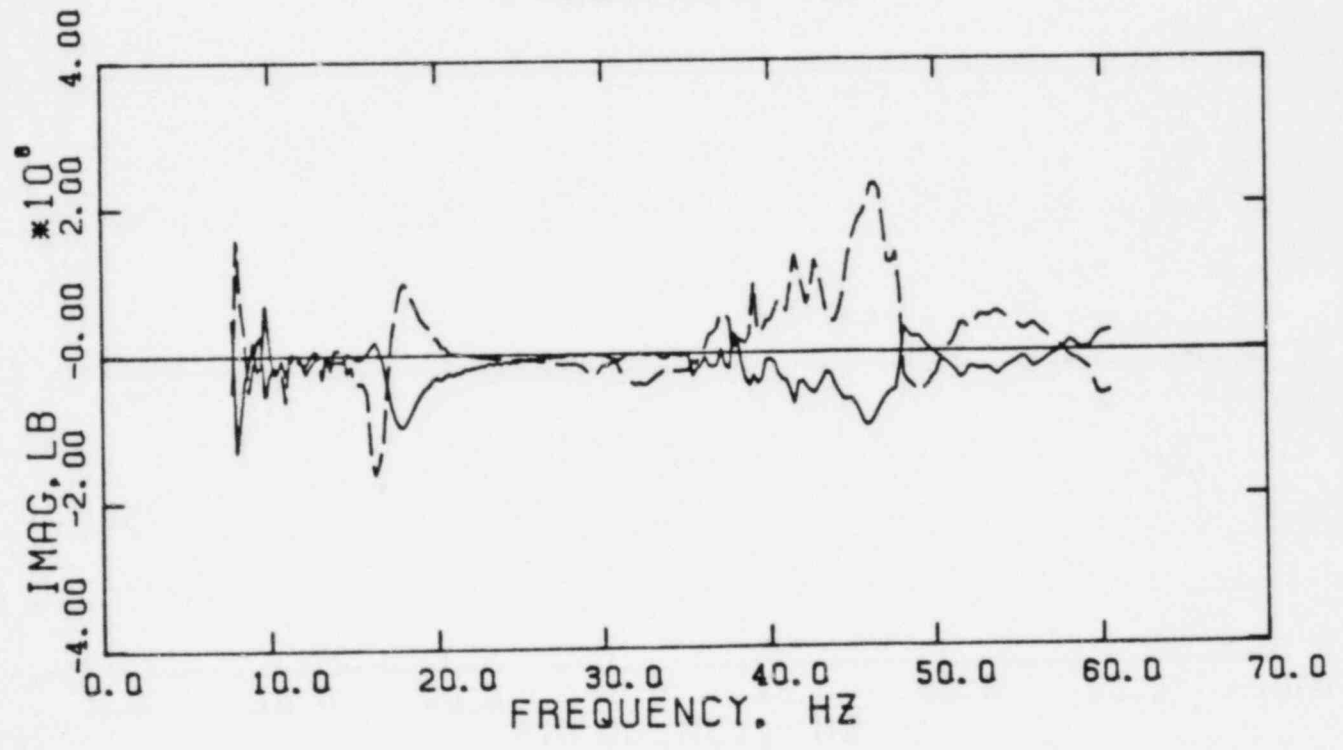
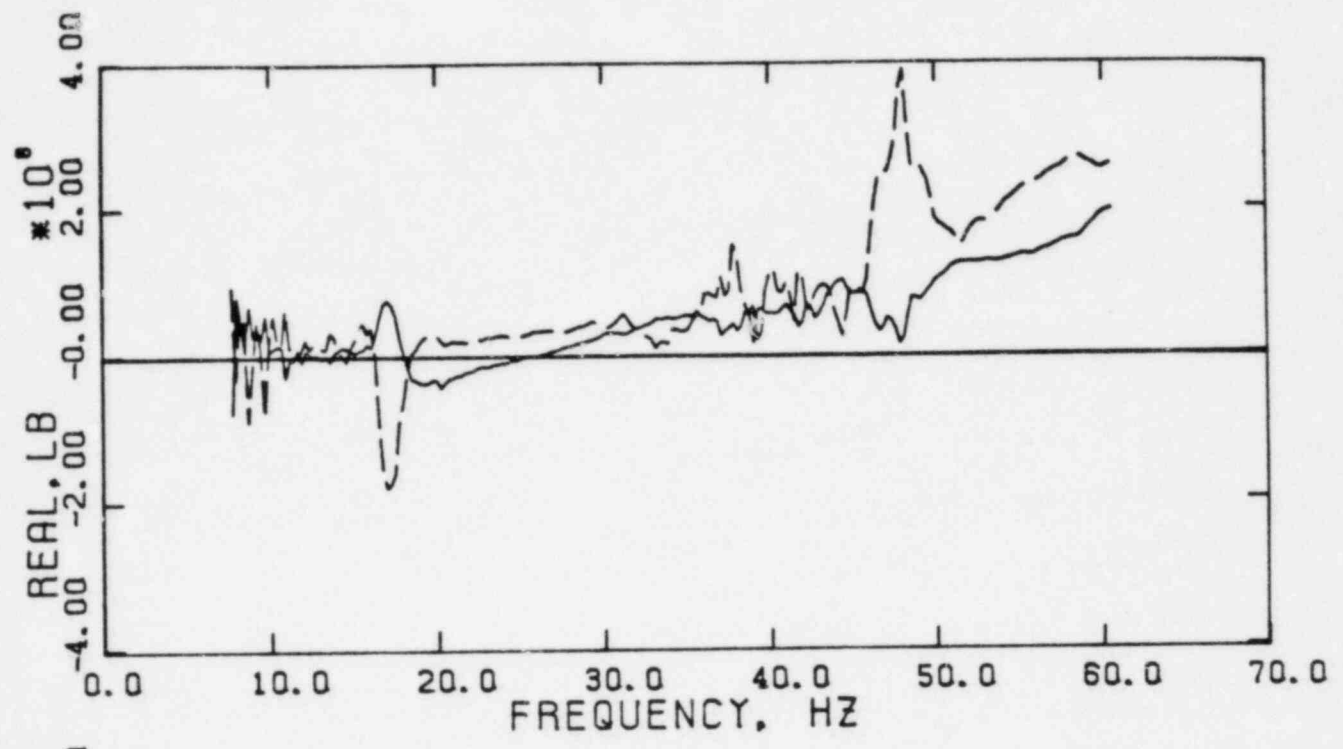
 The Earth Technology Corporation	PROJECT NO.: 83-164
	SCE&G
FOUNDATION IMPEDANCE, K_{11} , VERSUS FREQUENCY	
183	FIGURE 6

Approved by

Checked by

Drawn by

Compiled by



— K_{12}
- - - K_{21}



PROJECT NO.: 83-164

SCE&G

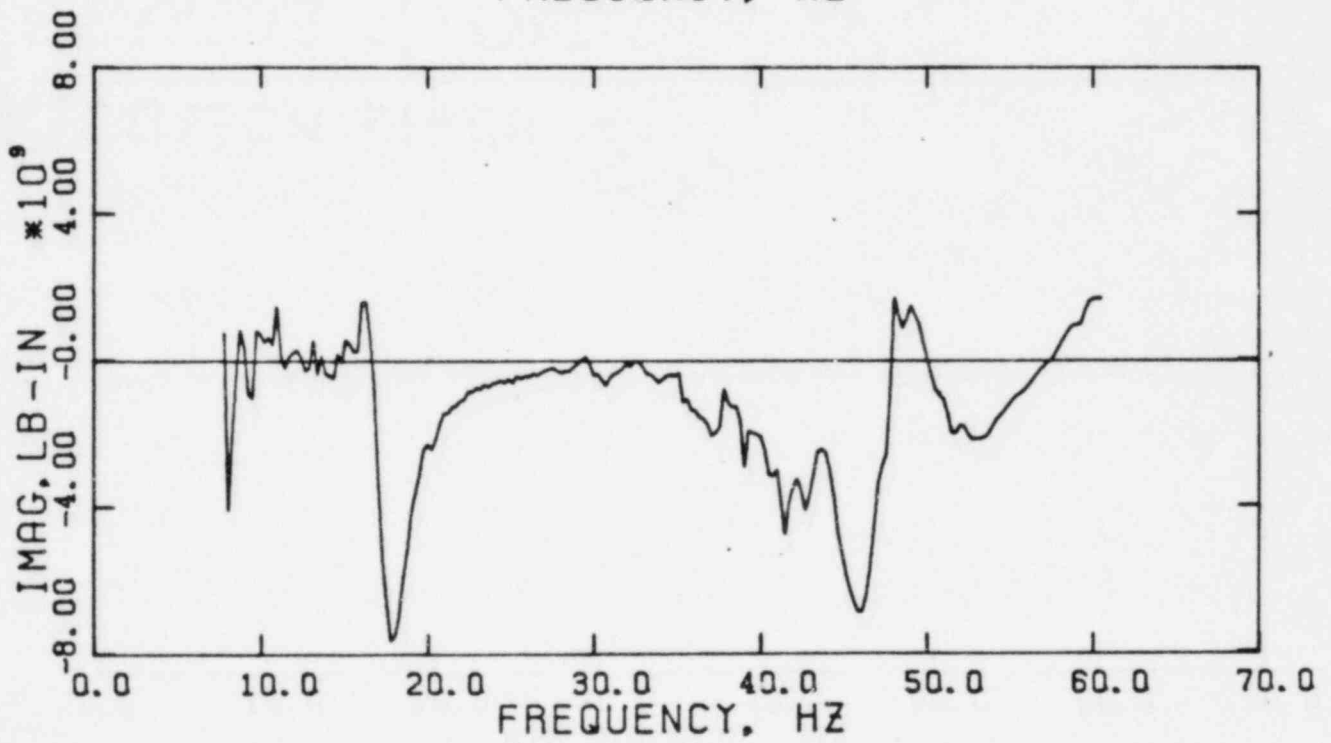
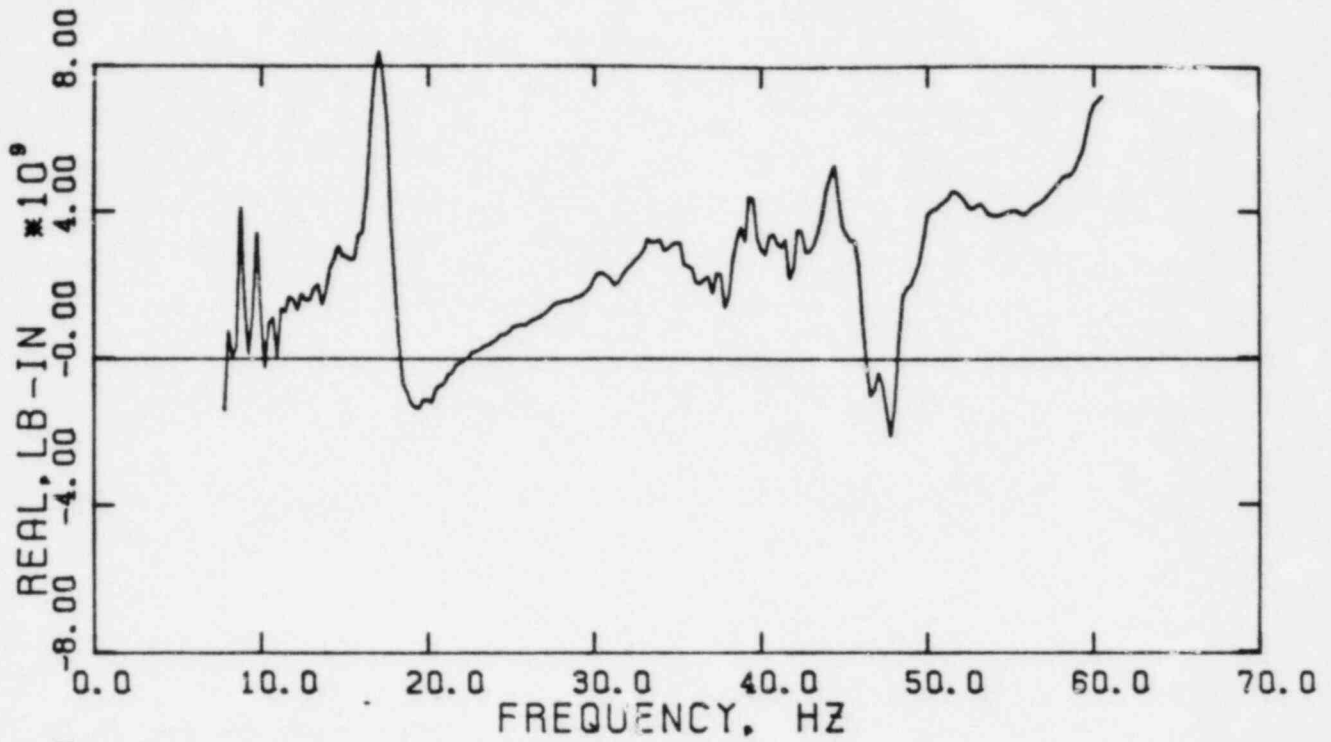
FOUNDATION IMPEDANCES,
 K_{12} AND K_{21}
VERSUS FREQUENCY

Approved by

Checked by

Drawn by

Compiled by



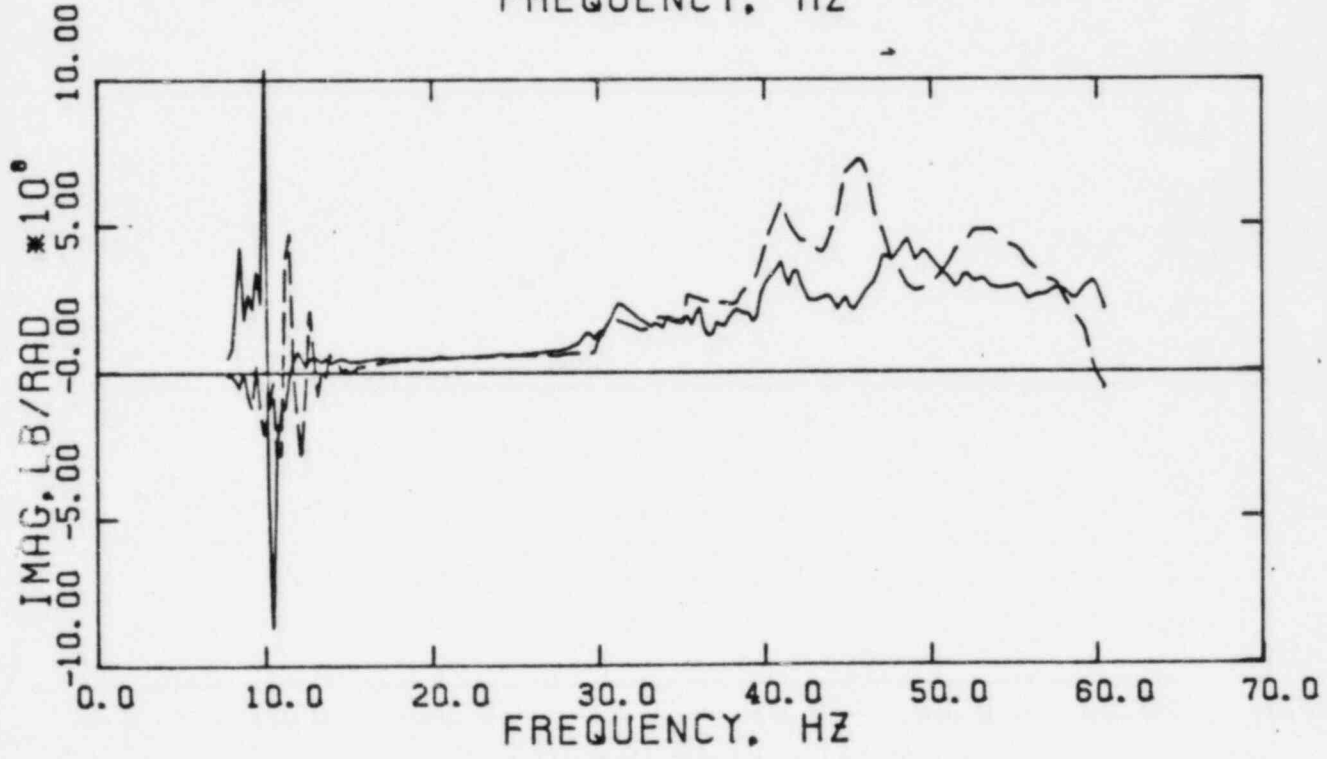
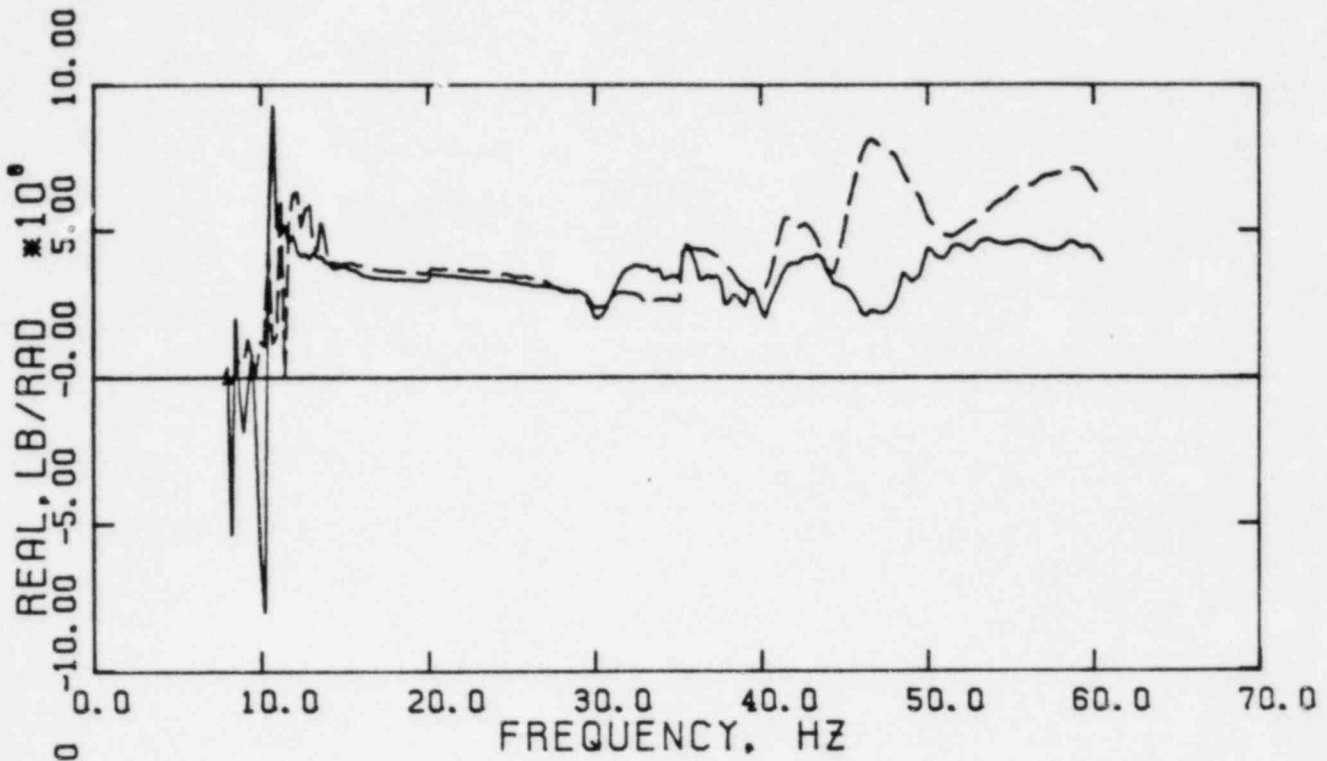
 The Earth Technology Corporation	PROJECT NO.: 83-164
	SCE&G
FOUNDATION IMPEDANCE, K22, VERSUS FREQUENCY	
1-83	FIGURE 8

Approved by

Checked by

Drawn by

Compiled by



_____ 1st EXPERIMENT (Eqn.5-13)
 - - - - - 2nd EXPERIMENT (Eqn.5-14)

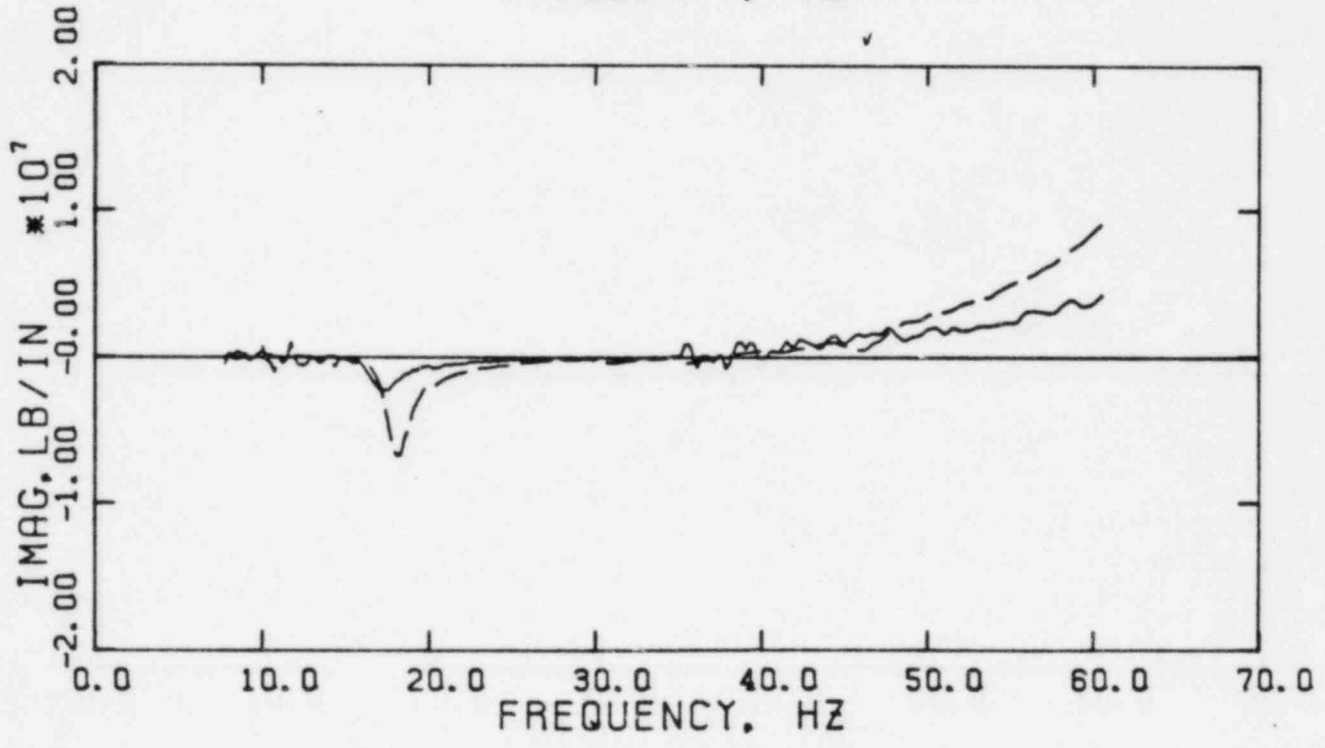
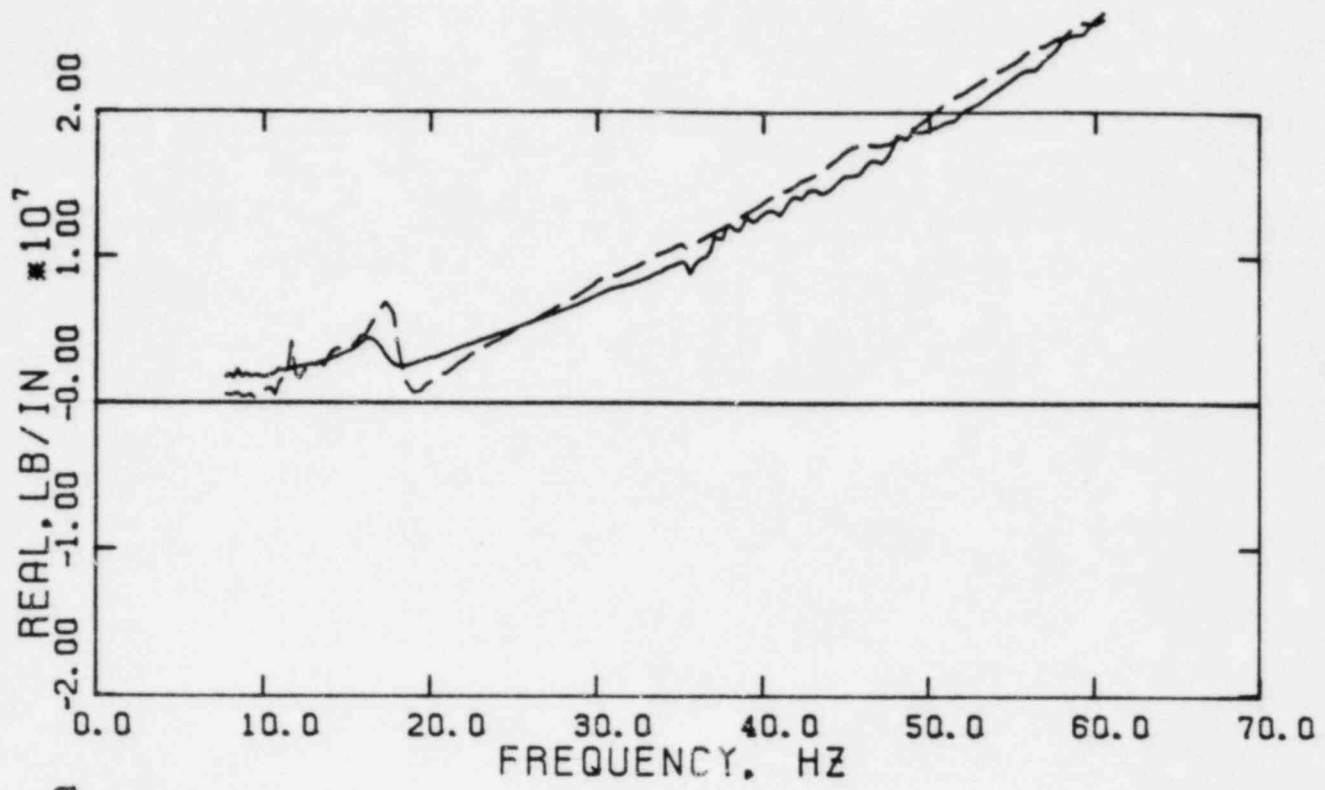
 The Earth Technology Corporation	PROJECT NO.:	83 164
	SCE&G	
ROTATIONAL STIFFNESS OF HUT, K_e , VERSUS FREQUENCY		
1-83	FIGURE 9	

Approved by

Checked by

Drawn by

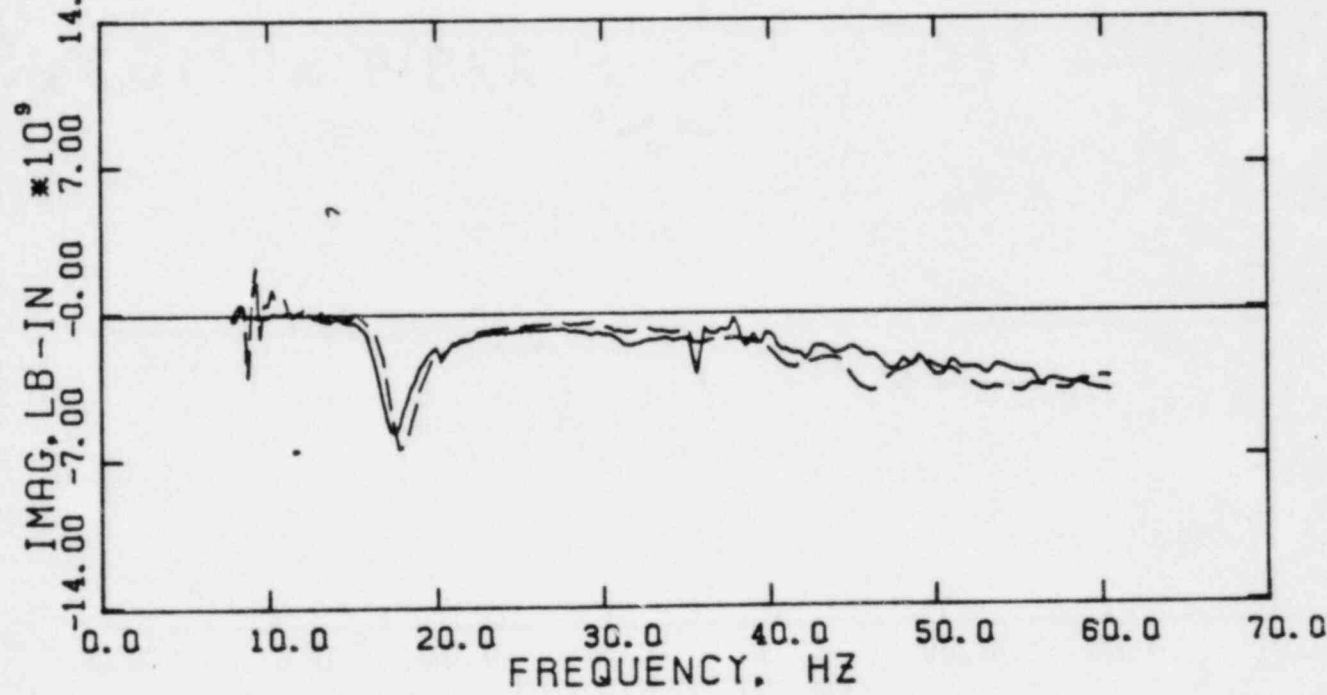
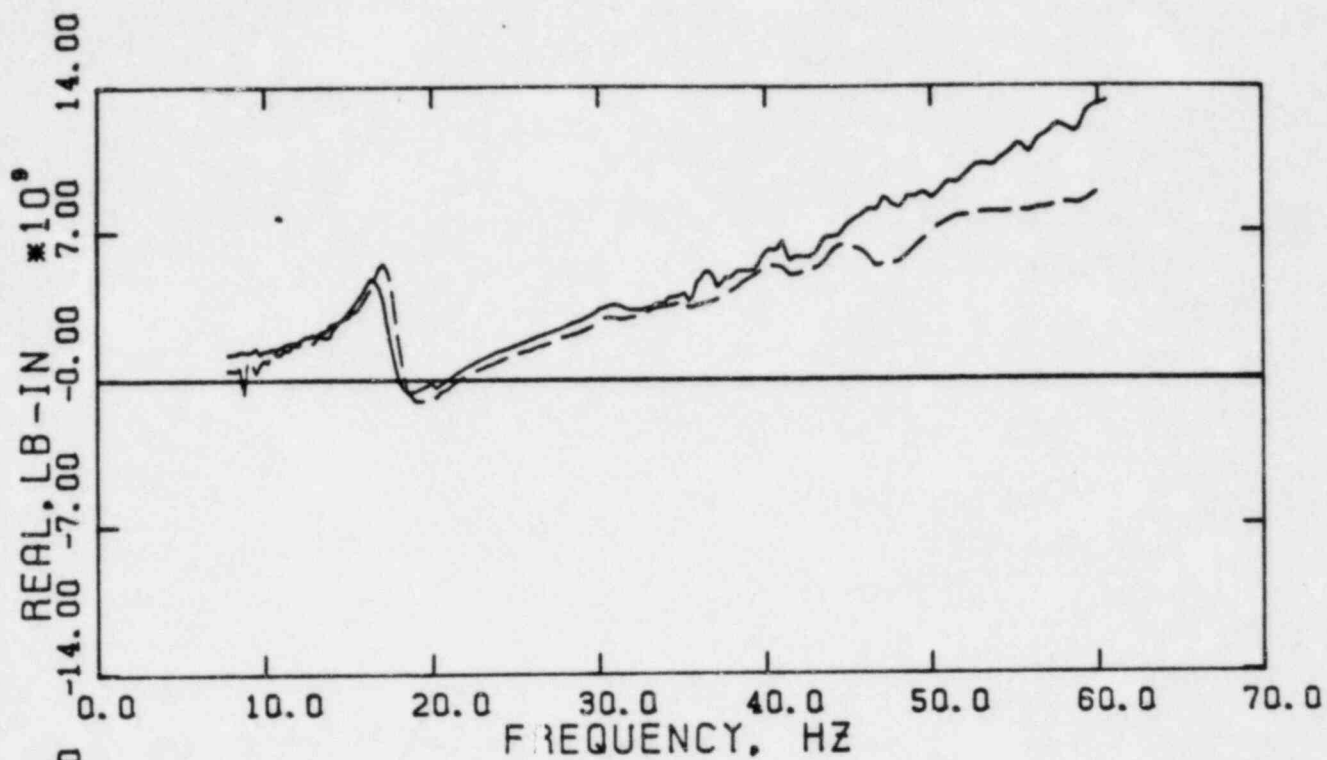
Compiled by



—— 1st EXPERIMENT (Eqn.5-15)
- - - 2nd EXPERIMENT (Eqn.5-16)

 The Earth Technology Corporation	PROJECT NO.:	83-164
	SCE&G	
FOUNDATION IMPEDANCE, K_{11} , VERSUS FREQUENCY ASSUMING $K_{12}=K_{21}=0$		
1-83	FIGURE 10	

Approved by _____
Checked by _____
Drawn by _____
Compiled by _____



———— 1st EXPERIMENT (Eqn.5-17)
----- 2nd EXPERIMENT (Eqn.5-18)

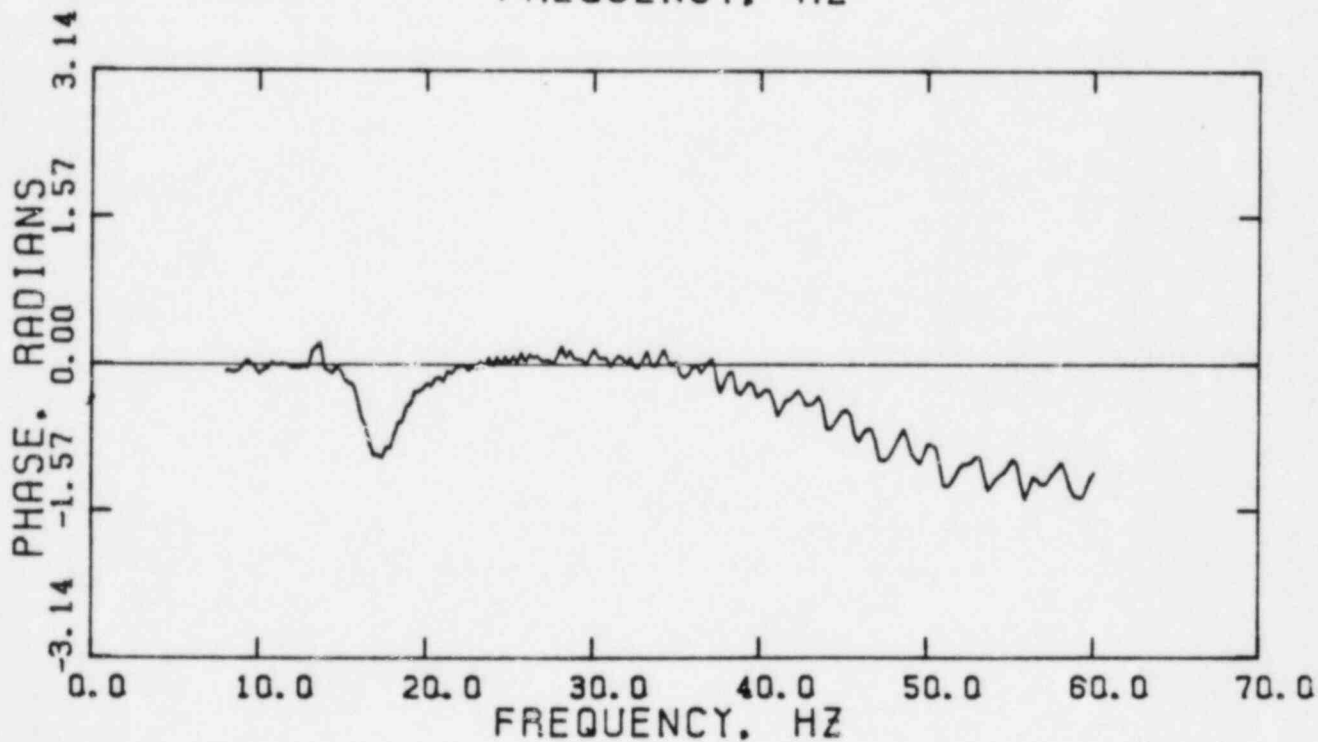
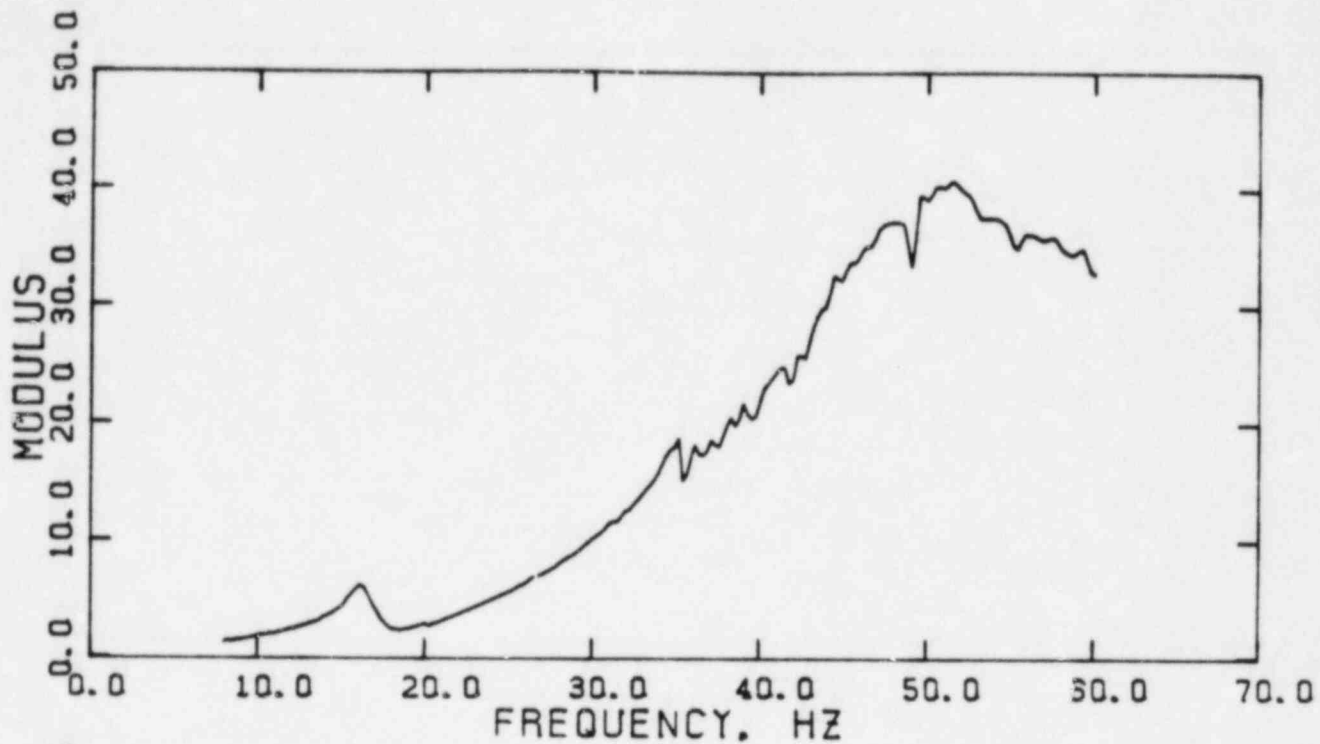
 The Earth Technology Corporation	PROJECT NO.:	83-164
	SCE&G	
FOUNDATION IMPEDANCE, K_{22} , VERSUS FREQUENCY ASSUMING $K_{12}=K_{21}=0$		
1-83	FIGURE 11	

Approved by

Checked by

Drawn by

Compiled by



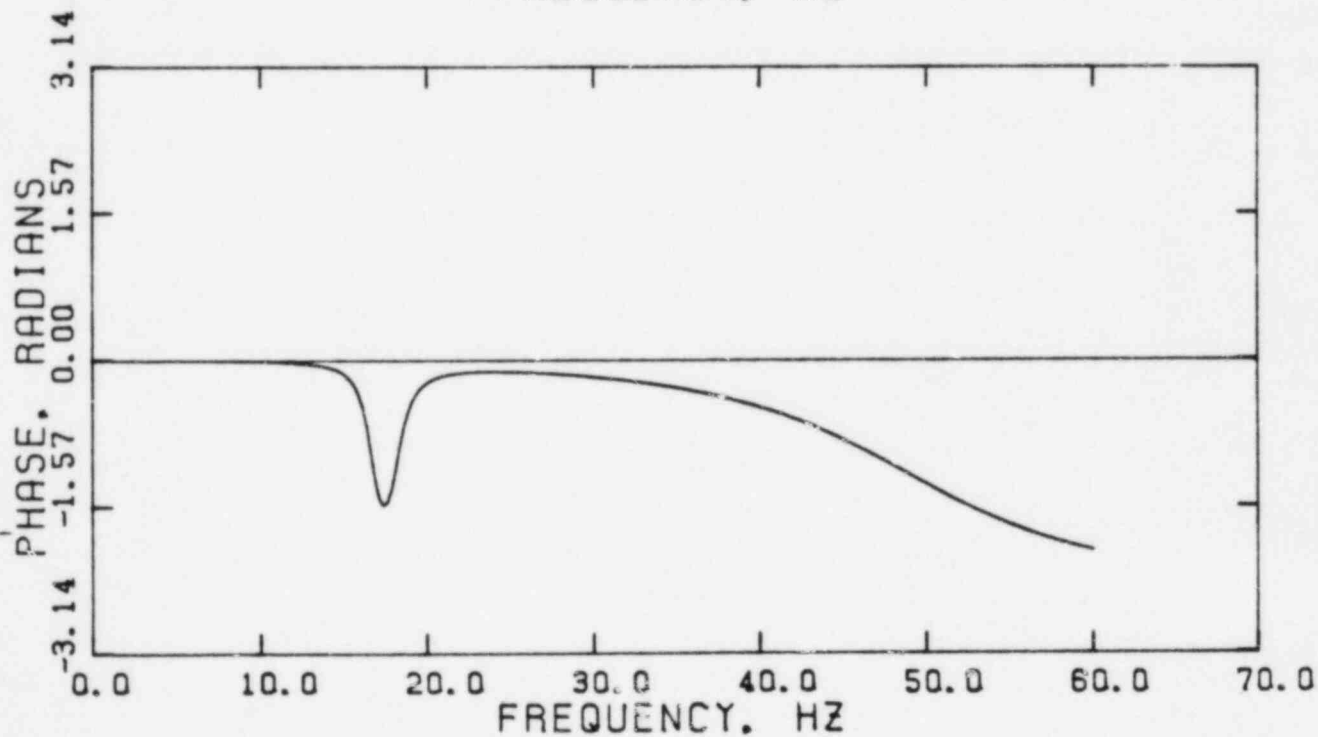
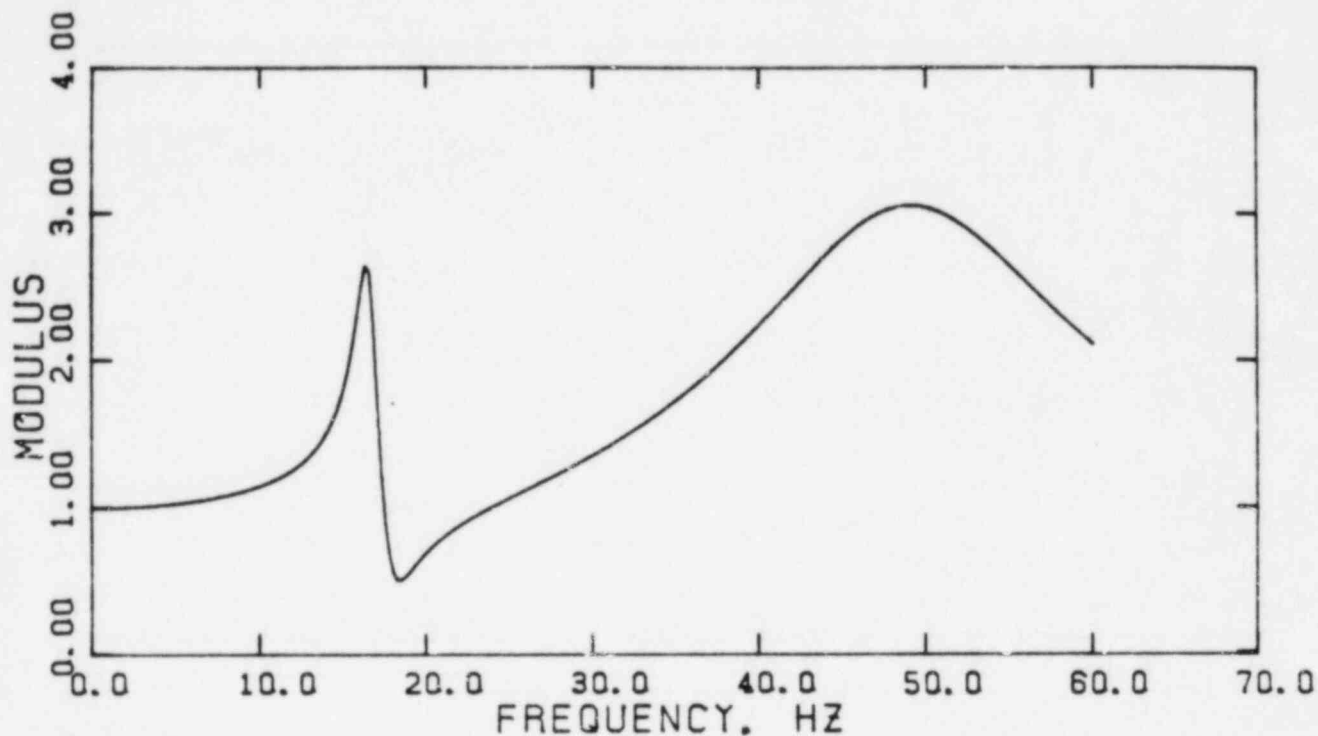
 The Earth Technology Corporation	PROJECT NO.: 83-164
	SCE&G
TRANSFER FUNCTION VS FREQUENCY STIFFNESS APPROACH X DIRECTION	
1-83	FIGURE 12

Approved by _____

Checked by _____

Drawn by _____

Compiled by _____



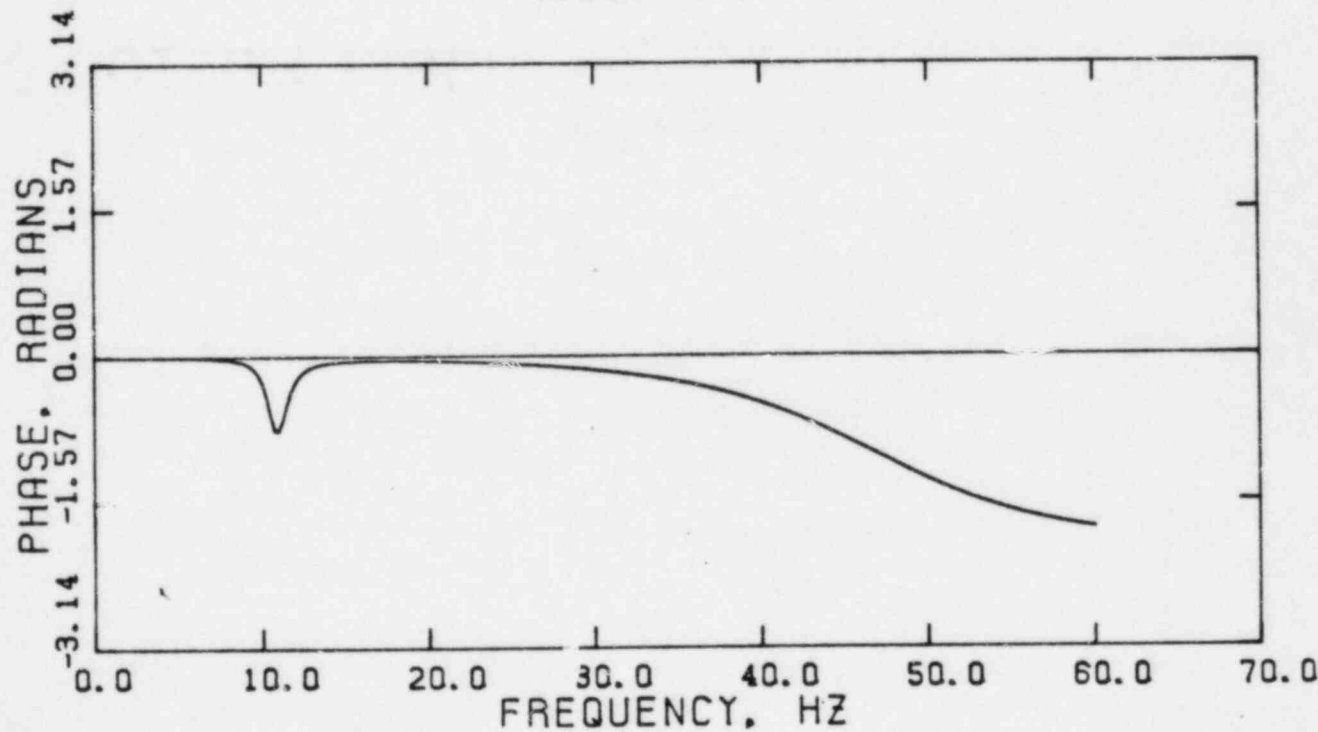
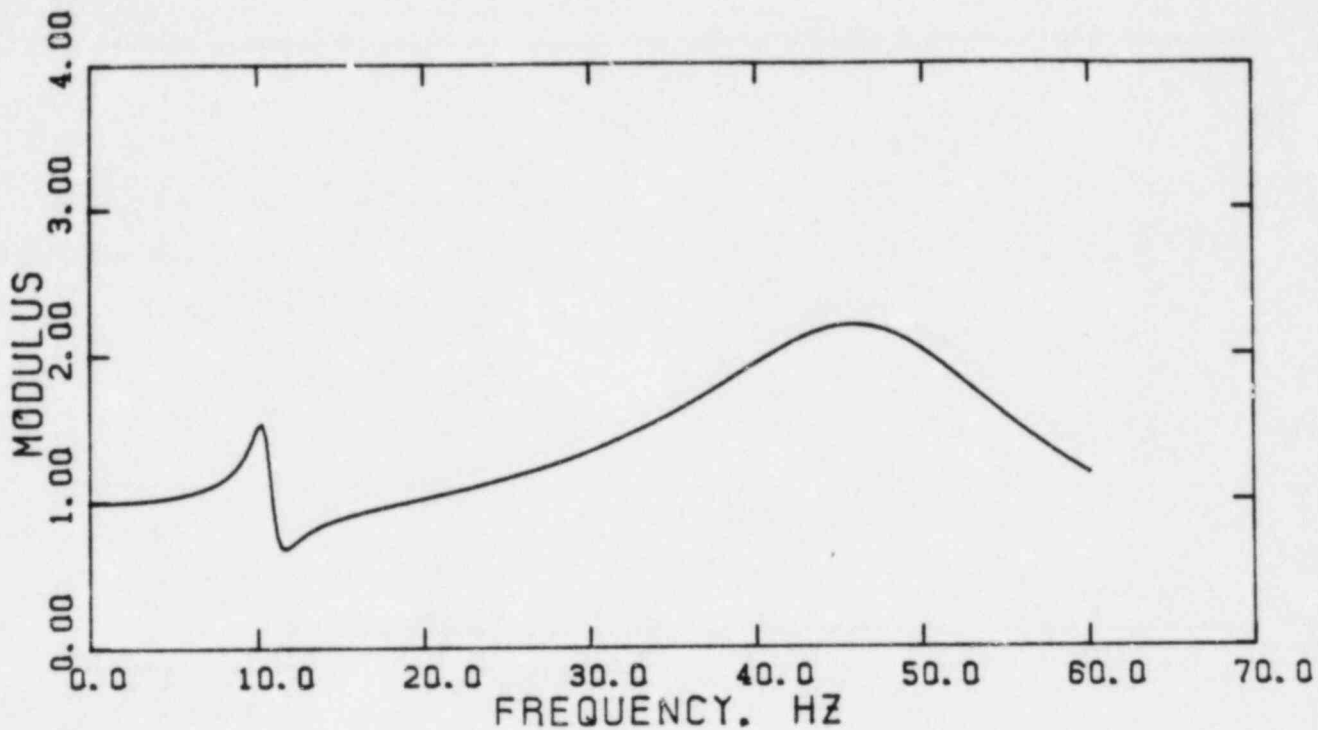
 The Earth Technology Corporation	PROJECT NO.: 83-166
	SGE&G
TRANSFER FUNCTION VS FREQUENCY MODAL APPROACH X DIRECTION	
1-83	FIGURE 13

Approved by _____

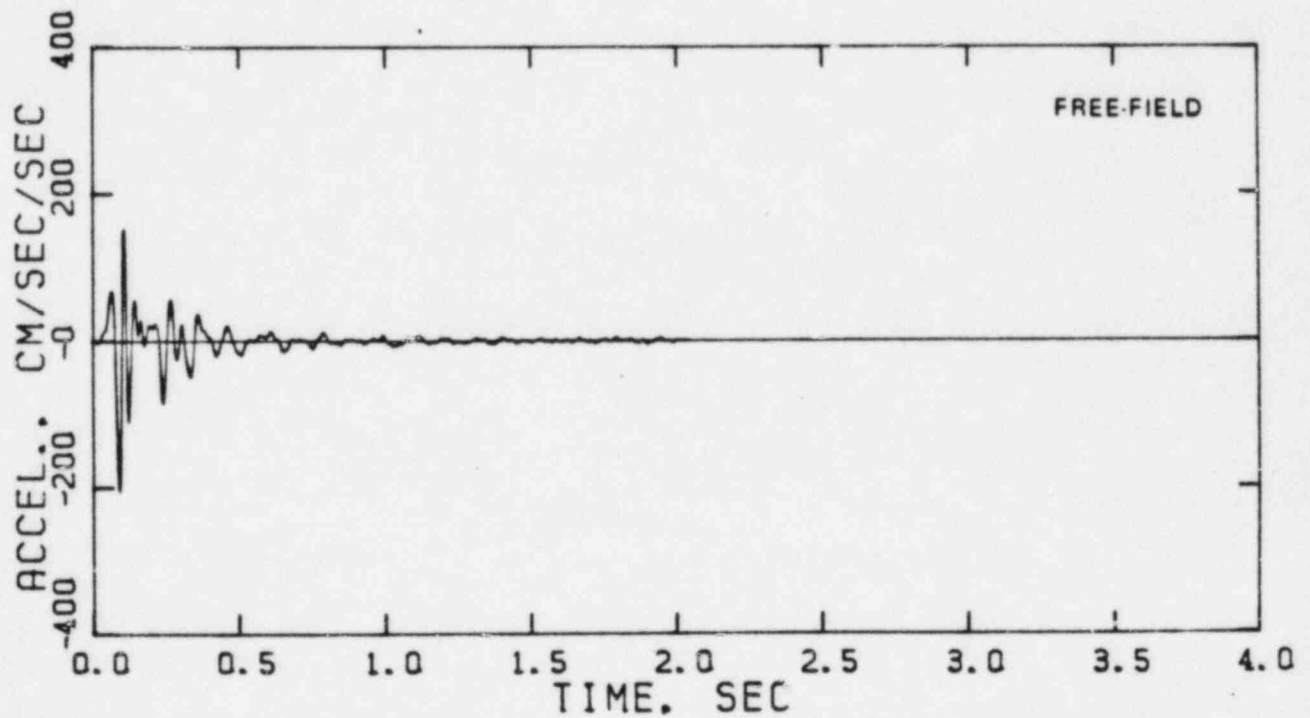
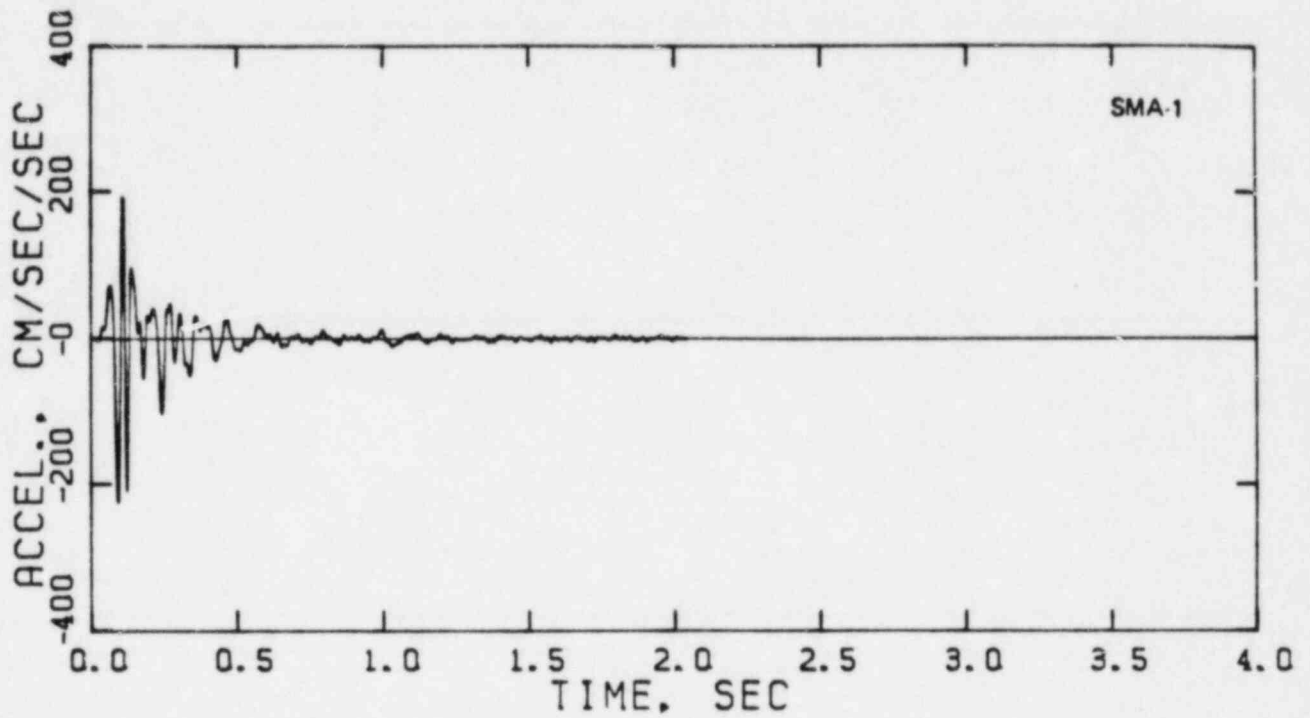
Checked by _____

Drawn by _____

Compiled by _____



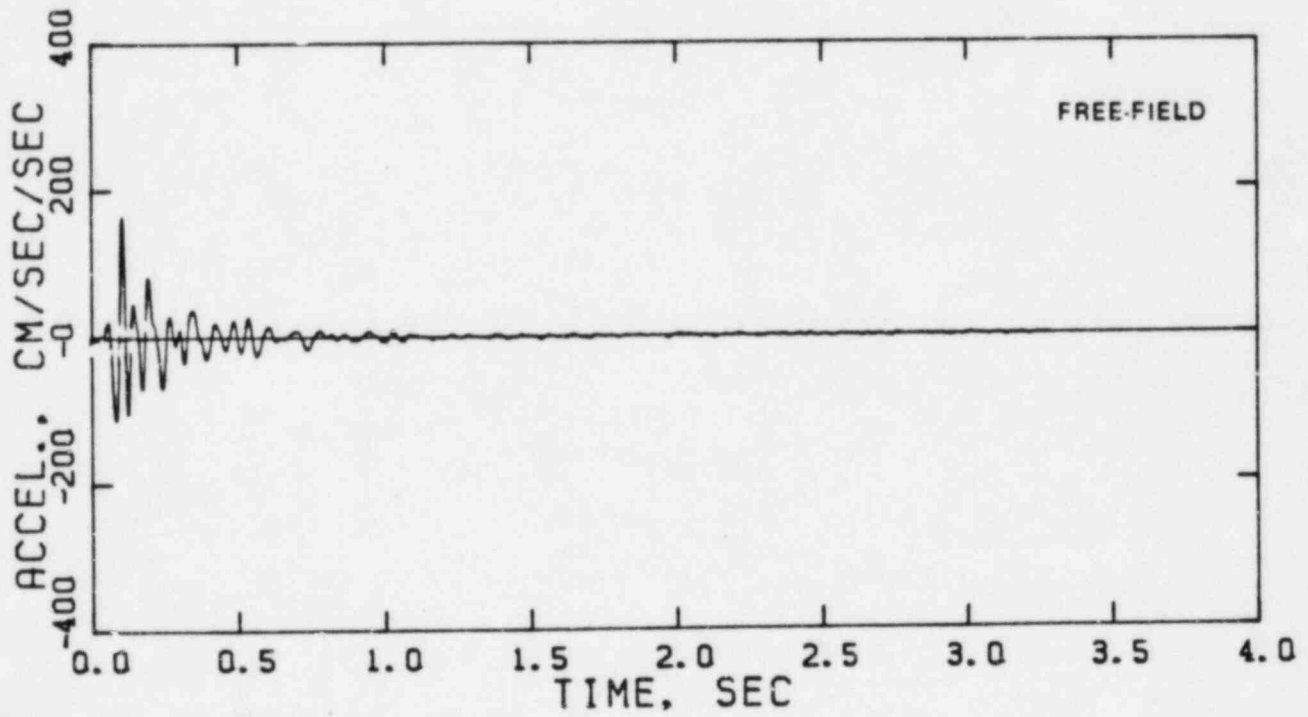
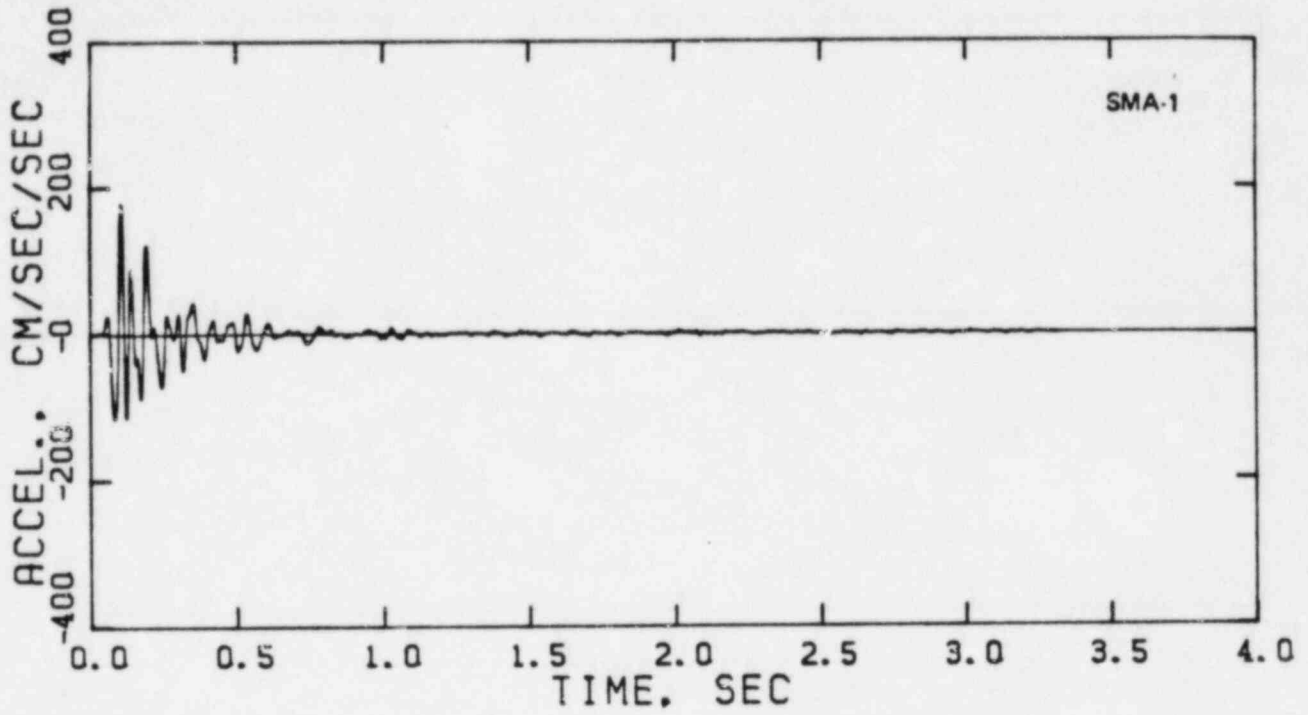
 The Earth Technology Corporation	PROJECT NO.: 83-164
	SCE&G
TRANSFER FUNCTION VS FREQUENCY MODAL APPROACH Y DIRECTION	
1-83	FIGURE 14



Drawn by _____

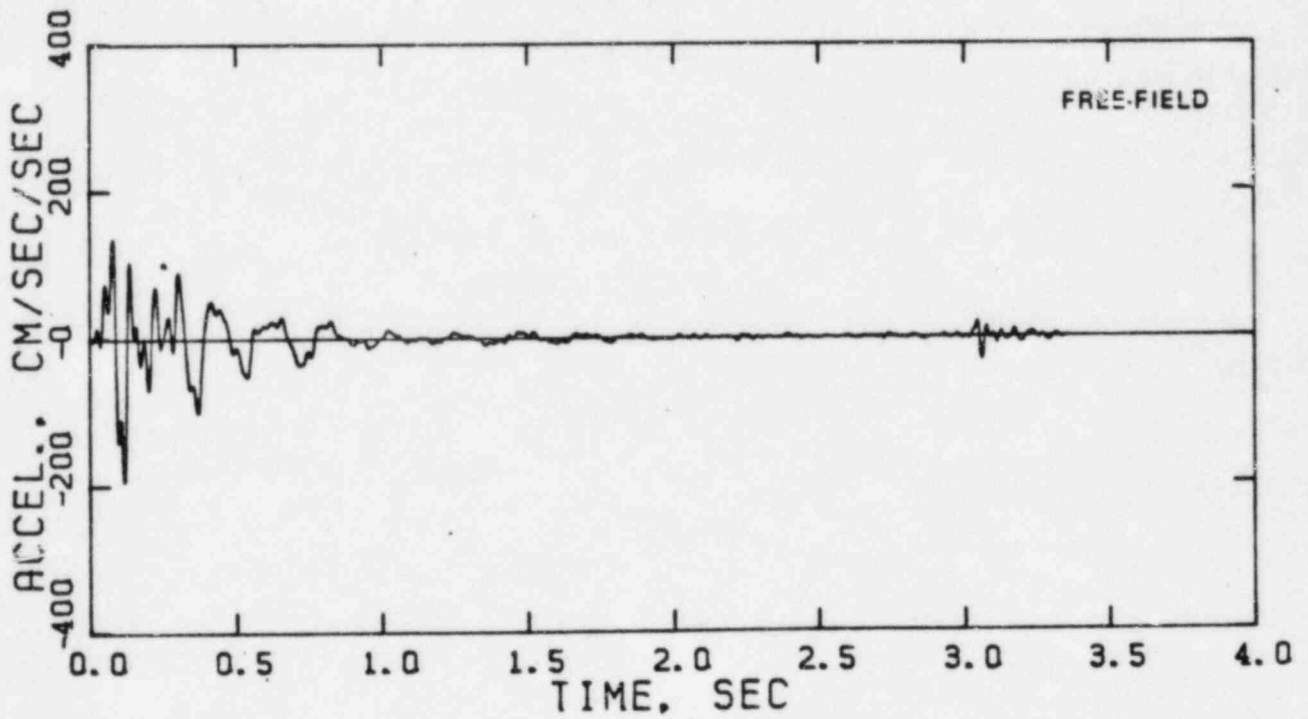
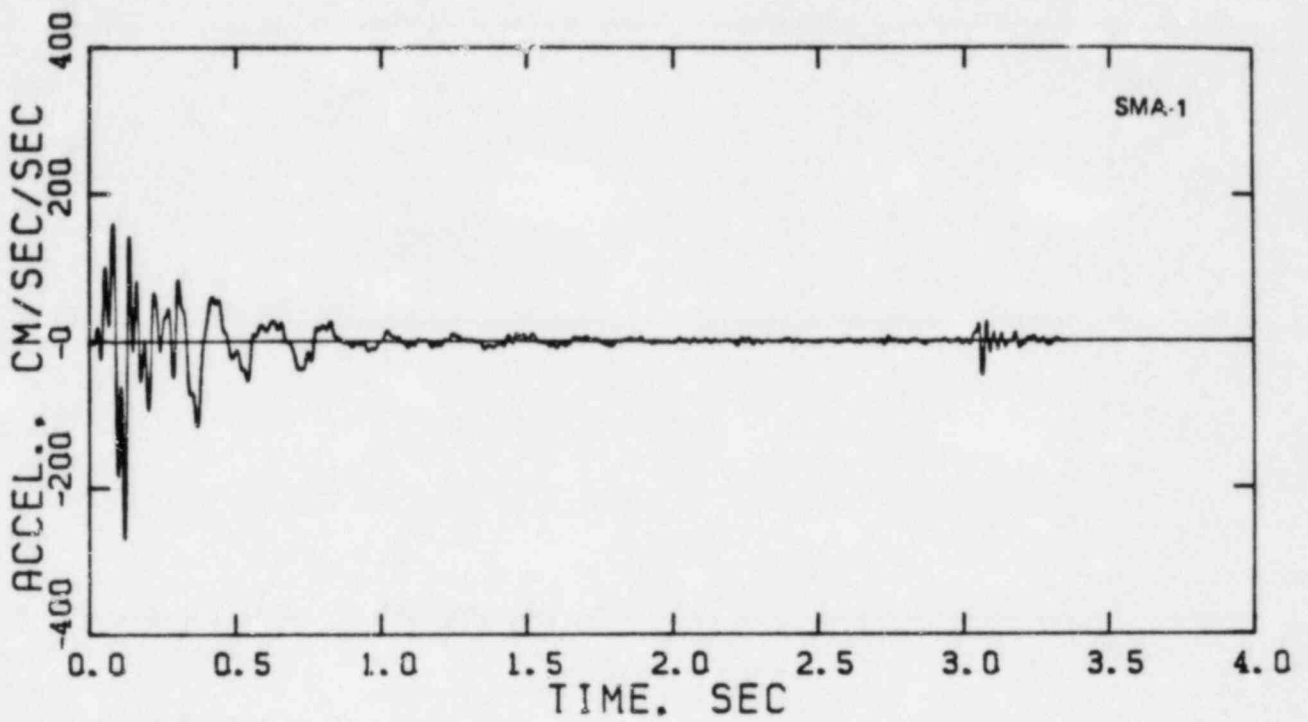
Compiled by _____

	PROJECT NO.:	R3 164
	S&C&G	
RECORDED SMA-1 VS COMPUTED FREE-FIELD ACCELEROGRAMS 090° DIRECTION 27 AUGUST 1978 EVENT		
1.83	FIGURE 13a	



	PROJECT NO.:	83-164
	SCE&G	
RECORDED SMA-1 VS COMPUTED FREE-FIELD ACCELEROGRAMS 090° DIRECTION 1978 AFTERSHOCK NO. 1		
1-83	FIGURE 15b	

Approved by _____
 Checked by _____
 Drawn by _____
 Compiled by _____

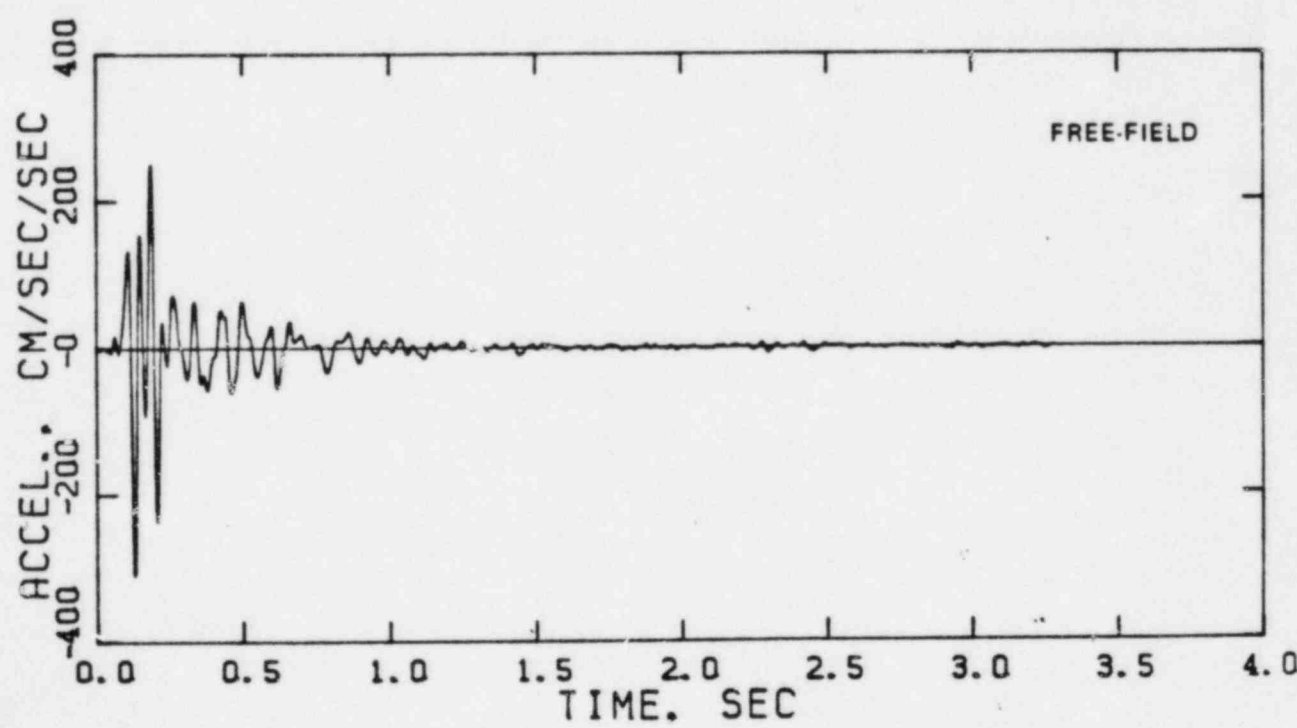
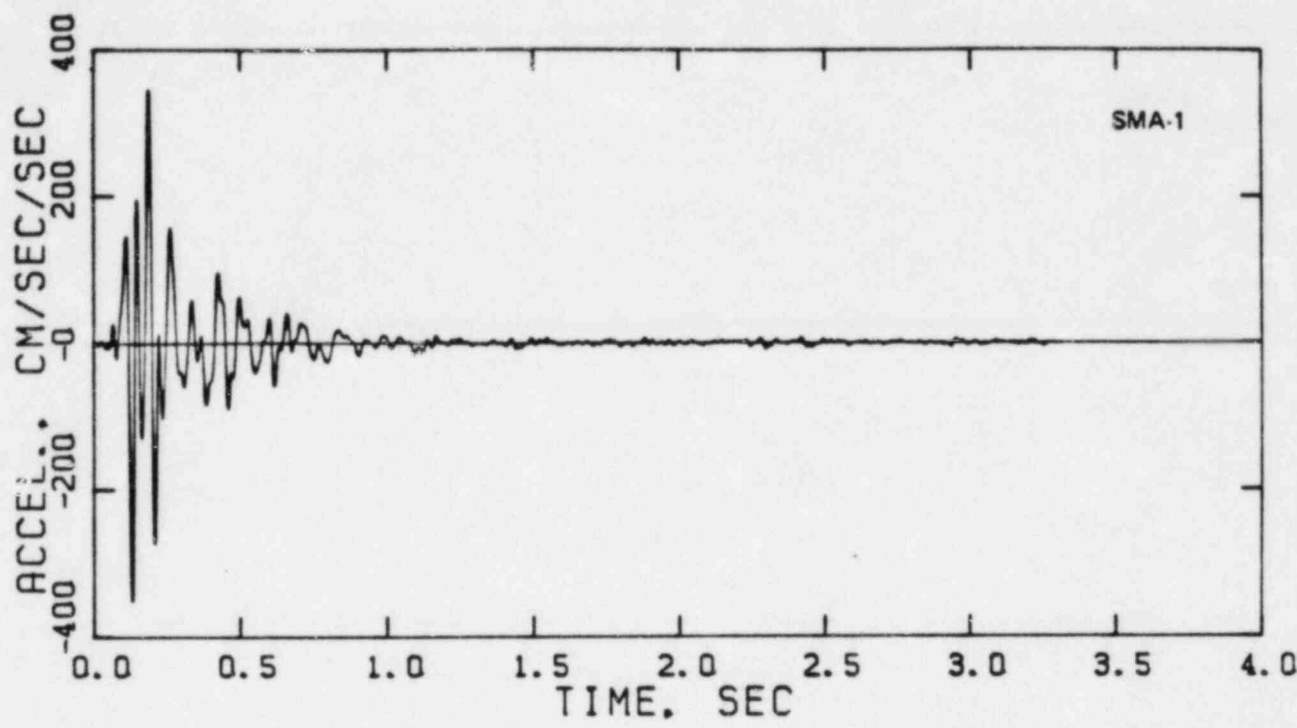


Drawn by _____

Completed by _____

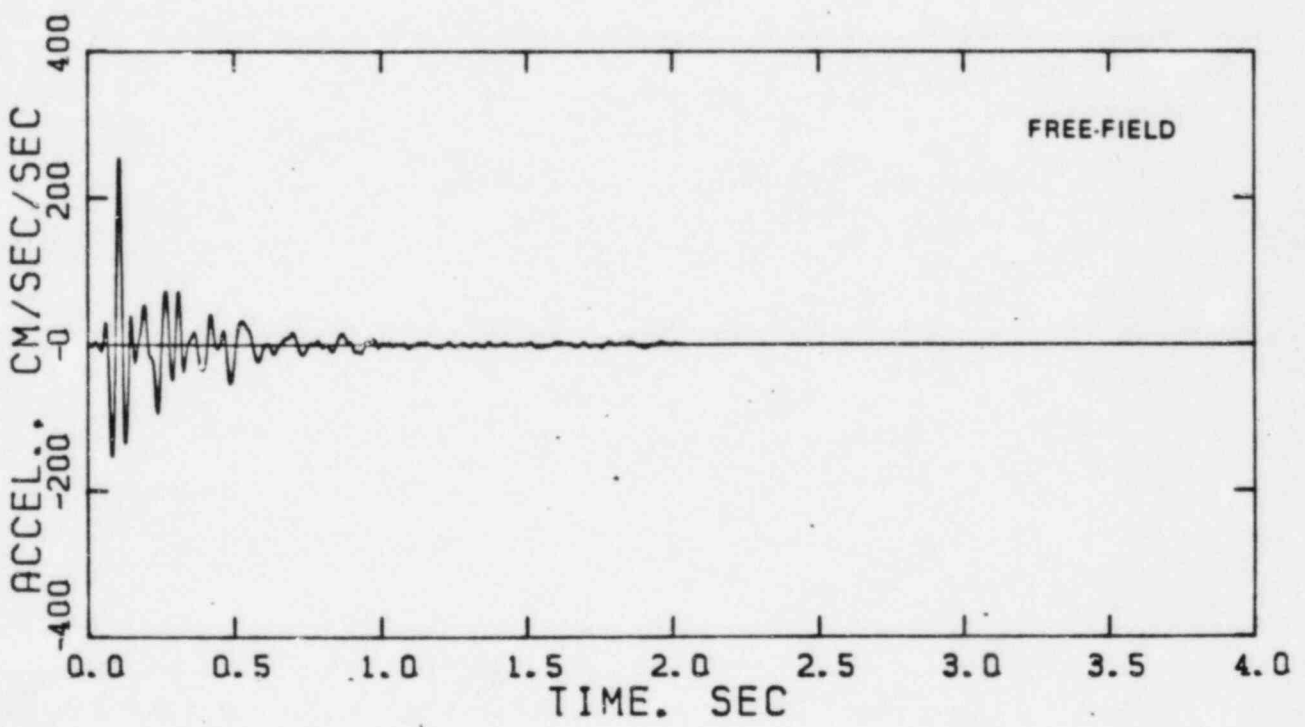
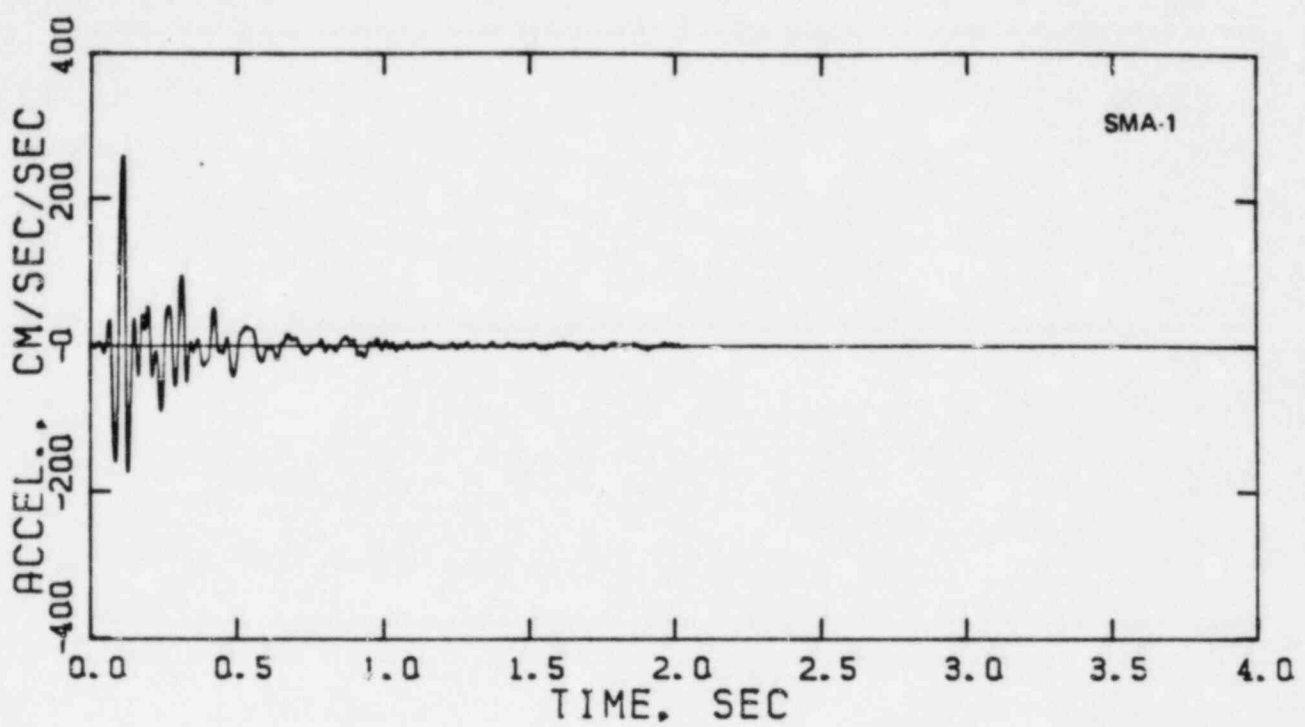
	PROJECT NO.:	83-164
	SCE&G	
RECORDED SMA-1 VS COMPUTED FREE-FIELD ACCELEROGRAMS 090° DIRECTION 1978 AFTERSHOCK NO. 2		
1-83	FIGURE 15c	

Approved by _____
Checked by _____
Drawn by _____
Compiled by _____

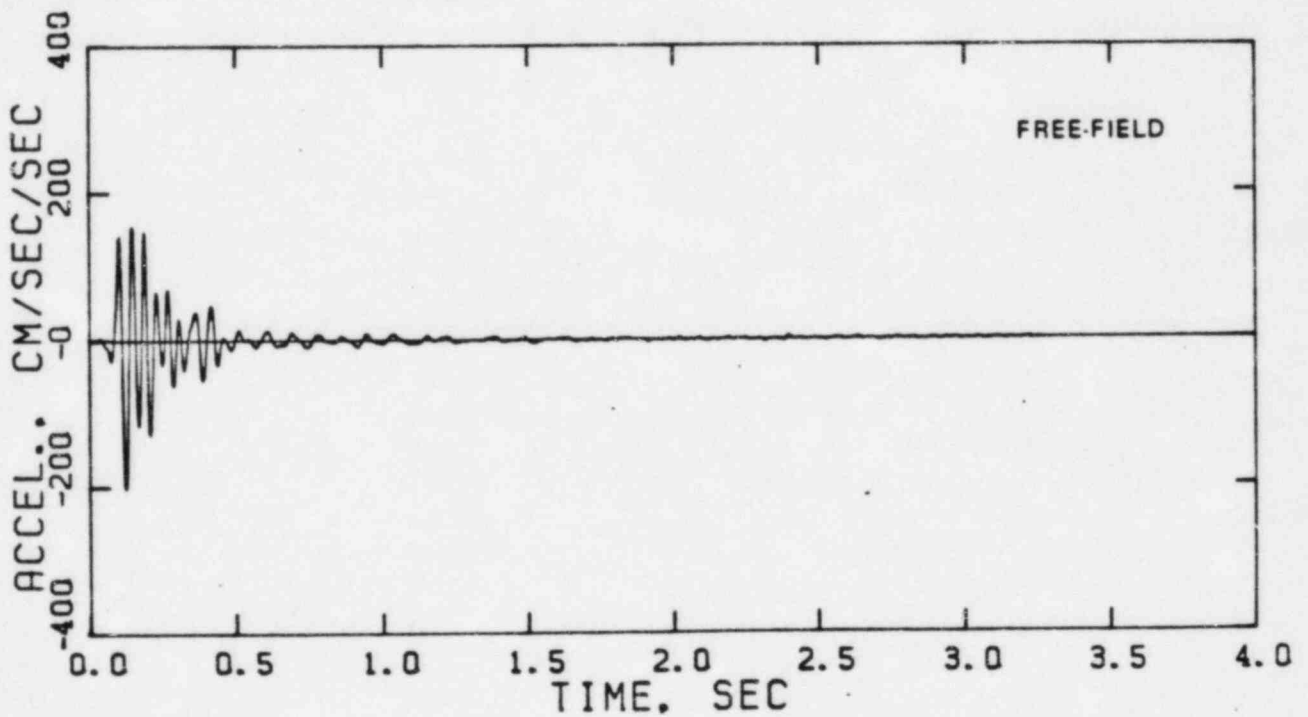
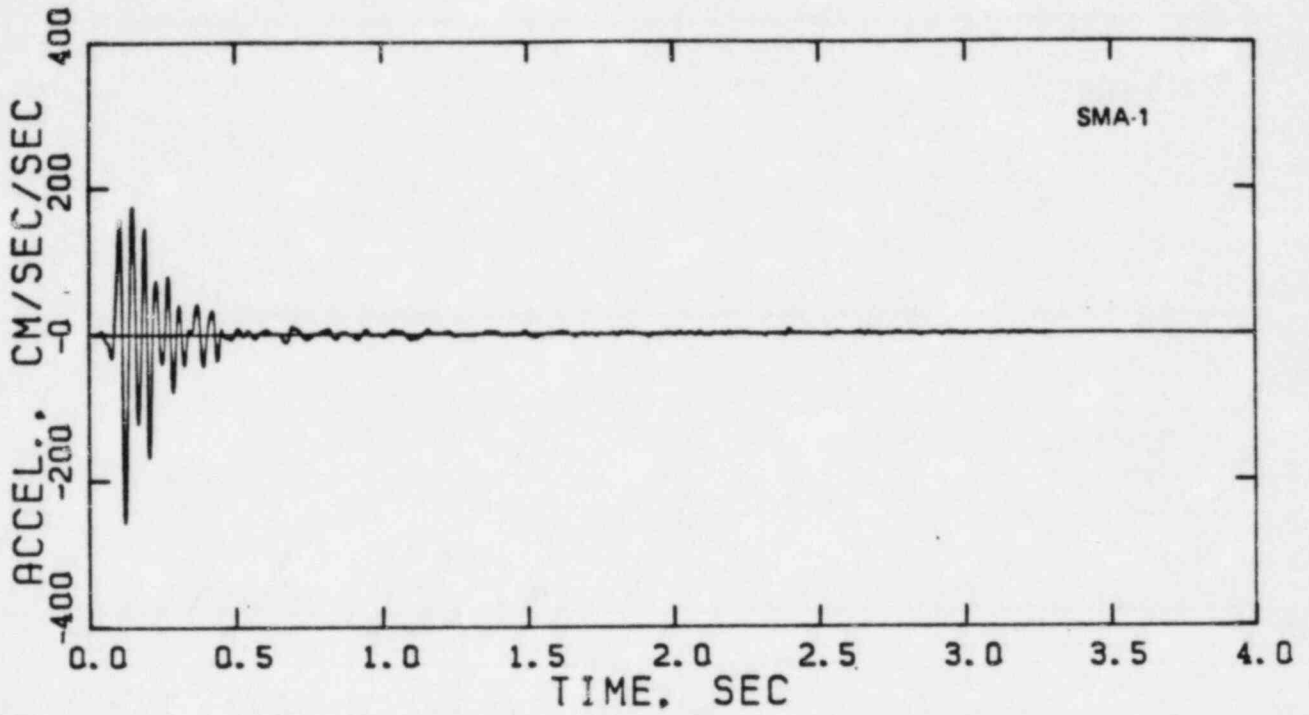


 The Earth Technology Corporation	PROJECT NO.: 83-164
	SCE&G
RECORDED SMA-1 VS COMPUTED FREE-FIELD ACCELEROGRAMS 090° DIRECTION 16 OCTOBER 1979 EVENT	
1-83	FIGURE 15d

Approved by _____
Checked by _____
Drawn by _____
Compiled by _____



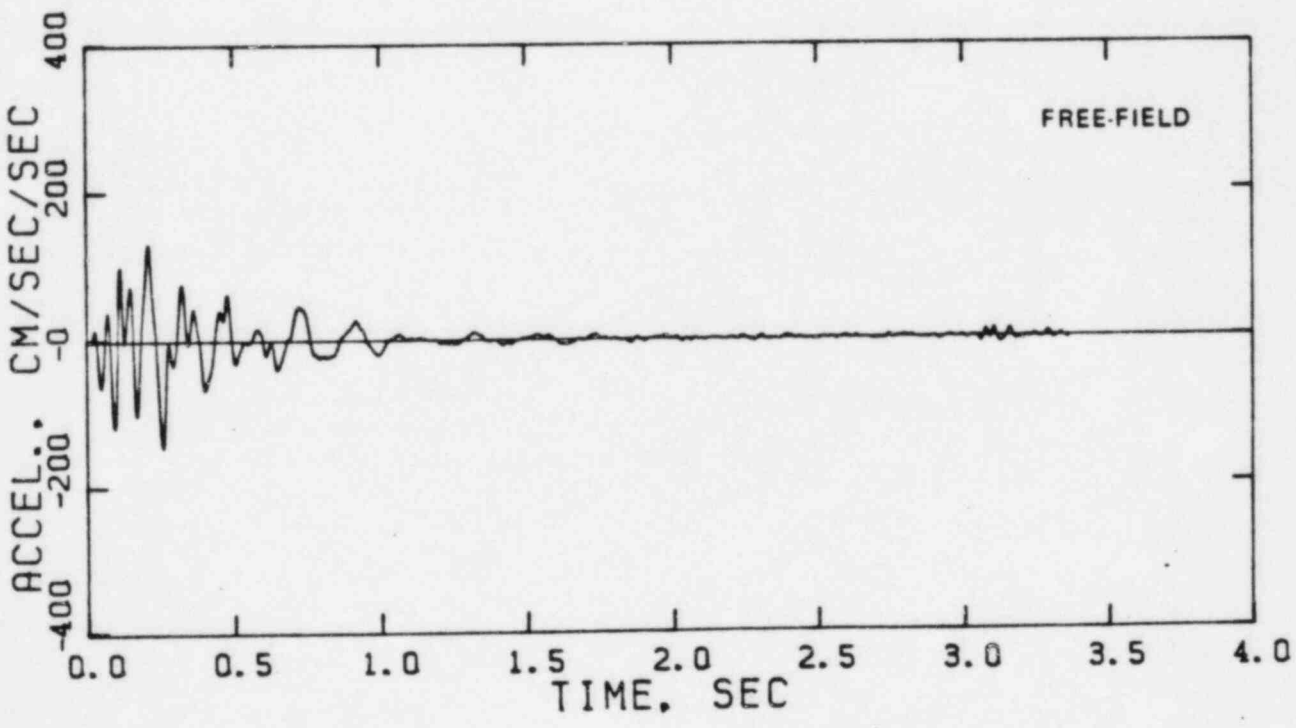
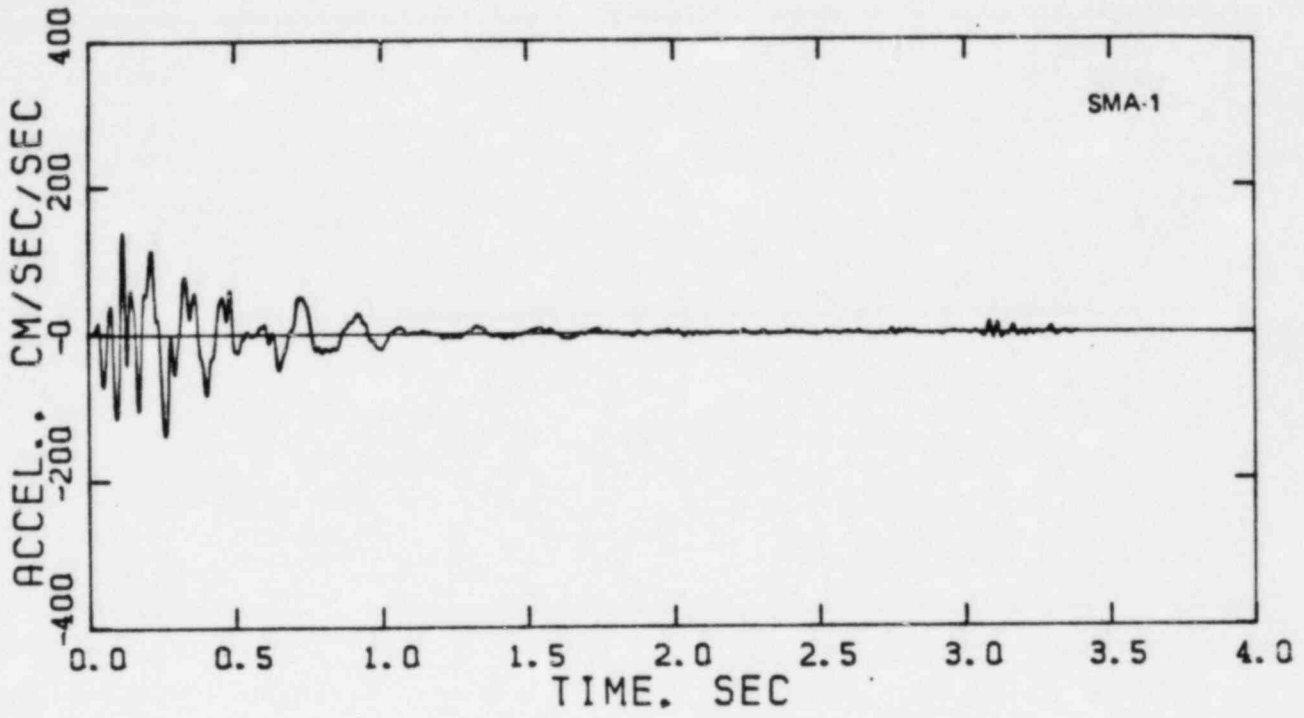
 The Earth Technology Corporation	PROJECT NO.: 83-164
	SCE&G
RECORDED SMA-1 VS COMPUTED FREE-FIELD ACCELEROGRAMS 180° DIRECTION 27 AUGUST 1978 EVENT	
1-83	FIGURE 16a



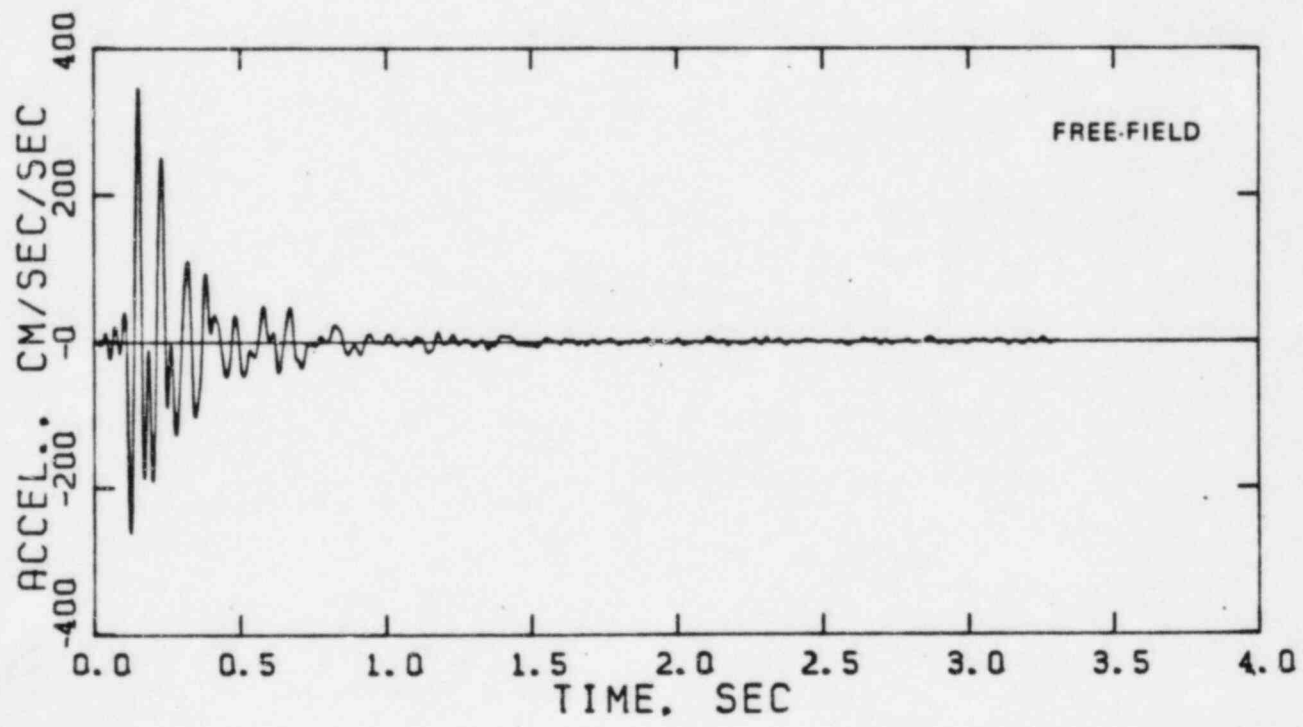
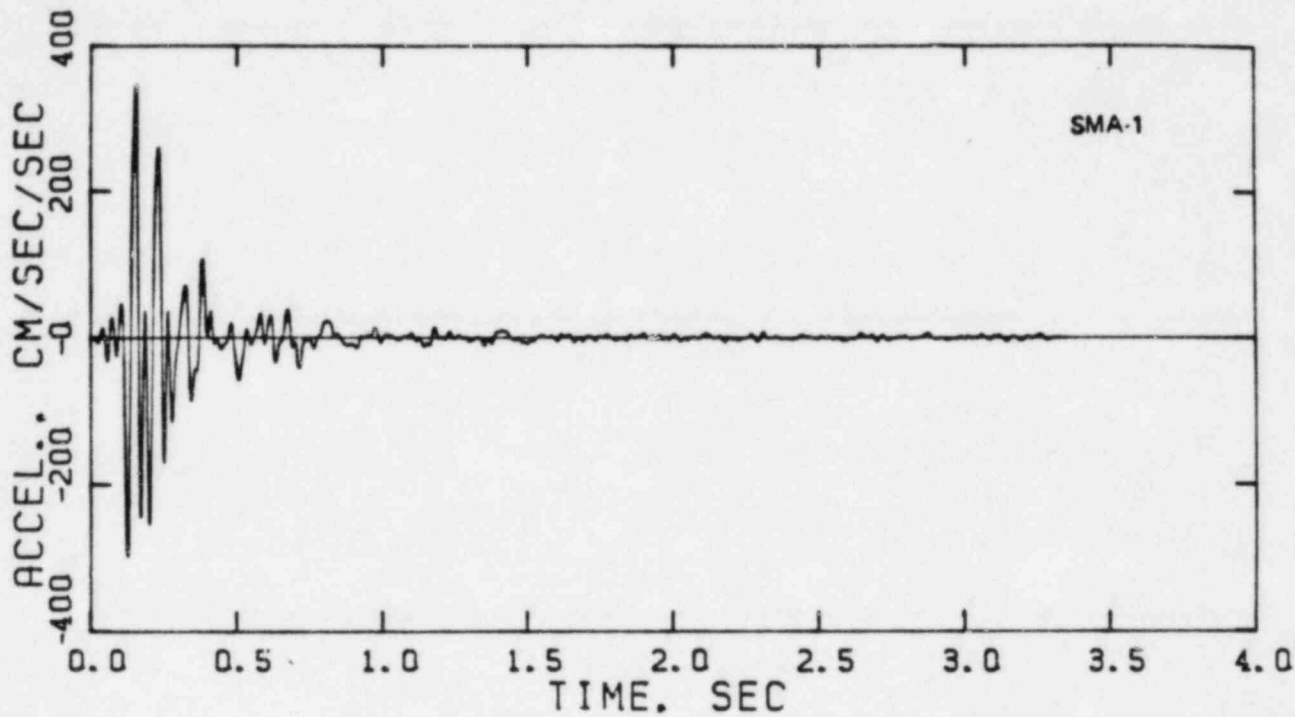
 The Earth Technology Corporation	PROJECT NO.:	83-164
	SCE&G	
RECORDED SMA-1 VS COMPUTED FREE-FIELD ACCELEROGRAMS 180° DIRECTION 1978 AFTERSHOCK NO. 1		
1-83	FIGURE 10b	

Approved by _____
 Checked by _____
 Drawn by _____
 Compiled by _____

Approved by _____
Checked by _____
Drawn by _____
Compiled by _____



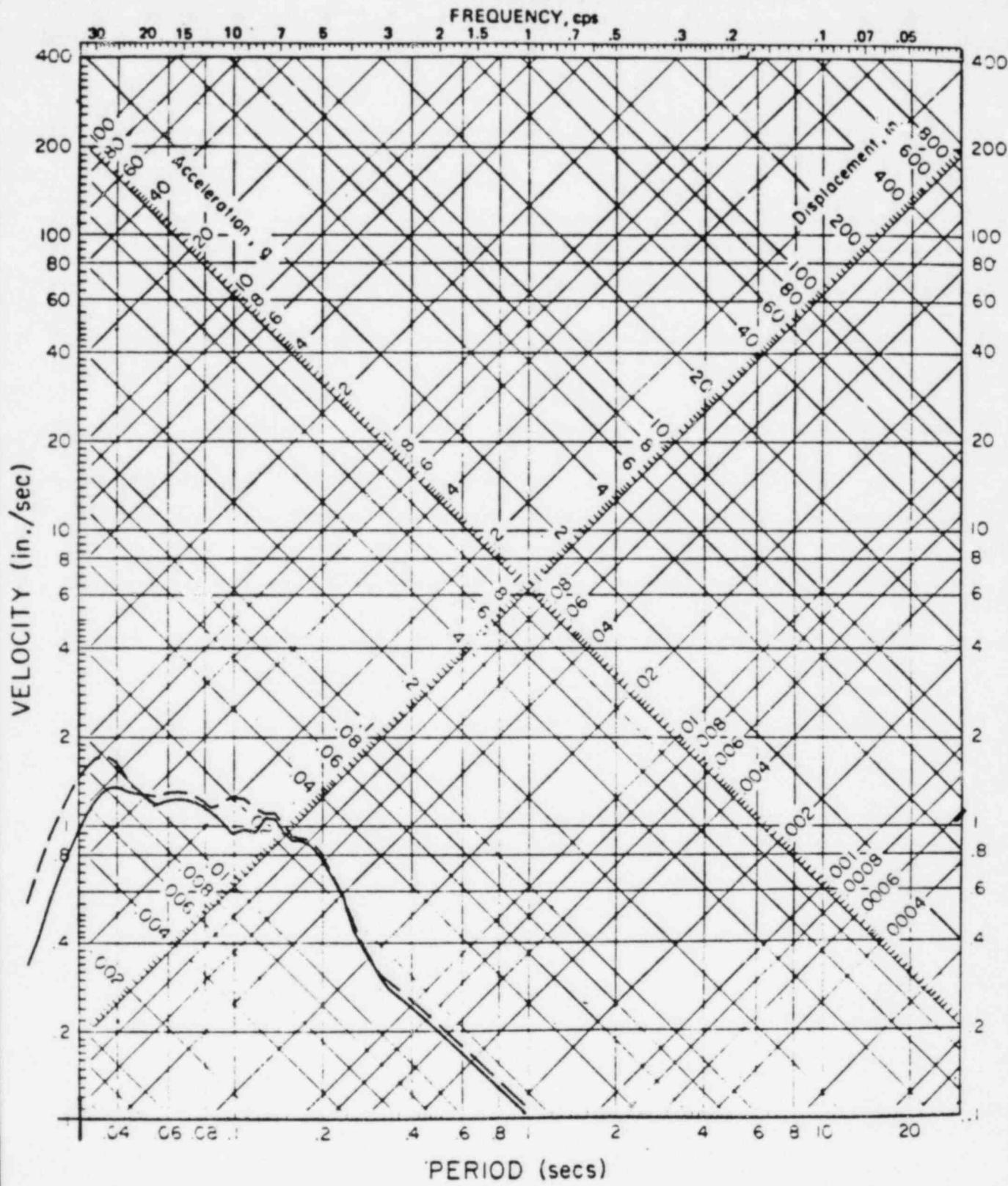
 The Earth Technology Corporation	PROJECT NO.: 83 164
	SCE&G
RECORDED SMA-1 VS COMPUTED FREE-FIELD ACCELEROGRAMS 180° DIRECTION 1978 AFTERSHOCK NO. 2	
1-83	FIGURE 16c



 The Earth Technology Corporation	PROJECT NO.: 83-164
	SCE&G
RECORDED SMA-1 VS COMPUTED FREE-FIELD ACCELEROGRAMS 180° DIRECTION 16 OCTOBER 1979 EVENT	
1-83	FIGURE 16d

Approved by _____
 Checked by _____
 Drawn by _____
 Compiled by _____

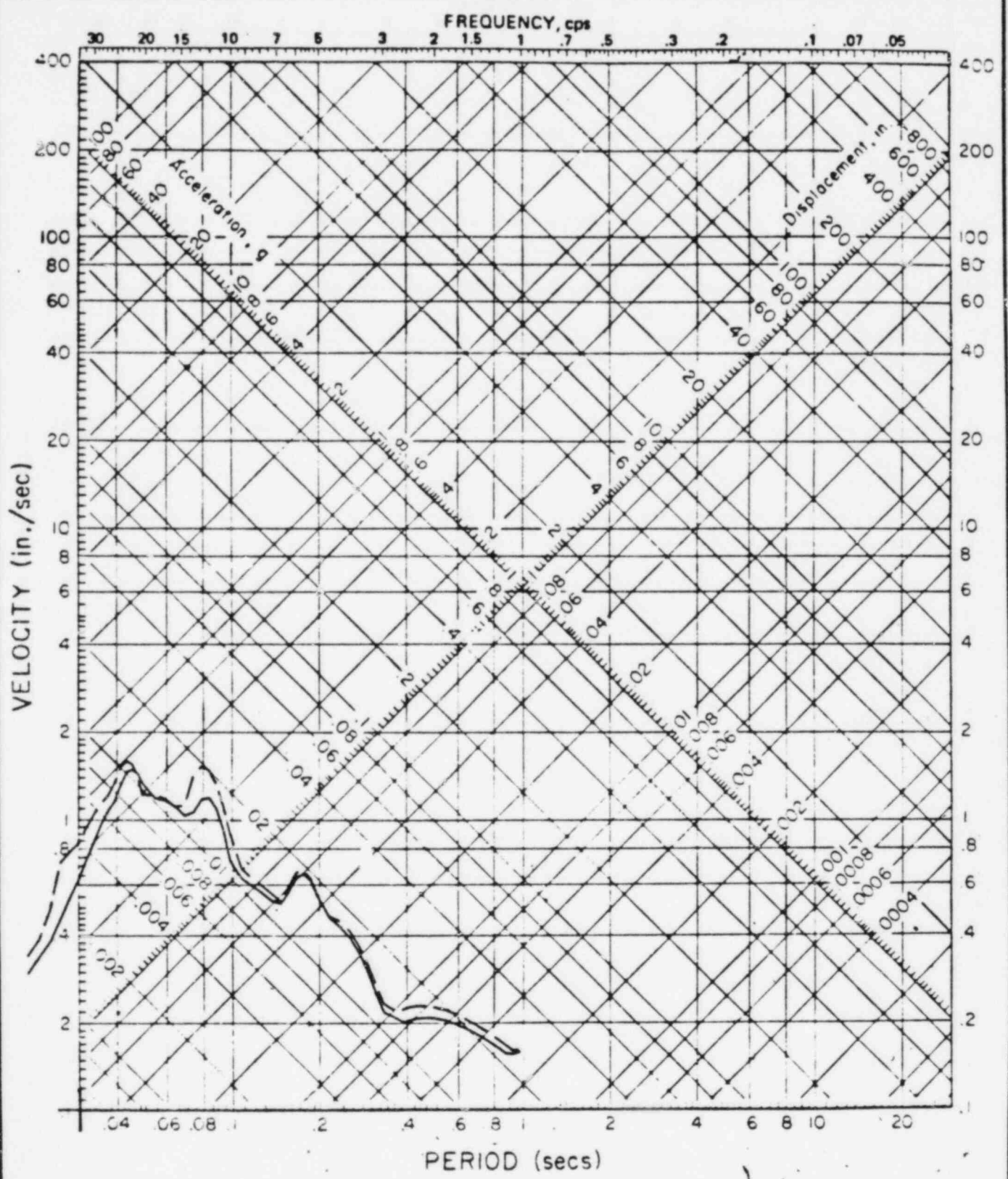
Approved by _____
Checked by _____
Drawn by _____
Compiled by _____



--- SMA-1
— FREE-FIELD

 The Earth Technology Corporation	PROJECT NO.: 82-164
	SGE&G
RESPONSE SPECTRA OF SMA-1 AND FREE-FIELD ACCELEROGRAMS 090° DIRECTION 27 AUGUST 1978 EVENT	
1-83	FIGURE 17a

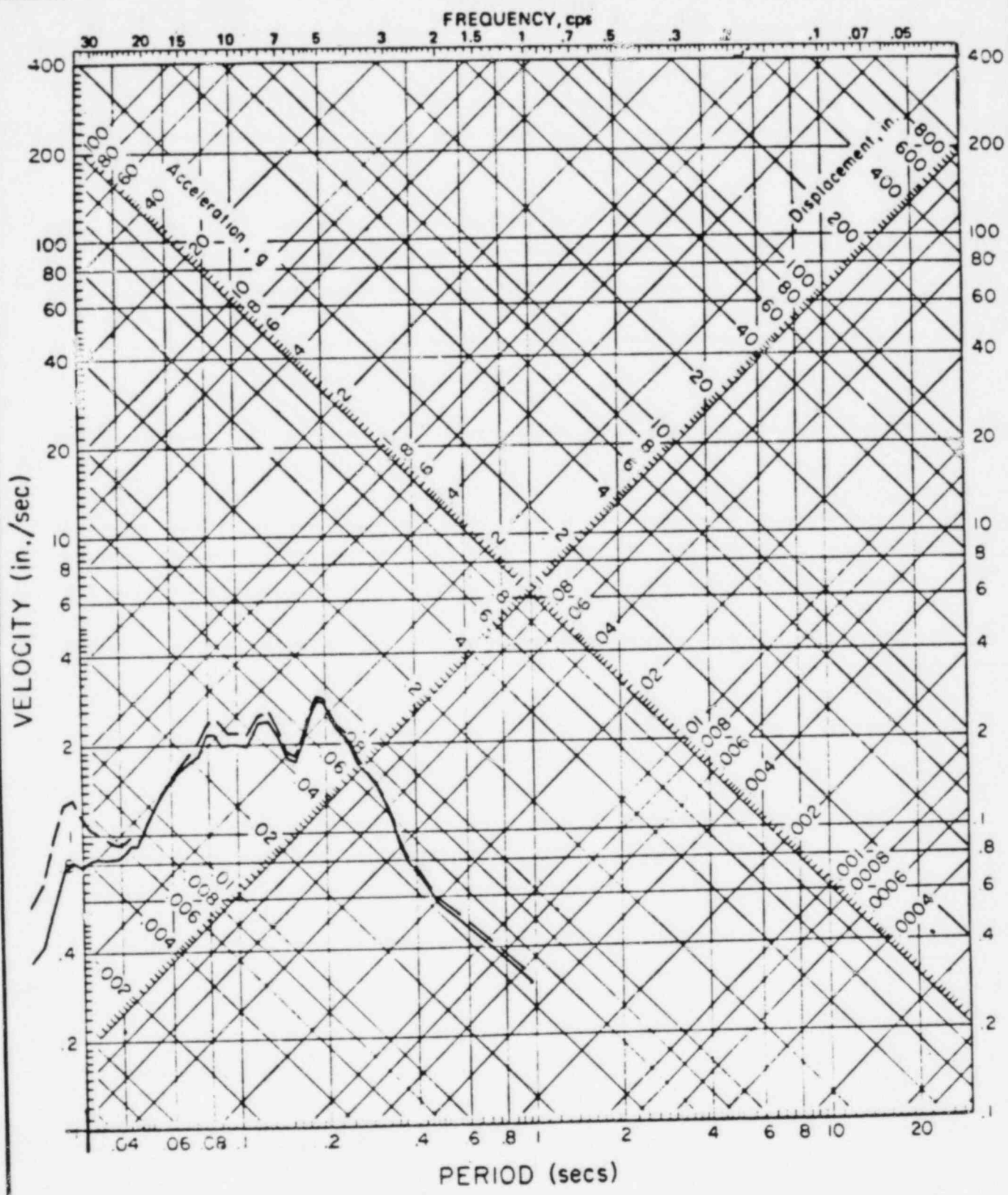
Approved by _____
Checked by _____
Drawn by _____
Compiled by _____



--- SMA-1
— FREE-FIELD

 The Earth Technology Corporation	PROJECT NO.: 83-164
	SCE&G
RESPONSE SPECTRA OF SMA-1 AND FREE-FIELD ACCELEROGRAMS 090° DIRECTION 1978 AFTERSHOCK NO. 1	
1-83	FIGURE 17b

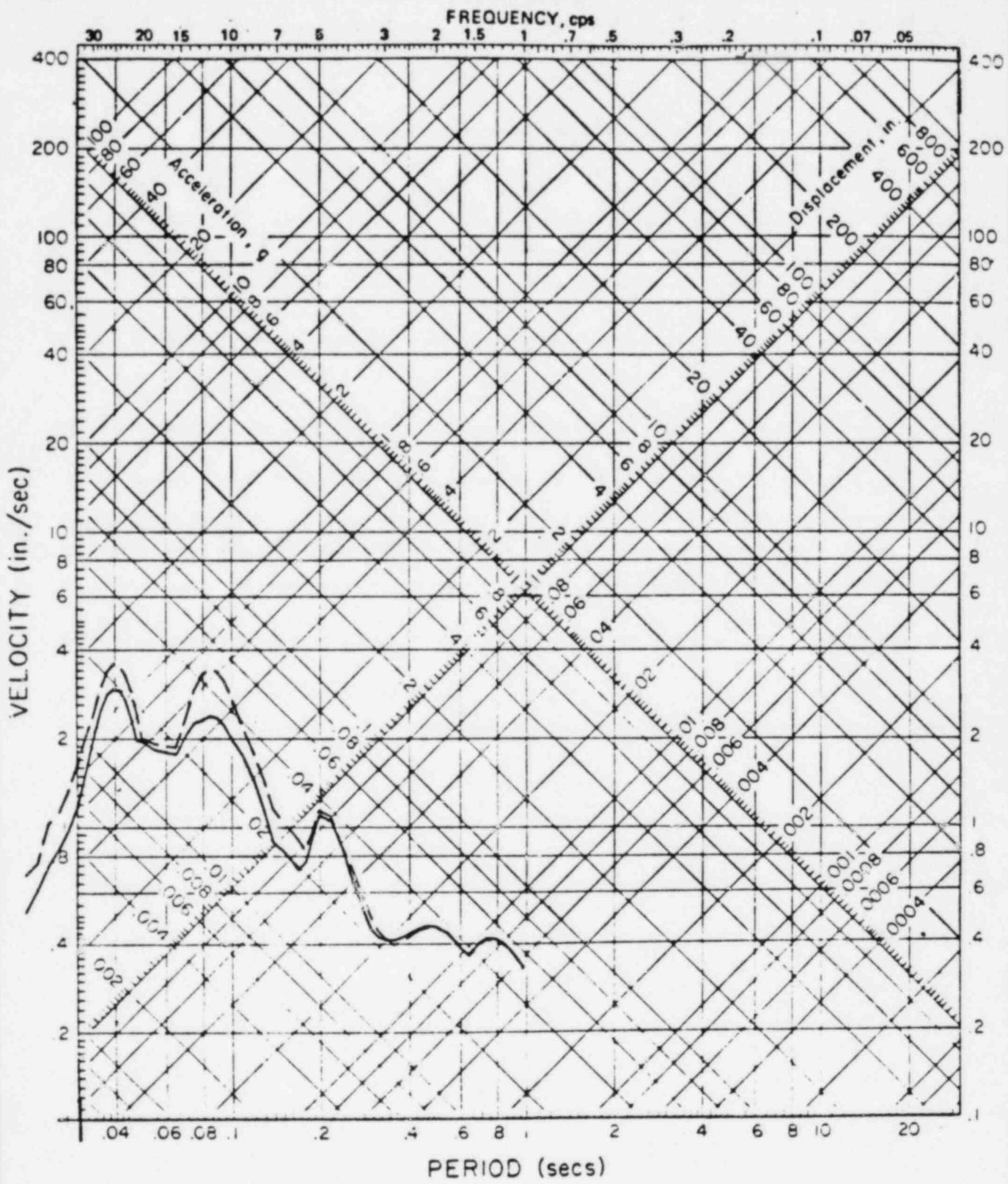
Approved by _____
Checked by _____
Drawn by _____
Compiled by _____



--- SMA-1
— FREE-FIELD

 The Earth Technology Corporation	PROJECT NO.: 83-164
	SCE&G
RESPONSE SPECTRA OF SMA-1 AND FREE-FIELD ACCELEROGRAMS 090° DIRECTION 1978 AFTERSHOCK NO. 2	
1-83	FIGURE 17c

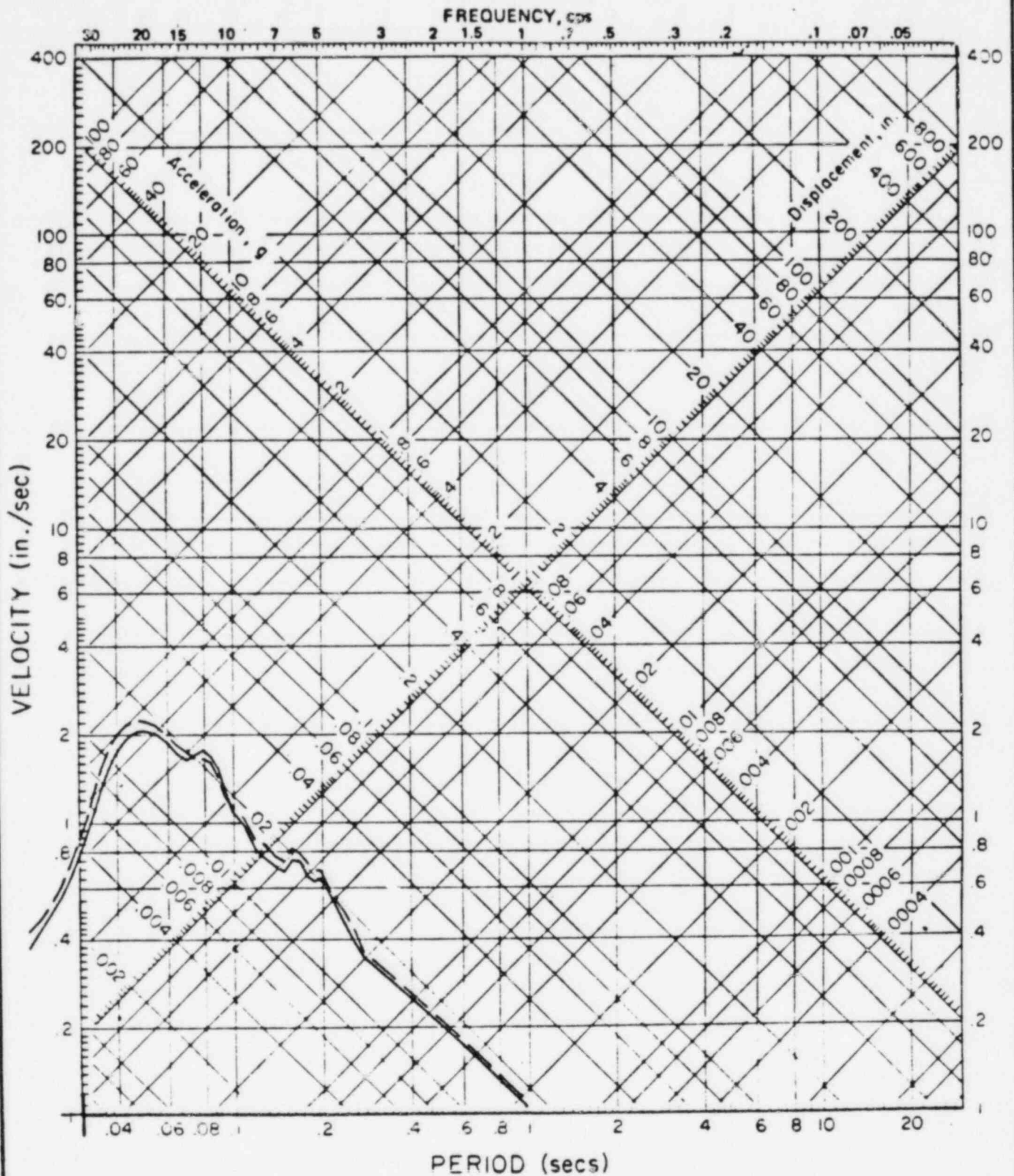
Approved by _____
Checked by _____
Drawn by _____
Compiled by _____



--- SMA-1
— FREE-FIELD

 The Earth Technology Corporation	PROJECT NO: 83 164
	SCE&G
RESPONSE SPECTRA OF SMA-1 AND FREE-FIELD ACCELEROGRAMS 090° DIRECTION 16 OCTOBER 1979 EVENT	
1-83	FIGURE 17d

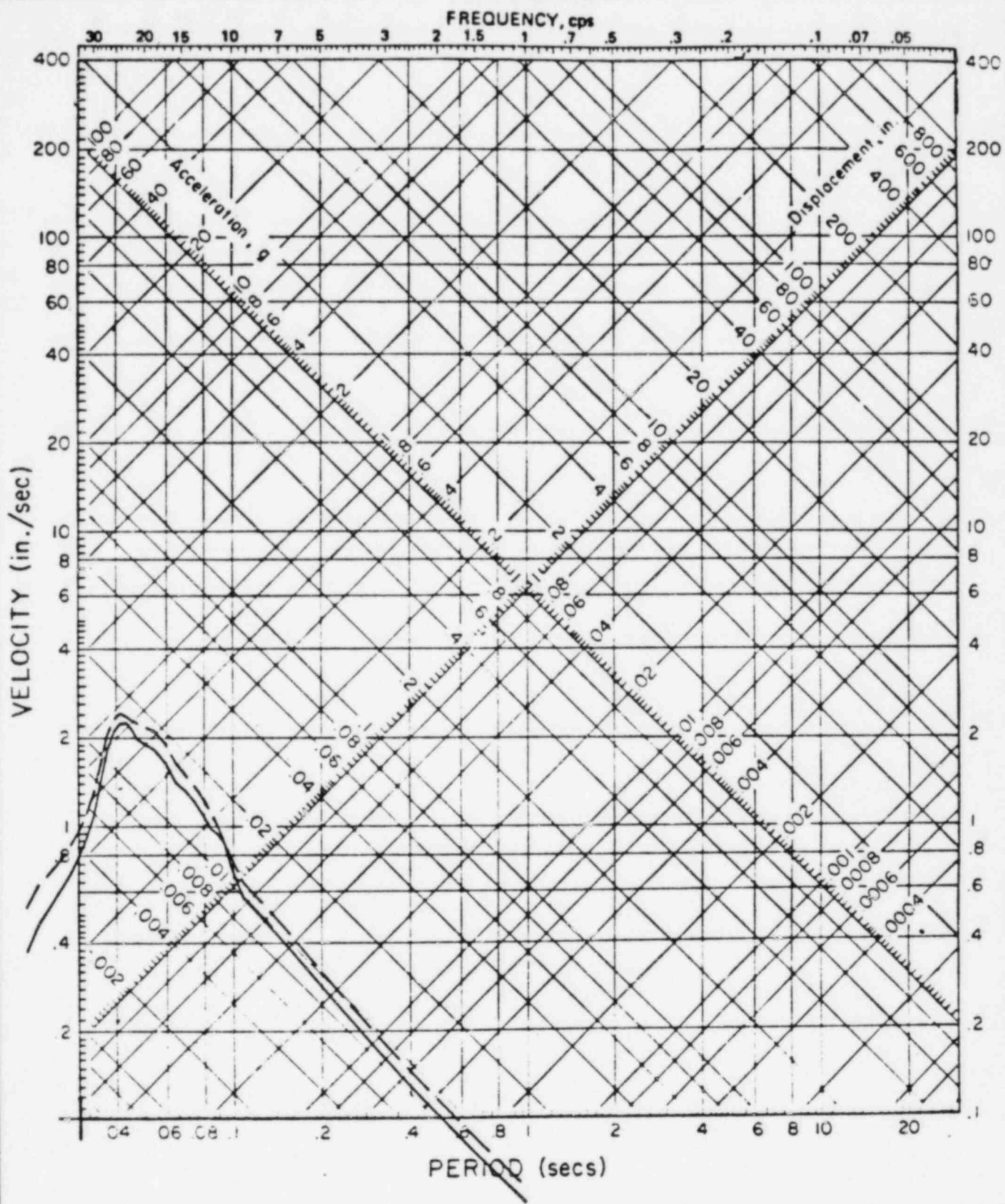
Approved by _____
Checked by _____
Drawn by _____
Compiled by _____



--- SMA-1
— FREE-FIELD

 The Earth Technology Corporation	PROJECT NO.: 83 164
	SCE&G
RESPONSE SPECTRA OF SMA-1 AND FREE-FIELD ACCELEROGRAMS 180° DIRECTION 27 AUGUST 1978 EVENT	
1-83	FIGURE 18a

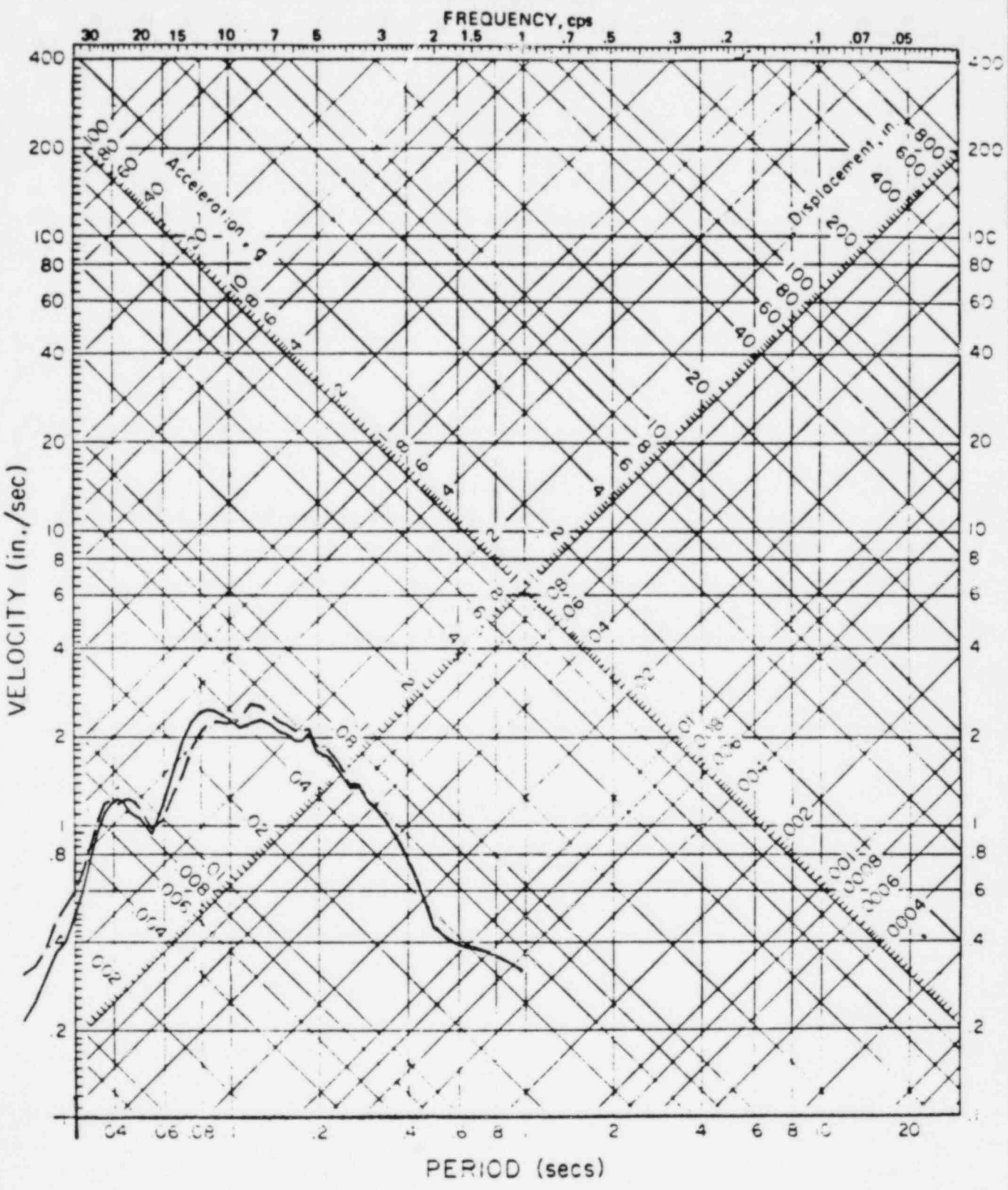
Approved by _____
Checked by _____
Drawn by _____
Compiled by _____



--- SMA-1
— FREE-FIELD

 The Earth Technology Corporation	PROJECT NO.: 83-164
	SCE&G
RESPONSE SPECTRA OF SMA-1 AND FREE-FIELD ACCELEROGRAMS 180° DIRECTION 1978 AFTERSHOCK NO. 1	
1-83	FIGURE 18b

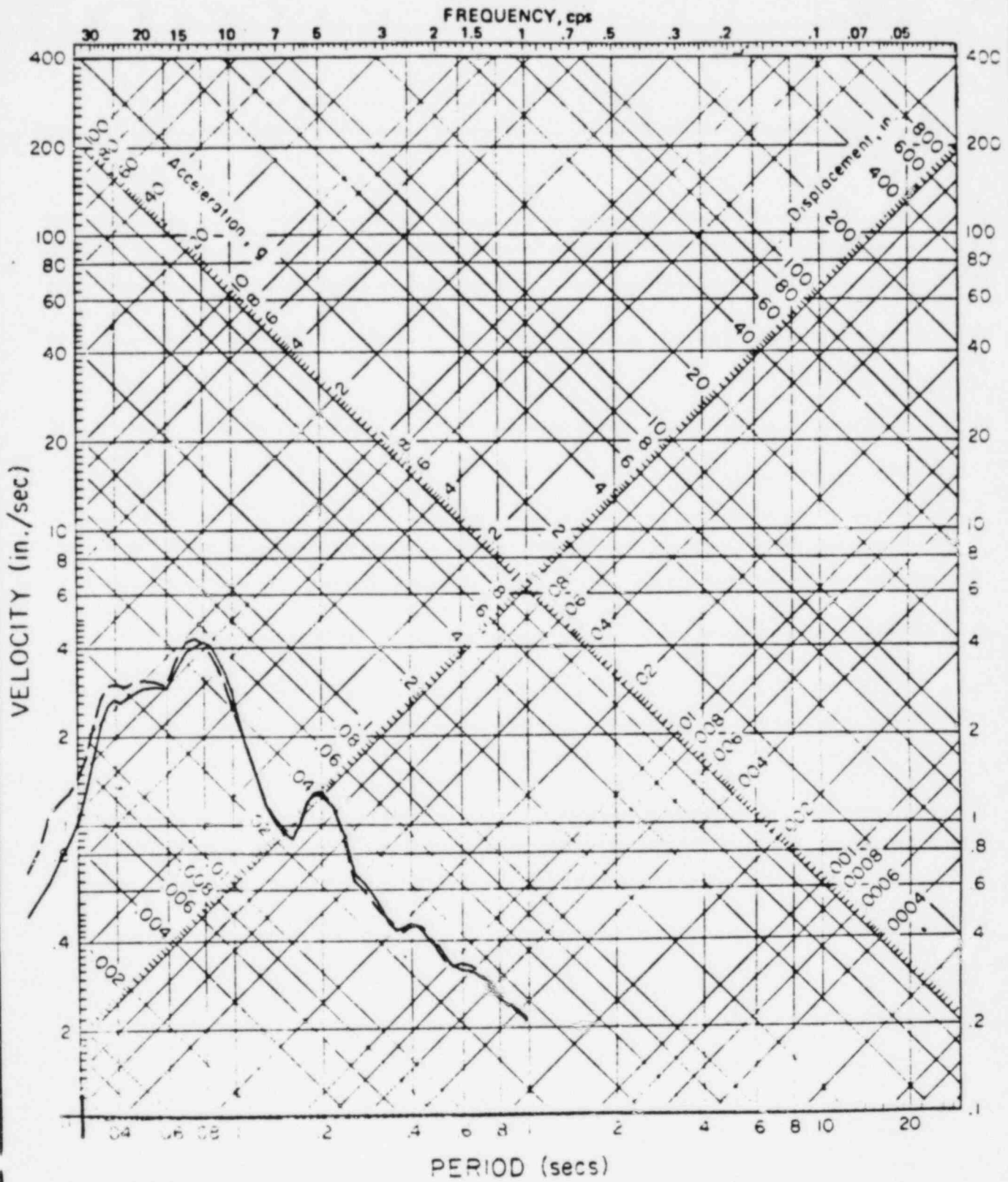
Approved by _____
Checked by _____
Drawn by _____
Compiled by _____



--- SMA-1
— FREE-FIELD

 The Earth Technology Corporation	PROJECT NO.: 83-164
	SCE&G
RESPONSE SPECTRA OF SMA-1 AND FREE-FIELD ACCELEROGRAMS 180° DIRECTION 1978 AFTERSHOCK NO. 2	
1-83	FIGURE 18c

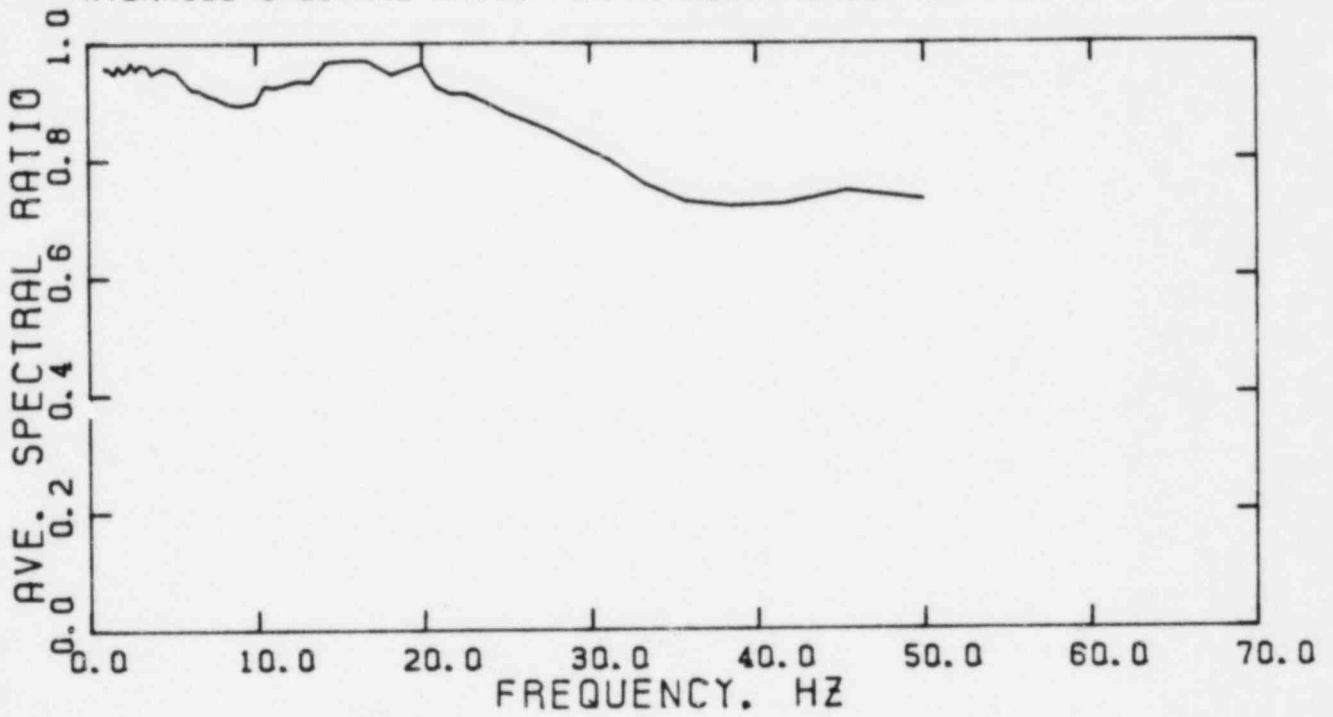
Approved by _____
Checked by _____
Drawn by _____
Compiled by _____



--- SMA-1
— FREE-FIELD

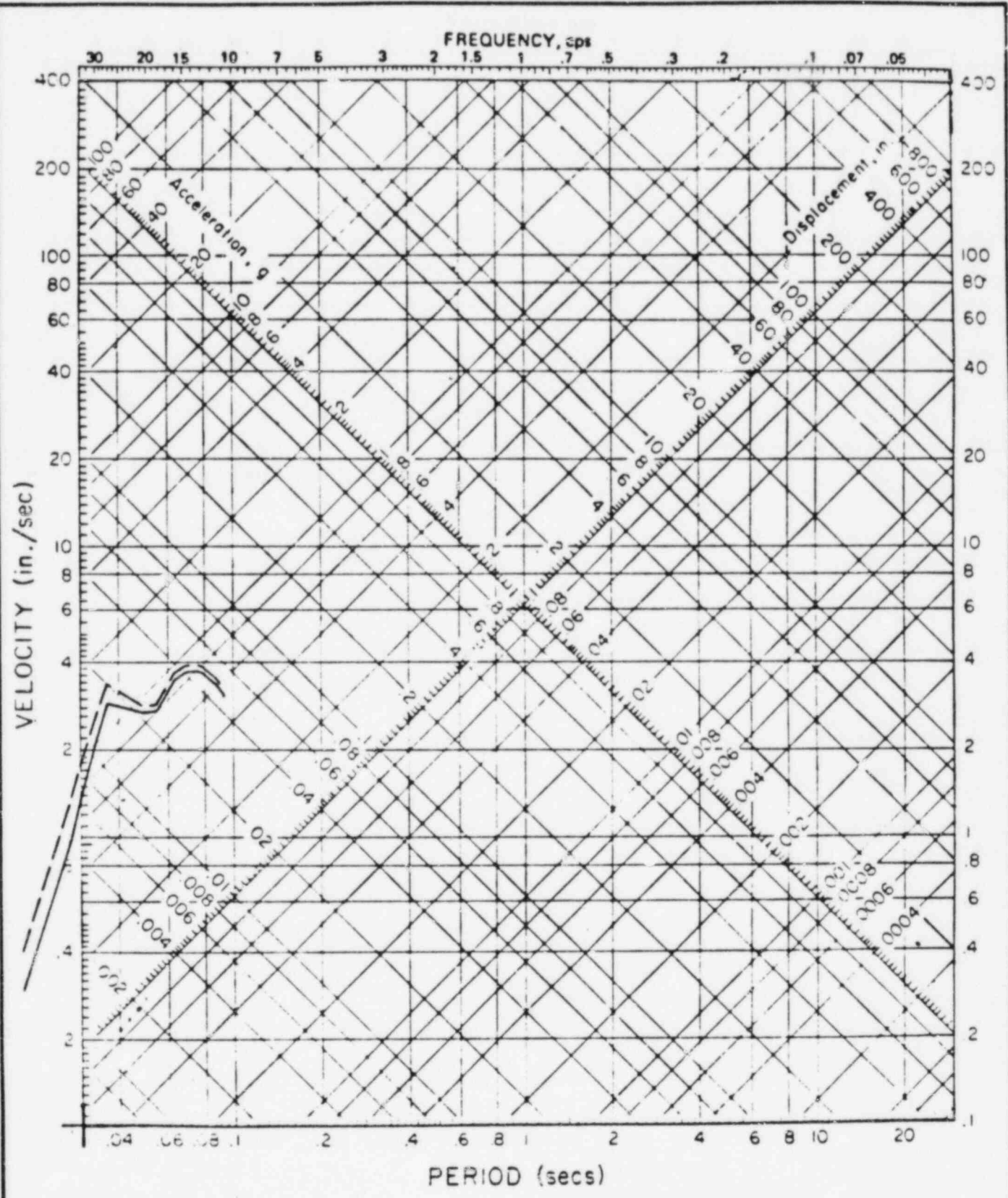
 The Earth Technology Corporation	PROJECT NO. : 83-164
	SCE&G
RESPONSE SPECTRA OF SMA-1 AND FREE-FIELD ACCELEROGRAMS 180° DIRECTION 16 OCTOBER 1979 EVENT	
183	FIGURE 18d

AVERAGED SPECTRAL RATIO FOR HORIZONTAL COMPONENTS



	PROJECT NO. 83-164
	SCE&G
AVERAGE RATIO OF THE FREE-FIELD TO SMA-1 RESPONSE SPECTRA	
1-83	FIGURE 19

Approved by _____
Checked by _____
Drawn by _____
Compiled by _____



--- NRC (1982) MONTICELLO SPECTRUM
— REDUCED SPECTRUM (FREE-FIELD)

	PROJECT NO.: 83-164
	SCE&G
REDUCED RESPONSE SPECTRUM RECOMMENDED FOR MONTICELLO ACCELEROGRAMS VS ORIGINAL NRC RECOMMENDED SPECTRUM	
183	FIGURE 20

URS

EXPERIMENTAL INVESTIGATION OF RELATIVE
RESPONSE OF ACCELEROGRAPH PAD, FREE FIELD
AND STRUCTURAL FOUNDATIONS
AT THE VIRGIL C. SUMMER NUCLEAR STATION

February 1983

prepared for

South Carolina Electric
and Gas Company
Columbia, South Carolina

prepared by

URS/John A. Blume & Associates, Engineers
2855 Telegraph Avenue
Berkeley, California 94705

NOTICE

This report is being released prior to completion of all QA documentation and thus must be treated as preliminary until QA release.

CONTENTS

<u>ITEM</u>	<u>PAGE</u>
I. INTRODUCTION AND BACKGROUND.	1
II. OBJECTIVES	3
III. EXPERIMENTAL PROCEDURES.	4
A. Shot and Recording Site Selection Criteria	4
B. Instrumentation Plan	6
C. Data Acquisition System	7
D. Operational Factors.	10
IV. DESCRIPTION OF DATA.	18
A. Representative Seismograms	18
B. Travel Times and Group Velocities.	19
C. Particle Motions	21
D. Polarization Filtering	23
E. Summary.	23
V. ANALYSIS METHODS	24
A. Calibration of Seismograms	24
B. Data Transfer and File Structure	24
C. Spectral Ratios-Theory and Methods Applied	25
D. Band Pass Filtering.	29
E. Free-Field and Foundation Motion for 16 October 1979 Earthquake	31
VI. RESULTS.	39
A. Introduction	39
B. Accelerograph Pad/Free-Field Spectral Ratios	39
C. Foundation/Free-Field Spectral Ratios.	43
D. Free-Field Motion for 16 October 1979 Earthquake	48
E. Foundation Response for 16 October 1979 Earthquake	48
F. Direct Pad/Foundation Structural Response.	49
VII. CONCLUSIONS.	50
VIII. REFERENCES	52

I. INTRODUCTION AND BACKGROUND

In October 1981, two explosion tests were conducted at the Virgil C. Summer Nuclear Station (VCSNS) and were reported in Applicants' Additional Seismic Testimony (1981).

The 1981 explosion tests (Tests 1 and 2) were designed primarily to investigate the possibility of anomalous site response where the USGS accelerograph station is located. The location of these tests is shown in Fig. I.1. In these experiments, seismometers were installed close to, but not on, the USGS accelerograph pad at the dam abutment. Motions recorded near the accelerograph pad were not discernibly anomalous in relation to motions recorded at free-field sites elsewhere.

In addition to an array of free-field recordings near the dam abutment, records were obtained on the Auxiliary Building foundation for Test 1 and on the Fairfield Pumped Storage Facility (hydroplant) foundation for Test 2. In both tests, there were significant reductions in the high-frequency foundation motions relative to free-field motions recorded at equal distances.

The analysis of the 1981 active field experiments presented in Applicants' Additional Seismic Testimony considered Fourier spectral modulus ratios of record pairs. In the 11 to 16 January 1982 Atomic Safety and Licensing Board (ASLB) hearing, a Board witness testified (Tr 5716) that the fundamental Rayleigh wave mode shape "could be very significant to the entire explanation for the reduction we see in the building," in comparison with the free field. On rebuttal, Applicants' witness testified (Tr 5992-5994) that the observed reductions are comparable for the P-wave train and for the train of S waves and surface waves, so that the reduction cannot be attributed entirely to the decrease with depth of the fundamental mode Rayleigh wave amplitude. Applicants' witness also testified that, in any case, explosive tests reported in FSAR Section 2.5.4.4.4 indicate that fundamental mode waves are not generated to any observable extent by explosions in the Monticello Reservoir area.

In its Partial Initial Decision (PID), 20 July 1982, the ASLB, following the NRC staff position, found that although "the analyses of blast test data demonstrated a trend toward significant reductions," these were not considered "conclusive in a quantitative sense so as to define the final magnitude of reduction" (Find. 48 at 43).

In November 1982, 3 series of explosion tests (Tests 3, 4, and 5) were conducted using 3 different shot point locations, and 3-component recordings were made on the foundations of 3 VCSNS structures, at free-field sites in the vicinity of the Nuclear Station, on the accelerograph pad, and at nearby free-field sites on the dam abutment. Motions generated by Test 5 were also recorded in the foundation of the hydroplant. Results of these tests are used to define the magnitude of the spectral reductions to be applied to the 16 October 1979 earthquake response spectra to obtain foundation response spectra.

II. PROGRAM OBJECTIVES

The objective of the 1982 tests was to spectrally compare the signals observed on the VCSNS foundations and on the dam abutment accelerograph pad, with free-field signals. Foundation/free-field spectral ratios were to be documented for different wave types, and for 3 basic foundation types: mat or fill concrete overlying bedrock, caissons through the saprolite to bedrock, and mat foundation on saprolite. The applicability of the explosion tests results to earthquake response of the foundations was to be assessed. Questions as to the response of the accelerograph pad relative to its immediate surroundings were to be resolved with data from a small-aperture seismic array at the dam abutment.

The free-field accelerograms were to be obtained by applying these transfer functions to accelerograms recorded on the USGS pad at the dam abutment. As an end result, accelerograms and corresponding response spectra for Virgil C. Summer Nuclear Station (VCSNS) building foundations at floor level were to be computed by applying empirical transfer functions to free-field accelerograms of reservoir-induced seismicity (RIS) events.

III. EXPERIMENTAL PROCEDURES

A. Shot and Recording Instrument Site Selection Criteria

The recording sites and shot locations were carefully chosen to satisfy the program objectives discussed above. In addition to meeting the specific requirements of these objectives, the shot locations had to fulfill the following general criteria:

- o The distance from the shots to each receiver had to be sufficiently large to allow a clear separation between the arrival times of compressional and shear waves;
- o For the Nuclear Station SSI tests, the shots had to be equidistant from structure foundations and free-field stations;
- o Tests had to be conducted at locations within the project boundary that were accessible by a large truck-mounted drill;
- o The blast holes had to be located such that there was little chance of causing damage to any structure, roads, or power lines.

The specific requirements of each shot location are discussed below. Figure III.A.1 shows the location of all shots and receivers, and Table III.A.1 gives the locations at which records were obtained for each shot. The explosives tests of November 1981 were previously designated as Shot Points 1 and 2.

A geologic map of the basement rocks, digitized from FSAR Figure 2.5-13, is shown in Figure III.A.2. The saprolite soil layer is extremely variable in thickness over this area, ranging from 0 to approximately 100 ft.

Shot Point 3 was located to provide a direct comparison between motions in the Virgil C. Summer Nuclear Station (VCSNS) foundations and motions in the free field around the plant.

The free-field recording sites were deployed along the arc of a circle centered at the shot point and passing through the Auxiliary Building (Figure III.A.3). The free-field stations were installed on both sides of the VCSNS and far enough from it (more than 3 overall foundation dimensions, or approximately 1200 ft) to insure that the response of the plant itself did not influence the free-field motions.

Shot Point 4 was placed equidistant from the USGS accelerograph pad and the foundation of the Auxiliary Building (Figure III.A.4). This arrangement allowed a direct comparison of the response of the pad relative to its own immediate free field, as well as a direct comparison of the pad motion with motions on that of the foundations of the VCSNS.

Shot Point 5 was located as close as practical to the computed epicenter of the 16 October 1979 earthquake, and was specifically intended to test the response of the USGS accelerograph pad relative to its free field (Figure III.A.5). Therefore, the explosively-generated seismic pulses impinging on the accelerograph pad have propagation paths identical or very similar to those of the 1979 earthquake, and the pad-to-free-field behavior is expected to replicate that of 1979 for each wave type; this is particularly the case for explosions detonated close to the hypocentral depth of the 1979 event. A recording station was also established on the foundation of the Fairfield Pumped Storage Facility during the Shot Point 5 experiments.

Pertinent details about the shots and receivers are presented in Tables III.A.i through 4. Table III.A.1 lists all recording sites and their identification labels, their grid coordinates and the specific tests for which data were recorded. Table III.A.2 gives charge weight, depth and detonation time for each test shot. Table III.A.3 gives the shot-to-receiver distances (as measured from the center of the array of drill holes) for those recording locations that were active for each series of tests. Table III.A.4 lists those stations which recorded data from specific test explosions.

Locations of seismometers installed in the VCSNS foundations* are shown in Figures III.A.6, 7 and 8 for the Auxiliary Building (AB), Diesel Generator Sump (GS) and Service Water Pumphouse (WP), respectively. Noise levels on these foundations were recorded during a preparatory site visit on 23-24 September 1982. Seismometers were installed in the Auxiliary Building foundation, at elevation 374 ft, as in the 1981 tests, but were located in an area (Room 74-08) that was quieter than the location monitored in 1981 (Room 74-09E). The Auxiliary Building is founded on lean concrete fill overlying bedrock. Figure III.A.7 is a section showing the seismometer location in the sump of the Diesel Generator Building at elevation 400 ft. The Diesel Generator Building is founded on caissons that penetrate the saprolite to bedrock. Figure III.A.8 is a plan showing the seismometer location at elevation 425 ft on the Service Water Pumphouse foundation, which is a mat foundation on saprolite.

B. Instrumentation Plan

The characteristics of the data acquisition system used for the confirmatory program were dictated by the following considerations:

- o A large amount of data was to be collected, and it would be necessary to rapidly review the adequacy of the data after each explosion.
- o There were large spatial separations of up to 7000 ft between data collection points, and it was essential that channels be recorded with a common time base.
- o The data acquisition system had to suppress a large amount of 60 Hz interference and other electrical noise generated by the dense network of high-voltage AC power transmission lines present in the area.
- o The data had to be acquired in a format that was suitable for subsequent transfer to a "main frame" computer for analysis.

* Throughout this report "foundation" refers to the structural basement floor level.

- o Because most of the instrumented sites were out in the open, it was necessary that the system be capable of operating in adverse weather conditions.
- o Each element of the recording network had to be checked and calibrated independently of other elements.
- o System reliability was an important consideration because of the logistical and other scheduling constraints.
- o The system had to be partially reconfigured between sets of test explosions without relocating the central recording equipment.

Several options were eliminated by the above factors. Telemetry was considered and rejected because of cost, difficulty of installation and potential reliability and calibration problems. The use of separate analog or digital 3-channel recorders at each site was not seriously considered because of problems previously experienced in using this type of equipment; it would have been particularly difficult and time consuming to verify that all instruments operated properly after each test explosion. A "hard-wired" analog signal transmission system was selected, feeding into a digital data acquisition system; the instrumentation fulfilled every requirement demanded by the program. The elements of the data acquisition are described in more detail in the next section.

C. Data Acquisition System

An overview of the entire system is shown in the block diagram in Figure III.C.1. Each element is described separately below.

Geophones. Mark Products Model L-22 geophones with a natural frequency of 2 Hz were chosen for the transducer. The 0.7 critically damped amplitude and phase response (obtained from an on-site

calibration) of a representative geophone is shown in Figure III.C.2. The voltage output of this self-generating device is proportional to the velocity of the geophone case. The L-22 geophone (suitably rugged and weatherproof for field use) exhibits no hysteresis and has excellent resolution of low-level motions.

Preamplifiers. The combination of low signal levels (microvolts) and long cable lengths in the high-noise environment of the VCSNS dictated that the signals be amplified before transmission to the recording site. Three-channel, twelve-volt powered preamplifiers were fabricated for this project because of the unavailability of suitable units from commercial sources. A differential output was necessary to drive the signal lines which were terminated by differential-input amplifiers at the central recording site. Preamplification and the use of individually-shielded, twisted-pair signal lines virtually eliminated the common problems of noise caused by ground loops and 60 Hz pickup. The preamplifiers had a fixed voltage gain of 200 and an input impedance of 860 ohms, a value selected for proper damping (0.7) of the geophones. A conventional 12-volt automobile battery was capable of powering a 3-channel preamplifier continuously for about 7 days.

Cable. Multiconductor shielded cable was used to transmit all signals to the recording site. The cable was simply laid on the ground surface and all splices and branches were made in weather-proof junction boxes. Screw-type terminal strips in the boxes were labeled according to a standard industrial color code for multiple-pair cable. A total of approximately 25,000 ft of cable was installed and few problems occurred. The most serious trouble encountered was severe damage to several cables caused by vehicle traffic inside the plant area; new sections of cable were spliced in and no further problems were experienced.

Amplifiers. Callex Model 178 instrumentation amplifiers were used in the final stage of amplification at the central recording site. Voltage gain of the 24 amplifiers was continuously adjustable from 3 to 1,000, and the gains were set to the desired values by measuring the transfer function of each amplifier with a Hewlett-Packard Model 3582 dual-channel spectrum analyzer. This gain-setting procedure also insured that the amplifiers were functioning properly just prior to acquiring the data for each set of explosive tests. The Model 178 amplifiers employ a differential input and have a very high common mode rejection. Total voltage amplification of the system (including the preamplifiers) ranged from 600 to 15,000.

Anti-alias Filters. The output of the final stage of amplification was fed to a Preston Scientific Model GMF-8-40, 24-channel, low pass, 8-pole, Butterworth filter with a cutoff frequency (-3dB) of 40 Hz. The attenuation rate above 40 Hz is 48 dB per octave. The transmission characteristics of the filters are represented by the plot in Figure III.C.3, obtained from a filter calibration.

Multiplexer. A Preston Scientific Model GM-91032, 32-channel multiplexer was the interface between the analog transducers, transmission system and signal conditioners, and the digital recording system. The multiplexer is an analog device, and operates under the control of the Hewlett-Packard Model 5451 (HP-5451) Fourier Analyzer (discussed in the next section) which was the principal data recorder. The multiplexer simultaneously samples and holds up to 32 channels, the number of active channels being set by switches on the unit. The voltage levels in each channel are then sequentially converted to a 12-bit digital signal by the HP-5451. It is important to note that all input channels in the multiplexer are sampled and held simultaneously, rather than sequentially, and no interchannel phase shift is introduced.

Digital Recording System. The primary recording system was the HP-5451 Fourier Analyzer with its internal hard disk storage (5Mb) and external tape drive (HP-7970E). The system is built around the Hewlett-Packard Model 2100 S computer and incorporates a 2-channel, 12-bit analog to digital converter, low pass filters, CRT display, dual 2.5 Mb disk drives and all necessary interfaces for plotter, printer and keyboard. The system can sample up to 100 kHz, a capacity far exceeding the requirement for this program. Each channel of the multiplexer is sampled at 5 msec intervals, and the data are transferred to either magnetic disk or digital tape in real time, along with file headers for later identification and retrieval. The data were acquired and stored as blocks of 2048 data points, corresponding to 10.24 seconds of recording time after each test explosion. The data acquisition is started when the analog-to-digital converter is triggered by a zero-time pulse generated by the firing pulse from the blasting machine at the explosion site. All data channels have, therefore, a common time base which starts at the instant of the explosion.

A significant advantage of this system is that all data channels could be displayed and reviewed immediately after each test shot in order to confirm that all channels operated. Furthermore, the data could be processed, e.g., Fourier transformed, to spot-check the results as they were obtained.

D. Operational Factors

The following sections discuss various aspects of field operations in the experimental program.

Drill Holes. Four holes were drilled at each of the three shot locations. A fifth hole was drilled at Site 5, but was abandoned because of drilling difficulties. The holes were cased down to the top of rock and then drilled with a 6-inch-diameter bit to a depth of

50 ft below the bottom of the casing. The hole depths therefore varied as the depth to rock varied; total depths ranged from about 110 to 210 ft, with the greatest bedrock relief at Site 5. The holes were drilled 50 ft apart in a line that was generally perpendicular to the source-receiver alignment. Preshot water levels were within a few tens of feet of ground surface in all holes, and the water provided the only stemming for the test explosions. In several instances, water was pumped into holes prior to loading repeat shots to compensate for the water blown out of the hole by the previous explosion.

The decision to drill 4 holes at each site reflected a balance between the need to improve signal-to-noise ratio (by averaging the data for many shots) and the practical constraint of drilling costs. Four holes would result in data with twice the signal-to-noise ratio as data from only one hole. Further, it was believed that some of the holes would survive the first explosion and allow repeat shots in the same hole. Repeat shots were fired in some holes, up to a maximum of 4 in hole 4A; conversely, some holes could not be reloaded because of damage from the first shot. A total of 8 to 10 shots was recorded for each group of 4 holes.

Explosives. An ammonium nitrate-based water gel explosive was used for all the test explosions. (Both DuPont Tovex and Ireco Iregel were used.) The bulk of the explosives were packaged in 5-inch diameter 30-lb bags. DuPont 1-lb HDP primers initiated by DuPont SSS seismograph blasting caps were used in all cases. A list of charge weights, depths and detonation times is given in Table III.A.2.

Zero-Time Pulse. The data acquisition system was triggered by a pulse originating in the blasting machine. The 225-volt firing pulse from the capacitor-discharge-type machine was transformed down to about 5 volts and transmitted over wire to the recording equipment.

Because DuPont SSS blasting caps fire less than 1 millisecond after application of the firing current, the sampling of the data started at virtually the instant of detonation.

Shot/Recording Procedures. The general procedure for recording any one shot was quite straightforward. Communications between the shot point and the recording point were maintained over South Carolina Electric and Gas's (SCE&G) FM radio net. As a first step, the integrity of the zero-time pulse-transmission system was verified by firing several blasting caps and observing the pulse on a storage oscilloscope in the recording shed. Subsequently, it was simply a matter of assembling the explosives and primer, loading the explosives in the hole, and confirming the readiness of the recording equipment. Ten seconds of ambient noise were recorded for each channel prior to every shot. A countdown from 10 was then broadcast over the radio net for every shot. The average time between shots fired in a sequence was 40 minutes, although the actual interval times varied from 10 minutes to over 2 hours.

Calibration. All calibration functions were performed on site with a Hewlett-Packard Model 5423A (HP-5423A) Structural Dynamics Analyzer. This instrument, the calibration of which is traceable to NBS through Hewlett-Packard, can be used as a versatile and fast, FFT-based, dual-channel spectrum analyzer. All calibrations were dynamic and broadband rather than single frequency and resulted in complete amplitude and phase response of the system elements over the full frequency spectrum of the measurements.

The geophones were calibrated by mounting them on an electrodynamic shaker together with a standard geophone^{*} as a reference. Band-limited random noise is used to excite the shaker, and the transfer

* The standard geophone was calibrated on site against a standard calibrated accelerometer.

function between each geophone and the reference standard is computed by averaging in the frequency domain. An annotated record of the amplitude and phase calibration is preserved on magnetic tape in the HP-5423A.

The preamplifiers and transmission cables are calibrated in a similar fashion using the random noise output of the HP-5423A; i.e., by measuring the complete transfer function of the preamplifier or cable. Finally, an end-to-end calibration is performed on each data channel by physically exciting each geophone with pseudo-random vibrations and comparing the response of one channel to another. The gains of the final amplifiers are set with a Hewlett-Packard Model 3582 (HP-3582) dual-channel analyzer; and the gain-setting potentiometer is adjusted until the amplitude of the transfer function between the amplifier's output and input, with random noise input, is equal to the desired level of amplification. The calibration of the HP-3582 is based on that of the HP-5423A.

TABLE III.A.1
COORDINATES OF RECORDING SITES

Receiver Location	ID	State Plane Coordinates		Shots Recorded
		North	East	
Hydroplant Foundation	HP	475,600	1,899,840	5 (all)
50 ft NW of USGS Pad	P1	474,856	1,900,673	5 (all)
USGS SMA Pad	P2	474,816	1,900,703	5 (all) 4-1 to 4-6
15 ft SE of USGS Pad	P3	474,806	1,900,713	4-3 to 4-6
50 ft SE of USGS Pad	P4	474,781	1,900,738	5 (all) 4-1, 4-2
250 ft SE of USGS Pad	P5	474,635	1,900,874	5 (all)
Free field, West of Met.	F1	472,785	1,902,300	3 (all)
290 ft NW of DSA Pad	FR	473,096	1,903,059	5 (all) 4-3 to 10 3 (all)
260 ft SW of DSA Pad	F2	472,811	1,903,131	4-1, 4-2
DSA Pad	DS	472,987	1,903,325	5 (all)
15 ft S of DSA Pad	F3	472,972	1,903,325	4 (all), 3 (all)
Downhole DSA	DR	472,984	1,903,325	5 (all), 4 (all), 3 (all)
Auxiliary Bldg. Foundation	AB	472,615	1,904,590	5 (all), 4 (all), 3 (all)
Diesel Generator Sump	GS	472,532	1,904,900	4 (all), 3 (all)
Service Water Pumphouse	WP	472,547	1,905,427	4 (all), 3 (all)
Free Field SE 3-1	F4	471,625	1,906,025	3 (all)
Free Field SE 3-2	F6	470,652	1,906,584	3 (all)
Free Field SE 4	F5	471,157	1,905,257	4 (all)

Note: The coordinates of the midpoint of the linear array of 4 drill holes at each shot point are as follows:

Shot Point 3	469,160	1,903,303
Shot Point 4	470,552	1,900,887
Shot Point 5	476,991	1,898,502

TABLE III.A.2

RECORD OF TEST EXPLOSIONS

<u>Shot No.</u>	<u>Hole</u>	<u>Charge Weight</u> ⁽¹⁾	<u>Depth</u> ⁽²⁾	<u>Date</u> ⁽³⁾	<u>Time</u> ⁽⁴⁾	<u>Remarks</u>
5-1	5E	1	21	10 Nov	15:30+	Abandoned hole, no usable signals
5-2	5D	13.5	108	10 Nov	16:23:00	
5-3	5D	13.5	46	12 Nov	13:46:30	
5-4	5C	122	116	12 Nov	14:53:30	
5-5	5B	122	157	12 Nov	15:29:30	Casing pushed up 20 ft during shot
5-6	5A	121	210	12 Nov	15:50:30	
5-7	5C	13.5	67	12 Nov	16:11:30	
5-8	5C	13.5	50	12 Nov	18:29:30	
5-9	5A	121	190	12 Nov	18:39:30	Signals clipped at some stations
4-1	4A	121	117	16 Nov	13:12:30	
4-2	4B	121	143	16 Nov	13:57:30	
4-3	4C	121	133	16 Nov	16:18:30	
4-4	4D	121	125	16 Nov	16:40:30	
4-5	4A	30	115	16 Nov	16:50:30	
4-6	4B	122	100	16 Nov	17:24:30	
4-7	4A	121	102	16 Nov	17:48:30	
4-8	4C	91	130	16 Nov	18:19:30	
4-9	4A	122	102	17 Nov	13:37:30	
4-10	4B	122	92	17 Nov	13:50:30	Partial detonation, 90 lbs of explosives ejected
3-1	3D	121	125	18 Nov	14:30:30	
3-2	3C	121	104	18 Nov	14:41:30	
3-3	3B	121	107	18 Nov	15:11:30	
3-4	3A	121	120	18 Nov	15:23:30	
3-5	3B	121	103	18 Nov	16:32:30	Partial detonation, 60 lbs of explosive ejected
3-6	3B	90	60	18 Nov	16:48:30	
3-7	3A	90	65	18 Nov	17:45:30	
3-8	3D	121	85	18 Nov	17:57:30	

Notes:

- (1) Total weight in lbs, including primer
(2) To center of charge (+) in ft
(3) 1982
(4) Eastern Standard Time

TABLE III.A.3

DISTANCES FROM CENTER OF TEST EXPLOSIONS
TO RECORDING SITES (FT)

<u>Receiver Location</u>	<u>ID</u>	<u>Shot Point 5</u>	<u>Shot Point 4</u>	<u>Shot Point 3</u>
Hydroplant Foundation	HP	1930	-	-
50 ft N of USGS Pad	P1	3045	-	-
USGS Pad	P2	3094	4268	-
15 ft SE of USGS Pad	P3	-	4258	-
50 ft SE of USGS Pad	P4	3144	4232	-
250 ft SE of USGS Pad	P5	3343	-	-
Free field, West of Met Tower	F1	-	-	3761
290 ft NW of DSA Pad	FR	5995	3345	3944
260 ft SW of DSA Pad	F2	-	3184	-
DSA Pad	DS	6268	-	-
15 ft S of DSA Pad	F3	-	3435	3812
Downhole DSA	DR	6270	3444	3824
Auxiliary Bldg. Foundation	AB	7498	4239	3687
Diesel Generator Sump	GS	-	4475	3731
Service Water Pumphouse	WP	-	4959	3998
Free Field SE 3-1	F4	-	-	3672
Free Field SE 3-2	F6	-	-	3604
Free Field SE 4	F5	-	4412	-

TABLE III.A.4
SHOT/RECEIVER COMBINATIONS FOR EXPLOSION TESTS

<u>Receiver Location</u>	<u>I D</u>	<u>SHOT</u>					
		<u>5-2</u>	<u>5-3</u>	<u>4-1,</u>	<u>4-3</u>	<u>4-7</u>	<u>3-1</u>
			<u>THRU</u>	<u>4-2</u>	<u>THRU</u>	<u>THRU</u>	<u>THRU</u>
Hydroplant Foundation	HP	x	x				
50 ft NW of USGS Pad	P1	x	x				
USGS SMA Pad	P2	x	x	x	x		
15 ft SE of USGS Pad	P3				x		
50 ft SE of USGS Pad	P4	x	x	x			
250 ft SE of USGS Pad	P5	x	x				
Free Field W 3	F1						x
290 ft NW of DSA Pad	FR	x	x		x	x	x
260 ft SW of DSA Pad	F2			x			
DSA Pad	DS		x				
15 ft S of DSA Pad	F3			x	x	x	x
DSA Downhole	DR		x	x	x	x	x
Auxiliary Building	AB	x	x	x	x	x	x
Diesel Generator	GS			x	x	x	x
Service Water Pumphouse	WP			x	x	x	x
Free Field SE 3-1	F4						x
Free Field SE 4	F5			x	x	x	
Free Field SE 3-2	F6						x

IV. DESCRIPTION OF DATA

A comprehensive study of the nature of the explosion test signals was undertaken to address more fully questions raised by Board witnesses in the 11-16 January 1982, Atomic Safety and Licensing Board (ASLB) hearing. The seismograms were analyzed by a variety of techniques for decomposing signals by wave type. Although the signals are characterized by prominent energy arrivals in P-wave and S-higher-mode surface wave intervals, the records were found to be too complex for further decomposition by particle-motion discriminants. It is evident that much of the complexity of the signatures is due to secondary waves generated in the immediate vicinity of the receiver sites. While the saprolite layer has a significant influence on the seismic signatures on a local scale, there is little or no coherent wave propagation within the saprolite layer over significant distances. Because of the complexity of the particle motions, the principal decomposition method chosen for further analysis was selection of separate P-wave and S-surface wave time windows by group velocity on each component of motion.

A. Representative Seismograms

Examples of the vertical, radial and transverse components of seismograms with good signal-to-noise ratios recorded for the 3 test series are shown in Figures IV.A.1 through 9 (see Section V.B for nomenclature). The traces for any one shot are plotted with true relative amplitudes. Visual inspection of these records leads to several important conclusions.

The most noticeable feature is that motions observed at the free-field sites typically exhibit larger amplitudes than the corresponding records obtained at the same distance on the foundations of the Virgil C. Summer Nuclear Station (VCSNS). This phenomenon is quite apparent, for example, in Figures IV.A.5 and 6 which show the horizontal components of motion from 2 of the explosions at shot point 4.

A comparison of the shot point 5 seismograms recorded in the foundation of the hydroplant (HP) with those recorded on the dam abutment (P1, P2, P4, P5), shown in Figures IV.A.7, 8, and 9, clearly shows that the amplitudes in the hydroplant are significantly lower than those on the abutment, even though the hydroplant station is much closer to the source (approximately 1900 ft) than the abutment (approximately 3100 ft).

From an inspection of these figures, it is apparent that there are two principal group arrivals, the first being the P wave and the second resembling the S and surface wave arrivals seen in typical reservoir-induced seismicity (RIS) earthquake seismograms recorded at comparable epicentral distances. This topic is discussed further in the next section.

B. Travel Times and Group Velocities

It is of interest to partition the seismograms into their fundamental wave types (P, S, surface) in order to examine the relative contribution of each wave type to the overall excitation of the VCSNS foundations. In particular, it is important to determine the relative contribution of fundamental mode Rayleigh waves because of a Board witness' testimony during the 11-16 January 1982, ASLB hearings (Tr 5716), suggesting that foundation-to-free-field reductions were explained by the smaller eigenfunction amplitudes at the foundation depth.

The principal discriminant that can be applied in order to identify wave types on the seismograms is simply to examine the propagation velocity of the principal (i.e., large amplitude) groups seen on the records. As discussed elsewhere, the particle motions of both earthquakes and explosion records of the various arrivals typically do not conform to classical seismological behavior. This complication is largely attributable to modification and transformation of the energy during propagation, but especially that near the receiver sites.

A travel-time plot was constructed for the dominant arrivals on typical records. Figure IV.B.1 shows the arrival times for the first P upkick on the vertical component and for the approximate onset of the S arrival. The travel-time curves in Figure IV.B.1 are drawn approximately along the lower bounds of the data points; these shorter travel times were observed at sites where the soil cover was thin (FR, F6), or where foundations were in contact with rock (HP and AB). The slightly longer travel times of points falling above the travel-time curves are due to propagation through the low-velocity saprolite.

The P and S velocities in Figure IV.B.1 of 18,200 and 10,250 ft/sec, respectively, are entirely reasonable for the granitic rocks that underlie the VCSNS site. These velocities correspond to a Poisson's ratio near 0.25, a value that is typical of crystalline rocks and atypical of soil or highly weathered rock. These velocities are confirmed by refraction surveys conducted on site by Dames & Moore (Preliminary Safety Analysis Report, Section 2.5.1, 1972).

The travel-time curves in Figure IV.B.1 have been superimposed on representative seismograms from shot point 3 shown in Figure IV.B.2. The superposition clearly illustrates the two dominant arrivals on the records.

Because seismic velocities in the saprolite are so much lower than in the granitic basement, group velocities of fundamental mode surface waves are much lower than those of the higher modes and of compressional and shear waves propagating in bedrock. Thus, fundamental-mode waves would arrive much later (at velocities of about 500 ft/sec) than the groups identified above. As will be shown below, the contribution of such waves to the explosion test signals is negligible.

If the coda termination time is defined as the point on the seismogram beyond which no further significant energy (<10 percent) arrives, then the velocity corresponding to this termination time places a lower limit on the group velocity that can be assigned to the transmission of energy at levels

capable of exciting the VCSNS structures. The velocity corresponding to the observed coda termination times is approximately 6000 ft/sec; no significant amount of energy propagates at velocities less than this value.

A clearly identifiable fundamental mode Rayleigh wave was observed at the tailrace site during explosion Test 2 in the October 1981 field experiments. In this case the shot-to-receiver distance was about 1100 ft and a continuous surface layer, consisting of dredge fill and saprolite, was present. This is the only case where fundamental mode surface waves were observed on any seismograms for Tests 1, 2, 3, 4 and 5. On the basis of the coda termination velocity of 6000 ft/sec and a fundamental mode surface wave velocity of 500 ft/sec observed in the 1981 test, it is concluded that almost all of the energy arrives from the source as body waves and higher mode surface waves propagating through rock rather than through the surficial layer of saprolite. It is also apparent that any fundamental mode Rayleigh waves present on the records for earthquakes and explosions are generated in the immediate vicinity of the receiver. This means that the observed reduction factors apply equally to earthquakes and explosions because both sources will generate them. These observations are consistent with the absence of a continuous and uniform layer of saprolite throughout the area. In fact, the saprolite shows large lateral variations in thickness, approaching zero in some locations.

C. Particle Motions

In order to investigate further the nature of the seismic wave arrivals, a study of seismic particle motion was conducted to see if waves of different types could be distinguished from one another by their characteristic particle motions. Results are shown on particle-motion plots in which the radial (R) component of ground motion (positive away from the source) is plotted as the abscissa (positive to the right) and the vertical component (V) as the ordinate (positive upward), with the epicenter located to the left of the origin. On such a plot, a simple P wave, characterized by longitudinal motion parallel with the direction of wave propagation from the source, should appear as pure rectilinear motion confined to the first and third quadrants of the plot.

SV waves, having displacement perpendicular to the direction of wave propagation and in the V-R plane, should appear as pure rectilinear motion confined to the second and fourth quadrants of the plot. Rayleigh waves have particle motion that is generally retrograde elliptical in the V-R plane, and should appear as counterclockwise motion about the origin in particle motion plots. A program PARTICLE was written in FORTRAN77 to construct particle motion plots of this kind.

First, an examination of the velocity records (Figure IV.C.1) computed from USGS SMA records for the earthquake of 16 October 1979, reveals that the whole-record plot shows quite chaotic motion. Figure IV.C.2 shows particle motions in the S-wave window; however, motion in the second and fourth quadrants, which would be characteristic of SV, is not prominent. The largest arrival on this portion of the record (near sample No. 70) appears to be rectilinear in quadrant 3, which is typical of P-wave motion. No clear Rayleigh wave is seen, except for one retrograde ellipse between samples 80 and 94 (Figure IV.C.2). This figure includes the largest arrivals on the accelerogram. Even for this smaller time window the motion is quite chaotic, except for the samples mentioned.

Particle motion as recorded during Test 5 on the USGS accelerograph pad (station P2) is then compared with the foregoing results. Test 5 produced a number of recordings from shots located near the instrumentally-determined hypocenter of the 1979 event. The whole-record particle motions shown in Figure IV.C.3 are complicated, but nevertheless are simpler than the earthquake data. Careful examination shows that the motion is elliptic retrograde, indicative of Rayleigh waves. Figure IV.C.4 shows the particle motions for the first 20 samples following the onset of P (the first arrival). The motion is rectilinear in the first quadrant for only the first 6 samples (0.03 sec) before becoming chaotic. Figure IV.C.5 shows the motions at the time of the largest arrivals on the records. The character of the motion apparently is a mixture of P and Rayleigh, producing a highly-eccentric retrograde ellipse. Comparing the motions on the pad with those for the same shot at site P4 (Figures IV.C.6 to 8) approximately 50 ft away from the pad,

it can be seen that the motions for the whole record shown in Figure IV.C.6 are dominantly elliptic retrograde. The largest arrival on the record at P4 which occurs in the S-wave window, seems to be quasi-P, i.e., almost rectilinear in the first and third quadrants, as shown in Figure IV.C.8. The particle motions for the 16 October 1979 earthquake exhibit a degree of complexity comparable to the particle motions for the explosion-generated waves.

D. Polarization Filtering

Polarization filtering has been used to investigate the particle motions of the records. In this method, a filter is constructed which rejects energy not showing the appropriate phase between radial and vertical components for the wave motion considered. For example, in the case of P waves, the motion should be up and away or down and toward the source. Therefore, if complex Fourier spectra are computed for the radial and vertical components, the phase angle between them should be zero. A program PHADIF, written in FORTRAN by Dennis O'Neill (O'Neill, 1982), forms a filter by rejecting each frequency for which the phase of the radial and vertical differ by more than some specified value. The output of the filter is large at those times when the vertical and radial are in phase but small at other times. Similarly, filters for SV and Rayleigh waves can be constructed based on phase differences. Application of this method to the explosion signals shows, as did the particle motion analysis, complex polarization of the wave trains atypical of simple seismic phases.

F. Summary

A comprehensive investigation of the particle motions produced by the explosion sources has revealed the complex nature of the seismograms recorded at the VCSNS. Because of the complexity of the particle motions, the decomposition method chosen for further analysis was simply selection of time windows by group velocity. This permits us to treat separately those waves that have traveled as P waves from those that have traveled to the receivers as S and higher mode waves.

V. ANALYSIS METHODS

A. Calibration of Seismograms

All seismometers (velocity transducers) were calibrated before field setup, and each recording channel (preamplifier-transmission line-amplifier) was field-calibrated before every shot sequence. The product of a seismometer's motor constant with total channel gain is the effective motor constant (in volts/cm/sec) of a given recording channel. Upon returning from the field, a program was written to divide each digital record by its associated effective motor constant. This task was performed on the same Hewlett-Packard Model 5451 (HP-5451) computer used for data acquisition, and calibrated disk files had a format and sequence identical to that of the raw data. True seismometer base motion is valid only in the frequency band from 5 to 40 Hz, in which the transducer response is constant (in both phase and amplitude). No correction for the instrumental response was done, as it was unnecessary for present purposes.

B. Data Transfer and File Structure

In order to facilitate data handling and computation, all 672 digital records required in this program were moved to files on a Prime 750 computer. This was accomplished by: (1) writing a digital magnetic tape having the desired file name and structure on the HP-5451, and (2) reading the tape and writing disk files on the Prime 750.

The files were named using the convention ("Tn.Smm.Rxys") that "T," "S," "R," and "S" are literals and the lower case letters denote variables: "n" (=3, 4, or 5) is the Test number; "mm" (=01 to 10) denotes shot number in the sequence; and "xy" is the receiving seismograph's identifier. The suffix "S" distinguishes signal data from noise data files with suffix "N." Each named file contains the 3 components of motion recorded for event (test-shot) Tn. Smm. at receiver Rxy. The 3 components are stored serially in the file,

in the sequence vertical (V), radial (R) and transverse (T). Each component record comprises 2048 data points at a sample interval of 0.005 second, for a record length of 10.24 seconds. The first data record in each file contains the file name, and the distance and azimuth from shot to receiver.

C. Spectral Ratios - Theory and Methods Applied

This section describes the methods used to compare motions at different recording sites. It is possible and meaningful to construct a "transfer function" between 2 sites, and in particular, between measurements made in the free field and upon foundations. Through this transfer function, it is then possible to estimate quantitatively the motions to be expected at a foundation site, starting with free-field motions.

Because a true transfer function is complex valued, one way to construct it is through the complex cross spectrum. Let $x(t)$ be ground motion as recorded at a particular site (e.g., the USGS pad) and let $y(t)$ be the linearly-dependent motions that would result at a different site. The signals $x(t)$ and $y(t)$, along with their complex Fourier spectra $X(f)$ and $Y(f)$, can be related linearly through the impulse response $h(t)$ with complex Fourier spectrum $H(f)$. The unknown time trace $y(t)$ can be computed from the input signal $x(t)$ and the transfer function. The estimate of y is the inverse Fourier transform of the result obtained by dividing Y with H . Brillinger (1981) and numerous other workers suggest the estimate:

$$\hat{H}(f) = Y(f)X'(f)/[X'(f)X(f)]$$

where ' denotes complex conjugation. Statistics associated with this estimate can be obtained from the coherence between X and Y , where coherence $R(X,Y:f)$ is defined as:

$$R(X,Y:f) = \frac{|X'(f)Y(f)|}{\sqrt{X'YYY'}}$$

The advantage of forming the estimate in this way is that uncorrelated noise in x and y will be reduced in the estimate of the transfer function. However, if x and y are only weakly correlated, then the linear dependence implicit in a transfer function will fail to apply. In spite of high signal-to-noise ratios, correlation is generally poor between stations recording the same shot. Therefore, estimates of the transfer function obtained in this way are not clearly applicable to this analysis.

An alternative method is available for the estimation of the transfer function via:

$$H(f) = [Y'(f)Y(f)/X'(f)X(f)]^{1/2}$$

In this case, the transfer function estimated is real and the phase information is lost. To complete the estimate of the transfer function, an ad-hoc assumption about the phase must be made. Note also that the effect of uncorrelated noise in either the x or y series will not be reduced by these estimates, and another way to reduce the effects of this unwanted noise must be found.

A program named SPECTRUM was written in FORTRAN77 for performing the computations needed in the estimation of amplitude spectral ratios. The procedure has been to compute ensemble averages of the spectral ratios from several shots. In this way, statistics can be developed for the ratios. The calculation scheme used in SPECTRUM is described later.

Plotting Format. Figure V.C.1 is a representative plot of the Fourier amplitude spectrum of the signal together with the corresponding noise spectrum (dashed line) obtained from the last one-fourth of the record. The time trace that was Fourier analyzed is shown below the spectral plot. The run number (306) is a reference to the QA cataloging scheme.

Figure V.C.2 is an example of a spectral modulus ratio. The title indicates the tests, shots, and statistics used in the computation. As the legend indicates, in this case a spectral noise correction was applied. This information is also listed in Table V.C.1.

Preprocessing. The user specifies an appropriate starting time and a sample record length for each trace, and 2 record segments of that length are then placed in working buffers. The mean value is subtracted from each signal prior to Fourier analysis.

Spectra. The data traces are converted to discrete Fourier transforms via the Cooley-Tukey (1965) fast Fourier transform method.

Noise Removal. Experimentation has shown that the best way to obtain the noise sample is from the last 512 points of the signal traces, which are sufficiently long (2048 points) that the event coda has dropped essentially to the preshot levels of noise. Because noise is primarily due to heavy machinery and depends on the starting, stopping and loading of this equipment, obtaining a noise sample from the end of the record is preferable to using a sample of noise that was recorded a few minutes before each explosion.

The steps followed in noise removal are as follows. First, power spectra are computed from the spectral amplitudes of the signal and a sample of noise. Second, at each frequency, both the numerator and denominator of the spectral ratio are computed by subtracting the noise power spectrum from the signal power spectrum and then taking the square root. To reduce the impact of spectral nulls, 2-point Bartlett (triangle) smoothing is applied before subtraction of the noise. Processing proceeds identically on the numerator and denominator power spectra. If the noise exceeds the signal at some frequency, then the value of the estimate is set to zero; smoothing will take care of the few points for which this is the case.

The approximate magnitude of this correction is illustrated by Figures V.C.3 through 6 which show the Fourier amplitude spectra of a 512-point time window at the foundation sites (AB, GS, and WP) and at a free-field site (FR), along with the corresponding noise samples (dashed lines) for comparison.

Smoothing. In addition to the light pre-smoothing to make the noise subtraction more stable, the final noise-corrected spectra are smoothed using a 6-point Bartlett (triangular) window. This smoothing is a convolution in the frequency domain and is, therefore, equivalent to a time domain multiplication by a window function (the square of a sinc function, $\sin x/x$)

Statistics. Lognormal statistics are appropriate for use here. Standard formulas are used to estimate the mean and standard error of the logs of the ratios. For plotting, the antilogs are taken so that the means shown are geometric, and the 84th percentile estimates are obtained from the mean value through multiplication and division of the mean by the geometric deviation.

The statistics of spectral modulus ratios can be computed to express the variability among different free-field sites, the variability among different shots in a shot sequence, or both. Figure V.C.7 gives the statistics of the accelerograph pad/free-field spectral modulus ratio in terms of the variability among free-field sites. In this calculation, one trial is the average pad/free-field ratio for a series of 6 Test 5 shots for a given free-field station and the number of trials is the number of free-field sites. Figure V.C.8 shows combined statistics for site-to-site and shot-to-shot variability. In this case, one trial is the spectral ratio for just one shot and one free-field site, and the number of trials is the multiplicity of sites and shots. Figure V.C.9 gives statistics of shot-to-shot variability of the spectral ratio. One trial in this case is, for one shot, the ratio of accelerograph pad spectral modulus to the average spectral modulus for all free-field sites, and the number of trials is the number of shots.

Comparing Figures V.C.7 and V.C.9, it can be seen that the site-to-site variability is of the same order but larger than the shot-to-shot variability. This indicates that geologic heterogeneity on a scale of tens of feet at the shot point location contributes less to the total variability, but not much less than does the heterogeneity of the dam abutment where the free-field recording array was deployed. The mean spectral ratios are similar for the 3 different statistical calculations, all being enveloped by the standard deviation bounds for shot-to-shot variability (Figure V.C.9).

For the spectral ratio results given subsequently that involve more than one free-field site, statistics are computed on a shot-to-shot basis and so the variability of free-field site motion is not included in the standard deviations.

D. Band-Pass Filtering

When the input time series is complicated, then narrow-band or band-pass filtering is a useful adjunct to conventional Fourier analysis. In this procedure, the time series under study is passed through a bank of narrow-band filters and the resulting outputs saved. A number of different time series similarly processed can be compared in amplitude, frequency, and time.

An advantage of band-pass filtering over Fourier analysis is that it provides more information than just the maximum amplitude of the filtered output (which scales with the Fourier spectral modulus). The distribution of the energy in time is also available, and in particular the approximate time at which the maximum amplitude associated with a particular frequency occurs. Thus, individual spectral ratios can be computed for waves propagating with the same group velocity. Subsets of relatively small time windows can also be selected for band-pass spectral analysis, and interference effects commonly observed using Fourier analysis are thereby alleviated. Another advantage of band-pass filtering is that it permits the portrayal of coherence of signals between stations. For receivers having approximately equal source distances,

body and surface wave coherence can be easily viewed for each band-pass frequency. The degree of coherence can indicate the degree to which geologic structural complexities have influenced the signal waveforms.

Filtering is accomplished by a frequency-domain Gaussian operator with constant bandwidth. The filter window function is given by:

$$F_n(\omega) = \exp \left[-\alpha \left(\frac{\omega - \omega_n}{\omega_n} \right)^2 \right]$$

where ω_n is the selected center frequency. A filter bandwidth is selected based on the degree of resolution desired in the frequency domain. A tradeoff exists between resolution in the time and frequency domains, and is controlled by the selection of α . For computational purposes, the filter is band-limited: truncation of $F_n(\omega)$ occurs at 30 dB down from the maximum filter response. This means, for example, that for a 30 dB cutoff at ± 3 Hz, 99.8 percent of the area under the Gaussian function would lie in a band of ± 3 Hz centered at ω_n and 90.4 percent would lie in a ± 1 Hz band.

A stable procedure to derive the amplitude and frequency of the filtered time series uses the "quadrature function" or "analytic signal." The Hilbert transform (Bracewell, 1965) is utilized to provide the envelope and instantaneous frequency of the filtered time trace. This procedure is used to compute the envelope and instantaneous frequency of the filtered data for any desired number of group velocity windows. It requires construction of the complex analytic signal $f(t) - iF_H(t)$, where F_H is the Hilbert transform of the band-passed time function $f(t)$. The envelope of the analytic signal is then $|f(t) - iF_H(t)|$. In practice, the analytic signal is easily produced by eliminating the negative frequency components of the Fourier transform before inverse transforming to generate the filtered time series.

E. Free-field and Foundation Motion for 16 October 1979 Earthquake

Free-field motion estimates, given as time histories and response spectra, were developed for the October 16, 1979 Monticello earthquake. These are based upon the dam abutment accelerograms of the 1979 earthquake and the spectral modulus ratio of free-field to accelerograph pad motion developed from the explosion tests. Steps taken to accomplish this task are listed below:

- (1) Compute Fourier transforms, $P(\omega)$ and $Q(\omega)$, of pad motions (90° and 180°) recorded during the 1979 earthquake.
- (2) Compute the average ratios, $R(\omega)$, average free-field-to-pad Fourier spectral moduli of explosion-generated horizontal motions.
- (3) Inverse Fourier transform $[P(\omega), Q(\omega)].R(\omega)$ to obtain free-field motions $\hat{p}(t)$; $\hat{q}(t)$.

The above procedure was also followed using Ertac's complex pad response functions, $H(\omega)$, measured parallel to the pad's axes. It was necessary first to rotate the 1979 accelerograms (90° and 180°) into the pad axes obtaining $p'(t)$ and $q'(t)$ in order to produce results to compare with Ertac's. Then $H(\omega)$ replaced $R(\omega)$ in step (2) above, and after step (3), $\hat{p}'(t)$, $\hat{q}'(t)$ were rotated back to 90° and 180° components for comparison with the first results.

Foundation motions were estimated for the Auxiliary Building, Diesel Generator Sump and Service Water Pumphouse from the 90° and 180° components of the 1979 earthquake as follows:

- (1) The free-field motion was Fourier-transformed (step 3 above) to obtain $\hat{P}(\omega)$, $\hat{Q}(\omega)$;

- (2) The average ratio of foundation to average horizontal-free-field Fourier spectral moduli was computed from the explosion-generated motions denoted by $F(\omega)$;
- (3) $F(\omega) \cdot [\hat{P}(\omega), Q(\omega)]$ was inverse Fourier-transformed to obtain $f(t)$ and $g(t)$, the foundation time histories;
- (4) The 5 percent damped response spectra were computed from $f(t)$ and $g(t)$.

TABLE V.C.1

LOG OF SPECTRAL MODULUS RATIO CALCULATIONS

Run #	Test	Shot #s	Receivers X/Y	Component	Code Revision #	Comments
1	4	3,4,5,6	P2/P3	V	2	Whole record (512 points) 6-point Bartlett smoothing window.
110	4	3,4,5,6	P2/P3	R	2	"
111	4	3,4,5,6	P2/P3	T	2	"
115	4	1,2	P2/P4	V	2	"
116	4	1,2	P2/P4	R	2	"
117	4	1,2	P2/P4	T	2	"
119	5	3,4,5,6,7,8	P2/P4	T	2	"
120	5	3,4,5,6,7,8	P2/P4	R	2	"
121	5	3,4,5,6,7,8	P2/P4	V	2	"
183	4+5	3,4,5,6,7,8 1,2 3,4,5,6	(5) P2/P1 P2/P4 P2/P5 (4) P2/P4 (4) P2/P3	R+T	2	Whole record (512 points) 6-point Bartlett smoothing window.
212	3	2,3,6,7,8	AB/F1 AB/F3 AB/F6 AB/FR	T	3	Whole record (512 points) 6-point Bartlett smoothing window. Power spectral noise was subtracted. 5 groups, 4 pairs per group.*
213	3	2,3,6,7,8	GS/F1 GS/F3 GS/F6 GS/FR	T	3	"
214	3	2,3,6,7,8	WP/F1 WP/F3 WP/F6 WP/FR	T	3	"

TABLE C.V.1 (Cont'd)

LOG OF SPECTRAL MODULUS RATIO CALCULATIONS

Run #	Test	Shot #s	Receivers X/Y	Component	Code Revision #	Comments
215	3	2,3,6,7,8	AB/F1 AB/F3 AB/F4 AB/F6 AB/FR	V	3	Whole record (512 points) 6-point Bartlett smoothing window. Power spectral noise was subtracted. 5 groups, 5 pairs per group.*
216	3	2,3,6,7,8	GS/F1 GS/F3 GS/F4 GS/F6 GS/FR	V	3	"
217	3	2,3,6,7,8	WP/F1 WP/F3 WP/F4 WP/F6 WP/FR	V	3	"
218	3	2,3,6,7,8	AB/F1 AB/F3 AB/F4 AB/F6 AB/FR	R	3	"
219	3	2,3,6,7,8	GS/F1 GS/F3 GS/F4 GS/F6 GS/FR	R	3	"
220	3	2,3,6,7,8	WP/F1 WP/F3 WP/F4 WP/F6 WP/FR	R	3	"
221	3	2,3,6,7,8	GS/AB	R+T	3	Whole record (512 points) 6-point Bartlett smoothing window. Power spectral noise was subtracted.*

TABLE C.V.1 (Cont'd)

LOG OF SPECTRAL MODULUS RATIO CALCULATIONS

Run #	Test	Shot #s	Receivers X/Y	Component	Code Revision #	Comments
222	3	2,3,6,7,8	WP/AB	R+T	3	Whole record (512) points 6-point Bartlett smoothing window. Power spectral noise was subtracted.*
223	3	2,3,6,7,8	AB/F1 AB/F3 AB/F6 AB/FR	R+T	3	Whole record (512 points) 6-point Bartlett smoothing window. Power spectral noise was subtracted. 5 groups, 8 pairs per group.*
224	3	2,3,6,7,8	GS/F1 GS/F3 GS/F6 GS/FR	R+T	3	"
225	3	2,3,6,7,8	WP/F1 WP/F3 WP/F6 WP/FR WP/FR	R+T	3	"
226	4	3,4,6 7,9	AB/P3 AB/F5 AB/F5	V	3	Whole record (512 points) 6-point Bartlett smoothing window. Power spectral noise was subtracted.*
227	4	3,4,6 7,9	AB/P3 AB/F5 AB/F5	R	3	"
228	4	3,4,6 7,9	AB/P3 AB/F5 AB/F5	R	3	"
229	4	3,4,6 7,9	AB/P3 AB/F5 AB/F5	R+T	3	"

TABLE V.C.1 (Cont'd)

LOG OF SPECTRAL MODULUS RATIO CALCULATIONS

Run #	Test	Shot #s	Receivers X/Y	Component	Code Revision #	Comments
230	4	3 7,9	GS/P3 GS/F5 GS/F5	V	3	Whole record (512) points 6-point Bartlett smoothing window. Power spectral noise was subtracted.*
231	4	3 7,9	GS/P3 GS/F5 GS/F5	R	3	"
232	4	3 7,9	GS/P3 GS/F5 GS/F5	T	3	"
233	4	3, 7,9	GS/P3 GS/F5 GS/F5	R+T	3	"
234	4	3,7,9	GS/AB	V	3	"
235	4	3,7,9	GS/AB	R	3	"
236	4	3,7,9	GS/AB	T	3	"
237	4	1,7,9	GS/AB	R+T	3	"
238	3	2,3,6,7,8	GS/AB	T	3	"
239	3	2,3,6,7,8	GS/AB	R	3	"
240	3	2,3,6,7,8	GS/AB	V	3	"
241	3	2,3,6,7,8	WP/AB	V	3	"
242	3	2,3,6,7,8	WP/AB	R	3	"
243	3	2,3,6,7,8	WP/AB	T	3	"
244	4	1,2,3,4,6	AB/P2	R+T	3	"

TABLE V.C.1 (Cont'd)

LOG OF SPECTRAL MODULUS RATIO CALCULATIONS

Run #	Test	Shot #s	Receivers X/Y	Component	Code Revision #	Comments
245	5	3,4,5,6,7,8	P2/P1 P2/P4 P2/P5	V	3	Whole record (512 points) 6-point Bartlett smoothing window. Power spectral noise was subtracted. 3 groups, 8 pairs per group.*
246	5	3,4,5,6,7,8	P2/P1 P2/P4	V	3	Whole record (512 points) 6-point Bartlett smoothing window. Power spectral noise subtracted. 6 groups, 3 pairs per group.*
247	5	3,4,5,6,7,8	P2/P1 P2/P4 P2/P5	V	3	Whole record (512 points) 6-point Bartlett smoothing window. Power spectral noise was subtracted.*
248	4	1,2,3,4,5,6	GS/P2 P2/P4 P2/P5	R+T	3	"
249	4	1,2,3,4,6	AB/P2 P2/P4 P2/P5	R+T	3	"
250	4	1,2,3,4,6	AB/P2	R	3	"
251	4	1,2,3,4,6	AB/P2	R	3	"
252	4	1,2,3,4,6	GS/P2	R	3	"
253	4	1,2,3,4,6	GS/P2	R	3	"
254	4	3,4,6	AB/P3	R+T	3	"

TABLE V.C.1 (Cont'd)

LOG OF SPECTRAL MODULUS RATIO CALCULATIONS

Run #	Test	Shot #s	Receivers X/Y	Component	Code Revision #	Comments
255	3	2,3,6,7,8	AB/FR	V	3	P-window (64 points). No smoothing. Power spectral noise was subtracted.*
256	3	2,3,6,7,8	AB/FR	V	3	S-window (128 points). 2-point Bartlett smoothing window. Power spectral noise was subtracted.*

* 2-point smoothing was applied prior to noise subtraction.

VI. RESULTS

A. Introduction

This section presents results concerning spectral modulus ratios, band-pass filtering, and foundation response spectra computed for the 16 October 1979 earthquake. First, the pad/free-field spectral ratios (both direct spectral modulus ratios and ratios of maximum envelope amplitudes from band-pass filtered records) are discussed. Next, the foundation/free-field modulus ratios are similarly discussed together with the additional consideration of time windows. These results provide the means to make a two-stage calculation of the foundation/pad spectral ratio. This end result is then compared to a direct, single-step calculation of the same ratio for the Auxiliary Building.

Free-field motions for the 16 October 1979 earthquake are computed by a deconvolution of the pad motion using the empirical transfer functions developed from the explosion test data. A separate deconvolution of the pad motion was performed using the transfer functions provided by Ertec. Response spectra for these 2 separate estimates of free-field motion are presented. Finally, foundation response spectra for the 1979 earthquake at the Auxiliary Building, Diesel Generator Sump, and Service Water Pumphouse are computed based upon the deconvolution of the 1979 pad motion. In addition, response spectra are computed on the basis of a direct transfer function (obtained from Test 4) between the USGS pad and the plant foundations.

B. Accelerograph Pad/Free-Field Spectral Ratios

In Tests 4 and 5, seismometers were placed on the accelerograph pad and in the immediate vicinity of the pad on the dam abutment. The sensors on the accelerograph pad (Station P2) were placed at the same location and elevation as the USGS SMA accelerograph. For Test 5, 3 stations were installed in a linear array in the azimuth of shot point 5, at locations 50 ft NW (P1), 50 ft SE (P4) and 250 ft SE (P5) in relation to the accelerograph pad

(see Figure III.A.5). In Test 4, site P4 was occupied for shots 1 and 2, and then the station was moved to a point (P3) 15 ft (approximately 3 pad dimensions) from the pad for shots 3 through 6. For shots 7 through 10, the P2 and P3 sites were unusable because of noise generated by the operation of the nearby Fairfield Pumped Storage Facility.

Fourier spectral modulus ratios were computed from the first 2.56 seconds (512 samples) of the shot records; the records were not corrected for the low level of ambient noise. The free-field spectral ratios exhibit substantial variation across the array. The topography and complexity of the bedrock geologic structure and of saprolite structure at the dam abutment probably contribute to the lack of coherence of seismic signals. Coherence is poor even for the pair P2 and P3, separated by 15 ft. Coherence functions and Fourier spectral ratios for P2 and P3 are shown in Figures VI.R.1 through 3 for the vertical, radial, and transverse components for Test 4. Spectral ratios for P2 and P4 (50 ft separation) in Figures VI.R.4 through 6 for Test 4 are only grossly similar. Substantial differences are observed when the spectral ratios for P2 and P4 for Test 4 are compared with the corresponding ratios for Test 5 shown in Figures VI.B.7 through 9. Pad-to-shot-point azimuths are 180° and 315° , respectively, for Tests 4 and 5.

On the basis of these comparisons, it is evident that the computed spectral ratios of pad to free field contain anomalous propagation effects that cannot readily be separated from the pad/soil response per se. The explosion test data neither resolve nor were intended to resolve the pad/soil interaction phenomena, nor do they separate any interaction phenomena from propagation effects. However, there is a sound rationale for using the pad/free-field explosion data to obtain a more robust estimate of expected or average free-field motion.

A grand average of Test 4 and Test 5 pad/free-field spectral modulus ratios for horizontal components was computed for all available data as shown in Figure VI.B.10. Test data included in this average for Test 5 are: P2/F1, P2/P4, and P2/P5 for shots 3, 4, 5, 6, 7, and 8; and Test 4 data

included are: P2/P4 for shots 1 and 2, and P2/P3 for shots 3, 4, 5, and 6. This spectral ratio is used to compute the foundation response spectra, using the USGS accelerograph data for the 16 October 1979 event as a starting point. A similar calculation was done using the Ertec pad/free-field complex transfer function.

Band-pass filtering analysis was performed for pad sites P2 and P3 for Test 4, shots 2, 3, 4 and 6. The proximity of P3 to P2 (15 ft) provides an excellent opportunity to study waveform coherence frequency-by-frequency using this technique.

Figures VI.B.11 through 14 show the envelope plots for the vertical, radial, and transverse components (numbered 1, 2 and 3) for sites P2 and P3. The first 256 points (1.28 sec) of signals from shots 2, 3, 4 and 6 are shown. The center frequencies selected for the band-pass filter (upper left of each trace) are indicated. The envelopes for P2 and P3 are given as solid and dashed traces, respectively. The numbers to the right of the traces give the maximum amplitude of the envelope for the 256-point window. The upper number corresponds to P2 (solid) and the lower to P3 (dashed). Some general remarks on the P2 and P3 envelopes follow.

- (1) The coherence of motion from one shot to another is generally very good and is higher at the lower frequencies.
- (2) The consistency of motions from one frequency to the next for a given shot and site is generally poor. Except for a few frequency bands (e.g., 24 to 30 Hz, vertical), the dominant amplitude generally moves in an irregular fashion over the time window. This means that over a broad range of frequencies, there is no single group arrival (or phase) that dominates in amplitude.

Figures VI.E.15 through 26 are the band-pass spectral ratios computed from the P2 and P3 envelopes. Four different time windows (0 to 1.28, 0.16 to 0.48, 0.48 to 0.80, and 0.80 to 1.28 sec) were selected for the spectral ratio calculation; these windows correspond to portions of the record that differ considerably in trace amplitude, dominant frequency, and group arrival time. For the vertical and radial components, selection of group velocity window generally has little effect on the trends of the spectral ratios. The transverse components exhibit considerably more scatter when compared in the 4 windows.

C. Foundation/Free-Field Spectral Ratios

Before presenting the foundation/free-field results, it is appropriate to discuss the differences between spectral ratios derived from different time windows of the seismograms. One objective of the test program was to compare spectral ratios for P waves, S waves, and surface waves. As noted in Section V.E, the complex nature of the recorded data allows consistent categorization only in terms of the major wave groups rather than by individual isolated phases. This discussion presents an example of the analysis of records on which easily identifiable groups travel at the P- and S-wave velocities. In Figures VI.C.1 through 5 are presented seismograms and spectra recorded at the sites AB (Auxiliary Building foundation) and FR (free field) for 5 shots of Test 3. The windowed first arrivals (P waves) at each site are presented, together with their amplitude spectra; the free-field spectra are indicated by a dashed line. The free-field signal amplitude is comparatively larger and its spectral modulus is higher over the entire frequency range shown. When these 5 ratios (i.e., AB and FR) are grouped individually (similar to the arrangement in Figure V.C.8), the result is the spectral ratio plot shown in Figure VI.C.6. Similarly, consider a window around the SV interval for the same records, shown in Figure VI.C.7 to 11, and the corresponding average ratio shown in Figure VI.C.12. The average P-wave spectral ratio in Figure VI.C.7 is very similar to the average SV-wave spectral ratio in Figure VI.C.12, and both are similar to the whole-record ratios given in the next section. A similar result is obtained when ratios are computed within group velocity windows using narrow-band filtering, as will be discussed. Collectively, these results support the use of whole-record modulus ratios for the estimation of foundation versus free-field ground-motion effects.

All foundation/free-field results reported below were obtained from Tests 3 and 4. In Test 3, 5 equidistant free-field stations were arrayed in an arc subtending an angle of 80° . (The transverse component at one free-field station, F4, was lost due to an amplifier malfunction.) Records with satisfactory signal-to-noise ratio were obtained in all 3 instrumented foundations for 5 of the 8 shots in Test 3. For Test 4 there were 2 free-field stations, separated by 80° and equidistant from the Auxiliary and Diesel

Generator Buildings; satisfactory signal-to-noise ratios existed at the Auxiliary Building for 5 shots, and at the Diesel Generator Building for 3 shots. The epicentral distance of the Service Water Pumphouse from Test 4 shots was about 500 ft greater than for the other foundations, and usable signals were not obtained on the horizontal components because of high levels of ambient noise.

Almost all results given below were obtained from the first 2.56 seconds (512 samples) of the records, and noise estimates were obtained from the last 2.56 seconds of the 10.24-second records. Signal spectral moduli both for foundation and free-field records were estimated by subtraction of power spectra and subsequently smoothed with a Bartlett window of halfwidth 6 points. Log normal statistics were computed for the ratio of foundation to average free-field spectral modulus, with the number of trials equal to the number of shots. The standard deviations shown in the figures express the variability between shots, but not between equidistant free-field sites.

Test 3 results for the Service Water Pumphouse are given in Figures VI.C.13, 14, 15 and 16 for the vertical, radial, transverse, and combined horizontal components. Foundation/free-field ratios are less than 1 for frequencies above about 5 Hz, and are generally less than 0.5 for the horizontal components. Figure VI.C.16 is adopted as the horizontal spectral modulus ratio for the Service Water Pumphouse/free field. This ratio was computed from the horizontal components for Test 3, shots 2, 3, 6, 7 and 8, and free-field stations F1, F3, F6, and FR.

Test 3 results for the Auxiliary Building foundation are shown in Figures VI.C.17, 18, 19 and 20 for the vertical, radial, transverse, and combined horizontal components. As in the case of the Service Water Pumphouse data, the spectral modulus ratios are basically reproducible from shot to shot in the test series.

The apparent fine structure in the Auxiliary Building/free-field spectral ratios seen in Test 3 is not reproduced in the corresponding results for Test

4, shown in Figures VI.C.21 through 24. For example, a prominent peak of about 1 at 20 Hz in the radial-component ratio for Test 3 does not appear on either horizontal component for Test 4. Similarly, the fine structure in the vertical component ratios is dissimilar for Tests 3 and 4. However, the general spectral ratio levels are not appreciably different.

Note that the free-field sites are different for the 2 tests and so differences in free-field site spectra contribute to the variation between Test 3 and Test 4 spectral ratios.

A third set of foundation/free-field spectral ratios (for a third azimuth [N30°E] and shot point distance [14,000 ft]) is available for the Auxiliary Building as a result of Test 1 conducted in 1981 (Applicants' Additional Seismic Testimony: Active Field Experiments, [1981]). In Test 1, seismograms were recorded at the dam abutment (close to P3). The Auxiliary Building/free-field spectral modulus ratios for Test 1 are similar to the Test 3 and Test 4 results in terms of average ratio (about 0.5 or less) in the band 5 to 40 Hz for horizontal components, with an overall tendency of the ratio to increase with frequency above 10 Hz; the Test 1 Auxiliary Building/free-field spectral ratio is shown later in the report.

To obtain an average horizontal spectral ratio for Auxiliary Building/free-field, results for combined horizontal components for Test 3 (Figure VI.C.20) and for Test 4 (Figure VI.C.24) were later averaged geometrically to compute response spectra. For Test 3 the data comprising this average are: shots 2, 3, 6, 7 and 8 and free-field stations F1, F3, F6 and FR; for Test 4, shots 3, 4 and 6 for P3 and F5 and shots 7 and 9 for F5. Free-field site P3 was unusable for shots 7 to 10 of Test 4 due to noise generated by operation of the Fairfield Pumped Storage Facility.

Test 3 results for the Diesel Generator Building are given in Figures VI.C.25 through 28 and the corresponding results for Test 4 are shown in Figures VI.C.29 through 32. Spectral ratios for the radial and transverse components exhibit peaks exceeding 1 at frequencies near 20 Hz and 10 Hz,

respectively, for Test 3; for Test 4, neither horizontal component has a maximum at either of these frequencies. The combined horizontal-component spectral ratio for Test 3 (Figure VI.C.28) uses the records for shots 2, 3, 6, 7 and 8 and free-field stations F1, F3, F6, and FR. For Test 4, the combined horizontal-component ratio (Figure VI.C.32) consists of data for shot 3 (sites P3 and F5) and shots 7 and 9 (site F5). As before, the Test 3 and Test 4 horizontal results were combined for the Diesel Generator/free-field spectral ratio to compute response spectra.

To examine the relative response of the various foundations, spectral ratios were computed for the Diesel Generator/Auxiliary Building for Test 3 (Figure VI.C.33 through 36) and Test 4 (Figures VI.C.37 through 40), and for the Service Water Pumphouse/Auxiliary Building for Test 3 (Figures VI.C.41 to 44). As in the case of the foundation/free-field results, the ratios differ considerably between Tests 3 and 4. The differences are smaller when the 2 horizontal components for each test are combined (Figures VI.C.36 and VI.C.40). The average Diesel Generator Sump/Auxiliary Building foundation spectral ratio is approximately 1.5 in the band 5 to 30 Hz. Service Water Pumphouse/Auxiliary Building ratios for all 3 components show similar form. From 5 to 40 Hz, the combined horizontal-component spectral ratio WP/AB decreases by an order of magnitude.

Of all 3 foundations, only the Service Water Pumphouse with mat foundation on saprolite shows response as high as, or higher than, free-field response at frequencies below 5 Hz. Compared to the theoretical ratio of about 1 (or higher, due to inertial resonance) at low frequency that applies to a structure embedded in an elastic halfspace, foundations of both the Auxiliary Building and Diesel Generator Building exhibit low response relative to the free field. In the frequency band of 10 to 40 Hz, the Service Water Pumphouse spectral reductions are even more pronounced than the Auxiliary Building/free-field reduction discussed earlier.

Horizontal-component spectral ratios were computed for the Auxiliary Building and Diesel Generator Sump relative to the UEGS pad (P2), as well as

the Auxiliary Building relative to P3 (all for shot point 4). The former allows one to compute a single-step, direct transfer function between the USGS accelerograph pad and the VCSNS foundations. Computation of response spectra using this direct transfer function serves as a method of confirming the two-step process, i.e., pad to free field, then free field to foundation. The AB/P3 spectral ratio was computed in order to compare it with the ratio between the same 2 locations that resulted from Test 1 in the 1981 field program. Combined horizontal-component spectral ratios AB/P2, GS/P2 and AB/P3 are shown in Figures VI.C.45, 46 and 47, respectively.

Figure VI.C.48 shows the north-south and east-west spectral ratios that were computed for the Auxiliary Building and Dam Abutment recordings for Test 1 in 1981; these 1981 records are reproduced in Figure VI.C.49. These spectral ratios can be compared directly with the combined horizontal-component spectral ratio AB/P3 shown in Figure VI.C.47. With the exception of the band from 0 to about 5 Hz, the agreement between the 2 ratios is good.

An analysis of foundation to free-field spectral ratios derived from band-pass filtered recordings for the Auxiliary Building, the Diesel Generator Building and free-field was performed for one Test 3 shot. This analysis examines the sensitivity of the foundation to free-field spectral ratios to the selection of time windows. Figures VI.C.50 to 67 show the band-pass spectral ratios for the selected windows. Three windows were selected for AB, GS and free field; the windows for AB and free-field are 0 to 1.28, 0 to 0.39 and 0.39 to 1.28 seconds; the three corresponding windows for GS are 0 to 1.28, 0 to 0.45, and 0.45 to 1.28 sec. The second and third windows correspond to group arrivals P and S⁺, respectively. Although the overall signal amplitudes for the P and S windows are different, the spectral ratios are very similar. The spectral characteristics also differ according to the component of motion, but the spectral ratios computed for the P and S⁺ windows are similar for each separate component. Comparison of Figures VI.C.50, C51, and C52 shows the character of the spectral ratios to be similar, whether the P and S windows are treated separately or whether the whole record is analyzed.

D. Free-Field Motion for 16 October 1979 Earthquake

The calculated free-field motion (in the 90° and 180° directions) for the 16 October 1979 earthquake was derived from the transfer functions developed from the explosion test data according to the method outlined in Section V.E. The 5 percent damped response spectra are shown in Figure VI.D.1. A comparison to the 5 percent damped response spectra for the 2 components of motion measured on the pad during the same event (Figure VI.D.2) indicates significant reductions.

The ratio of acceleration spectral values for the free field and the 16 October 1979 earthquake is shown in Figure VI.D.3. These values are approximately 1 from 0 to 10 Hz, 0.85 at 20 Hz, 0.75 at 25 Hz, and about 0.75 from 25 to 33 Hz. The results are almost identical for the 2 components of motion.

The 5 percent damped response spectra for the 2 components of the free-field motions generated using the transfer function (modulus and phase information) provided by Ertec are shown in Figure VI.D.4.

E. Foundation Response for 16 October 1979 Earthquake

The calculated foundation motions for the 2 horizontal components of the 16 October 1979 earthquake were obtained using the method outlined in Section V.E. The 5 percent damped response spectra (2 components at foundation floor levels) for the Auxiliary Building, the Diesel Generator Sump and the Service Water Pumphouse using the appropriate foundation to free-field spectral ratios discussed above, are shown in Figures VI.E.1 through 3.

The motion and response spectra for the foundation floor levels of all 3 structures are significantly less than those corresponding to the free field. The ratio of acceleration spectral values for the 16 October 1979 earthquake and the foundation motion in the Auxiliary Building are shown in Figure VI.E.4. The ratios are approximately 0.20 from 0 to 15 Hz and vary between 0.20 and 0.30 in the frequency range 15 to 33 Hz.

The corresponding spectral ratios for the Diesel Generator Sump are shown in Figure VI.E.5. The ratios are 0.3 or less from 0 to 15 Hz, increasing to a peak of 0.45 at approximately 24 Hz, and then decreasing to approximately 0.33 at 30 Hz and above. Similarly, the response spectral ratios for the Service Water Pumphouse foundation and the 1979 earthquake are shown in Figure VI.E.6. All ratios are below 0.4 in the frequency range from 4 to 33 Hz.

The equivalent spectra using the free-field motion derived with transfer functions from the Ertac report are shown in Figures VI.E.7 through 9 for the Auxiliary Building, Diesel Generator Sump and Service Water Pumphouse, respectively.

F. Direct Pad/Structural Foundation Response

It is of interest to compare the pad to structural foundation spectral ratios obtained directly from Test 4 in which the stations P2 and AB or GS are approximately equidistant from the shot point. It is apparent from the plot of spectral ratio of AB/P2 or GS/P2 (Figures VI.C.45 and 46) that the directly measured ratios are comparable to the cumulative effect of the pad to free-field ratio and the free-field to AB or GS foundation ratios, which confirms the two-stage procedure.

The 5 percent damped response spectra at foundation floor level for the Auxiliary Building and Diesel Generator Sump using these spectral ratios are shown in Figures VI.F.1 and 2, respectively. These are comparable to those obtained using the two-stage process.

VII. CONCLUSIONS

Seismic motions in the frequency band 5 to 40 Hz from shallow explosions in bedrock have significantly lower amplitudes in the foundations of the Virgil C. Summer Nuclear Station (VCSNS) than at equidistant points in the free field. Time and frequency domain analyses show that there are no discernible differences between the reductions of foundation motion relative to free-field motion for wave groups with velocities corresponding to P waves and P coda (18,000 ft/sec to 10,000 ft/sec), and wave groups corresponding to S and higher mode surface waves (10,000 ft/sec to 6,000 ft/sec). Very little of the total energy arrives in wave groups with velocity less than 6,000 ft/sec; in particular, there are no discernible later arrivals for groups with a velocity less than 1000 ft/sec which would correspond to fundamental-mode surface waves. There are no systematic differences between the reductions of foundation motion relative to free-field motion observed for the radial and transverse components: reductions of the horizontal components are systematically greater than for the vertical component.

Because reductions of the horizontal motions in the foundations are observed to be essentially the same for radial and transverse components and for both wave groups containing significant energy in the band 5 to 40 Hz (including body waves of different incidence angles), it is inferred that reductions of the same magnitude as observed for shallow explosion sources would be found for shallow earthquake sources. Thus, given free-field motions for the 16 October 1979 earthquake, the horizontal response of the VCSNS foundations can be calculated by applying the empirical foundation to free-field transfer functions measured in the experimental program.

Motions recorded on the USGS accelerograph pad at the dam abutment show significant amplifications in the band 5 to 40 Hz, compared with motions recorded nearby on saprolite at the dam abutment. The pad/free-field transfer function obtained from the seismographic data incorporates local site effects at the accelerograph pad as well as pad/soil response effects. Free-field motions calculated by applying the empirical pad/free-field transfer function

to the horizontal components of the 16 October 1979 accelerogram are approximately 20 percent lower than the recorded pad motions in the band 10 to 40 Hz.

Horizontal foundation/free-field spectral modulus ratios for 3 VCSNS buildings all show significant reductions in the band 5 to 40 Hz. For the Auxiliary Building foundation, the average ratio in the band 5 to 40 Hz is 0.5 or less for Tests 3 and 4. These results are very similar to those for Test 1 reported in Applicants' Additional Seismic Testimony (1981). Therefore, essentially the same reductions of foundation motion are obtained for a considerable range of distances and azimuths: 14,000 ft, 3,700 ft, and 4,300 ft; and 30°, 200°, and 240° respectively for Tests 1,3, and 4. Compared with the Auxiliary Building foundation, motions in the Diesel Generator Sump with foundations on caissons are approximately 50 percent larger in the band 5 to 30 Hz. Motions in the Service Water Pumphouse with mat foundation on saprolite are significantly higher than Auxiliary Building motions at low frequencies (below 10 Hz), but significantly lower at high frequencies (above 25 Hz).

Horizontal accelerograms, calculated for the VCSNS foundations by applying successively, the empirical accelerograph pad/free-field and the empirical foundation/free-field transfer functions to the 16 October 1979 earthquake accelerograms, show substantial reductions; the peak foundation accelerations are no more than one-third of the recorded peak pad accelerations. Similarly, horizontal-response spectral amplitudes in the band 5 to 40 Hz are substantially lower in all 3 foundations than on the accelerograph pad. This conclusion is confirmed by a direct comparison of Auxiliary Building foundation and accelerograph pad motions recorded in Test 4.

VIII. REFERENCES

- Active Field Experiments in Applicants' Additional Seismic Testimony, Vol. 2, South Carolina Electric and Gas Company, December 1981.
- Bracewell, R., 1965. The Fourier Transform and Its Applications, McGraw-Hill, New York.
- Brillinger, D.R., 1981. Time Series Data Analysis and Theory, Holden-Day, Inc., San Francisco.
- Cooley, J.W. and Tukey, J.W., 1965. An algorithm for the machine calculation of complex Fourier series, Math. Comput., Vol. 19, pp. 297-301.
- O'Neill, D., 1982. Development and Application of a Frequency Domain Phase-Difference Polarization Filter, Chapter 4, Ph.D. Dissertation, Pennsylvania State University.



FIGURE 11
 SOURCE LOCATIONS FOR EXPLOSION TESTS

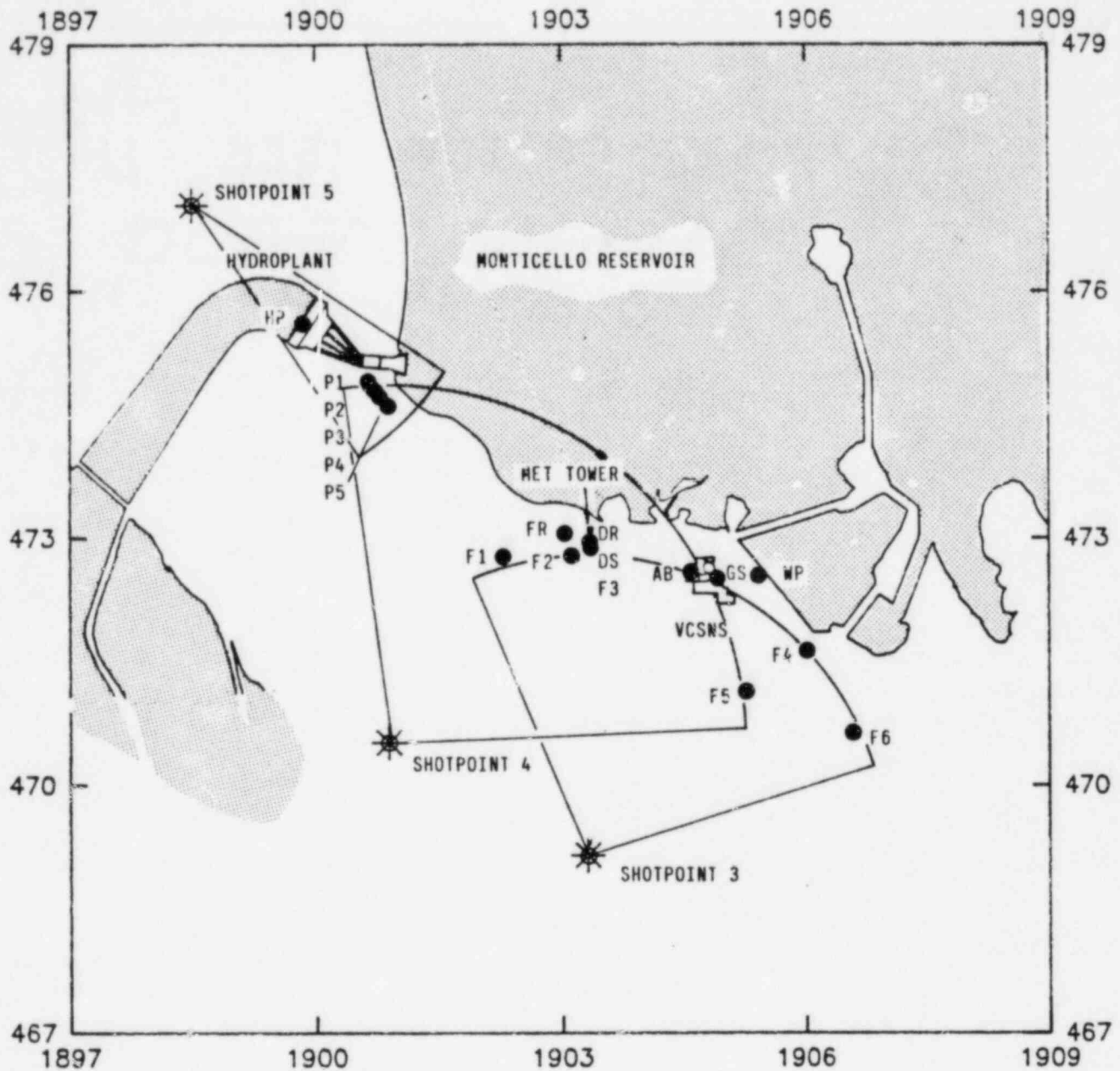
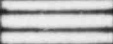
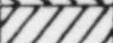


Figure III.A.1 Overview of Shotpoint and Receiver locations for 1982 Explosion Tests 3, 4 and 5.

COLOR	FORMATION
	CHARLOTTE BELT GNEISS
	GRANOFELS [foliated or gneissic rock of granitic texture and composition]
	MIGMATITE [mixture of granitic, gneissic and other rocks]
	GRANODIORITE [Adamellite]

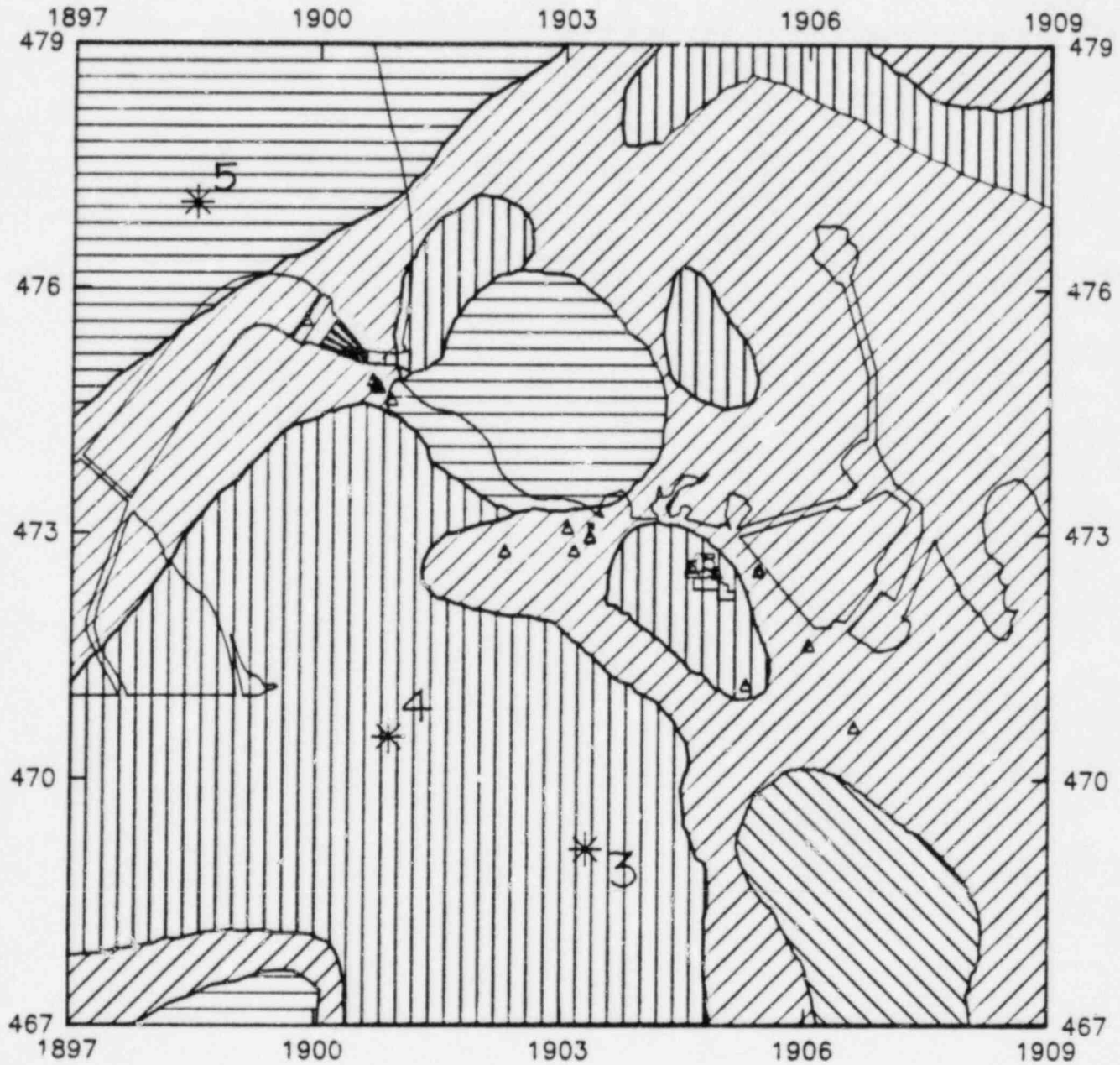


Figure III.A.2 Geologic Map of Test Area

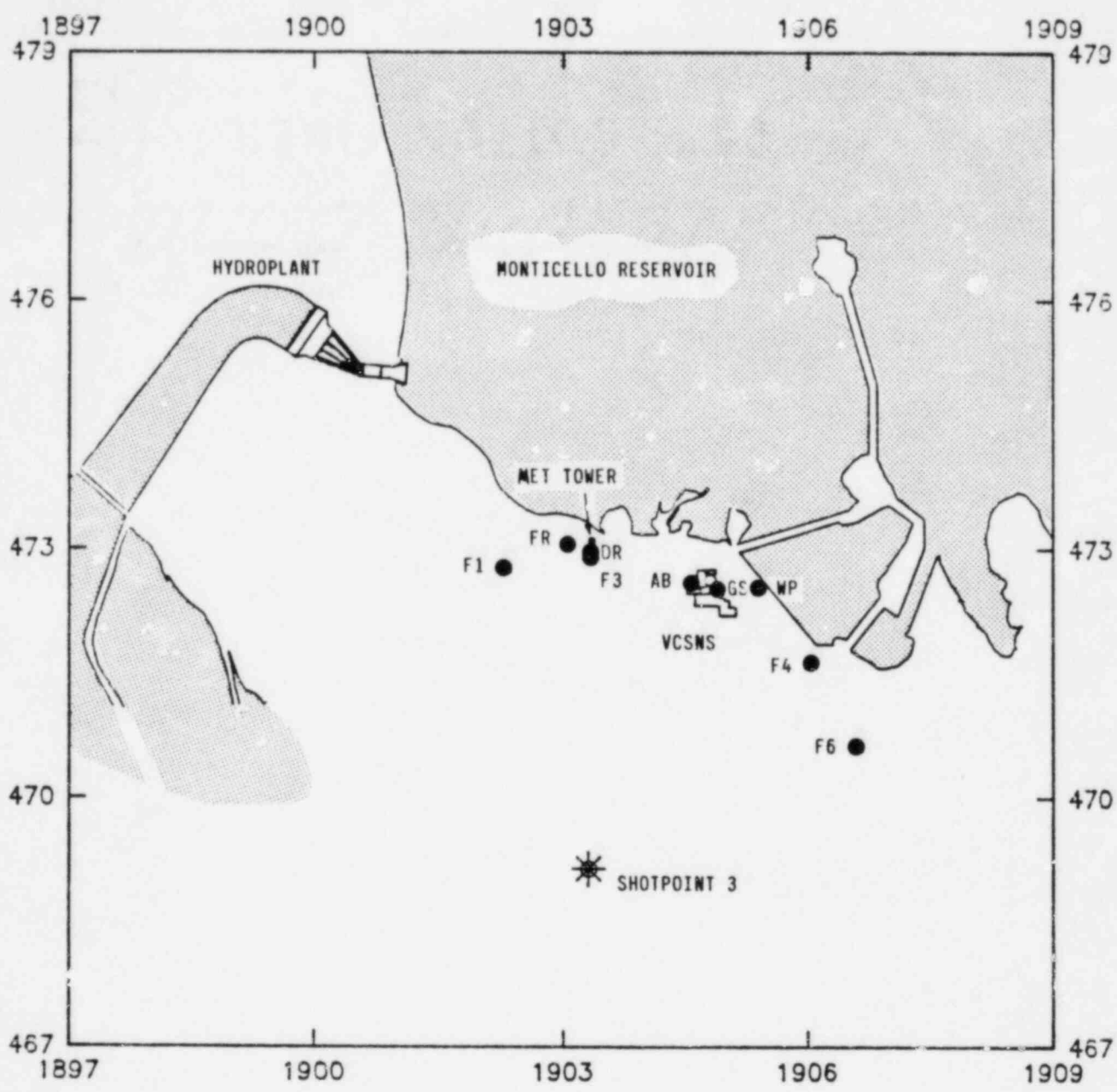


Figure III.A.3 Receiver locations for explosion test 3

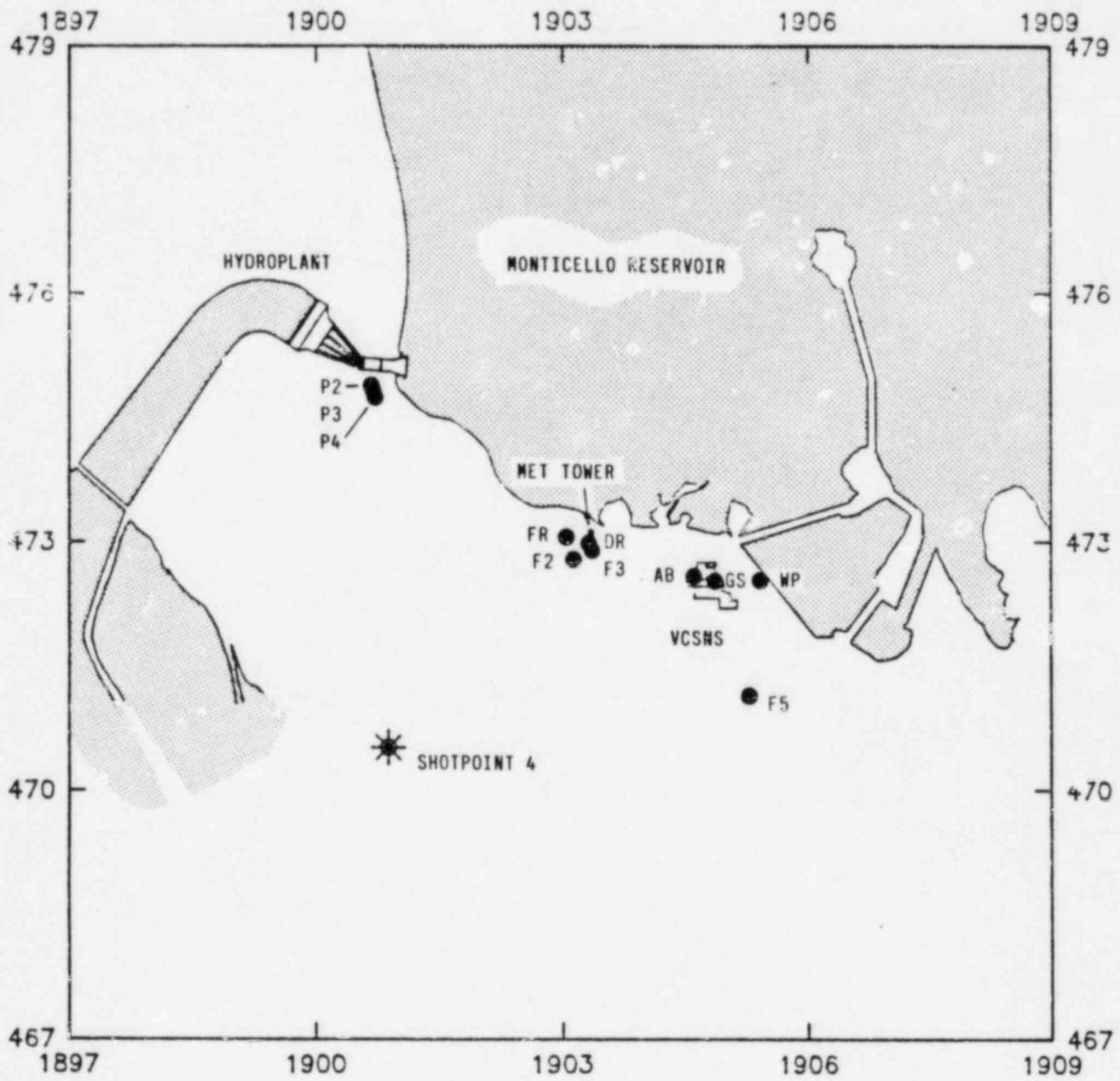


Figure III.A.4 Receiver locations for explosion test 4

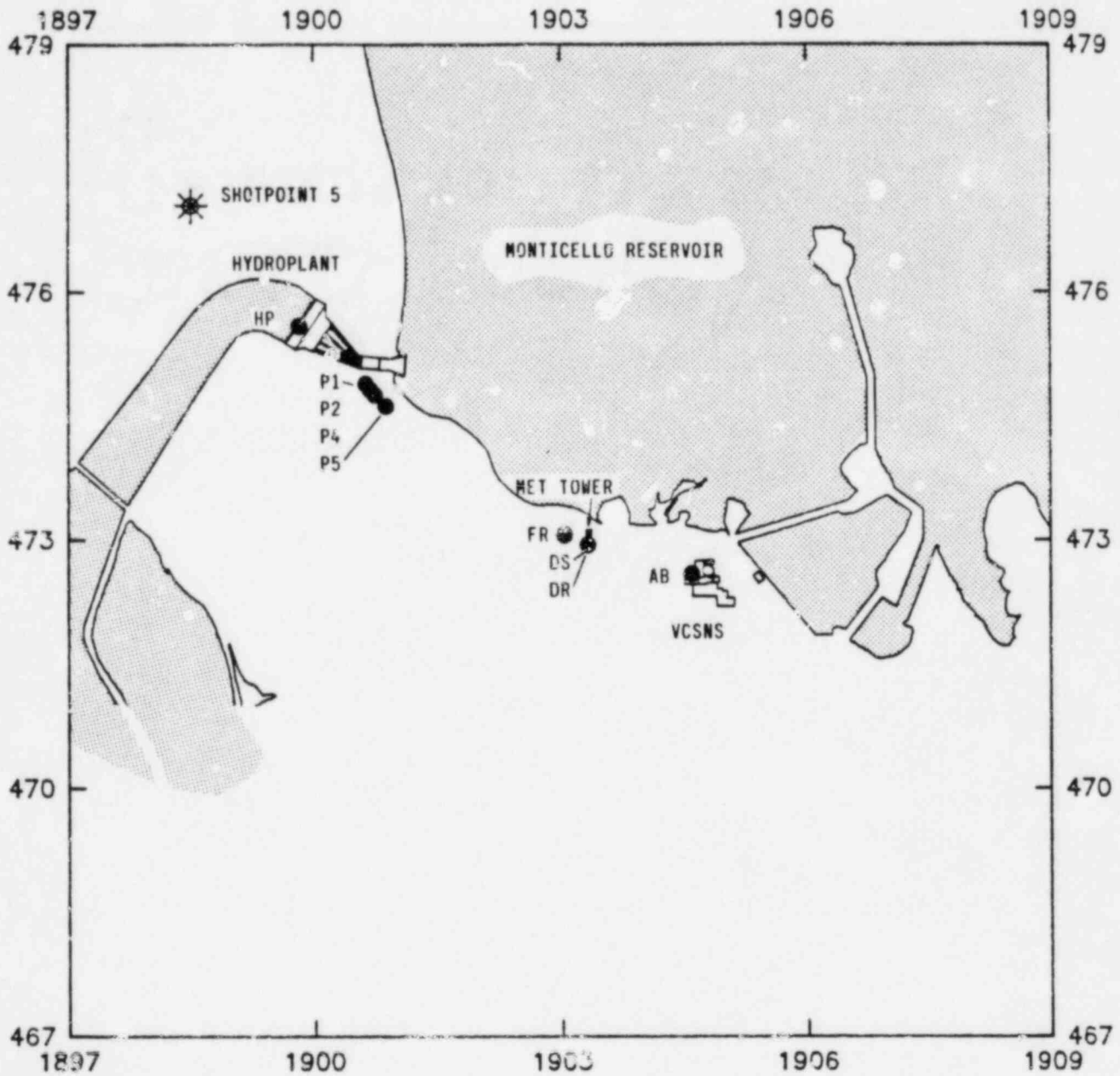


Figure III.A.5 Receiver locations for explosion test 5

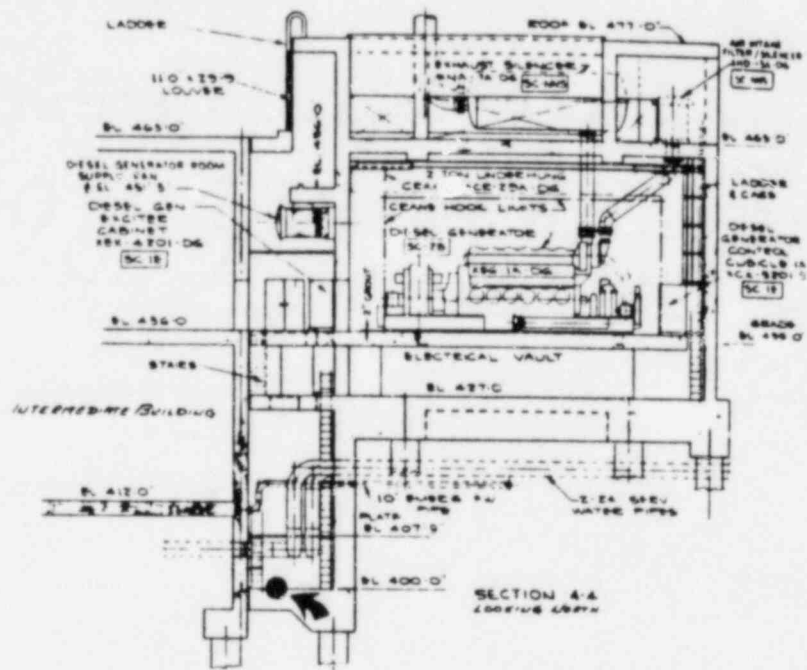


Figure III.A.7 Section showing instrument location in the sump of the Diesel Generator Building at elevation 400 ft.

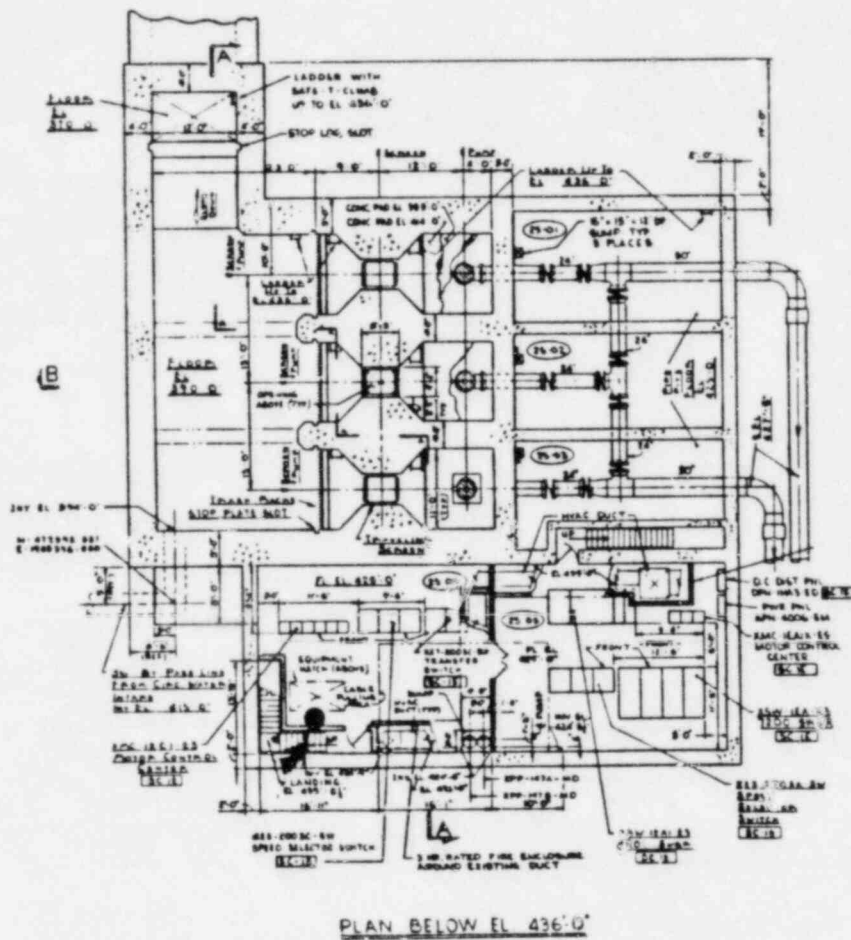


Figure III.A.8 Plan showing instrument location on the foundation of the Service Water Pumphouse at elevation 425 ft.

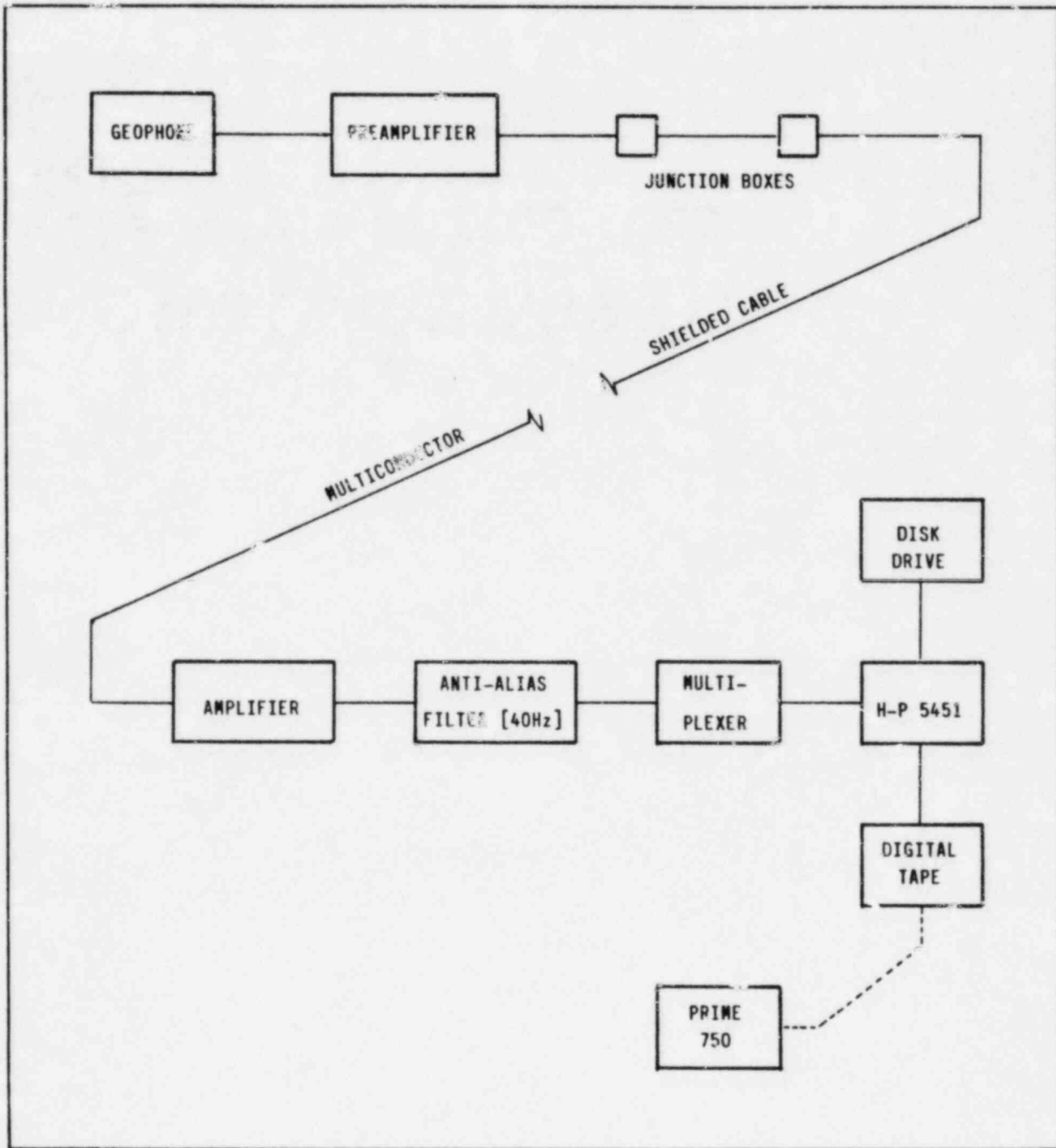


Figure III.C.1 Block schematic diagram of Data Acquisition System

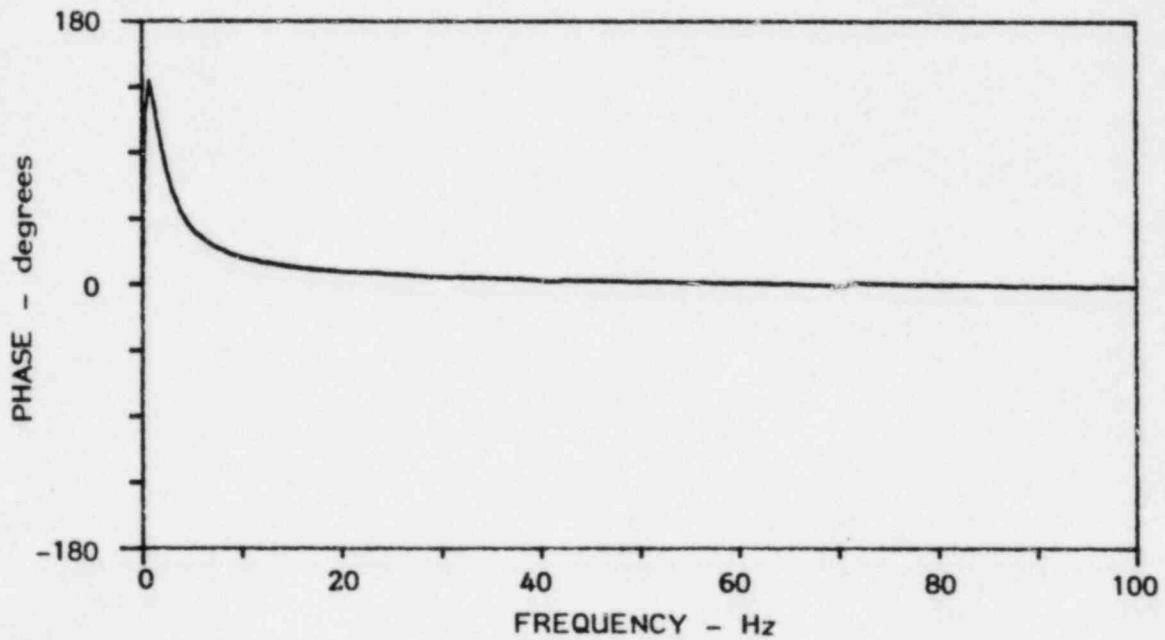
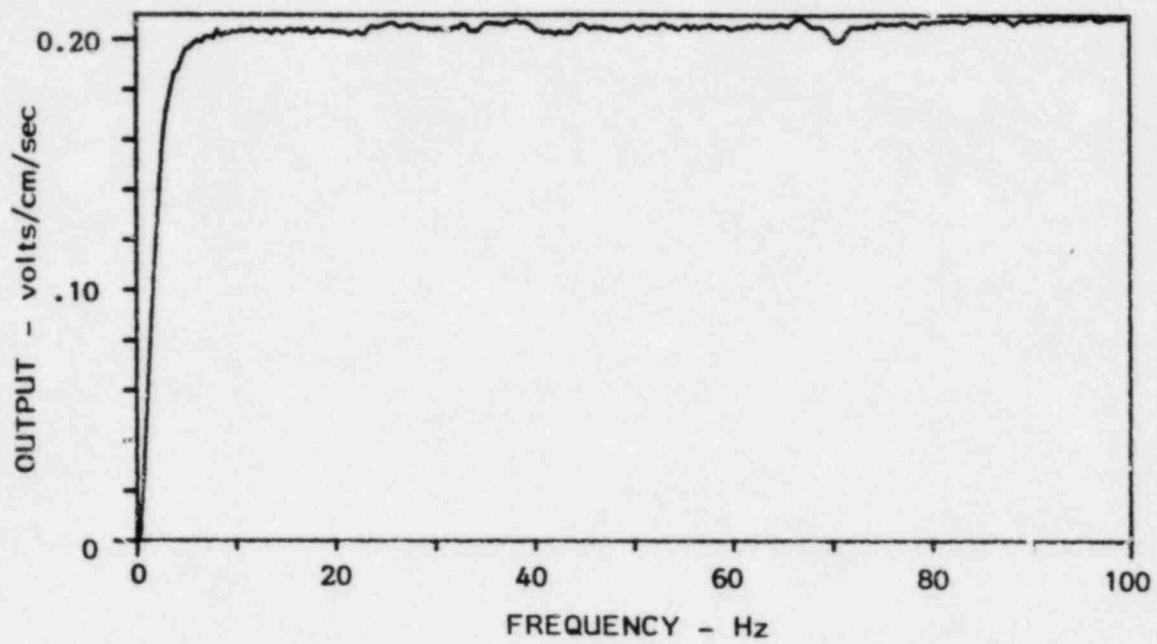


Figure III.C.2 Sensitivity and phase characteristics of typical L-22 geophone

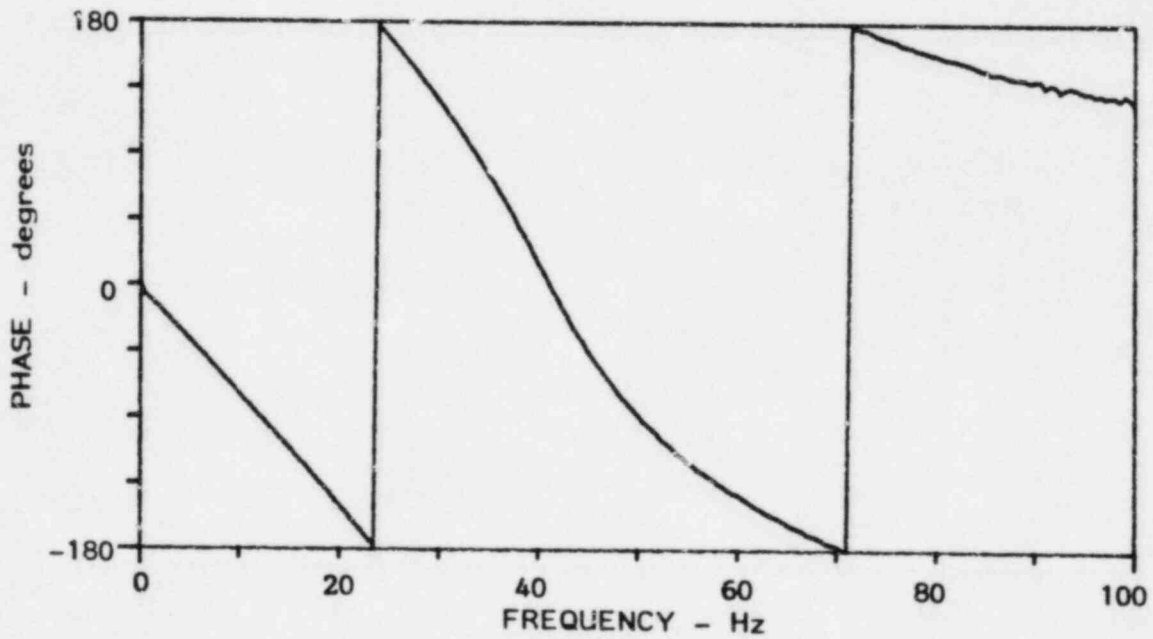
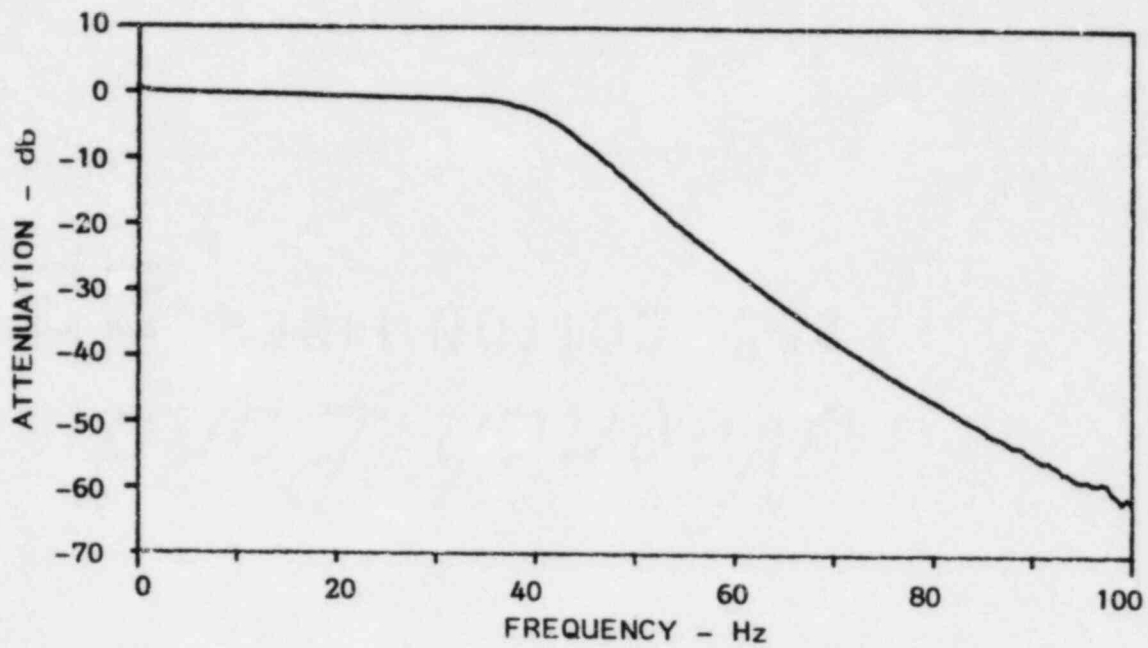


Figure III.C.3 Transmission characteristics of anti-alias filter

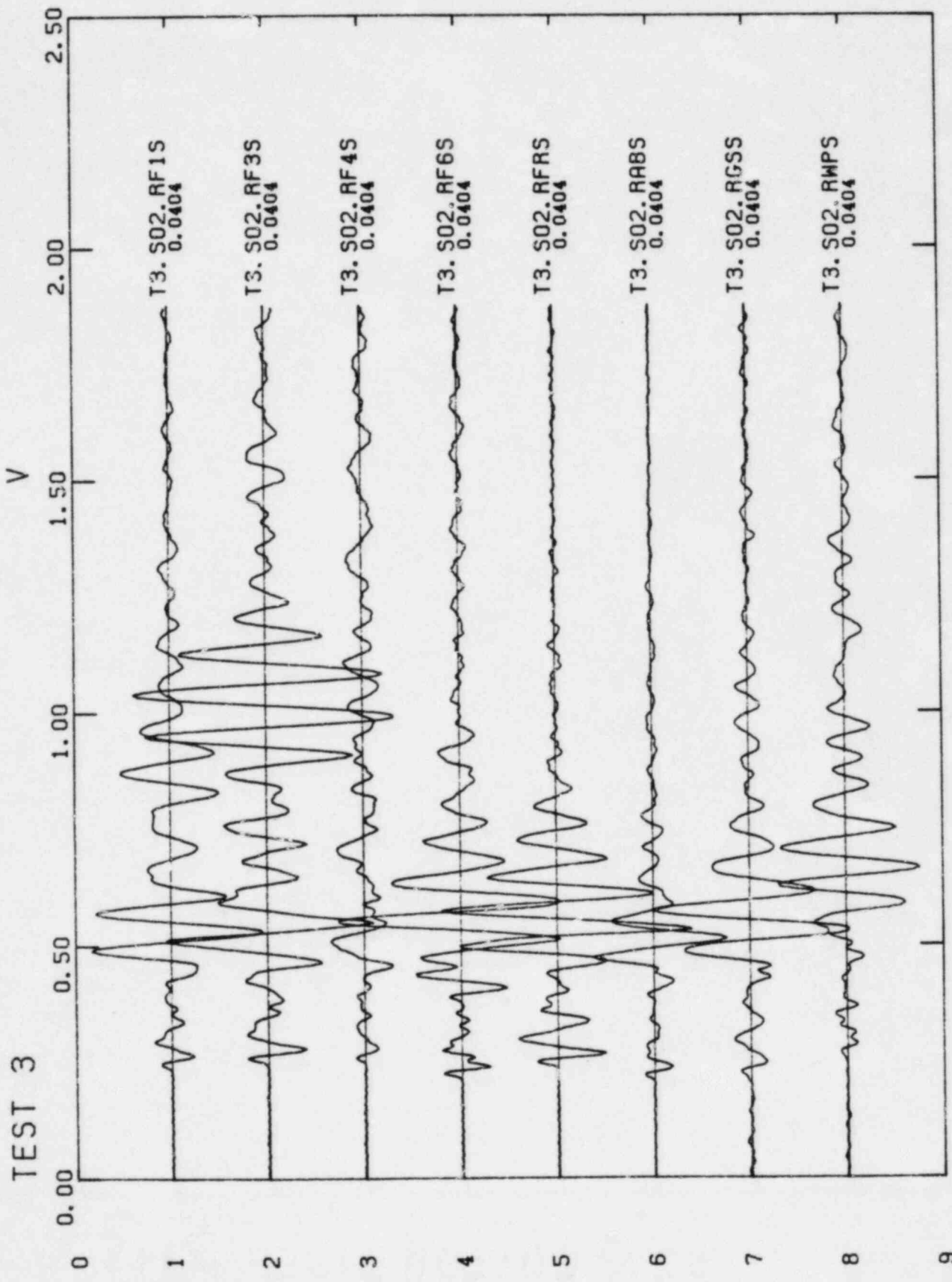


Figure IV.A.1 Representative seismograms for foundation and free-field sites from Test 3, Shot 2, vertical component. Vertical scale: 1"=0.040 cm/sec.

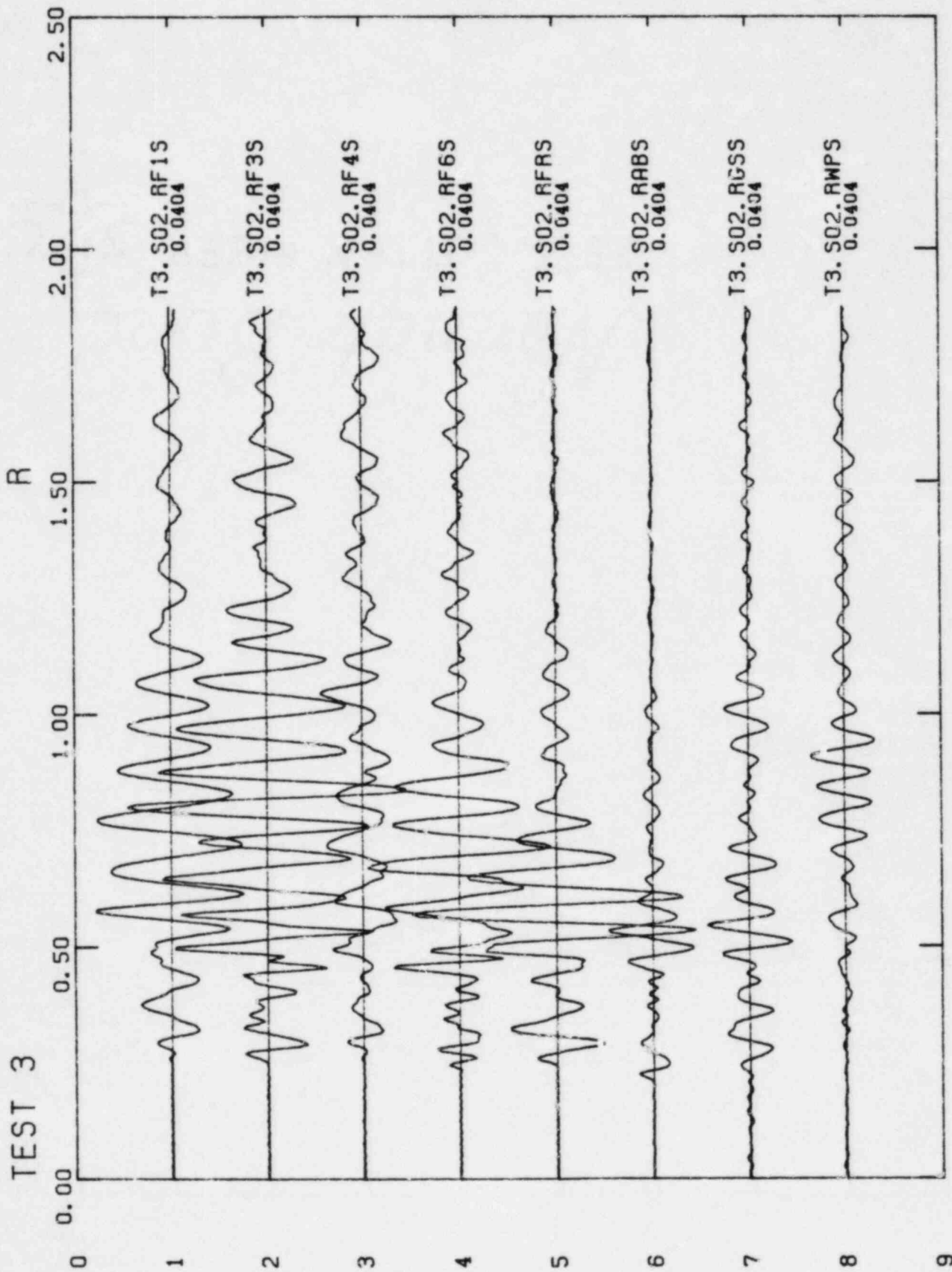


Figure IV.A.2 Representative seismograms for foundation and free-field sites from Test 3, Shot 2, radial component. Vertical scale: 1"=0.040 cm/sec.

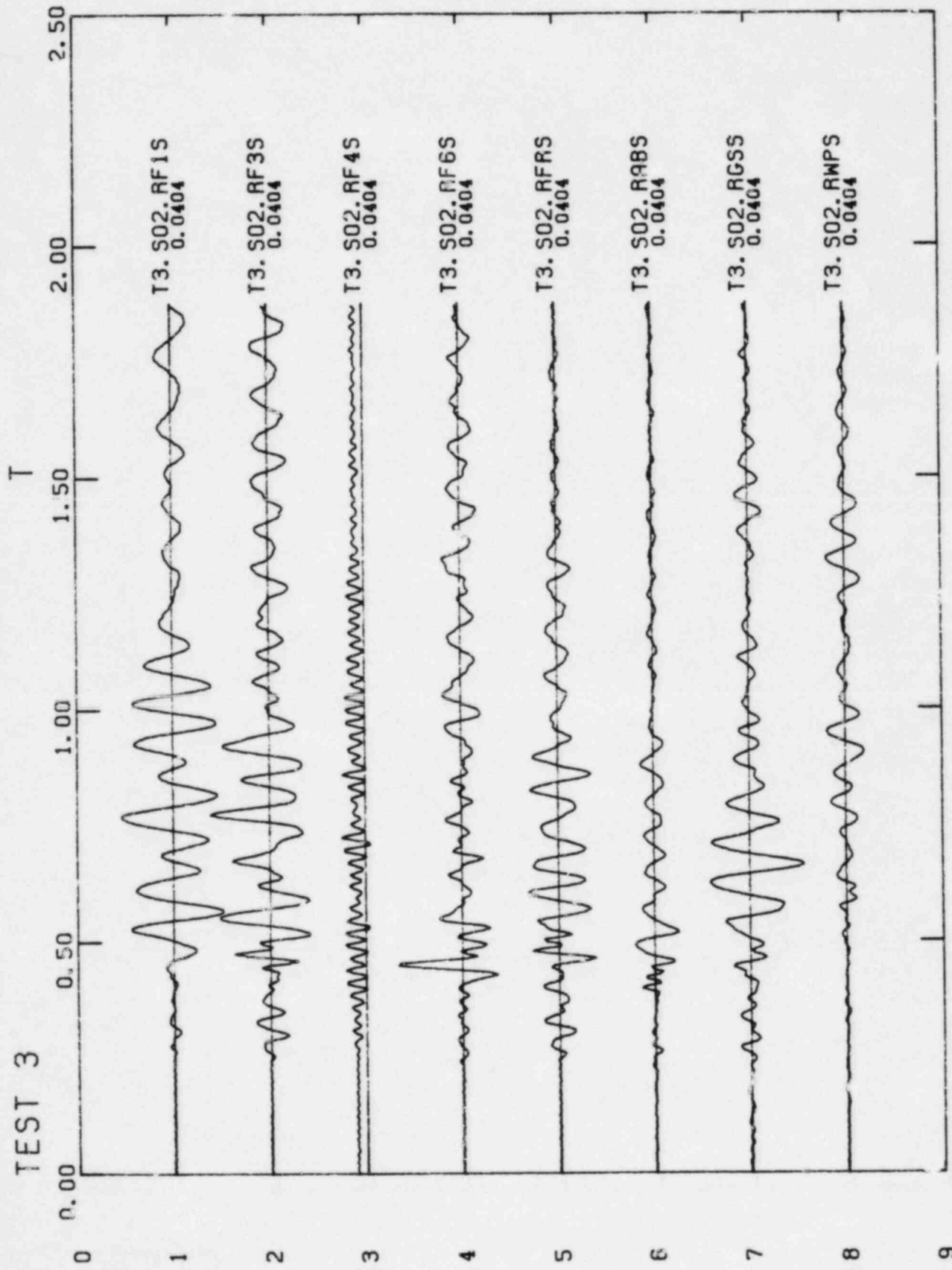


Figure IV.A.3 Representative seismograms for foundation and free-field sites from Test 3, Shot 2, transverse component. Vertical scale: 1"=0.040 cm/sec.

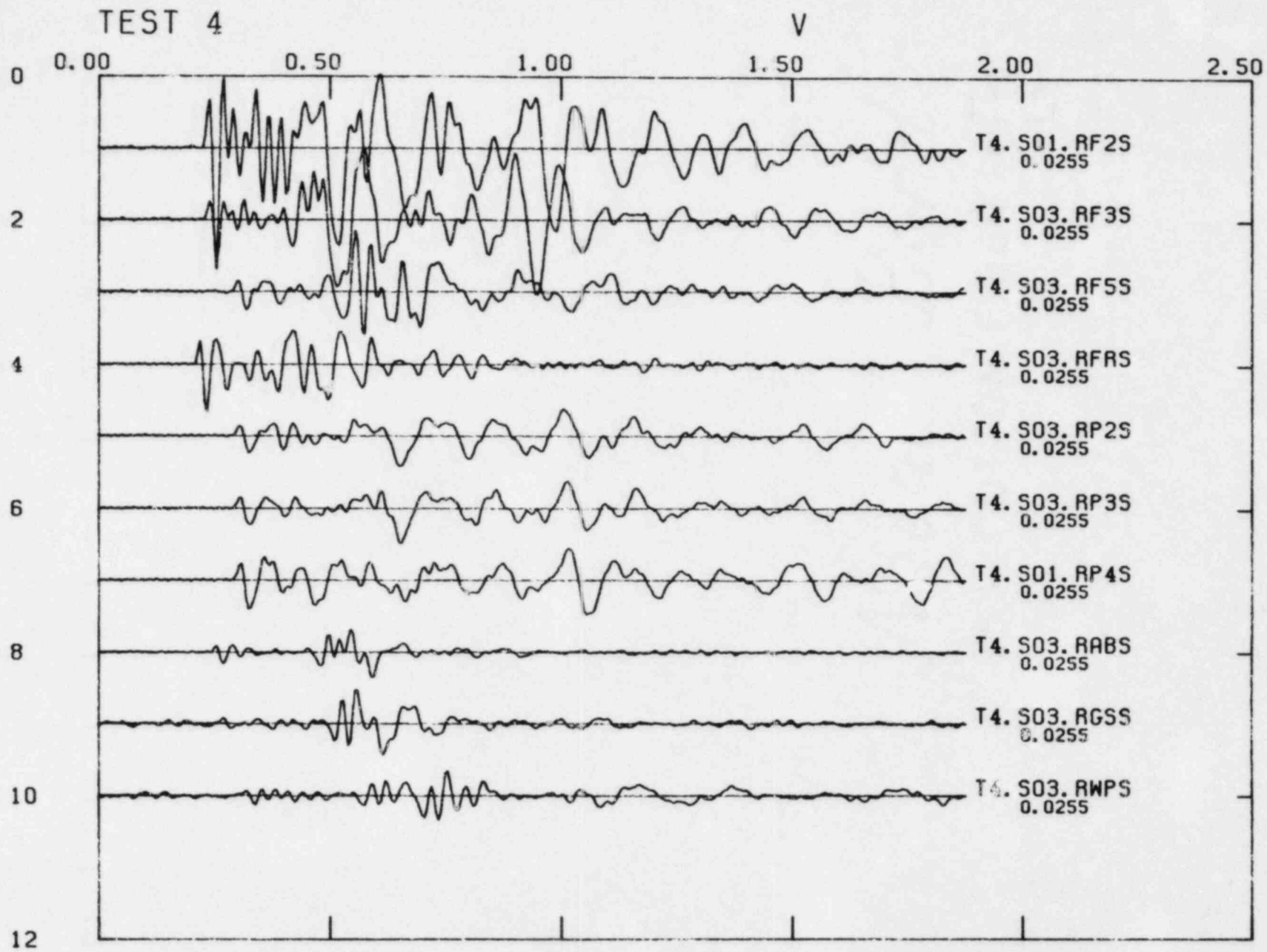


Figure IV.A.4 Representative seismograms for foundation and free-field sites from Test 4, Shots 1 and 3, vertical component. Vertical scale: 1"=0.026 cm/sec.

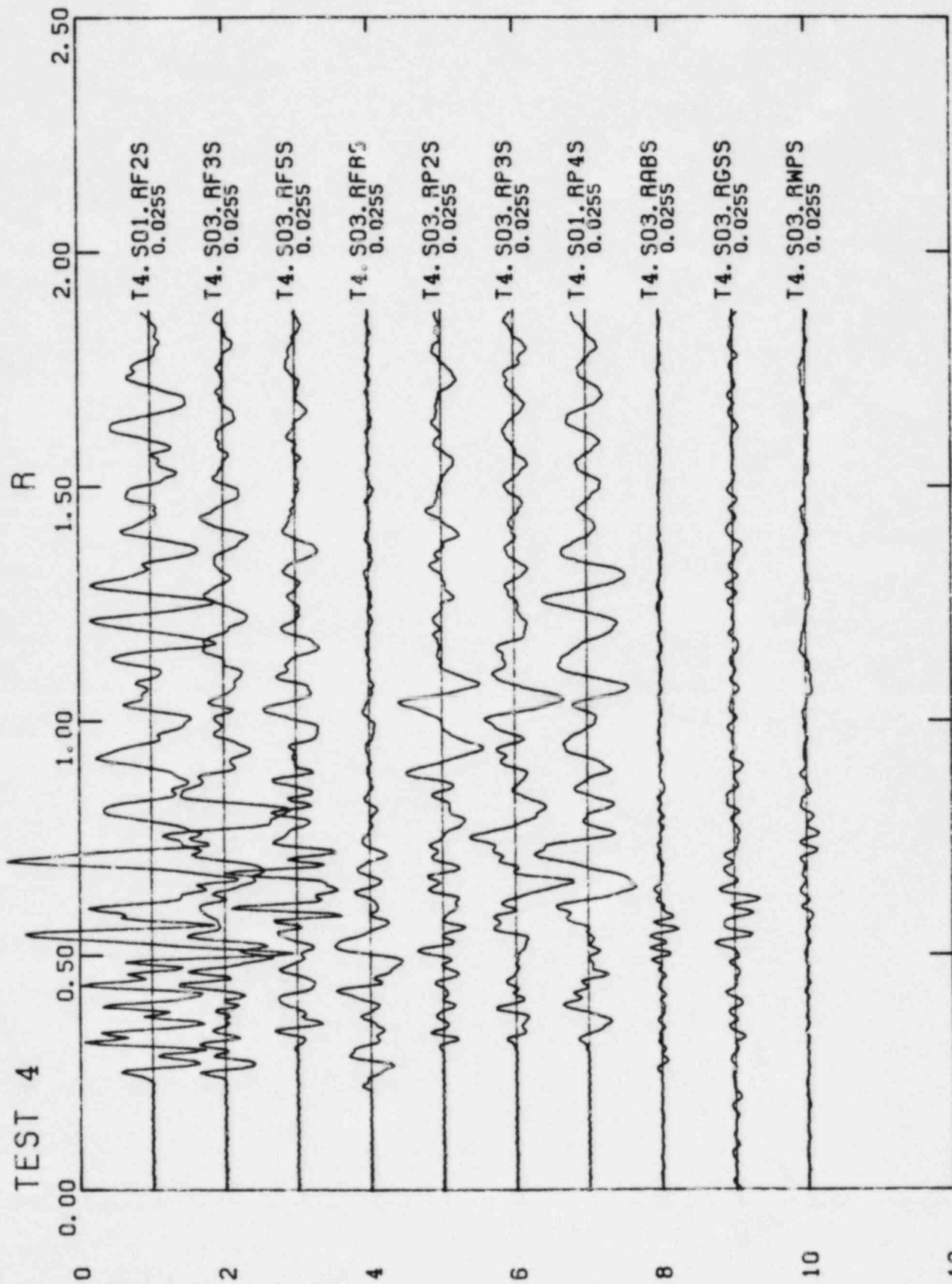


Figure IV.A.5 Representative seismograms for foundation and free-field sites from Test 4, Shots 1 and 3, radial component. Vertical scale: 1"=0.026 cm/sec.

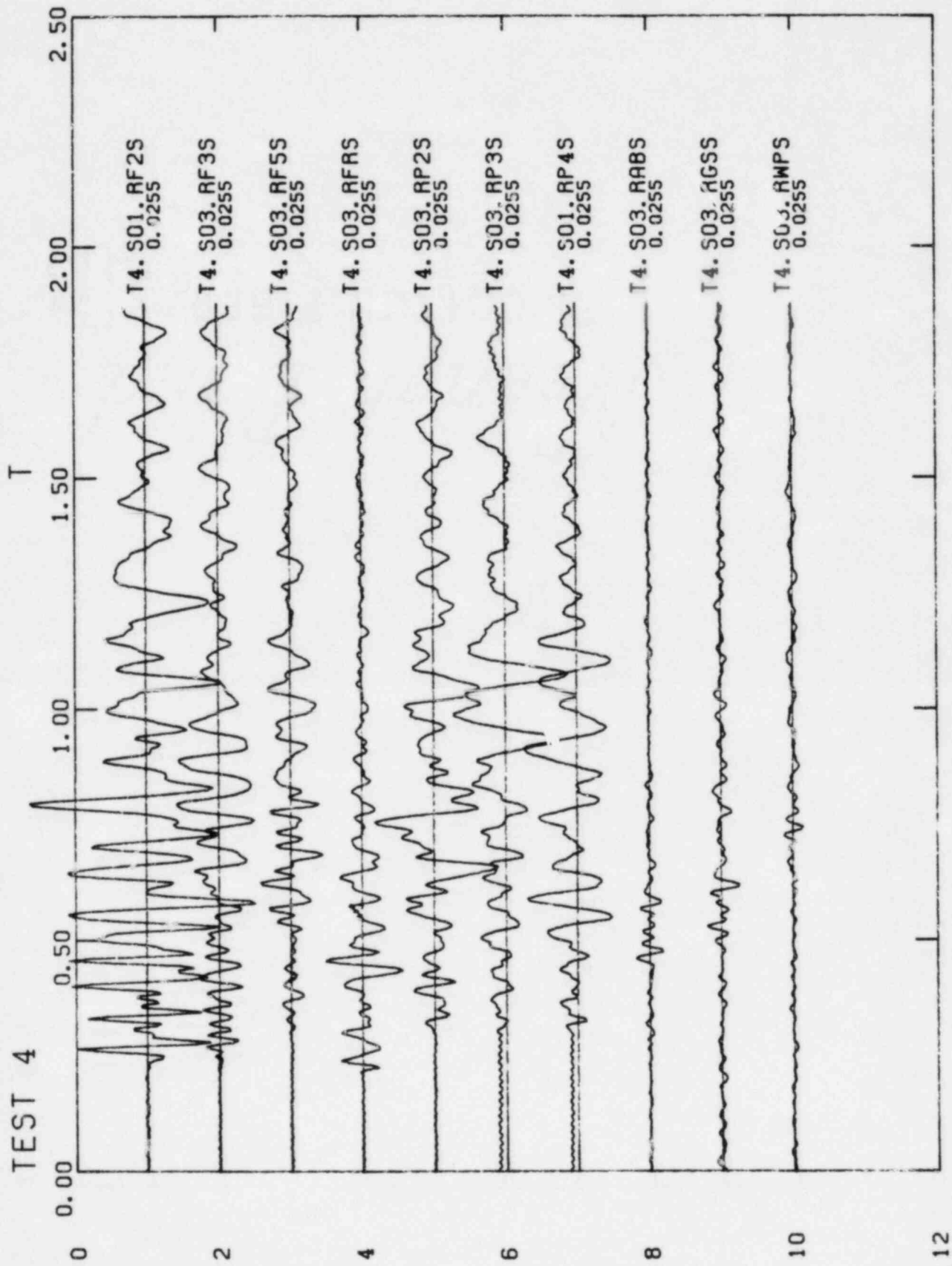


Figure IV.A.6 Representative seismograms for foundation and free-field sites from Test 4, Shots 1 and 3, transverse component. Vertical scale; 1"=0.026cm/sec.

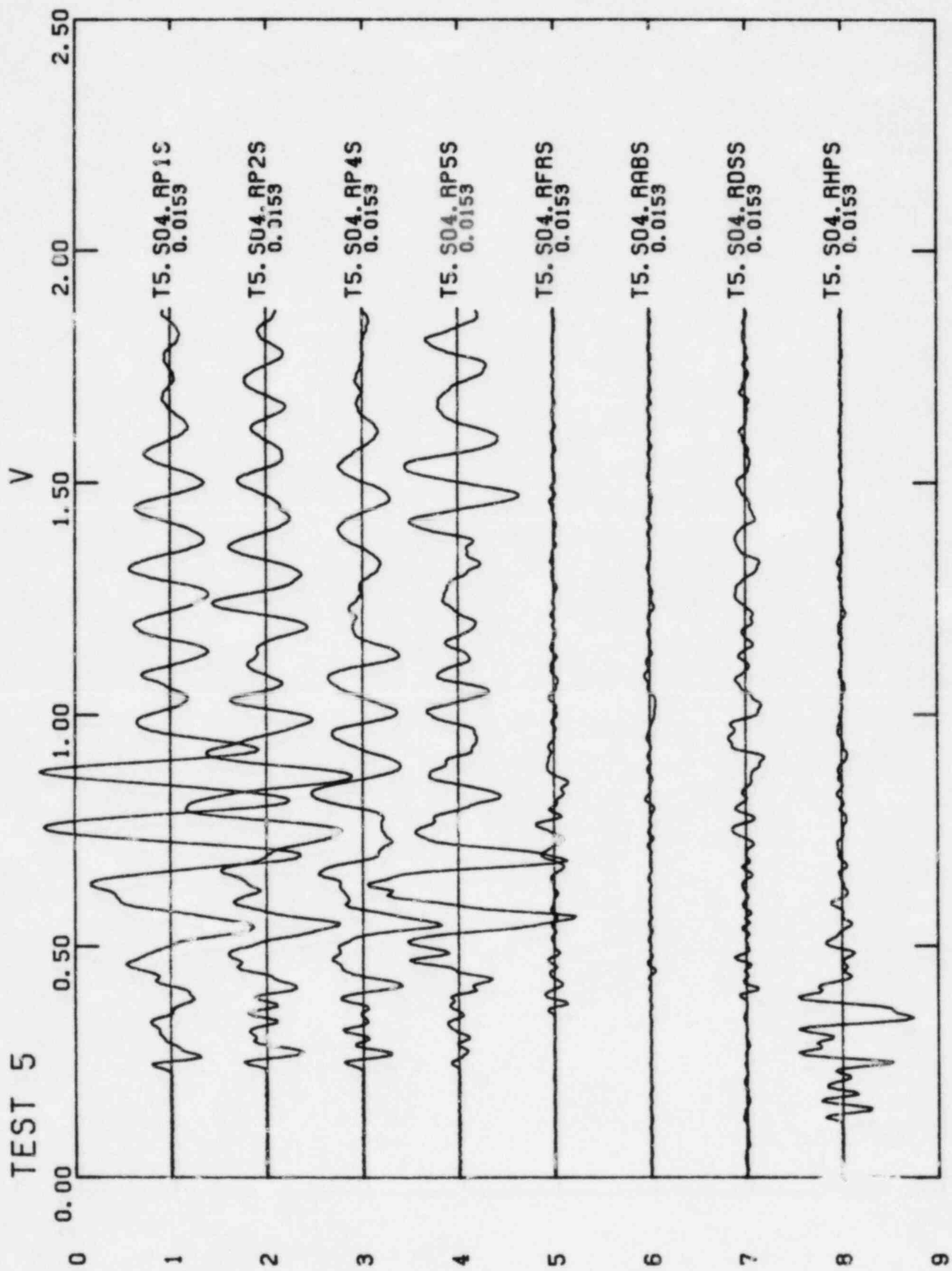


Figure IV.A.7 Representative seismograms for foundation and free-field sites from Test 5, Shot 4, radial component. Vertical scale: 1"=0.015 cm/sec.

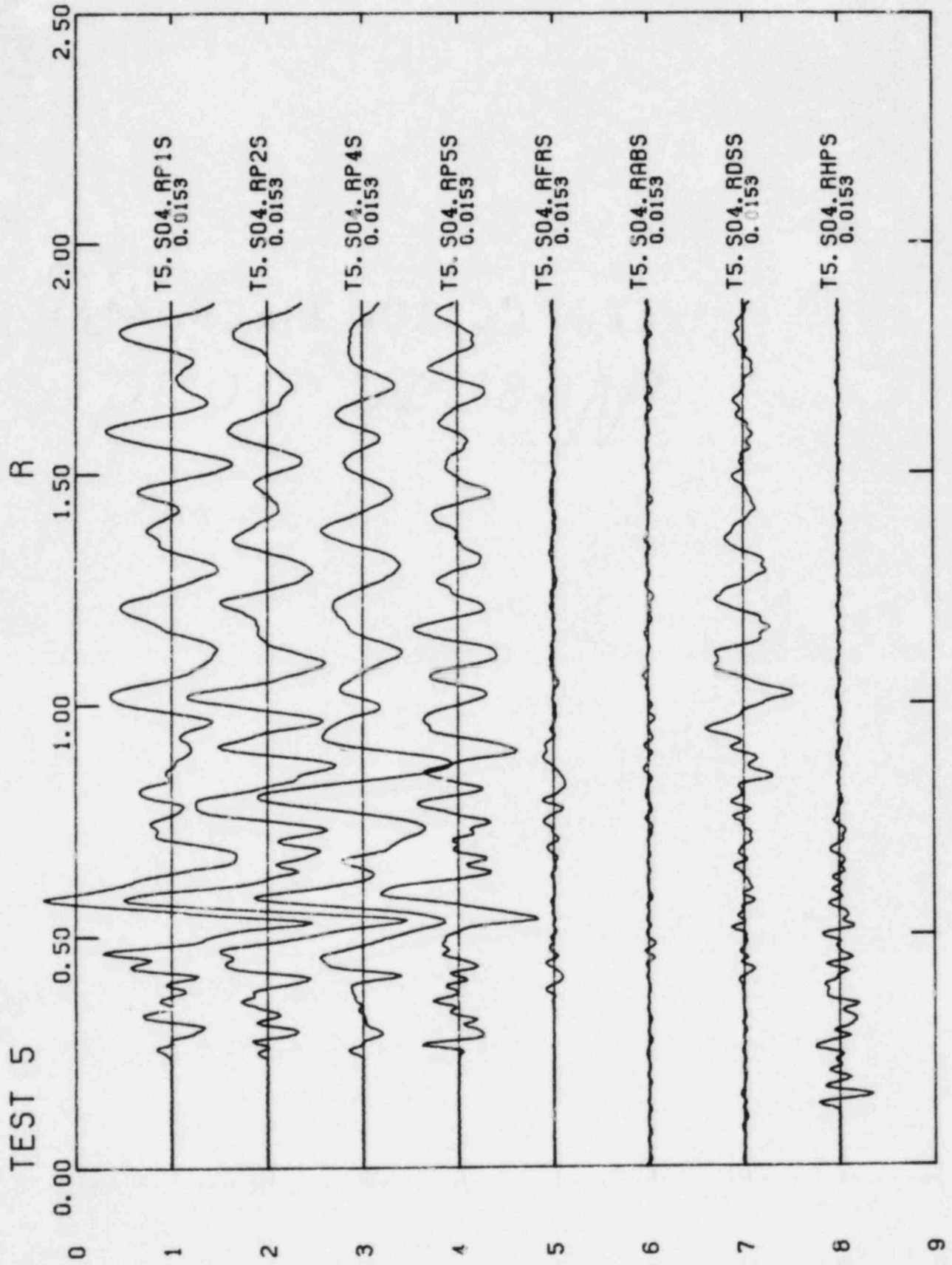


Figure IV.A.8 Representative seismograms for foundation and free-field sites from Test 5, Shot 4, vertical component. Vertical scale: 1"=0.015 cm/sec.

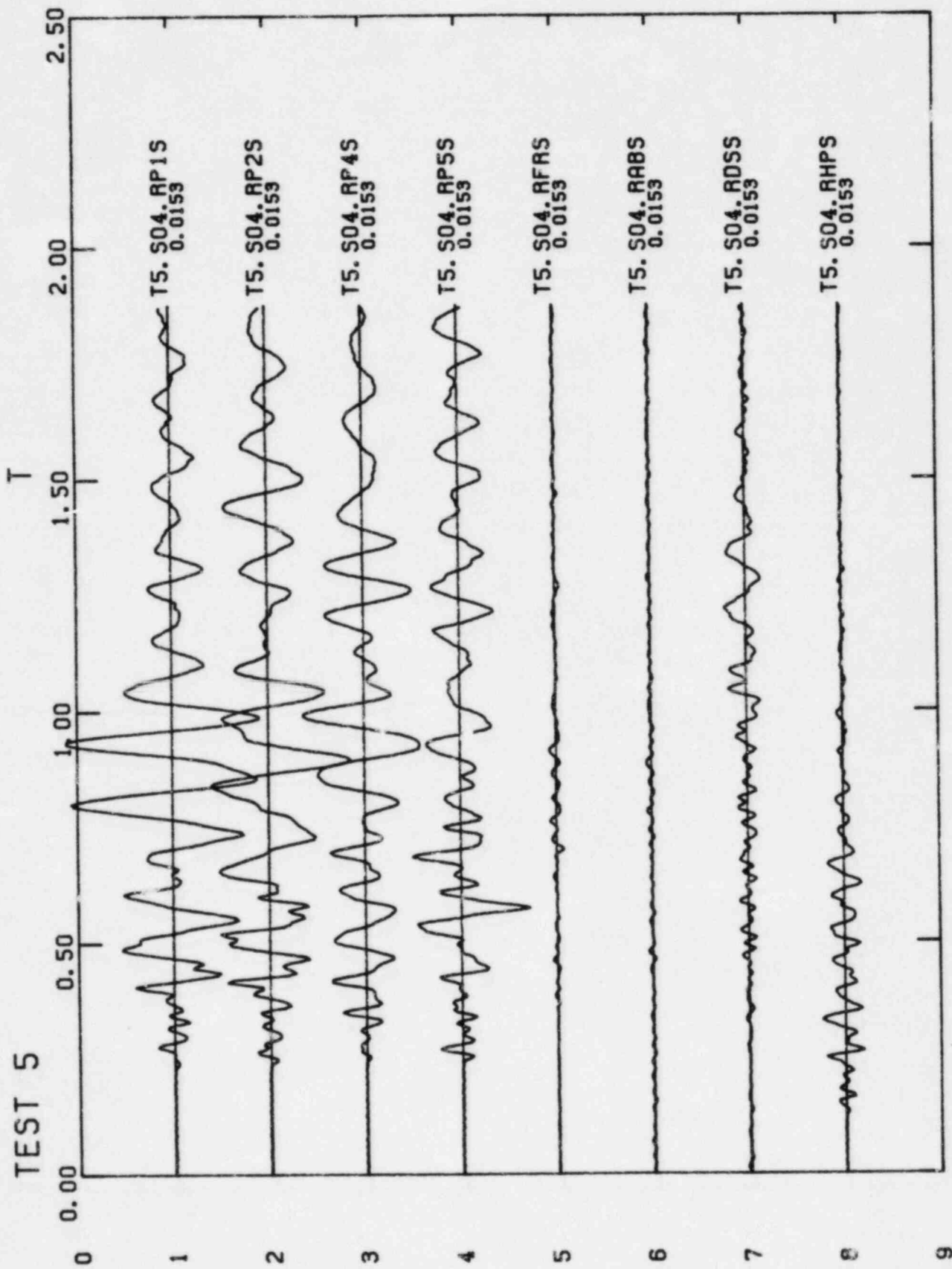


Figure IV.A.9 Representative seismograms for foundation and free-field sites from Test 5, Shot 4, transverse component. Vertical scale: 1"=0.015 cm/sec.

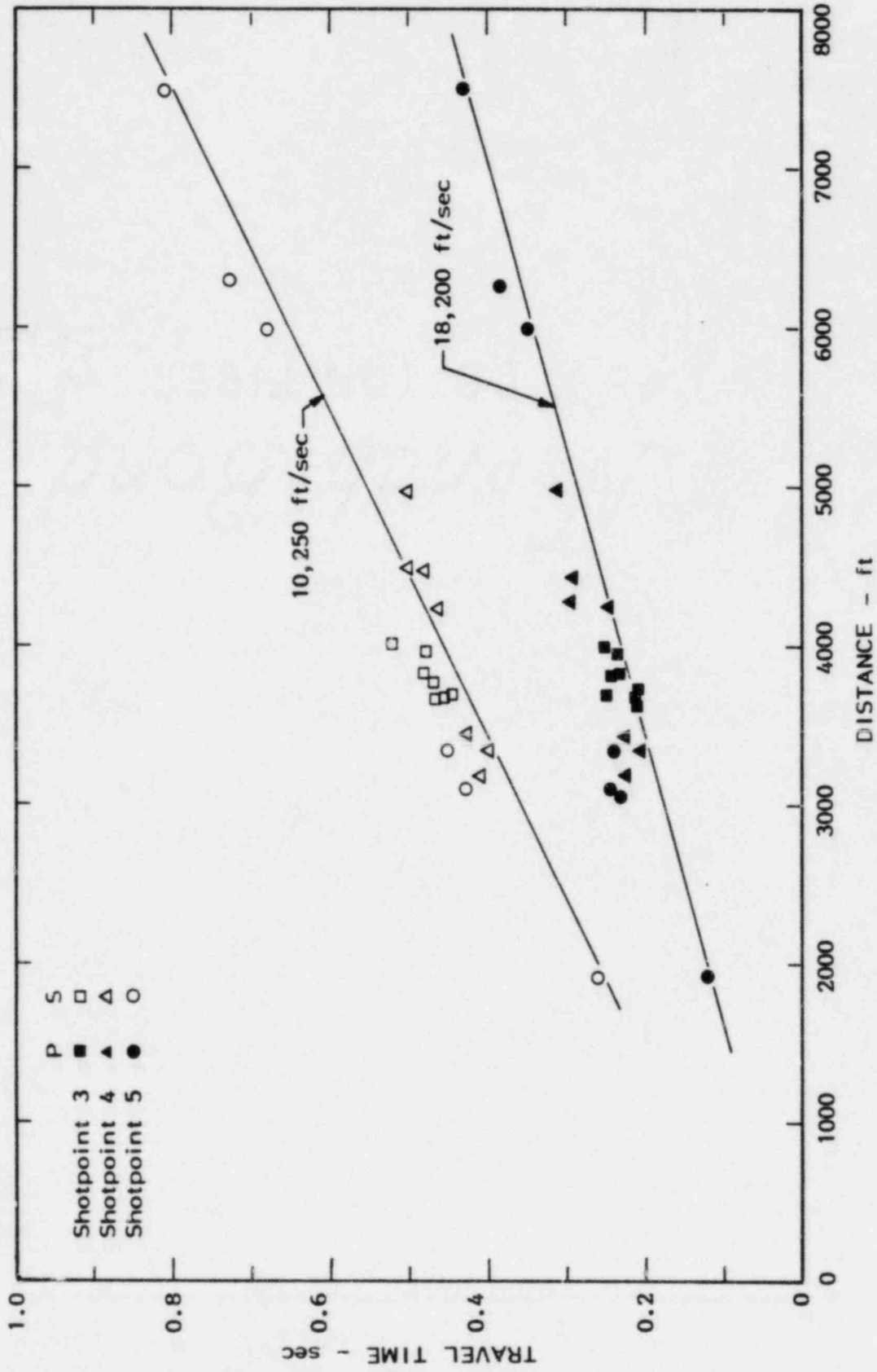


Figure IV.B.1 Travel time curves for the two principal phases on explosion records.

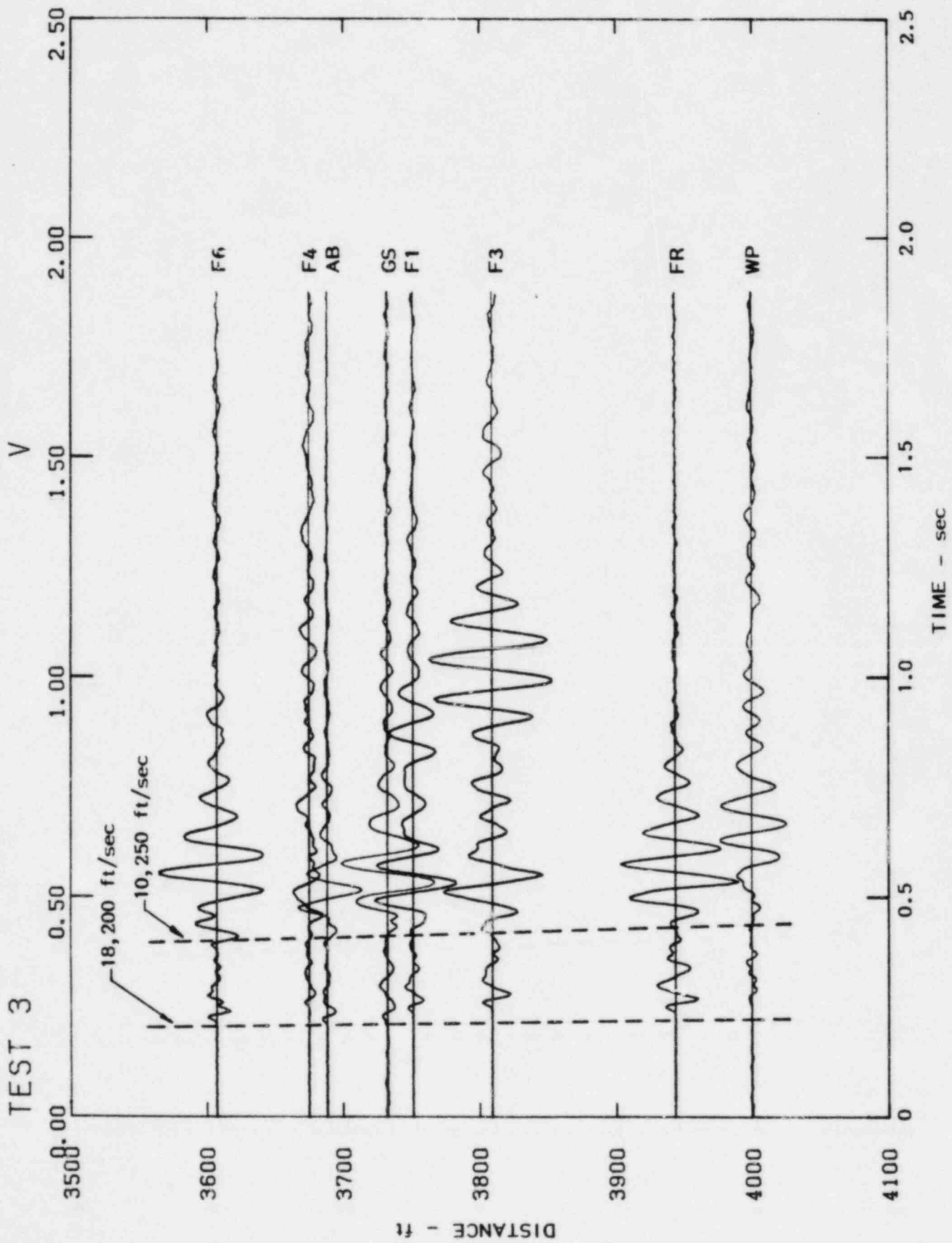
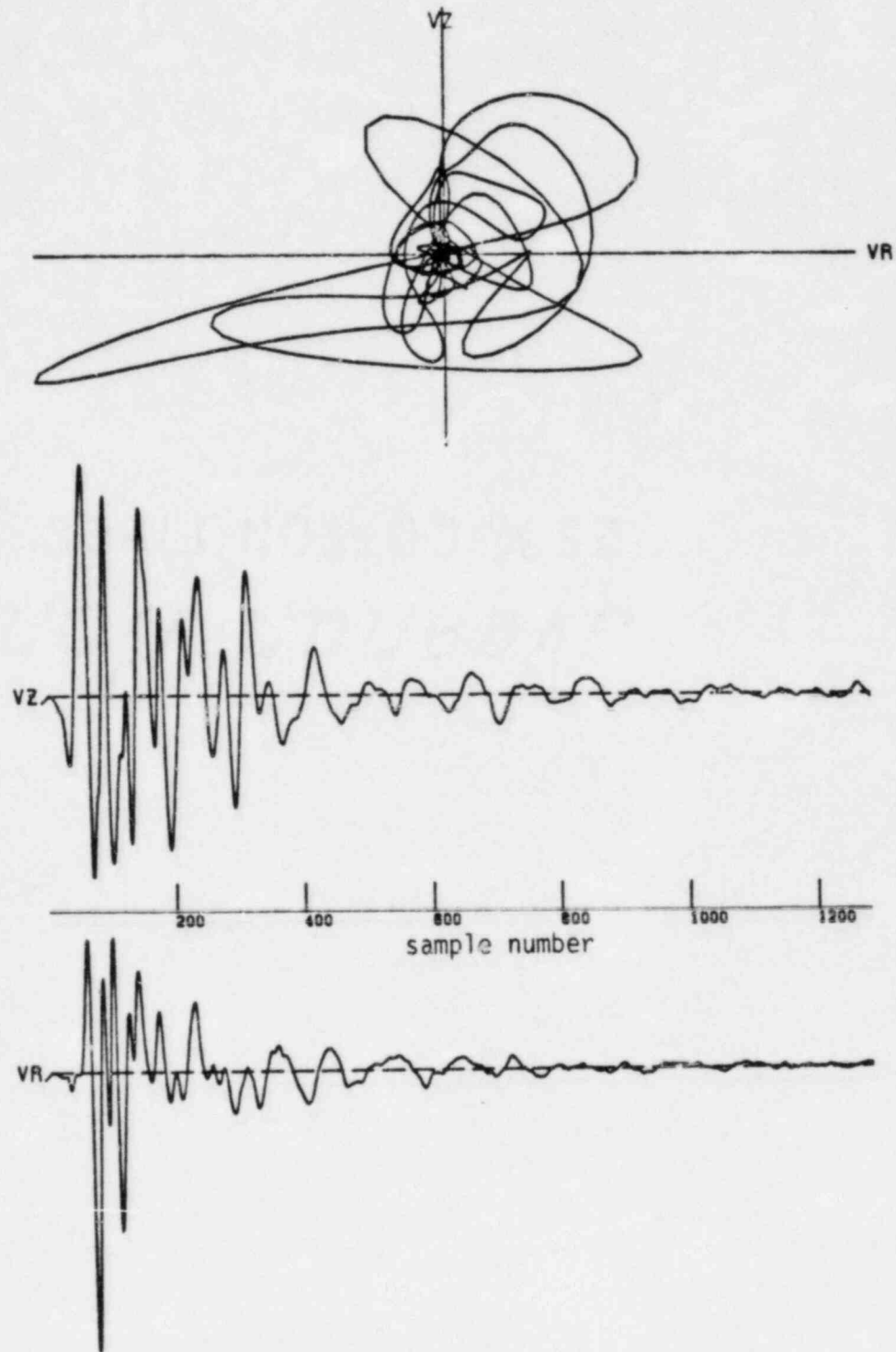
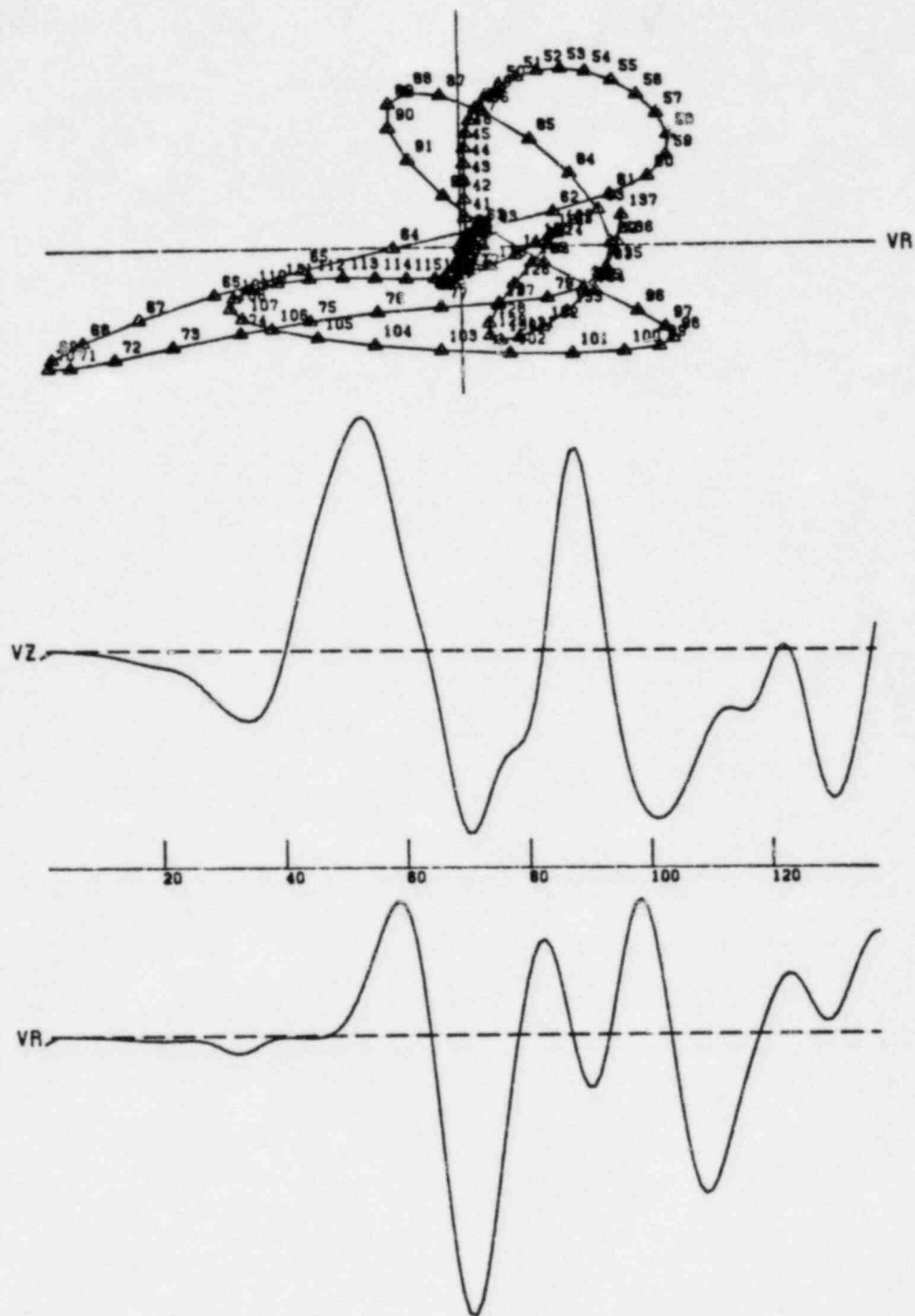


Figure IV.B.2 Vertical component of motion for Test 3, Shot 2.



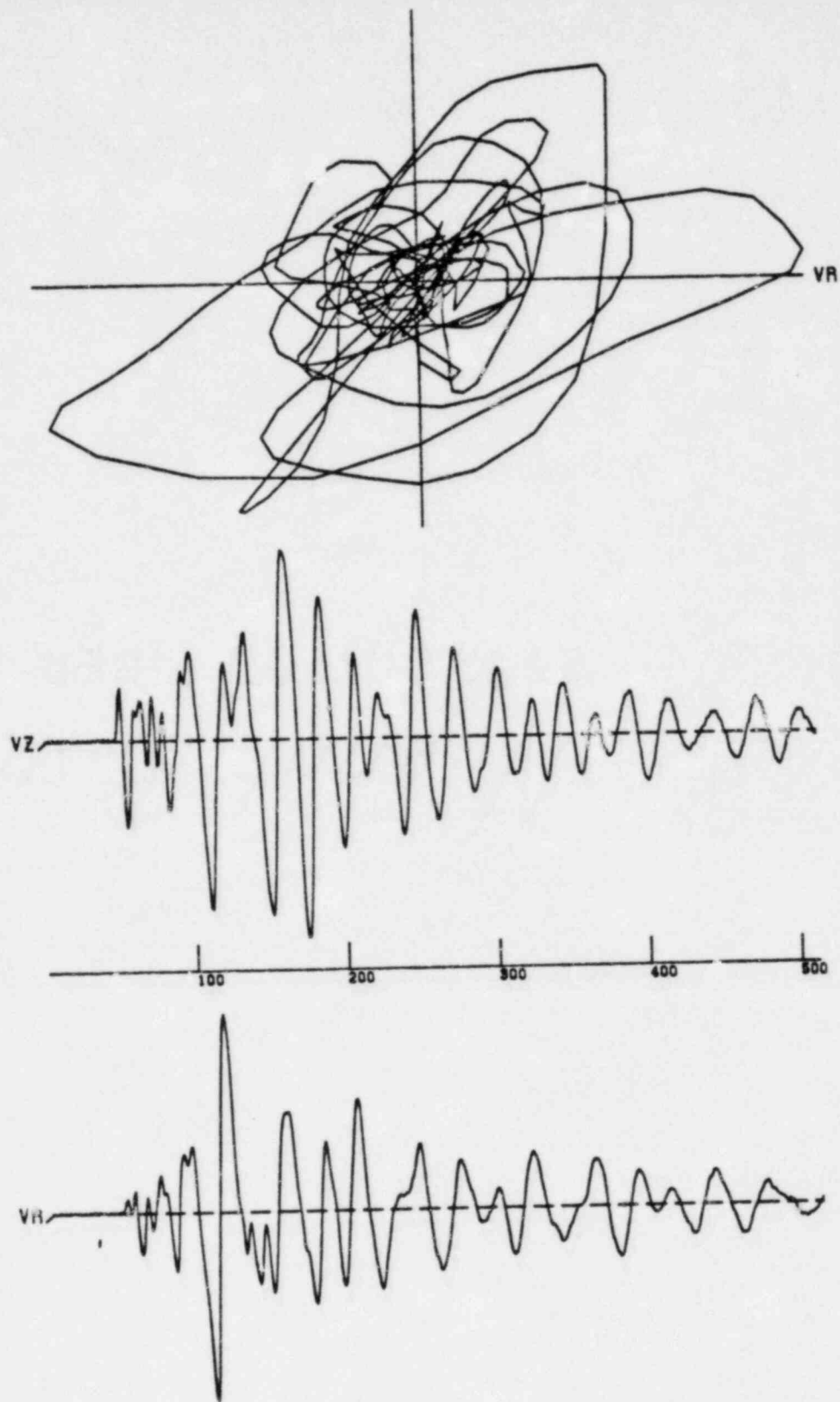
Note: Traces labelled VZ and VR are vertical and radial velocity.
The source is to the left on these plots.

Figure IV.C.1 Particle motion, 1979 accelerogram,
whole record



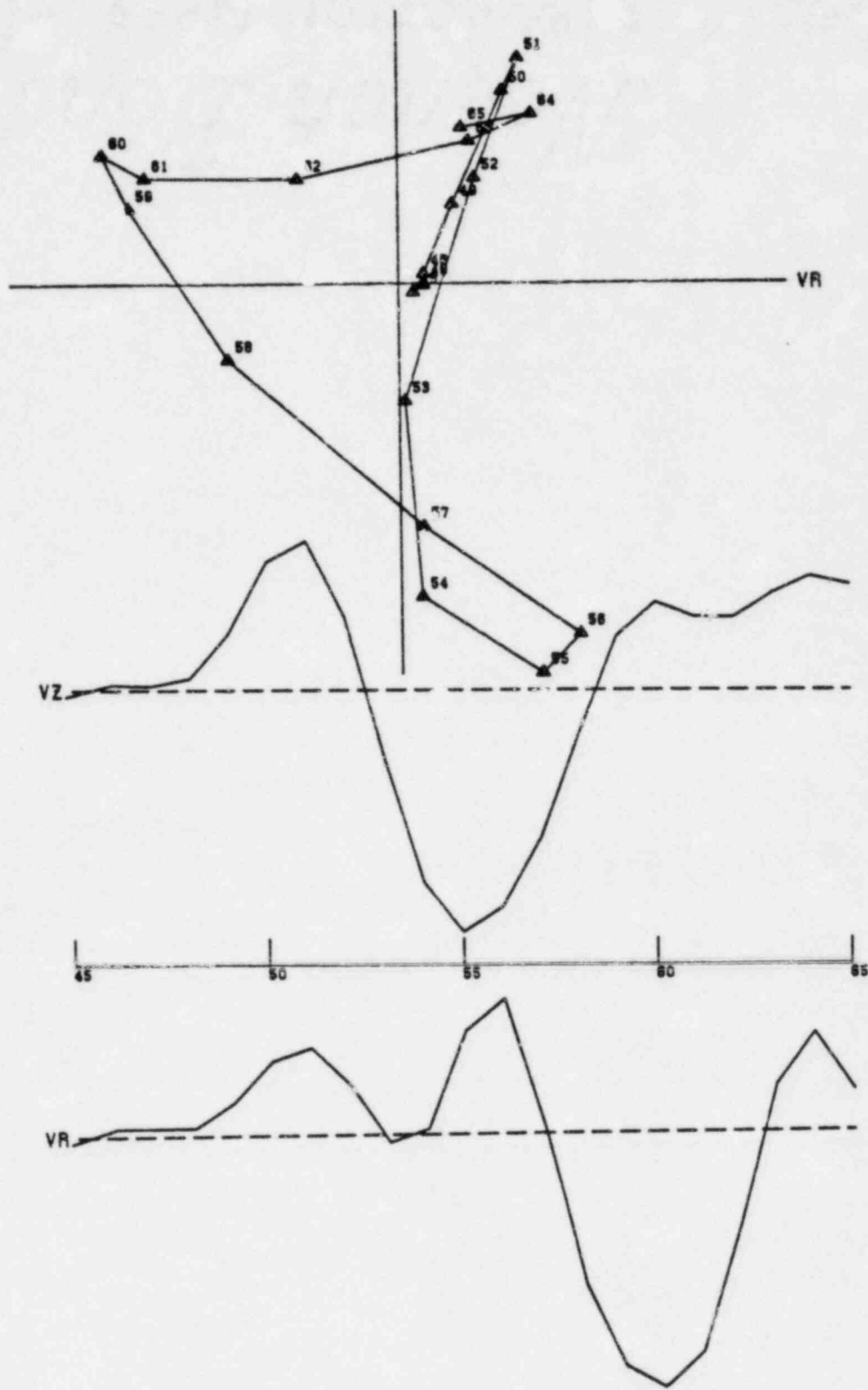
Note: Traces labelled VZ and VR are vertical and radial velocity.
 The source is to the left on these plots.

Figure IV.C.2 Particle motion, 1979 accelerogram,
 S-wave window



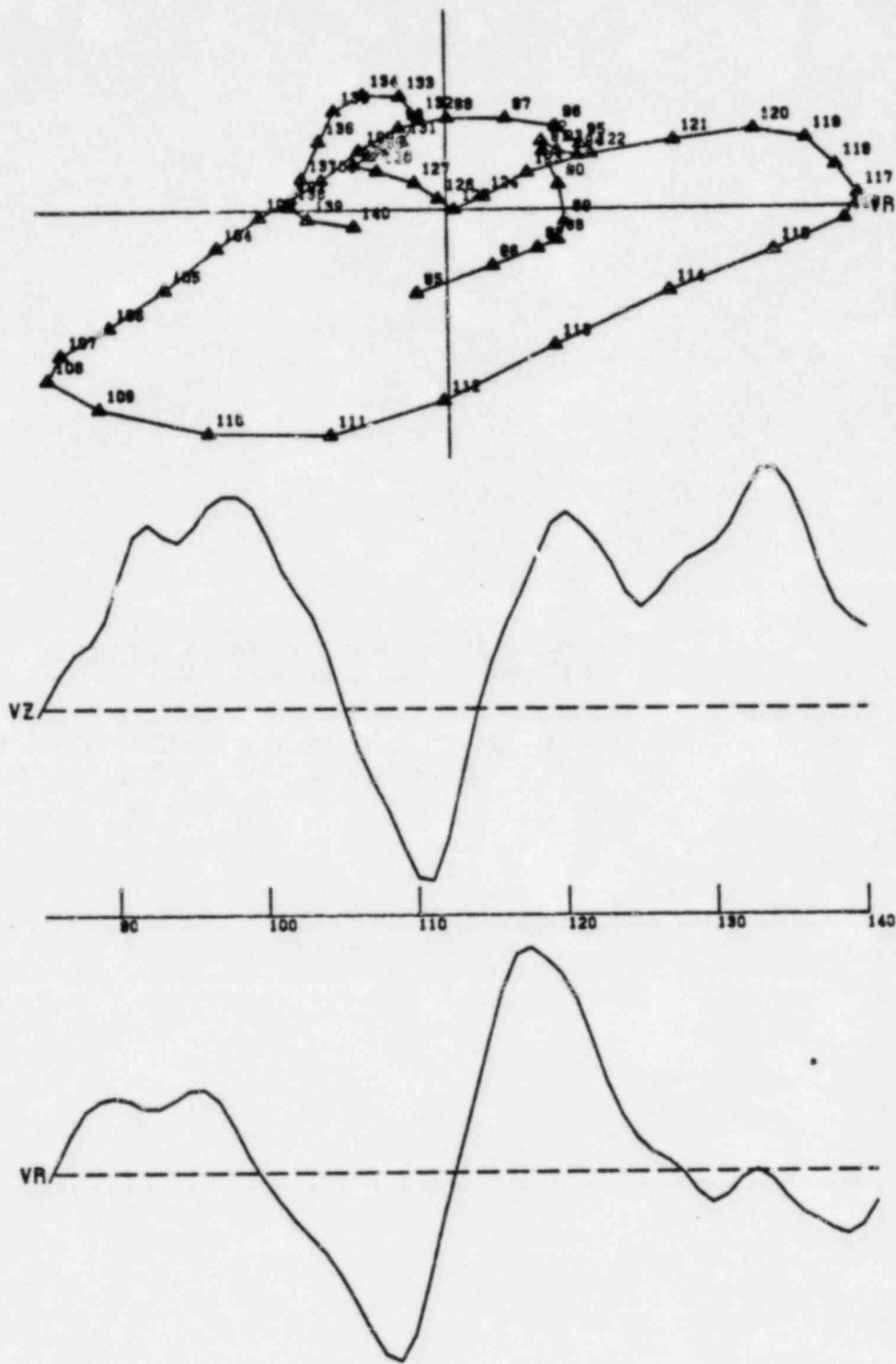
Note: Traces labelled VZ and VR are vertical and radial velocity.
The source is to the left on these plots.

Figure IV.C.3 Particle motion, T5.S04.RP2S (Pad),
whole record



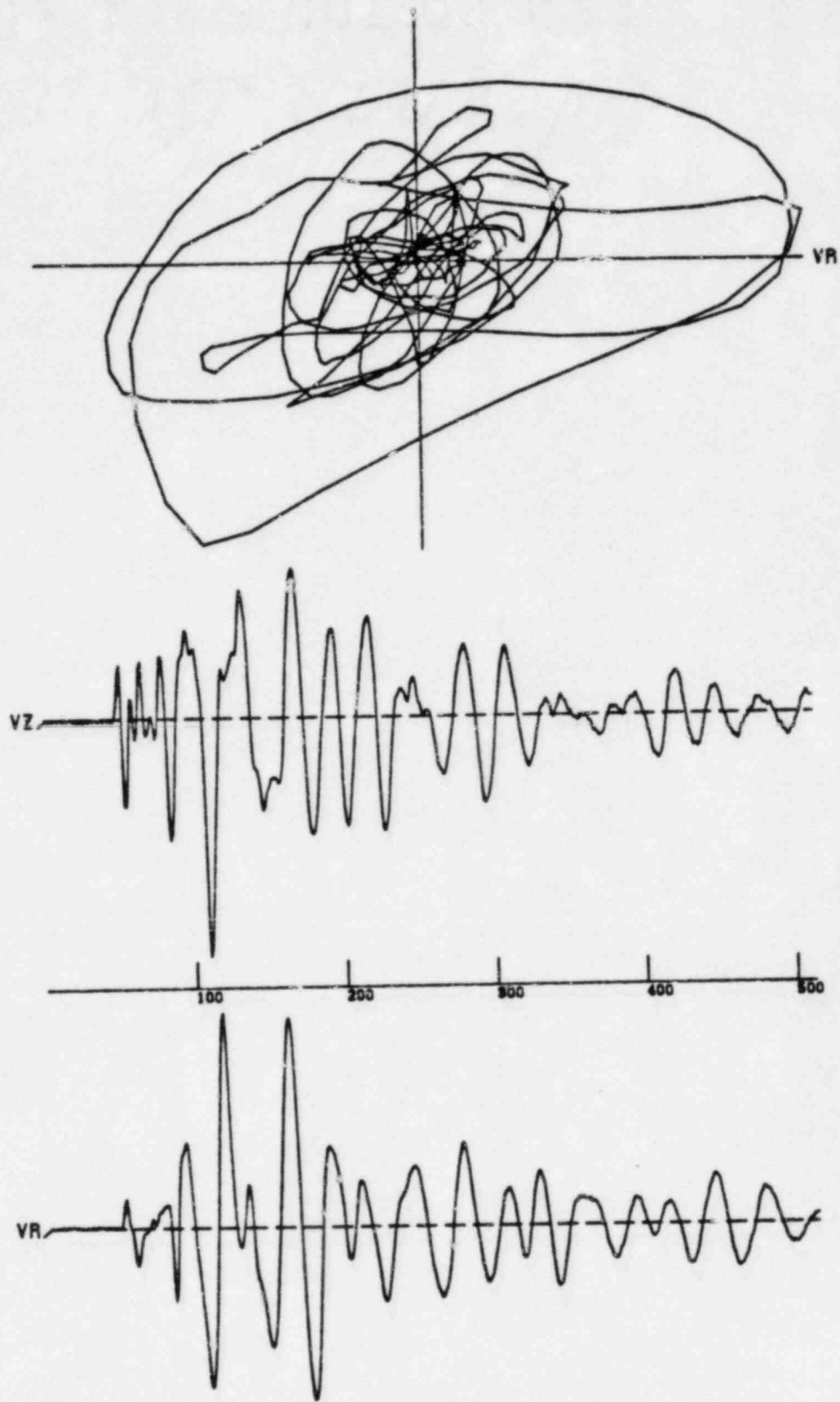
Note: Traces labelled VZ and VR are vertical and radial velocity.
The source is to the left on these plots.

Figure IV.C.4 Particle motion, T5.S04.RP2S (Pad),
P-wave onset



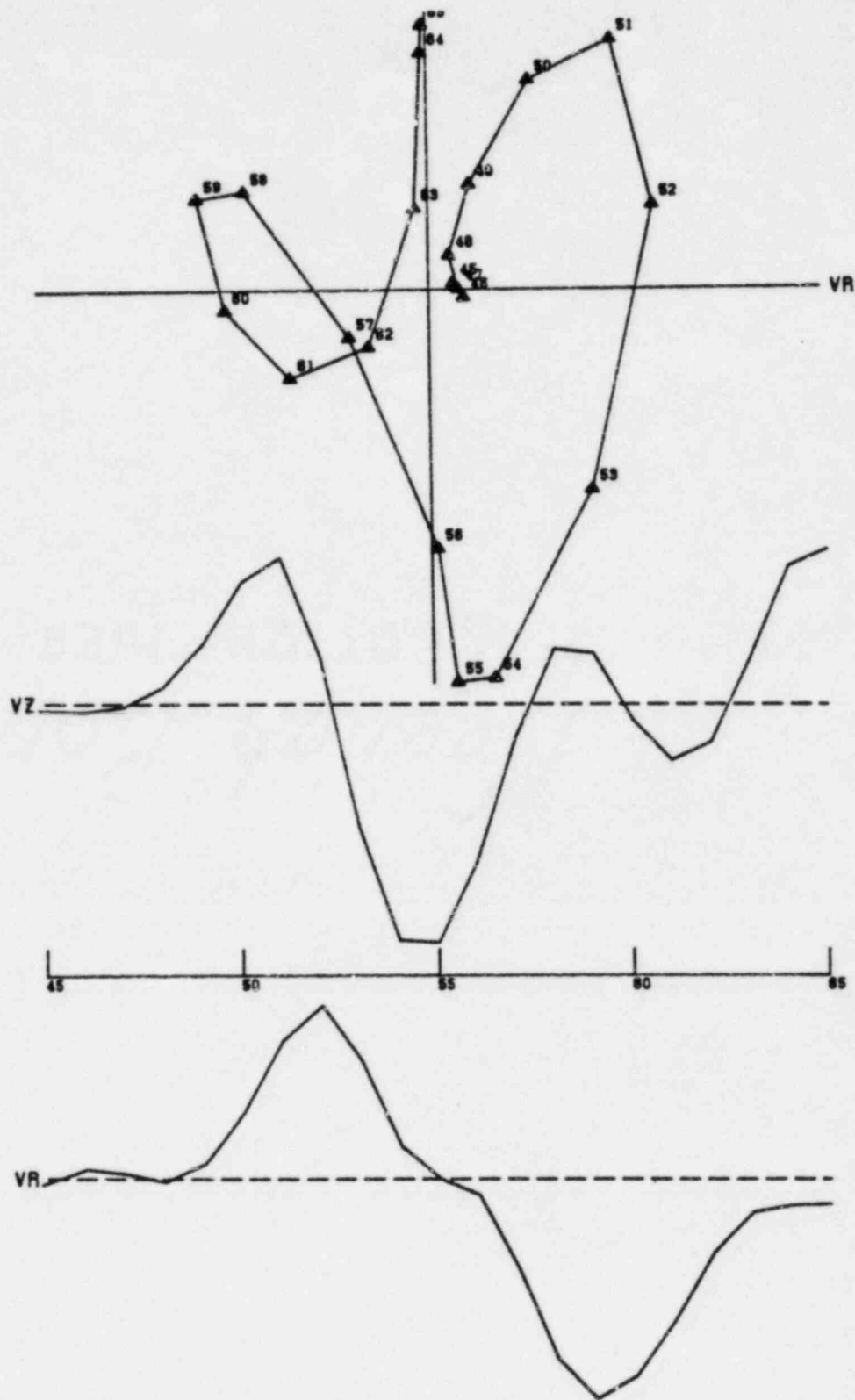
Note: Traces labelled VZ and VR are vertical and radial velocity.
The source is to the left on these plots.

Figure IV.C.5 Particle motion, T5.S04.RP2S (Pad),
S-wave window.



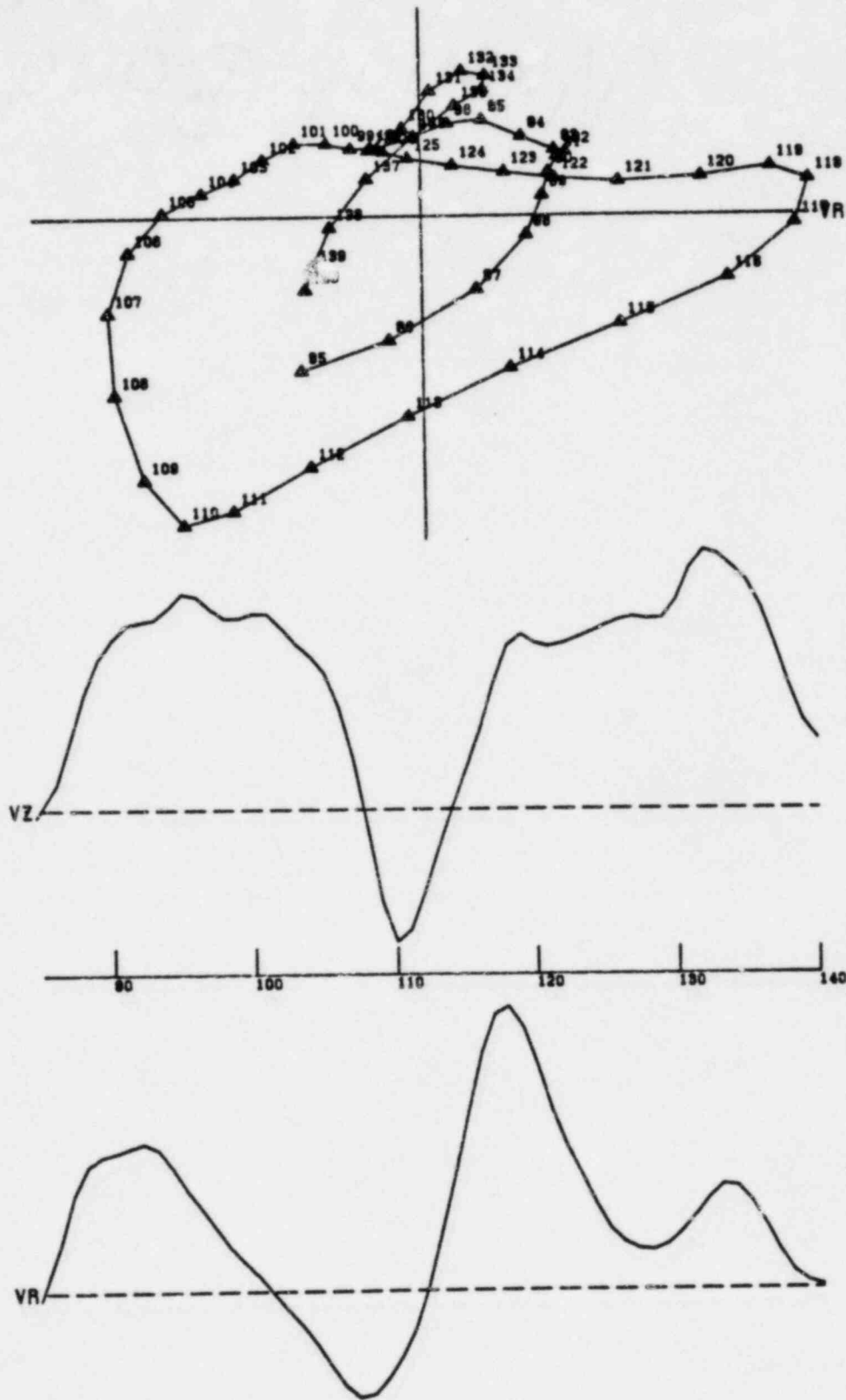
Note: Traces labelled VZ and VR are vertical and radial velocity.
The source is to the left on these plots.

Figure IV.C.6 Particle motion, T5.S04.RP4S (near Pad),
whole record



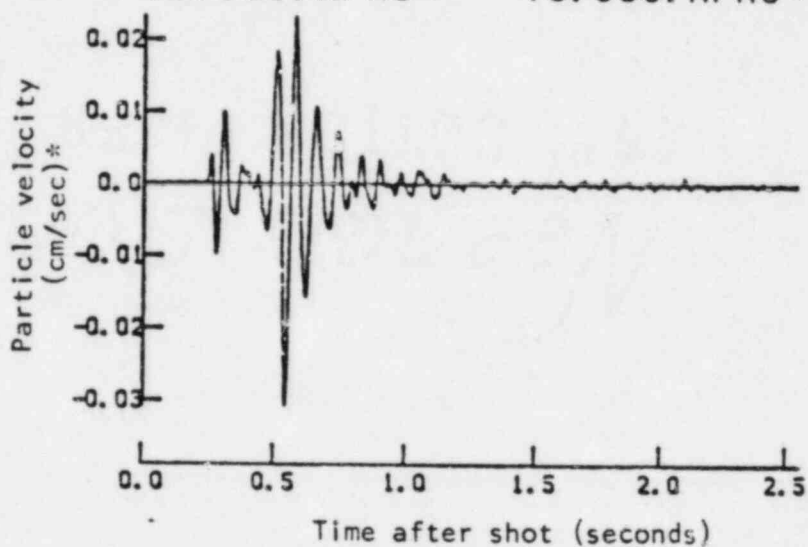
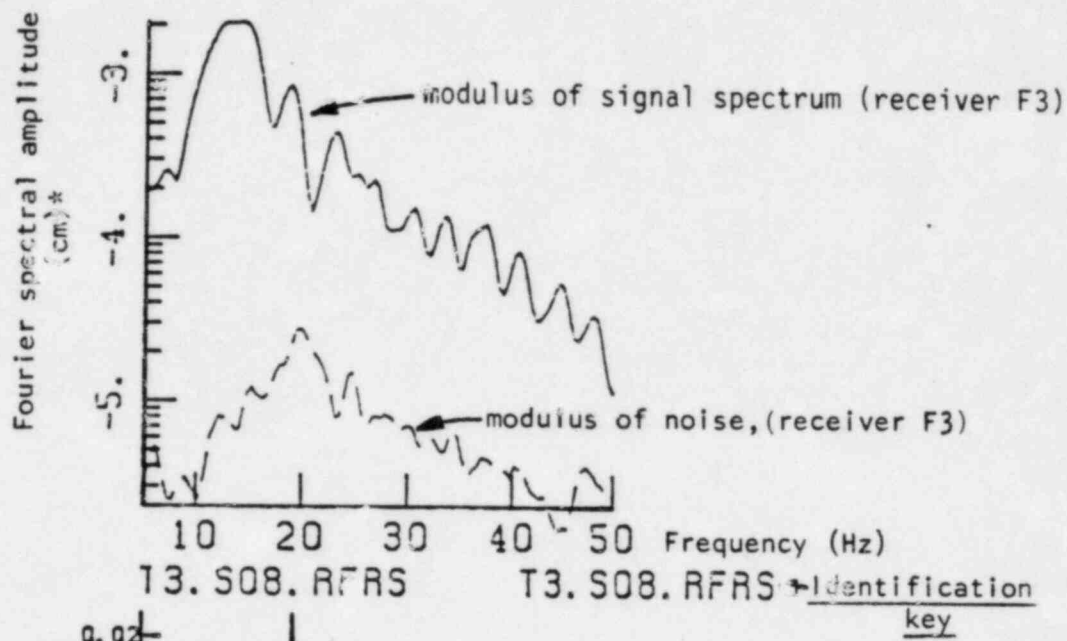
Note: Traces labelled VZ and VR are vertical and radial velocity.
The source is to the left on these plots.

Figure IV.C.7 Particle motion, T5.S04.RP4S (near Pad),
P-wave onset



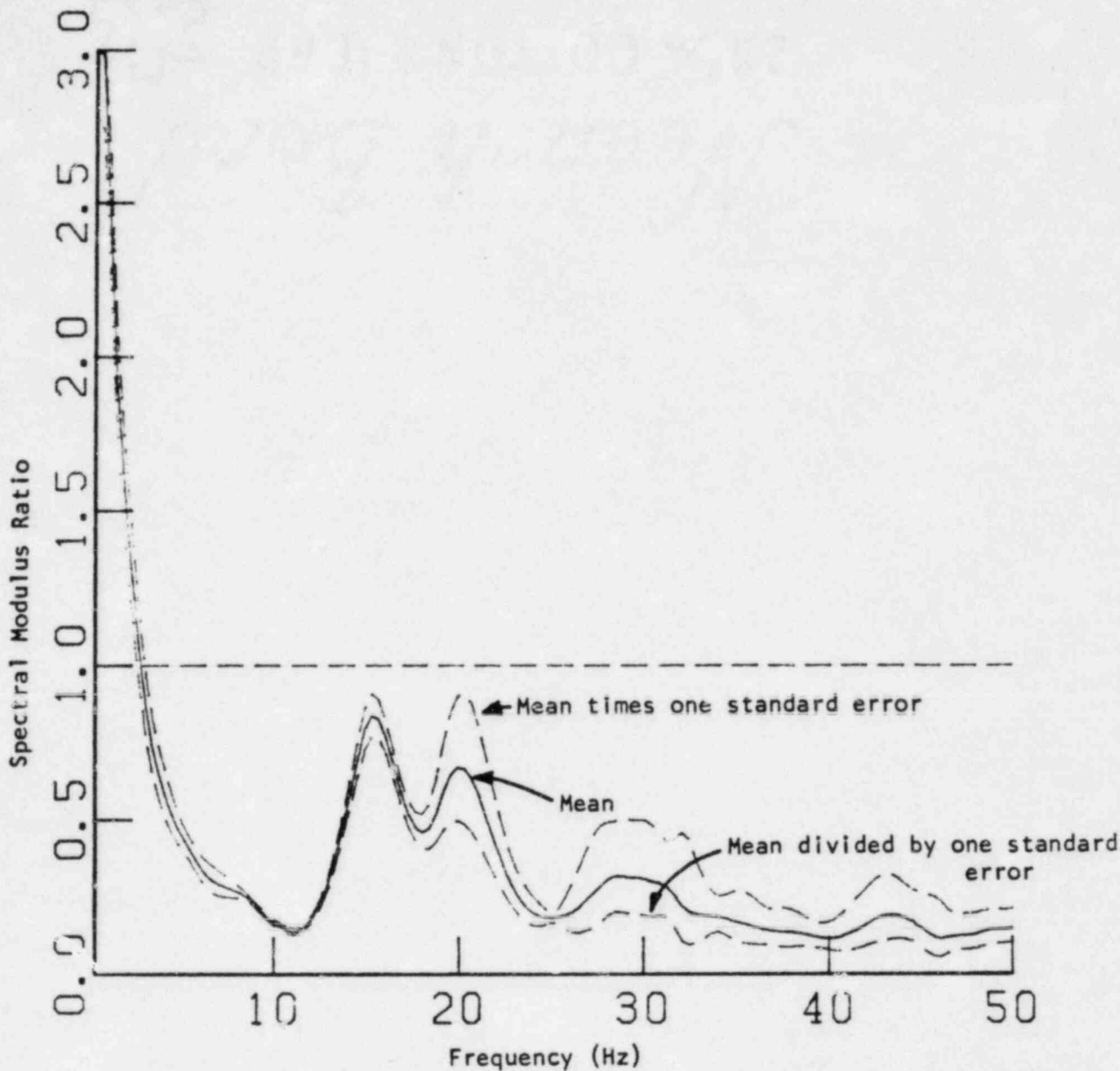
Note: Traces labelled VZ and VR are vertical and radial velocity.
The source is to the left on these plots.

Figure IV.C.8 Particle motion, T5.S04.RP4S (near Pad),
S-wave window.



internal run identifier → PLOT NO 30. RUN NO 306. ← QA catalog number

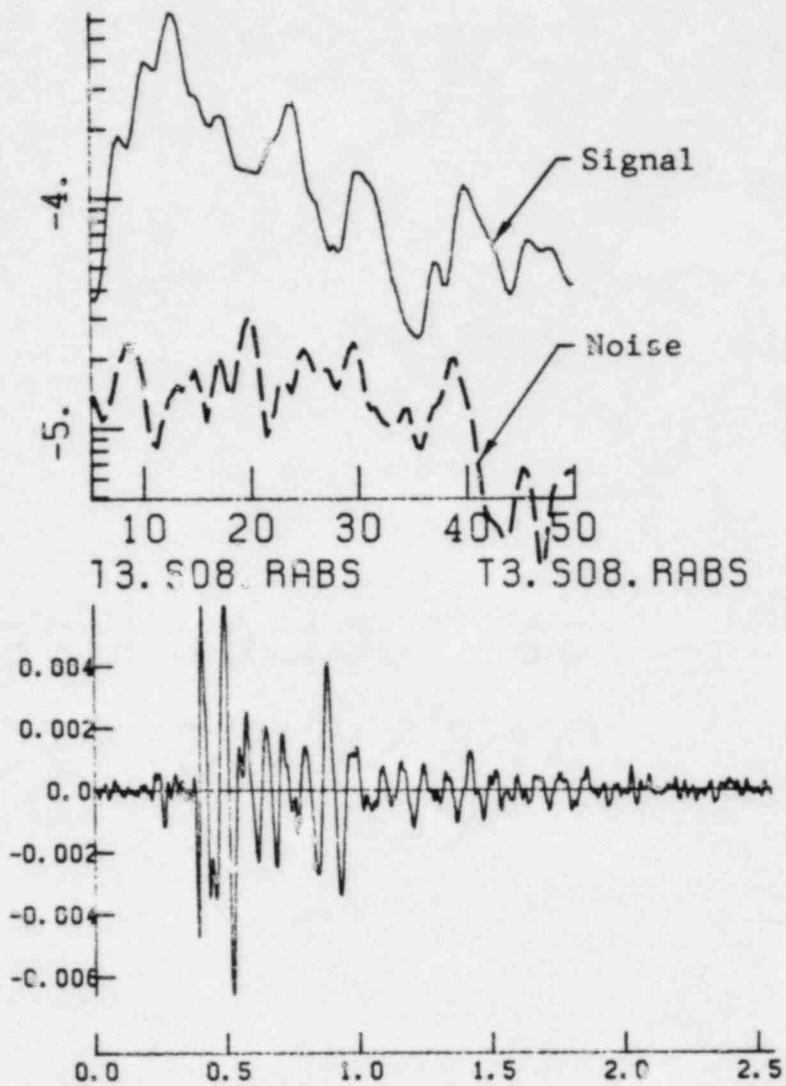
Figure V.C.1 Example of a spectral plot showing Fourier amplitudes of signal and noise. The lower figure shows the signal which was Fourier analyzed.



TEST 3. WP/FF, SHOTS 2, 3, 6, 7, 8, RADIAL Title
 RATIOS FROM MODULI IN GROUPS OF 5. ← Seismograms per
 RUN NO 220. ← QA catalog number trial
 POWER SPECTRAL NOISE SUBTRACTED

Figure V.3.2

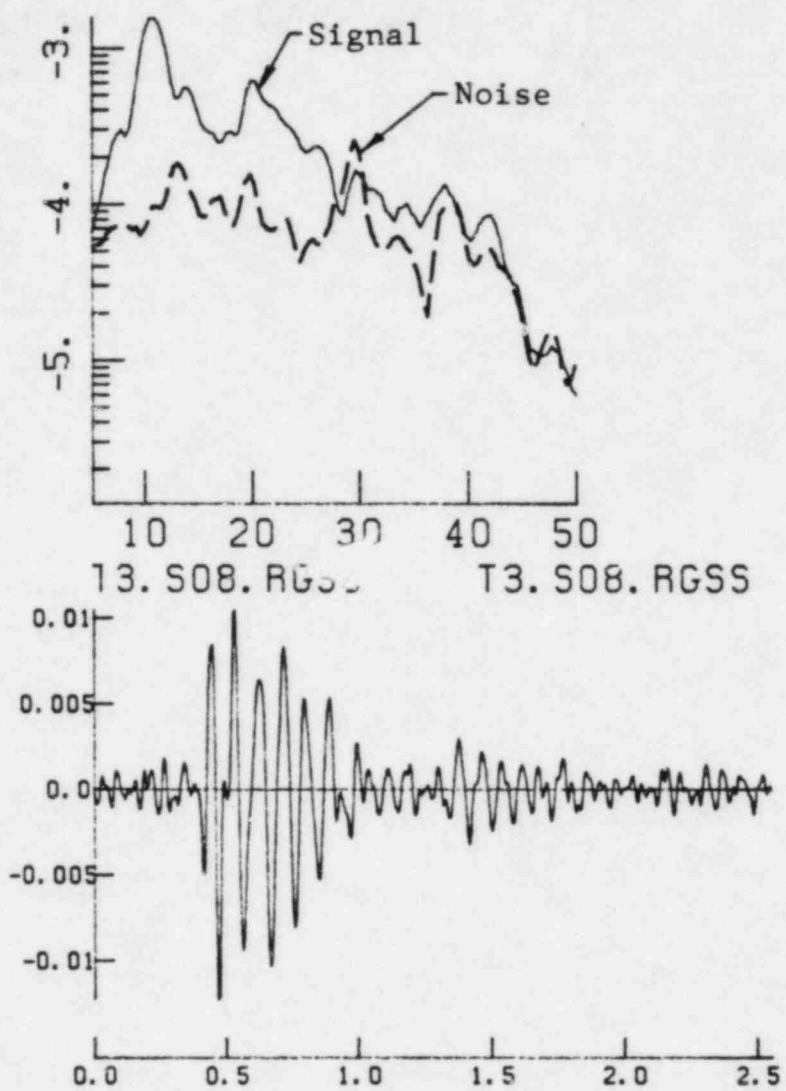
Description of spectral modulus plot.
 Given on each plot is the number of
 record pairs which make up one trial
 ratio (5 in the figure shown).



PLOT NO 22. RUN NO 305.

Figure V.C.3

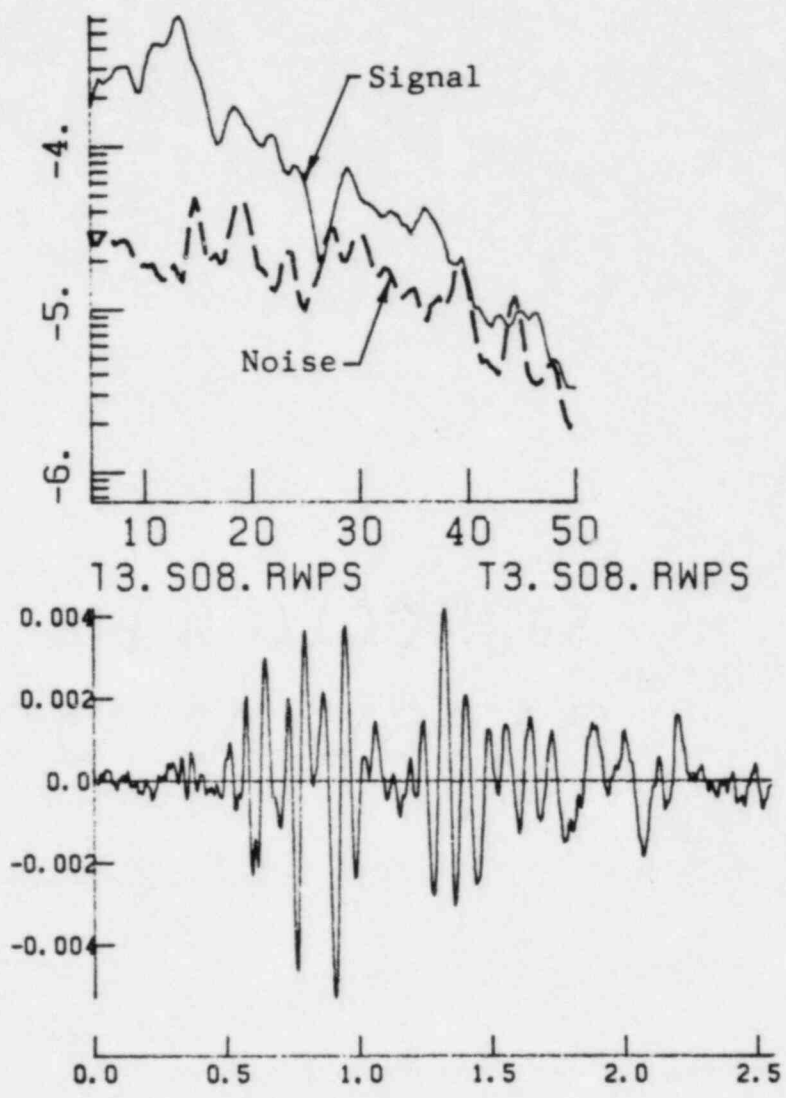
Example of a signal recorded at the foundation site AB. (Test 3, Shot 8, transverse component).



T3. S08. RGSS T3. S08. RGSS

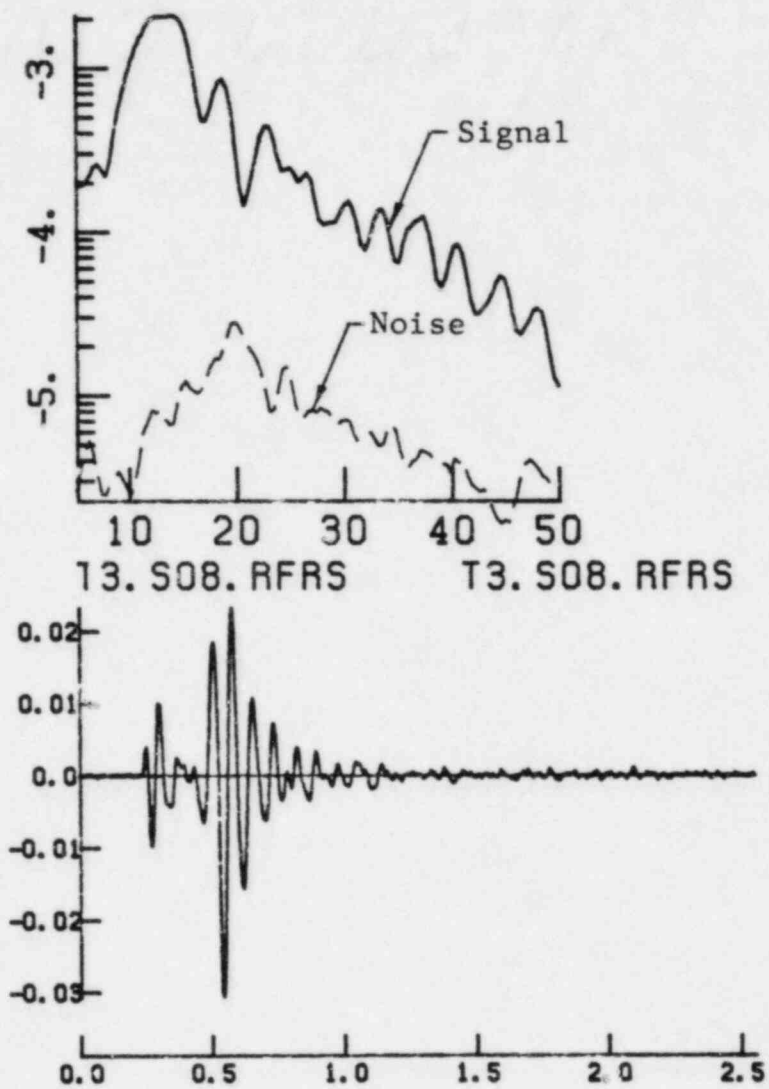
PLCT NO 23. RUN NO 305.

Figure V.C.4 Example of a signal recorded at the foundation site GS.



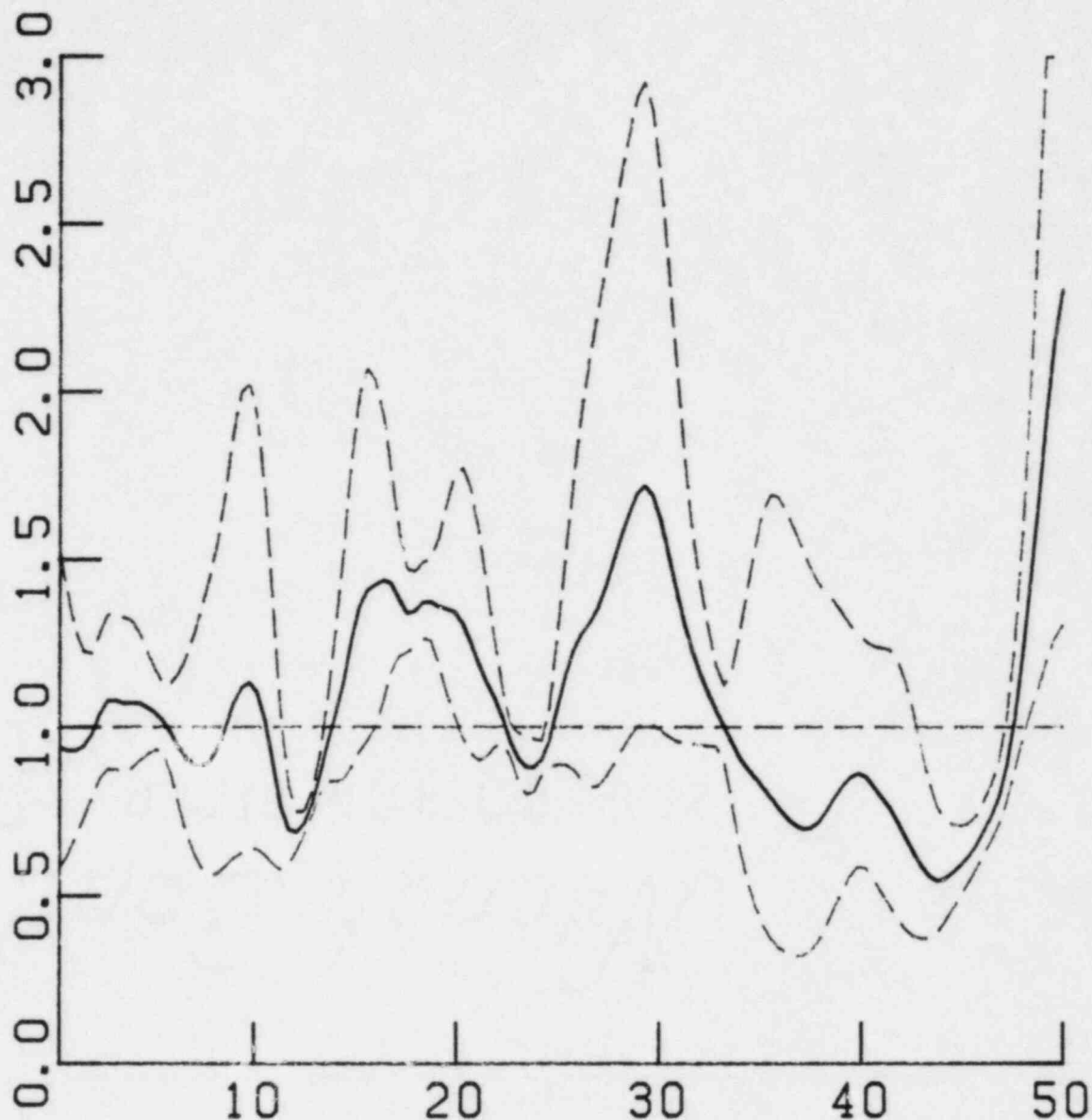
PLOT NO 24. RUN NO 305.

Figure V.C.5 Example of a signal recorded at the foundation site WP.



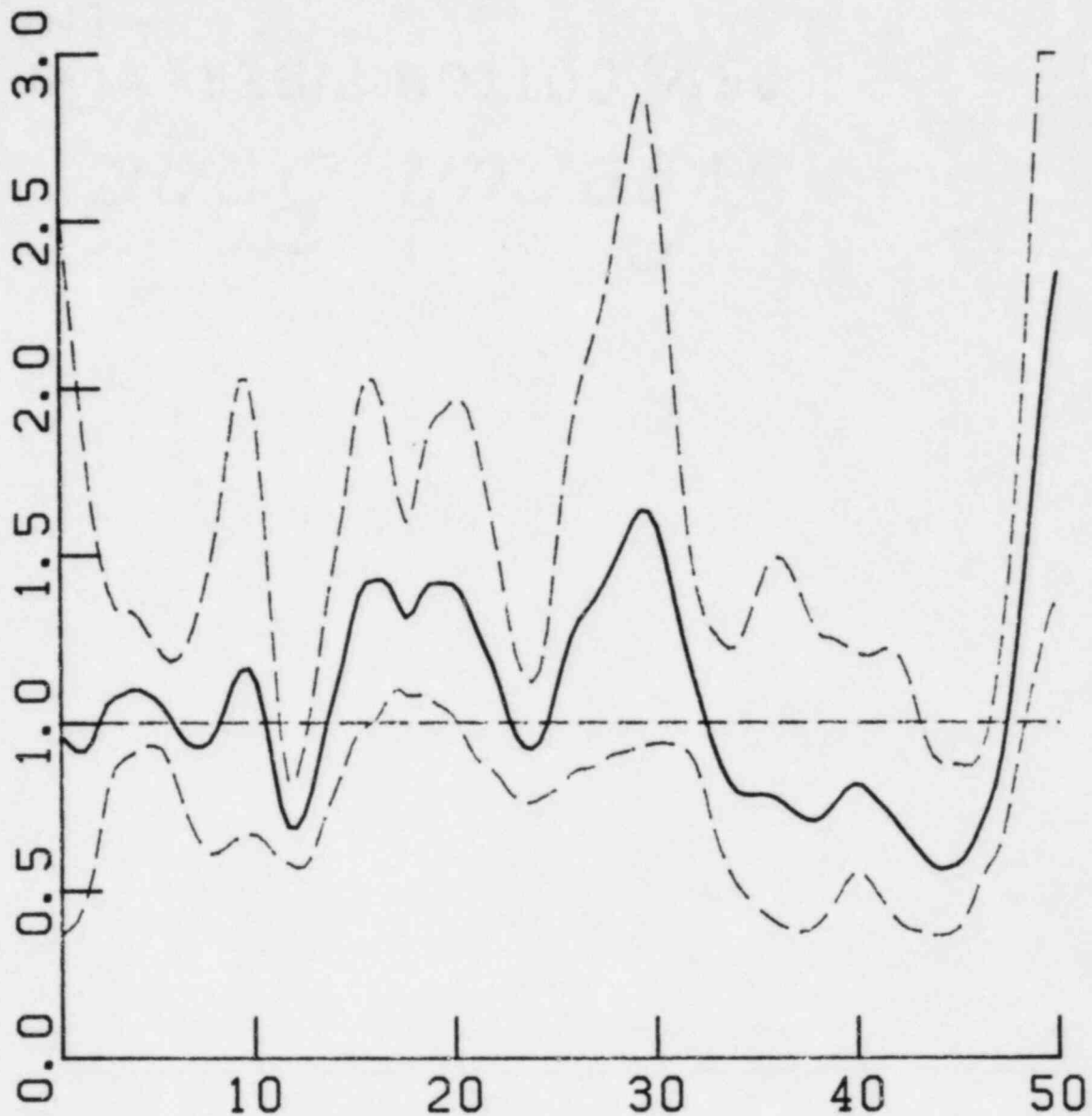
PLOT NO 30. RUN NO 306.

Figure V.C.6 Example of a signal recorded at the free-field site FR



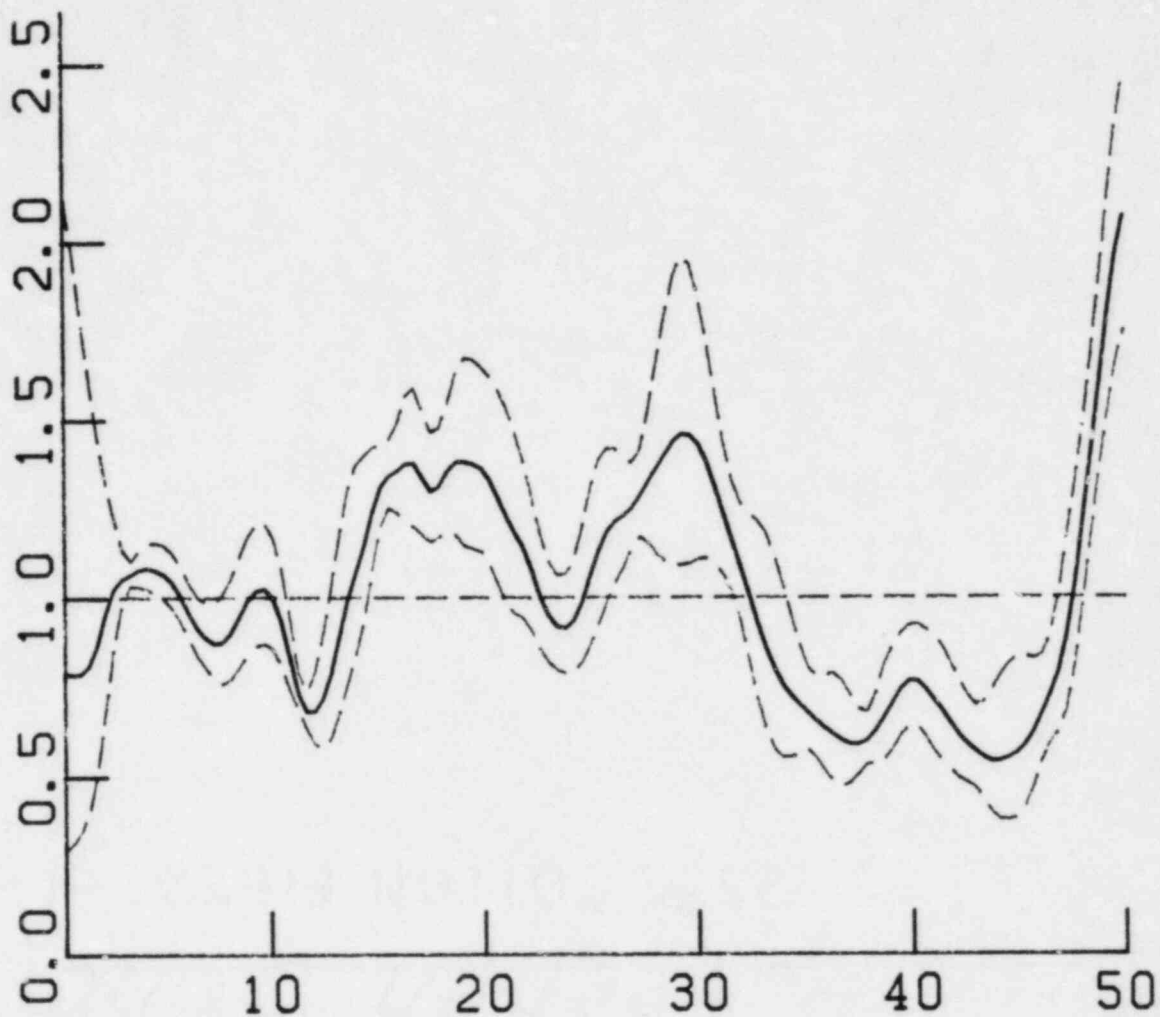
TEST 5 SHOTS 3, 4, 5, 6, 7, 8 P2/<P1, P4, P5> V
 RATIOS FROM MODULI IN GROUPS OF 6
 RUN NO 245.
 POWER SPECTRAL NOISE SUBTRACTED

Figure V.C.7 Spectral modulus ratio for Test 5, using the eighteen pairs of receiver sites indicated (6 shots, three pairs for each shot.) In this run the ratios are computed from 3 trials, each consisting of a numerator summation (over each shot) of the P2 spectral moduli divided by a denominator sum (over the same 6 shots) for each of the three free-field stations P1, P4, and P6. Dashed lines are the standard deviation for site-to-site variability.



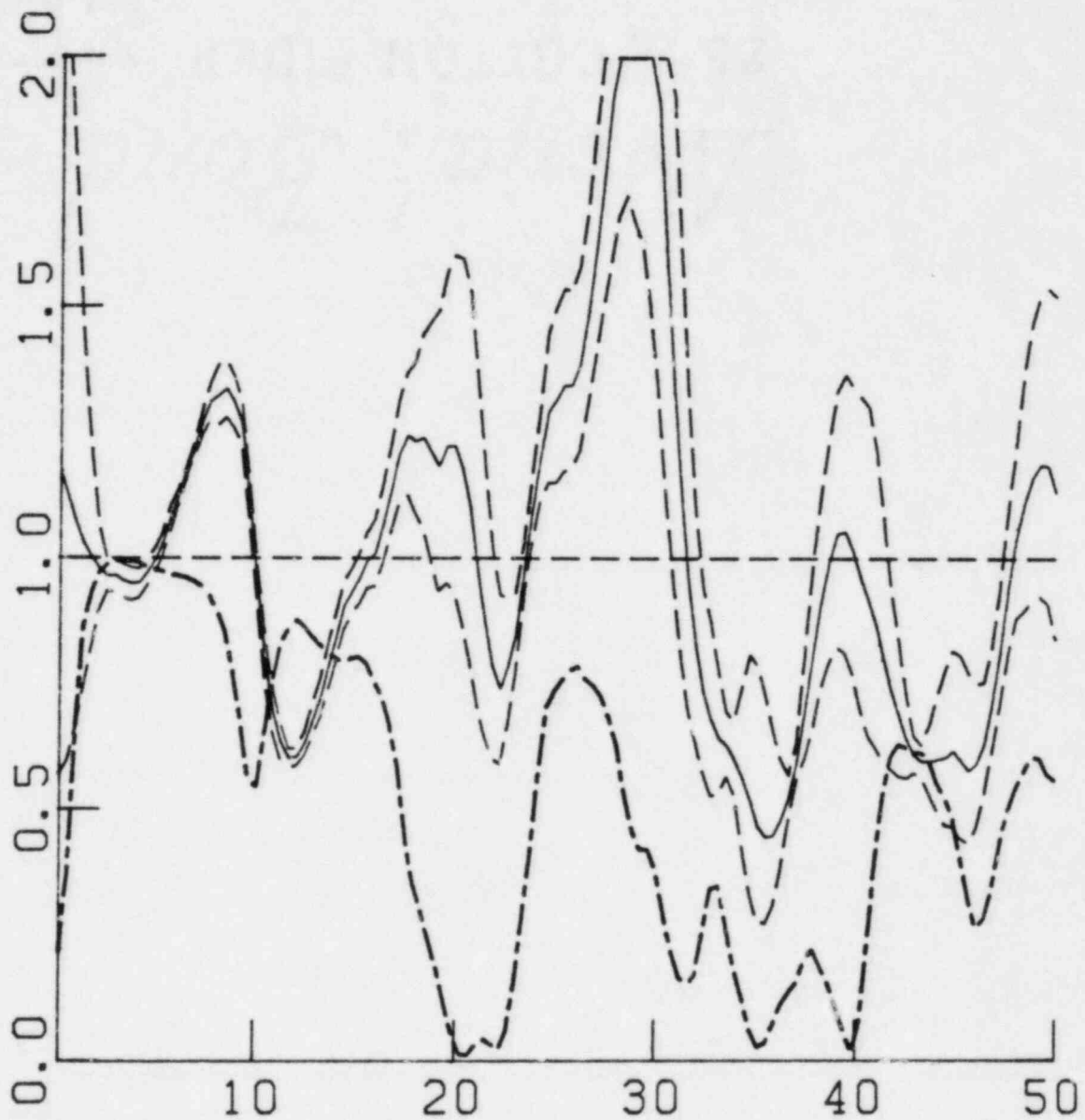
TEST 5 P2/<P1,P4,P5> NO GROUPS V
 RATIOS FROM MODULI INDIVIDUALLY
 RUN NO 247.
 POWER SPECTRAL NOISE SUBTRACTED

Figure V.C.8 Spectral modulus ratio for Test 5, using the same eighteen pairs of receiver sites as in Figure V.C.7, but with each trial consisting of a single receiver site pair. Dashed lines are the standard deviation for site-to-site and shot-to-shot variability combined.



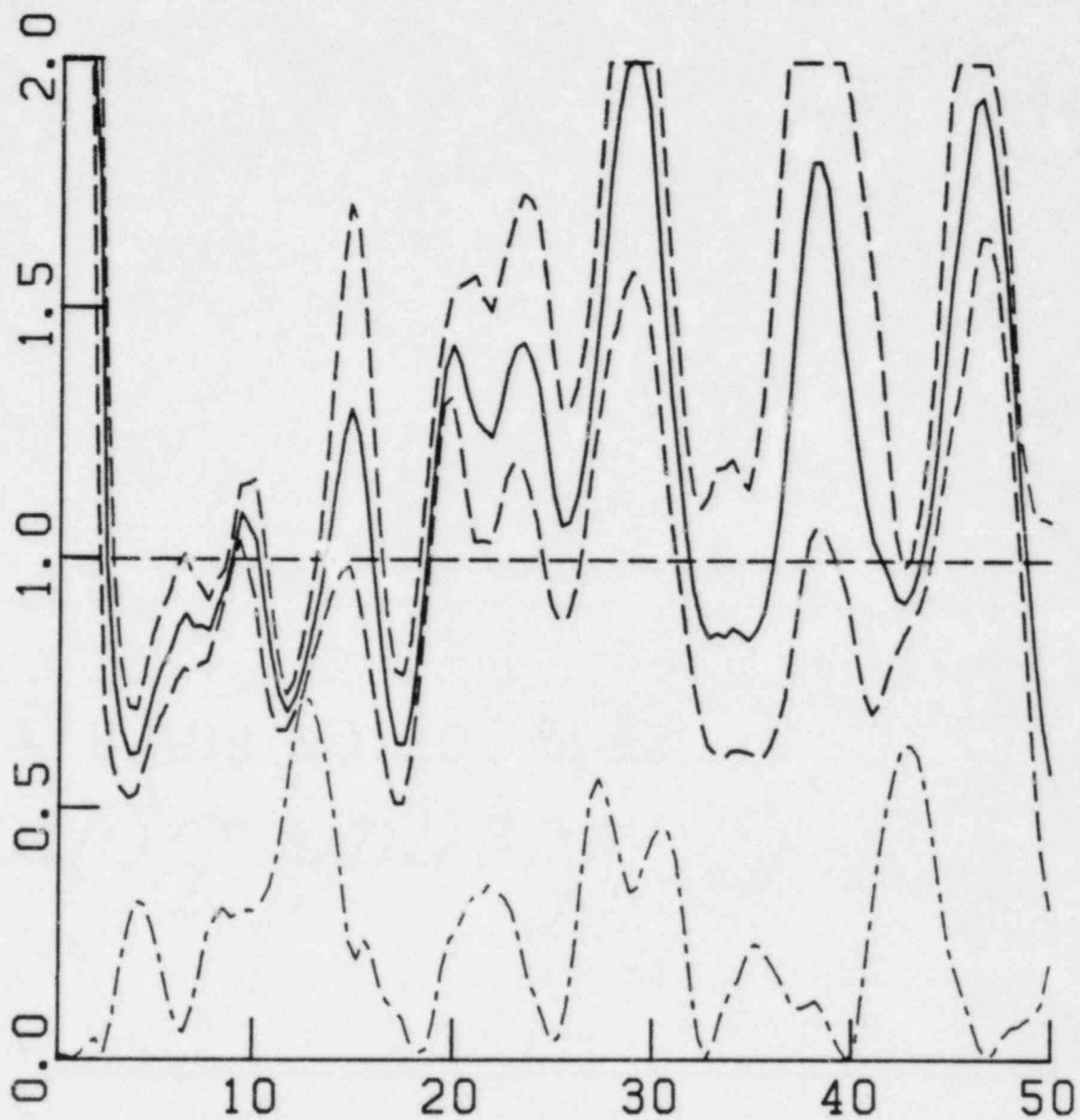
TEST 5 SHOTS 3, 4, 5, 6, 7, 8 P2/<P1, P4, P5> V
 RATIOS FROM MODULI IN GROUPS OF 3
 RUN NO 246.
 POWER SPECTRAL NOISE SUBTRACTED

Figure V.C.9 Spectral modulus ratio for Test 5, using the same eighteen pairs of receiver sites as in Figure V.C.7. In this case, one trial is the ratio of accelerograph pad to average free-field spectral modulus for one shot. Dashed lines are the standard deviation for shot-to-shot variability.



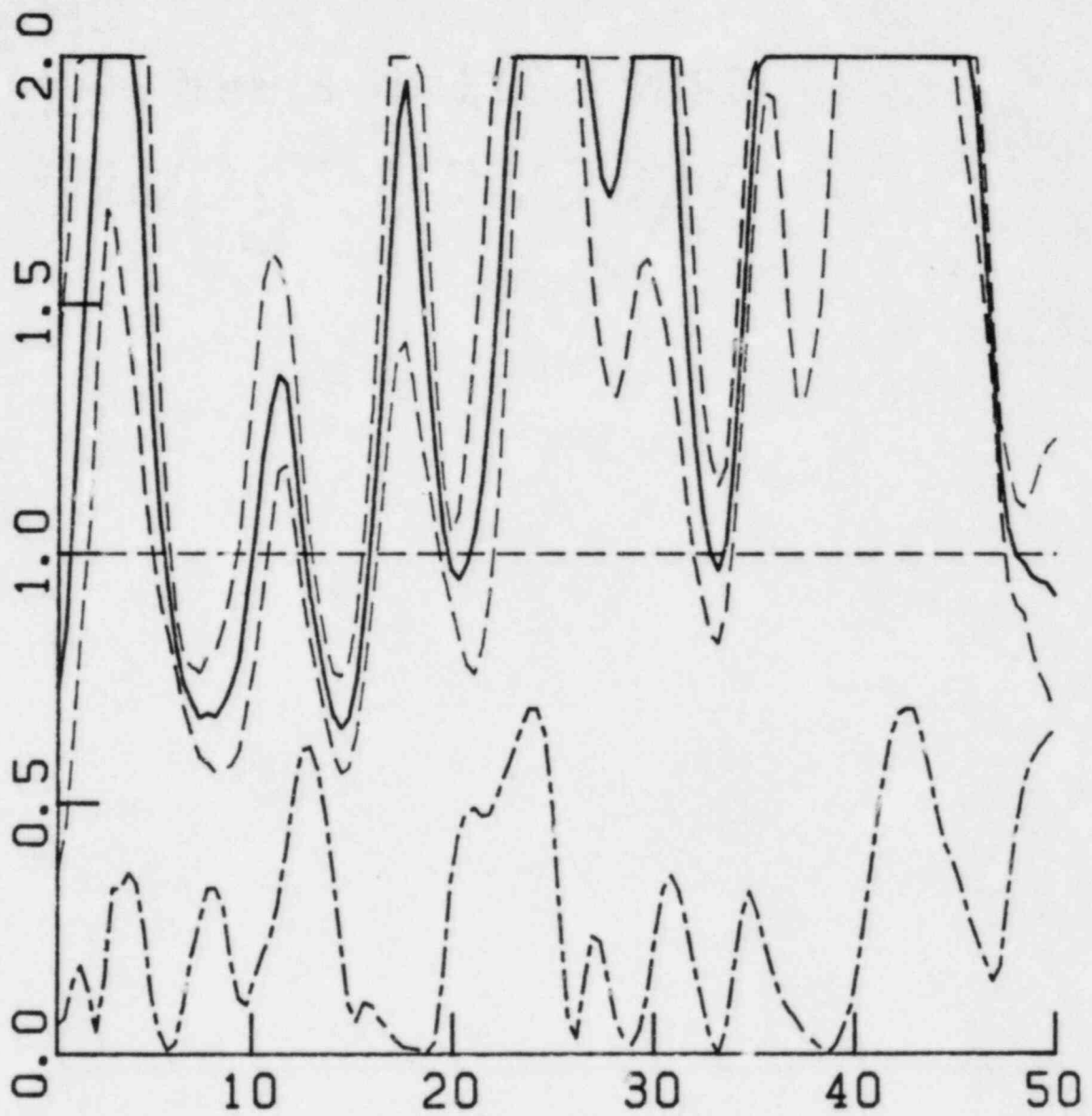
RATIOS FROM MODULI
 VERTICAL N = 4.
 RUN N 1.
 T4.S06.RP2S T4.S06.RP3S

Figure VI.B.1 Pad/Free-field spectral modulus ratio, vertical component, Test 4.



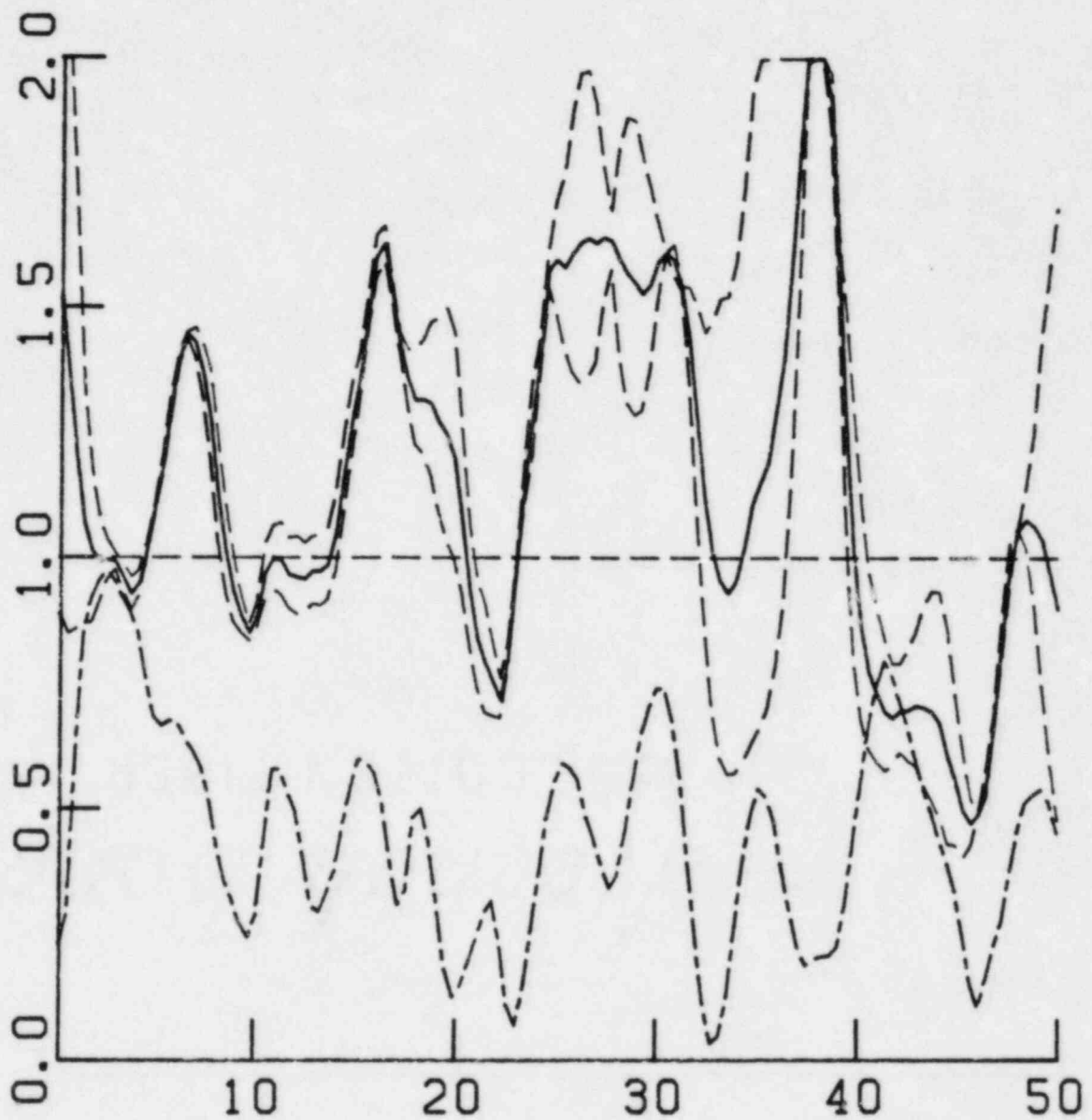
RATIOS FROM MODULI
 RADIAL N = 4.
 RUN N 110.
 T4. S06. RP2S T4. S06. RP3S

Figure VI.B.2 Pad/Free-field spectral modulus ratio, radial component, Test 4.



RATIOS FROM MODULI
 TRANSVERSE N = 4.
 RUN N 111.
 T4. S06. RP2S T4. S06. RP3S

Figure VI.B.3 Pad/Free-field spectral modulus ratio, transverse component, Test 4.



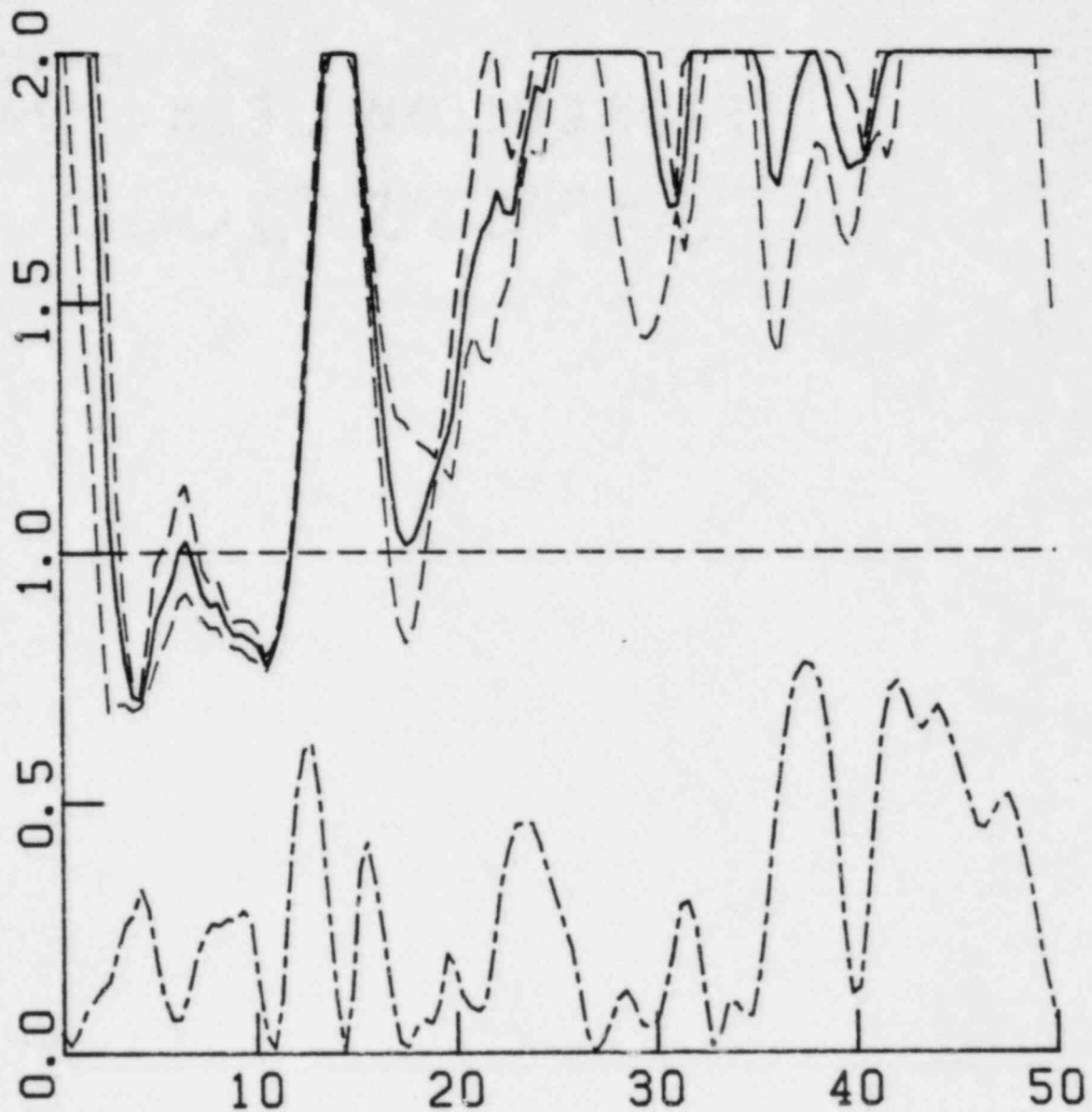
RATIOS FROM MODULI INDIVIDUALLY

VERTICAL N = 2.

RUN NO 115.

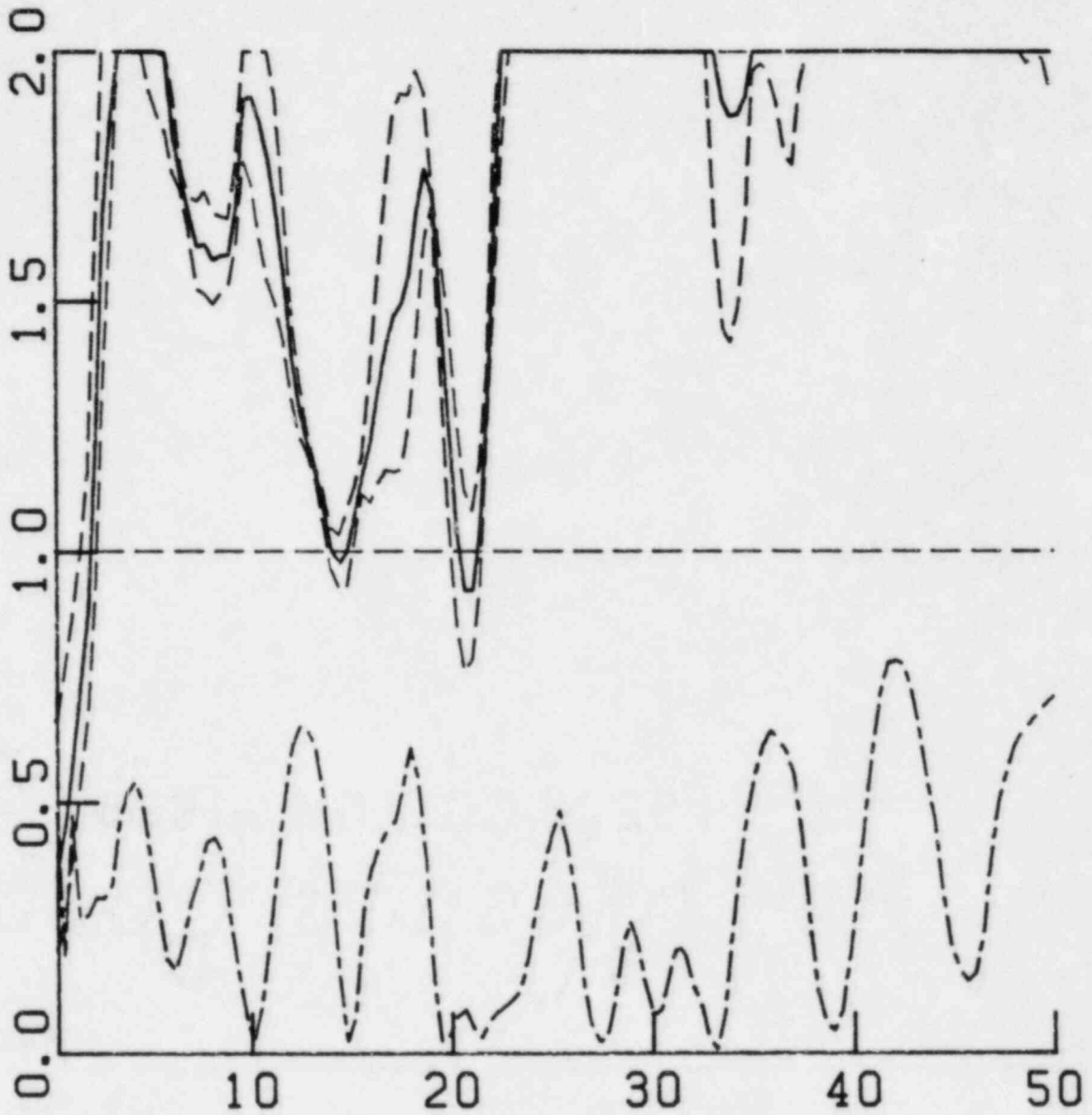
T4.S02.RP2S T4.S02.RP4S

Figure VI.B.4 Pad/Free-field spectral modulus ratio, vertical component, Test 4.



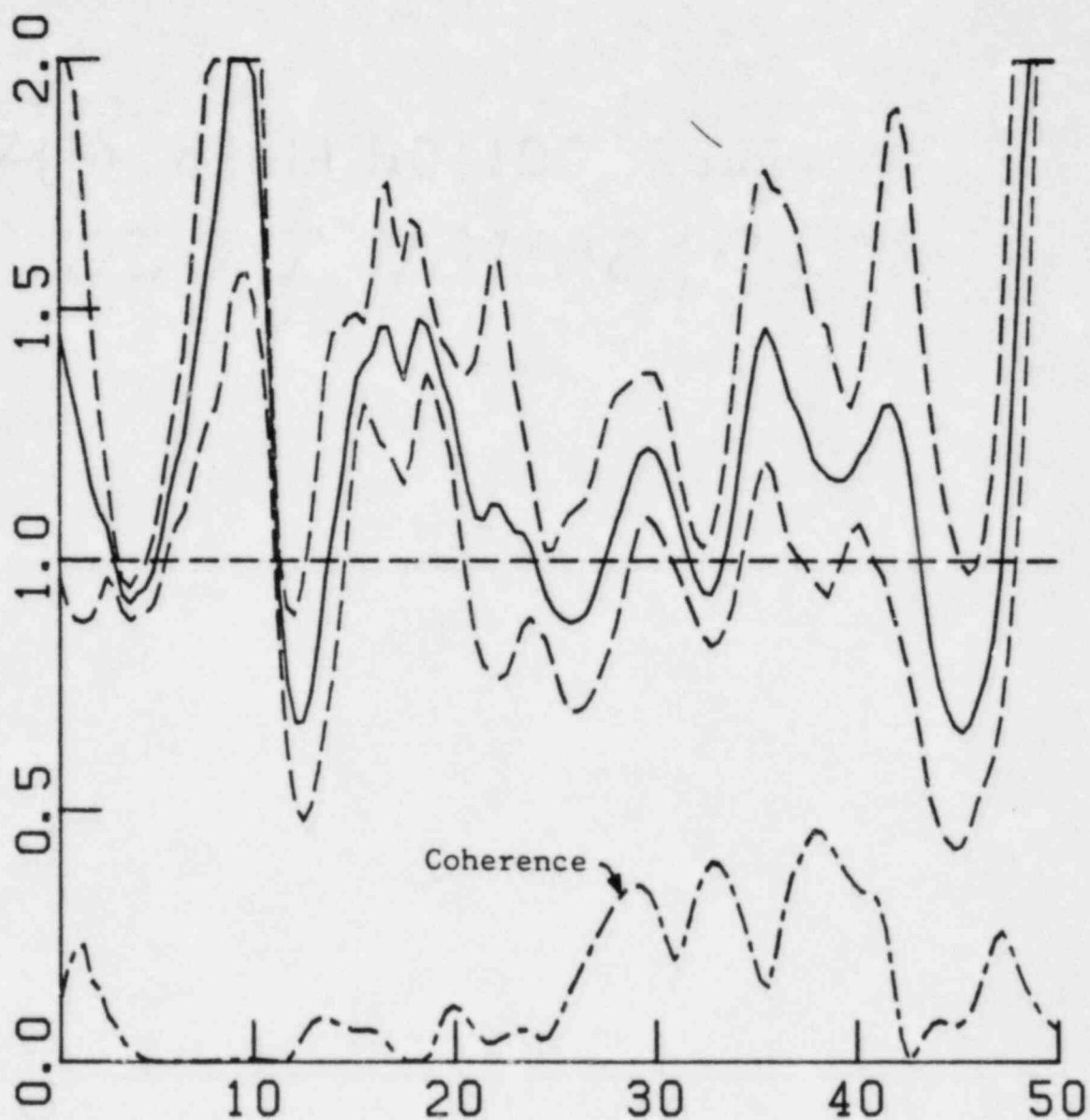
RATIOS FROM MODULI INDIVIDUALLY
 RADIAL N = 2.
 RUN NO 116.
 T4.S02.RP2S T4.S02.RP4S

Figure VI.B.5 Pad/Free-field spectral modulus ratio, radial component, Test 4.



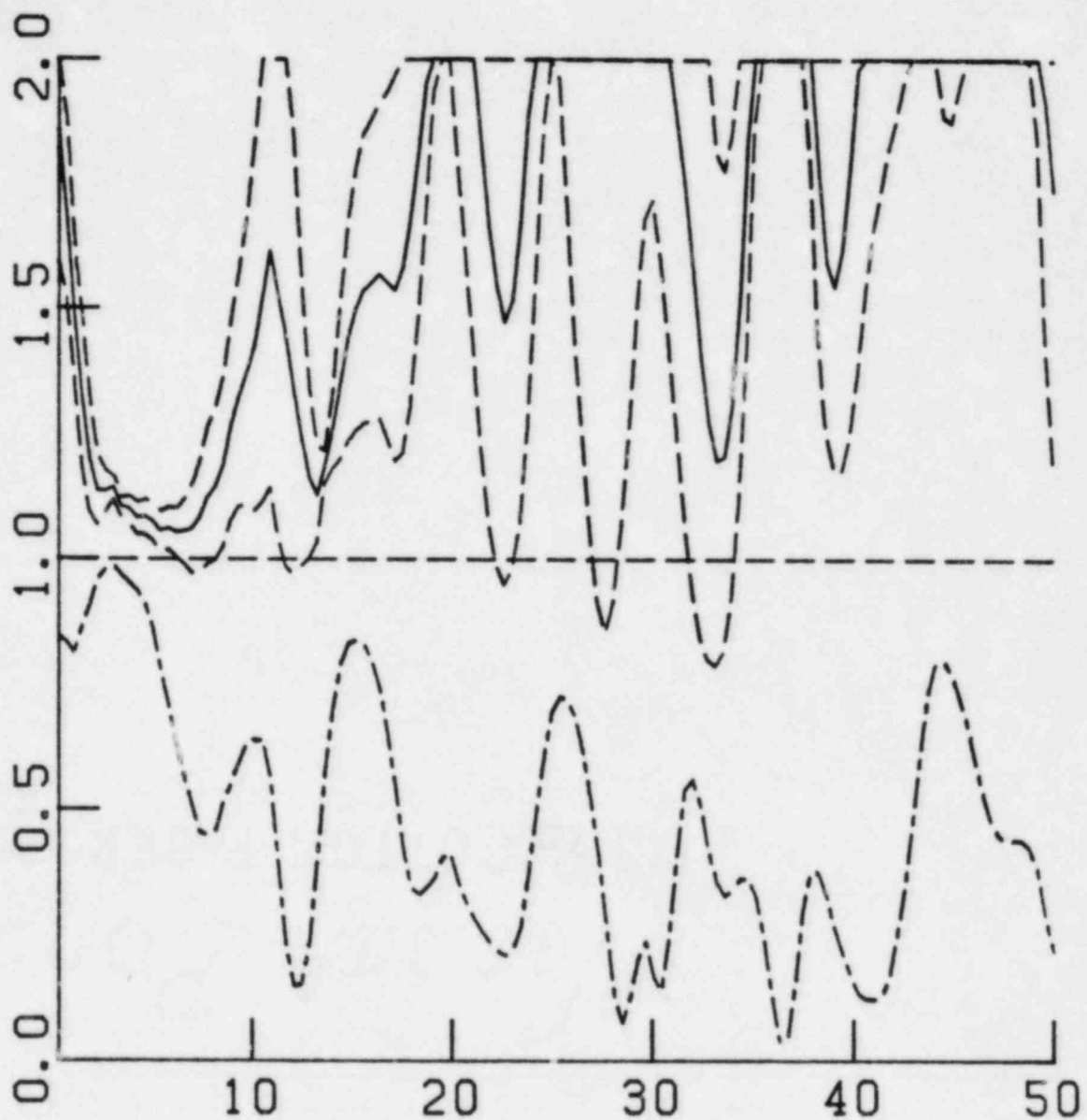
RATIOS FROM MODULI INDIVIDUALLY
 TRANSVERSE N = 2.
 RUN NO 117.
 T4. S02. RP2S T4. S02. RP4S

Figure VI.B.6 Pad/Free-field spectral modulus ratio, transverse component, Test 4.



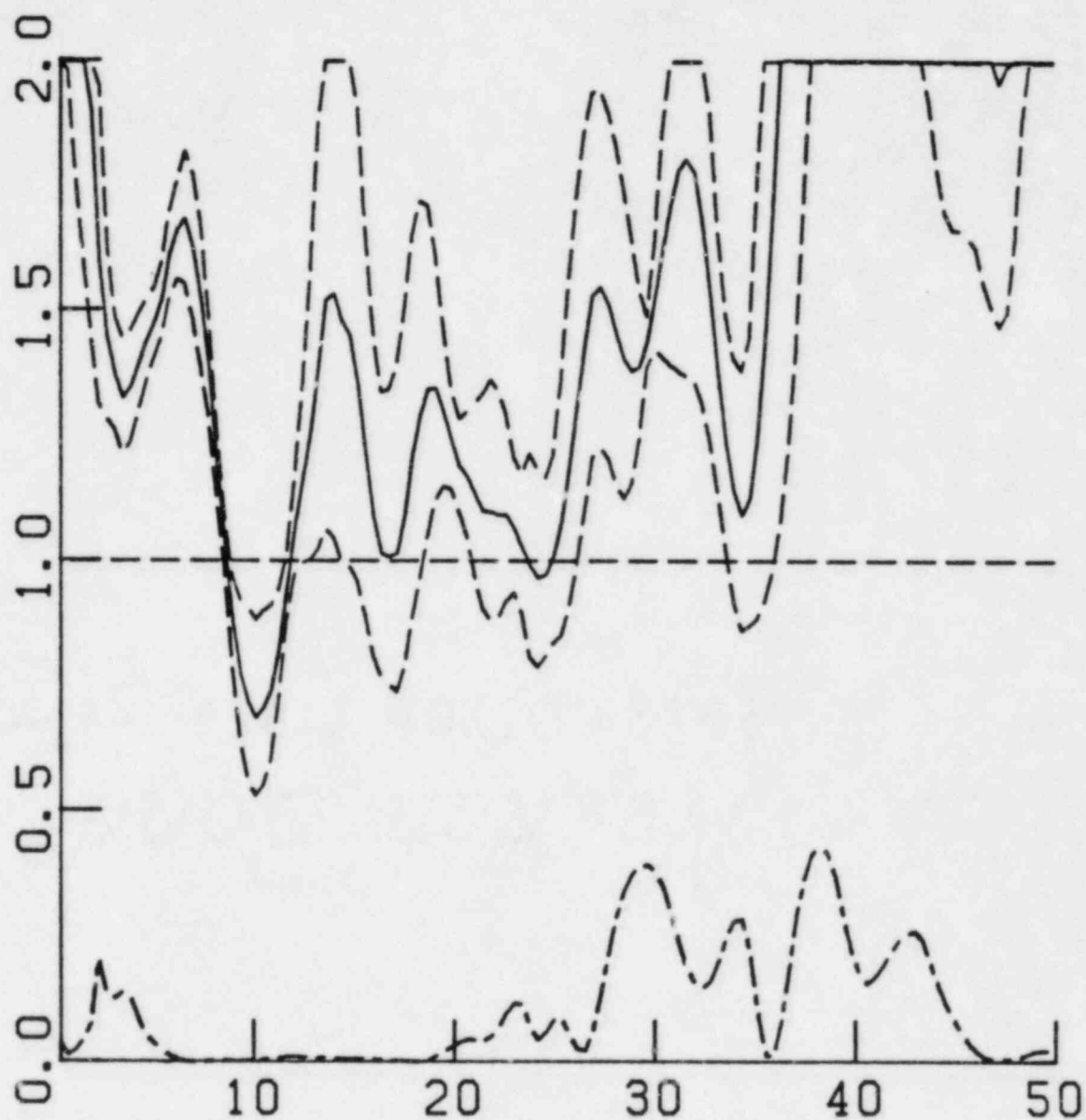
RATIOS FROM MODULI INDIVIDUALLY
 VERTICAL N = 6.
 RUN NO 121.
 T5.S08.RP2S T5.S08.RP4S

Figure VI.B.7 Pad/free-field spectral modulus ratio,
 vertical component, Test 5.



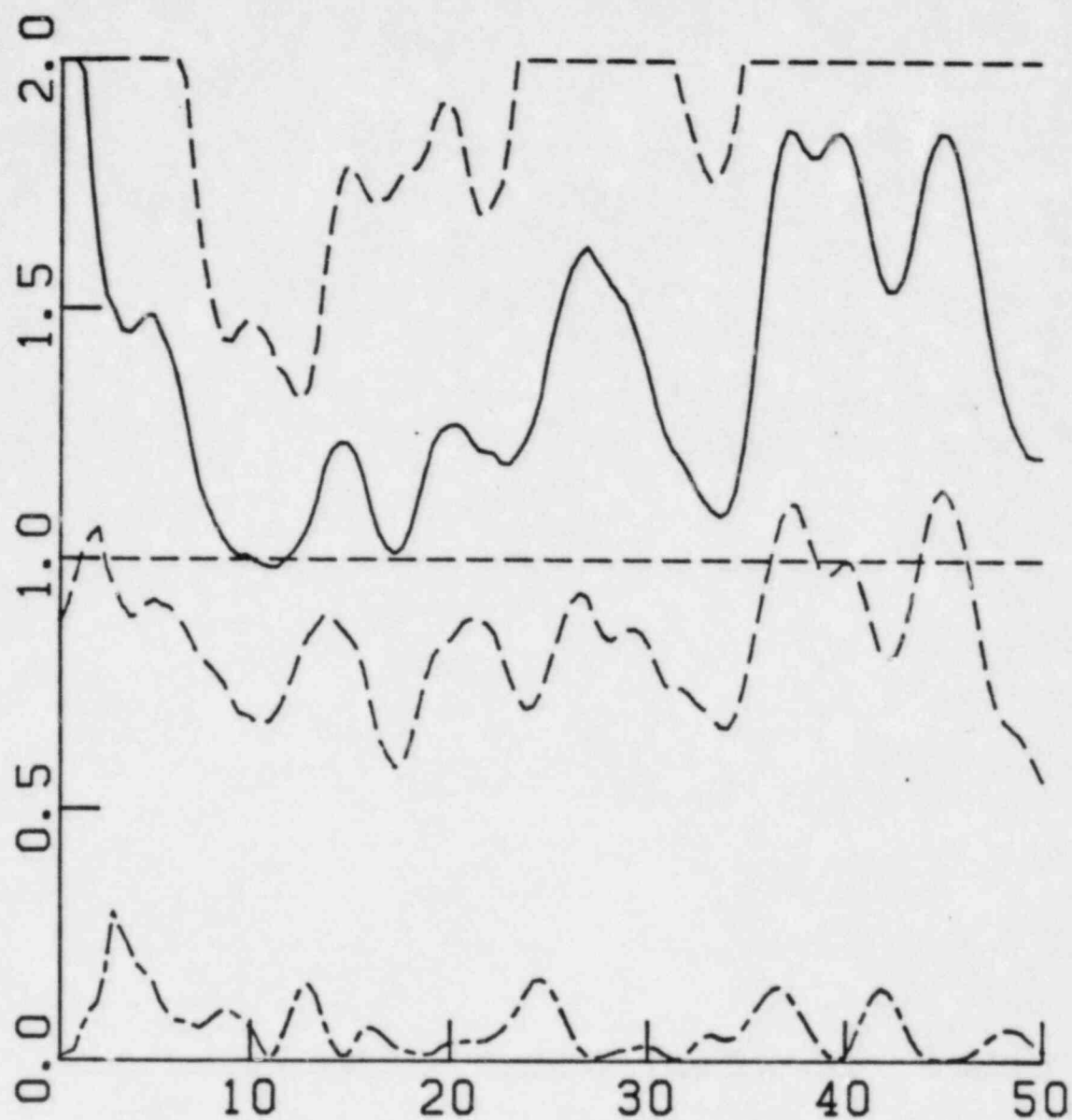
RATIOS FROM MODULI INDIVIDUALLY
 RADIAL N = 6.
 RUN NO 120.
 T5. S08. RP2S T5. S08. RP4S

Figure VI.B.8 Pad/Free-field spectral modulus ratio,
 radial component , Test 5.



RATIOS FROM MODULI INDIVIDUALLY
 TRANSVERSE N = 6.
 RUN NO 119.
 T5. S08. RP2S T5. S08. RP1S

Figure VI.B.9 Pad/Free-field spectral modulus ratio,
 transverse component, Test 5.



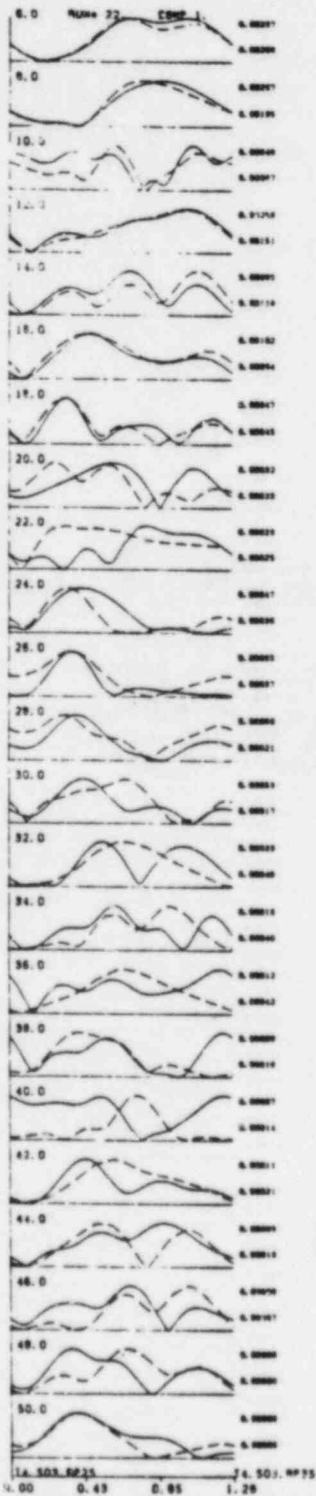
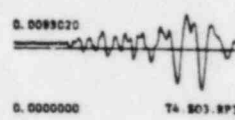
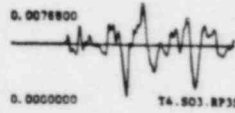
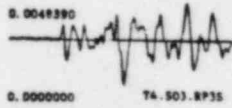
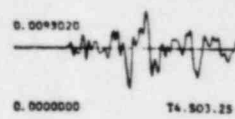
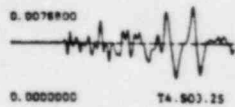
RATIOS FROM MODULI INDIVIDUALLY

TRANSVERSE N = 48.

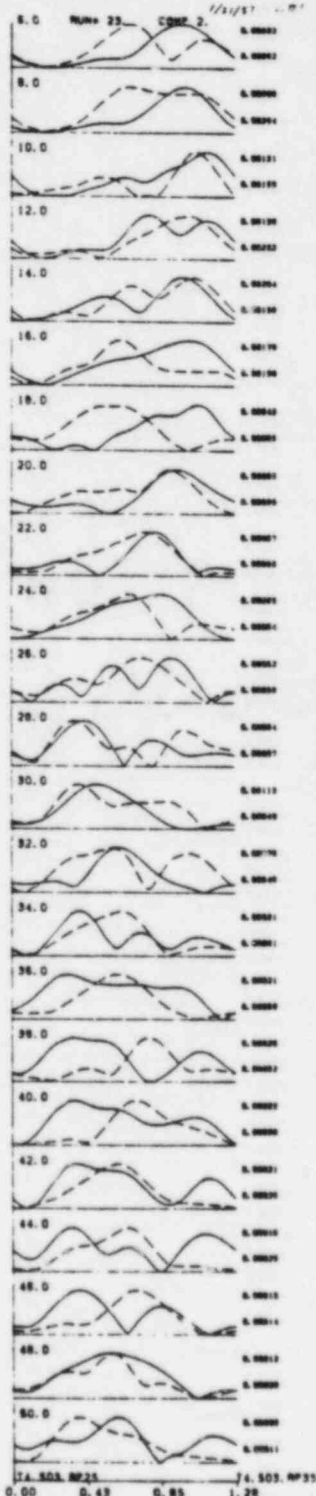
RUN NO 183.

T4. S06. RP2S T4. S06. RP3S

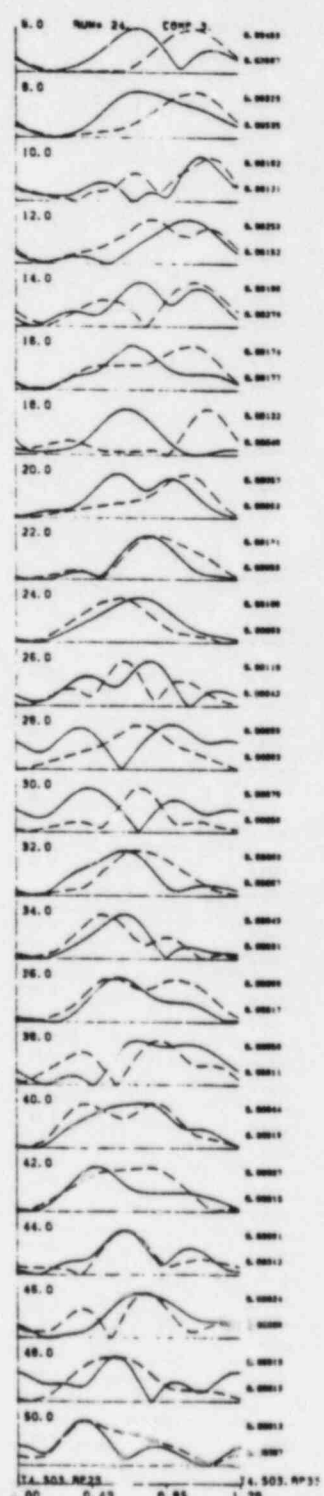
Figure VI.B.10 Pad/Free-field spectral modulus ratio, Radial and Transverse components combined. All Test 4 and Test 5 data are included and given equal weight. Dashed lines are standard deviations for the combined effects of shot-to-shot and site-to-site variability.



VERTICAL

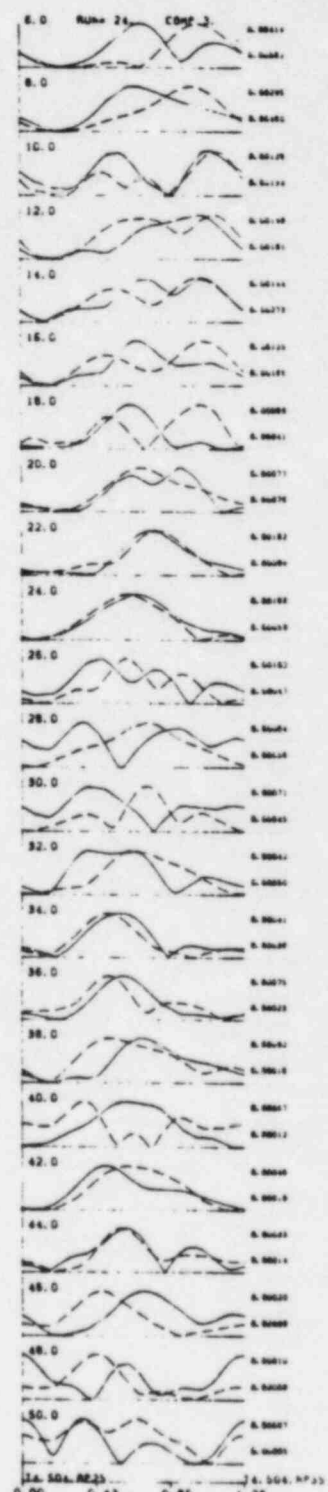
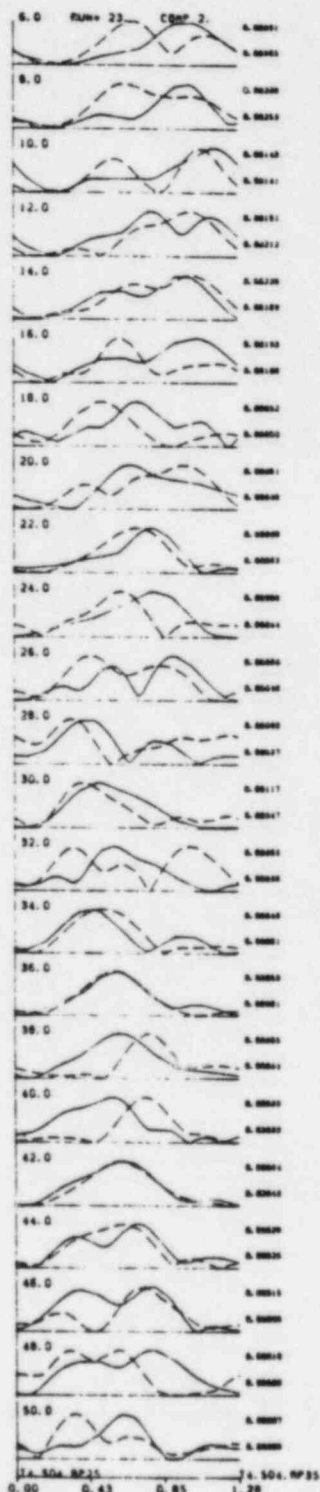
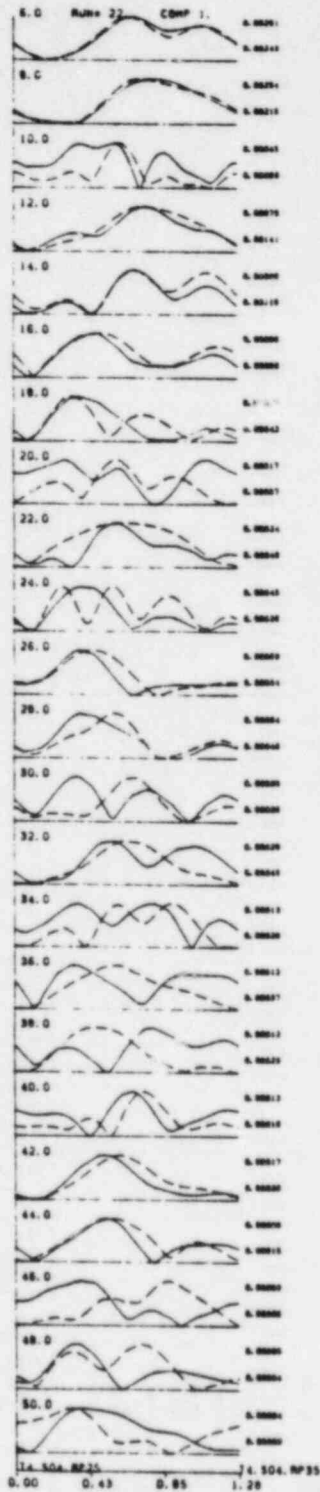
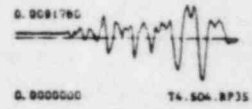
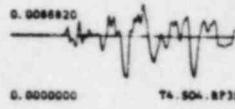
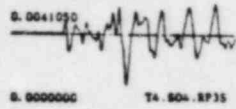
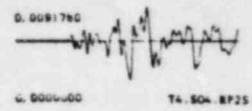


RADIAL



TRANSVERSE

Figure VI.B.II Band pass envelopes
P2 and P3, Test 4, Shot 3

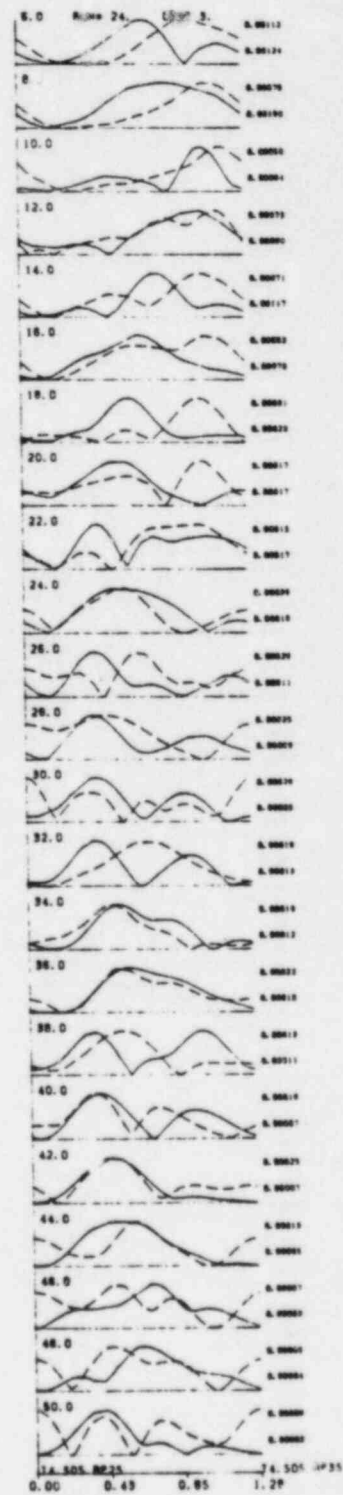
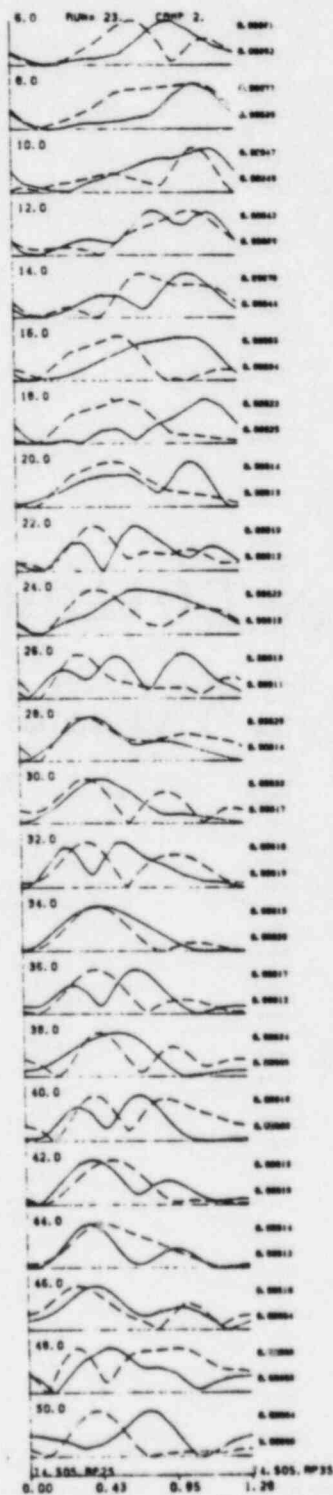
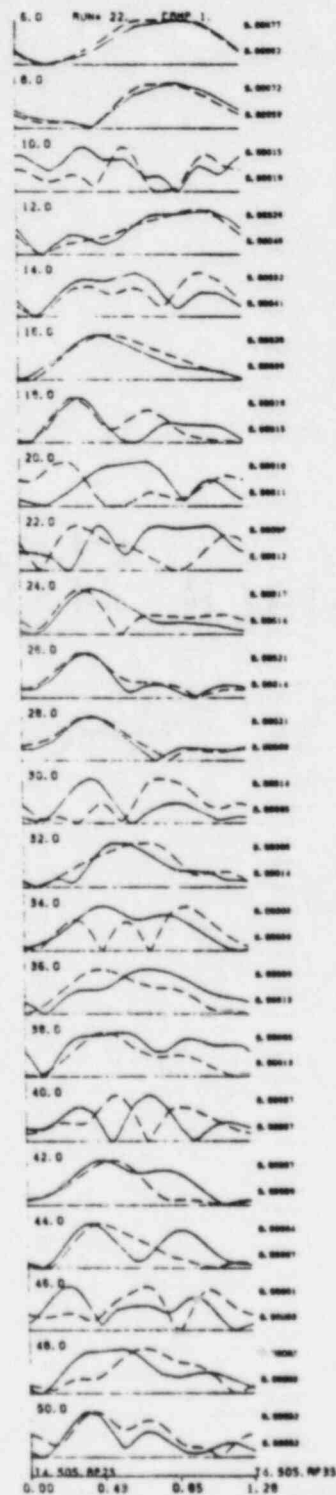
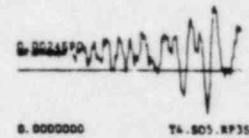
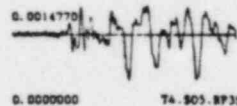
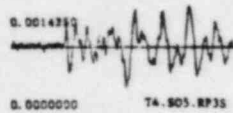
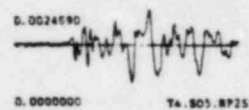


VERTICAL

RADIAL

TRANSVERSE

Figure VI.B.12 Band pass envelopes
P2 and P3, Test 4, Shot 4

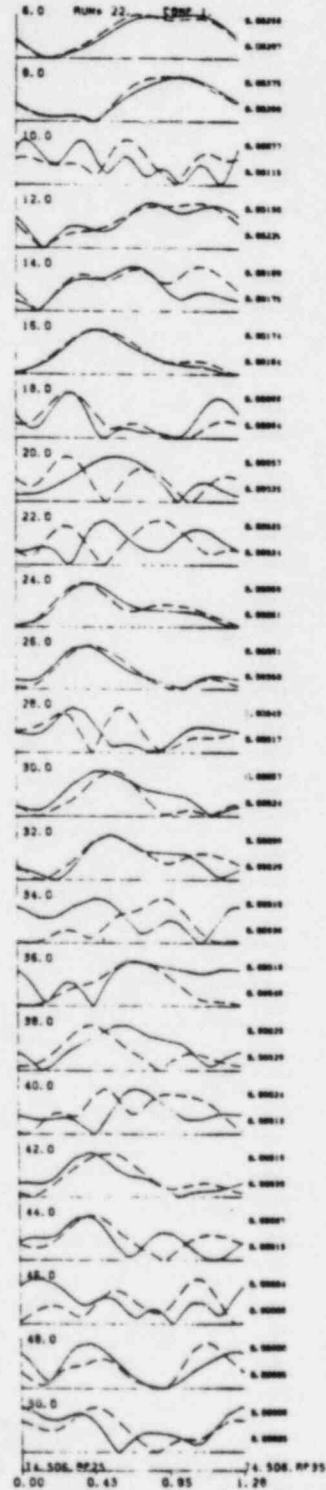
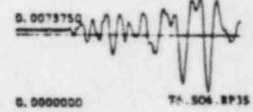
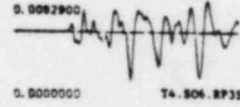
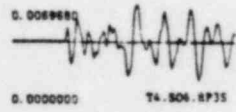
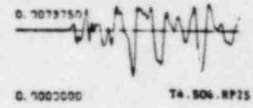
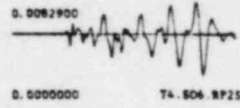
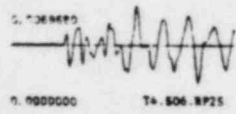


VERTICAL

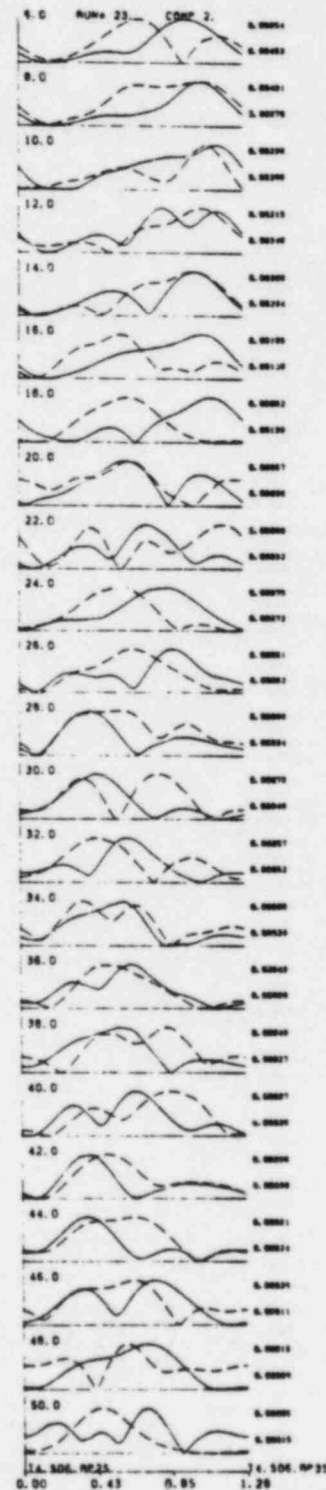
RADIAL

TRANSVERSE

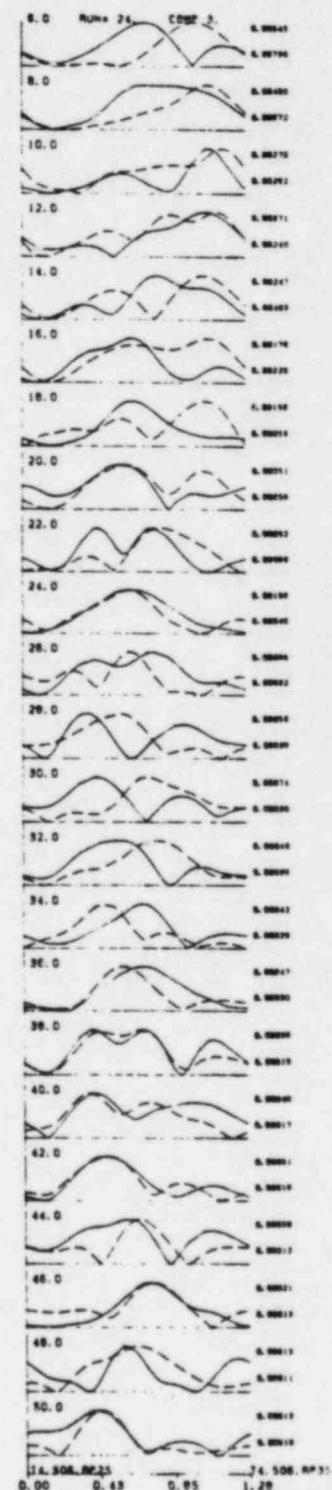
Figure VLB.13 Band pass envelopes
P2 and P3, Test 4, Shot 5



VERTICAL



RADIAL



TRANSVERSE

Figure VI.B.14 Band pass envelopes
P2 and P3, Test 4, Shot 6

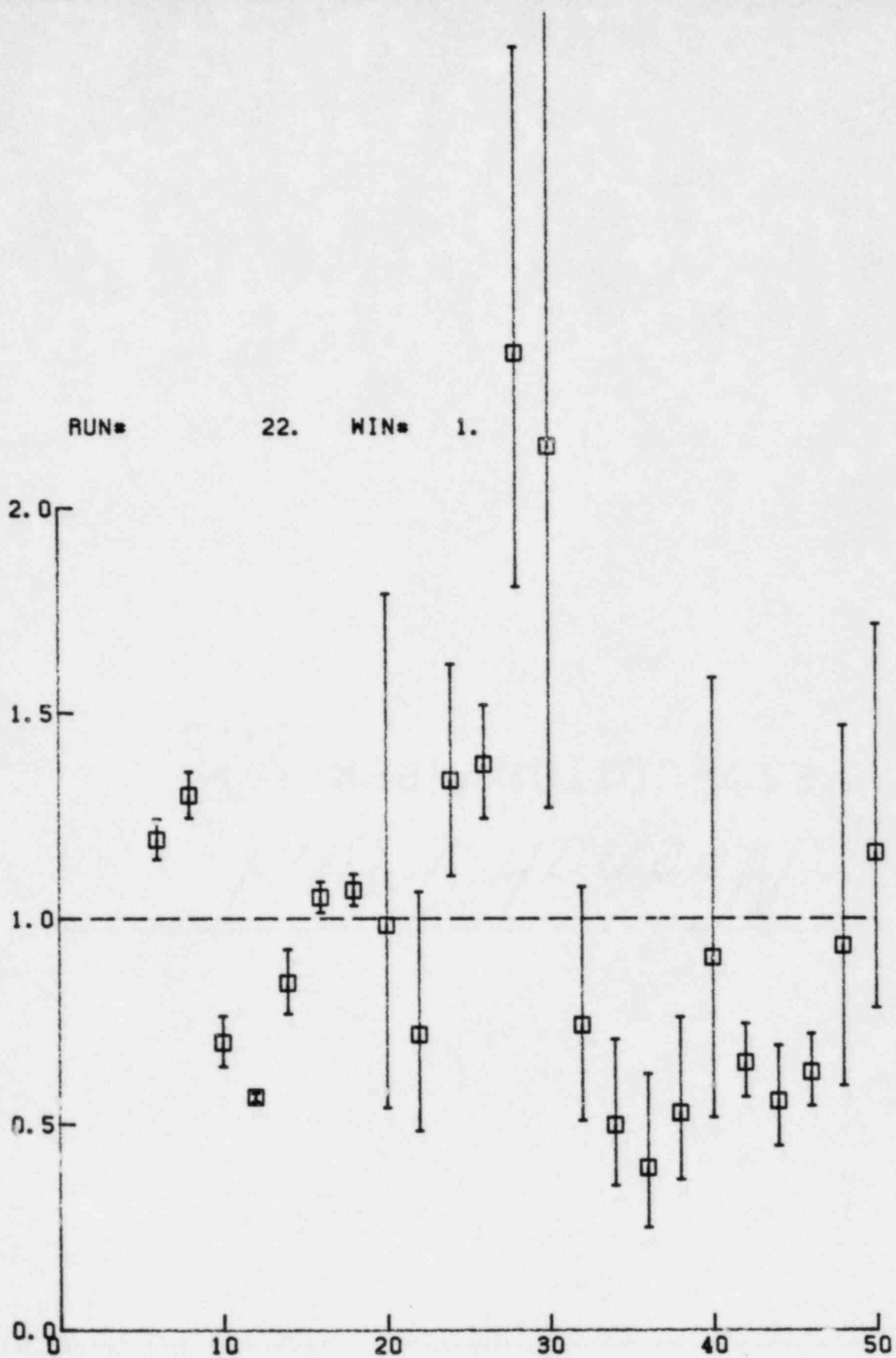


Figure VI. B.15 Test 4, vertical P2/P3 band pass spectral ratios, window 0-1.28 sec.

RUN# 22. MIN# 2.

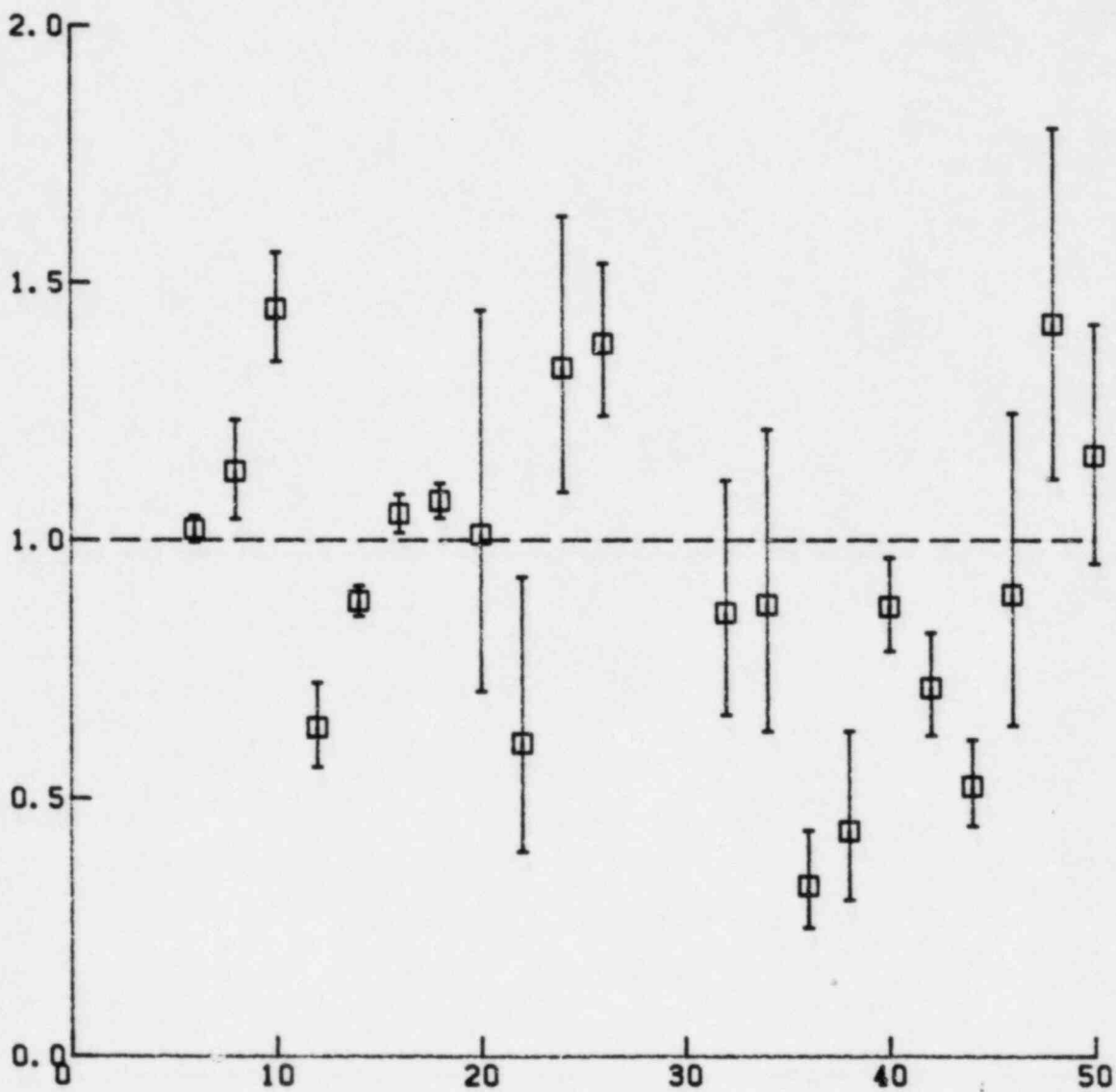


Figure VI.B.16 Test 4, vertical P2/P3
band pass spectral ratios
window 0.16-0.48 sec.

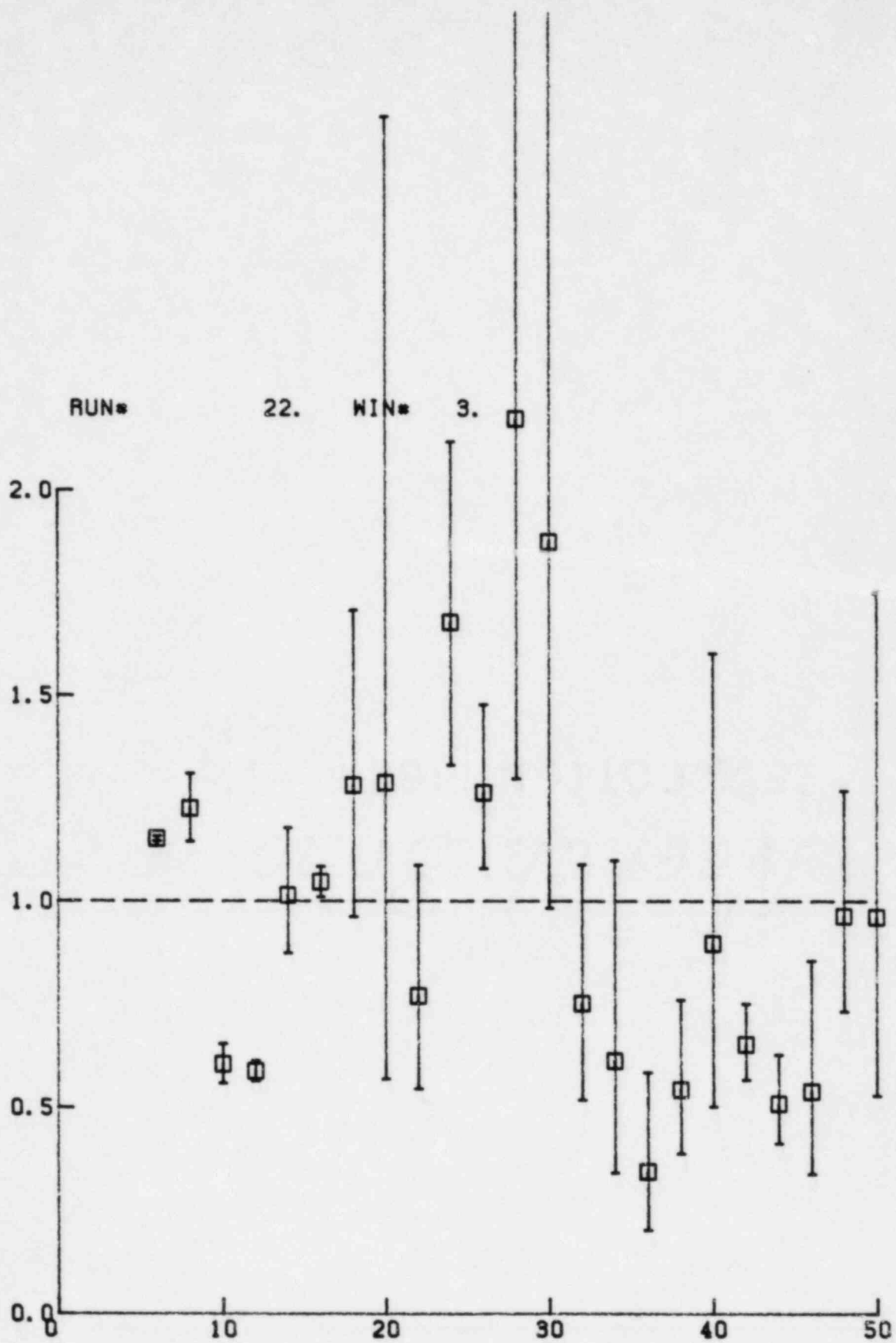


Figure VI.B.17 Test 4, vertical P2/P3
 band pass spectral ratios
 window 0.48-0.80 sec.

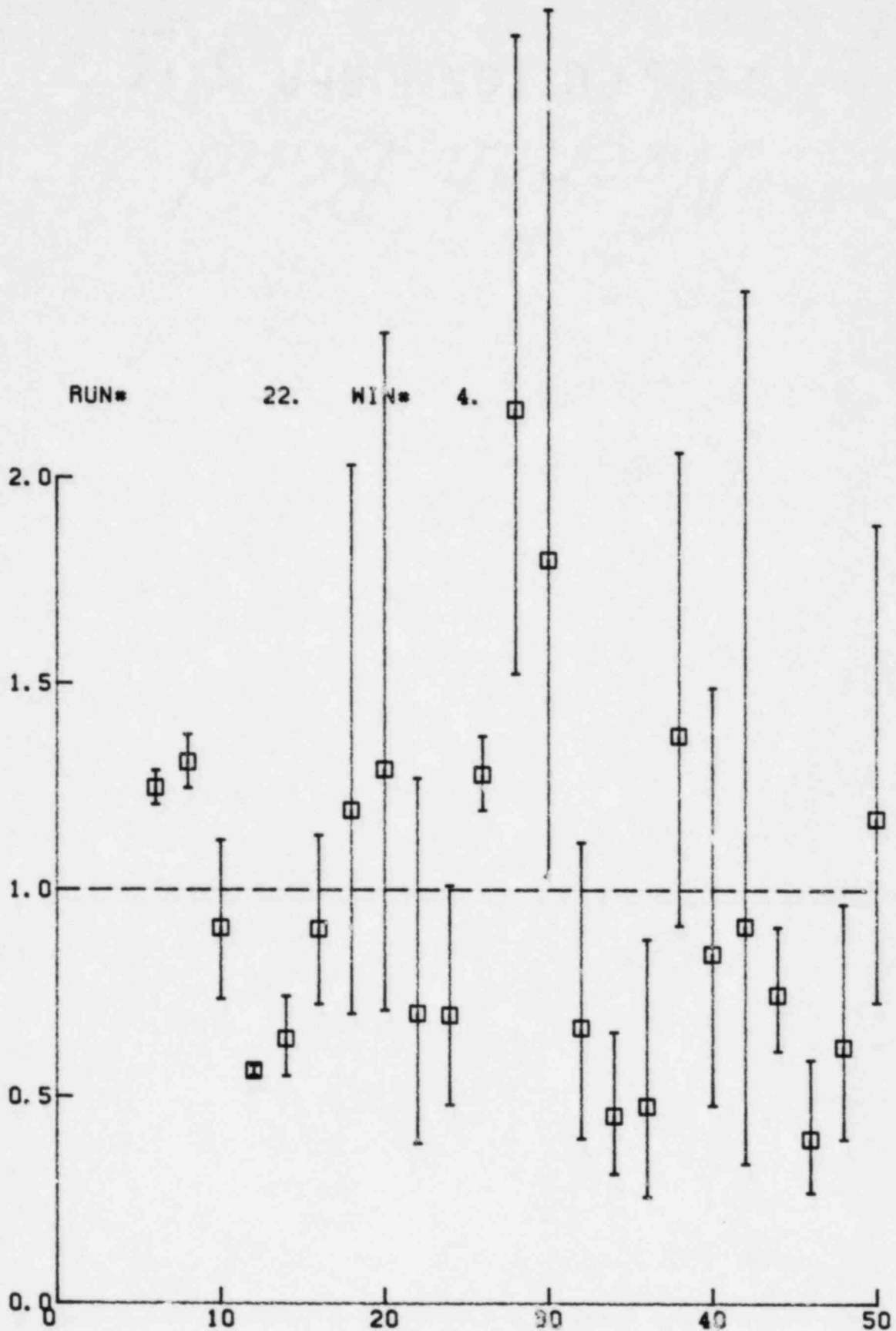


Figure VI.B.18 Test 4, vertical P2/P3 band pass spectral ratios window 0.80-1.28 sec.

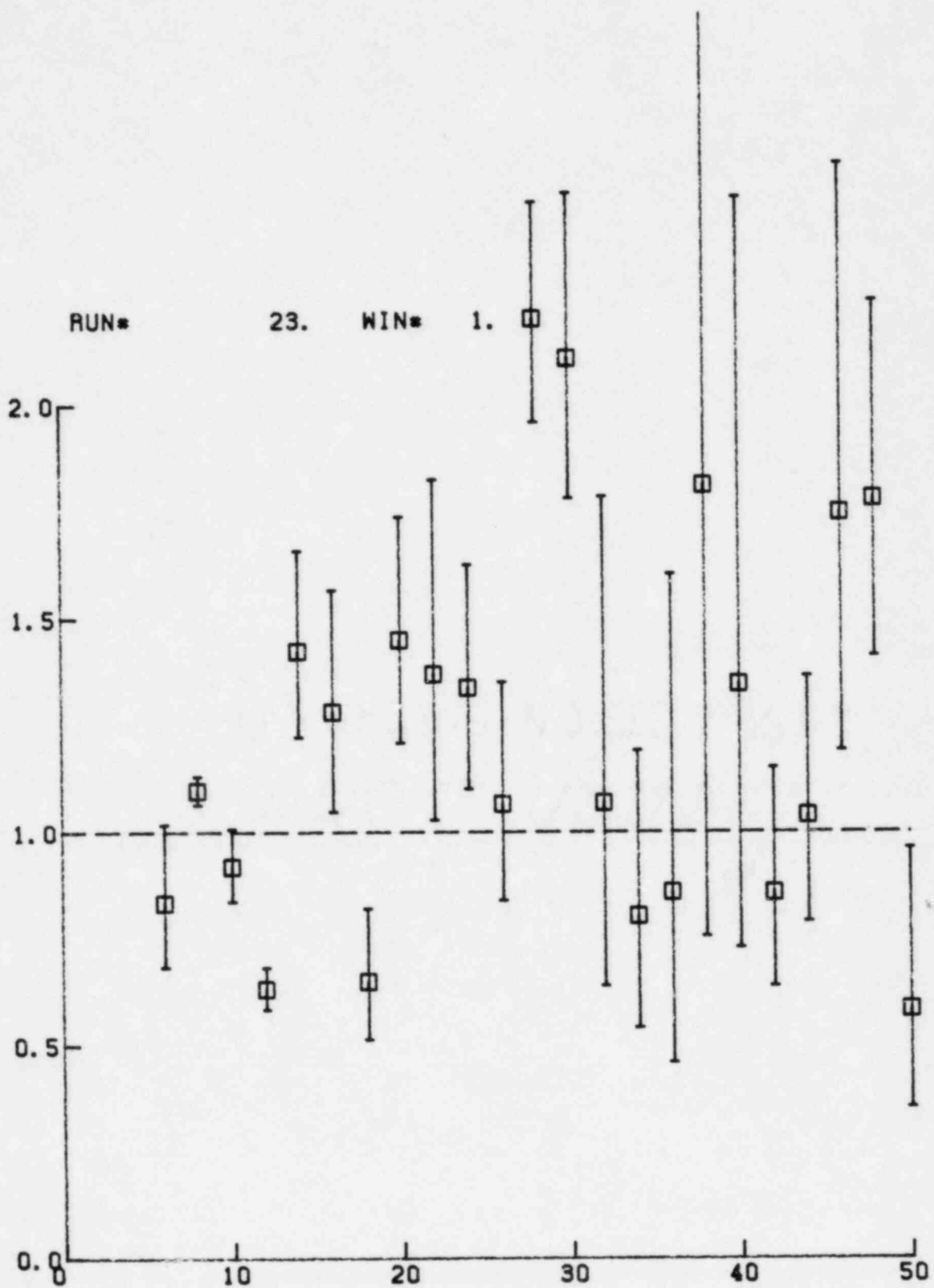


Figure VI.B.19 Test 4, radial P2/P3
band pass spectral ratios
window 0-1.28 sec.

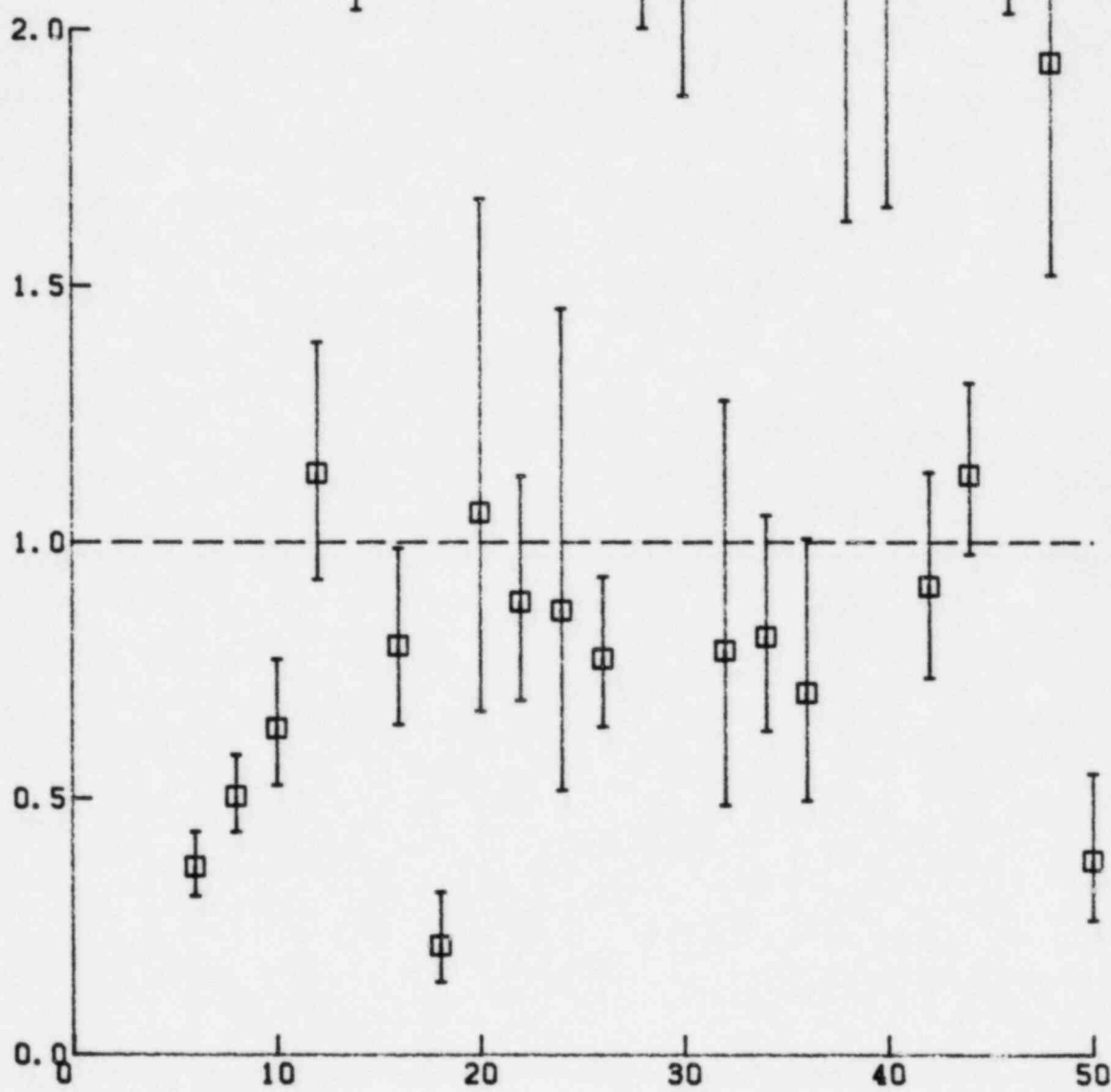


Figure VI.B.20 Test 4, radial P2/P3
band pass spectral ratios
window 0.16-0.48 sec.

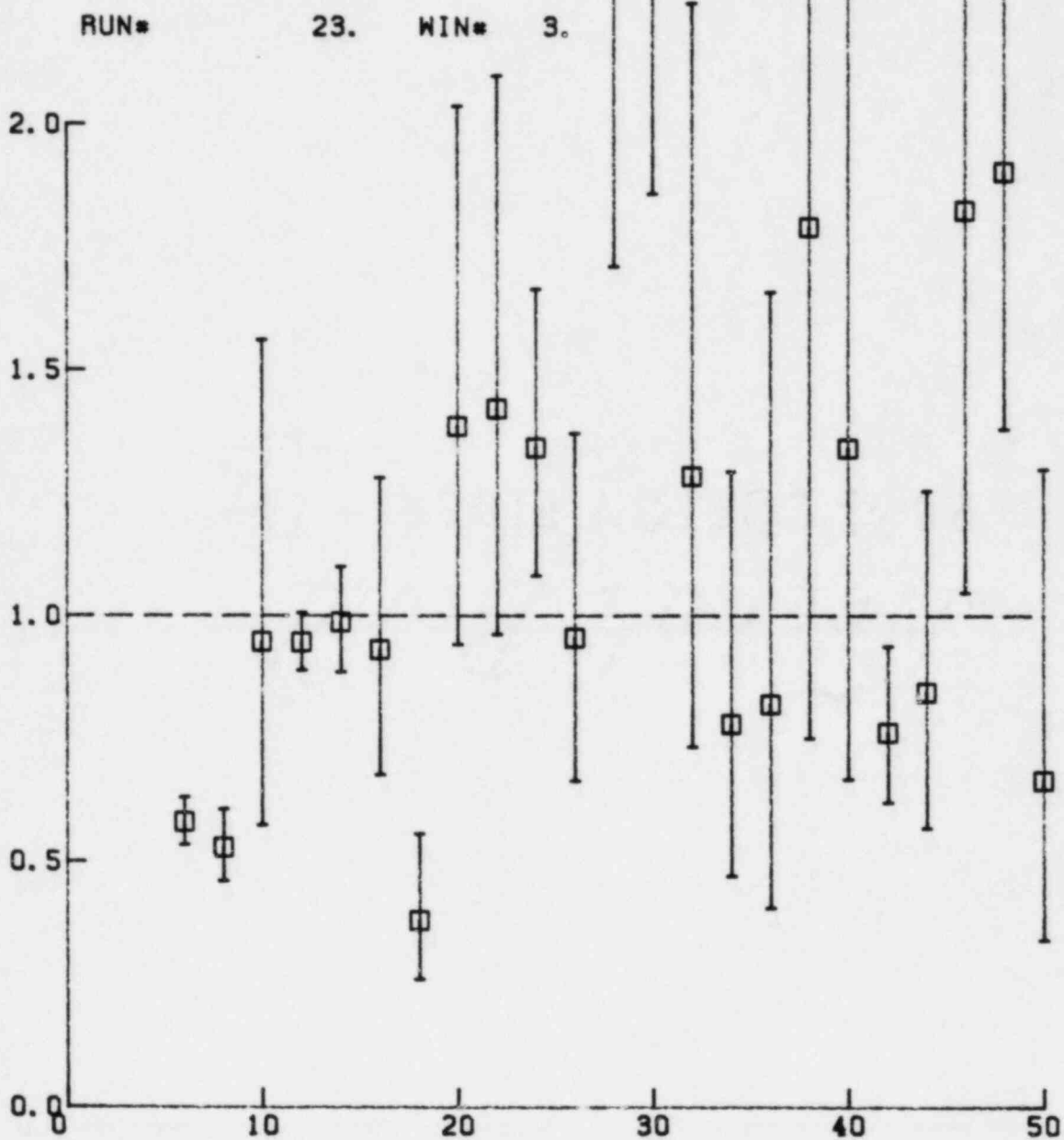


Figure VI.B.21 Test 4, radial P2/P3
band pass spectral ratios
window 0.48-0.80 sec.

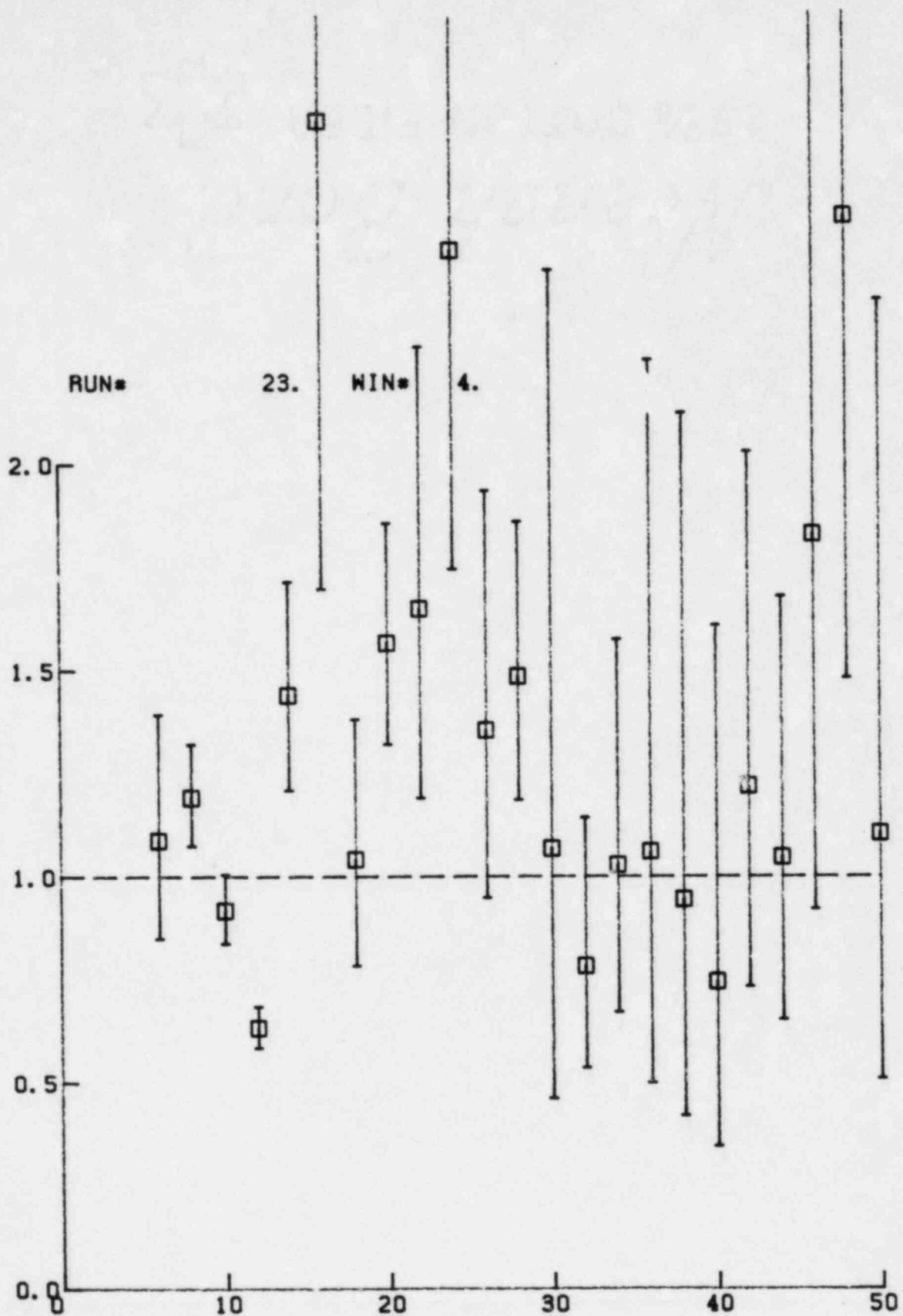


Figure VI.B.22 Test 4, radial P2/P3
band pass spectral ratios
window 0.80-1.28 sec.

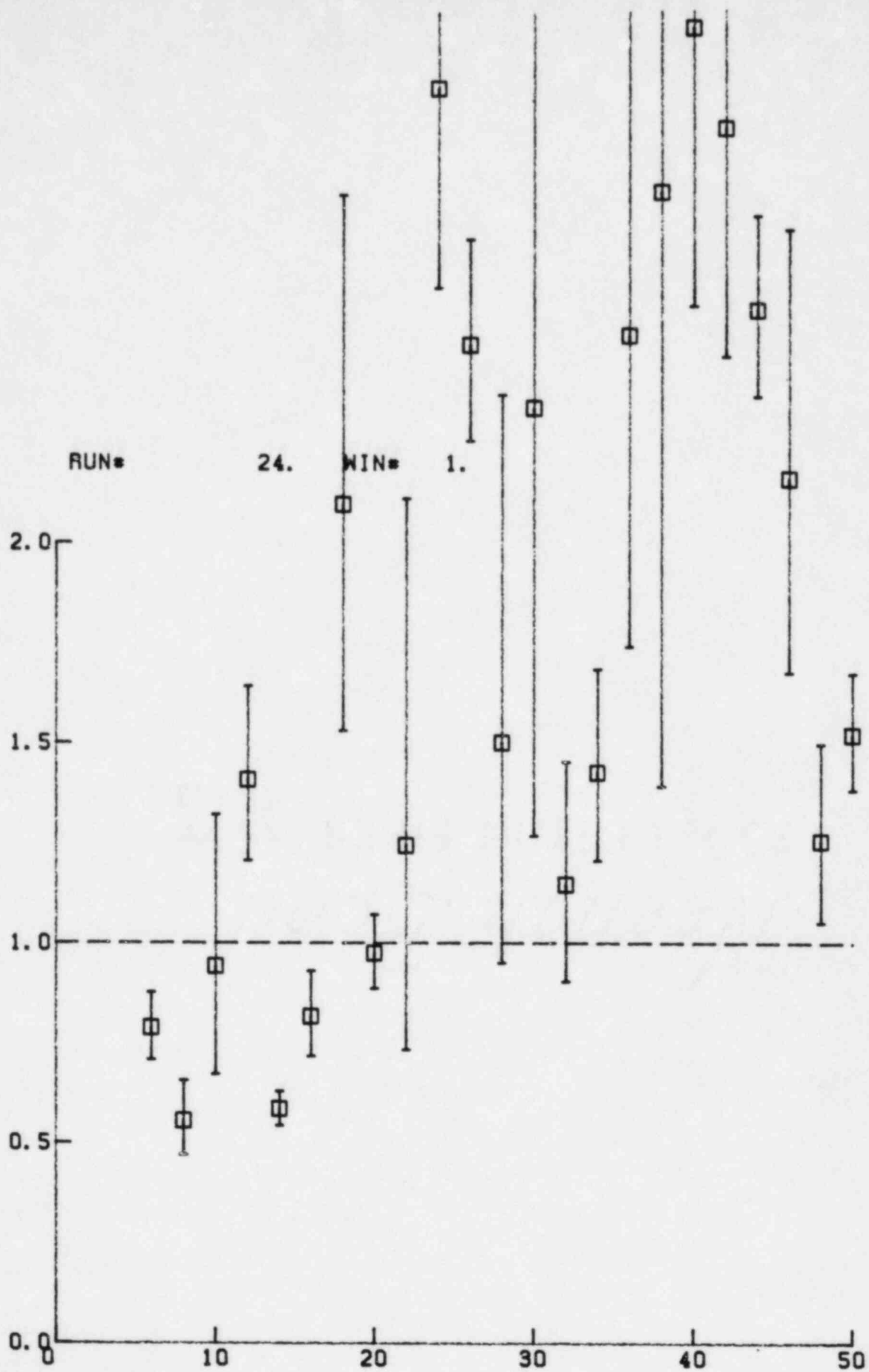


Figure VI.B.23 Test 4, transverse P2/P3 band pass spectral ratios window 0-1.28 sec.

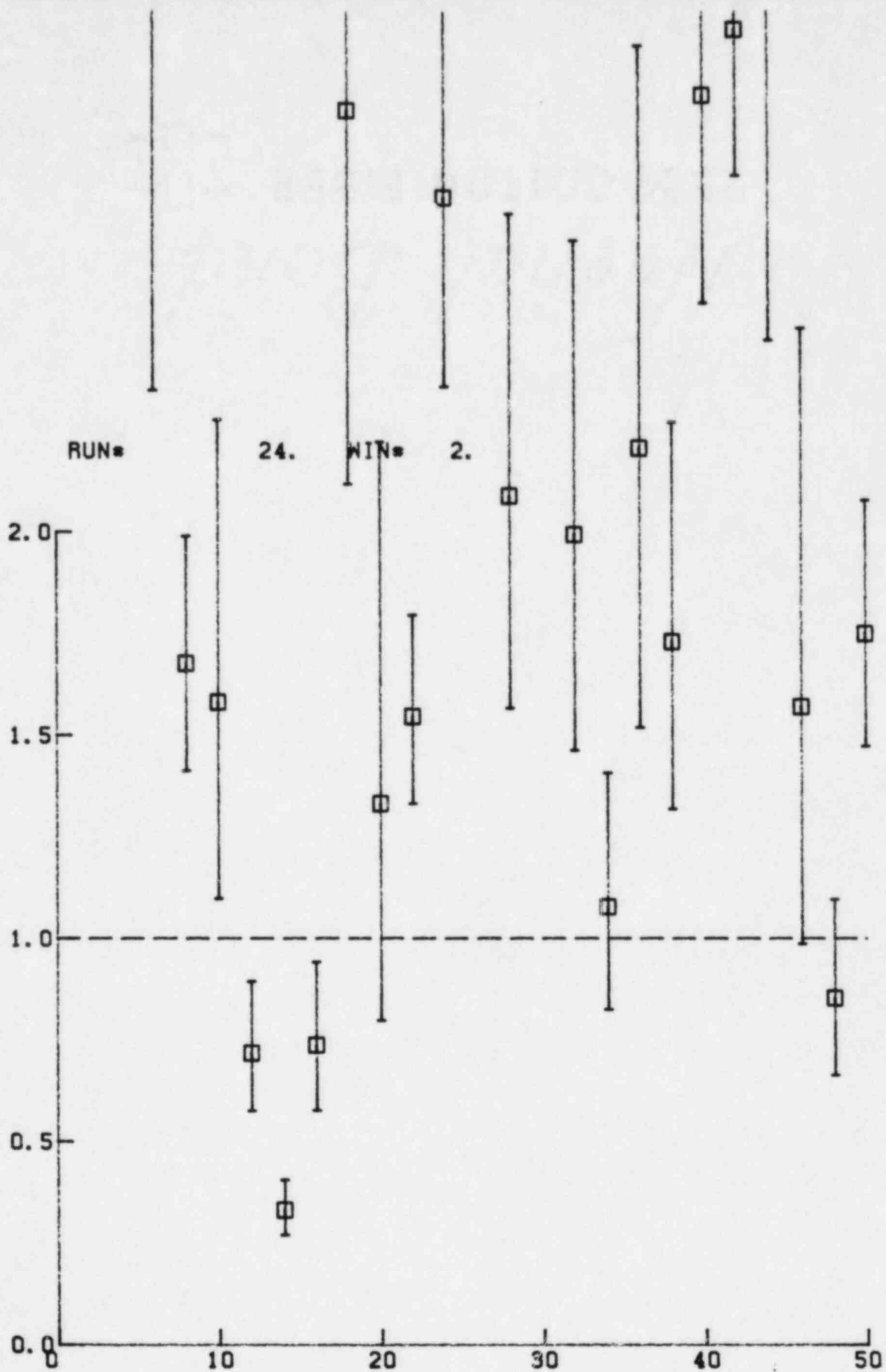


Figure VI.B.24 Test 4, transverse P2/P3
band pass spectral ratios
window 0.16-0.48 sec.

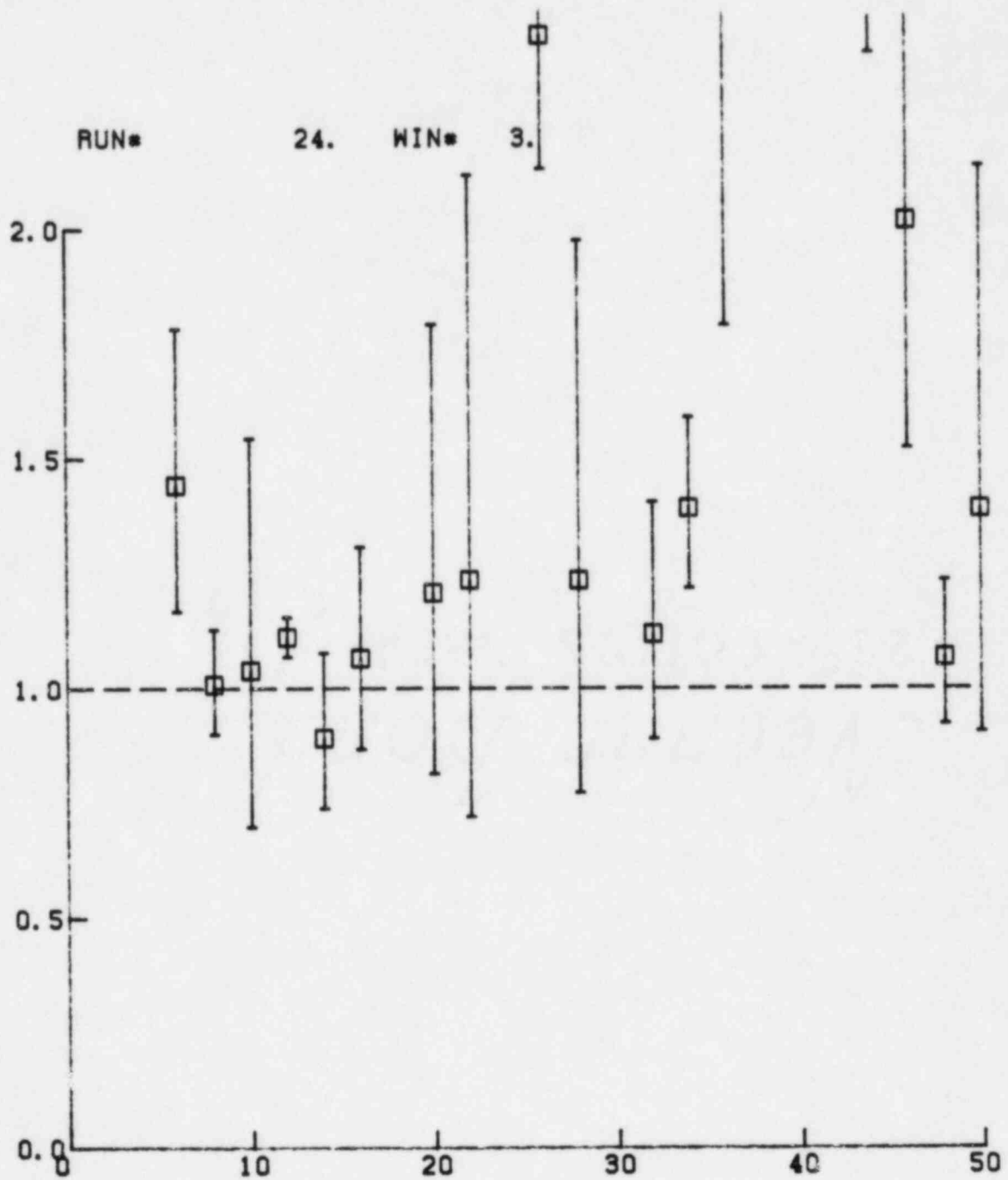


Figure VI.B.25 Test 4, transverse P2/P3
band pass spectral ratios
window 0.48-0.80 sec.

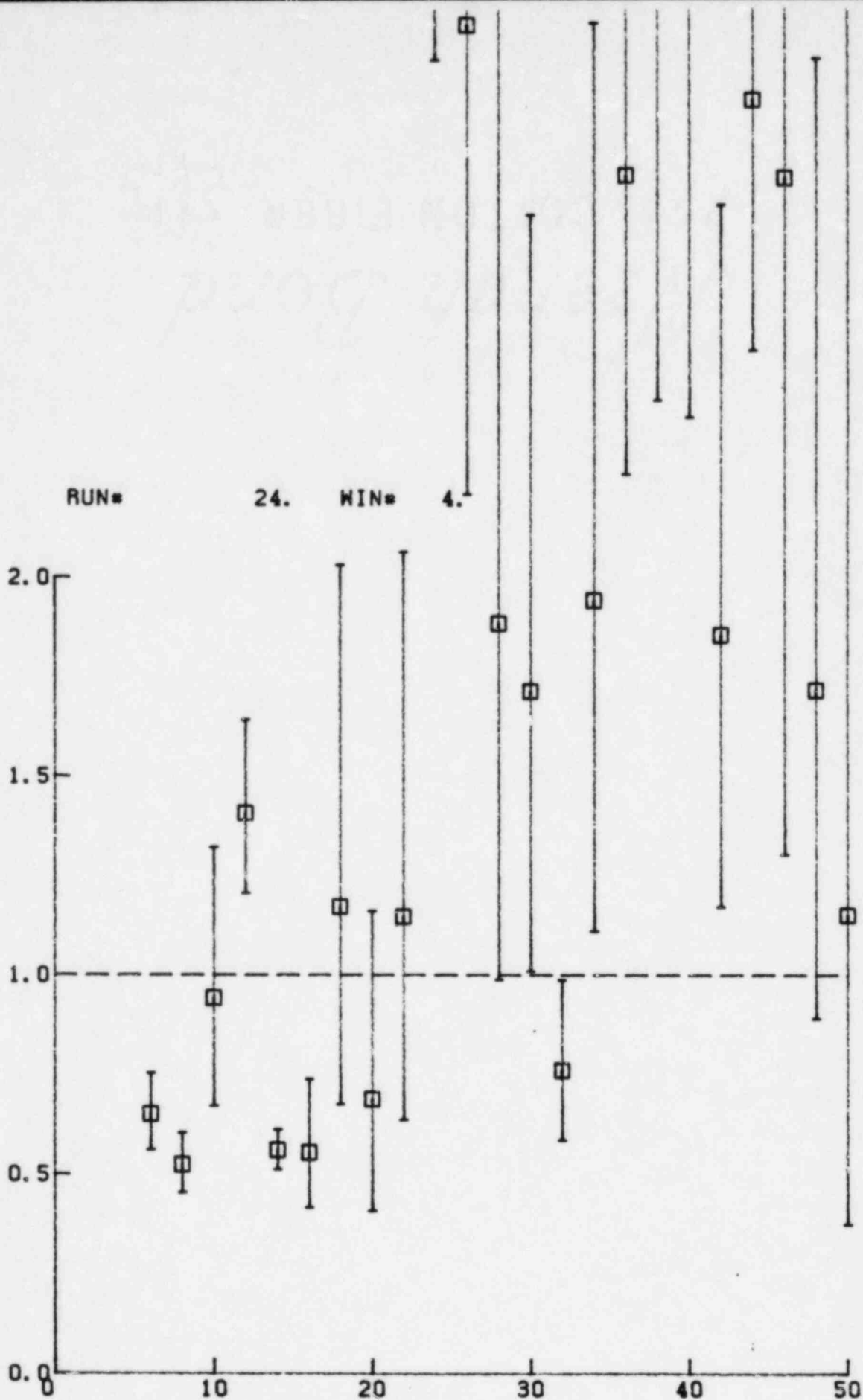
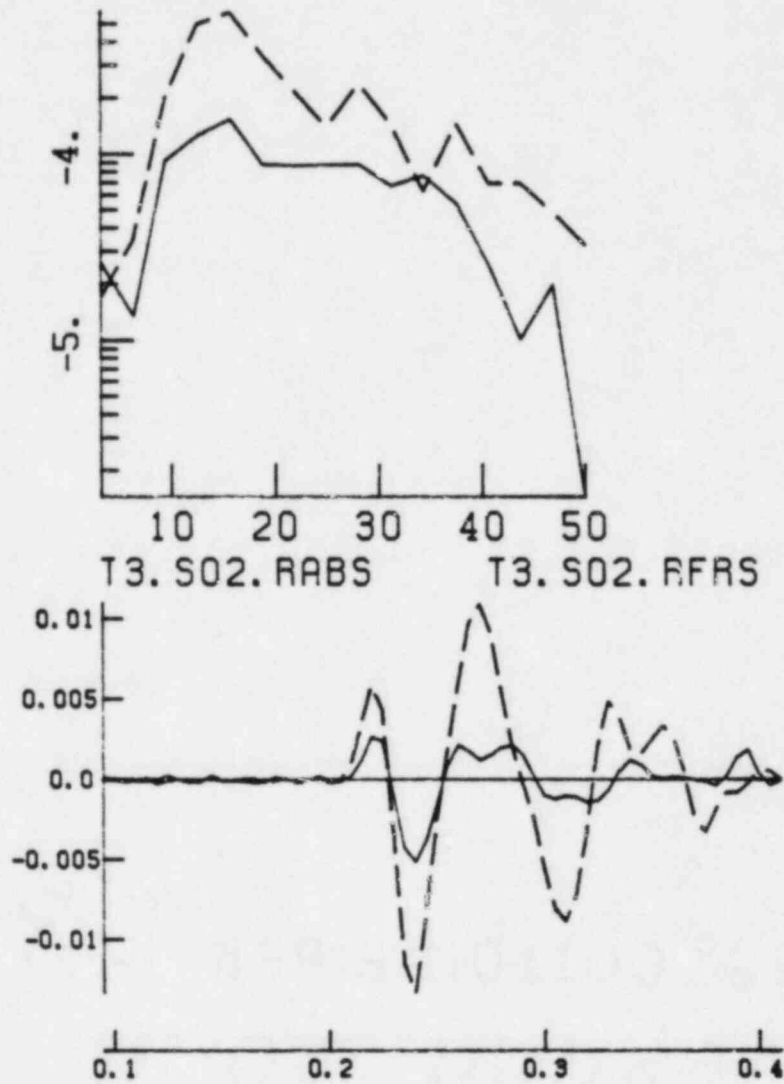
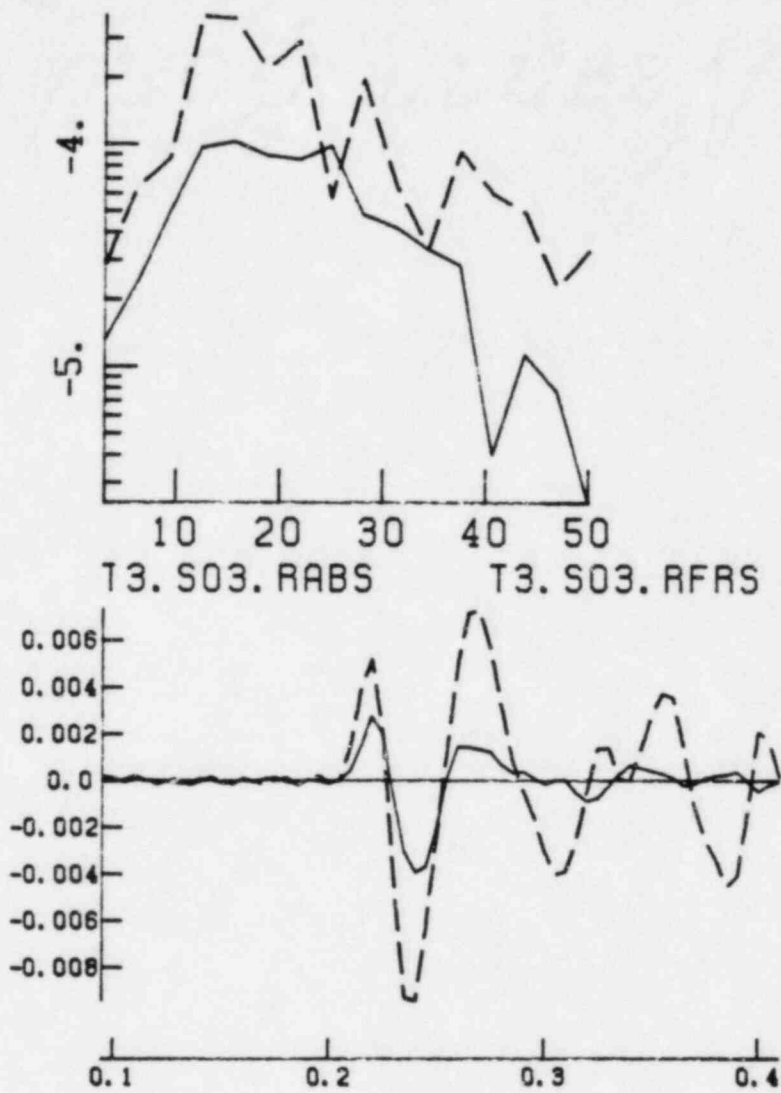


Figure VI.B.26 Test 4, transverse P2/P3
band pass spectral ratios
window 0.80-1.28 sec.



PLOT NO 1. RUN NO 255.

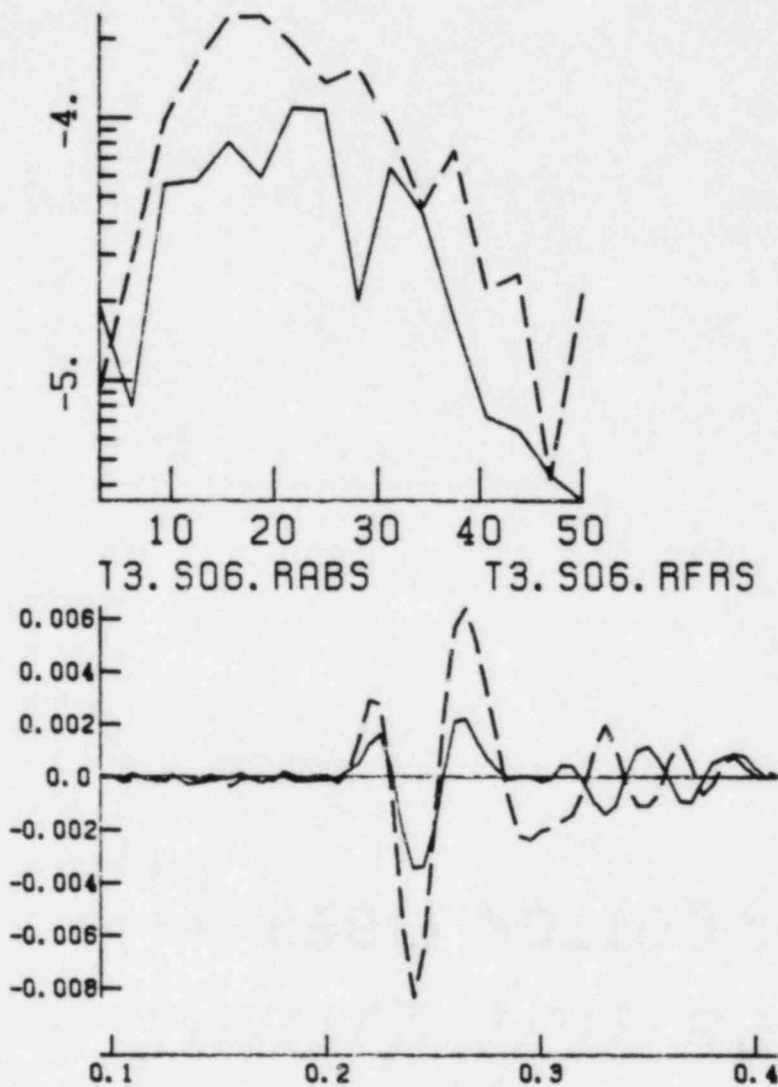
Figure VI.C.1 Seismic traces and Fourier amplitude spectra for Test 3, Shot 2, vertical component P-wave at sites AB (solid) and FR (dashed).



PLOT NO 2. RUN NO 255.

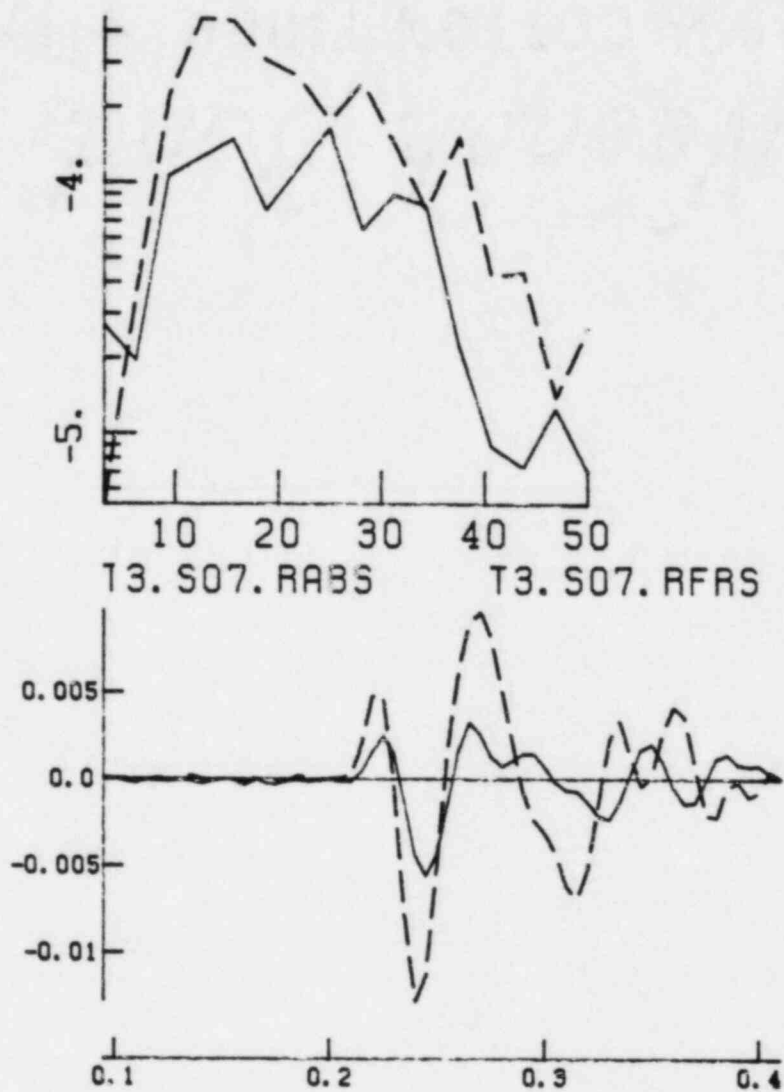
Figure VI.C.2

Seismic traces and Fourier amplitude spectra for Test 3, Shot 3, vertical component P-wave at sites AB (solid) and FR (dashed).



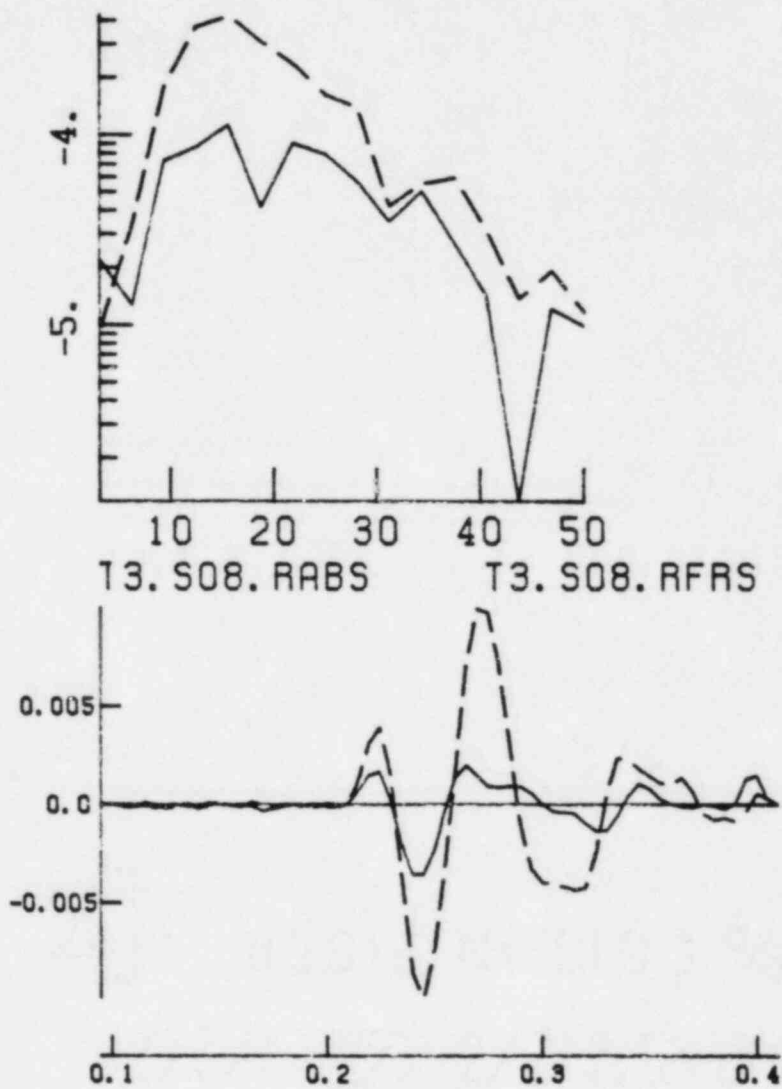
PLOT NO 3. RUN NO 255.

Figure VI.C.3 Seismic traces and Fourier amplitude spectra for Test 3, Shot 6, vertical component P-wave at sites AB (solid) and FR (dashed).



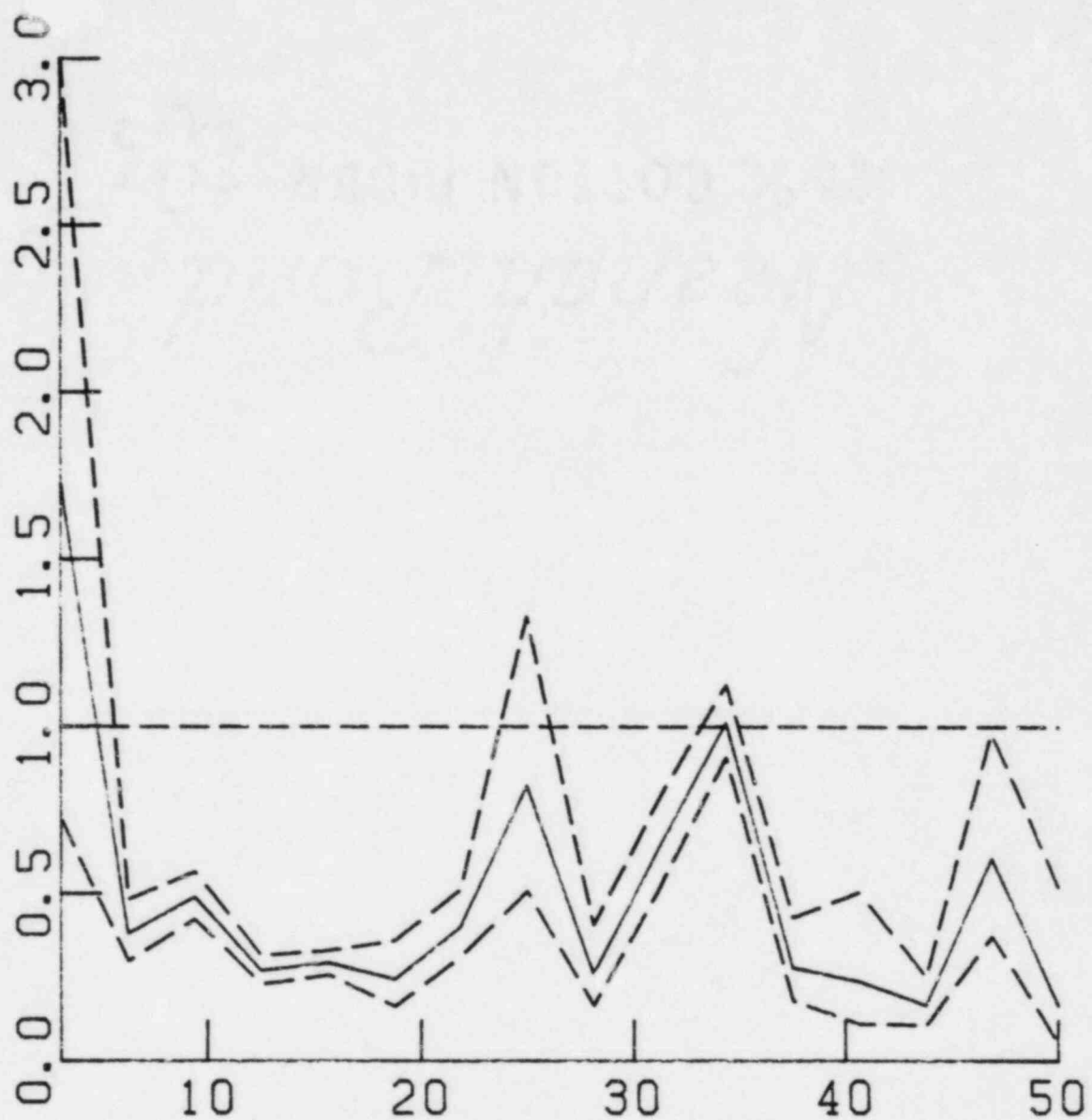
PLOT NO 4. RUN NO 255.

Figure VI.C.4 Seismic traces and Fourier amplitude spectra for Test 3, Shot 7, vertical component P-wave at sites AB (solid) and FR (dashed).



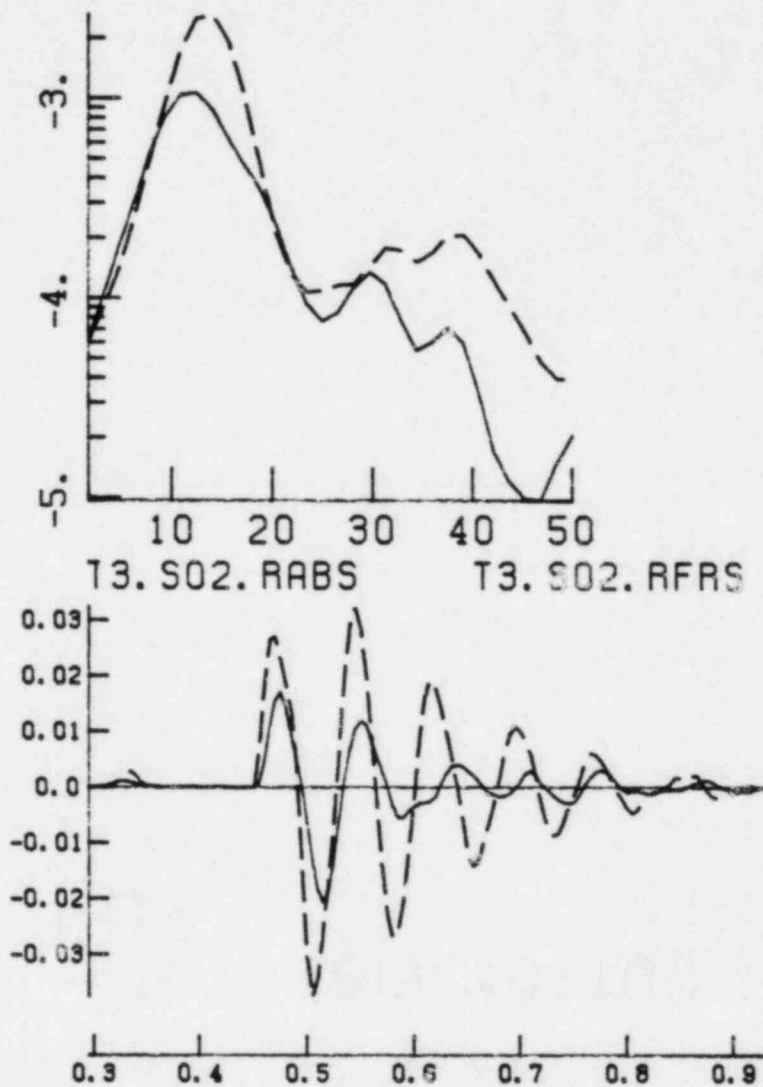
PLOT NO 5. RUN NO 255.

Figure VI.C.5 Seismic traces and Fourier amplitude spectra for Test 3, Shot 8, vertical component of P-wave at sites AB (solid) and FR (dashed).



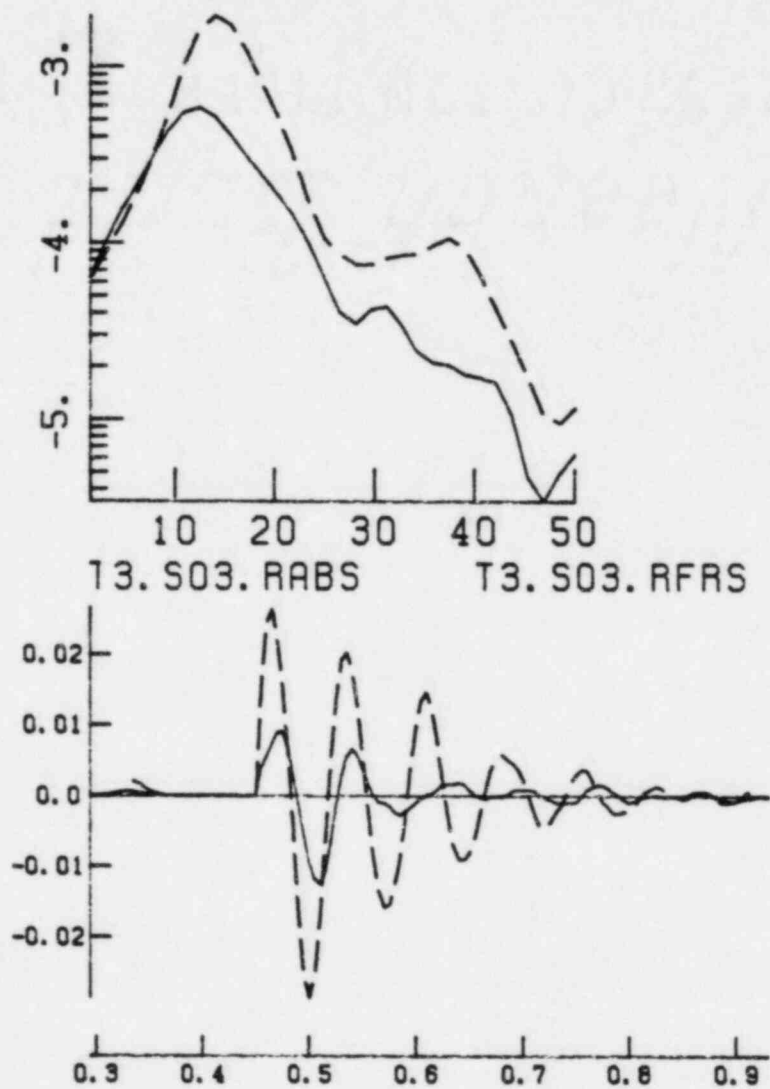
AB/FR TEST 3 SHOTS 2, 3, 6, 7, 8 Z P ONLY
 RATIOS FROM MODULI IN GROUPS OF 1
 RUN NO 255.
 POWER SPECTRAL NOISE SUBTRACTED

Figure VI.C.6 P-wave spectral ratio computed for AB and FR sites with five trials.



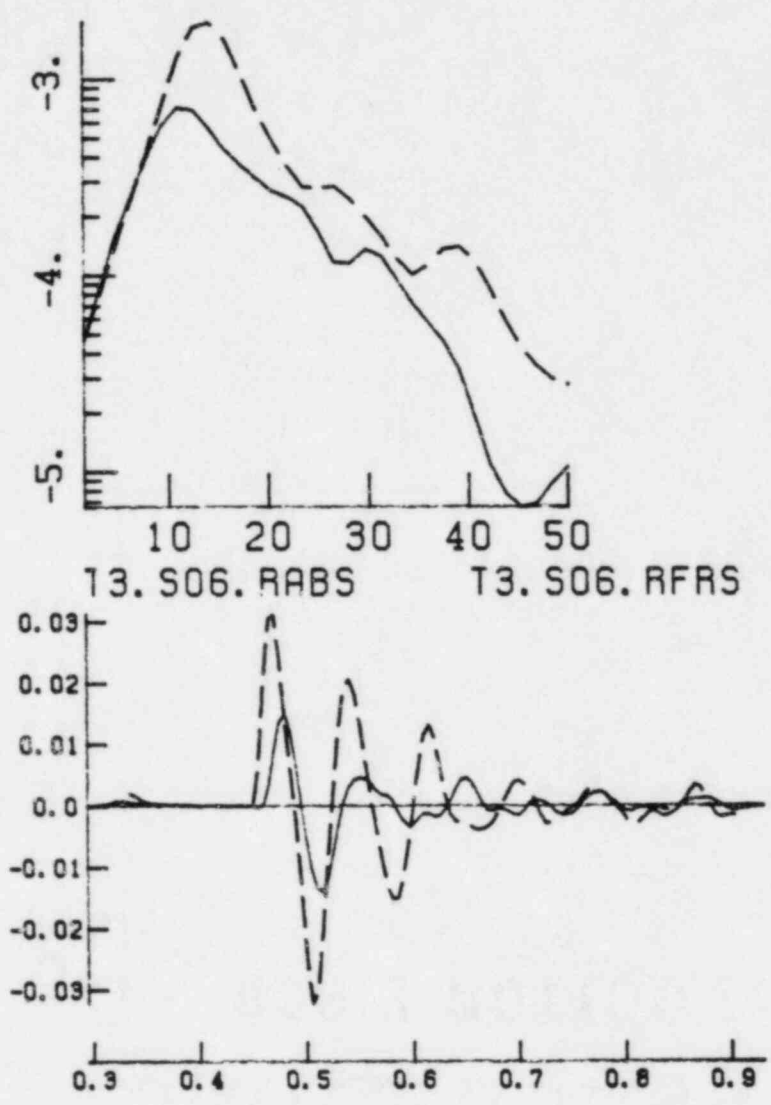
PLOT NO 1. RUN NO 256.

Figure VI.C.7 Seismic traces and Fourier amplitude spectra for Test 3, Shot 2, vertical component SV group at sites AB (solid) and FR (dashed).



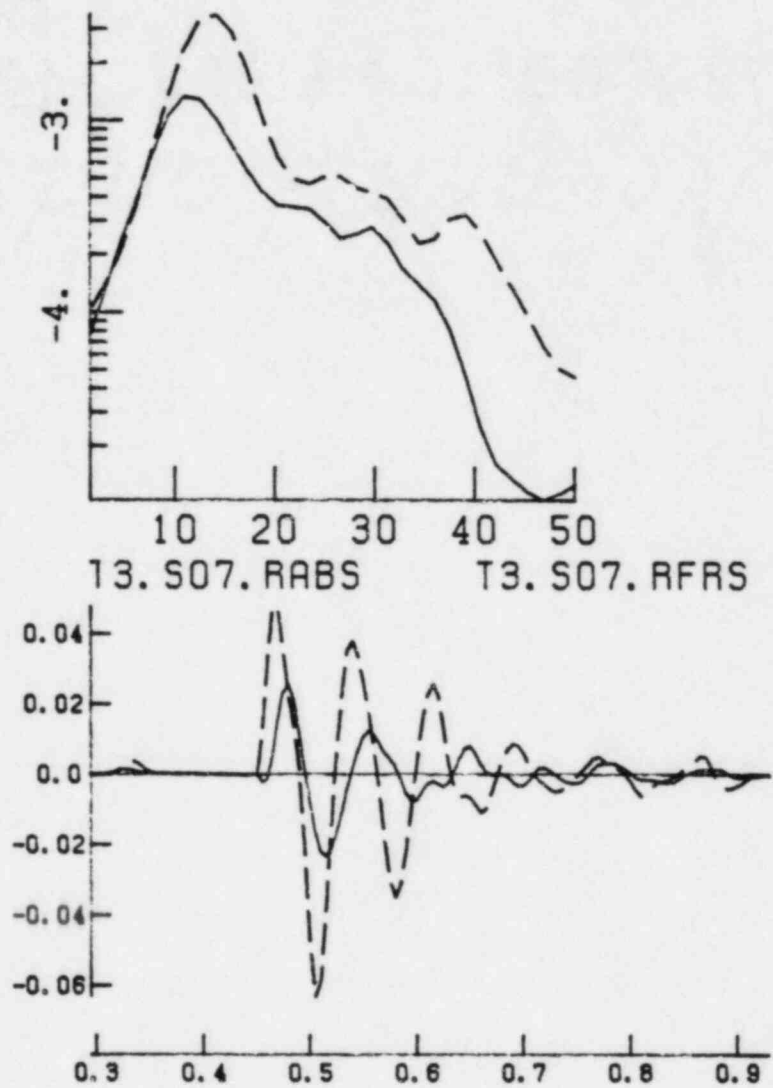
PLOT NO 2. RUN NO 256.

Figure VI.C.8 Seismic traces and Fourier amplitude spectra for Test 3, Shot 3, vertical component SV group at sites AB (solid) and FR (dashed).



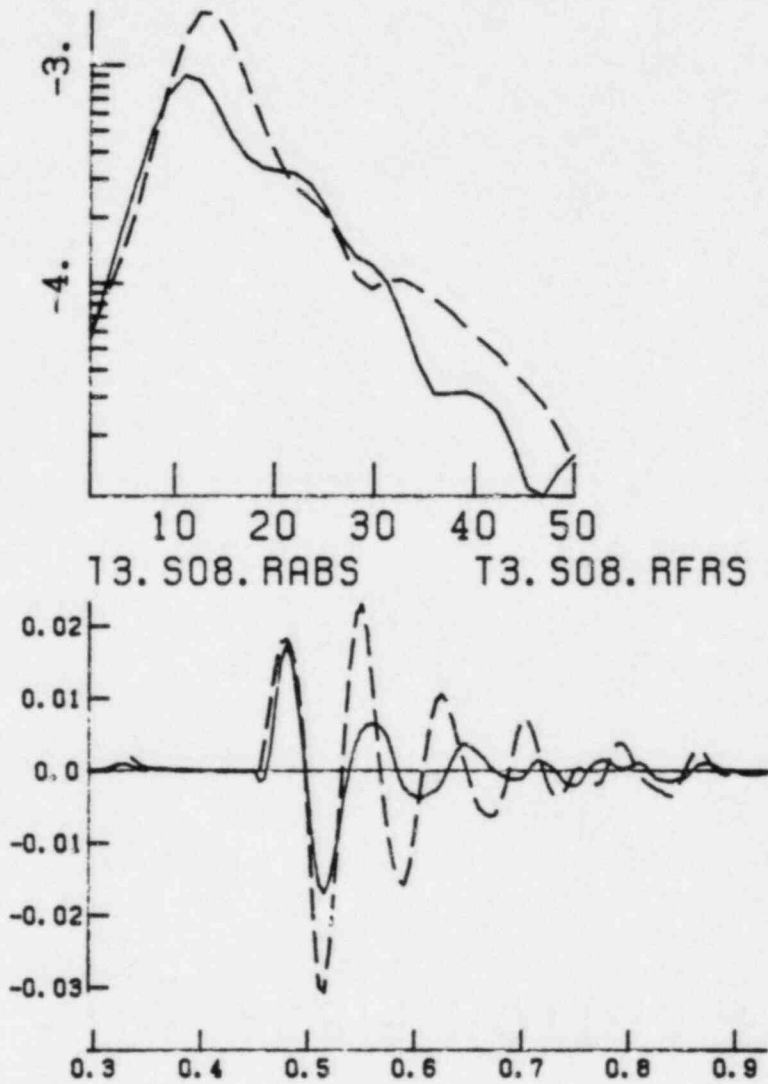
PLOT NO 3. RUN NO 256.

Figure VI.C.9 Seismic traces and Fourier amplitude spectra for Test 3, Shot 6, vertical component SV group at sites AB (solid) and FR (dashed).



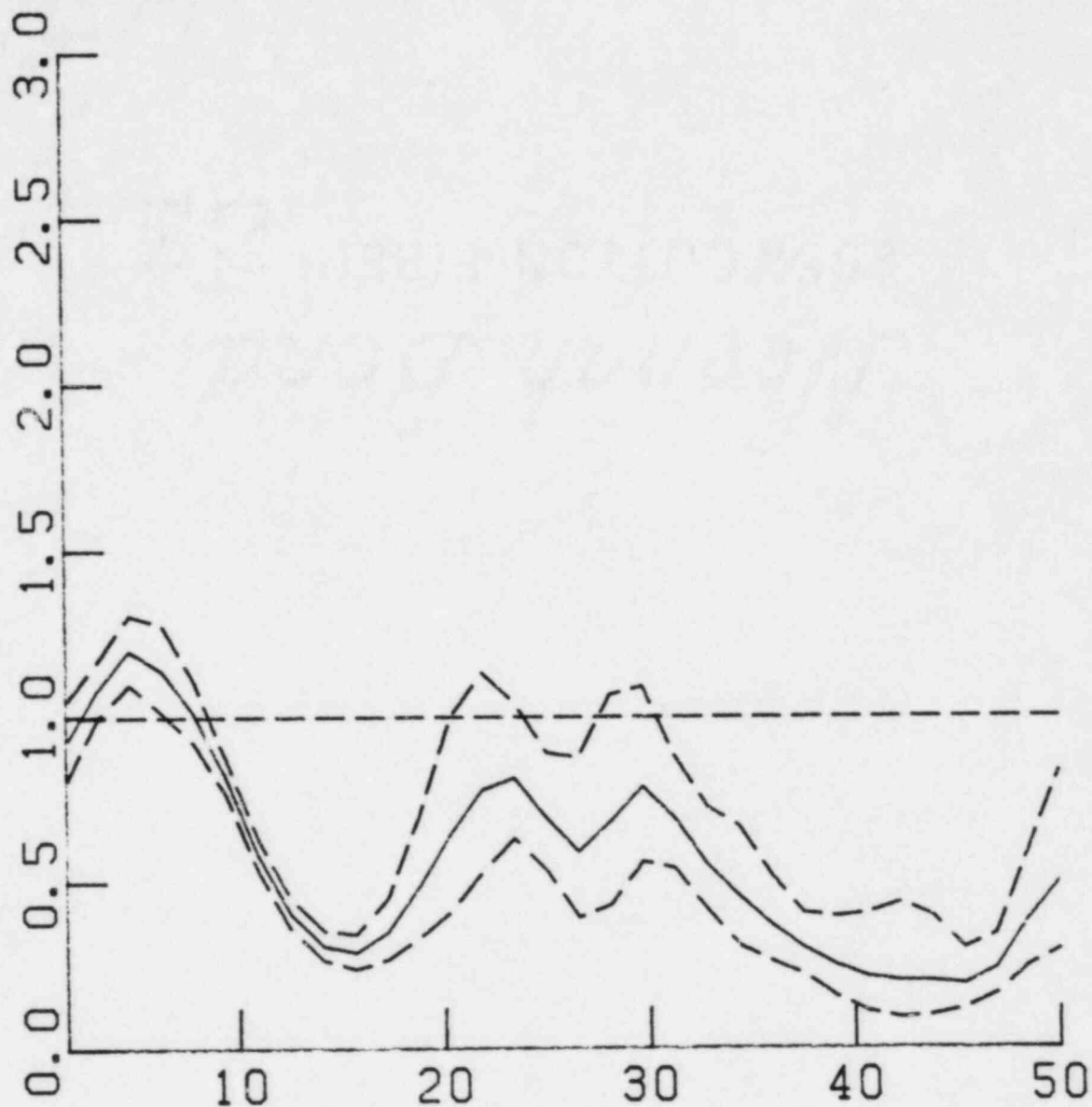
PLOT NO 4. RUN NO 256.

Figure VI.C.10 Seismic traces and Fourier amplitude spectra for Test 3, Shot 7, vertical component SV group at sites AB (solid) and FR (dashed)



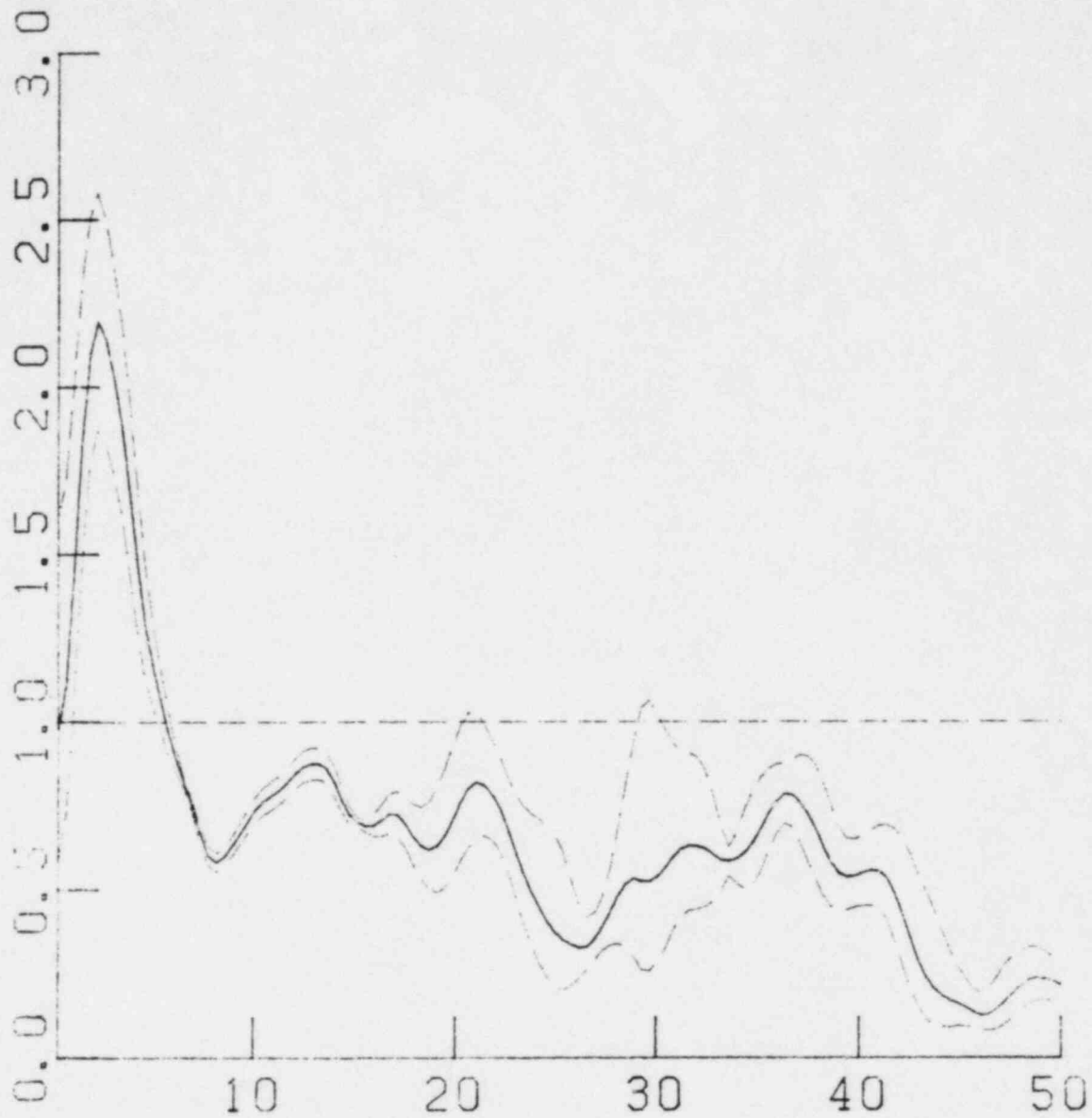
PLOT NO 5. RUN NO 256.

Figure VI.C.11 Seismic traces and Fourier amplitude spectra for Test 3, Shot 8, vertical component SV group at sites AB (solid) and FR (dashed).



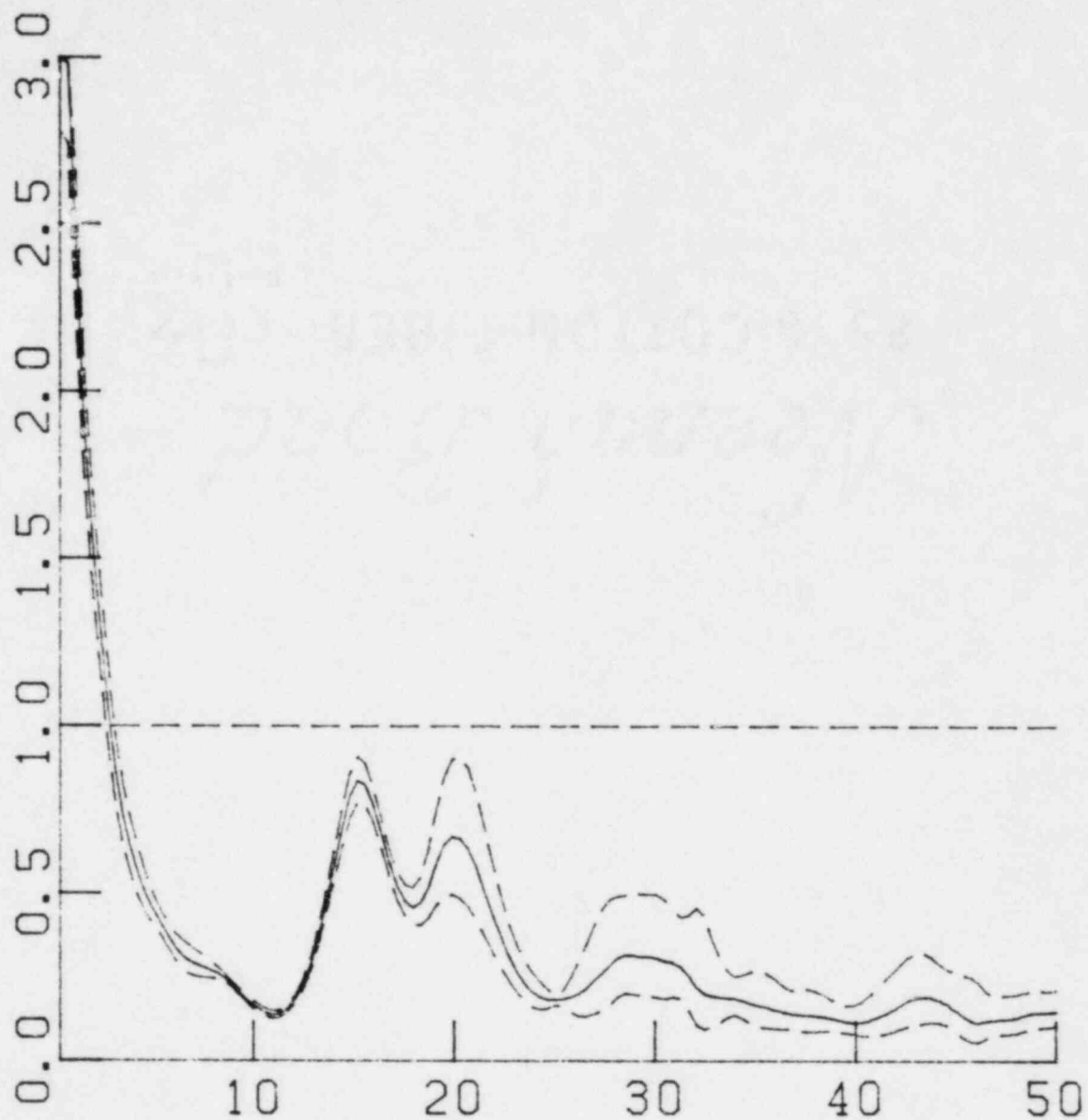
AB/FR TEST 3 SHOTS 2, 3, 6, 7, 8 Z P ONLY
 RATIOS FROM MODULI IN GROUPS OF 1
 RUN NO 256.
 POWER SPECTRAL NOISE SUBTRACTED

Figure VI.C.12 SV-wave spectral ratio computed for AB and FR sites with 5 trials.



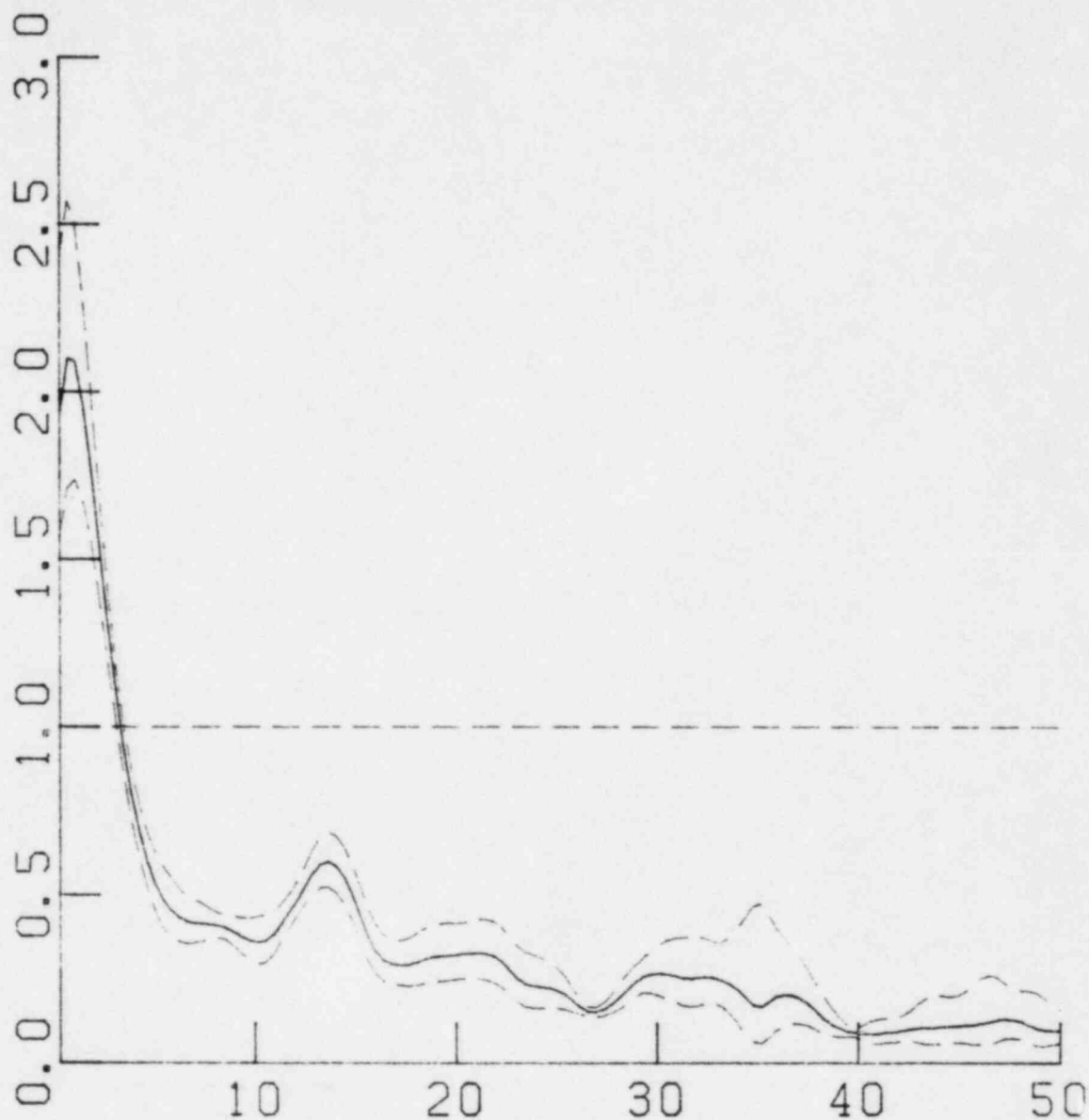
TEST 3, WP/FF, SHOTS 2,3,6,7,8, VERTICAL
 RATIOS FROM MODULI IN GROUPS OF 5.
 RUN NO 217.
 POWER SPECTRAL NOISE SUBTRACTED

Figure VI.C.13 Service Water Pumphouse/Free field spectral modulus ratio, vertical component, Test 3.



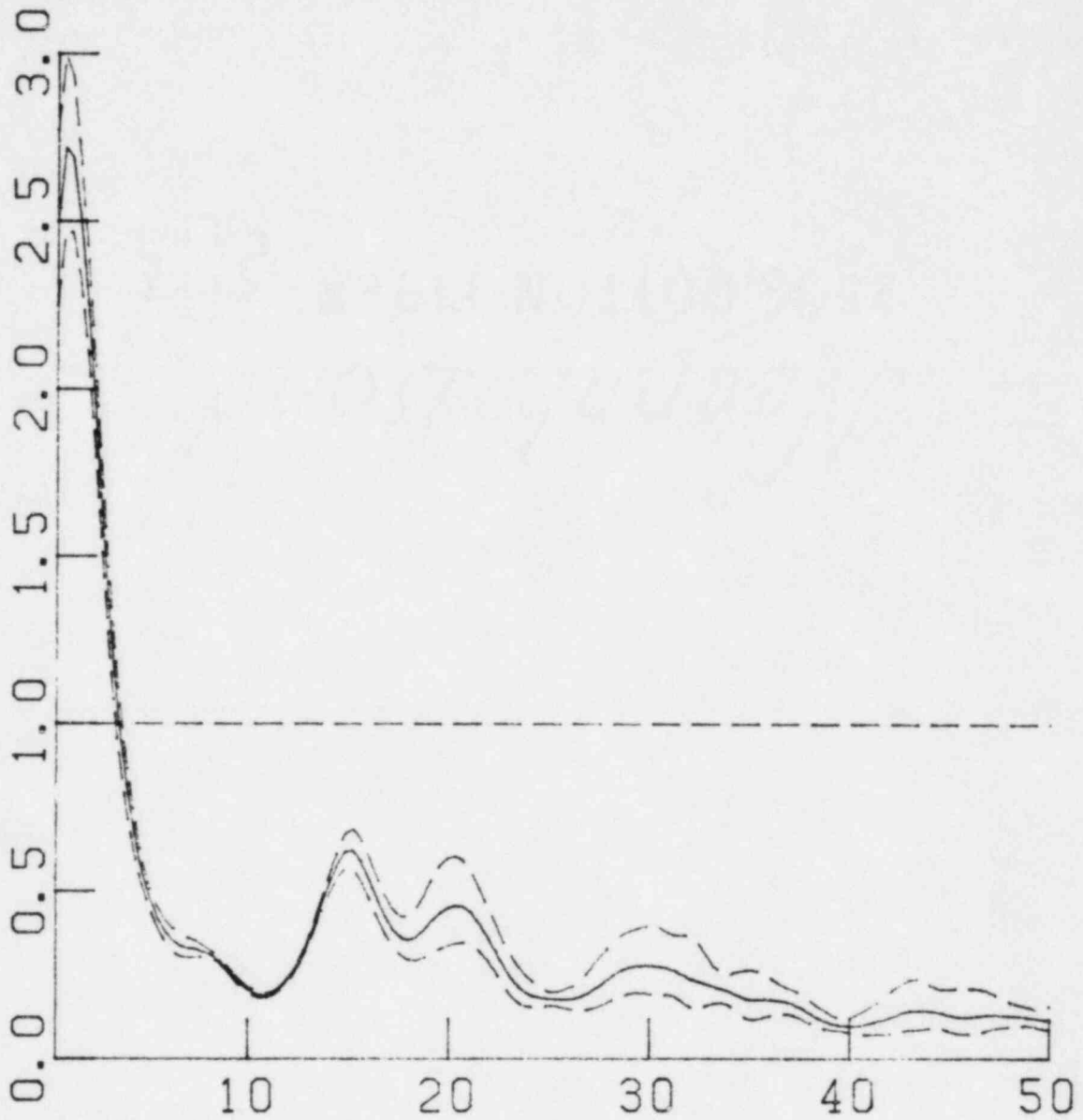
TEST 3, WP/FF, SHOTS 2, 3, 6, 7, 8, RADIAL
 RATIOS FROM MODULI IN GROUPS OF 5.
 RUN NO 220.
 POWER SPECTRAL NOISE SUBTRACTED

Figure VI.C.14 Service Water Pumphouse/Free field spectral
 modulus ratio, radial component, Test 3.



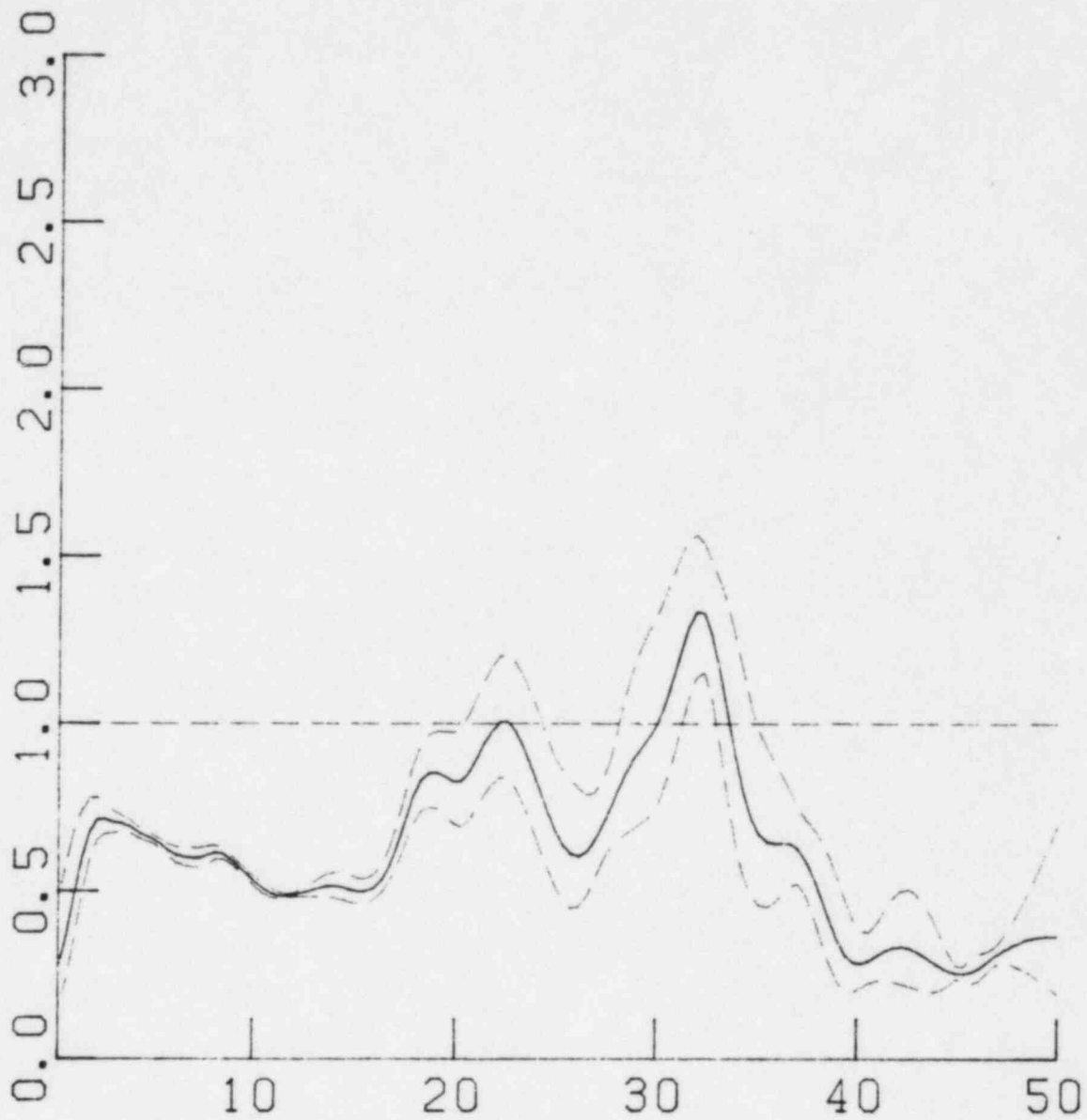
TEST3. WP/FF. SHOTS 2,3,6,7,8. TRANSVERSE
 RATIOS FROM MODULI IN GROUPS OF 4.
 RUN NO 214.
 POWER SPECTRAL NOISE SUBTRACTED

Figure VI.C.15 Service Water Pumphouse/Free field spectral
 modulus ratio, transverse component, Test 3.



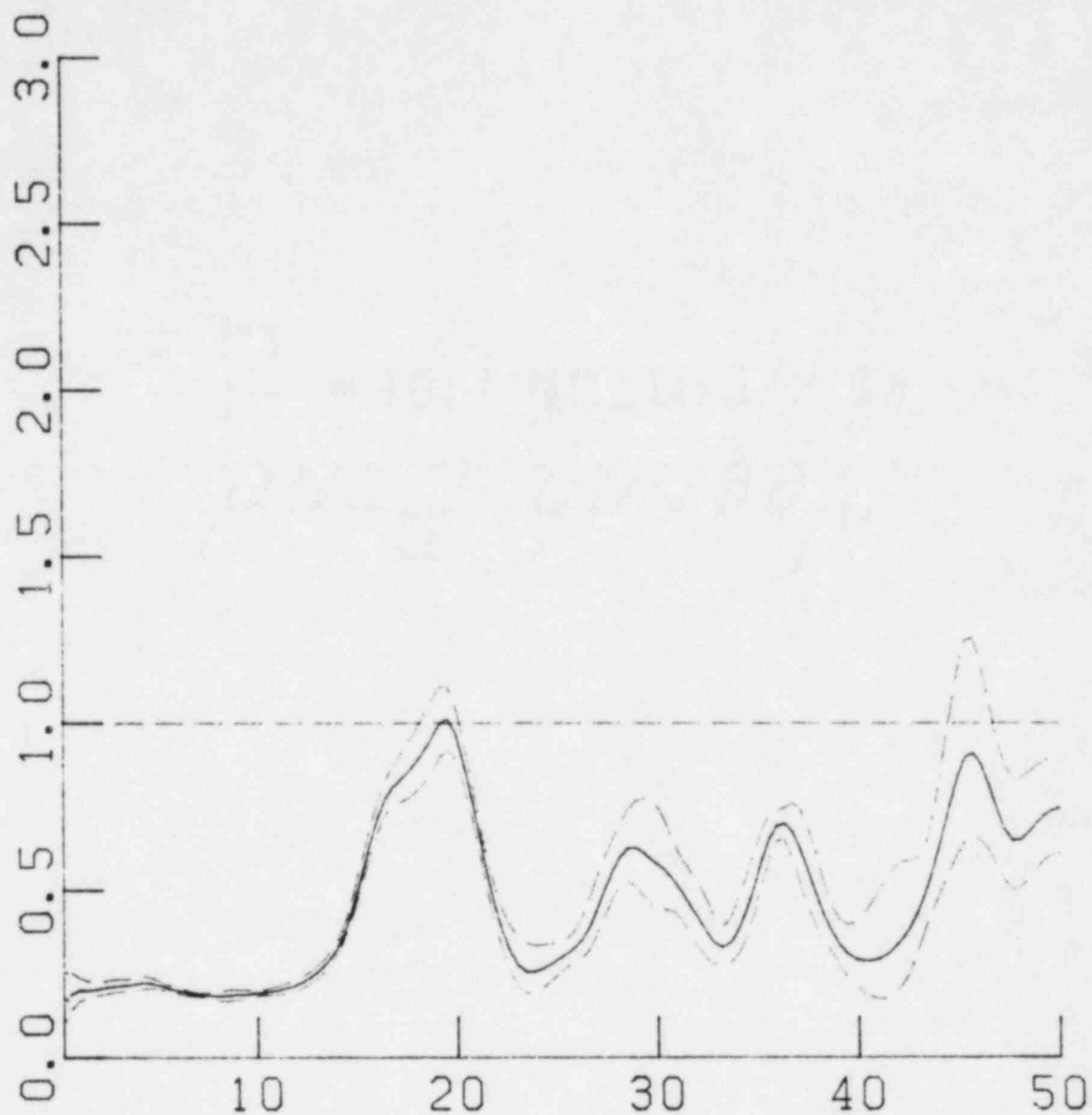
TEST 3, WP/FF, R, T COMB., GROUPED BY SHOT+CO
 RATIOS FROM MODULI IN GROUPS OF 8.
 RUN NO 225.
 POWER SPECTRAL NOISE SUBTRACTED

Figure VI.C.16 Service Water Pumpouse/Free field spectral modulus ratio, combined radial and transverse component, Test 3.



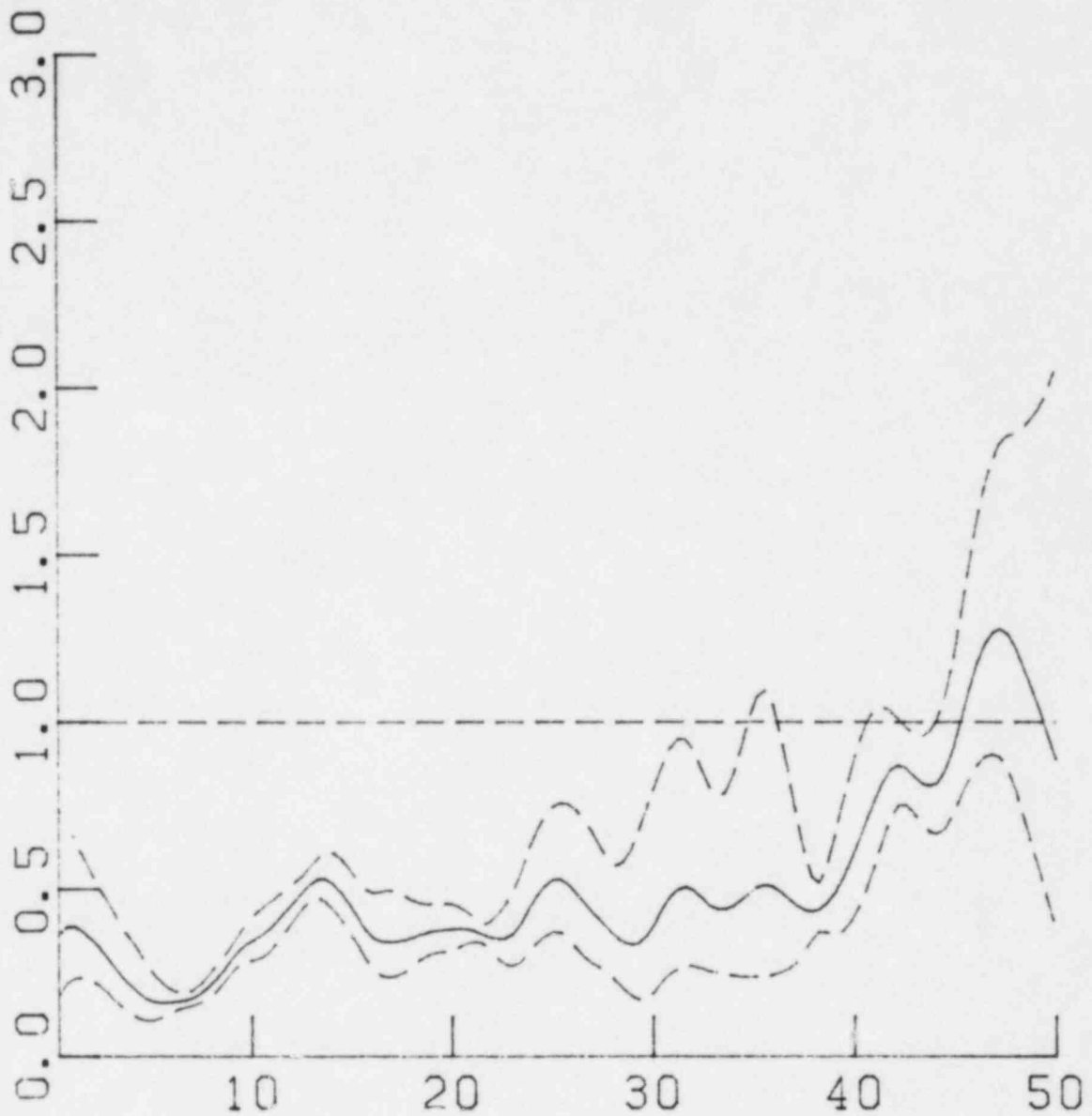
TEST 3, AB/FF, SHOTS 2, 3, 6, 7, 8, VERTICAL
 RATIOS FROM MODULI IN GROUPS OF 5.
 RUN NO 215.
 POWER SPECTRAL NOISE SUBTRACTED

Figure VI.C.17 Auxiliary Building/Free field spectral modulus ratio, vertical component, Test 3.



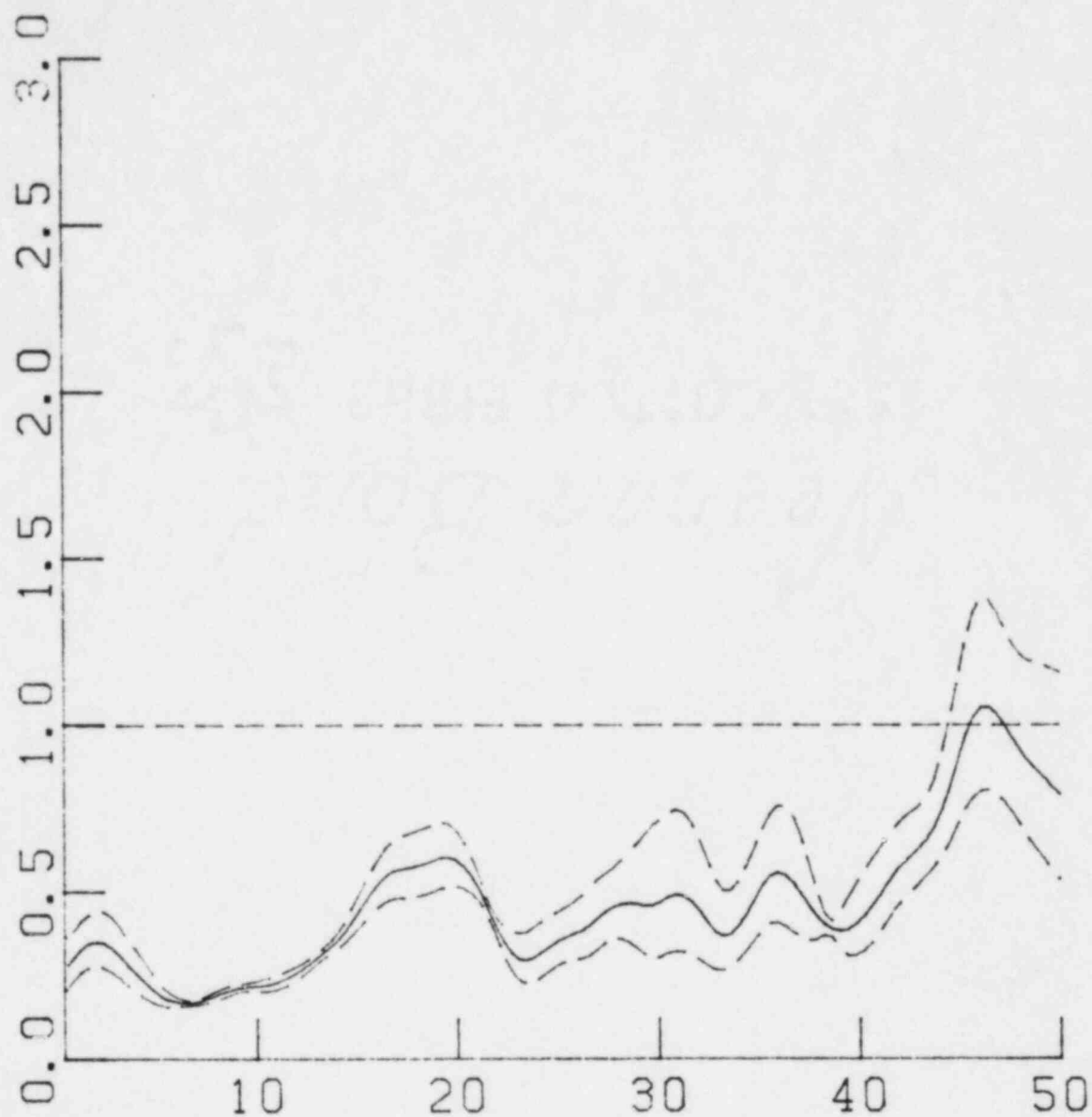
TEST 3. AB/FF. SHOTS 2,3,6,7,8. RADIAL
RATIOS FROM MODULI IN GROUPS OF 5.
RUN NO 218.
POWER SPECTRAL NOISE SUBTRACTED

Figure VI.C.18 Auxiliary Building/Free field spectral modulus ratio, radial component, Test 3.



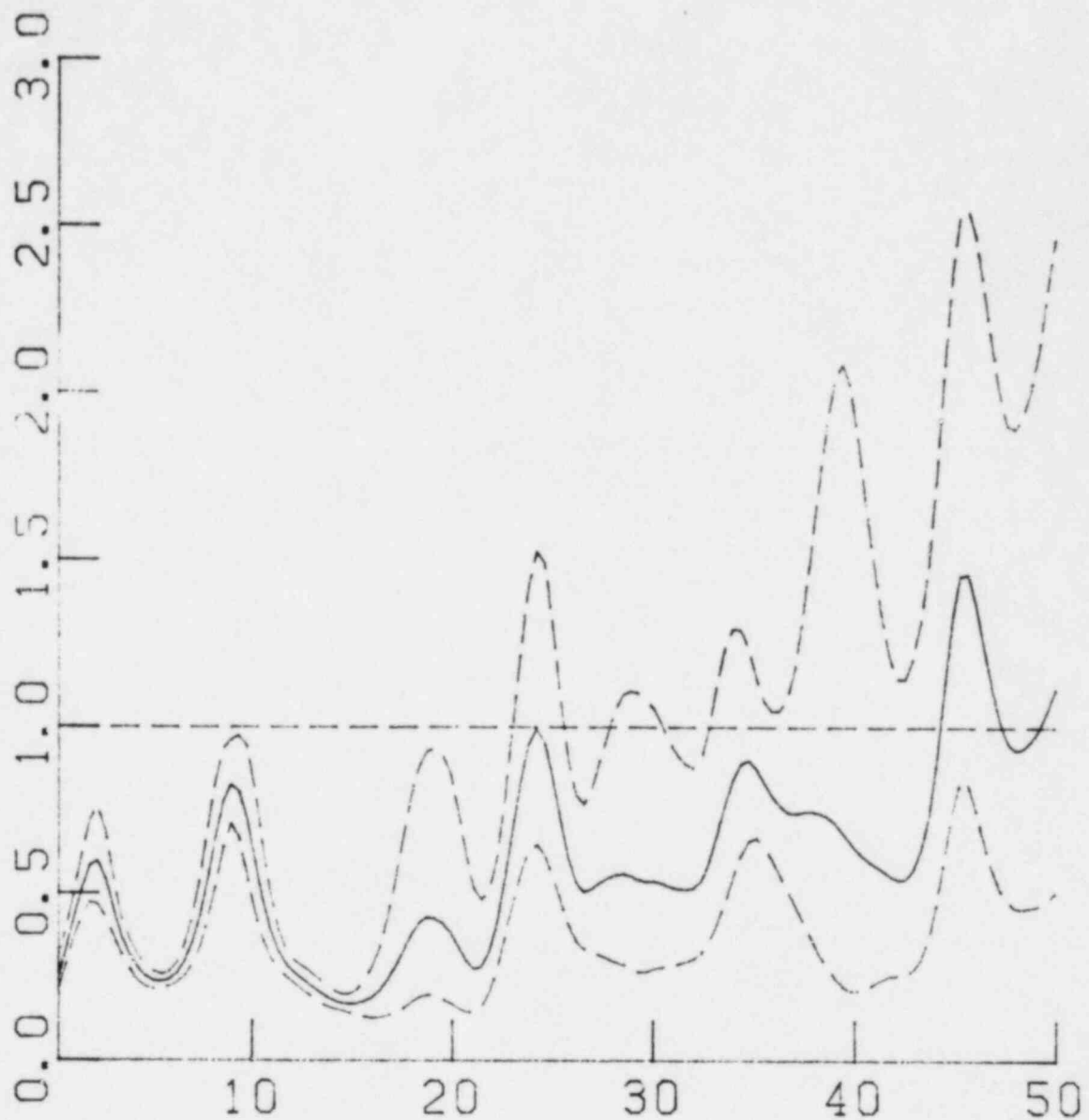
TEST3, AB/FF, SHOTS 2,3,6,7,8, TRANSVERSE
 RATIOS FROM MODULI IN GROUPS OF 4.
 RUN NO 212.
 POWER SPECTRAL NOISE SUBTRACTED

Figure VI.C.19 Auxiliary Building/Free field spectral modulus ratio, transverse component, Test 3.



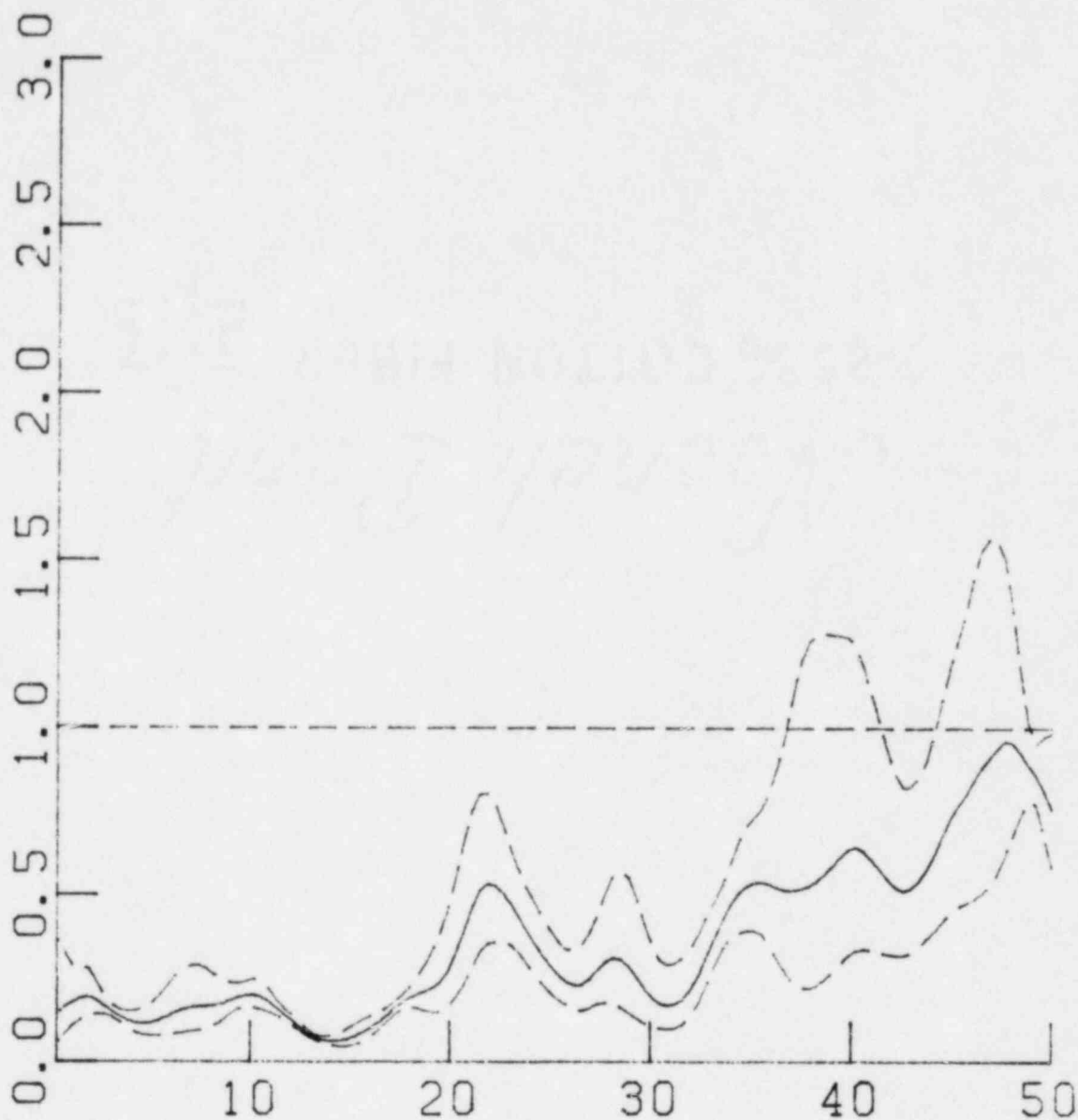
TEST 3, AB/FF, R, T COMB., GROUPED BY SHOT+CO
 RATIOS FROM MODULI IN GROUPS OF 8.
 RUN NO 223.
 POWER SPECTRAL NOISE SUBTRACTED

Figure VI.C.20 Auxiliary Building/Free field spectral modulus ratio, combined radial and transverse components, Test 3.



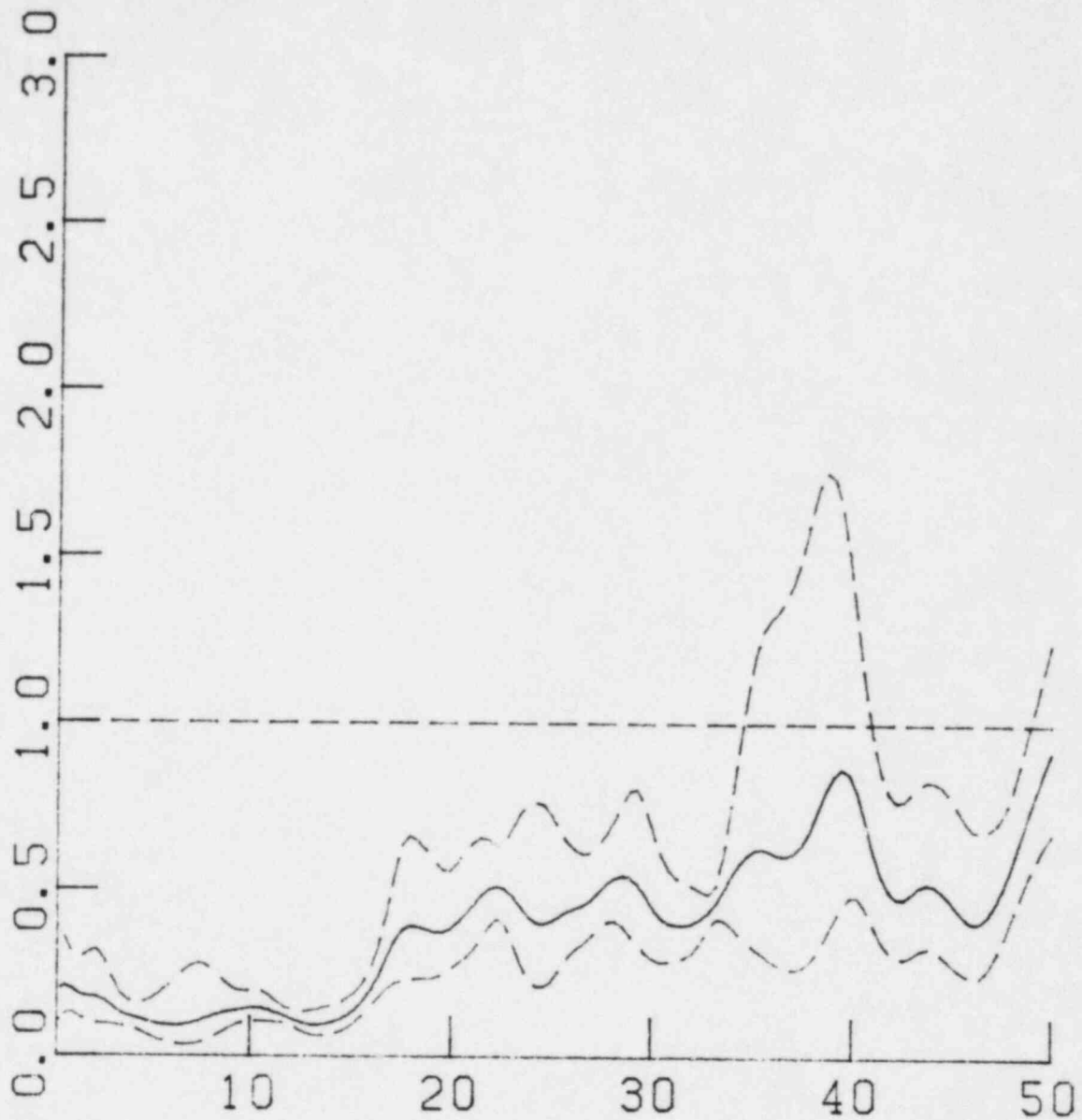
TEST 4 SHOTS 3, 4, 6, 7, 9 AB/<P3, F5> V
 RATIOS FROM MODULI INDIVIDUALLY
 RUN NO 226.
 POWER SPECTRAL NOISE SUBTRACTED

Figure VI.C.21 Auxiliary Building/Free field spectral modulus ratio, vertical component, Test 4.



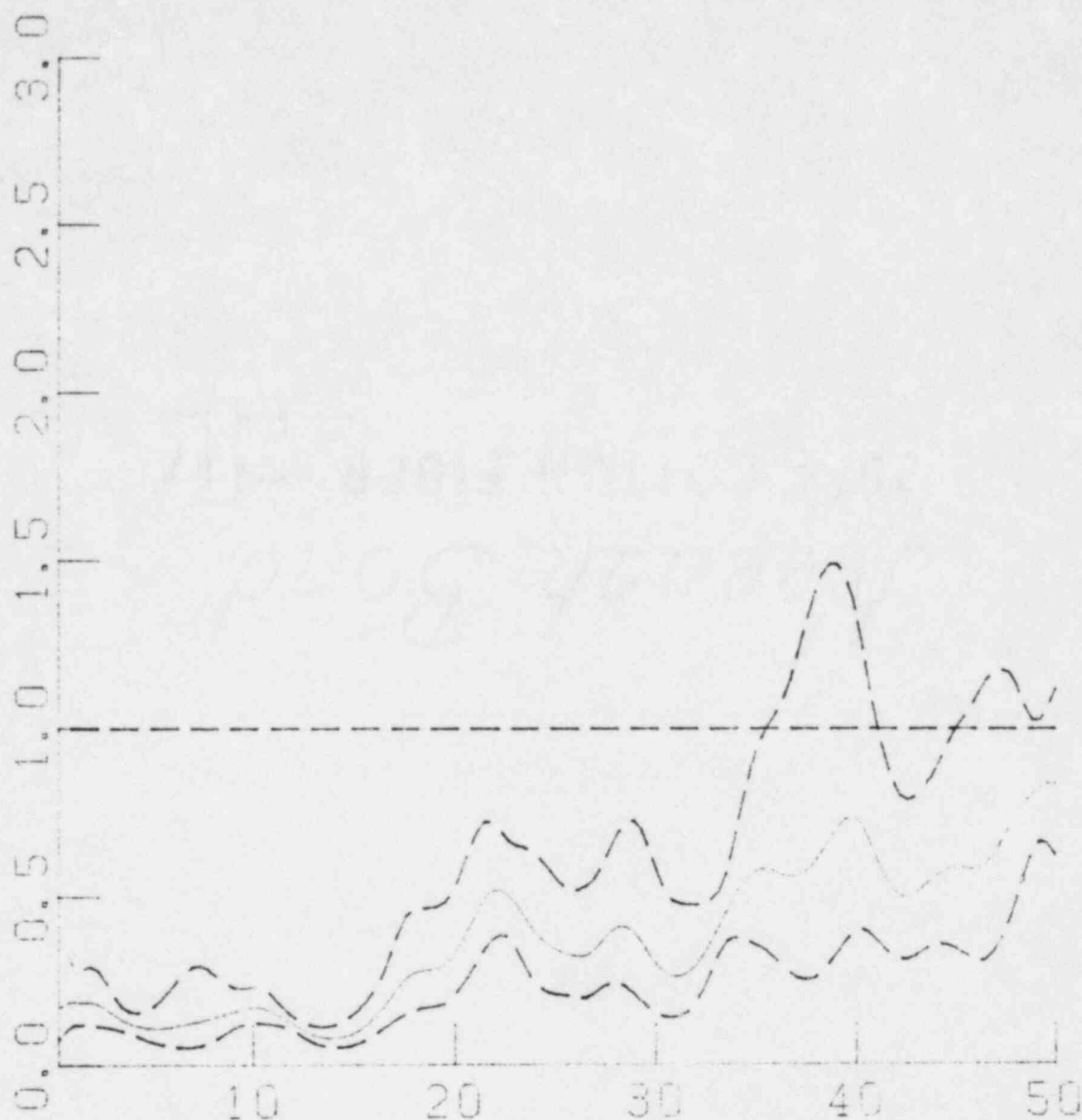
TEST 4 SHOTS 3, 4, 6, 7, 9 AB/<P3, F5> R
 RATIOS FROM MODULI INDIVIDUALLY
 RUN NO 227.
 POWER SPECTRAL NOISE SUBTRACTED

Figure VI.C.22 Auxiliary Building/Free field spectral modulus ratio, radial component, Test 4.



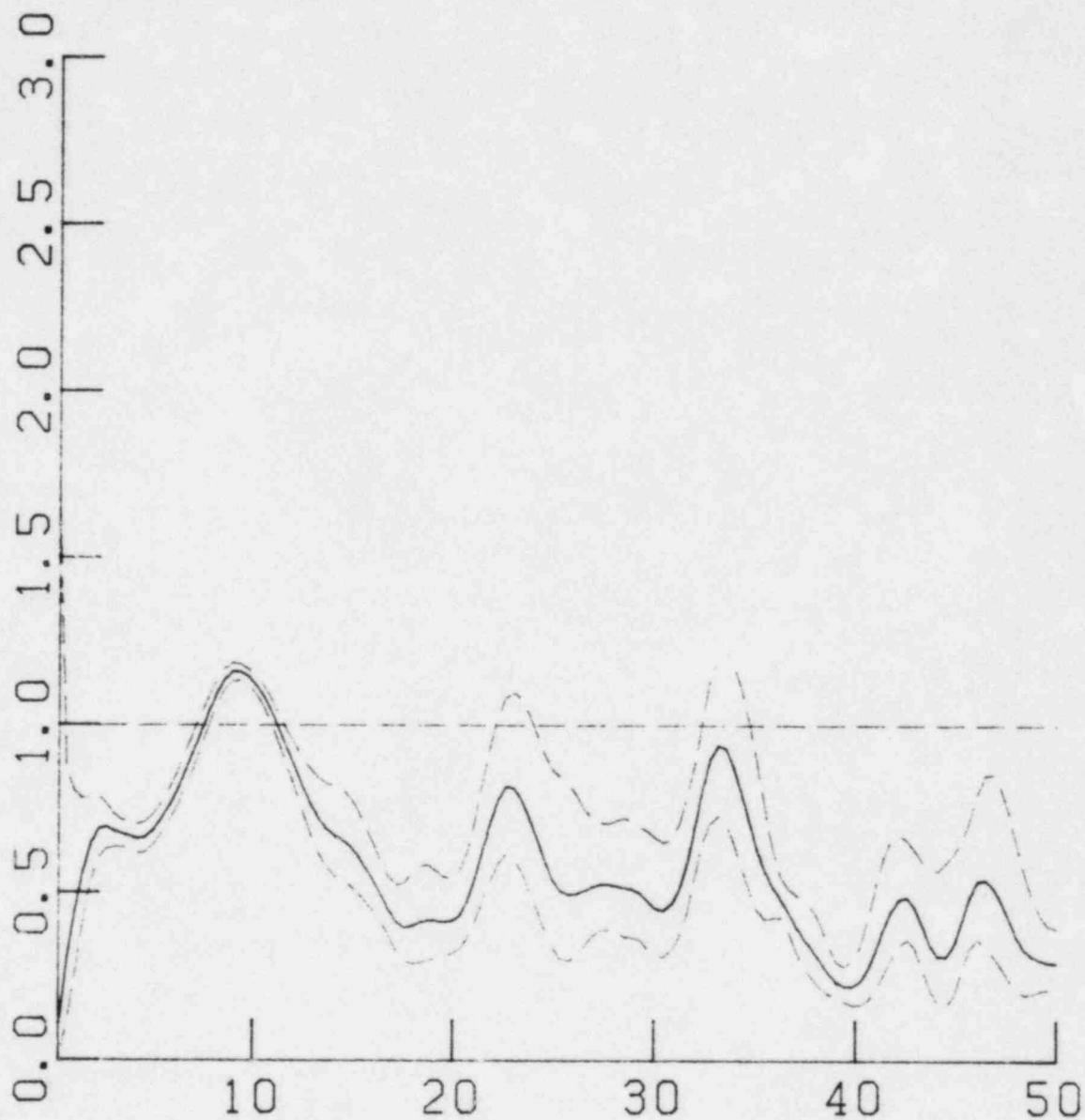
TEST 4 SHOTS 3, 4, 6, 7, 9 AB/<P3, F5> T
 RATIOS FROM MODULI INDIVIDUALLY
 RUN NO 228.
 POWER SPECTRAL NOISE SUBTRACTED

Figure VI.C.23 Auxiliary Building/Free field spectral modulus ratio, transverse component, Test 4.



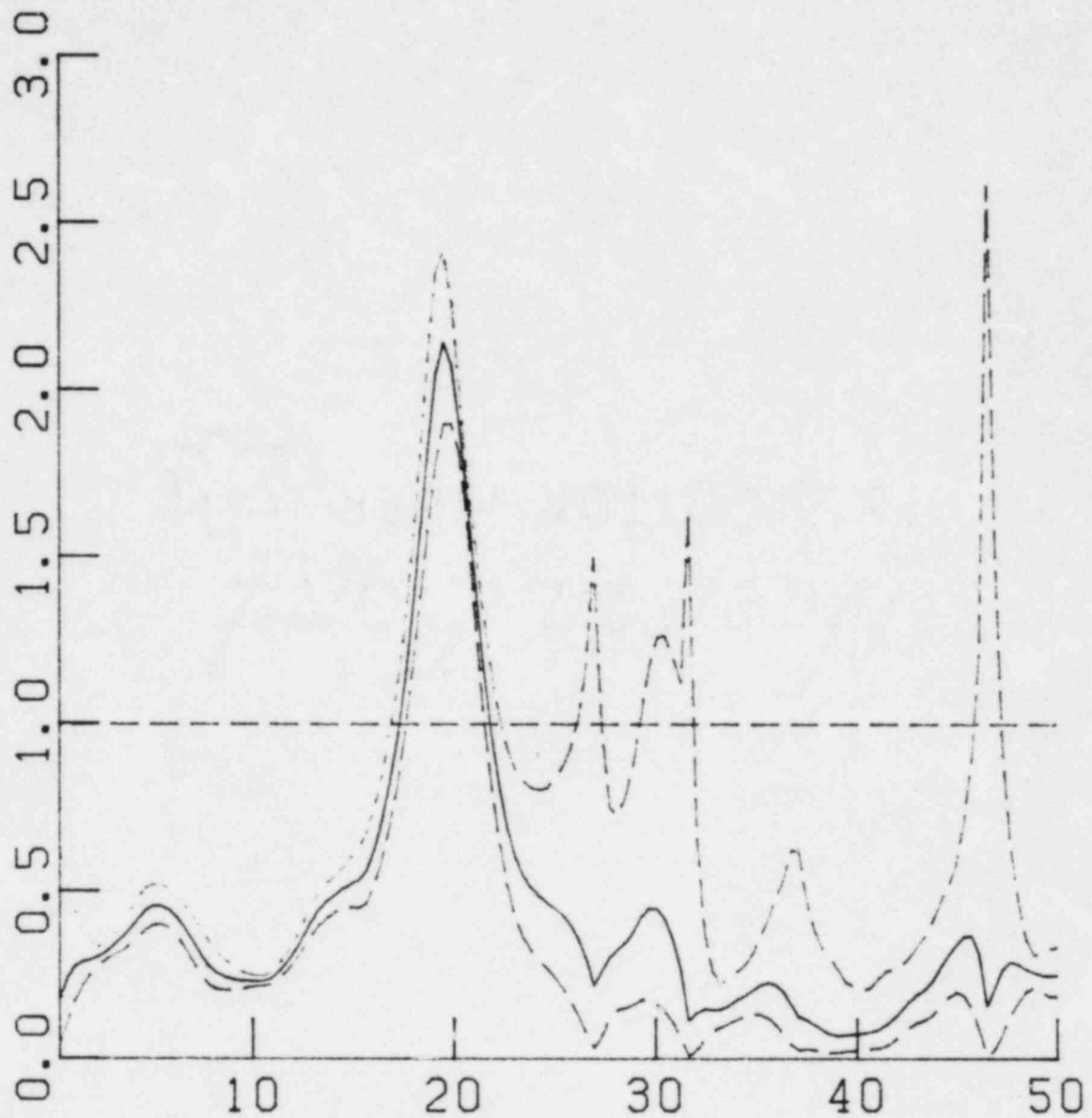
TEST 4 AB/<P3, F5> R, T COMB. NO GROUP.
 RATIOS FROM MODULI INDIVIDUALLY
 RUN NO 229.
 POWER SPECTRAL NOISE SUBTRACTED

Figure VI.C.24 Auxiliary Building/Free field spectral modulus ratio, combined radial and transverse components, Test 4.



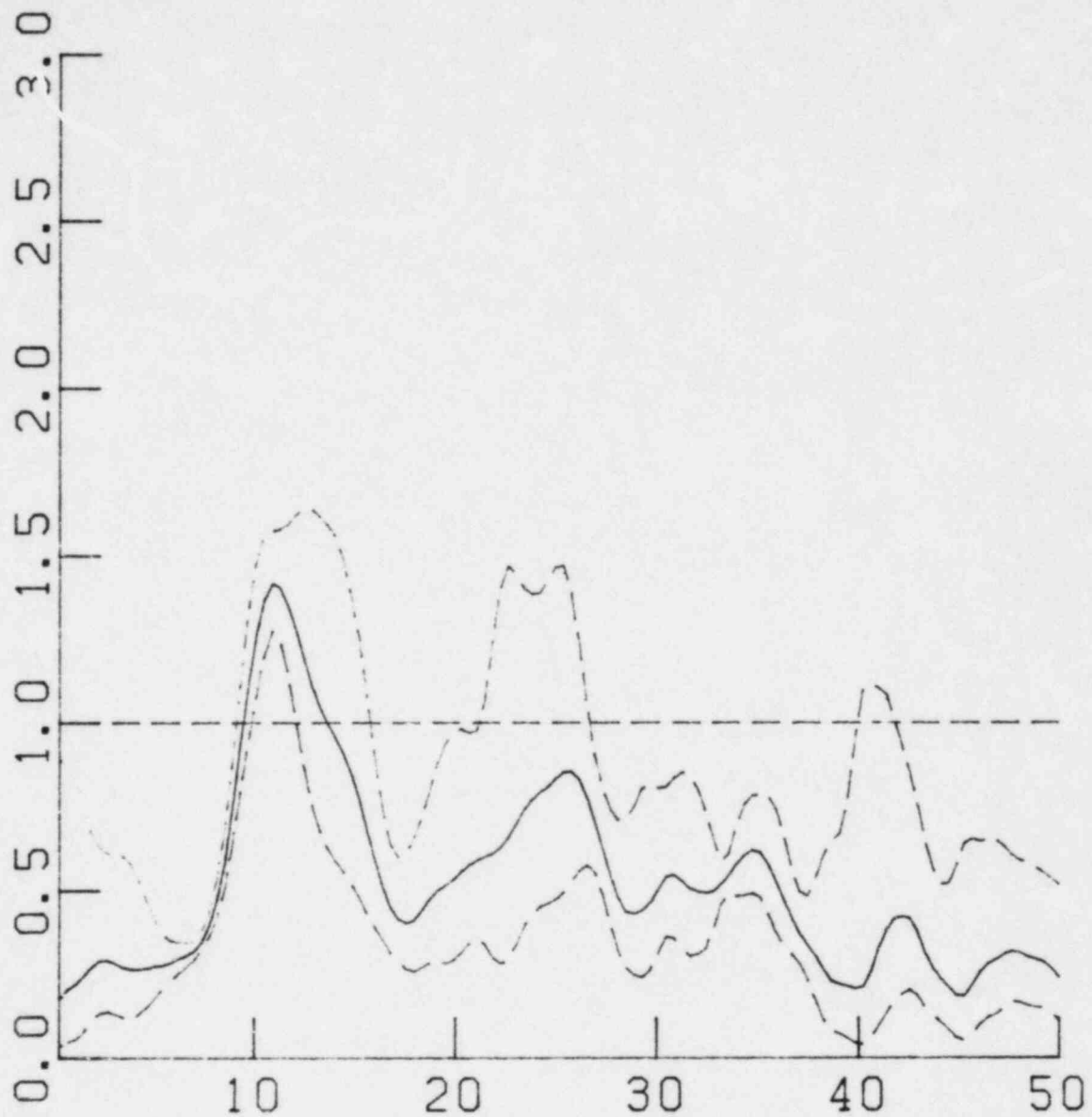
TEST3, GS/FF, SHOTS 2,3,6,7,8, VERTICAL
 RATIOS FROM MODULI IN GROUPS OF 5.
 RUN NO 216.
 POWER SPECTRAL NOISE SUBTRACTED

Figure VI.C.25 Diesel Generator Sump/Free field spectral modulus ratio, vertical component, Test 3.



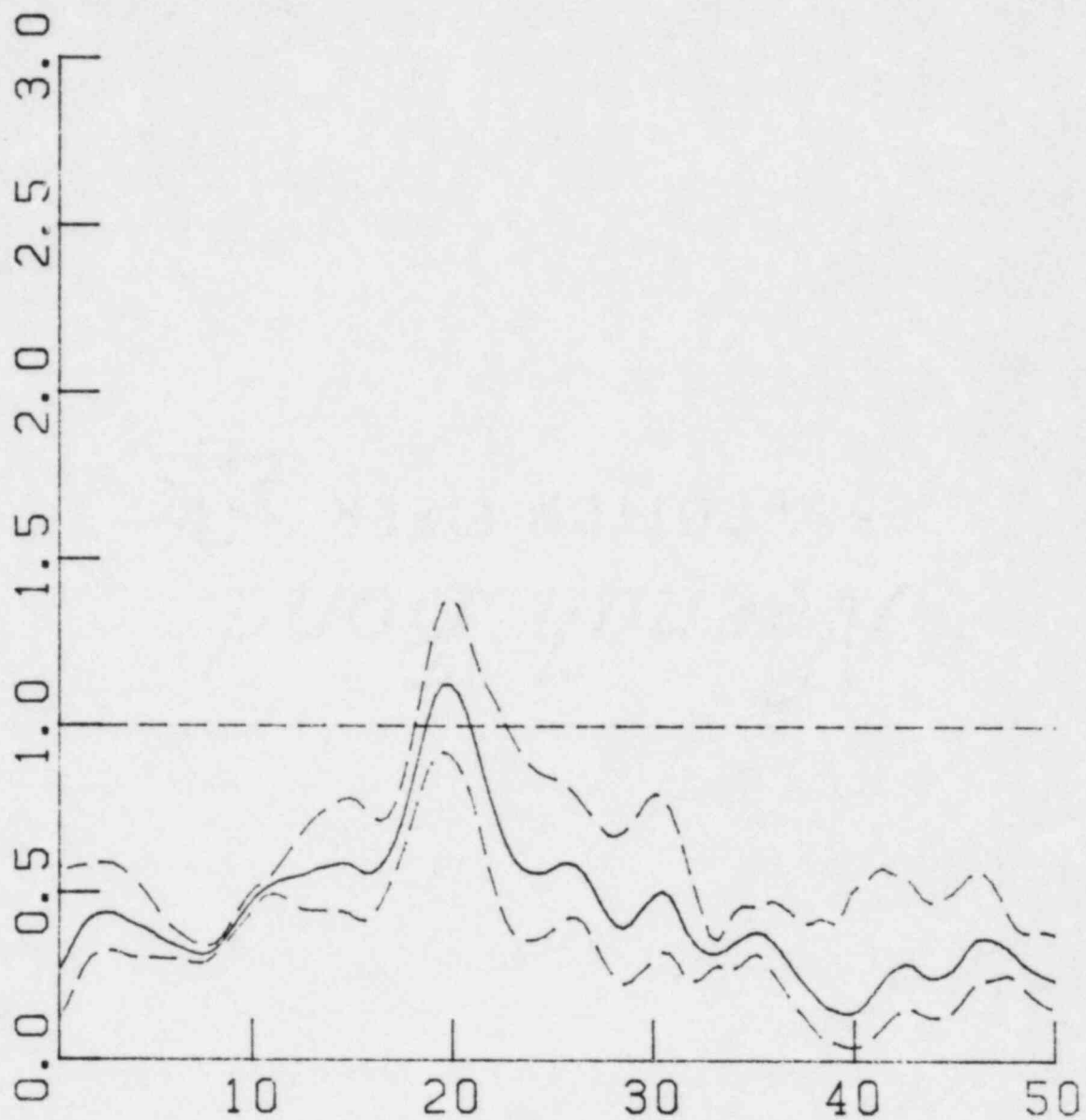
TEST 3, GS/FF, SHOTS 2,3,6,7,8, RADIAL
 RATIOS FROM MODULI IN GROUPS OF 5.
 RUN NO 219.
 POWER SPECTRAL NOISE SUBTRACTED

Figure VI.C.26 Diesel Generator Sump/Free field spectral
 modulus ratio, radial component, Test 3.



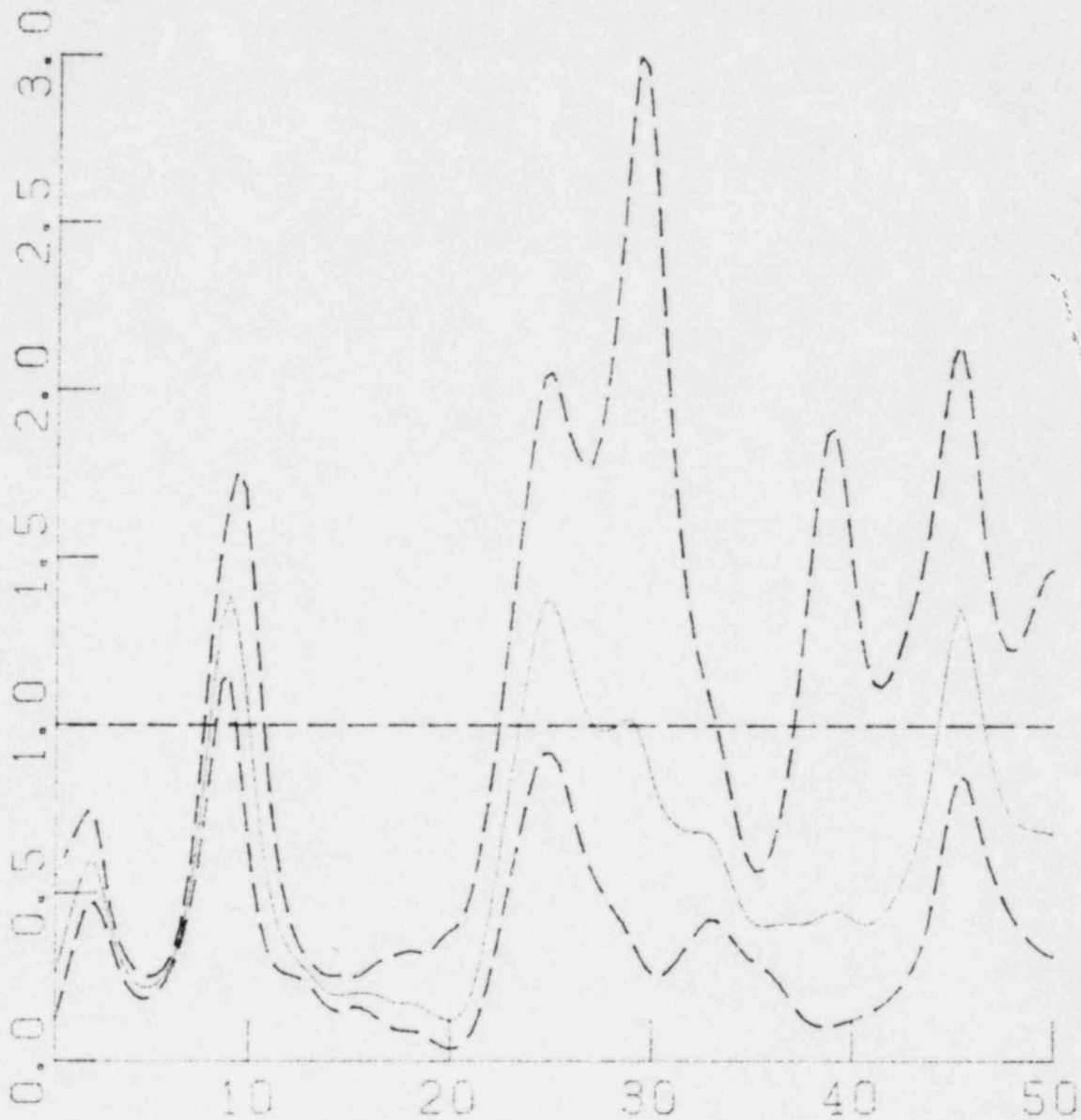
TEST3, GS/FF, SHOTS 2,3,6,7,8, TRANSVERSE
 RATIOS FROM MODULI IN GROUPS OF 4.
 RUN NO 213.
 POWER SPECTRAL NOISE SUBTRACTED

Figure VI.C.27 Diesel Generator Sump/Free field spectral
 modulus ratio, transverse component, Test 3.



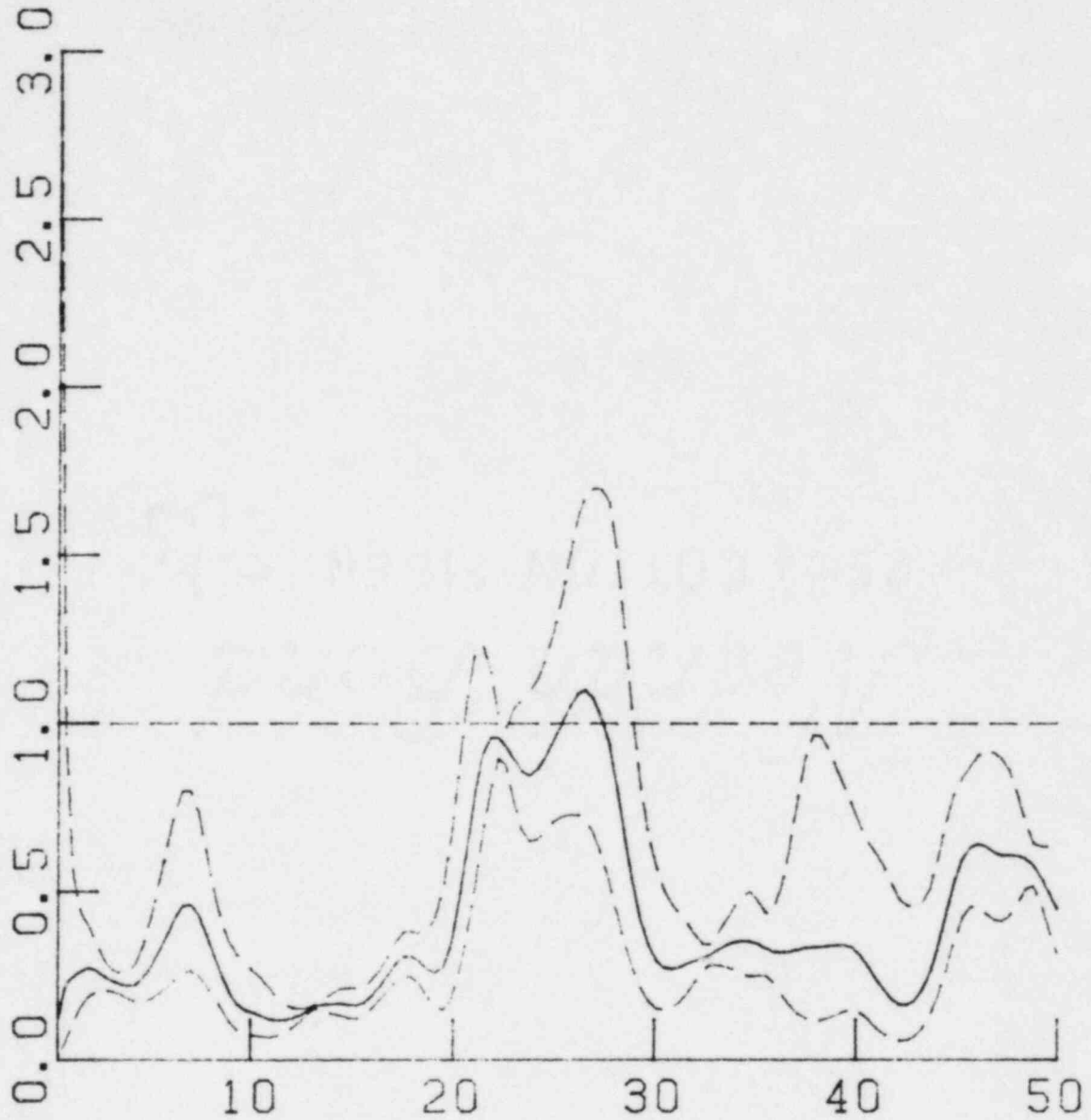
TEST 3, GS/FF, R, T COMB., GROUPED BY SHOT+CO
 RATIOS FROM MODULI IN GROUPS OF 8.
 RUN NO 224.
 POWER SPECTRAL NOISE SUBTRACTED

Figure VI.C.28 Diesel Generator Sump/Free field spectral modulus ratio, combined radial and transverse components, Test 3.



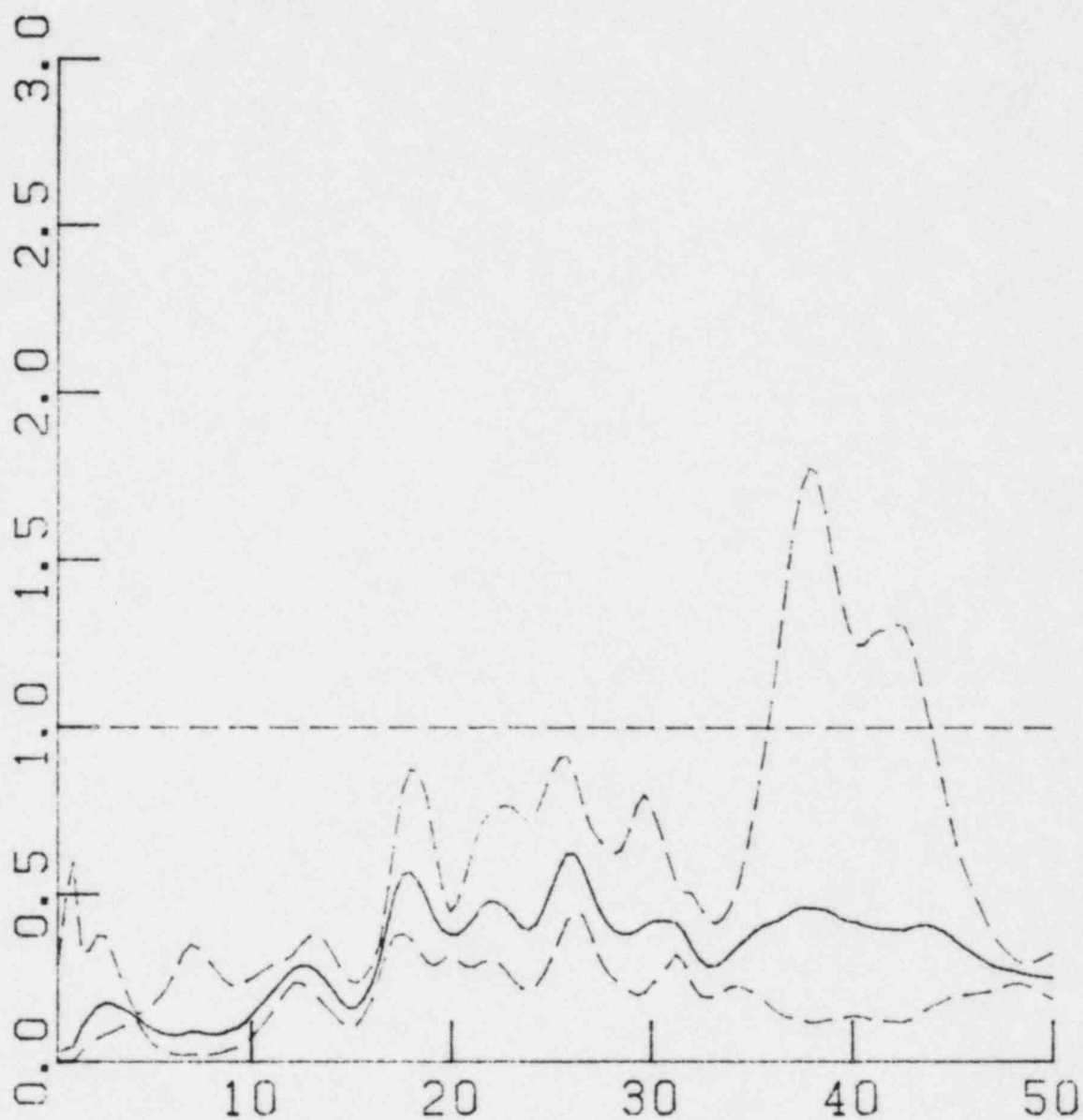
TEST 4 SHOTS: 3 GS/⟨PB, FE⟩ & 7.9 GS/FS V
 RATIOS FROM MODULI INDIVIDUALLY
 RUN NO 230.
 POWER SPECTRAL NOISE SUBTRACTED

Figure VI.C.29 Diesel Generator Sump/Free field spectral modulus ratio, vertical component, Test 4.



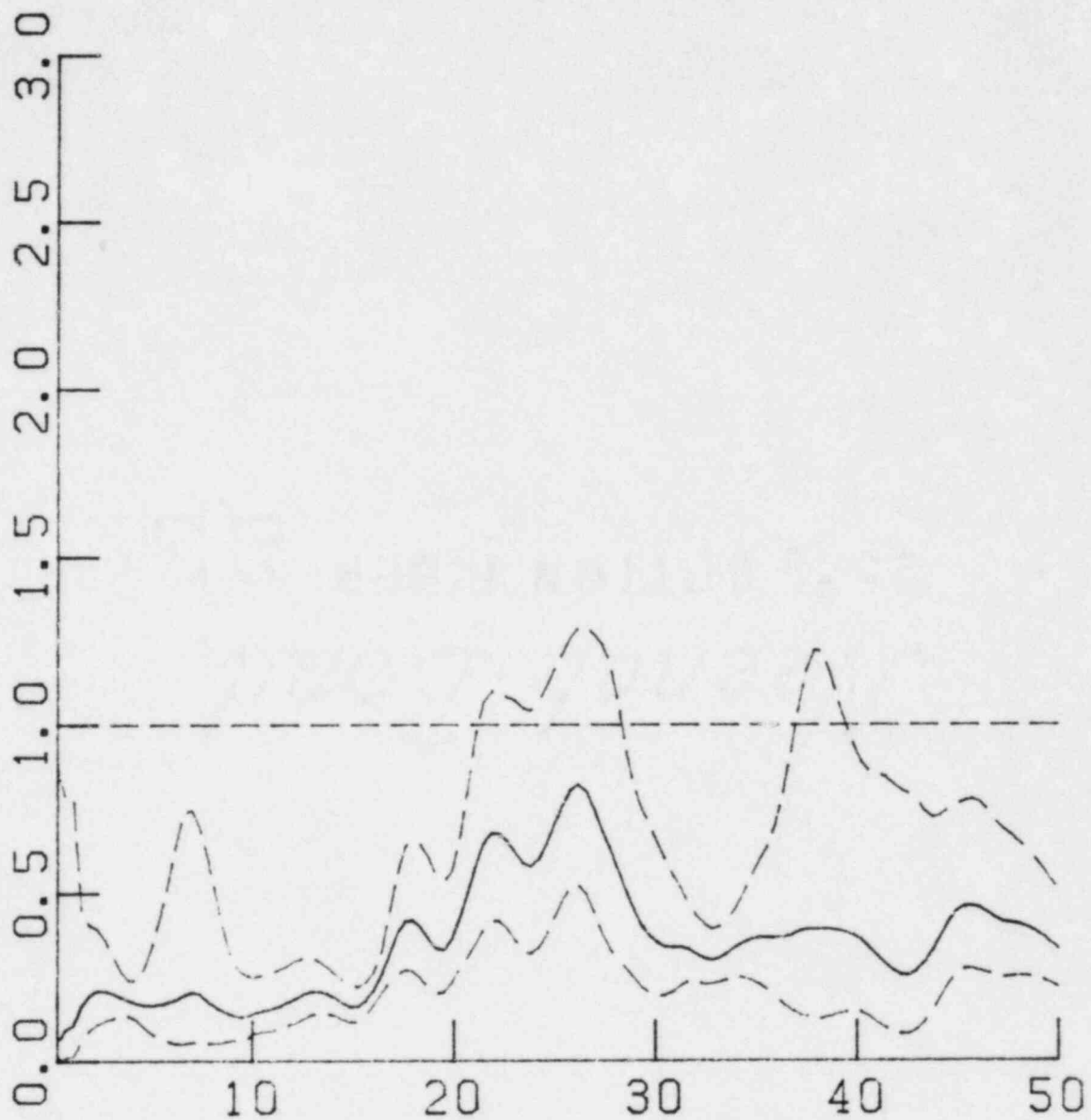
TEST 4 SHOTS: 3 GS/<P3, F5> & 7.9 GS/F5 R
 RATIOS FROM MODULI INDIVIDUALLY
 RUN NO 231.
 POWER SPECTRAL NOISE SUBTRACTED

Figure VI.C.30 Diesel Generator Sump/Free field spectral modulus ratio, radial component, Test 4.



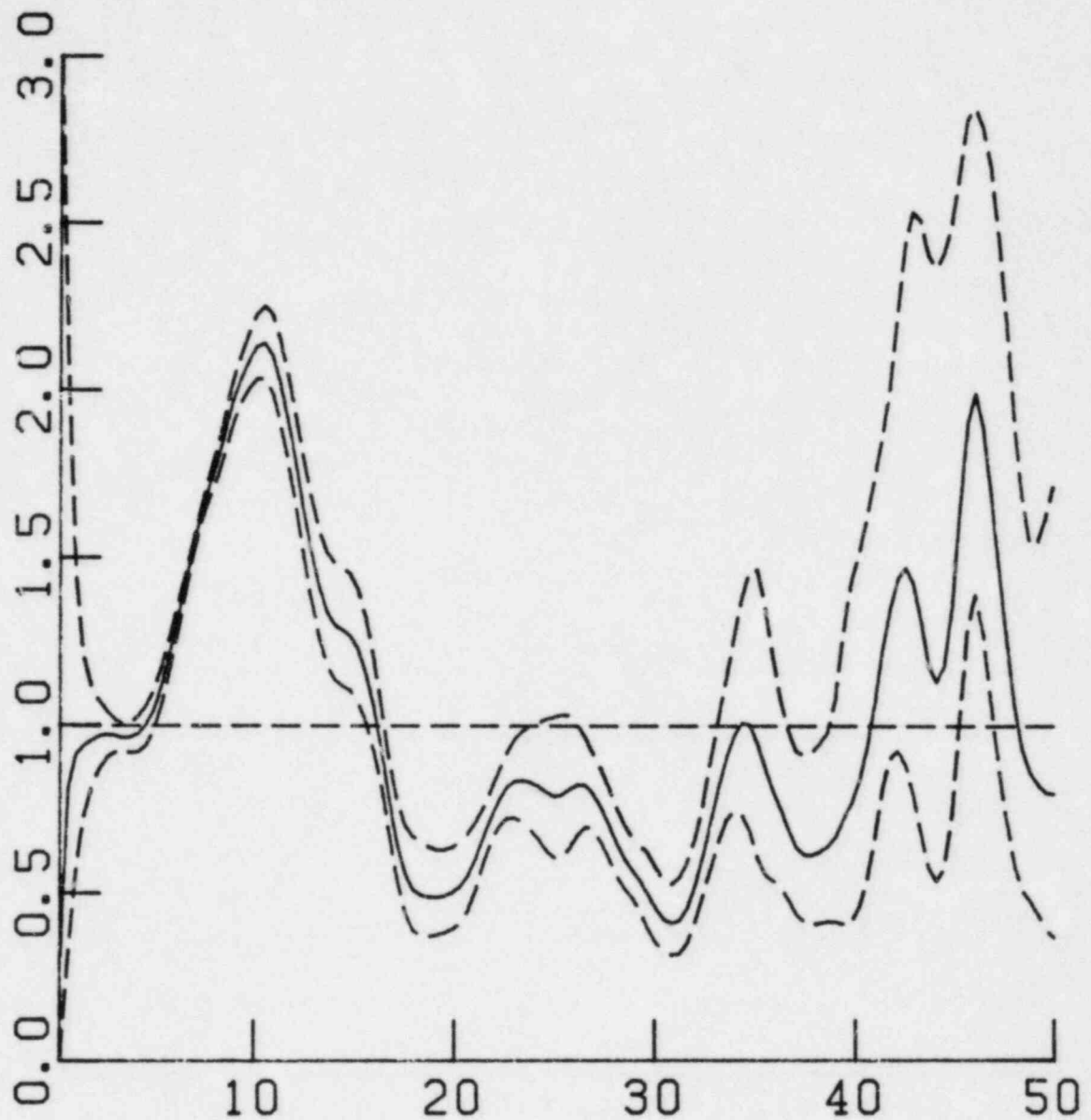
TEST 4 SHOTS: 3 GS/<P3, F5> & 7, 9 GS/F5 T
 RATIOS FROM MODULI INDIVIDUALLY
 RUN NO 232.
 POWER SPECTRAL NOISE SUBTRACTED

Figure VI.C.31 Diesel Generator Sump/Free field spectral modulus ratio, transverse component, Test 4.



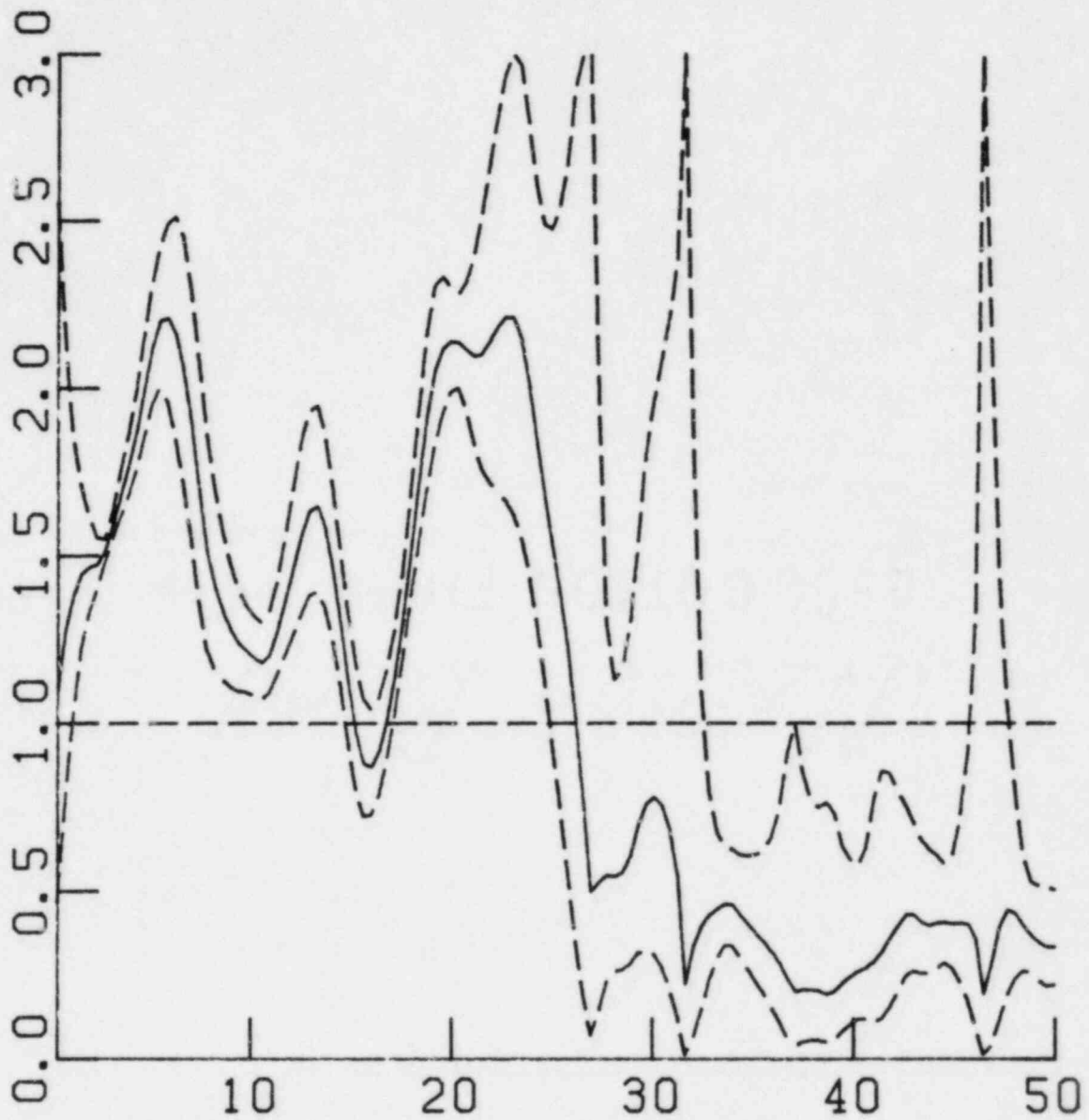
TEST 4 SHOTS: 3 GS/<P3, F5> & 7.9 GS/F5 R+T
 RATIOS FROM MODULI INDIVIDUALLY
 RUN NO 233.
 POWER SPECTRAL NOISE SUBTRACTED

Figure VI.C.32 Diesel Generator Sump/Free field spectral modulus ratio, combined radial and transverse components, Test 4.



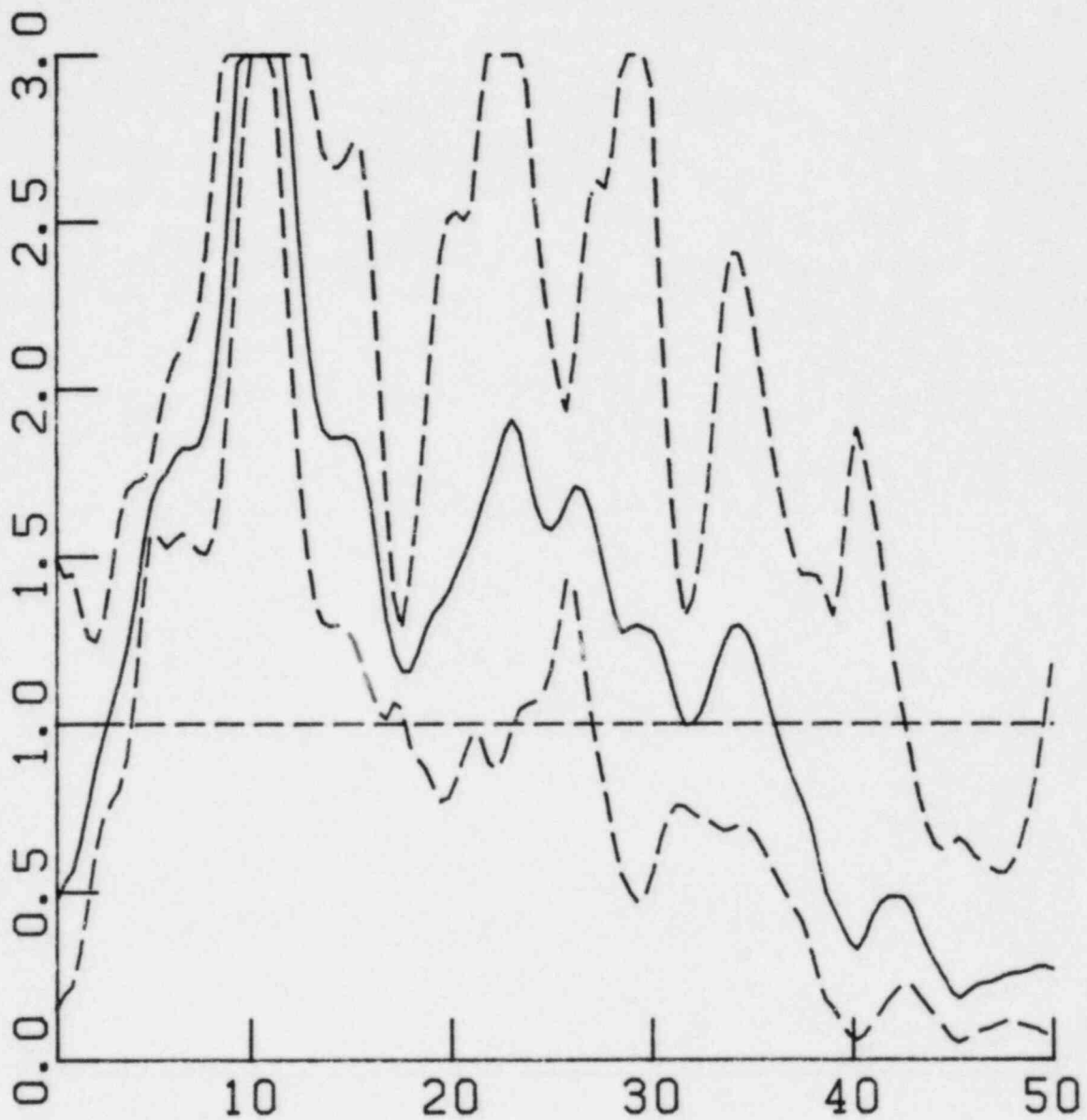
TEST 3 SHOTS 2, 3, 6, 7, 8 GS/AB , V NO GROUP.
 RATIOS FROM MODULI INDIVIDUALLY
 RUN NO 240.
 POWER SPECTRAL NOISE SUBTRACTED

Figure VI.C.33 Diesel Generator Sump/Auxiliary Building
 spectral modulus ratio, vertical component,
 Test 3.



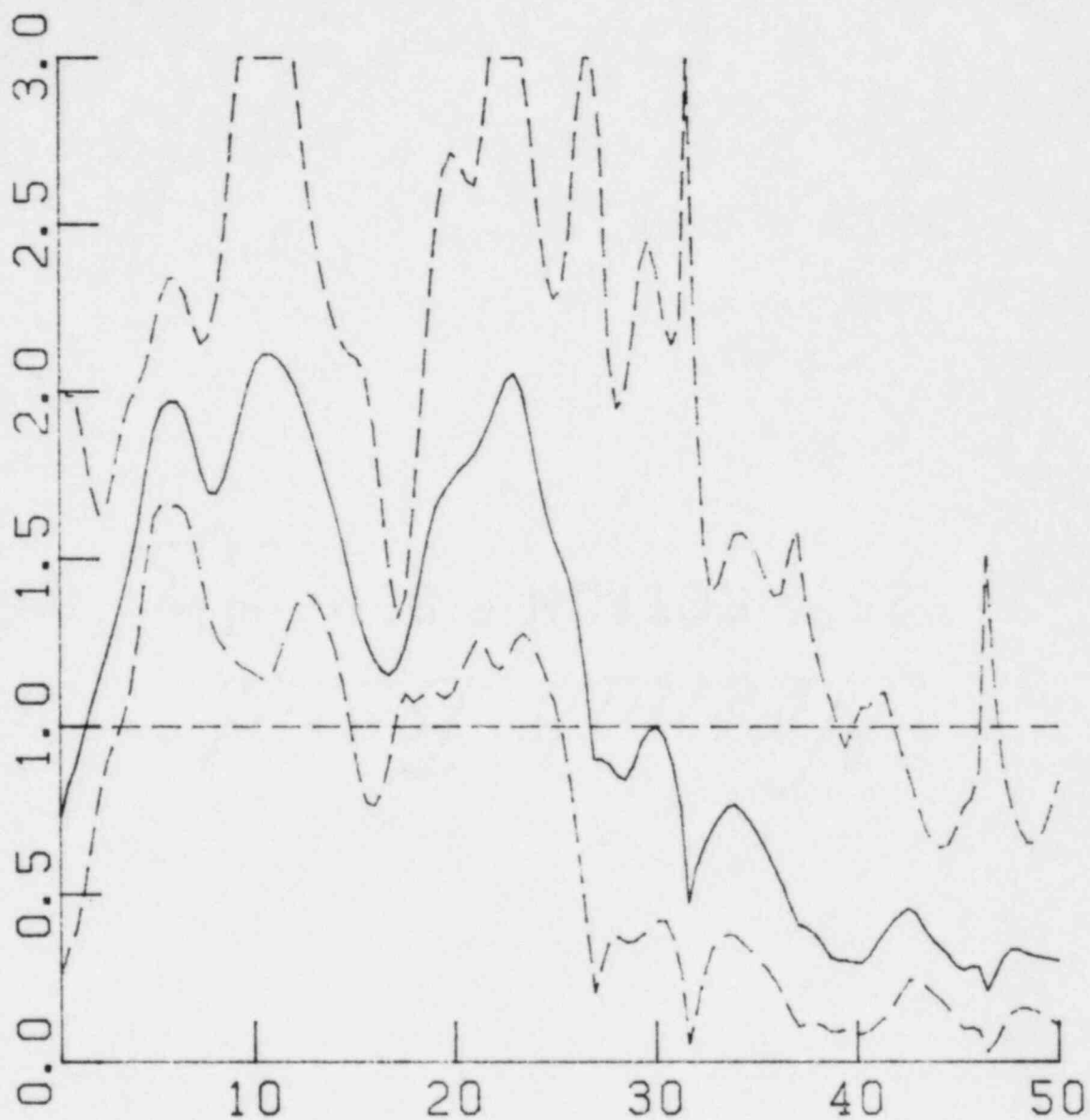
TEST 3 SHOTS 2, 3, 6, 7, 8 GS/AB , R NO GROUP
 RATIOS FROM MODULI INDIVIDUALLY
 RUN NO 239.
 POWER SPECTRAL NOISE SUBTRACTED

Figure VI.C.34 Diesel Generator Sump/Auxiliary Building
 spectral modulus ratio, radial component,
 Test 3.



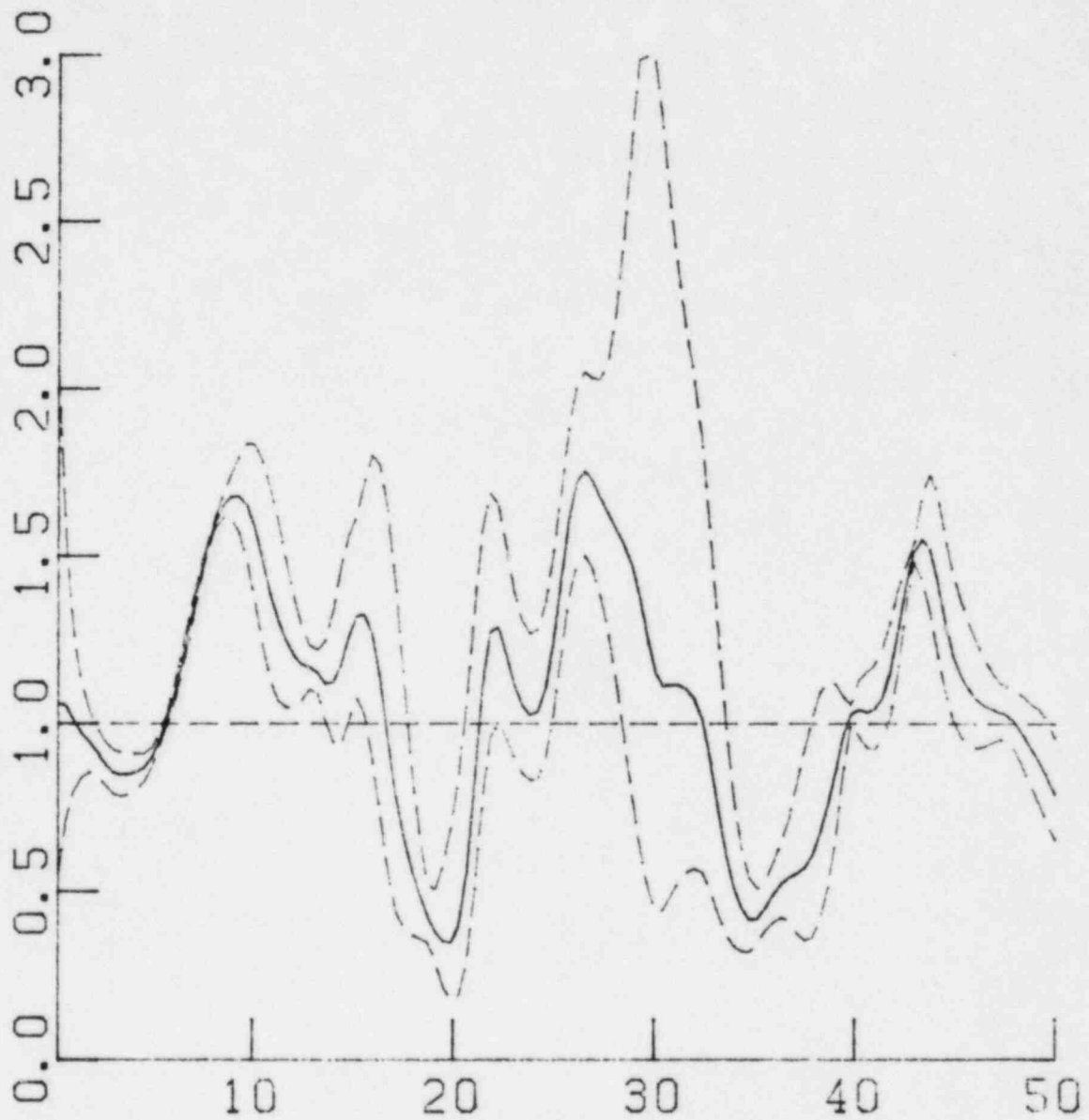
TEST 3 SHOTS 2,3,6,7,8 GS/AB , T NO GROUP.
 RATIOS FROM MODULI INDIVIDUALLY
 RUN NO 238.
 POWER SPECTRAL NOISE SUBTRACTED

Figure VI.C.35 Diesel Generator Sump/Auxiliary Building,
 spectral modulus ratio, transverse component,
 Test 3.



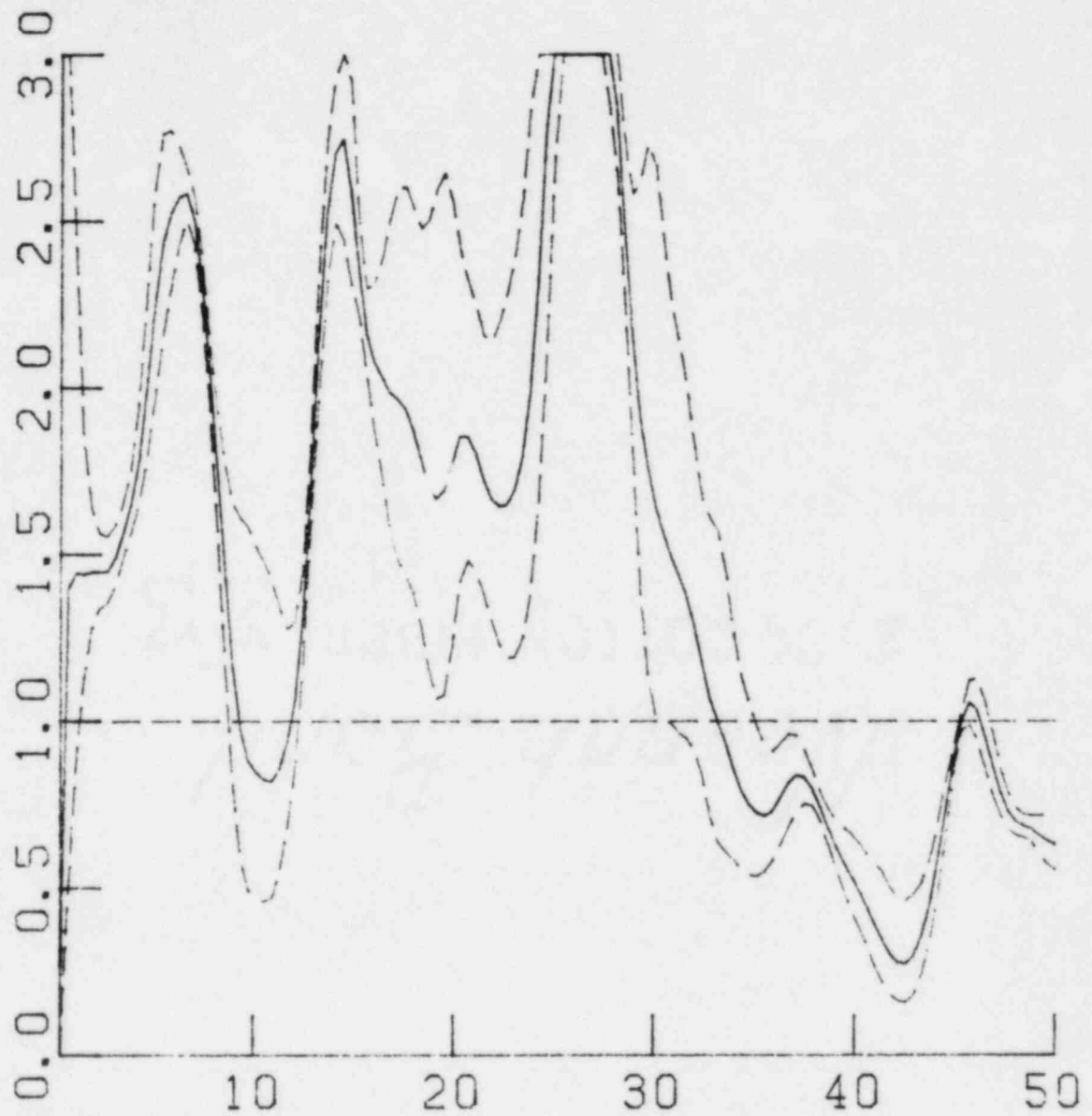
TEST 3, GS/AB, R, T COMB., NO GROUPING
 RATIOS FROM MODULI INDIVIDUALLY
 RUN NO 221.
 POWER SPECTRAL NOISE SUBTRACTED

Figure VI.C.36 Diesel Generator Sump/Auxiliary Building,
 spectral modulus ratio, combined radial
 and transverse components, Test 3.



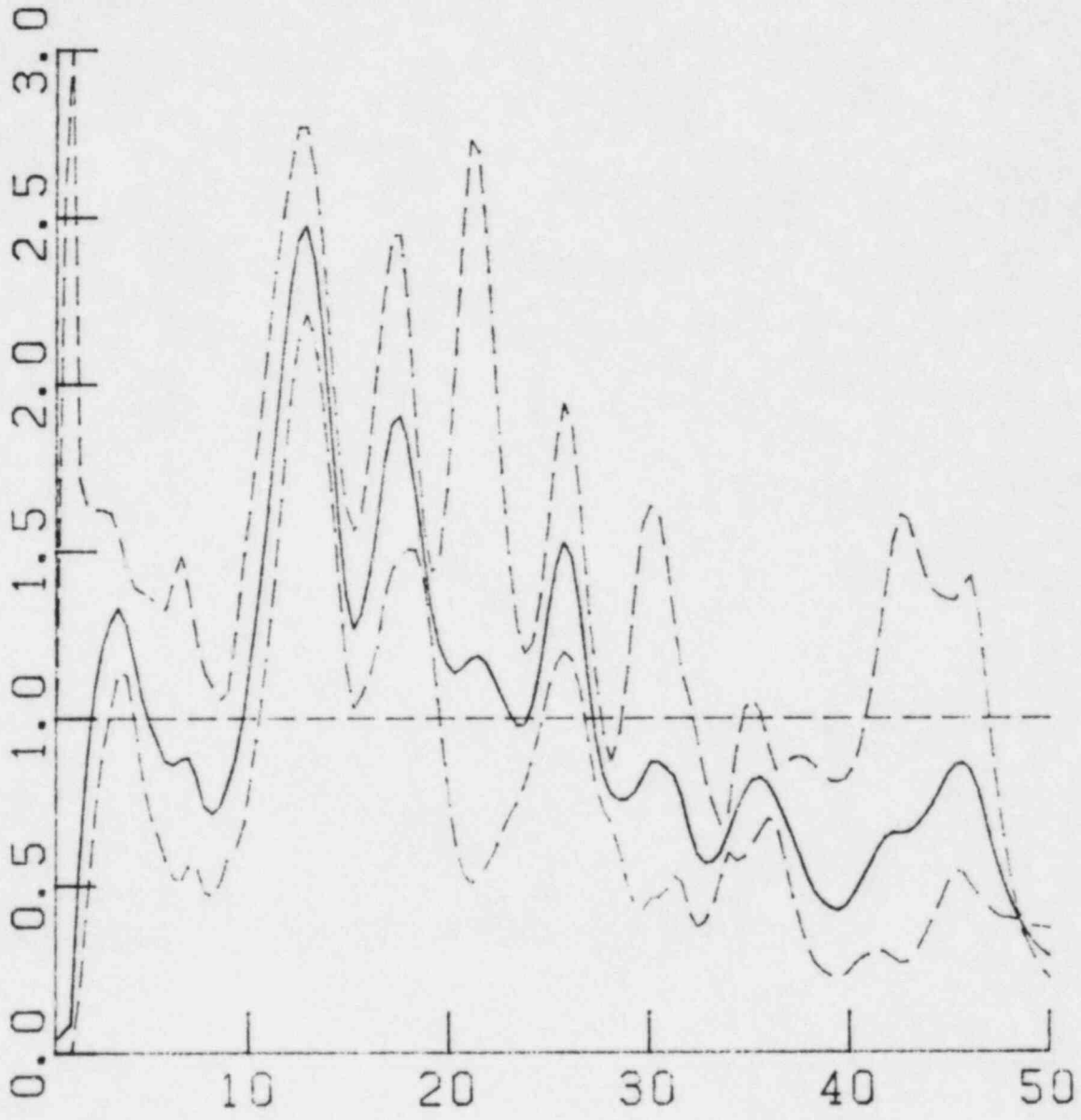
TEST 4 SHOTS 3, 7, 9 GS/AB V
 RATIOS FROM MODULI INDIVIDUALLY
 RUN NO 234.
 POWER SPECTRAL NOISE SUBTRACTED

Figure VI.C.37 Diesel Generator Sump/Auxiliary Building,
 spectral modulus ratio, vertical component,
 Test 4.



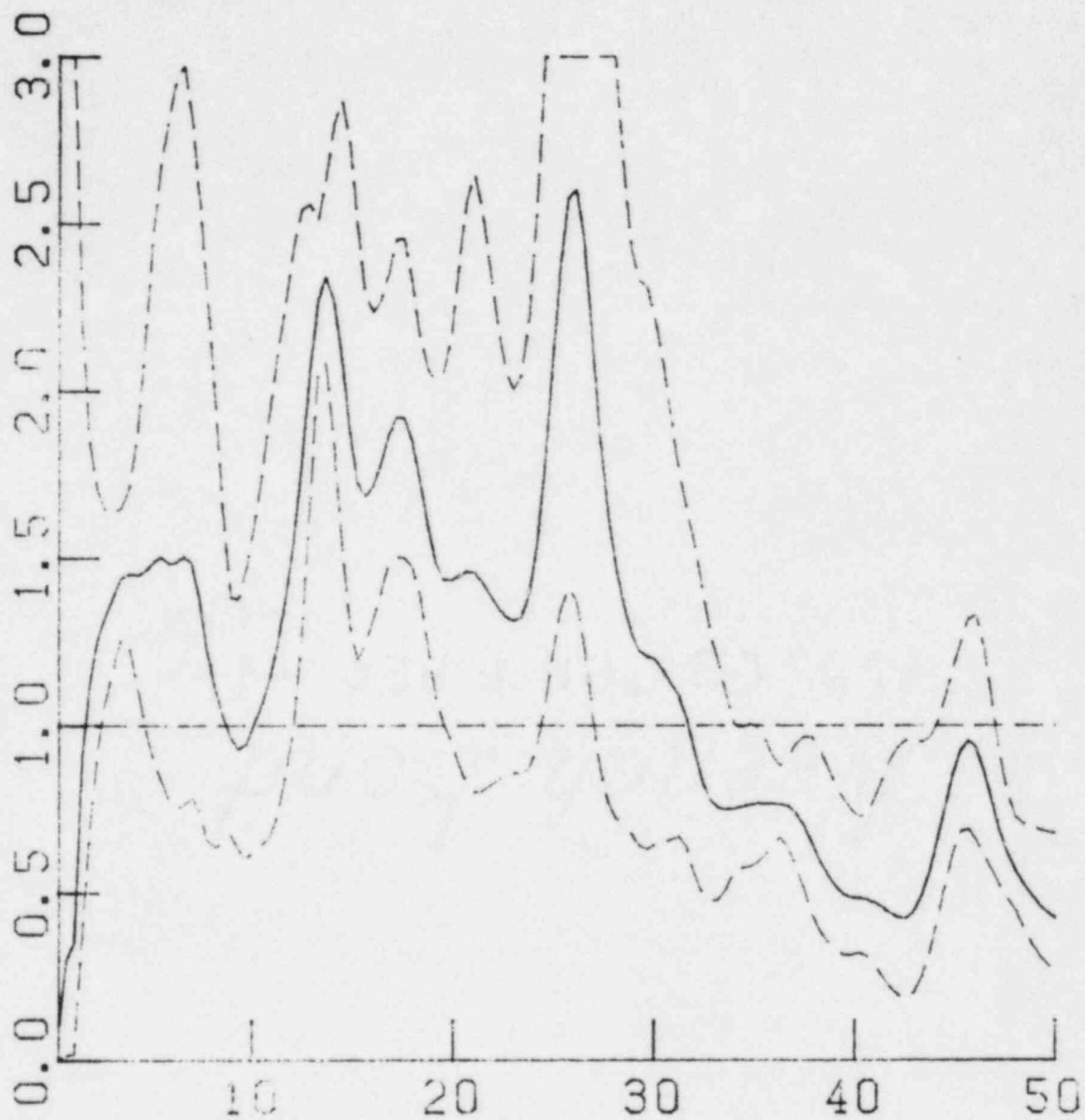
TEST 4 SHOTS 3, 7, 9 GS/AB R
 RATIOS FROM MODULI INDIVIDUALLY
 RUN NO 235.
 POWER SPECTRAL NOISE SUBTRACTED

Figure VI.C.38 Diesel Generator Sump/Auxiliary Building,
 spectral modulus ratio, radial component,
 Test 4.



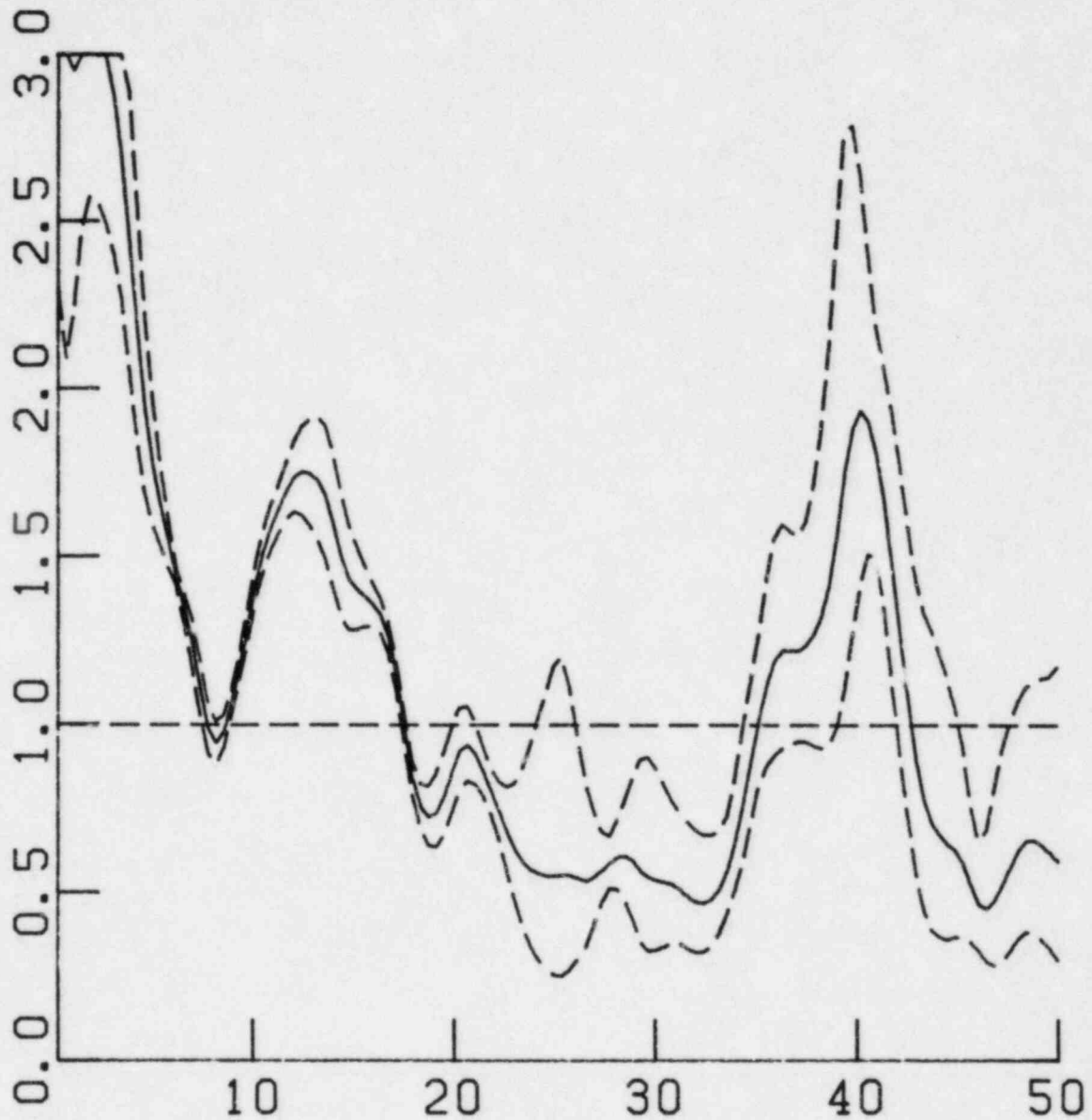
TEST 4 SHOTS 3,7,9 GS/AB T
 RATIOS FROM MODULI INDIVIDUALLY
 RUN NO 236.
 POWER SPECTRAL NOISE SUBTRACTED

Figure VI.C.39 Diesel Generator Sump/Auxiliary Building,
 spectral modulus ratio, transverse component,
 Test 4.



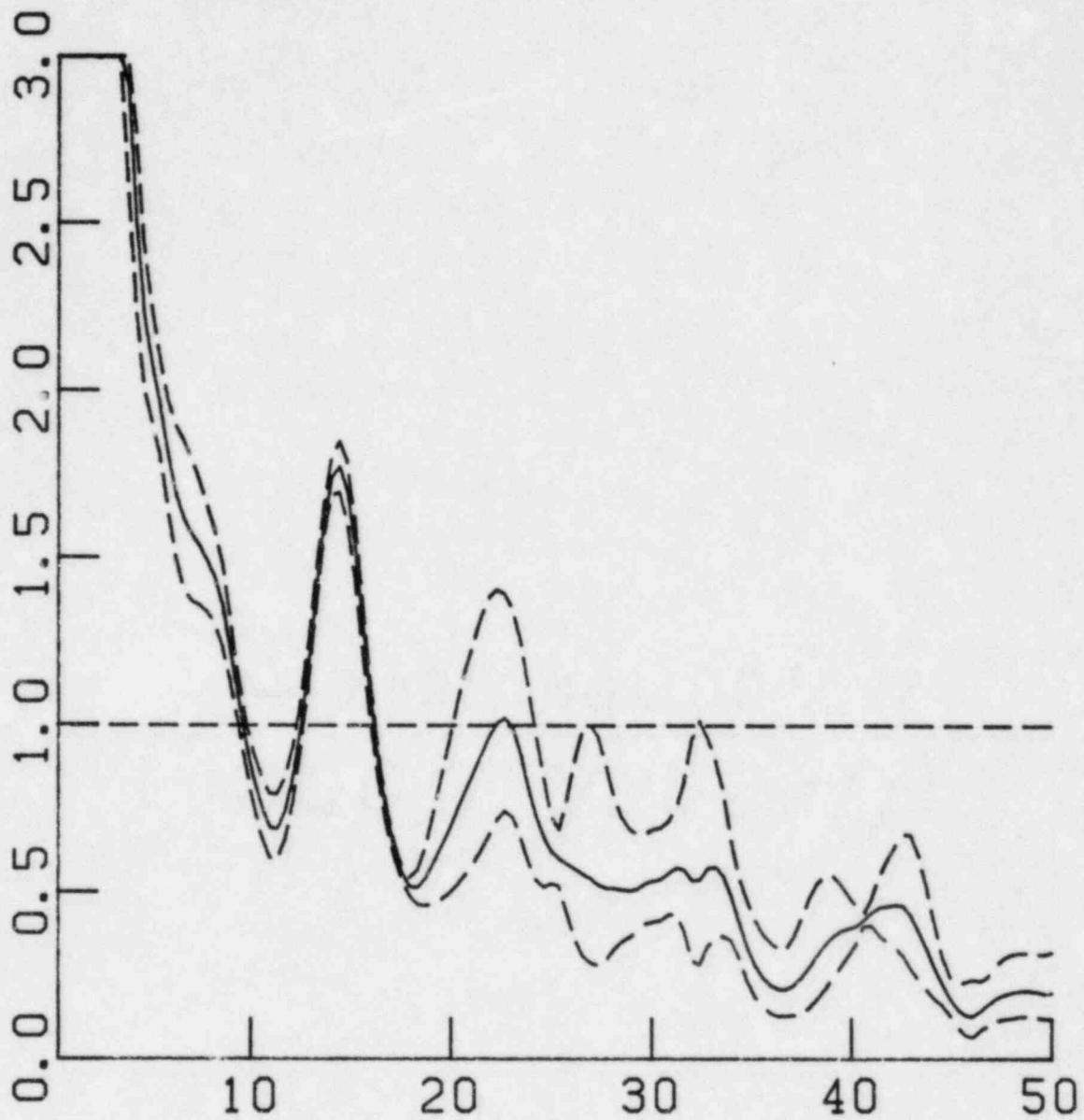
TEST 4 SHOTS 3, 7, 9 GS/AB R. T COME.
 RATIOS FROM MODULI INDIVIDUALLY
 RUN NO 237.
 POWER SPECTRAL NOISE SUBTRACTED

Figure VI.C.40 Diesel Generator Sump/Auxiliary Building,
 spectral modulus ratio, combined radial and
 transverse components, Test 4.



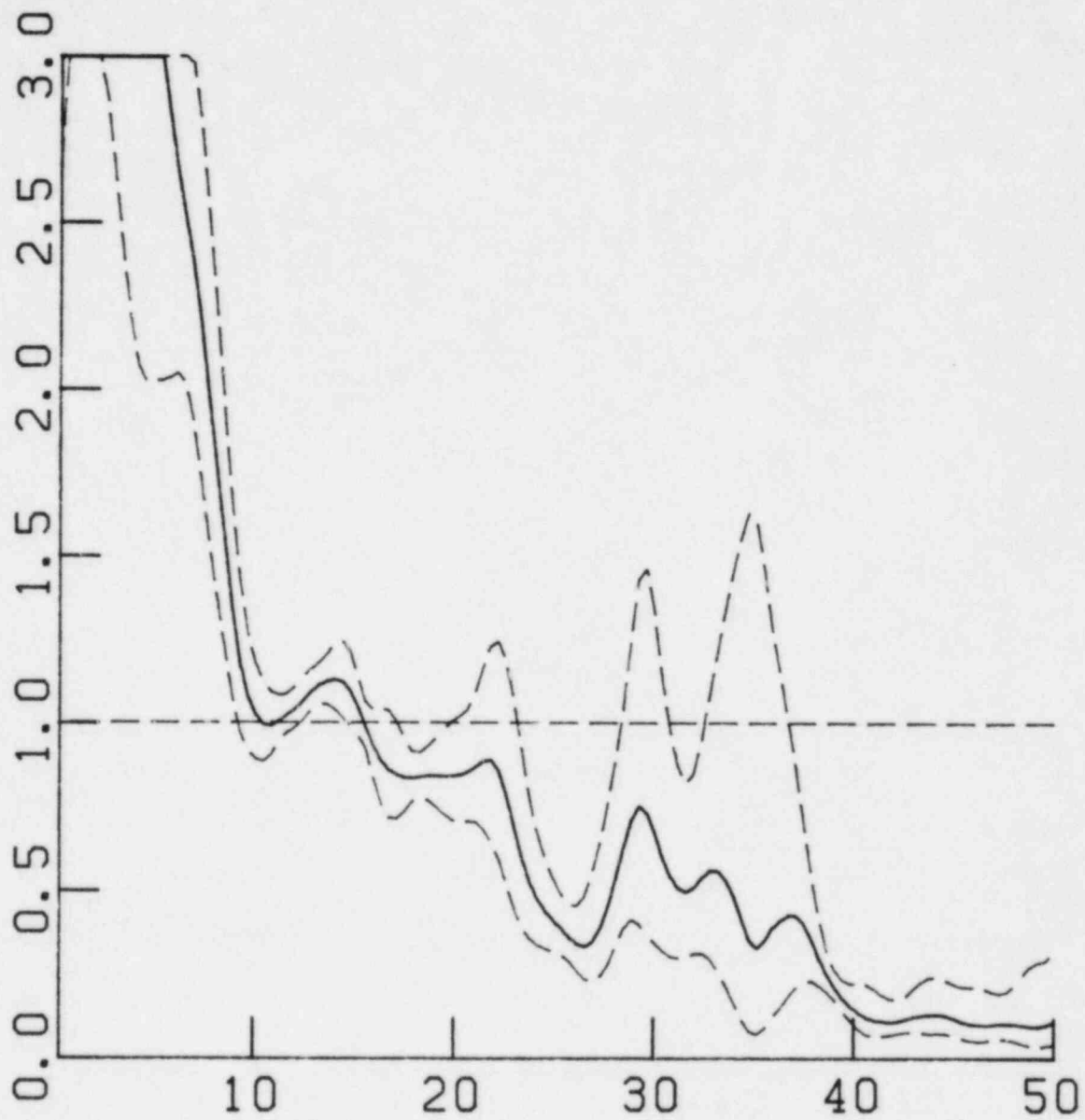
TEST 3 SHOTS 2, 3, 6, 7, 8 WP/AB , V NO GROUP.
 RATIOS FROM MODULI INDIVIDUALLY
 RUN NO 241.
 POWER SPECTRAL NOISE SUBTRACTED

Figure VI.C.41 Service Water Pumphouse/Auxiliary Building,
 spectral modulus ratio, vertical component,
 Test 3.



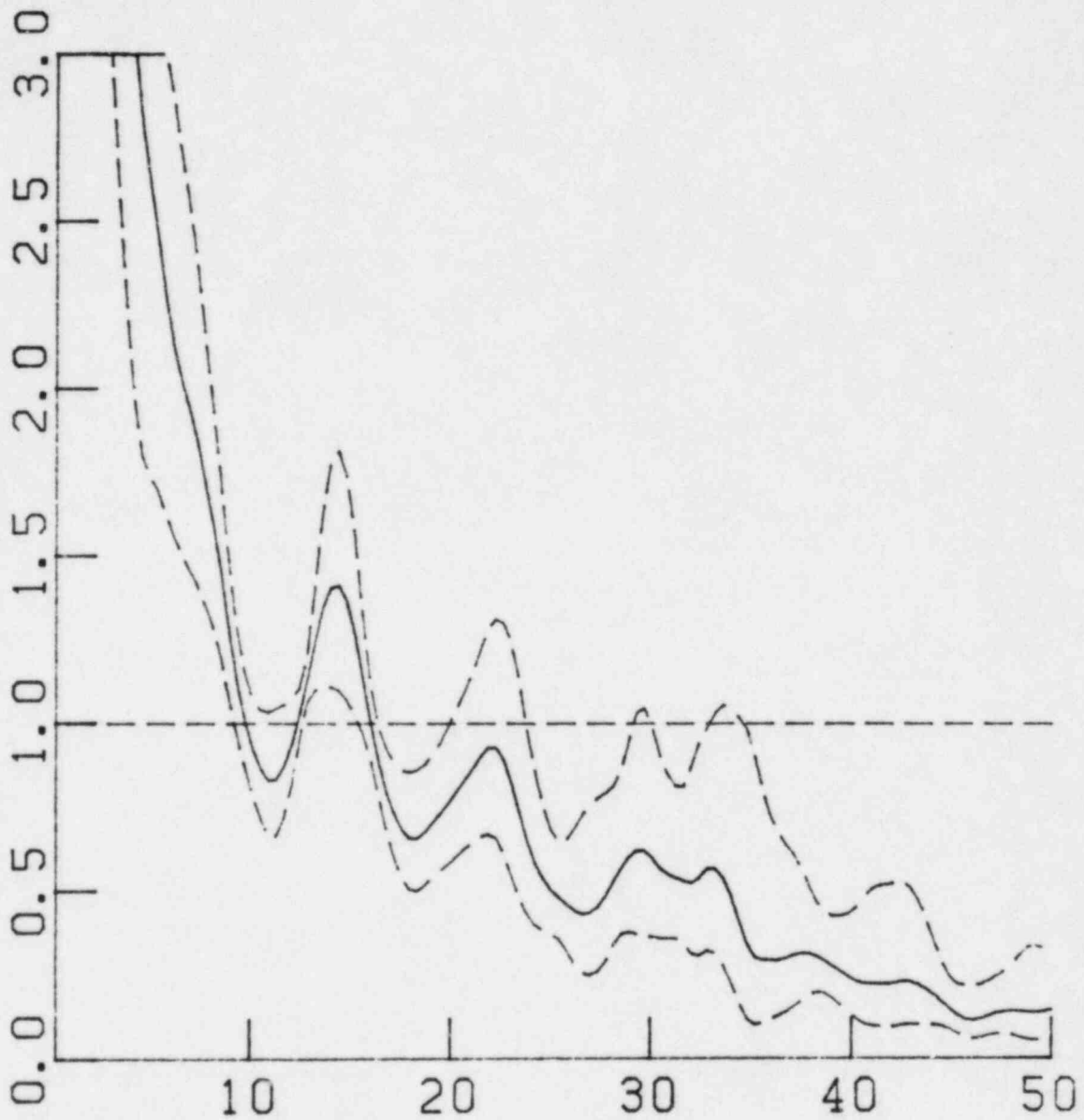
TEST 3 SHOTS 2, 3, 6, 7, 8 WP/AB , R NO GROUP.
 RATIOS FROM MODULI INDIVIDUALLY
 RUN NO 242.
 POWER SPECTRAL NOISE SUBTRACTED

Figure VI.C.42 Service Water Pumphouse/Auxiliary Building,
 spectral modulus ratio, radial component,
 Test 3.



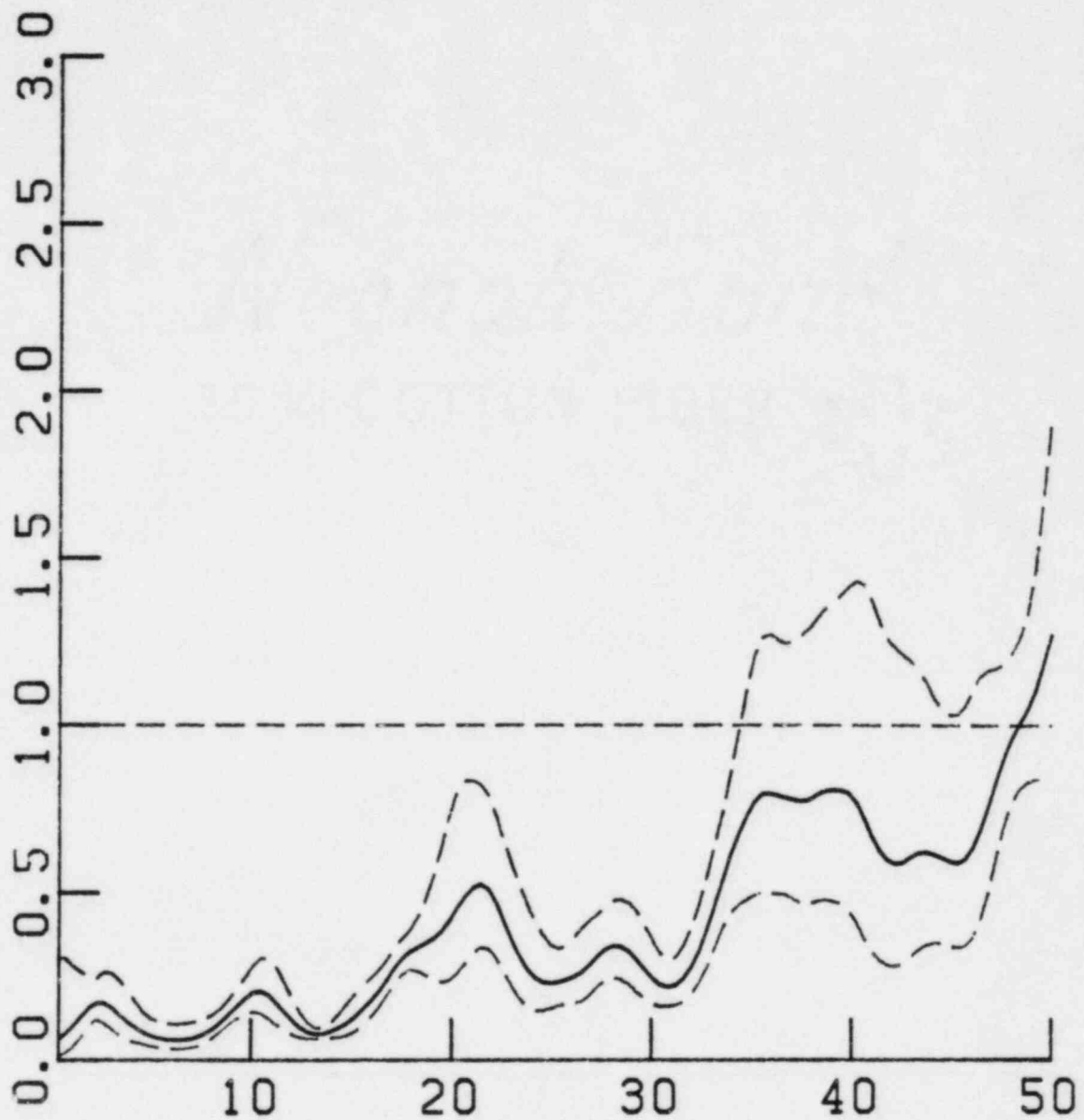
TEST 3 SHOTS 2, 3, 6, 7, 8 WP/AB , T NO GROUP.
 RATIOS FROM MODULI INDIVIDUALLY
 RUN NO 243.
 POWER SPECTRAL NOISE SUBTRACTED

Figure VI.C.43 Service Water Pumphouse/Auxiliary Building,
 spectral modulus ratio, transverse component,
 Test 3.



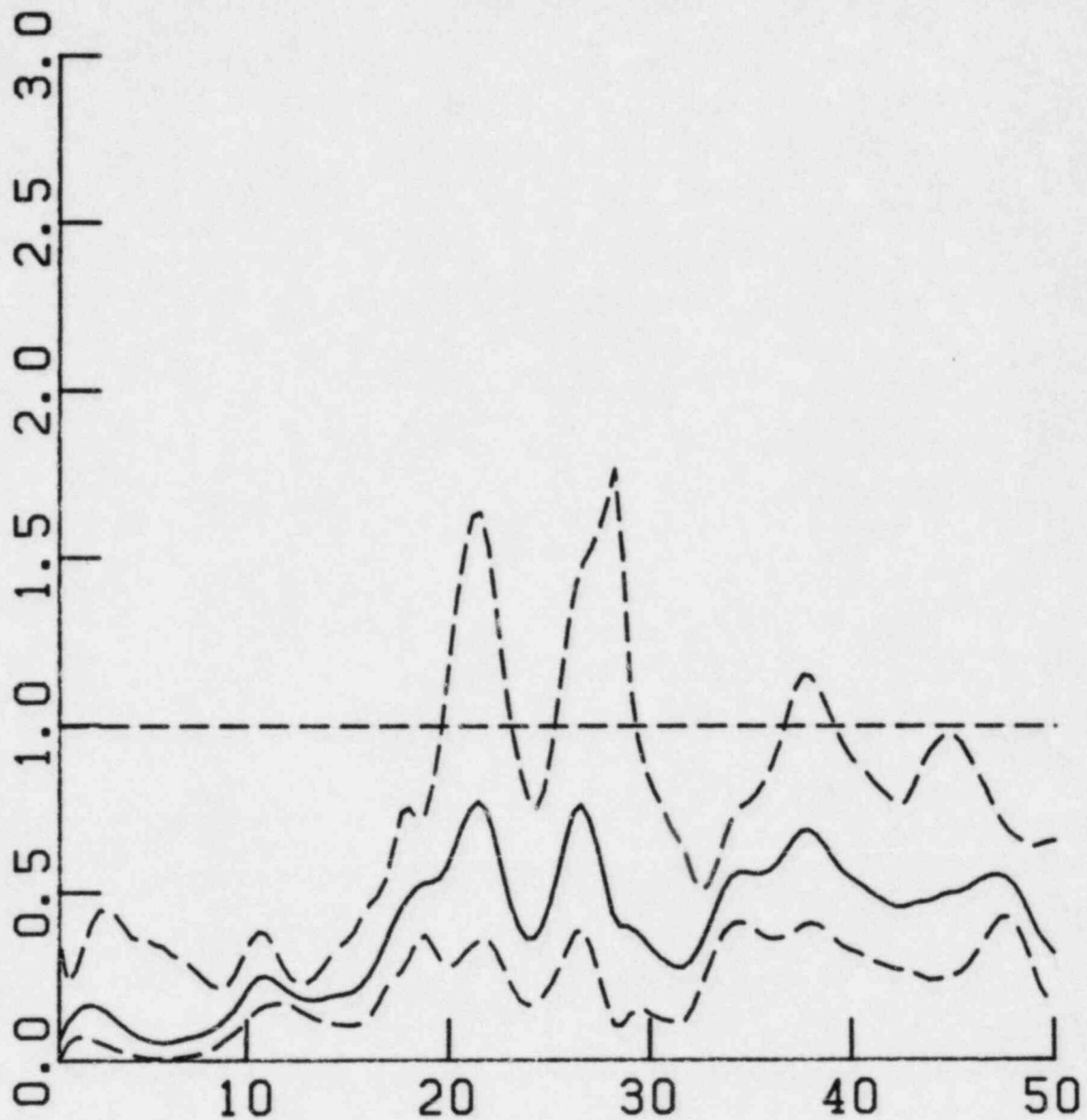
TEST 3, WP/AB, R, T COMB., NO GROUPING
 RATIOS FROM MODULI INDIVIDUALLY
 RUN NO 222.
 POWER SPECTRAL NOISE SUBTRACTED

Figure VI.C.44 Service Water Pumphouse/Auxiliary Building, spectral modulus ratio, combined radial and transverse components, Test 3.



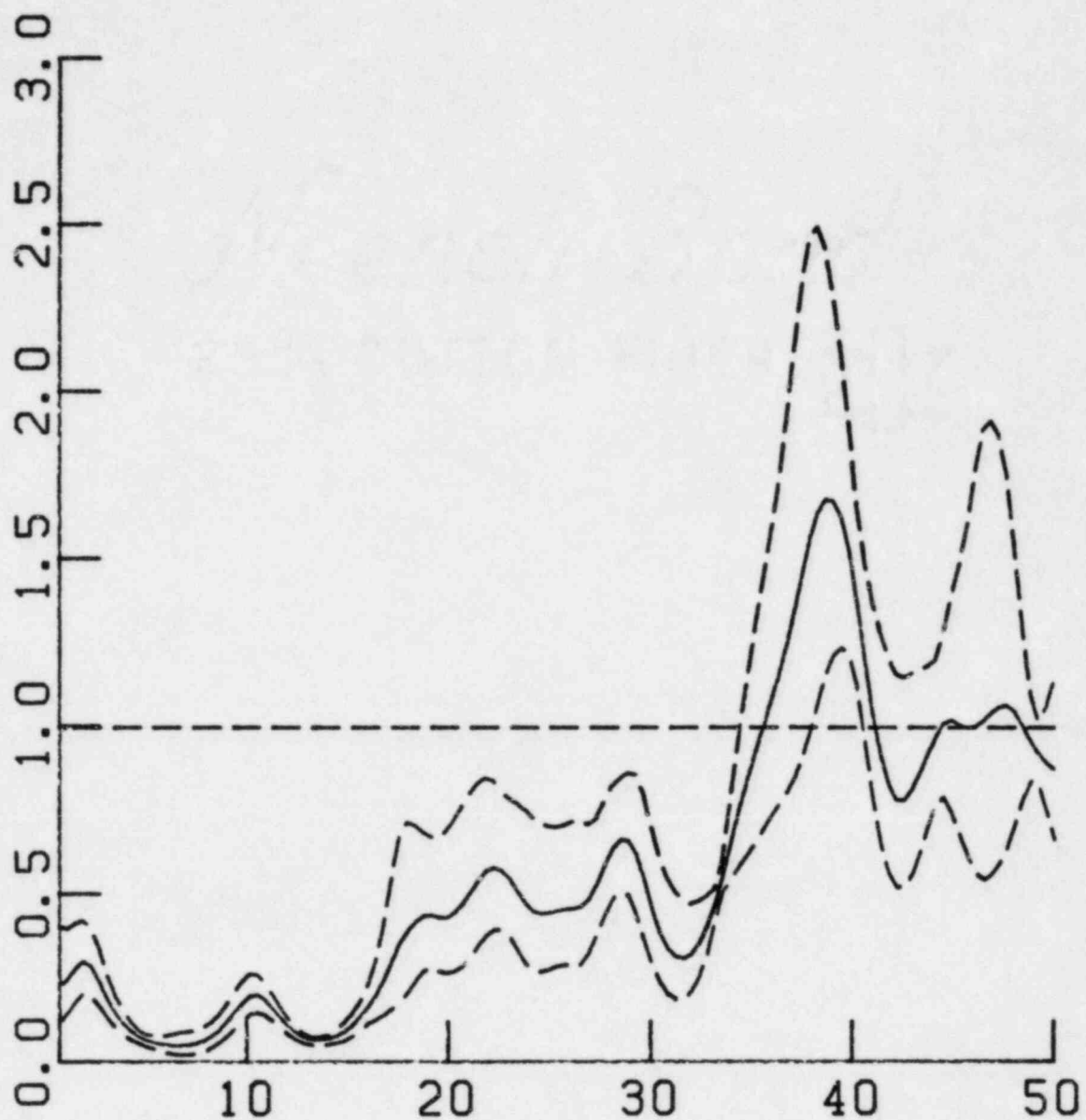
TEST 4 SHOTS 1, 2, 3, 4, 6 AB/P2 R+T.
 RATIOS FROM MODULI INDIVIDUALLY
 RUN NO 244.
 POWER SPECTRAL NOISE SUBTRACTED

Figure VI.C.45 Auxiliary Building/Pad spectral modulus ratio, combined radial and transverse components, Test 4.



TEST 4 SHOTS 1, 2, 3, 4, 6 GS/P2 R+T.
 RATIOS FROM MODULI INDIVIDUALLY
 RUN NO 248.
 POWER SPECTRAL NOISE SUBTRACTED

Figure VI.C.46 Diesel Generator Sump/Pad spectral modulus ratio, combined radial and tranverse components, Test 4.



TEST 4 SHOTS 3,4,6 AB/P3 R+T.
 RATIOS FROM MODULI INDIVIDUALLY
 RUN NO 254.
 POWER SPECTRAL NOISE SUBTRACTED

Figure VI.C.47 Auxiliary Building/Free field, Dam Abutment spectral modulus ratio, combined radial and transverse components, Test 4.

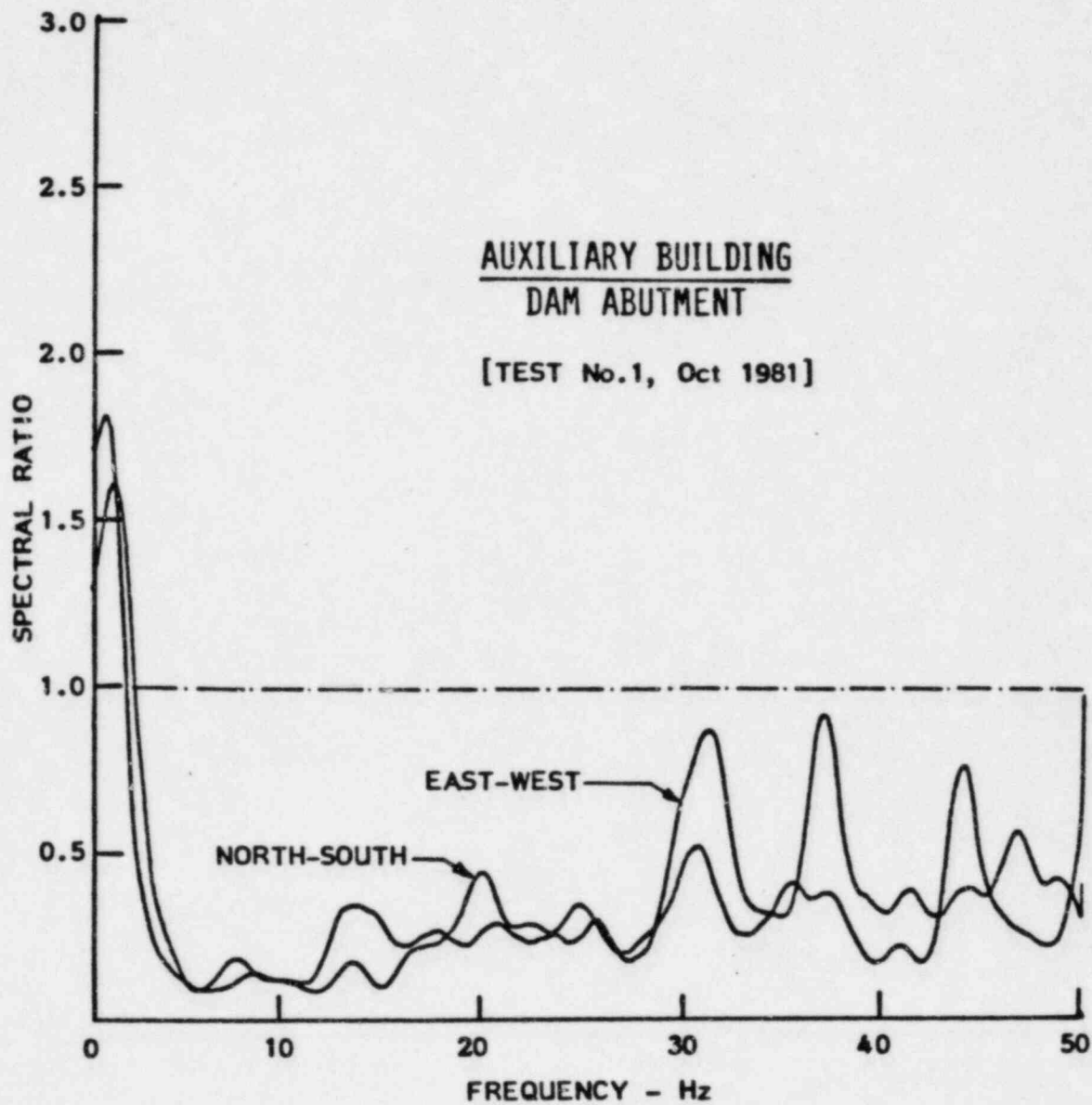


Figure VI.C.48 Horizontal component spectral ratios between Auxiliary Building and Dam Abutment obtained from Test 1, October, 1981.

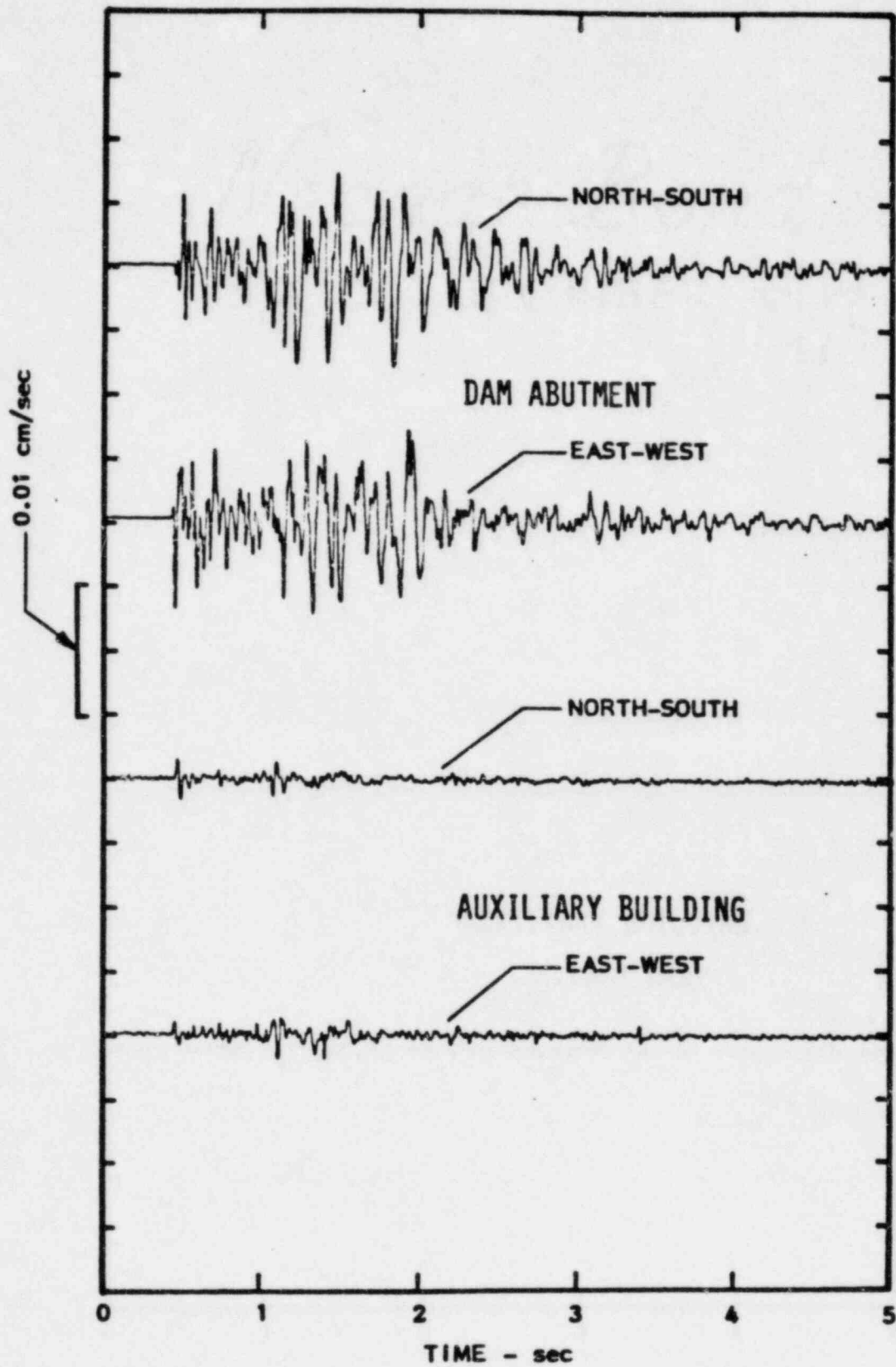


Figure VI.C.49 Horizontal components of motions generated at Dam Abutment and in Auxiliary Building by Test 1, October, 1981. Locations were equidistant from explosion.

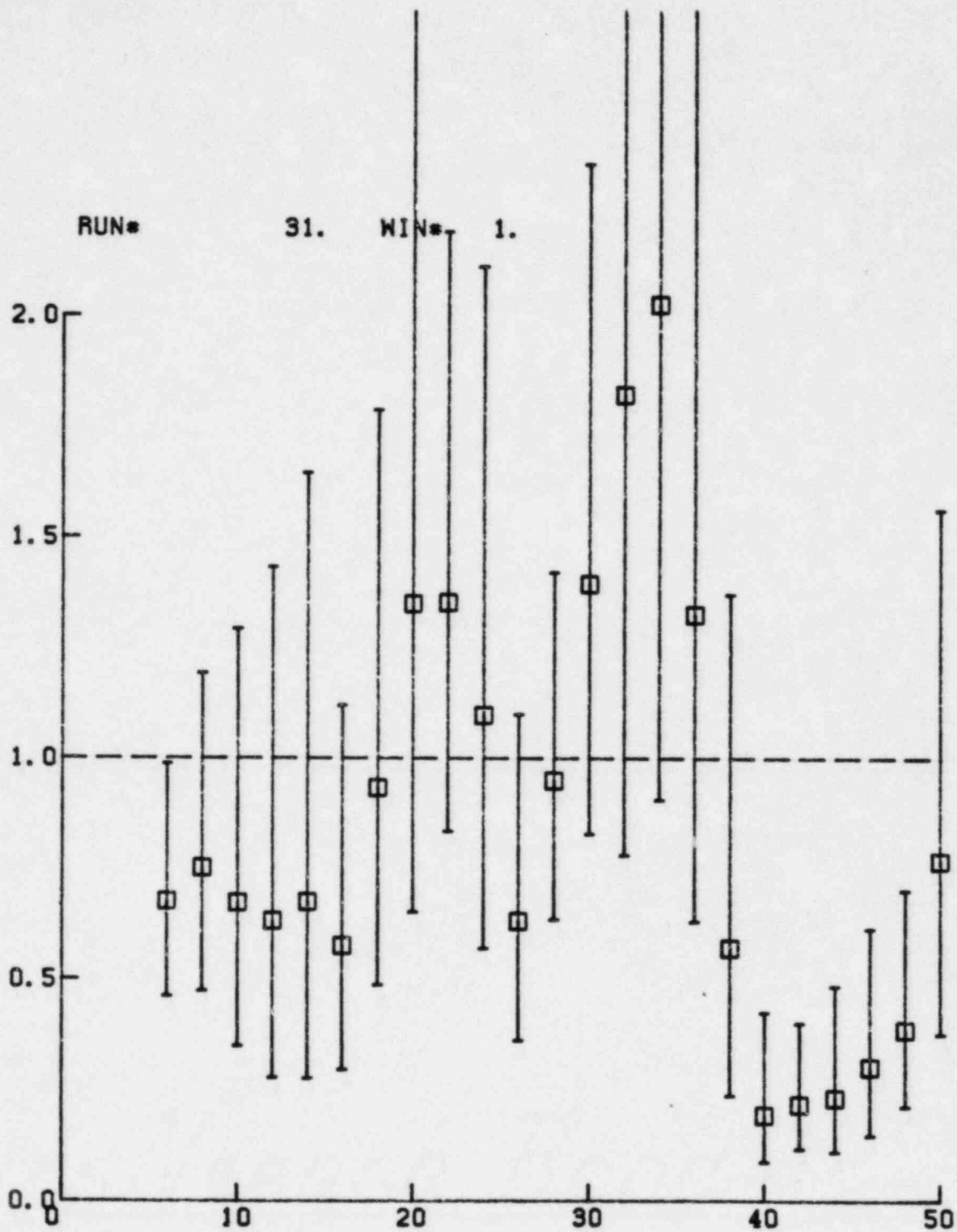


Figure VI.C.50 Test 3, vertical AB/FF band pass spectral ratios, window 0-1.28 sec.

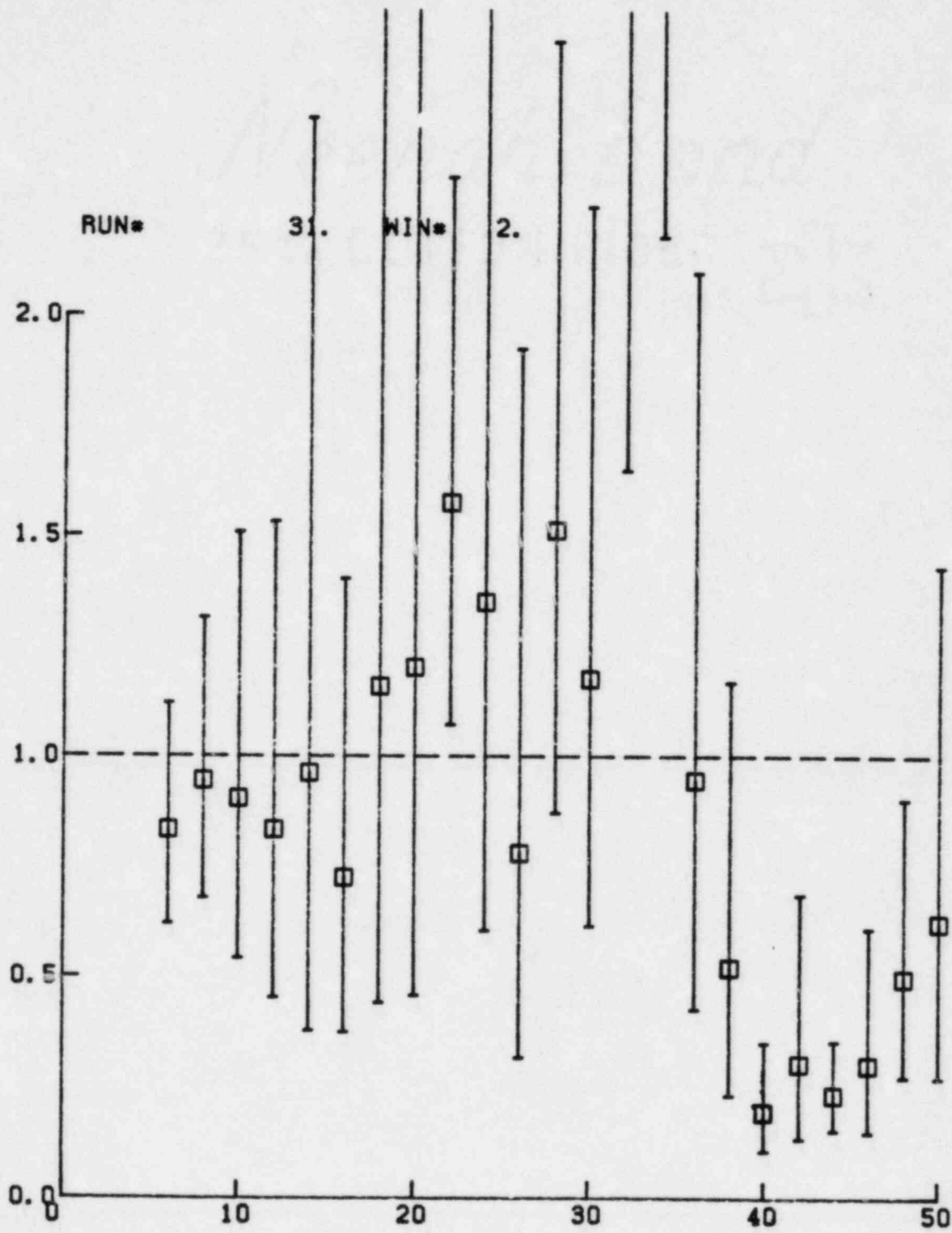


Figure VI.C.51 Test 3, vertical AB/FF
band pass spectral ratios,
window 0-0.39 sec.

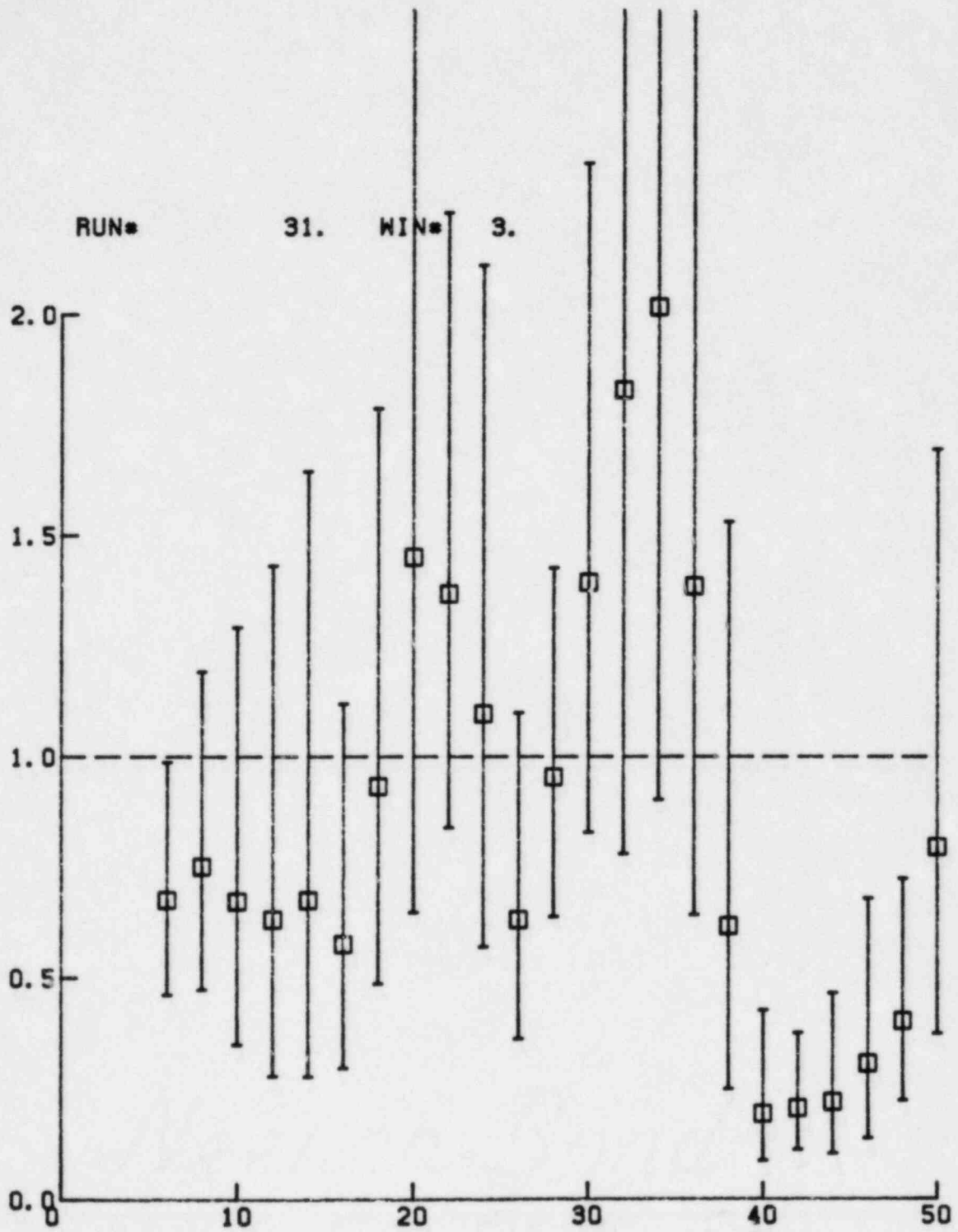


Figure VI.C.52 Test 3, vertical AB/FF band pass spectral ratios window 0.39-1.28 sec.

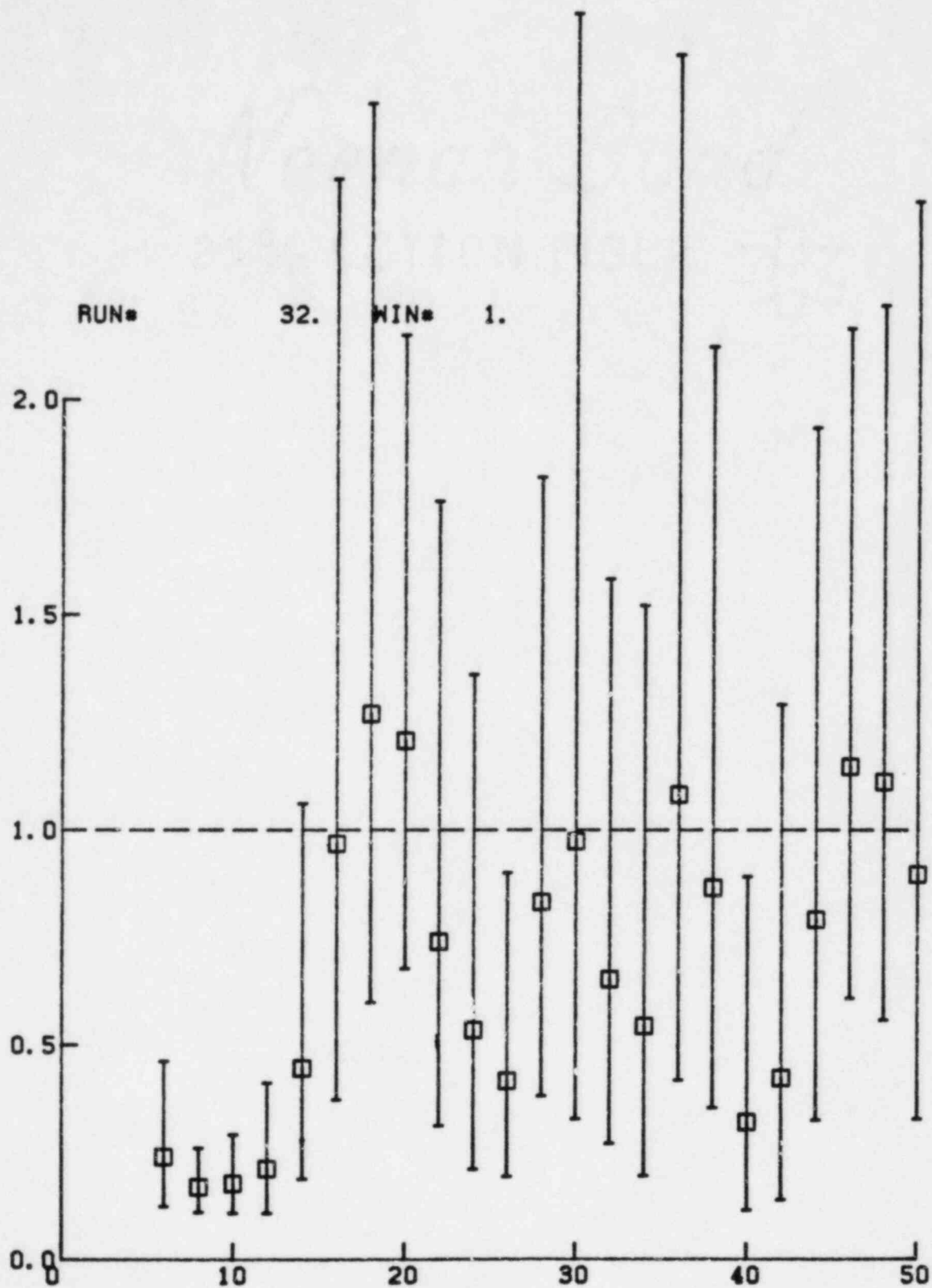


Figure VI.C.53 Test 3, radial AB/FF
band pass spectral ratios
window 0-1.28 sec.

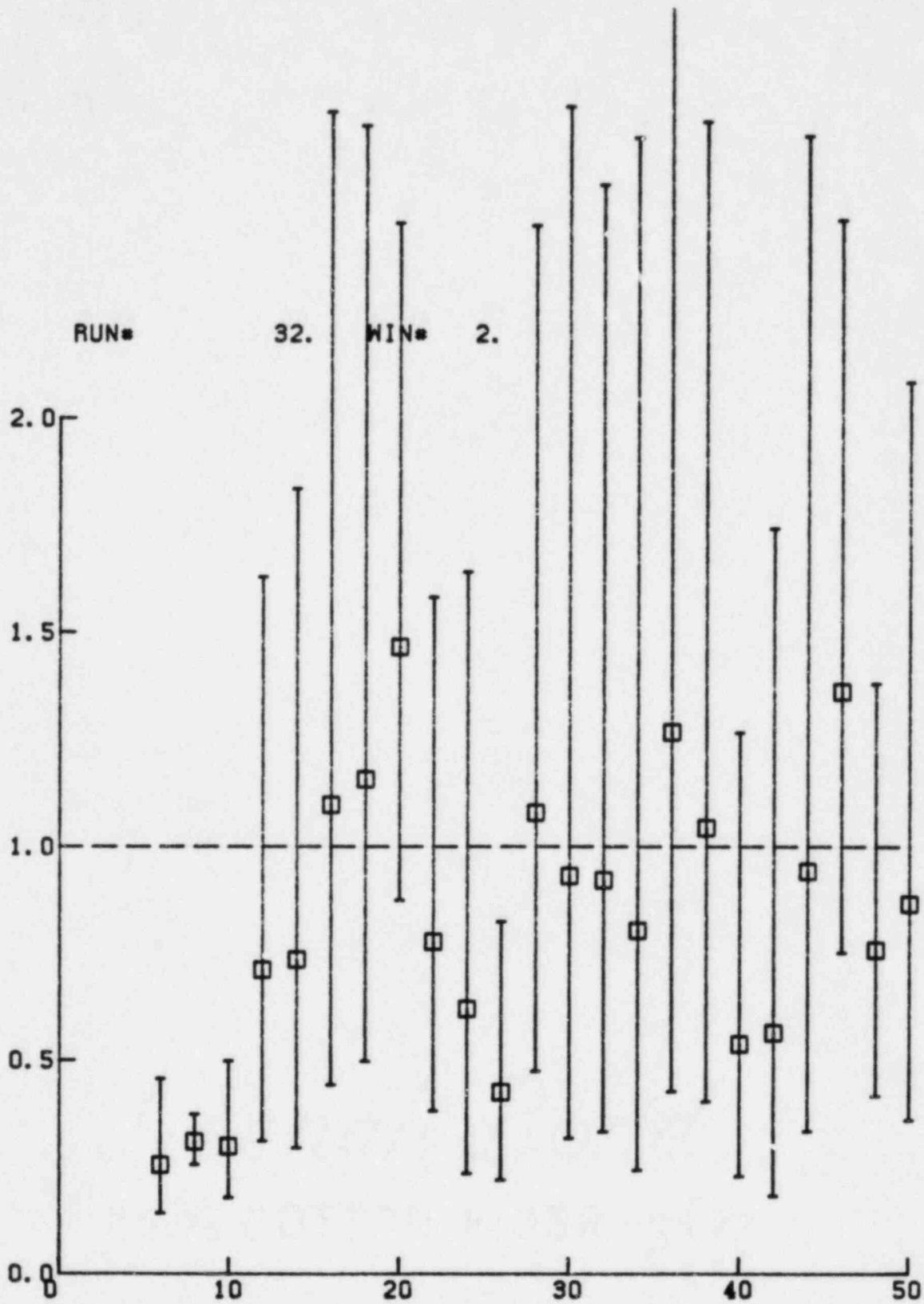


Figure VI.C.54 Test 3, radial AB/FF band pass spectral ratios window 0-0.39 sec.

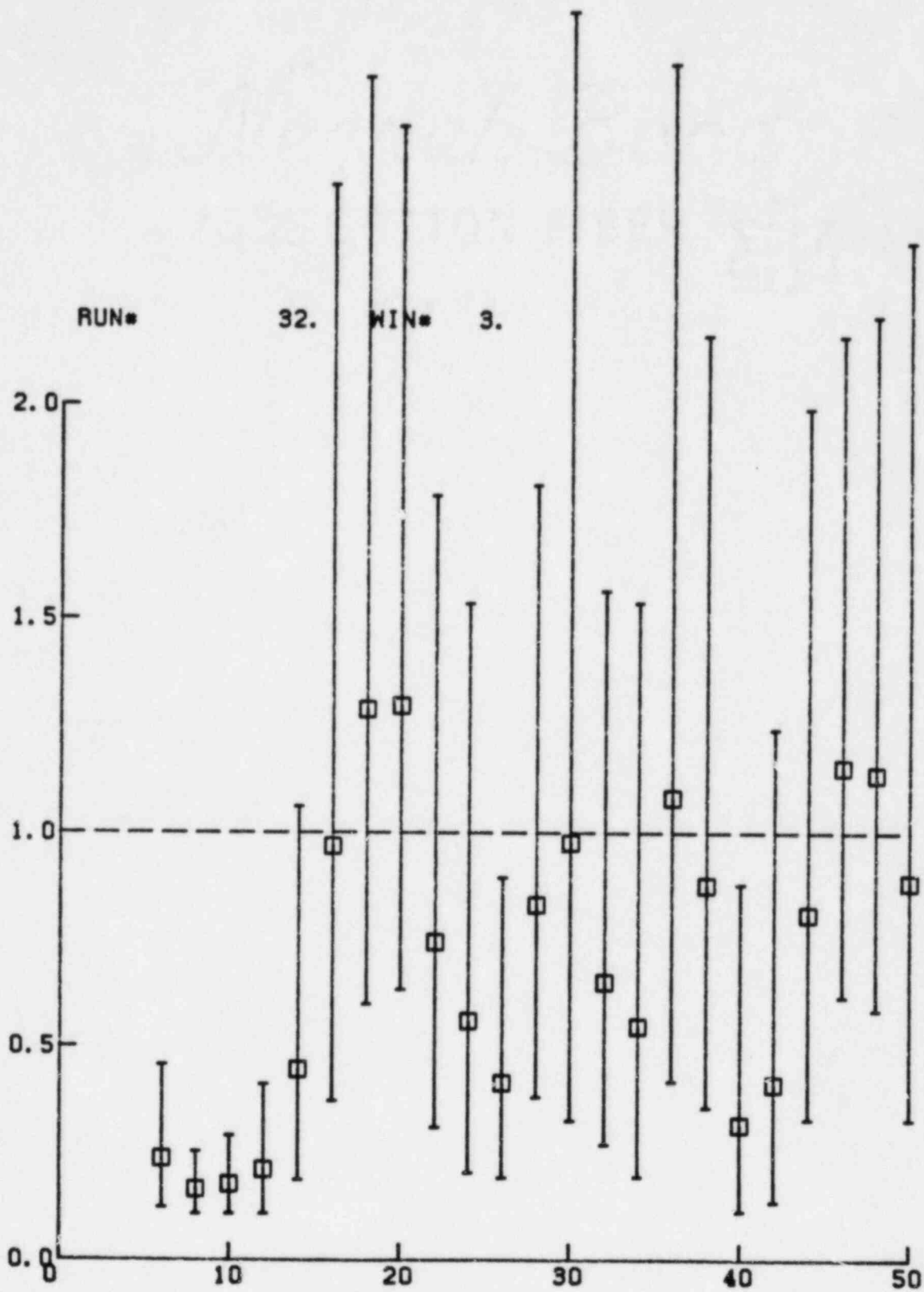


Figure VI.C.55 Test 3, radial AB/FF
band pass spectral ratios
window 0.39-1.28 sec.

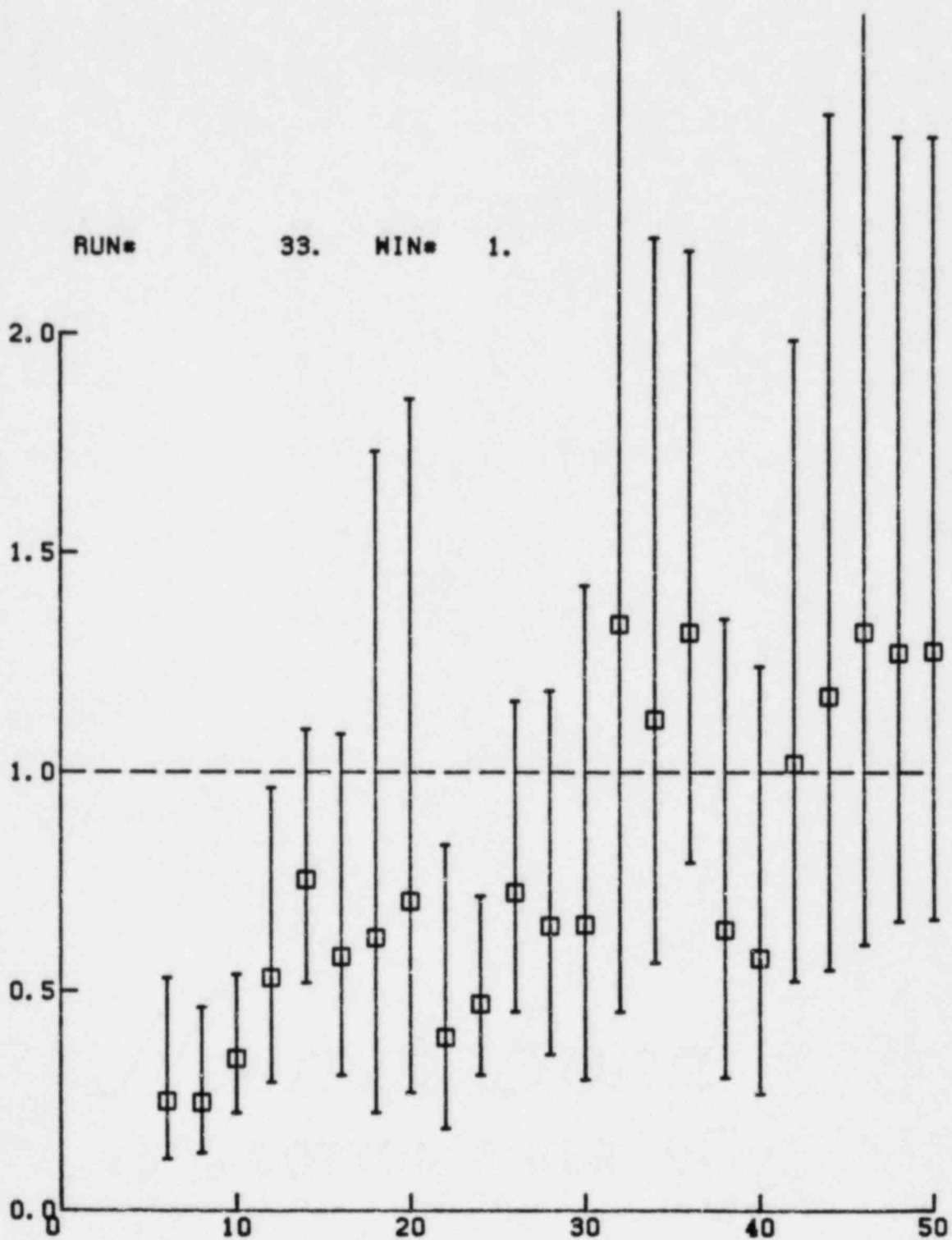


Figure VI.C.56 Test 3, transverse AB/FF
band pass spectral ratios
window 0-1.28 sec.

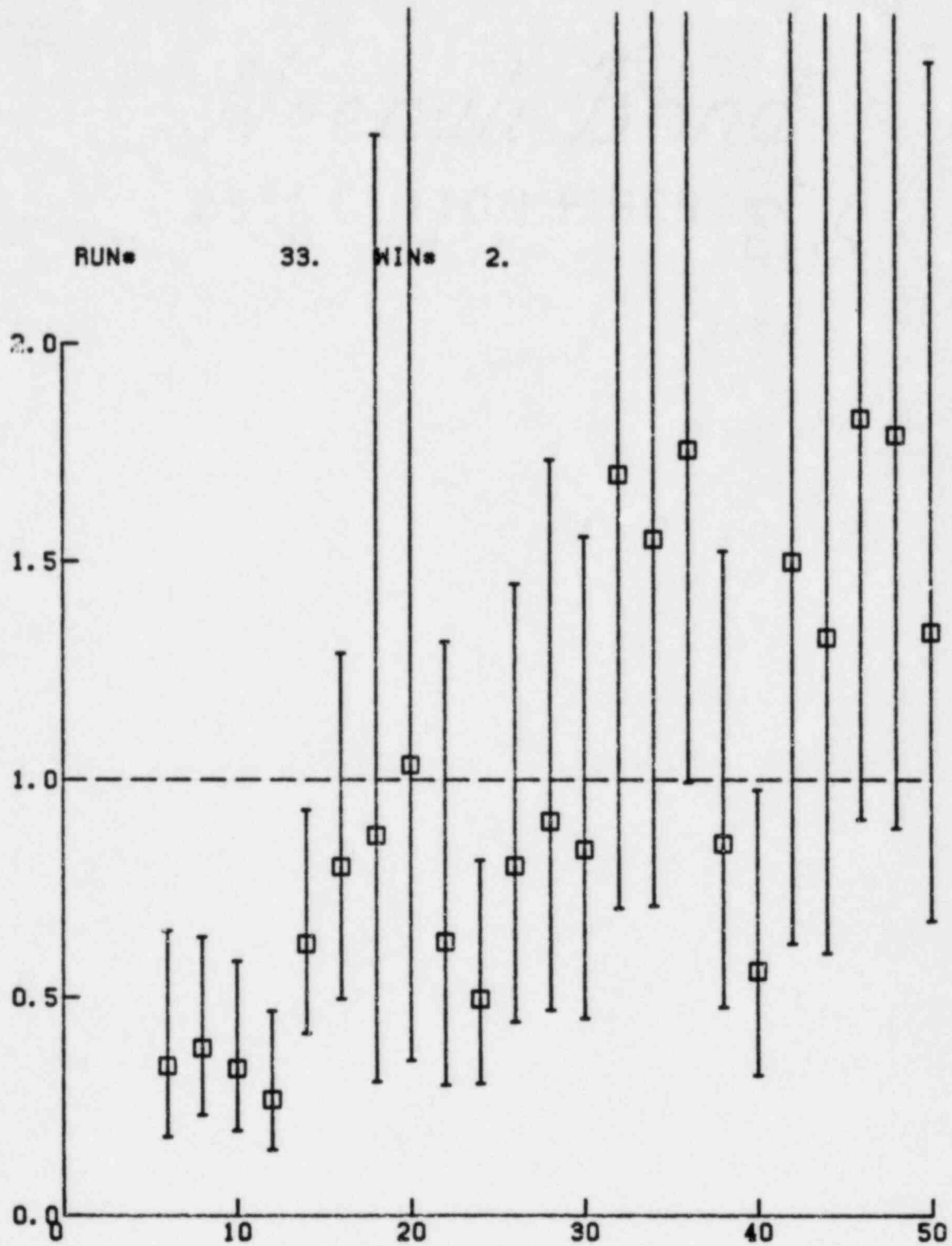


Figure VI.C.57 Test 3, transverse AB/FF
band pass spectral ratios
window 0-0.39 sec.

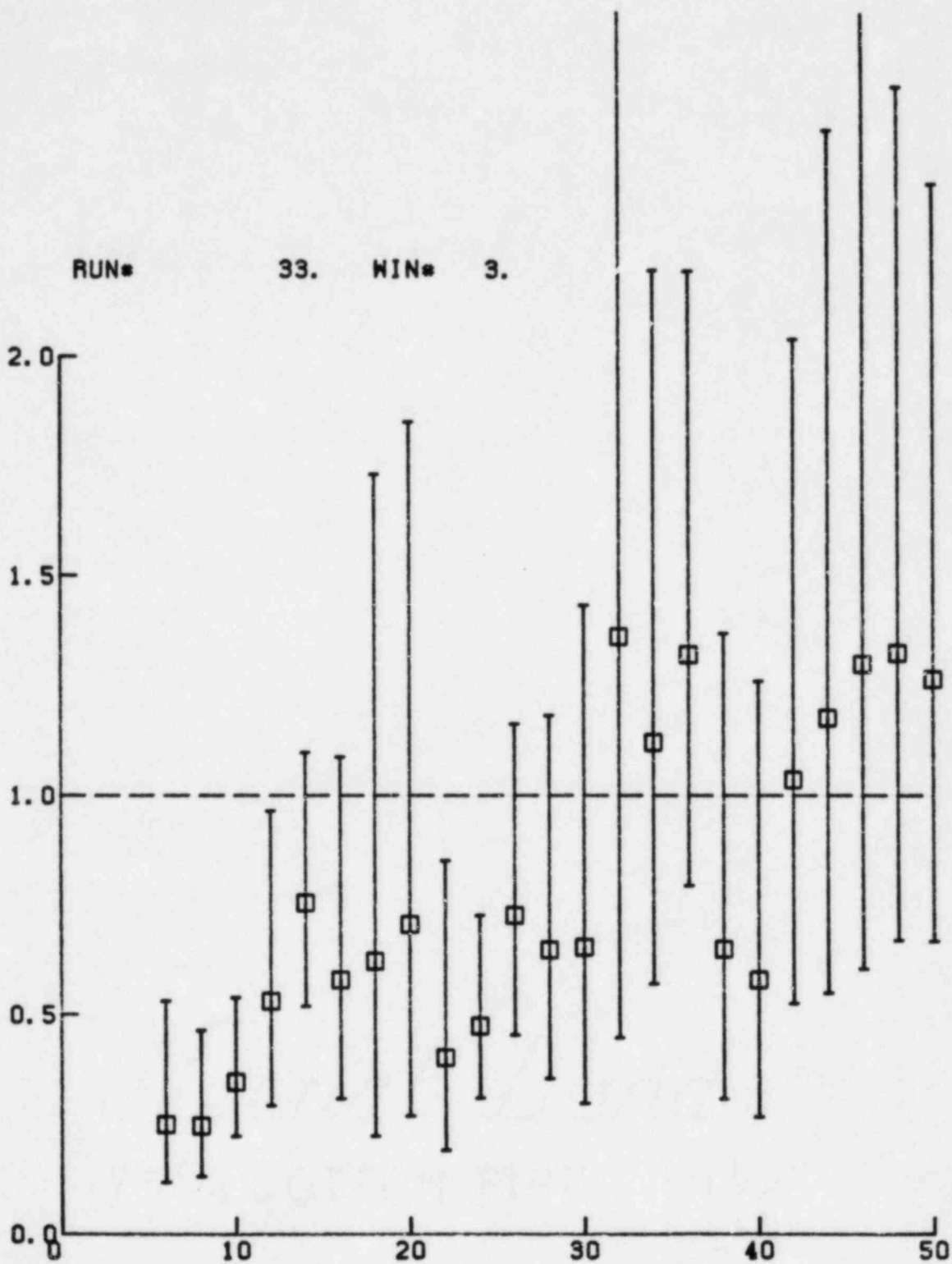


Figure VI.C.58 Test 3, transverse AB/FF
band pass spectral ratios
window 0.39-1.28 sec.

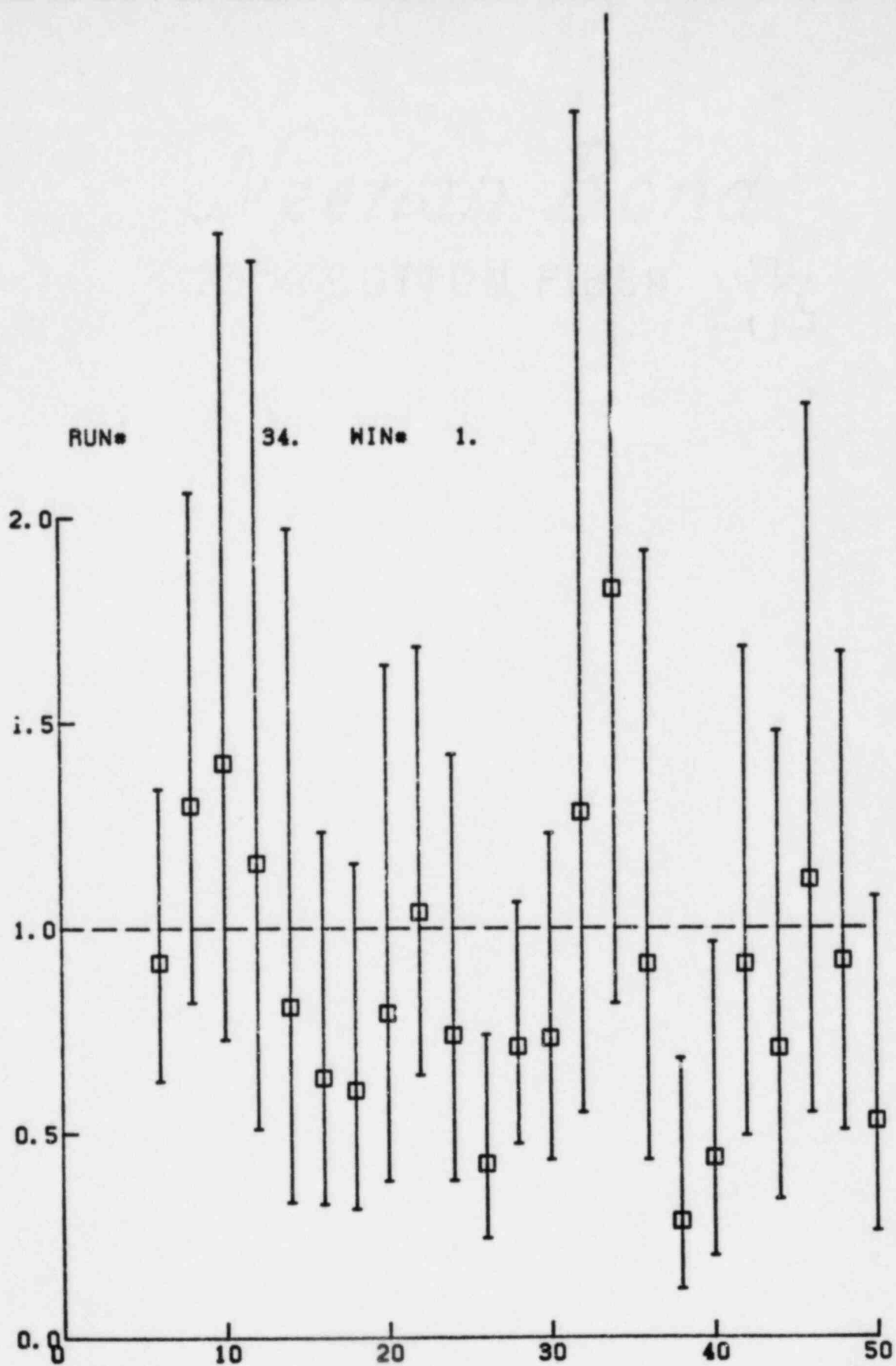


Figure VI.C.59 Test 3, vertical GS/FF band pass spectral ratios, window 0-1.28 sec.

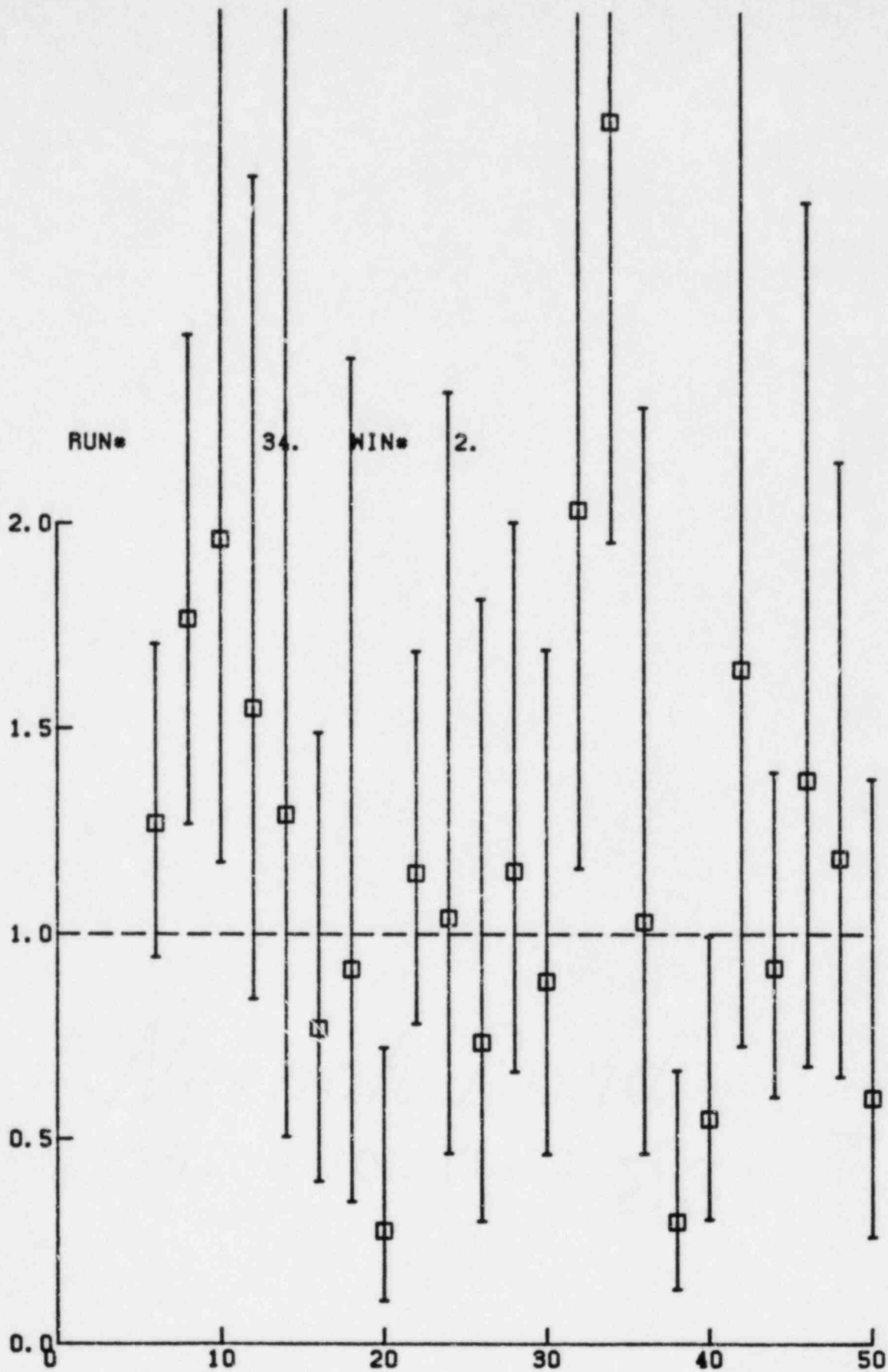


Figure VI.C.60 Test 3, vertical GS/FF band pass spectral ratios window 0-0.45 sec.

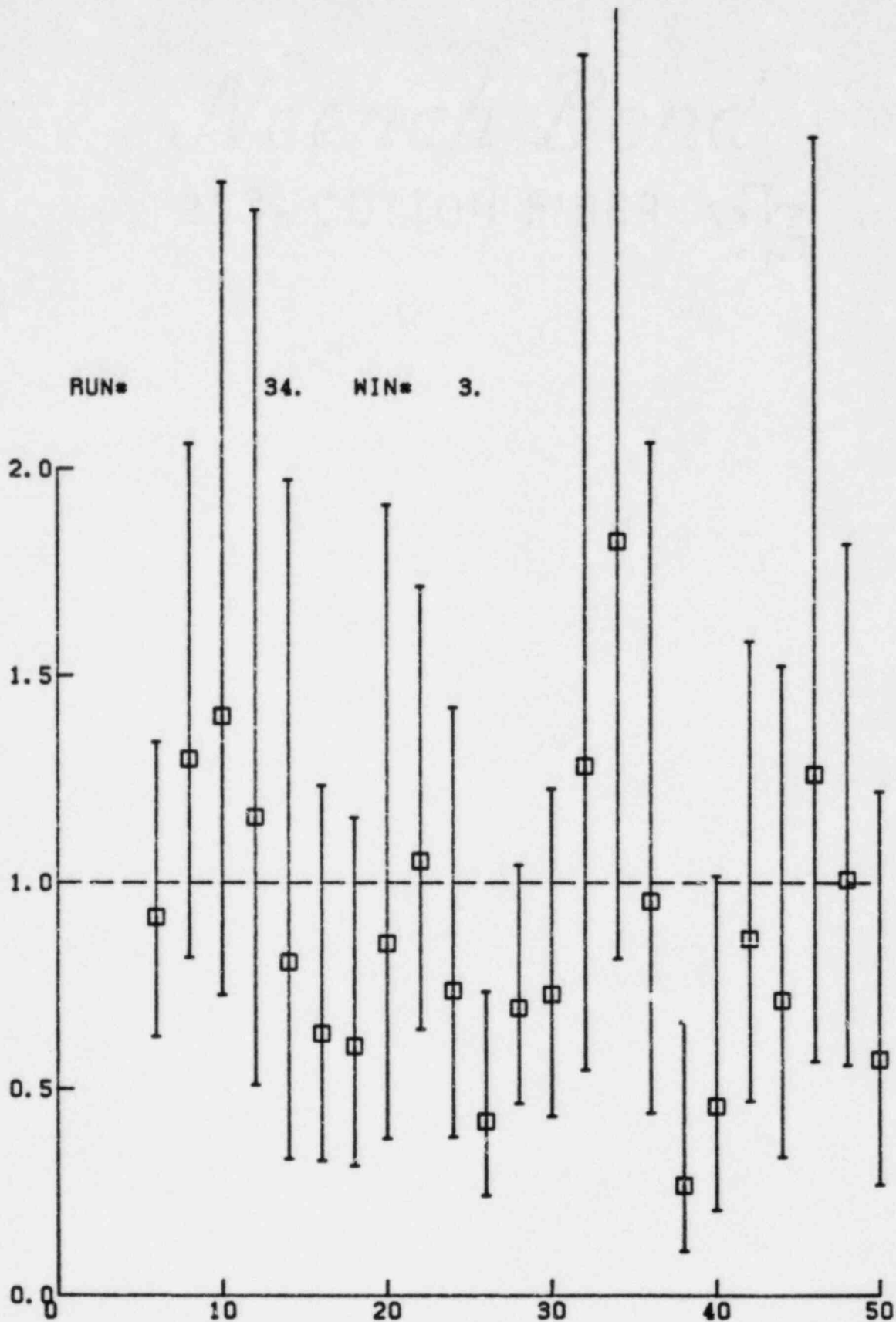


Figure VI.C.61 Test 3, vertical GS/FF
band pass spectral ratios
window 0.45-1.28 sec.

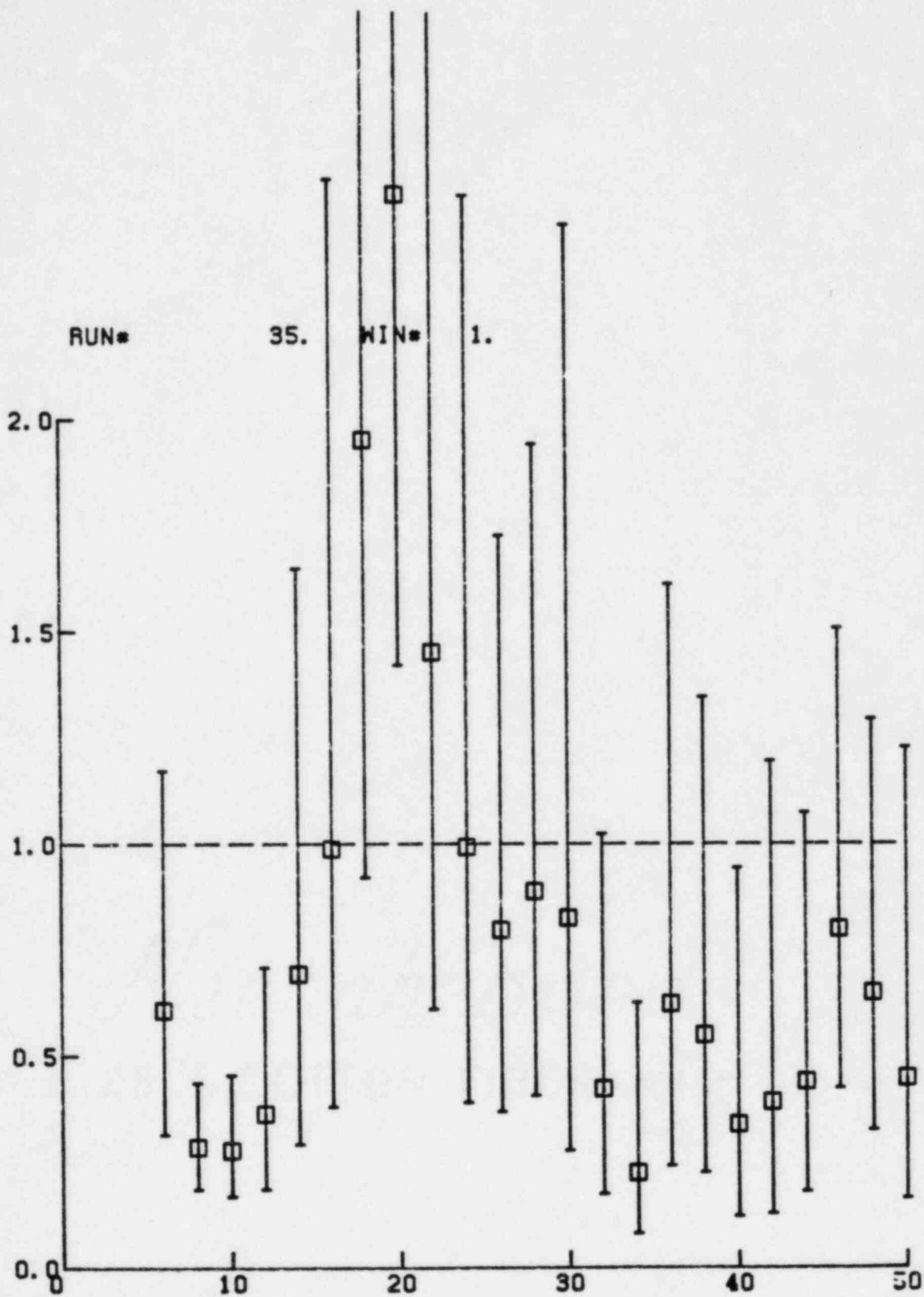


Figure VI.C.62 Test 3, radial GS/FF
band pass spectral ratios
window 0-1.28 sec.

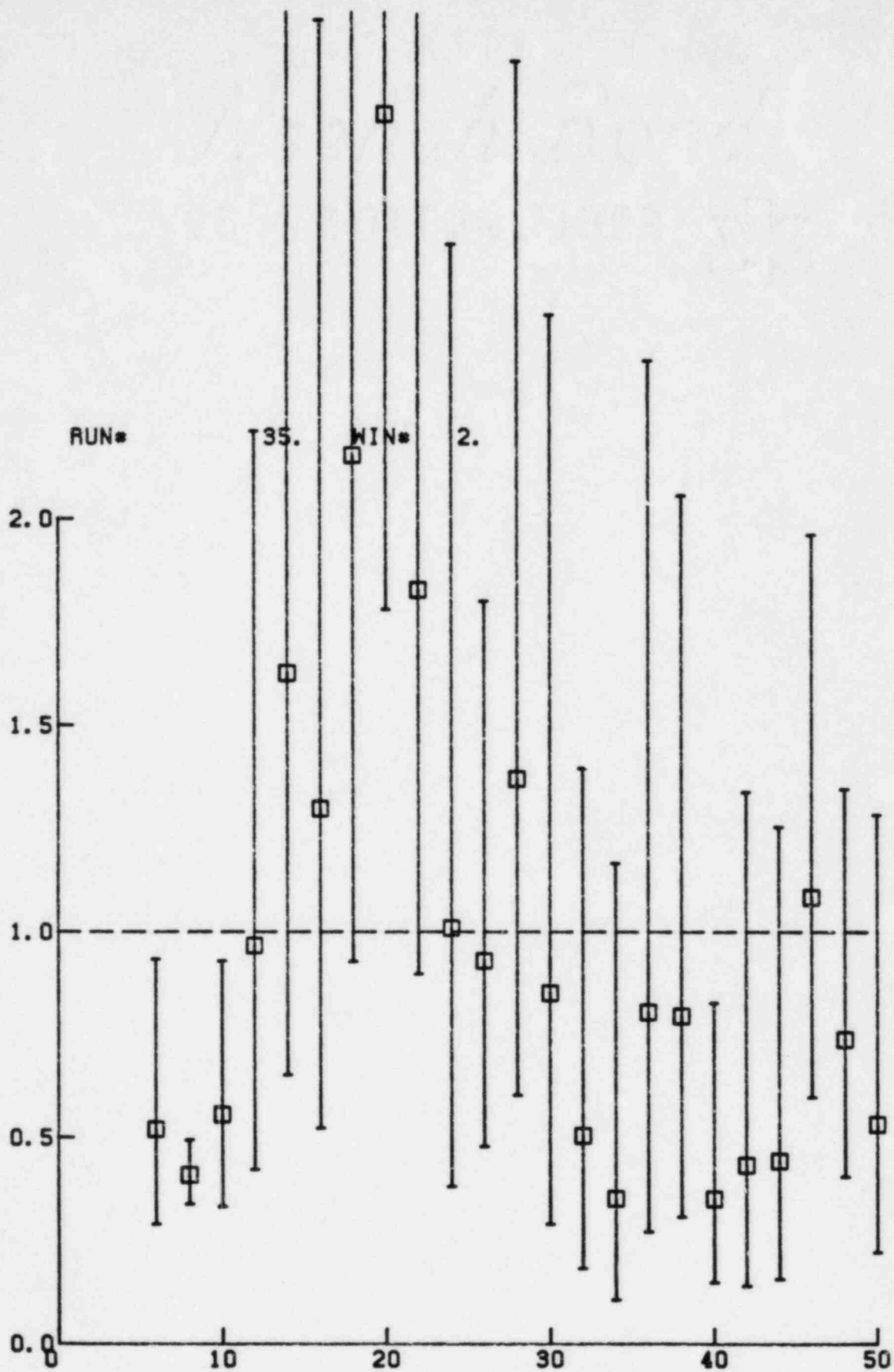


Figure VI.C.63 Test 3, radial GS/FF
band pass spectral ratios
window 0-0.45 sec.

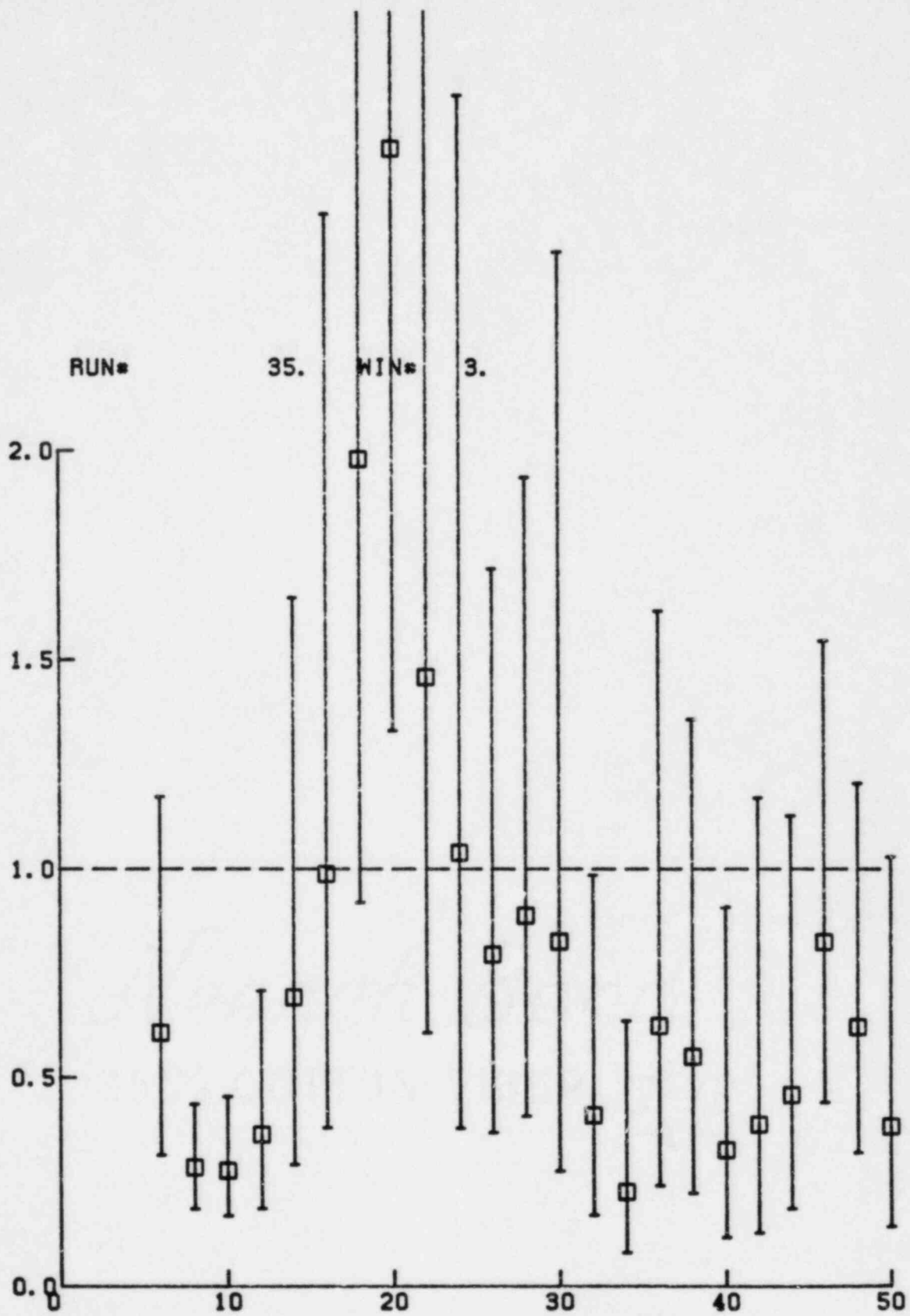


Figure VI.C.64 Test 3, radial GS/FF
band pass spectral ratios
window 0.45-1.28 sec.

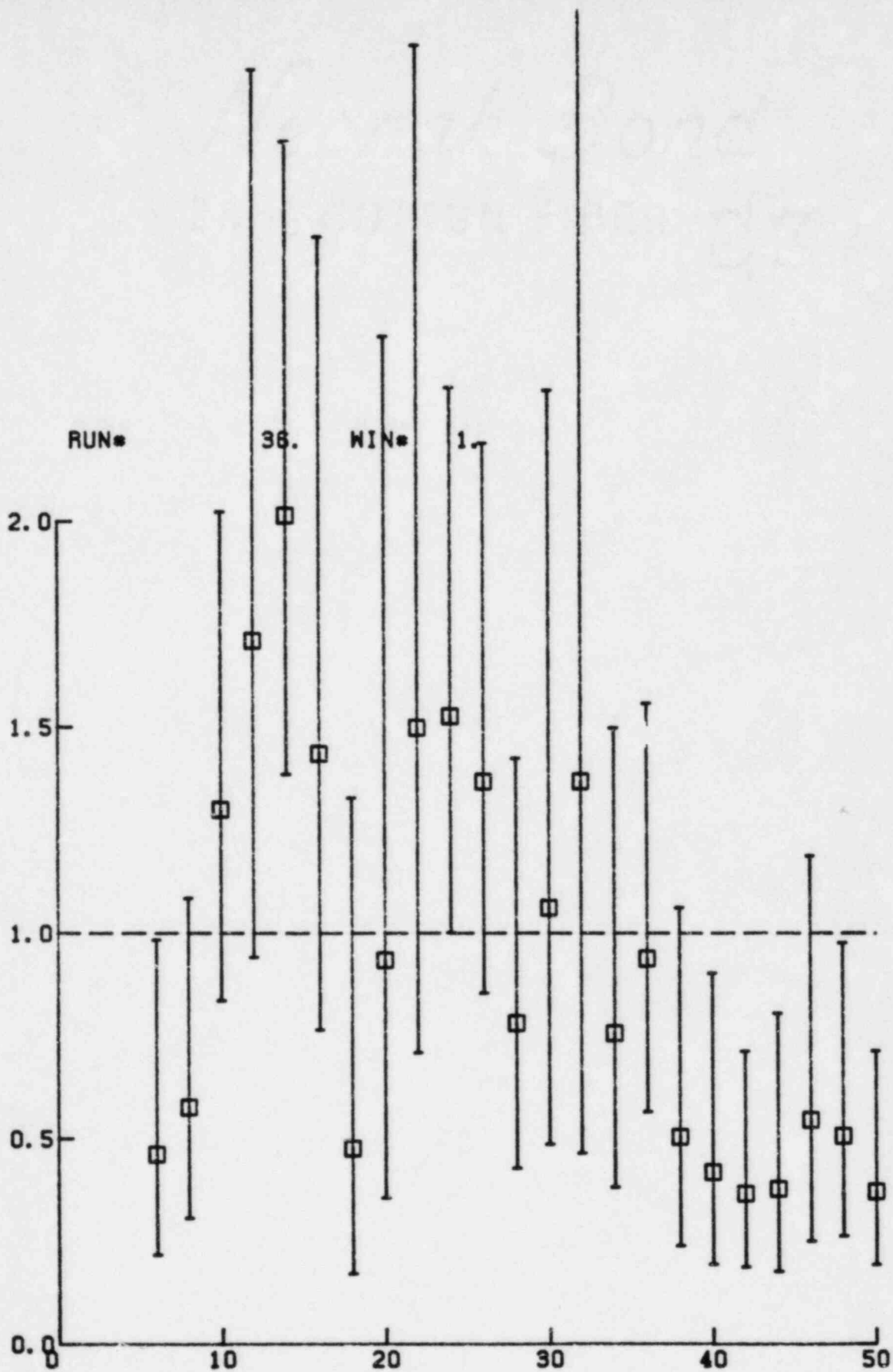


Figure VI.C.65 Test 3, transverse GS/FF
band pass spectral ratios
window 0-1.28 sec.

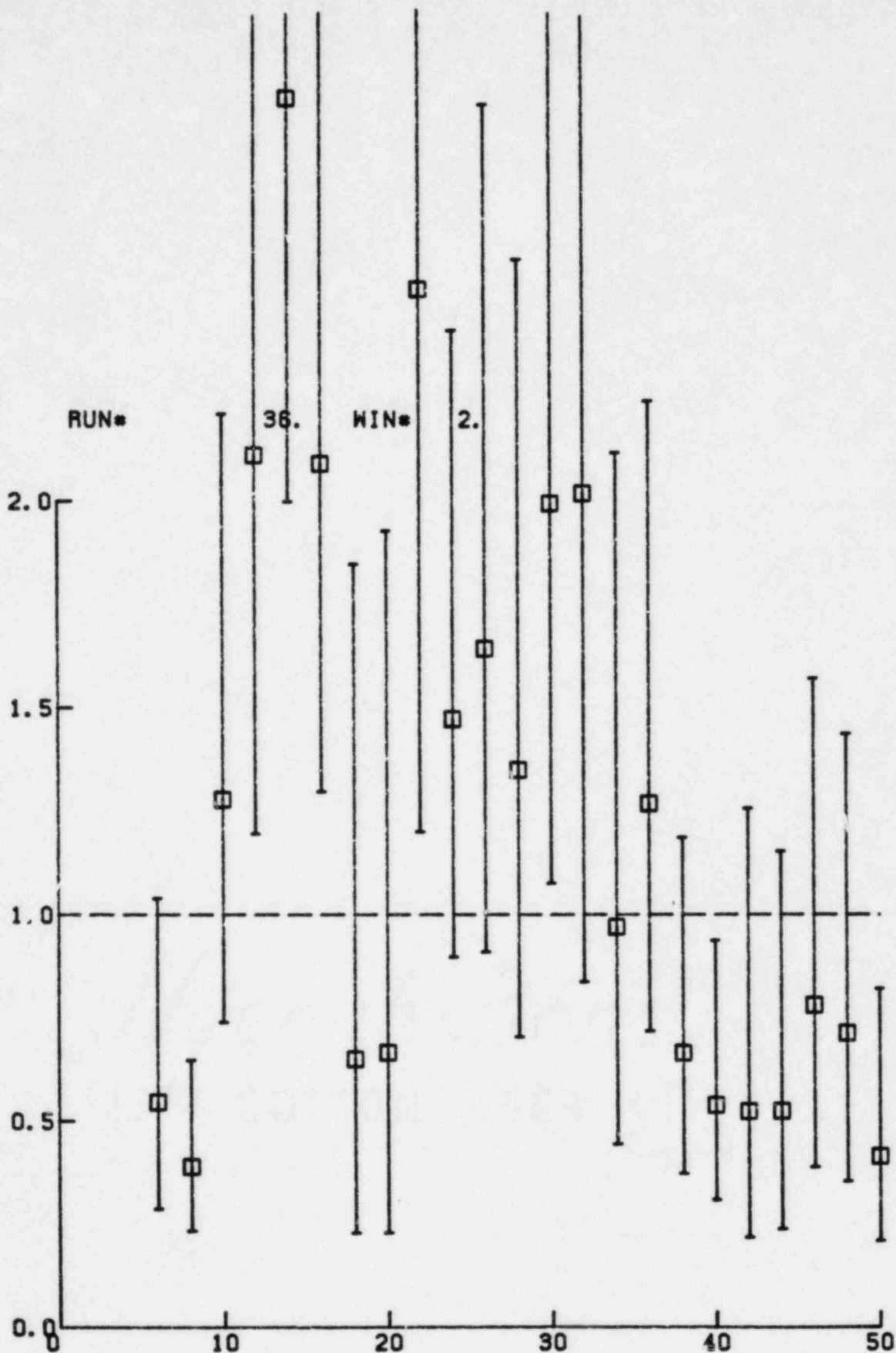


Figure VI.C.66 Test 3, transverse GS/FF
band pass spectral ratios
window 0-0.45 sec.

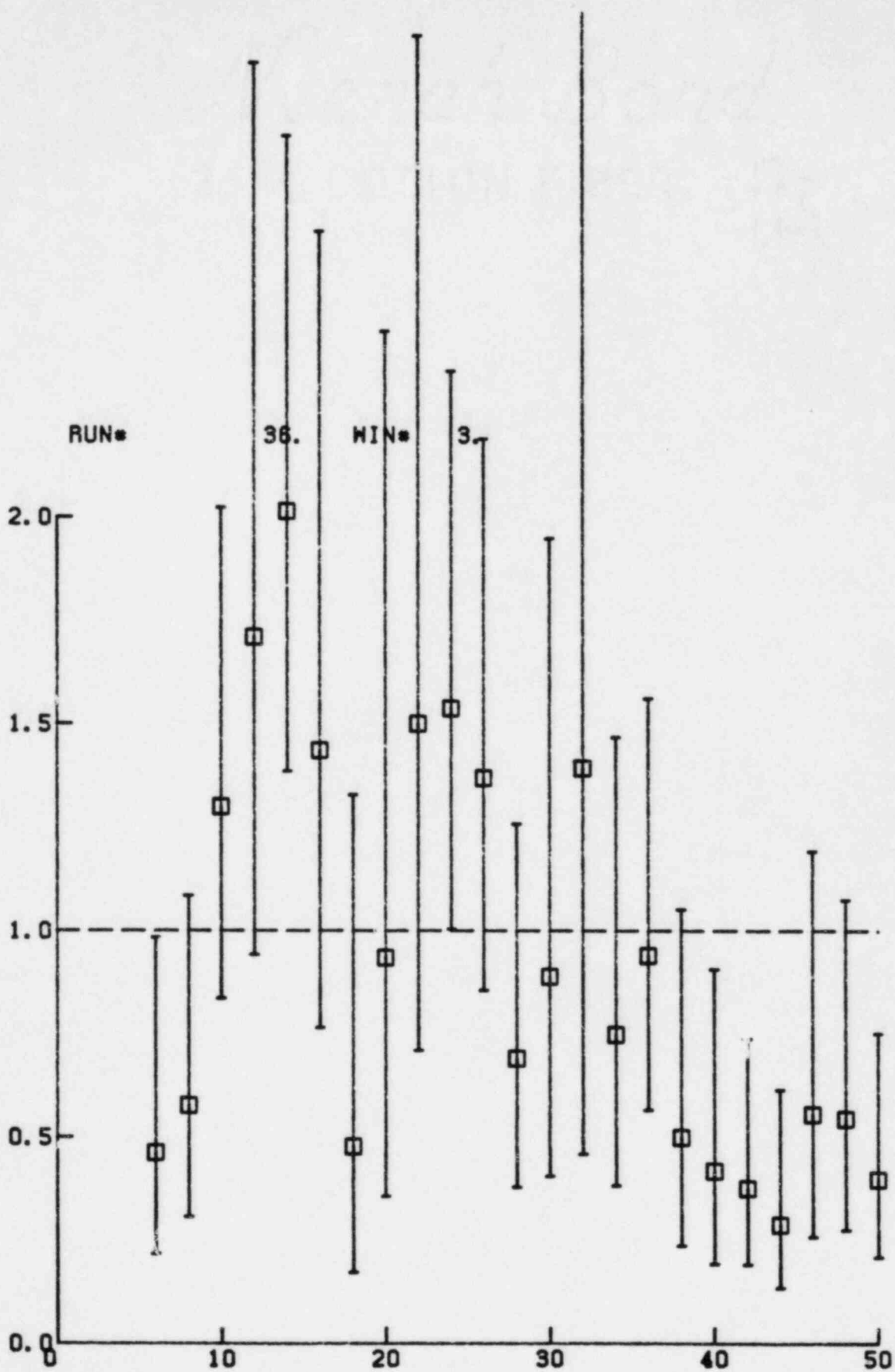


Figure VI.C.67 Test 3, transverse GS/FF
band pass spectral ratios
window 0.45-1.28 sec.

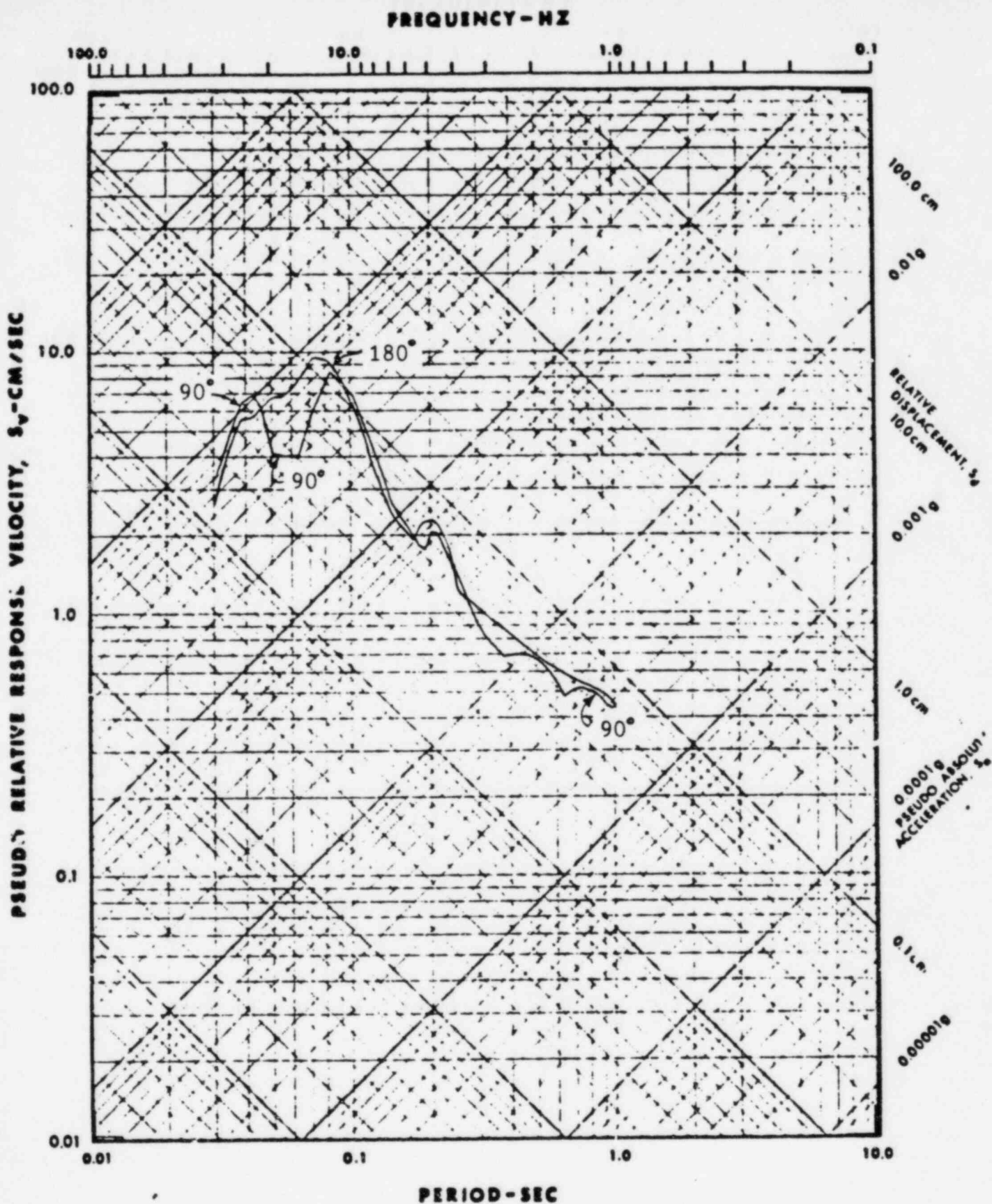


Figure VI.D.1 Derived Free-Field Response Spectra for 10/16/79 Earthquake (5% Damping)

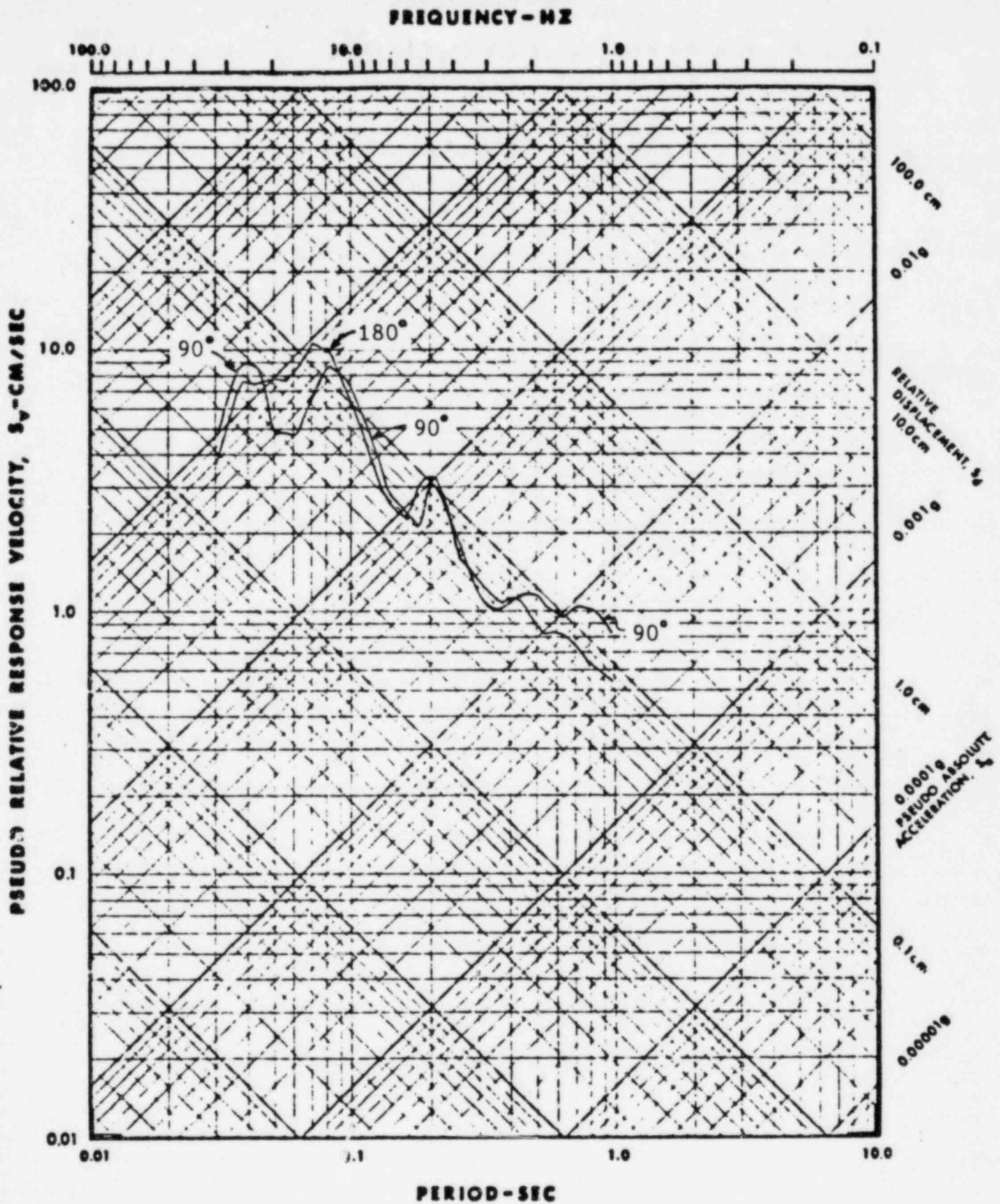


Figure VI.D.2 USGS Pad Response Spectra for 10/16/79 Earthquake (5% Damping)

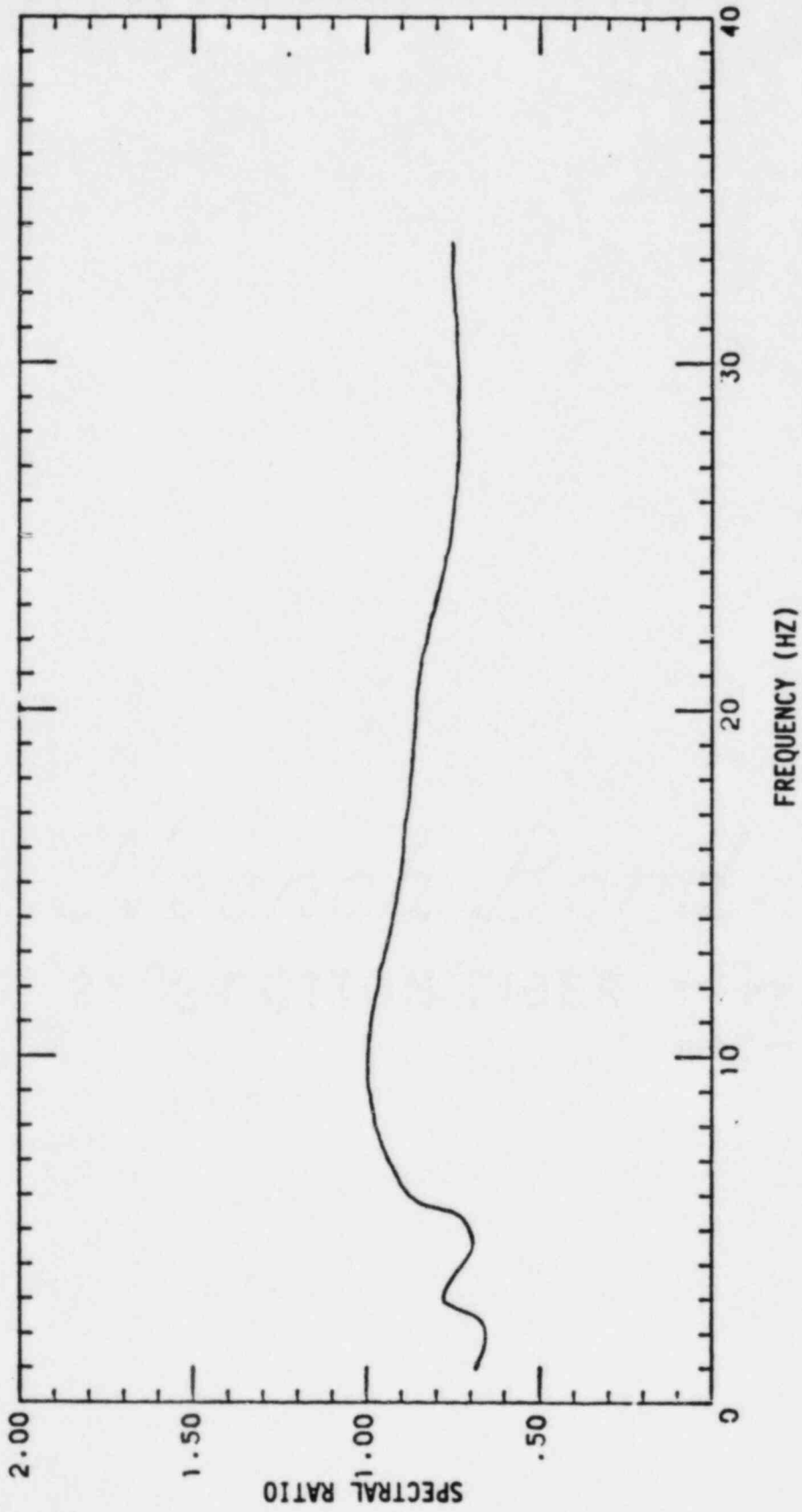


Figure VI.D.3: Averaged Ratio of the Free-Field to the USGS Pad Response Spectra (5% Damped)

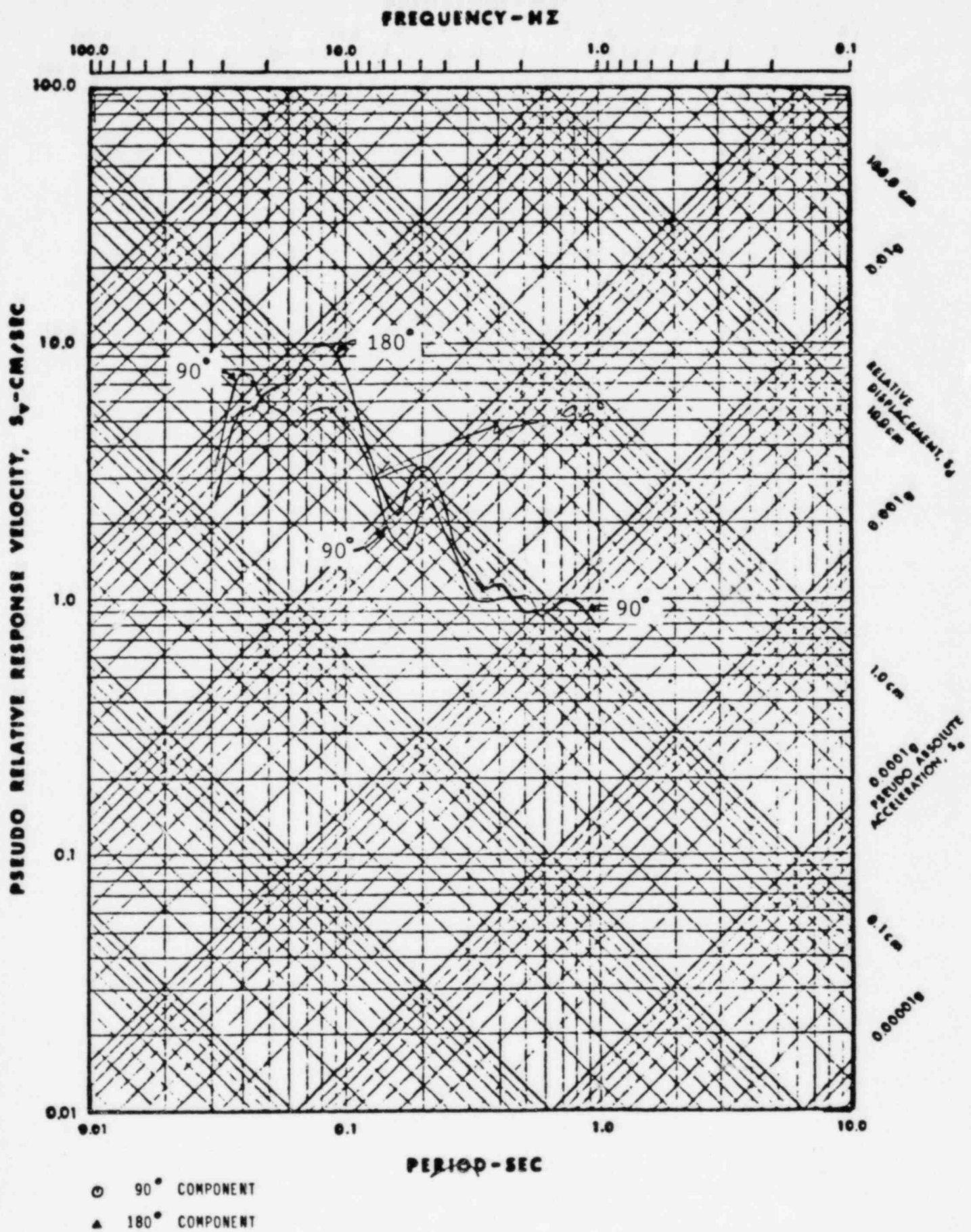


Figure VI.D.4 Free-field Response Spectra for 10/16/79 Earthquake from Ertec Pad to Free-field Transfer Function (5% Damping)

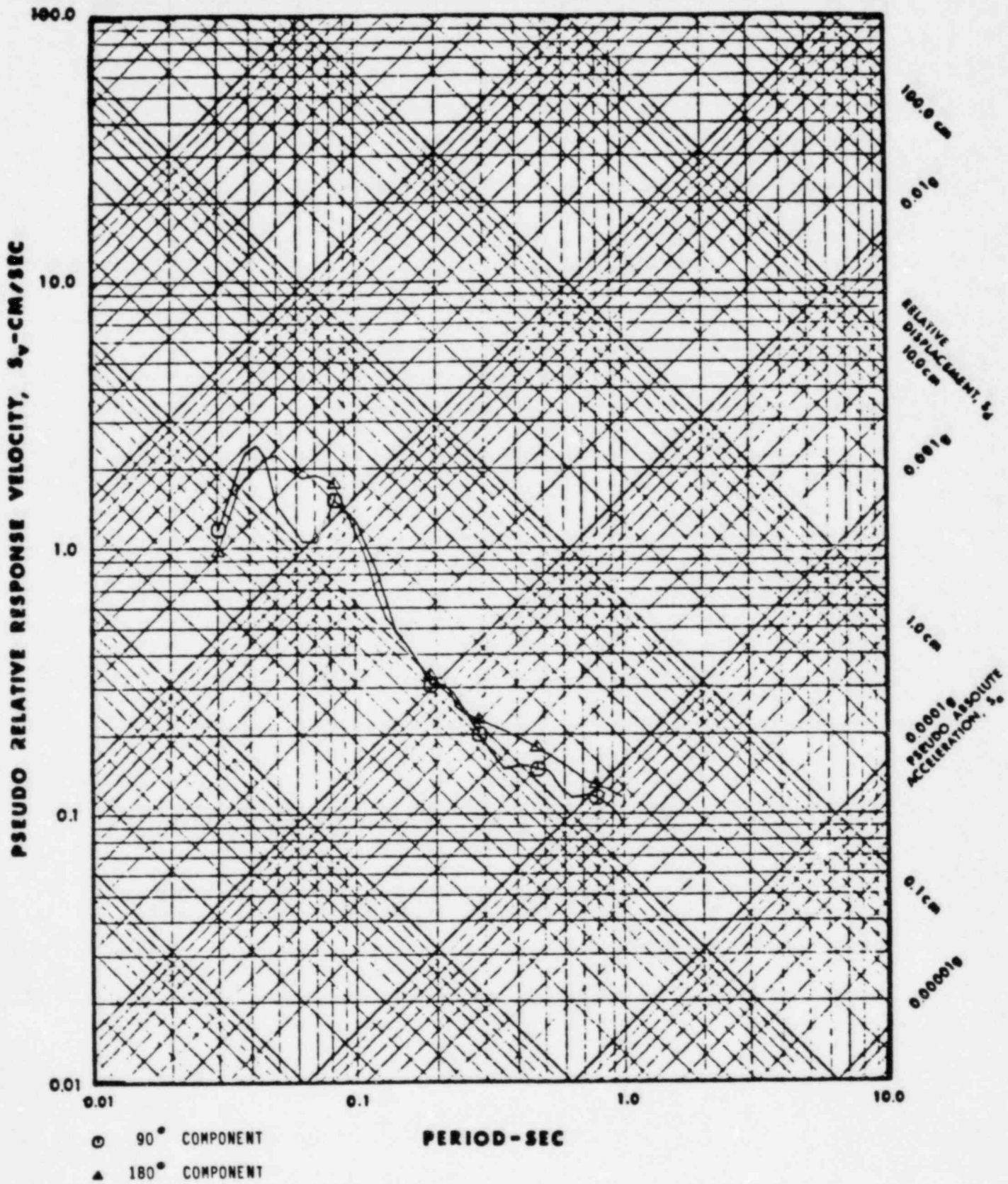


Figure VI.E.1

Derived Auxiliary Building Foundation Response Spectra (5% Damping) for 10/16/79 Earthquake using Two-Stage Approach.

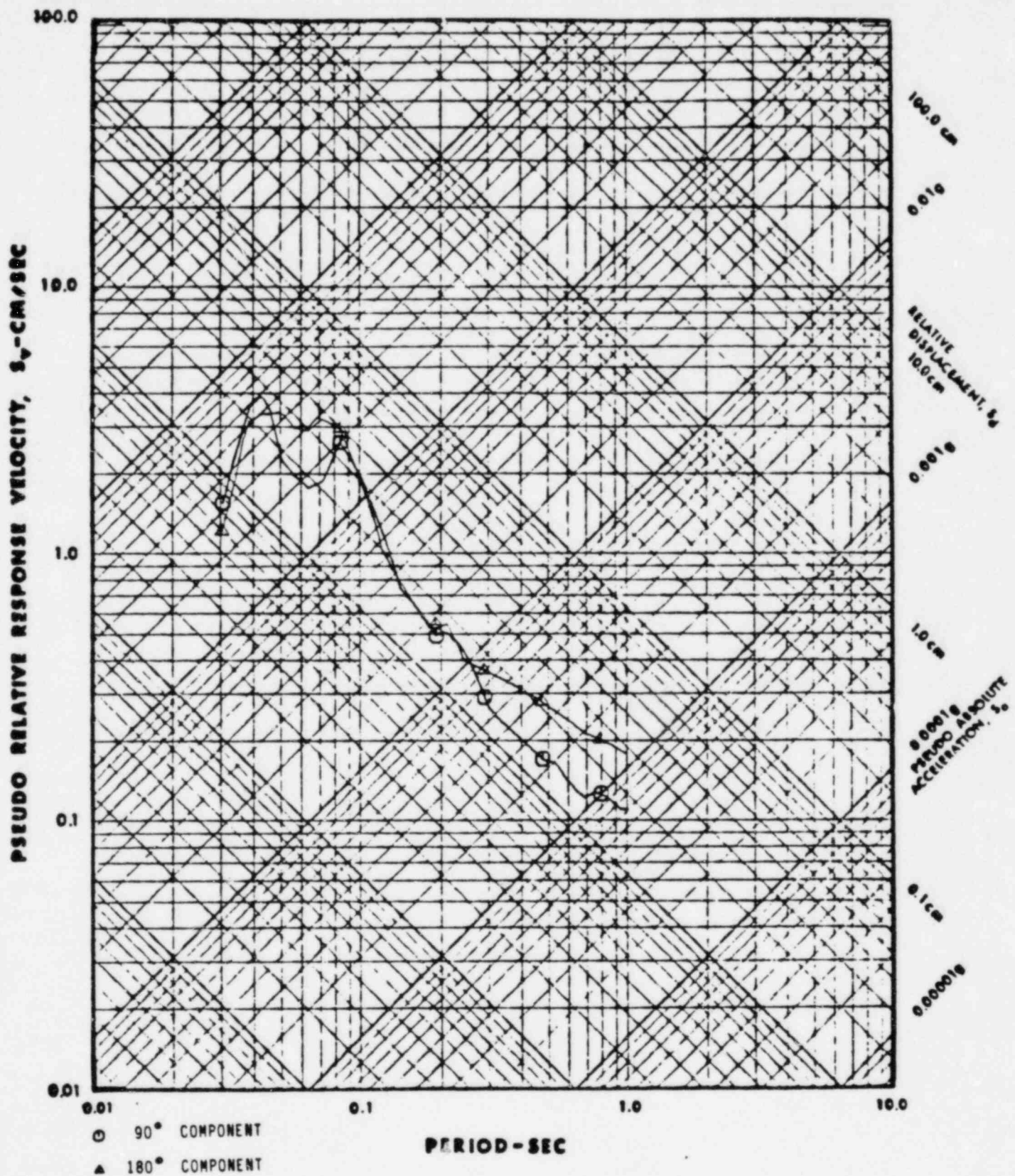


Figure VI.E.2 Derived Diesel Generator Sump Foundation Response Spectra (5% Damping) for 10/16/79 Earthquake using Two-Stage Approach.

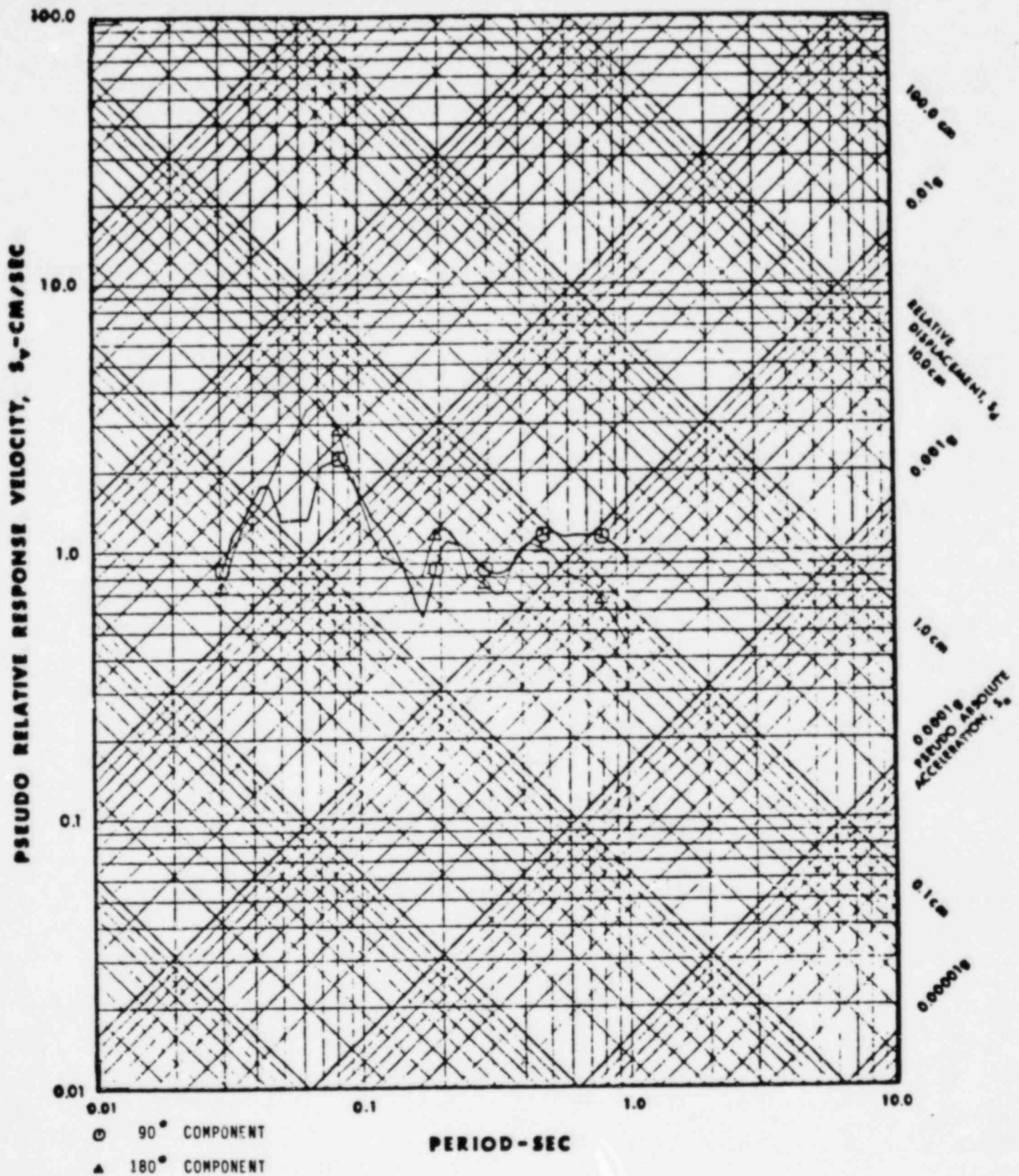


Figure VI.E.3 Derived Service Water Pumphouse Foundation Response Spectra (5% Damping) for 10/16/79 Earthquake using Two-Stage Approach.

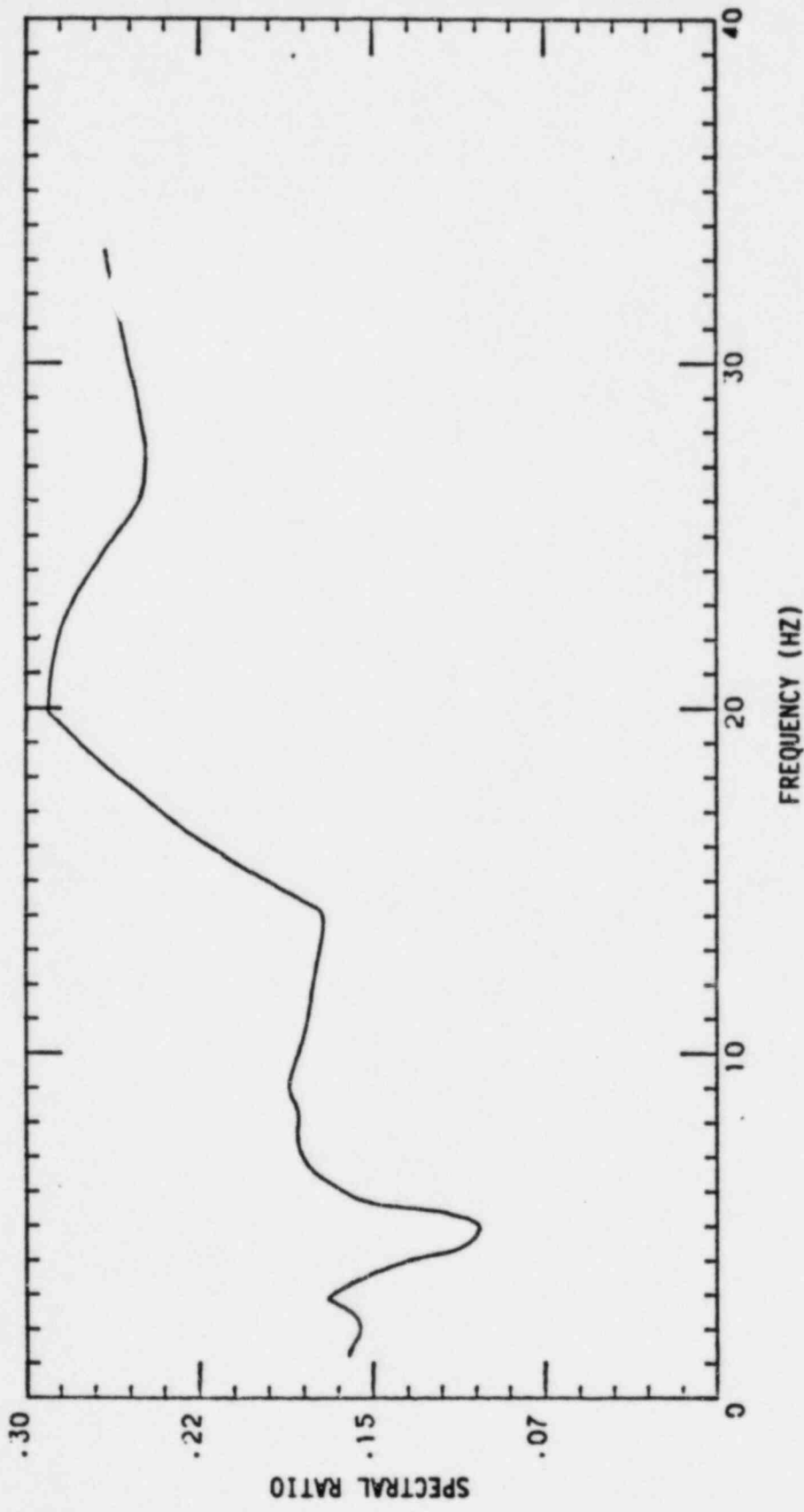


Figure VI.E.4: Averaged Ratio of the USGS Pad to the Auxiliary Building Foundation Response Spectra (5% Damped)

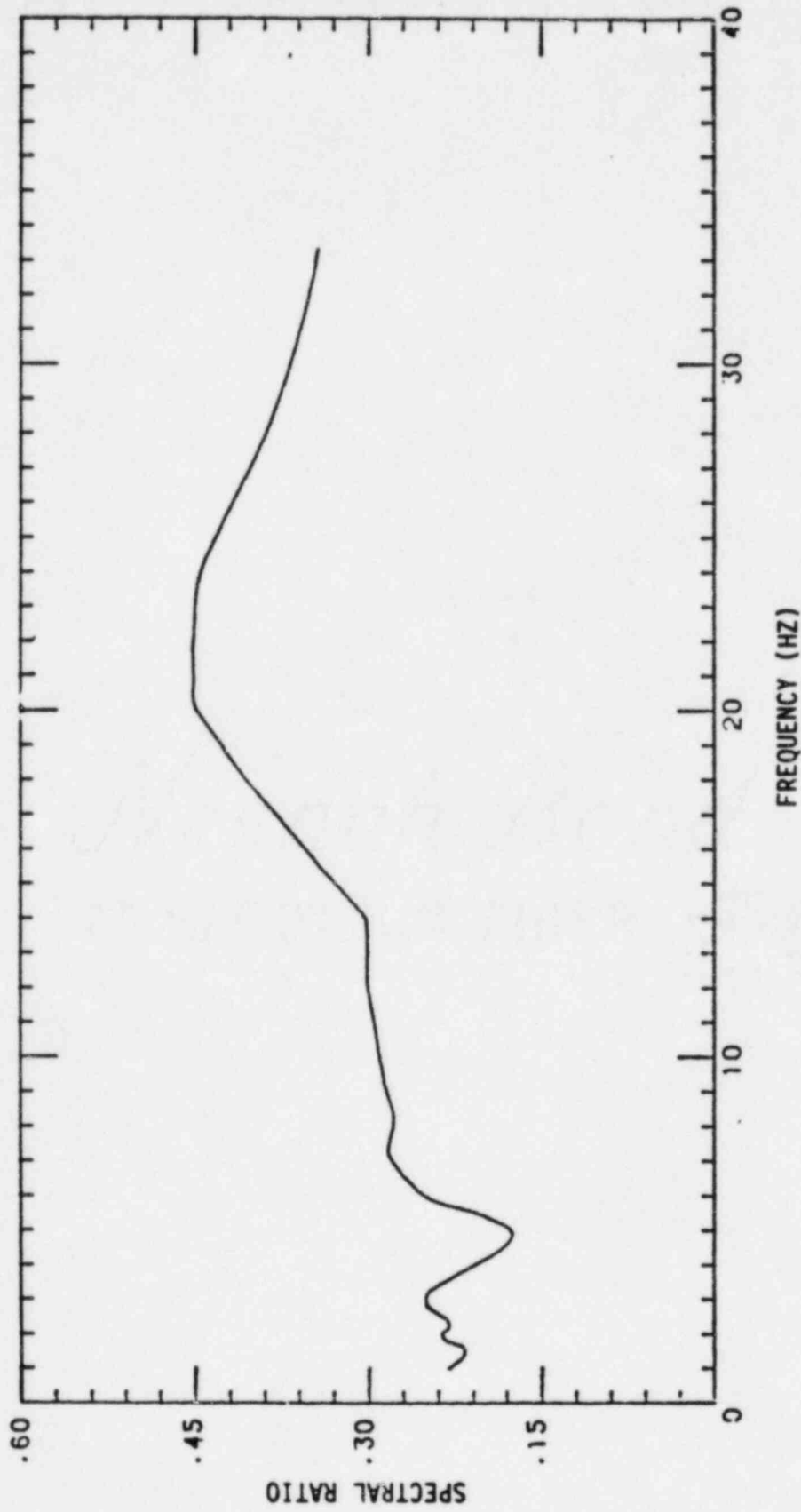


Figure VI.E.5: Averaged Ratio of the USGS Pad to the Diesel Generator Sump Foundation Response Spectra (5% Damped)

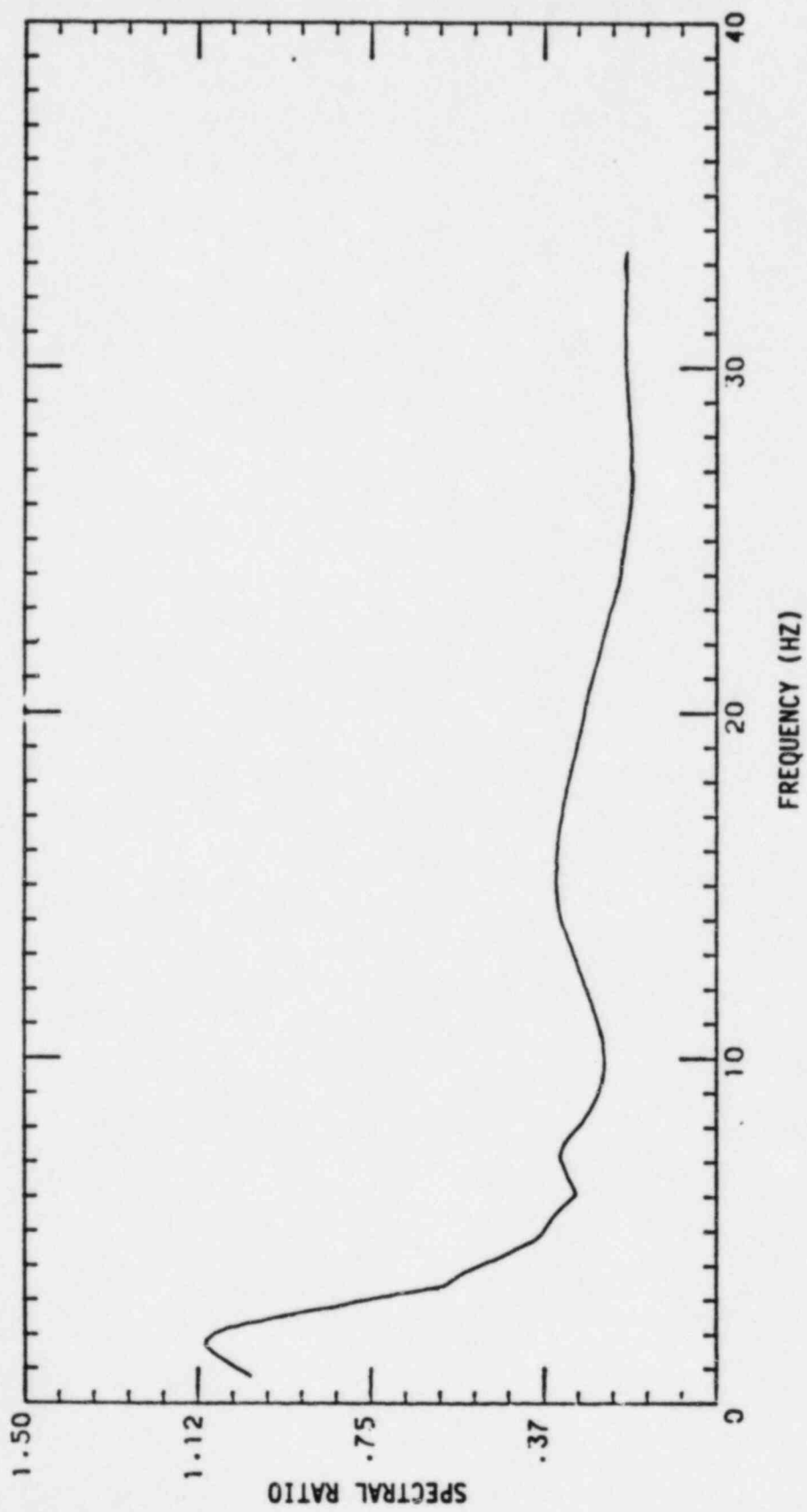


Figure VI.E.6: Averaged Ratio of the USGS Pad to the Service Water Pump House Foundation Response Spectra (5% Damped)

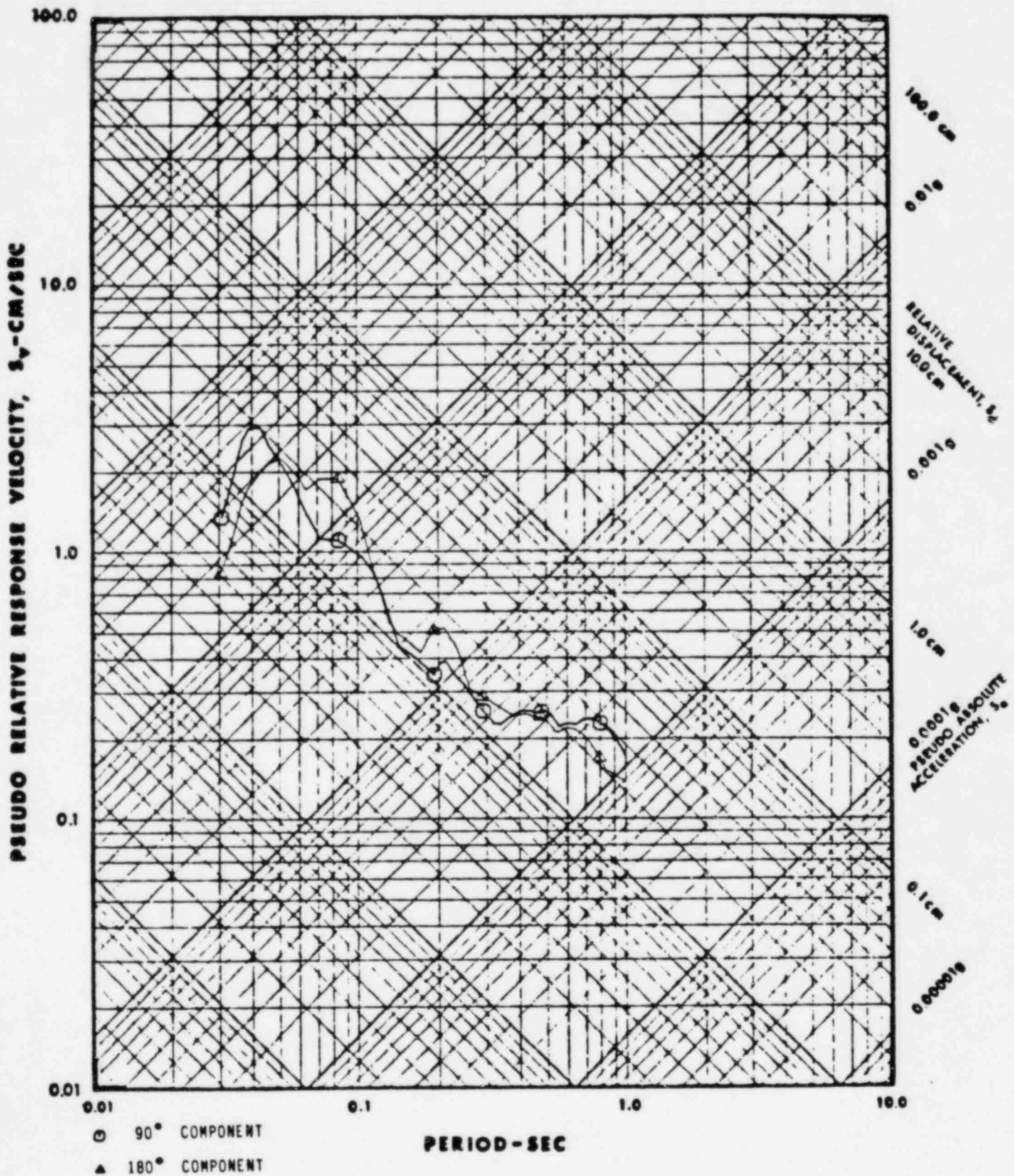


Figure VI.E.7 Derived Auxiliary Building Foundation Response Spectra (5% Damping) for 10/16/79 Earthquake using Two-Stage Approach with Ertec Pad/Free-Field Transfer Function.

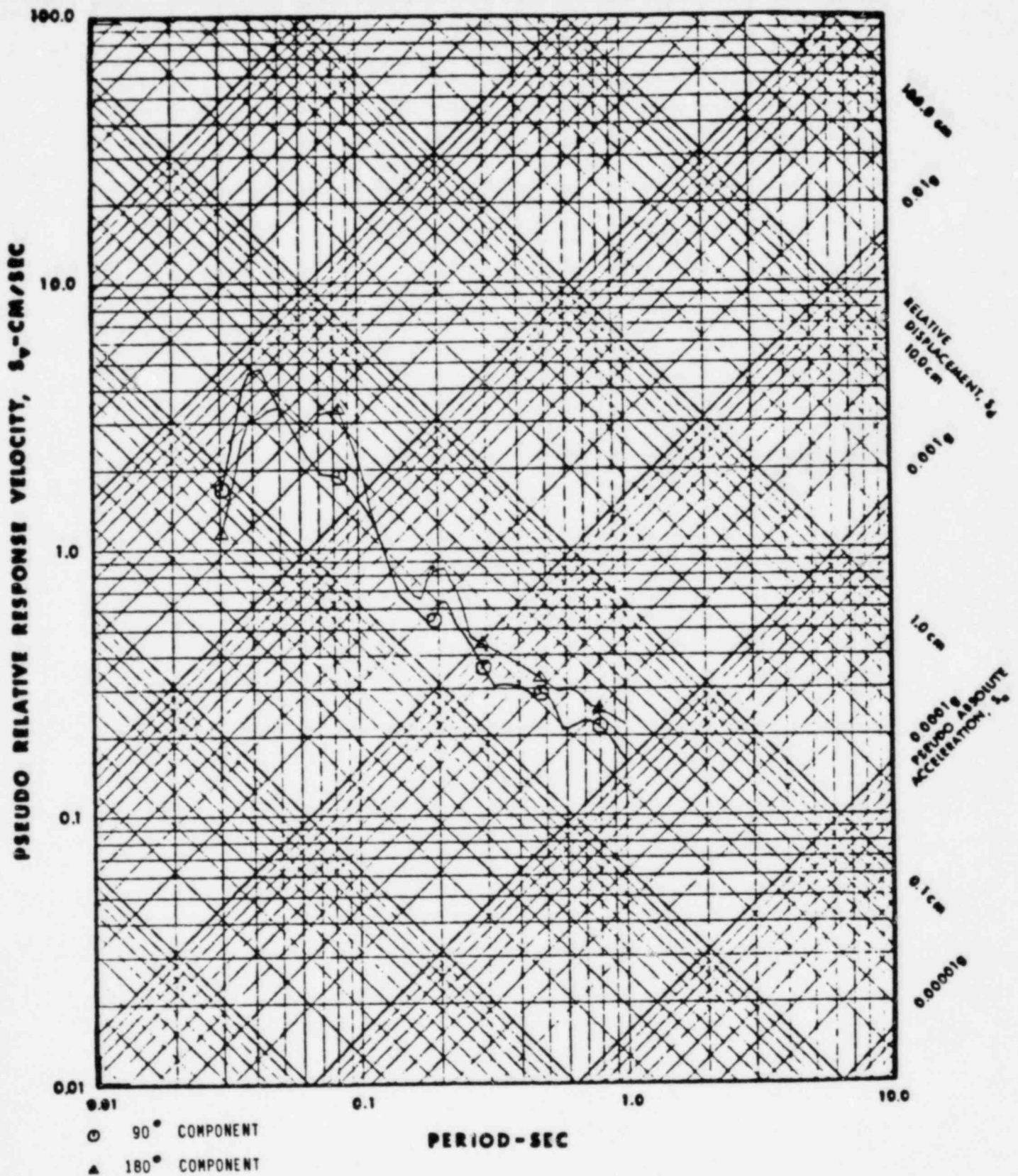


Figure VI.E.8

Derived Diesel Generator Sump Foundation
 Response Spectra (5% Damping) for 10/16/79
 Earthquake using Two-Stage Approach with
 Ertec Pad Free-Field Transfer Function .

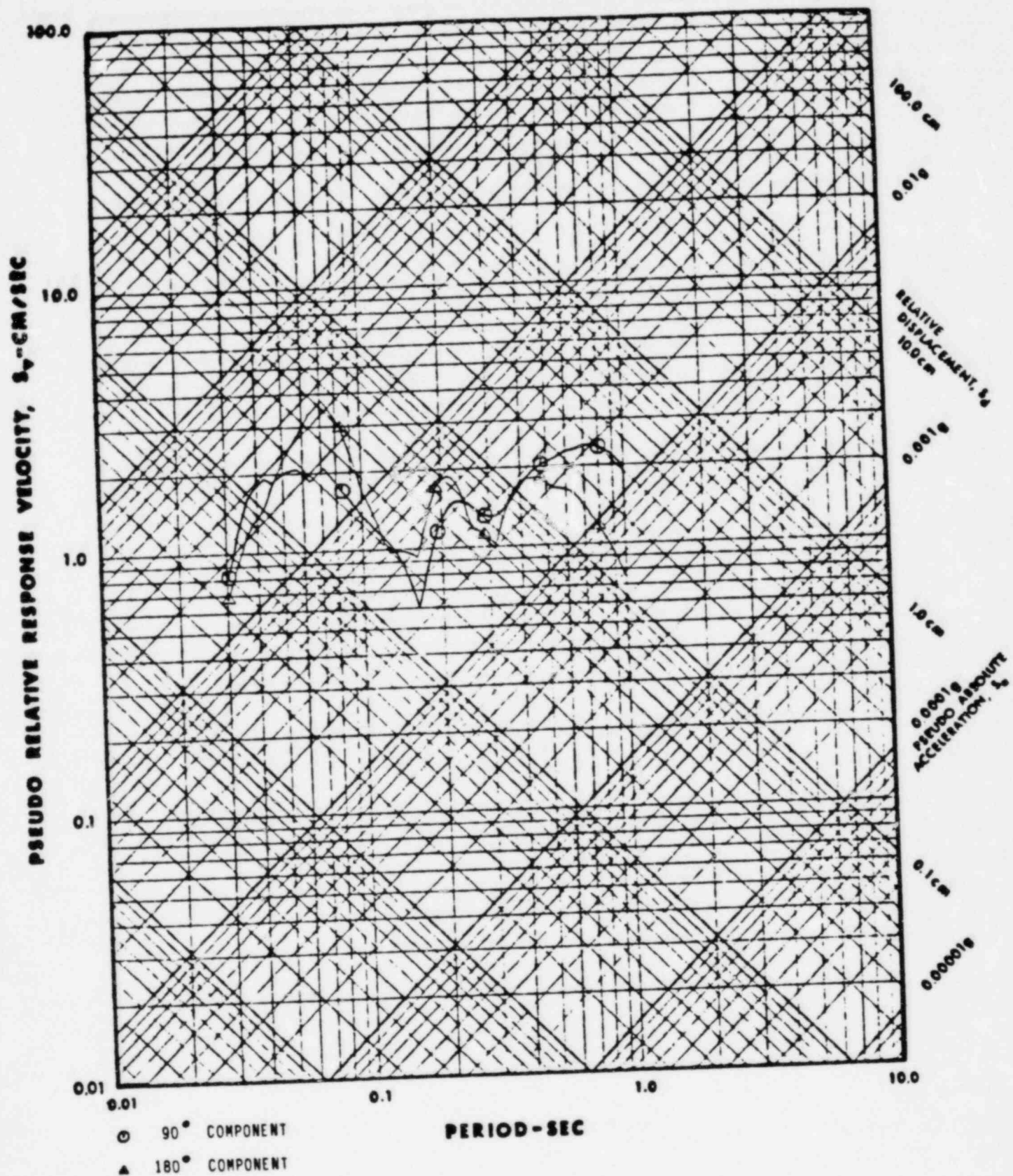


Figure VI.E.9

Derived Service Water Pumphouse Foundation Response Spectra (5% Damping) for 10/16/79 Earthquake using Two-Stage Approach with Ertec Pad/Free-Field Transfer Function.

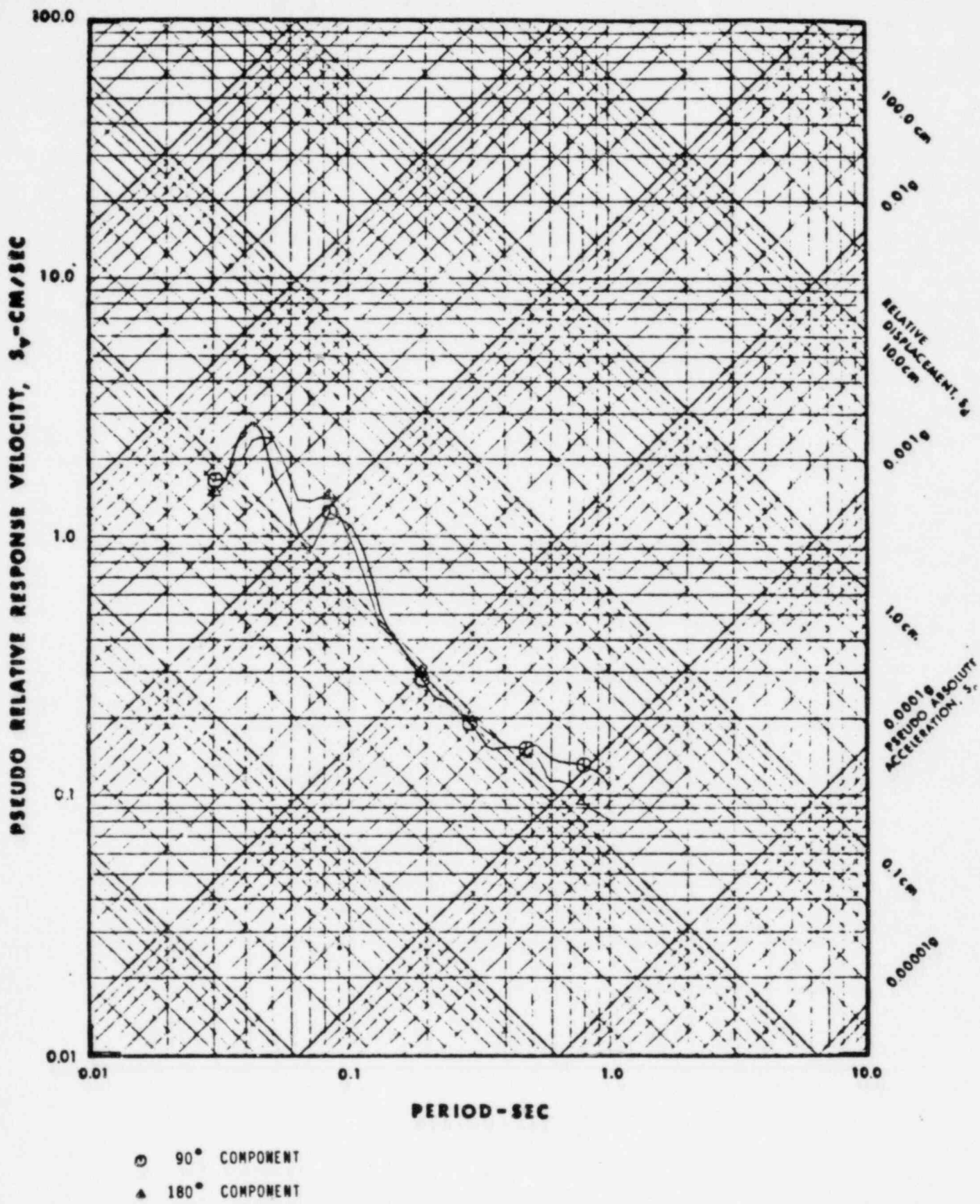


Figure VI.F.1 Auxiliary Building Foundation Response Spectra for 10/16/79 Earthquake using Direct Approach (5% Damping)

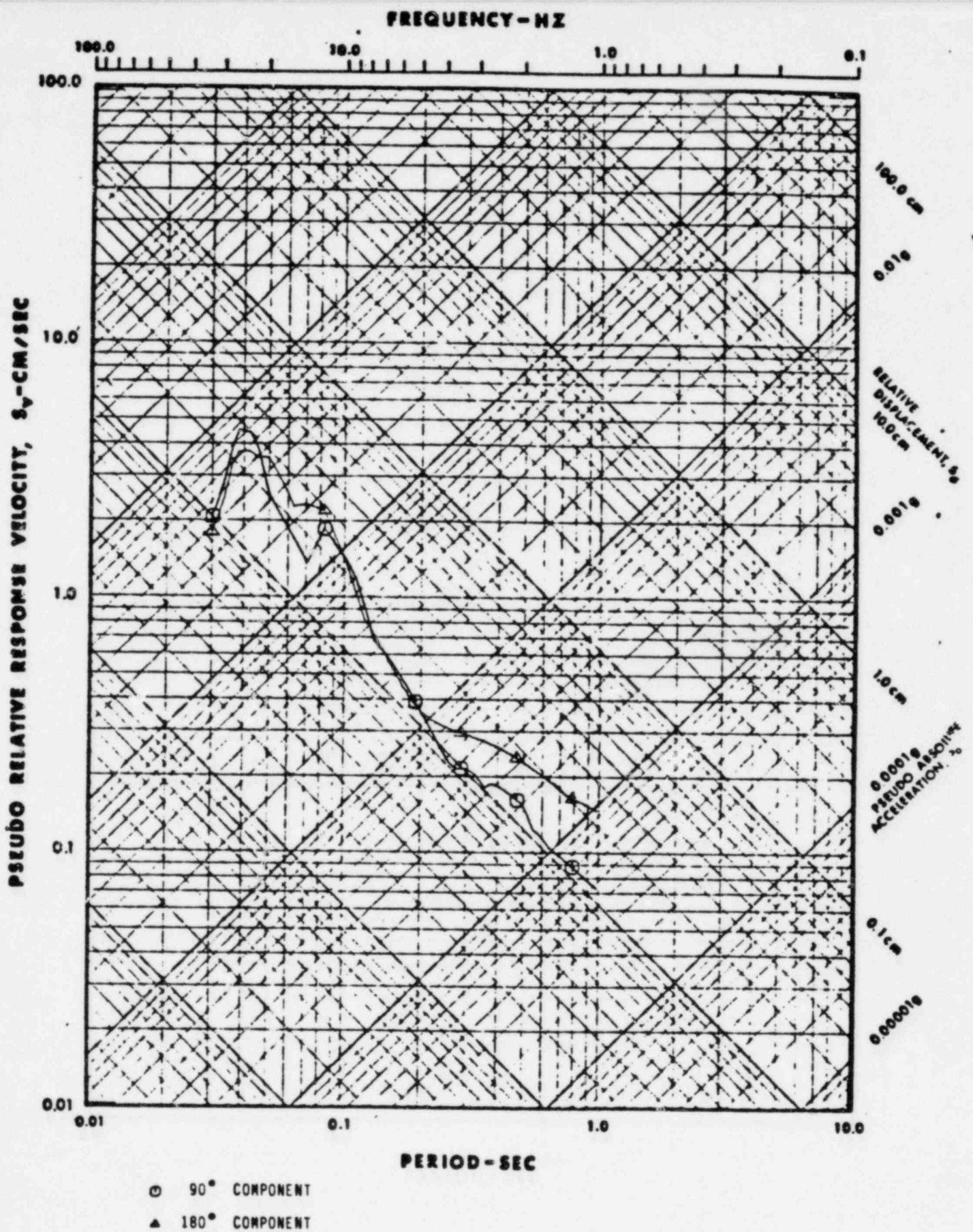


Figure VI.F.2 Diesel Generator Sump Foundation Response Spectra for 10/16/79 Earthquake using Direct Approach (5% Damping)

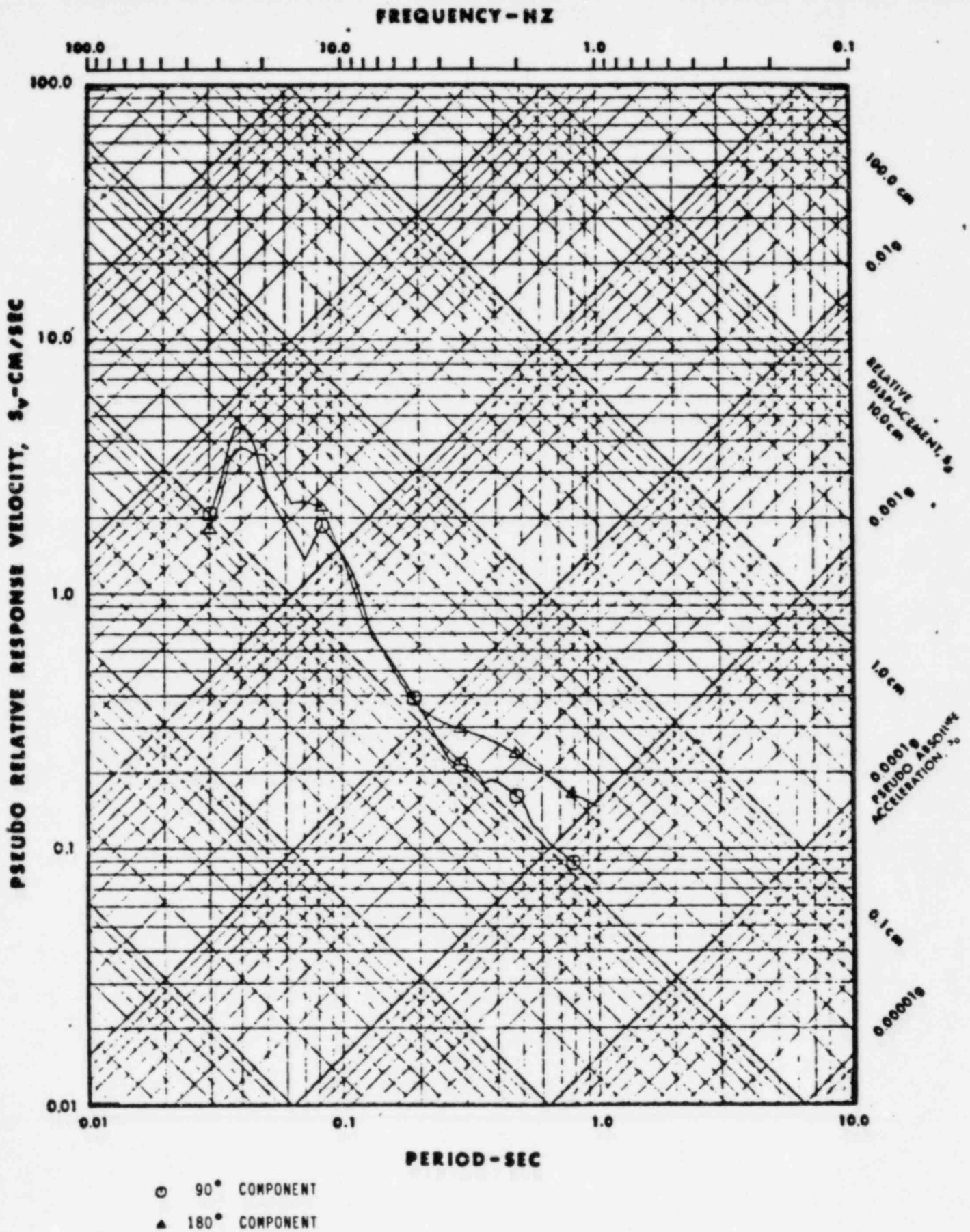


Figure VI.F.2 Diesel Generator Sump Foundation
Response Spectra for 10/16/79 Earthquake
using Direct Approach (5% Damping)